Karlsruhe Institute of Technology

Spatially resolved immobilization of metallopolymers – Spiropyrans for light sensitive metal complexes and STED-inspired laser lithography

Zur Erlangung des akademischen Grades eines
DOKTORS DER NATURWISSENSCHAFTEN
(Dr. rer. nat.)

von der KIT-Fakultät für Chemie und Biowissenschaften
des Karlsruher Instituts für Technologie (KIT)

genehmigte
DISSERTATION
von

Dipl.-Chem. Rouven Müller

aus
Karlsruhe, Deutschland

1. Referent:	Prof. Dr. Christopher Barner-Kowollik
2. Referent:	Prof. Dr. Peter W. Roesky
Tag der mündlichen Prüfung:	09.05.2019

Wir haben verlernt, die Augen auf etwas ruhen zu lassen.
Deshalb erkennen wir so wenig.

Jean Giono (1895 - 1970)

Die vorliegende Arbeit wurde von März 2015 bis Mai 2019 unter Anleitung von Prof. Dr. Christopher Barner-Kowollik am Institut für Technische Chemie und Polymerchemie des Karlsruher Instituts für Technologie (KIT) – Universitätsbereich angefertigt.

Ich erkläre hiermit, dass die vorliegende Arbeit im Rahmen der Betreuung durch Prof. Dr. Christopher Barner-Kowollik selbstständig von mir verfasst und keine anderen als die angegebenen Quellen und Hilfsmittel verwendet wurden. Wörtlich oder inhaltlich übernommene Stellen sind als solche durch Zitate kenntlich gemacht. Die Satzung des Karlsruher Instituts für Technologie (KIT) zur Sicherung guter wissenschaftlicher Praxis wurde beachtet. Die elektronische Version der Arbeit stimmt mit der schriftlichen überein und die Abgabe und Archivierung der Primärdaten gemäß Abs. A (6) der Regeln zur Sicherung guter wissenschaftlicher Praxis des KIT beim Institut gesichert. Ich versichere, dass ich keine vorausgegangenen Promotionsversuche unternommen habe und mich derzeit auch nicht in einem weiteren, laufenden Promotionsverfahren befinde.

. . . .
Ort, Datum

. . . .
Name

Abstract

Photochemistry has been employed in macromolecular and surface science with great success. The usage of light enables the clean, spatially, and temporarily resolved performance of chemical reactions.

In the first part of the present thesis, the photo triggered nitrile imine-mediated tetrazole-ene cycloaddition (NITEC) enables for the first time the spatially resolved surface immobilization of multiple metallopolymers on a single surface. The metallopolymers are prepared *via* reversible-addition-fragmentation chain-transfer (RAFT) polymerization of suitable ligand monomers and subsequent metal loading. In preliminary studies, the need of capping the RAFT group by hetero-*Diels–Alder* chemistry, employing photo generated *o*-quinodimethanes, is demonstrated as the key point to successfully perform the NITEC photoligation on the surface. Through this approach of RAFT polymerization and post-modification steps, α-ω-functionalized metallopolymers based on platinum, palladium, as well as gold are synthesized. The fabrication of gold metallopolymer surfaces is feasible through a post- or pre-loading approach, leading to the same surface structure, which is demonstrated by time-of-flight secondary ion mass spectrometry (ToF-SIMS), as well as X-ray photoelectron spectroscopy (XPS) mappings. In contrast, platinum and palladium metallopolymer surfaces are only obtained *via* the pre-loading approach. As part of the investigation of the photoligation process, the impact of the *Beer–Lambert* law on the surface ligation is investigated. The quantification of this effect is achieved by the combination of the absorption spectrum of the solution containing the metallopolymer and the spectral irradiance of the employed irradiation source. In addition to monofunctional metallopolymer surfaces, the preparation of bi- and even trifunctional metallopolymer surfaces is demonstrated by consecutive NITEC photoligation chemistry.

The synthesis of new spiropyran-based metal complexes of zinc, nickel, calcium, as well as lanthanum is the subject of the second part of this thesis. It is shown that the complex stoichiometries obtained *via* X-ray crystallography do not necessarily equal the situation in solution. For this, the solution stoichiometries for the synthesized complexes were investigated with Job's method of continuous variations. Subsequently, the photochemistry of spiropyran-metal complexes is investigated by coupling of UV-Vis, as well as NMR spectroscopy with the *in situ* irradiation of the complexes with a high-power UV LED. The LED-NMR method is significantly improved compared to the setups described in literature regarding the light intensity reaching the analyte solution inside the NMR spectrometer. The understanding of the photochemistry of the described spiropyran-metal complexes in this thesis is the first step for the application in functional materials.

In the last part of the present thesis, the spirothiopyran photoswitch is introduced for the spatially resolved lithographic encoding of surfaces *via* photoligation chemistry with a maleimide species. The application of a functionalized maleimide and subsequent surface-initiated polymerization enables the lithographic encoding of glass substrates with polymer brushes. With this approach, line structures feature brush heights between 25–50 nm with a width down to 0.4 µm can be prepared. Importantly, the possibility to trigger the reaction between the spirothiopyran and the maleimide either at around 365–410 nm or *via* two photon absorption at 820 nm is a great benefit for the toolbox of photolithographic protocols. In a second investigation, it is shown that the incorporation of the spirothiopyran photoswitch into a polymer opens up the possibility to employ the system in direct laser writing applications. While the photoligation chemistry with a suitable maleimide photoresist can be used to prepare free-standing 3D structures, the spirothiopyran photoresist itself can also form stable 3D structures *via* supramolecular aggregation. In addition, this new photoresist does enable the laser lithographic writing with sub-diffraction resolution.

Zusammenfassung

Photochemie wurde bereits mit großem Erfolg im Gebiet der Polymerchemie als auch bei der Funktionalisierung von Oberflächen eingesetzt. Der Einsatz von Licht ermöglicht eine saubere, ortsaufgelöste sowie zeitlich kontrollierte Durchführung von chemischen Reaktionen.

Im ersten Teil der vorliegenden Dissertation wird die lichtgesteuerte Nitrilimin vermittelte Tetrazol-En Cycloaddition (NITEC) erstmals für die ortsaufgelöste Verankerung mehrerer Metallopolymere auf einer einzigen Oberfläche verwendet. Die Metallopolymere werden durch reversible Additions-Fragmentierungs-Kettenübertragungspolymerisation (RAFT-Polymerisation) von passenden Ligandenmonomeren und anschließender Metallbeladung erhalten. In Vorstudien wird gezeigt, dass die Reaktion der RAFT-Gruppe mit *ortho*-Quinodimethanderivaten in einer hetero-*Diels–Alder*-Reaktion einen Schlüsselschritt für die darauffolgende NITEC-Reaktion an der Oberfläche darstellt. Durch diesen Ansatz aus RAFT-Polymerisation und anschließender Modifizierung werden α-ω-funktionelle Platin-, Palladium- und Goldmetallopolymere hergestellt. Die Herstellung von, mit Goldmetallopolymeren funktionalisierten, Oberflächen ist dabei entweder durch die Vor- oder Nachbeladung des Ligandenpolymers mit dem Metallvorläufer zugänglich. Die so erhaltenen Oberflächen zeigen eine übereinstimmende Oberflächenstruktur, wie durch Flugzeit-Sekundärionen-Massenspektrometrie (ToF-SIMS) und Röntgen-Photoelektronen-Spektroskopie (XPS) gezeigt werden konnte. Im Gegensatz dazu sind die entsprechenden platin- und palladiumbasierten Metallopolymer-Oberflächen nur über die bereits zuvor metallbeladenen Polymere zugänglich. Ebenso wurde der Einfluss des Gesetzes von Lambert-Beer auf die Oberflächenverankerung mittels dieser lichtgesteuerten Kupplungsreaktion untersucht. Die Quantifizierung dieses Einflusses ist durch die Kombination der Absorption der eingesetzten Metallopolymerlösungen und der Lichtintensität der eingesetzten Strahlungsquelle möglich. Zusätzlich zu den einfach funktionalisierten Oberflächen wurden zwei- und dreifach funktionalisierte Metallopolymer-Oberflächen über die stufenweise Durchführung von NITEC-Reaktionen realisiert.

Die Synthese neuer spiropyranbasierter Metallkomplexe von Zink, Nickel, Calcium und Lanthan bildet den Kern des zweiten Abschnittes dieser Dissertation. Es wird gezeigt, dass die durch Röntgenstrukturanalyse erhaltenen Stöchiometrien nicht notwendigerweise mit der Struktur in Lösung übereinstimmen. Dafür wird die Stöchiometrien in Lösung über die Jobsche Methode der kontinuierlichen Variation untersucht. Im Folgenden wird die Photochemie der Metallkomplexe durch die Verwendung von UV-Vis- als auch durch NMR-Spektroskopie unter gleichzeitiger Bestrahlung mit einer UV-LED untersucht. Die verwendete LED-NMR-Methode konnte im Vergleich zu in der Literatur beschriebenen Aufbauten verbessert werden, wobei die im NMR-Probenkopf ankommende Lichtintensität deutlich gesteigert wurde. Das Verständnis der Photochemie der beschriebenen spiropyranbasierten Metallkomplexe in dieser Arbeit stellt den ersten Schritt für die Anwendung dieser Molekülklasse in funktionellen Materialien dar.

Im letzten Teil dieser Dissertation wird die Anwendung des Spirothiopyran-Photoschalters in der ortsaufgelösten Verankerung auf Oberflächen durch die Reaktion mit Maleimid-Molekülen beschrieben. Durch die Verwendung eines funktionalisierten Maleimids und anschließender oberflächeninitiierter Polymerisation sind Glasoberflächen zugänglich, welche mit Polymerbürsten funktionalisiert sind. Über diesen Ansatz sind Linienstrukturen mit einer Höhe von 25–50 nm und einer Breite von 0.4 µm zugänglich. Hervorzuheben ist die Möglichkeit, die Spirothiopyran-Maleimid-Reaktion entweder im Bereich von 365–410 nm oder, mittels Zwei-Photonen-Absorption, bei 820 nm zu steuern. In einer zweiten Untersuchung wird gezeigt, dass der Einbau des Spirothiopyran-Photoschalters in einen Photolack den Einsatz im Bereich des Direkten Laserschreibens ermöglicht. Die Verwendung eines passenden Maleimid-Photolacks ermöglicht die Herstellung von freistehenden 3D-Strukturen. Zusätzlich wird gezeigt, dass der Spirothiopyran-Photolack selbst zur Ausbildung stabiler 3D-Strukturen über die Bildung von supramolekularen Aggregaten verwendet werden kann, wobei die Verwendung dieses neu entwickelten Photolacks das laserlithographische Schreiben mit einer Auflösung unterhalb der Beugungsgrenze ermöglicht.

Contents

Abbreviations **XV**

1 Introduction **1**

2 Theoretical background **3**

2.1 Polymer chemistry 3
  2.1.1 Basic concepts in polymer chemistry 4
  2.1.2 Free radical polymerization 7
  2.1.3 Reversible-deactivation radical polymerization 12
    2.1.3.1 Reversible-addition-fragmentation chain-transfer polymerization 12
  2.1.4 Metallopolymers 17
2.2 Photochemistry 21
  2.2.1 Physical description of photochemical processes 22
  2.2.2 Photochromic molecules 27
    2.2.2.1 Spiropyrans 30
  2.2.3 Photo triggered ligation techniques 37
    2.2.3.1 Thioaldehydes 41
    2.2.3.2 Nitrile imine-mediated tetrazole-ene cycloaddition . . 44
    2.2.3.3 *ortho*-Quino dimethanes 48
    2.2.3.4 Spirothiopyrans 51
2.3 3D laser lithography below the diffraction limit 54
  2.3.1 The principle of STED 54
  2.3.2 From direct laser writing towards STED-inspired lithography . . 56
    2.3.2.1 Direct laser writing 56
    2.3.2.2 STED-inspired lithography 57
2.4 Spatially resolved surface functionalization 62
  2.4.1 Substrates 63
  2.4.2 Silicon surfaces 64
    2.4.2.1 Activation strategies 64
    2.4.2.2 Formation of self-assembled monolayers 65
    2.4.2.3 Post-modification techniques 66
    2.4.2.4 Polymers on surfaces 67
    2.4.2.5 Surface-immobilized metallopolymers 70

3 Spatially resolved multiple metallopolymer surfaces by photolithography 73
3.1 Development of a surface ligation protocol 74
3.1.1 Phenacylsulfide approach 75
3.1.2 NITEC approach 81
3.2 Metallopolymer synthesis 86
3.3 Surface attachment 94
3.3.1 Post-loading approach 94
3.3.2 Pre-loading approach 97
3.4 Conclusion 113

4 Light-sensitive spiropyran-metal complexes 115
4.1 Synthesis of spiropyran-metal complexes 117
4.2 Photochemistry of spiropyran-metal complexes 126
4.2.1 LED-UV-Vis investigations 126
4.2.2 LED-NMR spectroscopy 128
4.3 Conclusion 138

5 Photocaged ligation *via* spirothiopyrans 139
5.1 Surface photoligation 141
5.2 Fabrication of 3D microstructures 147
5.3 Linewidth reduction through STED-inspired lithography 156
5.4 Conclusion 159

6 Concluding remarks 163

7 Experimental section 165
7.1 Materials 165
7.2 Analysis 167
7.3 Synthesis of small molecules 172
7.4 Polymerizations 180
7.5 Surface reactions 184

Bibliography 187

List of Figures 205

List of Tables 221

List of Schemes 223

A Appendix 227
A.1 Pulse sequence for LED-NMR kinetic experiments 227
A.2 Setup for LED-UV-Vis measurements 228
A.3 Setup for LED-NMR measurements 229
A.4 MATLAB Script for absorption corrected spectral intensity 229

A.5 NMR spectra 236
A.6 UV-Vis spectra 251
A.7 Emission spectra 254
A.8 SEC chromatograms 258
A.9 ToF-SIMS and XPS analysis 263
    A.9.1 Monofunctional patterning 265
    A.9.2 Bifunctional patterning 283
    A.9.3 Trifunctional patterning 296

Publications and conference contributions **305**

Acknowledgements **307**

Abbreviations

2PII	Two-color photo-initiation/inhibition
Đ	Dispersity index
δ	Chemical shift
Δ	Thermal heating
ϵ	Molar attenuation coefficient
$\hat{\mu}$	*Dipole-moment operator*
μCP	Microcontact printing
τ	Lifetime
Φ	Quantum yield
a.u.	Arbitrary units
A	Absorbance
AFM	Atomic-force microscopy
AIBN	Azobisisobutyronitrile
AM	Acrylamide
AN	Acrylonitrile
APTES	(3-Aminopropyl)triethoxysilane
ATRP	Atom transfer radical polymerization
AuNPs	Gold nanoparticles
$\mathrm{Br(CH_2)_3OTBDMS}$	3-Bromopropoxy-*tert*-butyl-dimethylsilane
c	Speed of light
$c\mathrm{C_6H_{12}}$	Cyclohexane
C_X	Transfer constant towards a species X
CDI	1,1′-Carbonyldiimidazole
CDSTSP	4-Cyano-4-((dodecylsulfanylthiocarbonyl)sulfanyl)pentanoic acid
COD	1,5-Cyclooctadiene
COSY	Correlation spectroscopy
CPADB	4-Cyanopentanoic acid dithiobenzoate
CRP	Controlled radical polymerization

CSIRO	Commonwealth Scientific and Industrial Research Organization
CT	Charge-transfer
CTA	Chain transfer agent
CW	Continuous wave
DCC	*N*,*N*′-Dicyclohexylcarbodiimid
DCM	Dichloromethane
DEAD	Diethyl azodicarboxylate
DETC	7-Diethylamino-3-thenoyl coumarine
DG	Donating group
DIAD	Diisopropyl azodicarboxylate
DIC	*N*,*N*′-Diisopropylcarbodiimide
DLW	Direct laser writing
DMAP	4-Dimethylaminopyridine
DMF	Dimethylformamide
DMSO	Dimethylsulfoxide
EAL	Effective attenuation length
EDC·HCl	1-Ethyl-3-(3-dimethylaminopropyl)carbodiimide hydrochloride
ESI-MS	Electrospray ionization mass spectrometry
EtOAc	Ethyl acetate
EWG	Electron withdrawing group
FCF	*Franck-Condon* factor
FWHM	Full width at half maximum
h	Planck constant
HEMA	2-Hydroxyethyl methacrylate
HMBC	Heteronuclear multiple bond correlation
HMQC	Heteronuclear multiple quantum correlation
HOMO	Highest occupied molecular orbital
HR-ESI-MS	High-resolution electrospray ionisation mass spectrometry
I	Light intensity
IC	Internal conversion
ISC	Intersystem crossing
ITO	Indium tin oxide
ITX	Isopropylthioxanthone
k_d	Rate coefficient of the initiator decomposition
k_i	Rate coefficient initiation

k_p	Rate coefficient propagation
k_t	Rate coefficient termination
K_{eq}^{λ}	Photo-dynamic equilibrium constant
K_{eq}^{Δ}	Thermal equilibrium constant
L	“Livingness”
LAM	“Less activated” monomer
LDA	Lithium diisopropylamide
LED	Light-emitting diode
LG	Leaving group
LUMO	Lowest unoccupied molecular orbital
M_{if}	Transition dipole moment
$\bar{M}_\mathrm{n}$	Number-average molecular weight
$\bar{M}_\mathrm{w}$	Weight-average molecular weight
MA	Methyl acrylate
MAA	Methacrylic acid
MADIX	Macromolecular design *via* the interchange of xanthates
Mal-OH	2-(2-Hydroxyethyl)-3a,4,7,7a-tetrahydro-1*H*-4,7-epoxyisoindole-1,3(2*H*)-dione
MAM	“More activated” monomer
MAP	Multiphoton absorption polymerization
MC	Merocyanine
MeCN	Acetonitrile
MMA	Methyl methacrylate
MOF	Metal–organic framework
MWD	Molecular weight distribution
N_A	Avogadro constant
NA	Numerical aperture
o-NB	*o*-Nitrobenzyl
o-NBA	*o*-Nitrobenzaldehyde
NICAL	Nitrile imine-carboxylic acid ligation
NIL	Nanoimprint lithography
NIR	Near-infrared
NITEC	Nitrile imine-mediated tetrazole-ene cycloaddition
NMP	Nitroxide-mediated polymerization
NMR	Nuclear magnetic resonance

NSL	Nanosphere lithography
NVP	*N*-Vinylpyrrolidone
OPA	One photon absorption
PEG	Polyethylene glycol
PEGMEMA	Poly(ethylene glycol) methyl ether methacrylate
PDA	Polydopamine
PEDA	Photoenolization/*Diels–Alder*
PFP	Pentafluorophenol
PI	Photoinitiator
PLED	Polymer light-emitting diode
PMDETA	*N*,*N*,*N*′,*N*″,*N*″-Pentamethyldiethylenetriamine
PMMA	Poly(methyl methacrylate)
PS	Polystyrene
PSS	Photostationary state
PTFE	Polytetrafluoroethylene
o-QM	*o*-Quinone methide
R_i	Rate of initiation
R_p	Rate of propagation
R_t	Rate of termination
RAFT	Reversible-addition-fragmentation chain-transfer
RAPID	Resolution augmentation through photo induced deactivation
RDRP	Reversible-deactivation radical polymerization
ROMP	Ring-opening metathesis polymerization
ROP	Ring-opening polymerization
S	Singulet
$\mathrm{S_N2}$	Bimolecular nucleophilic substitution
SAM	Self-assembled monolayer
SCNP	Single-chain nanoparticle
SE	Stimulated emission
SEC	Size-exclusion chromatography
SEM	Scanning electron microscopy
SI-ATRP	Surface-initiated atom-transfer radical polymerization
SP	Spiropyran
STED	Stimulated emission depletion
STP	Spirothiopyran

Sty	Styrene
T	Triplet
TAD	Triazolinedione
TEA	Triethylamine
Tet-acid	4-(2-(4-Methoxyphenyl)-2*H*-tetrazol-5-yl)benzoic acid
THF	Tetrahydrofuran
tht	Tetrahydrothiophen
ToF-SIMS	Time-of-flight secondary ion mass spectrometry
TPA	Two photon absorption
UCNPs	Upconverting nanoparticles
UHV	Ultra-high vacuum
UV-Vis	Ultraviolet-visible
VAc	Vinyl acetate
VR	Vibrational relaxation
$\bar{X}_\mathrm{n}$	Number-average degree of polymerization
$\bar{X}_\mathrm{w}$	Weight-average degree of polymerization
XPS	X-ray photoelectron spectroscopy

CHAPTER 1

Introduction

Photochemistry is playing an increasing role in chemistry, as well as in material science. The development of new light triggered reactions, such as photoligations, or the usage of light as a stimulus in chemical systems has evolved as an emerging research field in organic chemistry, including the synthesis of macromolecular architectures. The current thesis is exploiting photochemistry for different applications in the realm of material science, as well as small molecules. In Chapter 3, the light-triggered nitrile imine-mediated tetrazole-ene cycloaddition (NITEC) is shown to be a versatile photoligation method for the spatially resolved encoding of multiple metallopolymers on a single functionalized surface. In fact, additional usage of another photoligation chemistry, namely the photo induced generation of *ortho*-quino dimethanes followed by a *Diels–Alder* reaction, was necessary for the success of the developed surface encoding protocol. As such, these versatile photoligation methods enabled the preparation of hitherto undescribed functional surfaces for potential applications in heterogeneous catalysis or small molecule sensing devices. In contrast, Chapter 4 is investigating the photochemistry of spiropyran-derived metal complexes. The understanding of these light sensitive complexes is a crucial step towards the development of functional materials. Therefore, the aim of Chapter 4 is to gain a deeper understanding of the photochemistry of this material class. However, the driving force behind these investigations is the application in macromolecular scaffolds and the creation of unprecedented highly functional metallopolymers with an inherent light-sensitivity. In Chapter 5, the photoligation chemistry of spirothiopyrans (STPs) and maleimides is introduced for the spatially resolved encoding of surfaces. While there are many surface photoligation protocols available, such as the NITEC reaction employed in Chapter 3, the ability to trigger the photoligation with varying wavelengths is an active research field. With this respect, the possibility to trigger the STP-maleimide reaction in the near-infrared at 750–820 nm *via* two-photon excitation is a valuable addition for the toolbox of photoligation protocols. In addition, the incorporation of STPs into a macromolecular scaffold enables laser lithographic writing with sub-diffraction resolution.

CHAPTER 2

Theoretical background

The following chapter will provide an overview of the chemistry, the methods, and theoretical concepts employed in the current thesis. An introduction will be given to polymerization techniques with a particular focus on reversible-deactivation radical polymerization methods for the controlled fabrication of macromolecular matter. An additional section is specifically dedicated to the field of metallopolymer chemistry. Subsequently, the theoretical basis for photochemical transformations is given. The chemistry of spiropyrans (SPs) will be presented, a prominent class of photochromic molecules employed in Chapter 4 and 5 of the present thesis. Furthermore, modern photo triggered ligation techniques will be the subject of Section 2.2.3, which have been used in Chapter 3 and 5 of the current work. The concepts of 3D laser lithography and ways to overcome the diffraction limit in resolution will be discussed in Section 2.3 (see also Chapter 5). Finally, routes towards spatially resolved surface functionalization employed in Chapter 3 will be the subject of Section 2.4.

2.1 Polymer chemistry

Polymers have ever since played an important role in life on earth, e.g. in the form of DNA, RNA, proteins, or polysaccharides. While not being recognized as polymers for a long time, the beginning of today's polymer science can be dated back into the 19$^{\mathrm{th}}$ century. Thomas Hancock discovered that natural rubber does become more fluid when being masticated in 1820. Only a few years later, in 1839, Charles Goodyear found that the elastic properties of natural rubber can be significantly improved by heating with elemental sulfur, a process nowadays known as vulcanization. This process was subsequently patented by his brother Nelson Goodyear in 1851. In 1892, another patent was issued on the dissolving and following regeneration of cellulose by Charles Cross, Clayton Beadle, and Edward Bevan. While all of these processes utilize natural based polymers, Leo Baekeland commercialized the first fully synthetic polymer in 1910, based on phenols and formaldehyde, with the name *Bakelite*. During World War I, the production of the first synthetic rubber from 2,3-dimethylbutadiene started in Germany. The common belief during that time was that the properties of the polymeric material resulted from strong physically associated aggregates of small molecules. Hermann Staudinger introduced the word *macromolecule* to describe the polymer characteristics in the 1920s, a concept being highly controversial at that time. Nevertheless, further studies conducted by Wallace Carothers and others strengthened the picture of polymers as drawn by Staudinger. With the beginning of the 1930s, the concept of macromolecules and polymers has been accepted and established the field as a new discipline in science. This results in the Nobel Prize for Chemistry for Hermann Staudinger in 1953 and for Paul Flory in 1974, who made a substantial impact in the theoretical description of macromolecules. From then onwards, advances in polymer chemistry have increased enormously and have led to the highly specialized fields of polymer chemistry today, both in industry and academia.

2.1.1 Basic concepts in polymer chemistry

Polymers are by definition large molecules (macromolecules or polymers) composed of repeated structural units (monomers), which are connected by covalent bonds. The very large amount of polymerizable monomers, which determine the properties of the polymer, yields a broad range of polymers and possible combinations. As a consequence of this variety of polymeric materials, it becomes clear that there is not just one single way to characterize them all.

Polymerization mechanism Polymers can be classified by the reaction mechanism of formation into *step-growth polymerizations* and *chain-growth polymerizations*.

In *step-growth* polymerizations, the chains grow in stepwise reactions, which can occur between any of the molecular species being present in the polymerization mixture. Examples for such a mechanism are *polycondensation* and *polyaddition* polymerizations. In *step-growth* polymerizations, the degree of polymerization increases only little at low functional group conversion, to ultimately reach high degrees close to full conversion of the functional groups. The monomers form oligomers which eventually react to long polymer chains. As such, a high degree of polymerization, i.e. high conversion of functional groups, is necessary for the production of long chains. *Step-growth* polymerizations are therefore very demanding on *clean* reactions with high conversions, as well as high purity of the starting materials. A theoretical correlation between the number-average degree of polymerization $\bar{X}_\mathrm{n}$ and the extent of the reaction p is given by the *Carothers's equation* (see Equation (2.1). Equation (2.1a) is describing the case of an equal number of functional groups, while a more general representation is given by Equation (2.1b). Here, r reflects the *reactant ratio* between two functional groups N_A and N_B as $r = N_\mathrm{A}/N_\mathrm{B}$.

$$\bar{X}_\mathrm{n} = \frac{1}{1-p} \tag{2.1a}$$

$$\bar{X}_\mathrm{n} = \frac{1+r}{1+r-2rp} \tag{2.1b}$$

On the other hand, *chain-growth* polymerizations feature a polymer chain with a reactive end-group. Monomers are repeatedly adding to such chain-ends, resulting in a growing polymer chain. Ionic polymerizations, as well as radical polymerizations belong to this class of polymerization mechanism. The kinetic aspects of *chain-growth* polymerizations will be discussed in Section 2.1.2 in the context of free radical polymerization (FRP). From all of these mechanisms, free radical polymerization is by far the most important polymerization technique, especially in industry and large-scale applications.

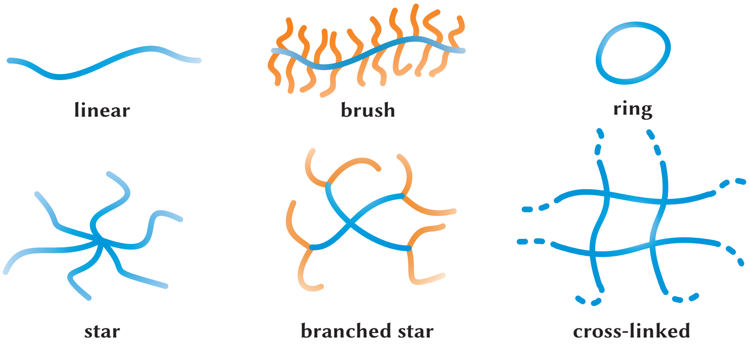

Figure 2.1. Different kinds of polymer topologies. (a) linear, (b) brush, (c) ring, (d) star, (e) cross-linked, and (f) branched star.

Polymer topology An alternative way to characterize polymers is their molecular topology, of which different possibilities are depicted in Figure 2.1. Polymer topologies can be described as *linear* in the case were there is only a single linear chain. *Brush* polymers feature a core polymer chain on which several secondary polymer chains are attached to. These can consist of the same monomer or feature other chemical functionalities as the core. (a) If the individual polymer chains are connected at both chain ends, *ring* polymers are formed. *Star* polymers feature a central core unit on which multiple polymer chains are attached to. If the star has additional branching points except the core, *branched star* polymer architectures are obtained. Finally, if the polymer chains are connected *via* many individual points towards each other, ultimately leading to a single molecule. The resulting structure is a *cross-linked* polymer, i.e. a polymer network.

Physical polymer properties A more physical way of dividing polymers into different classes is based on their melting properties. *Thermoplastics* are either amorphous or semicrystalline polymers. In contrast, *elastomers* are amorphous polymers which are weakly cross-linked. They are flexible but cannot be melted and are insoluble. Finally, *thermosets* are highly cross-linked polymers, which are also insoluble, cannot be melted, and cannot be reversibly reshaped without destroying the material.

Polymer composition Another way to classify polymers is based on their molecular composition as depicted in Figure 2.2. If the polymer chain is composed of a single monomeric repeating unit, it is referred as a *homopolymer.* When two or more monomers are incorporated into the polymer, the general structure is described as a *copolymer.* Such a polymer still consists of single linear chains, while the order of the individual monomeric repeating units dictates the nomenclature. *Statistical copolymers* exhibit a random distribution of the monomers inside the polymer chain. On the other hand, *alternating copolymers* feature a strict alternation of the different monomers. Finally, if the different monomers are assembled into blocks consisting of one monomer followed by another block of a second monomer, *block copolymers* are obtained. When the copolymer features a *brush*-like topology with one monomer building up the core chain and another one the attached side chains, the polymer is classified as a *graft copolymer.*

Molar mass distribution The molecular weight (MW) of polymers made synthetically is in all cases not homogeneous but exhibits a molecular weight distribution (MWD). As the mechanical properties of the polymers are associated directly with the MW and MWD, it is important to know as much as possible about the shape of the respective distribution. The MW and the MWD are described by the *number-average molecular weight* $\bar{M}_\mathrm{n}$, the *weight-average molecular weight* $\bar{M}_\mathrm{w}$, and the *dispersity index* $Đ$, which

---

(a) In the latter case, the structure is referred to as a *graft* polymer, see discussion under *Polymer composition.*

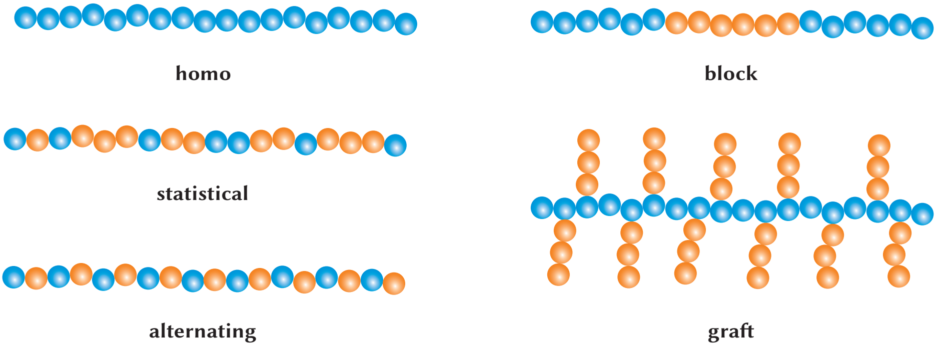

homo

block

statistical

graft

alternating

Figure 2.2. Examples of various polymer compositions as described in the text.

are defined by Equation (2.2a), (2.2b), and (2.2c), respectively.[1] In Equation (2.2a), n_i is the number of molecules having a MW M_i, and the weight fraction w_i in Equation (2.2b) is the mass of molecules with the MW M_i divided by the total mass of molecules in the ensemble.

$$\bar{M}_\mathrm{n} = \frac{\sum n_i M_i}{\sum n_i} \tag{2.2a}$$

$$\bar{M}_\mathrm{w} = \frac{\sum w_i M_i}{\sum w_i} \tag{2.2b}$$

$$Đ = \frac{\bar{M}_\mathrm{w}}{\bar{M}_\mathrm{n}} \tag{2.2c}$$

In addition, the degree of polymerization averages are important for polymer characterization. The *number-average* and *weight-average degrees of polymerization* are given by Equation (2.3a) and (2.3b), respectively. In both equations, M_0 is the average of the MW of the repeating units.

$$\bar{X}_\mathrm{n} = \frac{\bar{M}_\mathrm{n}}{M_0} \tag{2.3a}$$

$$\bar{X}_\mathrm{w} = \frac{\bar{M}_\mathrm{w}}{M_0} \tag{2.3b}$$

2.1.2 Free radical polymerization

As already mentioned in the introduction of Section 2.1.1, FRP is one of the major polymerization mechanism that is employed in various polymerization techniques, such as in bulk, in emulsion, in solution etc. Since a broad range of monomers are available, FRP represents the mostly used technology in polymer synthesis. FRP also features a high tolerance of functional groups and mild as well as facile reaction conditions, as for instance compared to ionic polymerizations.

Mechanism The mechanism of FRP can be divided in four steps, namely *initiation*, *propagation*, *chain transfer*, and *termination* (see Scheme 2.1).

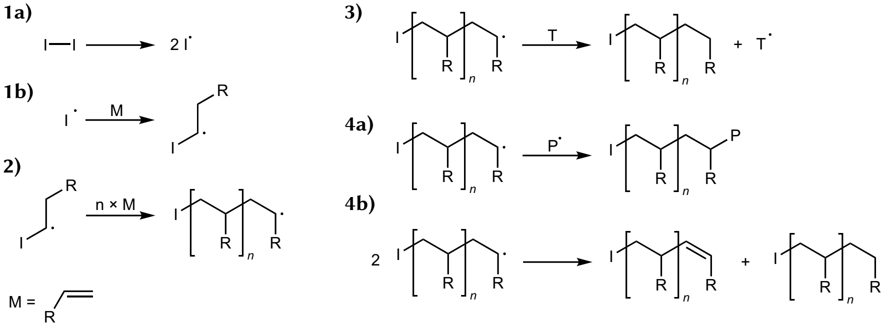

Scheme 2.1. The four steps in a FRP mechanism. *Initiation* can be divided in two steps, namely the formation of radicals by an initiator molecule I_2 (1a) and the addition to a double bond of a monomer M (1b). 2) *Propagation* of the polymerization, adding more monomers to the propagating chain. 3) *Chain transfer* reactions can occur with transfer agents T. *Termination via combination* of two radical species (4a) and through a *disproportionation* process (4b).

The *initiation* process is divided into two steps. First, the employed initiator forms radicals through either *homolytic scission* of a single bond, or *via* a *single-electron transfer process* from an ion or molecule. Commonly employed initiators form radicals *via* the homolytic scission. This process is often triggered either by heat (*thermolysis*) or by irradiation with light (*photolysis*). Prominent molecules for this class of initiation include for example peroxides and azo compounds, such as benzoyl peroxide or azobisisobutyronitrile (AIBN). Once the radicals are formed, the second step of the *initiation* is the addition of the initiator derived radicals onto a double bond of a monomer (see 1b) in Scheme 2.1).

During *propagation*, subsequent addition of additional monomer units to the chain results in the formation long polymer chains. *Chain transfer* reactions can occur with various species present during the polymerization process. Here, the active radical center from a growing chain is transferred onto another molecule T, which can be either an initiator, monomer, solvent, or an intentionally added so-called *transfer agent* molecule. The new radical species $T^\bullet$ can again participate in the polymerization process, e.g. re-initiating *via* addition to a further monomer unit. If the transfer reaction generates a radical at the backbone of a previously formed polymer chain, side polymer chains are generated upon addition of monomer units to yield branched polymer chains.

As depicted in Scheme 2.1, two radicals must react in a bimolecular reaction in *termination* processes. This results in an irreversible loss of the active radical center and termination of the polymerization process, which can occur in two ways. *Recombination* involves the coupling of two growing chain ends forming a single polymer chain with a MW that is the sum of the two chains reacting with each other. On the other hand, *disproportionation* refers to a process in which an active polymer chain is abstracting a hydrogen atom from another chain, thus creating an unsaturated and a saturated polymer chain, respectively. In principle, both *termination* processes can occur simultaneously in a polymerization. However, the extent of each termination mechanism depends on the monomer and the polymerization conditions. Generally, vinylic monomers, such as acrylates, tend to terminate *via recombination*, while in α-methyl vinyl monomers, such as methacrylates , *disproportionation* is favored. The reason for this behavior is the steric hindrance in α-methyl vinyl derived radicals and the additional three β-hydrogen atoms of the methyl group, from which H-abstraction can occur. In addition, the *recombination* has a lower activation energy as compared to the *disproportionation* process and is therefore favored at lower temperatures.

Kinetics The kinetic description of the FRP allows the calculation of the *polymerization rate* R_p and the *number-average degree of polymerization* $\bar{X}_\mathrm{n}$, among other parameters. The FRP can be divided into three regimes, namely the *initiation* phase, the *steady-state*, and the *termination* phase. In the *initiation* phase, the concentration of radicals formed *via* the decomposition of the initiator increases, until the formation of radicals equals the reduction of radicals due to termination processes. At this state, the *steady-state* regime is reached. During progression of the polymerization, the increasing viscosity of the system results in an increased polymerization rate, as a result of reduced diffusion hindering the termination of radicals. As such, the radical concentration increases, leading to an *auto-acceleration*, being referred to as the *Trommsdorff–Norrish effect* or *gel effect*. At this stage, the *steady-state* assumption fails, and the *termination* phase starts. If the heat transfer is insufficient, the reaction temperature will increase drastically, ultimately resulting in thermal overheating.

As the processes in FRPs are very complex, several assumptions are made in order to simplify the equations. First, the radical concentration during the polymerization is to be considered chain-length independent, resulting in a constant k_p. Second, the decrease of monomer concentration during the *initiation* phase is neglected, implying the monomer decrease during polymerization is exclusively caused by the *rate of propagation* R_p. Finally, the *steady-state* assumption means that the formation of new radicals $\mathrm{R}^\bullet$ equals the reduction of radicals $\mathrm{M}^\bullet$ inside the reaction mixture, resulting in Equation (2.4). $\mathrm{M}^\bullet$ refers to any radical species being present in the reaction mixture.

$$\frac{\mathrm{d}[\mathrm{R}^\bullet]}{\mathrm{d}t} = -\frac{\mathrm{d}[\mathrm{M}^\bullet]}{\mathrm{d}t} \tag{2.4}$$

The *rate of initiation* R_i can be described *via* Equation (2.5). In the first line, the initiation is expressed in terms of the bimolecular reaction with the rate k_i and the concentration of the radical $\mathrm{R}^\bullet$ and the monomer M. However, the formation of the radicals during decomposition of the initiator (see 1a) in Scheme 2.1) is the rate determining step in the initiation. Substitution of this elemental reaction step for a thermally triggered initiator results in the second line of Equation (2.5), with f being the *initiator efficiency*, i.e. the fraction of formed radicals actually starting a growing chain.

$$\begin{aligned} R_\mathrm{i} = \frac{\mathrm{d}[\mathrm{R}^\bullet]}{\mathrm{d}t} &= k_\mathrm{i}[\mathrm{R}^\bullet][\mathrm{M}] \\ &= 2fk_\mathrm{d}[I] \end{aligned} \tag{2.5}$$

The *rate of termination* R_t is given by the bimolecular reaction between two radical species $\mathrm{M}^\bullet$ in Equation (2.6). The rate coefficient k_t is the sum of the rate coefficient for *combination* and *disproportionation.*

$$R_\mathrm{t} = -\frac{\mathrm{d}[\mathrm{M}^\bullet]}{\mathrm{d}t} = 2k_\mathrm{t}[\mathrm{M}^\bullet][\mathrm{M}^\bullet] \tag{2.6}$$

$$\begin{aligned} R_\mathrm{p} = -\frac{\mathrm{d}[\mathrm{M}]}{\mathrm{d}t} &= k_\mathrm{p}[\mathrm{M}][\mathrm{M}^\bullet] \\ &= k_\mathrm{p}\sqrt{\frac{R_\mathrm{i}}{2k_\mathrm{t}}}[M] \\ &= k_\mathrm{p}\sqrt{\frac{fk_\mathrm{d}}{k_\mathrm{t}}}[M]\sqrt{[I]} \end{aligned} \tag{2.7}$$

For the *rate of propagation* R_p, Equation (2.7) can be written. Making use of the *steady-state* assumption for the radical concentration, i.e. Equation (2.4), (2.5), and (2.6), an expression for the *steady-state rate of polymerization* can be derived. (a) Based on these equations, the *number-average degree of polymerization* can be calculated *via* the ratio between R_p and R_t. The result is presented in Equation (2.8), with q being the fraction of termination reactions occurring through *disproportionation.* The index 0 in $\bar{X}_{\mathrm{n},0}$ refers to the fact that no *chain transfer* is considered here.

(a) It should be noted that the expression for the *rate of initiation* is only valid for thermal initiation. Other forms of Equation (2.5) must be used for photo- or redox-initiated polymerizations, see also [2].

$$\bar{X}_{\mathrm{n},0} = \frac{R_\mathrm{p}}{R_\mathrm{t}} = \frac{k_\mathrm{p}}{(1+q)\sqrt{fk_\mathrm{d}k_\mathrm{t}}}[M][I]^{-1/2} \tag{2.8}$$

As such, two important conclusions can be drawn from the above equations:

$$R_\mathrm{p} \propto [M]\sqrt{[I]} \quad \text{and} \quad \bar{X}_\mathrm{n} \propto [M][I]^{-1/2}$$

So far, the equations have excluded *chain transfer* in the description of the kinetic process. In doing so, several terms must be added in the denominator of Equation (2.8), with $R_\mathrm{tr,I}$, $R_\mathrm{tr,S}$, and $R_\mathrm{tr,M}$ describing the rate of transfer to initiator, solvent, and monomer, respectively, leading to Equation (2.9).

$$\bar{X}_\mathrm{n} = \frac{R_\mathrm{p}}{R_\mathrm{t} + R_\mathrm{tr,I} + R_\mathrm{tr,S} + R_\mathrm{tr,M}} \tag{2.9}$$

In defining a so-called *transfer constant* C_X towards a species X *via*

$$C_\mathrm{X} = \frac{k_\mathrm{tr,X}}{k_\mathrm{p}} \tag{2.10}$$

and by taking the reciprocal of Equation (2.8), Equation (2.11) can be written, which is known as the *Mayo equation.* Here, $\bar{X}_\mathrm{n}$ is the *number-average degree of polymerization* including the effect of chain transfer.

$$\frac{1}{\bar{X}_\mathrm{n}} = \frac{1}{\bar{X}_{\mathrm{n},0}} + C_\mathrm{M} + C_\mathrm{I}\frac{[I]}{[M]} + C_\mathrm{S}\frac{[S]}{[M]} \tag{2.11}$$

So-called *chain transfer agents* (CTAs) having a high C_tr value are intentionally added to the polymerization mixture in FRP processes to control (decrease) the MW. Compounds employed as CTAs are for example aliphatic thiols, such as 1-dodecanethiol (see also Chapter 5). The polymers made *via* a FRP exhibit a rather broad *dispersity index Đ.* In addition, the end group functionality, as well as the molecular architecture cannot be controlled. In order to improve these shortcomings, more advanced radical polymerization techniques have been developed, which will be discussed in the following section.

2.1.3 Reversible-deactivation radical polymerization

Living polymerization, of which anionic polymerization represents the archetype, are classified by the absence of *termination* and *transfer* processes. In addition, controlled polymerization methods are defined by their capability to gain control over the molecular weight, end group functionality, and by achieving low dispersities, in contrast to conventional FRP.

Reversible-deactivation radical polymerizations (RDRP), being formerly referred to as *controlled radical polymerizations* (CRP) achieve such criteria by drastically reducing the probability of *termination* events during polymerization.

The reduction in *termination* in RDRP protocols is achieved *via* different approaches. In atom transfer radical polymerization (ATRP) and nitroxide-mediated polymerization (NMP), the strong reduction of the active radical concentration favors *propagation* over *termination*, which is second order in terms of the radical concentration (see Equation (2.6). This is achieved *via* reversible end-capping of the growing chain radicals. In reversible-addition-fragmentation chain-transfer (RAFT) polymerization, a CTA is added, which leads to a rapid exchange of an end-capped radical with a free chain radical.

As the *termination* is sufficiently suppressed in all of the above mentioned polymerization techniques, RDRP protocols show some of the characteristic features of true *living polymerizations* (e.g. anionic polymerization), such as (I) low $Đ$ values, (II) a linear increase of $\bar{X}_\mathrm{n}$ with conversion, and (III) the polymerization kinetic is pseudo-first-order with respect to monomer. The RAFT polymerization was employed in all chapters of the present thesis and will thus be discussed in more detail in the following section.

2.1.3.1 Reversible-addition-fragmentation chain-transfer polymerization

The RAFT polymerization was introduced by the Moad, Thang, and Rizzardo in 1998 at the Commonwealth Scientific and Industrial Research Organization (CSIRO) in Australia.[3] At the same time, Charmot and co-workers described a polymerization termed MADIX (macromolecular design *via* the interchange of xanthates), which essentially follows the same mechanism as RAFT, employing xanthates as CTAs.[4] RAFT polymerization is based on a FRP with the addition of a CTA, which imposes a degenerative transfer system over the FRP process.[5]

Mechanism The RAFT mechanism is depicted in Scheme 2.2.[5] The *initiation* (**1**), *propagation* (**3**), and *termination* (**5**) reactions are the same as for the FRP described in Scheme 2.1. After the *initiation*, the radical species $\mathrm{P}_n^\bullet$ add to the RAFT agent (the

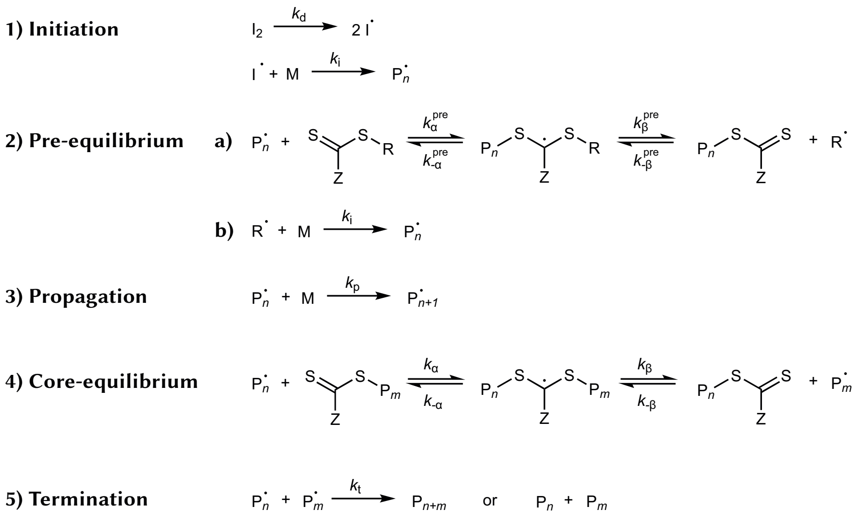

Scheme 2.2. Mechanism of a RAFT polymerization, starting with the *initiation* (1). Growing polymer chains are transformed into macroRAFT agents in the *pre-equilibrium* (**2a**) and the released $R^\bullet$ radicals re-initiate upon addition to monomer (**2b**). *Propagation* (**3**) and *termination* (**5**) events are overlaid by the *core-equilibrium* (**4**), in which constant addition/fragmentation between active polymer chains $P_n^\bullet$ and $P_m^\bullet$ and dormant CTA bearing polymer chains occurs.

CTA) in the *pre-equilibrium* (**2a**). Typical CTAs are thiocarbonylthio group containing molecules equipped with a Z- and a R-group, refer to the discussion below. Here, it is important that the rate of the addition/fragmentation of the *pre-equilibrium* is fast as compared to the *propagation* and that the released $R^\bullet$ radical does efficiently re-initiate *via* addition to monomer (**2b**). As such, all growing chains are effectively transformed in so-called macroRAFT agents (or macroCTAs), having a CTA as an end-group. The macroRAFT agents are also called *dormant chains*, as they do not have active radical chain ends. In order to ensure that all growing propagating chains are attached to a RAFT group, the initiator is added in lower amounts than the RAFT agent. In the *core-equilibrium* (**4**), all propagating polymer chains, here $P_n^\bullet$ and $P_m^\bullet$, constantly undergo reversible addition/transfer with dormant chains. The constant and rapid exchange results in the simultaneous and steady grow of all polymer chains and a control over the evolution of the MW. In addition, *termination* events are still present, but have become very unlikely due to the rapid and degenerated chain-transfer in the *core-equilibrium*.

Kinetics A key difference between RAFT and other RDRP protocols, such as ATRP and NMP, is the use of a radical initiator. As such, the number of termination events is directly proportional to the number of radicals introduced into the system *via* the initiator. In addition, a termination event in RAFT does not lead to a “dead” chain as in ATRP or NMP, as it still bears the CTA group, i.e. the number of polymer chains equipped with a CTA chain end stays the same throughout the polymerization. As a result, the number of “living” and “dead” chains in RAFT can be predicted *a priori* by the number of introduced radicals. Equation (2.12) gives an expression for the “livingness” L of a RAFT polymerization, i.e. the fraction of living chains.[6]

$$L = \frac{[\mathrm{CTA}]_0}{[\mathrm{CTA}]_0 + 2f\,[\mathrm{I}]_0 \left(1 - e^{-k_\mathrm{d} t}\right) \left(1 - \frac{q}{2}\right)} \tag{2.12}$$

Here, $[\mathrm{CTA}]_0$ and $[\mathrm{I}]_0$ are the initial concentrations of the chain transfer agent and the initiator, respectively and q the *termination parameter* introduced in Equation (2.8). The *rate of propagation* R_p of a RAFT polymerization is the same as in the FRP (see Equation (2.7), as the number of radicals is also the same.

In a RAFT polymerization, the target *degree of polymerization* $\bar{X}_\mathrm{n}$ has an impact on the number of living chains L. With all other parameters being the same, a higher target in $\bar{X}_\mathrm{n}$ results in a decrease in L. As such, RAFT is an ideal technique for the synthesis of low to medium MW polymers. The $\bar{M}_\mathrm{n}$ in RAFT is given by Equation (2.13), with the conversion p and M_M and M_CTA as the MW of the monomer and CTA, respectively. The exact expression in Equation (2.13a) including the effect of the initiator, can be simplified, resulting in Equation (2.13b).[5,6]

$$\bar{M}_\mathrm{n} = p\,\frac{[\mathrm{M}]_0}{[\mathrm{CTA}]_0 + 2f\,[\mathrm{I}]_0 \left(1 - e^{-k_\mathrm{d} t}\right) \left(1 - \frac{q}{2}\right)}\,M_\mathrm{M} + M_\mathrm{CTA} \tag{2.13a}$$

$$\approx p\,\frac{[\mathrm{M}]_0}{[\mathrm{CTA}]_0}\,M_\mathrm{M} + M_\mathrm{CTA} \tag{2.13b}$$

Monomers and CTA design An advantage of the RAFT process is its ability to cover a wide range of polymerizable monomers. However, the careful choice of the RAFT agent is crucial for a successful polymerization and depends on the class of monomers to be polymerized. These can be divided in “more activated” monomers (MAMs) and “less activated” monomers (LAMs).[6] MAMs are for example conjugated double bonds, such as in butadiene or styrene or a carbonyl group next to the vinyl moiety, such as in (meth)acrylates or (meth)acrylamides. Monomers featuring a hetero atom (such as oxygen, nitrogen, ...) bound to the vinyl group belong to the class of LAMs. Examples are vinyl acetate or *N*-vinylpyrrolidone. The majority of RAFT processes are conducted with (meth)acrylates, (meth)acrylamides, and styryl derivatives. The most commonly employed RAFT agents for such monomers are dithioesters, dithiobenzoates, or trithiocarbonates.

a) Selection guidelines

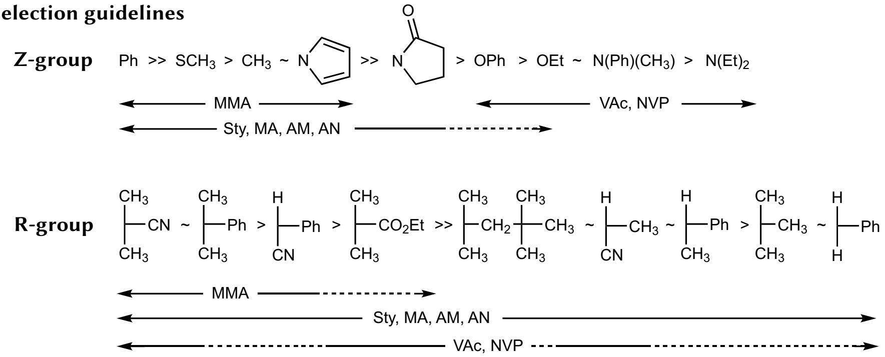
Z-group
Ph >> SCH3 > CH3 ~ N >> N > OPh > OEt ~ N(Ph)(CH3) > N(Et)2
O
MMA
VAc, NVP
Sty, MA, AM, AN
R-group
CH3 CN CH3
CH3 Ph CH3
H Ph CN
CH3 CO2Et CH3
CH3 CH2 CH3 CH3 CH3 CH3
H CH3 CN
H Ph CH3
CH3 CH3 CH3
H Ph H
MMA
Sty, MA, AM, AN
VAc, NVP

b) Examples of RAFT agents

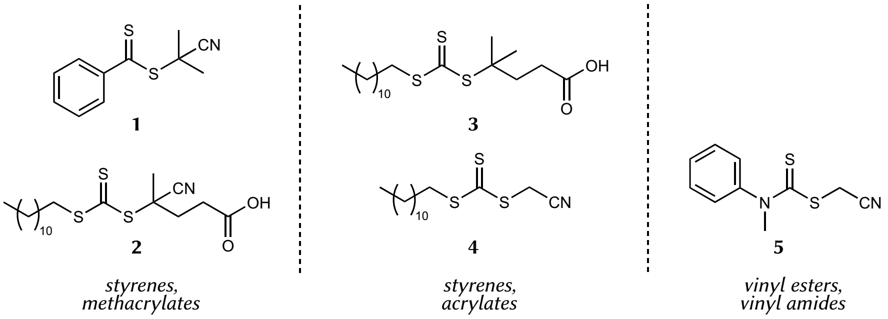
S
CN
S
1
S
S
S
OH
O
10
3
S
CN
S
S
OH
O
10
2
S
S
S
CN
10
4
S
N
S
CN
5
styrenes, methacrylates
styrenes, acrylates
vinyl esters, vinyl amides

Figure 2.3. a) Guidelines for the selection of suitable R- and Z-groups depending on the monomer structure. For the Z-groups, values of k_α decrease and k_β increase from left to right. For the R-groups, k_β decrease from left to right. Abbreviations: MMA = methyl methacrylate, Sty = styrene, MA = methyl acrylate, AM = acrylamide, AN = acrylonitrile, VAc = vinyl acetate, and NVP = *N*-vinylpyrrolidone. Adapted with permission from [7]. © 2012 American Chemical Society. b) Examples of RAFT agents for the monomer classes described below.

The key aspect of a RAFT polymerization is the suitable choice of the R- and Z-group with respect to the monomer according to the following criteria: 1) the CTA and macroCTA should have a reactive C=S double bond (high k_α^{pre} and k_α)[a] , 2) the intermediate radicals should fragment rapidly without side reactions (high k_β^{pre} and k_β)[a], and 3) the R$^\bullet$ radical in the *pre-equilibrium* efficiently re-initiates the polymerization.[5] The Z-group is mainly responsible for the activation of the C=S double bond and the stabilization of the intermediate radical. For the R-group, it is important that re-initiation of the polymerization after the fragmentation in the *pre-equilibrium* is efficient. Therefore, the R-group needs to be a good leaving group compared to the monomer fragment. Typically, mimics of the employed initiator fragments are good candidates for the R-group. A guideline for the selection of suitable Z- and R-groups with respect to the monomers is presented in Figure 2.3a). Different Z- and R-groups are drawn depending on their ability to control the polymerization of the monomers depicted below. Bold arrows indicate good control, while dashed lines correspond to poor control.[7]

---

[a] For a definition of the rate coefficients, see Scheme 2.2.

Examples of CTAs are depicted in Figure 2.3b). 2-Cyano-2-propyl benzodithioate (**1**) and 4-cyano-4-((dodecylsulfanylthiocarbonyl)sulfanyl)pentanoic acid (**2**) are versatile CTAs for the polymerization of the MAM monomers such as styrenes and methacrylates. Other MAM monomers, as for example acrylates, need less stabilized CTAs, such as the trithiocarbonates 4-(((dodecylthio)carbonothioyl)thio)-4-methylpentanoic acid (**3**) and cyanomethyl dodecyl carbonotrithioate (**4**). For the RAFT polymerization of LAMs, such as vinyl acetates, the dithiocarbamate CTA cyanomethyl methyl(phenyl)carbamodithioate (**5**) can be employed.

Post-modification The RAFT moiety does not only enable the controlled radical polymerization but can also be exploited for further post-modification of the polymer.[8] Given that almost all polymers of a RAFT process are equipped with CTA derived end-groups, i.e. a R-group on the α-, and a Z-group on the ω-chain end, tailor-made CTAs are versatile post-modification points. For certain applications, it is of interest to remove the thiocarbonylthio group, due to stability reasons or the inherent color of the sulfur-containing moieties. Transformation of the RAFT group into various other functional groups is also possible *via* different reagents. Other protocols use the RAFT end-group as a ligation point for the attachment of small molecules or the formation of block copolymers *via* an additional end-functionalized polymer. Figure 2.4 summarizes several approaches for the post-modification *via* the RAFT group.[5,6,8]

Transformation into free thiols or the product of a S_N2 reaction is possible *via* addition of nucleophiles, such as amines,[9] azides,[10] or hydroxides.[11] The thiols can be used in subsequent thiol-ene[12] or thiol-yne chemistry[13] or oxidized towards disulfide bridges upon addition of an oxidizing agent.[14] Monteiro and co-workers demonstrated that the formation of disulfide bridged block copolymers can also be reversible.[15] Radical cleavage of the RAFT group in the presence of a radical $I^\bullet$ and H-donors results in the formation of a hydrogen terminated polymer chain.[16] Discekici *et al.* demonstrated the selective one-pot conversion of a trithiocarbonate CTA to a thiol or hydrogen chain-end, depending on the reaction conditions.[17] The access to hydroxyl functionalized polymers is possible

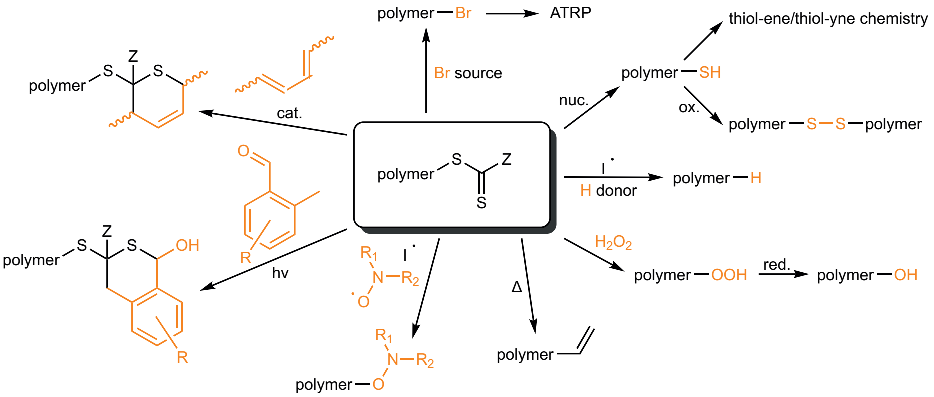
polymer—Br
ATRP
Br source
thiol-ene/thiol-yne chemistry
polymer—SH
nuc.
ox.
polymer—S—S—polymer
Z
polymer
S
S
cat.
O
polymer
S
Z
S
I•
H donor
polymer—H
Z
polymer
S
S
OH
R
R
hν
R1
N—R2
O•
I•
H2O2
polymer—OOH
red.
polymer—OH
Δ
R1
N—R2
polymer—O
polymer

Figure 2.4. Examples for the post-modification of the RAFT group into various other functional groups as described in the text.

via treatment of the RAFT group with H_2O_2 and subsequent reduction.[18] Thermolysis of the polymer eliminates the RAFT group and introduces a terminal alkene, but requires high temperatures ranging from 150–250 °C.[19] Upon treatment with a radical source $I^{\bullet}$, the generated polymer centered radical can also be trapped with nitroxide molecules for subsequent NMP polymerizations.[20] Lee *et al.* showed the direct conversion of the RAFT group into a bromine functionalized polymer for a second polymerization *via* an ATRP protocol.[21] The C=S double bond of the RAFT group can undergo *Diels–Alder* reactions with dienes in the presence of a catalyst.[22] If the Z-group of the RAFT agent is sufficiently activating the C=S double bond, the *Diels–Alder* reaction can proceed without catalyst at room temperature.[23] Photo triggered *Diels–Alder* reactions as described in Section 2.2.3.3 allow the capping of the RAFT group with small molecules[24] or the ligation with other polymers.[25]

2.1.4 Metallopolymers

The field of metallopolymers bridges the gap between organic polymer chemistry and inorganic coordination chemistry.[26] As such, these materials combine the properties of the two chemistries, but also feature new properties, which single polymers or metal complexes have not.

Synthetic hurdles plagued the metallopolymer filed for decades, as it was hard to prepare high MW metallopolymers.[27] Most metallopolymers prepared from the mid to late 20th century had a low MW and were insoluble in common organic solvents. In-depth characterization *via* nuclear magnetic resonance (NMR) spectroscopy and size-exclusion chromatography (SEC) was therefore not possible. In the 1960s and 1970s, a lot of side-chain ferrocene-containing polymers from vinyl-, acrylate-, and methacrylate-ferrocene containing monomers were described due to the facile preparation of ferrocene derivatives *via* S_N reactions.[28] Manners and coworkers were the first to synthesize well-defined high MW metallopolymers through thermal, transition metal-catalyzed, and anionic ring-opening polymerization (ROP) techniques.[29] With the advent of RDRP techniques, the preparation of well-defined metallopolymer architectures became possible.[27,30] Depending on the type of incorporation into the polymer, metallopolymers can be classified according to Rehan[31] and Wolf,[32] as depicted in Figure 2.5.

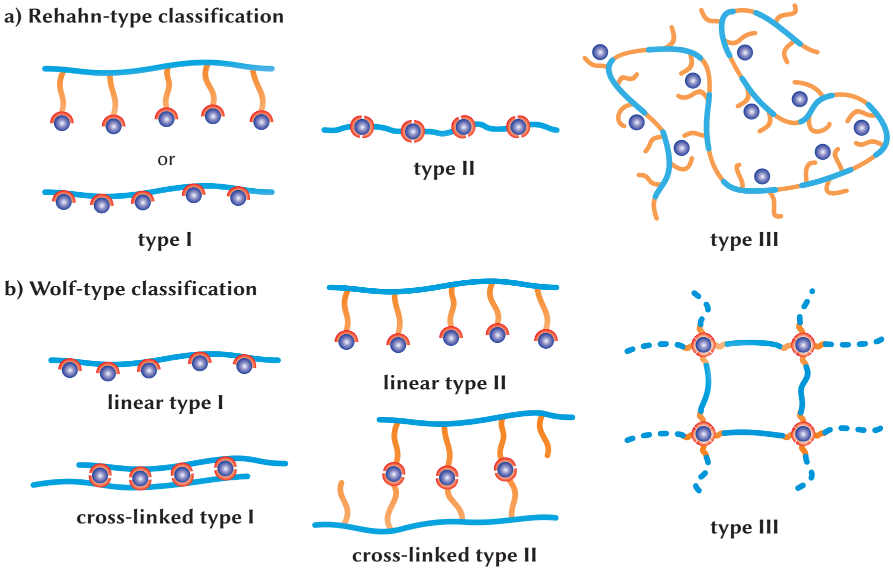

Figure 2.5. Classifications of metallopolymers according to Rehan (a) and Wolf (b).

Rehan and co-workers were the first, who introduced a structural classification based on the metal-polymer interactions. Here, metal complexes are either directly attached to the polymer backbone or *via* a spacer (*type I*). *Type II* metallopolymers feature metal complexes as part of the polymer backbone. Finally, *type III* metallopolymers describe the binding *via* physical interactions.

Wolf proposed an updated and generalized classification, as depicted in Figure 2.5b). Linear metallopolymers are classified into those in which the metal complex directly attached to the backbone (*linear type I*) and those with an additional spacer (*linear type II*). Likewise, this subdivision is also made for cross-linked metallopolymers *via* the metal complex (refer to *cross-linked type I* and *cross-linked type II* in Figure 2.5b). Finally, *type III* metallopolymers, initially named coordination polymers, are nowadays known as metal–organic frameworks (MOFs).[33] In the rest of the current thesis, the classification according to Wolf will be used.

Due to the wide range of possible metallopolymer architectures, this overview will focus on the preparation of *linear type I* and *II* metallopolymers *via* RAFT polymerization. The complexation with metal ions can either be performed prior of after the polymerization. Both strategies were followed in Chapter 3 of the current thesis. In Chapter 4, *linear type I* ligand polymers have been metal loaded in a subsequent step in order to yield *cross-linked type I* metallopolymers with the aim of exclusive intra-chain cross-linking.

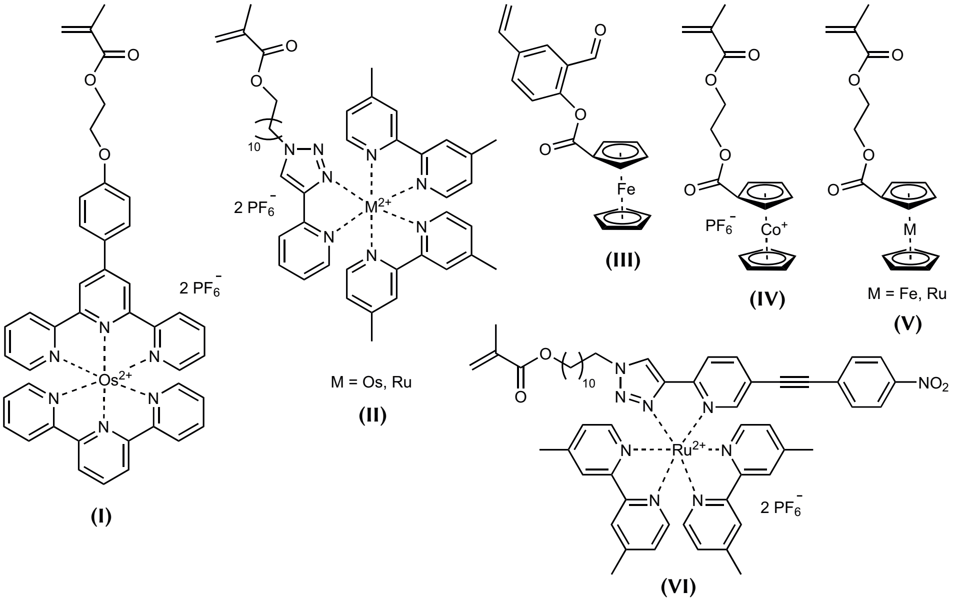

Figure 2.6. Selection of metal complex bearing monomers, which were directly polymerized in a RAFT process.

Metallopolymers *via* RAFT polymerization While metallopolymers can be prepared *via* different RDRP methods,[27] such as ATRP[34] and NMP,[35] this overview will describe approaches employing the RAFT polymerization. Figure 2.6 shows various metal complex containing monomers, which were employed in RAFT polymerizations.

$\mathrm{Os}^{+\mathrm{II}}$-bis-terpyridine functionalized methacrylate (**I**) was polymerized with 2-cyano-2-propyl benzodithioate as RAFT agent. The authors characterized the metallopolymer *via* SEC, electrospray ionization mass spectrometry (ESI-MS), and NMR spectroscopy and determined the redox potentials in film casting experiments.[36] Schubert and co-workers prepared Os$^{+\mathrm{II}}$-, as well as Ru$^{+\mathrm{II}}$-containing metallopolymers *via* the monomer structure (**II**).[37] They incorporated additional Ir$^{+\mathrm{III}}$ into the ruthenium containing metallopolymer and performed hydrogen evolution experiments. The energy transfer was investigated in the Os$^{+\mathrm{II}}$-metallopolymer *via* excitation-emission correlation spectroscopy. Lu and co-workers polymerized a ferrocene-containing styrene derivative (**III**) in a RAFT process with a narrow *Đ* of 1.2 and determined the end-group fidelity *via* desorption-ionization time-of-flight mass spectroscopy.[40] Zhang *et al.* made block copolymers of the cobaltocenium- (**IV**) and ferrocene-functionalized methacrylate (**V**). They demonstrated the reversible redox chemistry for the cobaltocenium units and made spherical micelles *via* self-assembly.[41] Tang and co-workers combined RAFT and ATRP protocols for the corresponding ruthenocene-containing monomer (**V**) and fabricated amphiphilic

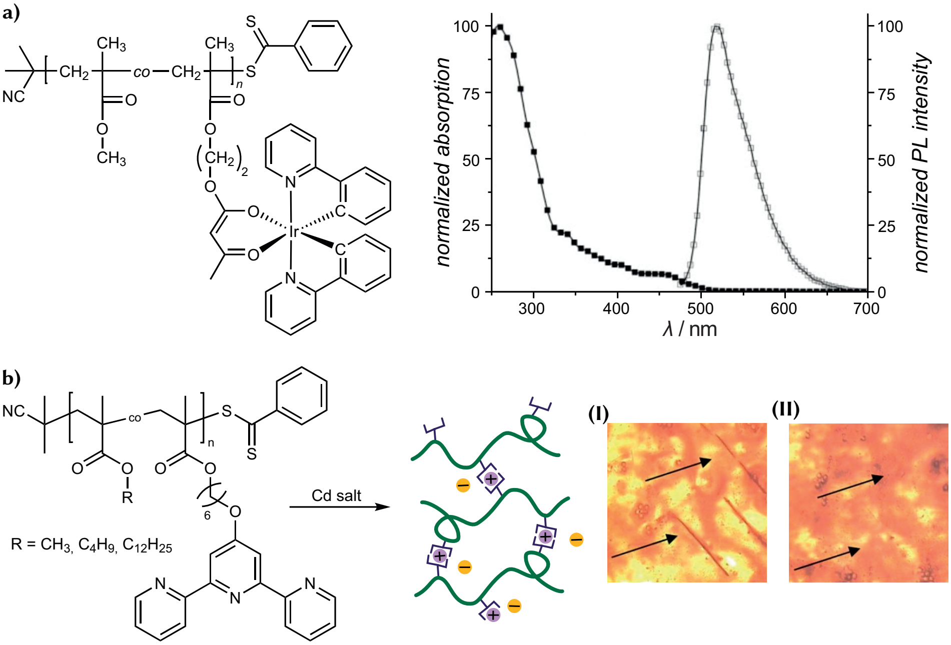

Figure 2.7. a) Phosphorescent Ir$^{+\mathrm{III}}$ emitter containing metallopolymer *via* a post-loading approach. The inset shows the polymer structure, as well as the UV-Vis and emission spectra. Adapted with permission from [38]. © 2010 Wiley-VCH Verlag GmbH & Co. KGaA. b) Polymer structure of a terpyridine containing copolymer and subsequent metal complexation with cadmium resulting in network formation with self-healing capabilities. Pictures after scratching (**I**) and after annealing at 100 °C for 16 h (**II**). [39] – Adapted by permission of The Royal Society of Chemistry.

diblock copolymers for self-assembled morphologies.[34f] Happ *et al.* copolymerized the luminescent ruthenium monomer (**VI**) with an organic 1,3-thiazole donor system and demonstrated the donor-acceptor properties with an energy transfer efficiency of >70 %.[42]

While these examples were fabricated *via* direct polymerization of a metal complex containing monomer, several strategies were described, which incorporated the metal into a ligand functionalized polymer after the polymerization (see Figure 2.7). Schubert and coworkers synthesized a phosphorescent $\mathrm{Ir}^{+\mathrm{III}}$ emitter containing metallopolymer.[38] They first copolymerized an acetoacetate ligand and performed subsequent metal loading with an $\mathrm{Ir}^{+\mathrm{III}}$ precursor complex in solution (see Figure 2.7a). The successful metallopolymer formation was evidenced by NMR spectroscopy, ultraviolet-visible (UV-Vis) measurements, and emission spectroscopy, as well as SEC. The authors proposed the application of the material for polymer light-emitting diodes (PLEDs). Bode *et al.* synthesized a terpyridine functionalized polymer *via* RAFT polymerization.[39] Subsequent complexation with a cadmium salt led to the formation of a polymeric network through inter-chain cross-linking. Scratches in the network vanished after heating at elevated temperature for several hours (see Figure 2.7b) (**I**) and (**II**), respectively).

2.2 Photochemistry

The following section provides basic concepts in photochemistry, covering the photochemical and -physical principles relevant for the present thesis. After a historical reflection, a physical description of photochemical processes is presented. Various models describing the complex photochemical systems are discussed (see Section 2.2.1) and the chemistry of photochromic molecules employed in the current thesis is explained in Section 2.2.2. Finally, examples of photo triggered ligation protocols which are employed in Chapter 3 of the current work are presented in Section 2.2.3.

Long before humans, nature took advantage of the unique opportunities offered by photochemistry and uses the energy delivered *via* photons to trigger and modify a plethora of reactions, the arguably most well-known being photosynthesis. The first observations occurred mainly by accident and coincidence. In 1777, Carl W. Scheele observed that violet light was superior in darkening silver chloride to any other wavelength employed. In the beginning of the 20th century, the theoretical concepts developed by Einstein, Planck, Stark, Bodenstein and others opened a new era of photochemistry.[43] A limiting factor at that time was the insufficient availability of analytical techniques and light sources emitting light with defined wavelengths.

Many advantages of photochemistry and the impact on chemical synthesis were already outlined in that time by Giacomo Luigi Ciamician (1857–1922). His statements made 100 years ago seem today as a prophecy:[44]

> “It is thus possible that using the irradiation energy might become interesting in another way. When all of the coal will have been burnt, it may become necessary to resort to exploiting light energy for the progress of society.”

One of the first systematic studies in the field of photochemistry was conducted by Norrish and coworkers in the late 1930s.[45] Since that time, progress in experimental and analytical techniques stimulated each other and has led to the wide area of photochemistry existing today. In many cases, photochemistry can achieve what ground-state chemistry is incapable of and contributes enormously to the chemical reaction toolbox.

2.2.1 Physical description of photochemical processes

Light is electromagnetic radiation, characterized by a wavelength λ, a frequency ν, and a speed c, which are related by the relationship given in Equation (2.14).

$$\lambda\nu = c \tag{2.14}$$

The value of c is the speed of light, which is a natural constant (2.998×10^{8} m s^{-1} in vacuum). Einstein proposed that light energy is quantized in small portions called photons. The photon is the quantum of light and the smallest possible amount of light at a given frequency ν. The energy E of one photon is related to the frequency ν by the *Einstein equation*, with $h = 6.63\times10^{-34}$ Js being the *Planck's constant* (see Equation (2.15).

$$E = h\nu \tag{2.15}$$

This description of light as an ensemble of individual photons is critical for the understanding of photochemistry and is expressed in the two laws of photochemistry:

1) Only absorbed light is effective in photochemical transformations (*Grotthuss–Draper* law).

2) Light absorption is a quantum process. Usually, one photon is absorbed by a single molecule (*Stark–Einstein* law).

A depiction of the electromagnetic spectrum and the corresponding frequencies ν, wavelengths λ, and energies E is given in Figure 2.8, with description of the various wavelength regimes and a zoom-in into the visible light region and the respective perception of colors.

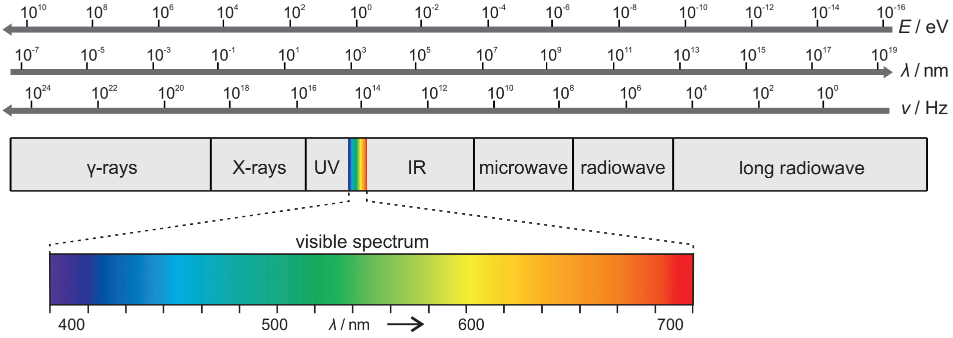

10^{10} 10^{8} 10^{6} 10^{4} 10^{2} 10^{0} 10^{-2} 10^{-4} 10^{-6} 10^{-8} 10^{-10} 10^{-12} 10^{-14} 10^{-16}
E / eV
10^{-7} 10^{-5} 10^{-3} 10^{-1} 10^{1} 10^{3} 10^{5} 10^{7} 10^{9} 10^{11} 10^{13} 10^{15} 10^{17} 10^{19}
λ / nm
10^{24} 10^{22} 10^{20} 10^{18} 10^{16} 10^{14} 10^{12} 10^{10} 10^{8} 10^{6} 10^{4} 10^{2} 10^{0}
ν / Hz
γ-rays
X-rays
UV
IR
microwave
radiowave
long radiowave
visible spectrum
400
500
λ / nm
600
700

Figure 2.8. The electromagnetic spectrum with the energy in electron volt (eV), the equivalent wavelength (nm) and the corresponding frequency (Hz). The spectrum is separated into different regimes as described in the gray horizontal bar. A zoom-in into of the visible light region is depicted below with the different perception of colors.

Beer–Lambert's law describes the absorption of a monochromatic light beam of intensity I_0 by a solution of concentration c after a path length b through the medium, leading to the reduced intensity I. Taking the logarithm of Equation (2.16a) leads to a linear correlation between I and I_0 (see Equation (2.16b). A is called the *absorbance* and ϵ the *molar attenuation coefficient*. It is important to note, that the *Beer–Lambert's* law only holds true for diluted solutions in which no concentration-dependent aggregation does occur (see also Section 2.2.2.1).

$$I = I_0 \cdot 10^{-\epsilon bc} \tag{2.16a}$$

$$A = \log\left(\frac{I_0}{I}\right) = \epsilon bc \tag{2.16b}$$

After the initial absorption of a photon with the energy $h\nu$ by a molecule A into the excited state A*, several processes can occur. Some general cases are depicted in Figure 2.9, with the speed of a potential photo reaction defined by the respective rate law constants.

The different rate coefficients in Figure 2.9 such as k_p, k_r, and k_nr are part of the respective rate laws, defining the rate of product formation P, radiative deactivation, and non-radiative deactivation, the latter two leading back to the ground state molecule A. Note that the term luminescence summarizes fluorescence, phosphorescence, as well as chemiluminescence.[46] The product P does not necessarily need to be a ground state molecule but can also be the outcome of a transformation into another excited state, such as triplet states. Each process in Figure 2.9 is called a *primary process* for which a quantum yield (Φ_i) can be defined by Equation (2.17a) and Equation (2.17b). As such, Φ_i represents the efficiency of a photochemical process.

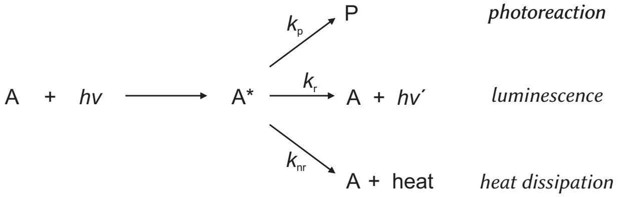

Figure 2.9. Primary steps after the interaction between light with the energy $h\nu$ and a molecule A. A chemical reaction with the rate constant k_p leads to the formation of product P (top). Luminescence associated with the rate k_r to the ground state A and release of a photon with energy $h\nu$ (middle). Non-radiative deactivation can occur *via* heat dissipation with a rate k_nr (bottom).

$$\Phi_\mathrm{i} = \frac{\text{Number of molecules undergoing process i}}{\text{Total number of photons absorbed}} \tag{2.17a}$$

$$\Phi_\mathrm{p} = \frac{k_\mathrm{p}}{k_\mathrm{p} + k_\mathrm{r} + k_\mathrm{nr}} \tag{2.17b}$$

Another important quantity is the *lifetime* $\tau(\mathrm{A}^*)$ of the respective excited state A^*, as given by Equation (2.18). It is the inverse of the sum of all rate deactivation rate constants.

$$\tau(\mathrm{A}^*) = \frac{1}{k_\mathrm{p} + k_\mathrm{r} + k_\mathrm{nr}} \tag{2.18}$$

Φ_i and τ of the respective primary steps are correlated *via* k_i (refer to Equation (2.19)).

$$k_\mathrm{i} = \frac{\Phi_\mathrm{i}}{\tau(\mathrm{A}^*)} \tag{2.19}$$

Rigorous treatment of photochemical processes with quantum chemistry results in the so-called transition dipole moment M_if of an initial state i and a final state f (see first line of Equation (2.20).[43] M_if answers the question whether a photochemical process is in principle possible or not. Ψ_i and Ψ_f are the wave functions of the initial and the final state, respectively and $\hat{\mu}$ the *dipole-moment operator.*

$$\begin{aligned} M_{\mathrm{if}} &= \int \Psi_{\mathrm{i}}\hat{\mu}\Psi_{\mathrm{f}}\mathrm{d}\tau \\ &= \int \phi_{\mathrm{i}}\hat{\mu}\phi_{\mathrm{f}}\mathrm{d}\tau_{\mathrm{e}} \int S_{\mathrm{i}}S_{\mathrm{f}}\mathrm{d}\tau_{\mathrm{s}} \int \theta_{\mathrm{i}}\theta_{\mathrm{f}}\mathrm{d}\tau_{\mathrm{N}} \end{aligned} \tag{2.20}$$

The *Born-Oppenheimer* approximation enables the separation of the electronic wave function from the wave function of the nuclei, which is denoted as θ.[47] Further split of the electronic wave function into a one electron wave function ϕ and a spin function S leads to the expression given for M_{if} in the second line of Equation (2.20). The first integral called the *electronic transition moment*, the middle one the *spin overlap integral*, while the square of the third integral is known as the *Franck–Condon* factor (FCF).[48]

For a specific transition i → f to occur, the transition dipole moment must be non-zero. The selection rules for electronic transitions are the result of the *electronic transition moment*. The *spin overlap integral* states that during an electronic transition, the spin multiplicity must be preserved. In cases where this rule is violated, the transition is called *spin forbidden*. This is especially relevant for molecules containing heavy atoms, like some of the metal complexes used in the present thesis. The intensity of the actual transition can be estimated *via* the FCF, which is known as the *Franck–Condon* principle.[48a,b,49]

When applying the *Born–Oppenheimer* approximation, it is possible to visualize the energy of the ground and excited electronic state with respect to the nuclear coordinates.[47] An example is depicted in Figure 2.10a). The potential energy curves of the ground and the excited state are visualized by the bold lines in yellow and red, respectively. An absorption results in a so-called *vertical transition*, which reflects the fact that the nuclei are considered at fixed position during electronic excitations in the *Born–Oppenheimer* approximation. The nuclei coordinates of the relaxed energies of the ground state differ from those of the excited state, leading to an intensity pattern of the possible transitions into various vibrational states as shown on the left side of the energy axis. The intensity distribution of the various transitions can be calculated by the FCF.

While the picture drawn in Figure 2.10a) may be illustrative for small molecules, it fails with increasing molecular size. A suitable presentation of such systems is obtained by the so-called *Jablonski* diagram.[50] An example is depicted in Figure 2.10b) with the energy levels of the various excited states relative to the ground state S_0 in yellow. The gray lines represent excited vibrational states.

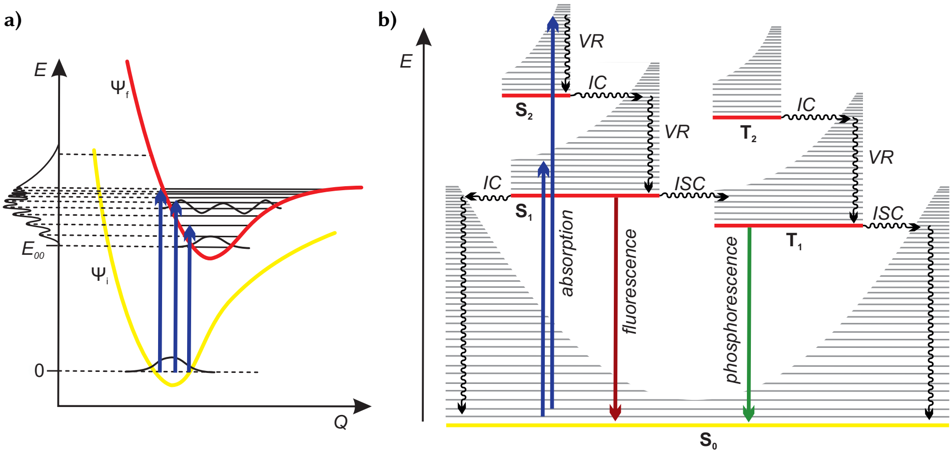

Figure 2.10. a) Schematic explanation of vertical electronic transitions from a ground state Ψ_i to an excited state Ψ_f. E is the energy scale and Q the nuclear coordinates of the respective molecule. E_ab represents the energy of a vibronic transition from $\Psi_{\mathrm{v=a}} \leftarrow \Psi_{\mathrm{v=b}}$. b) *Jablonski* diagram, depicting the energy levels of a molecule with the possible intramolecular photo processes as described in the text. Adapted with permission from [43]. © 2014 Wiley-VCH Verlag GmbH & Co. KGaA.

Excitation from the S_0 state into excited singlet states S_1 or S_2 can occur upon irradiation.(a) The distribution into the respective vibrational levels is dictated by the FCFs. The combination of an electronic and vibrational transition is referred to as *vibronic transition*. Fast *vibrational relaxation* (VR) brings the excited molecules to the lowest vibrational level in the respective state. From a here, *internal conversion* (IC) denotes the isoenergetic radiationless transition between two electronic states having the same multiplicity, e.g. from S_1 to S_0. On the other hand, *intersystem crossing* (ISC) describes the isoenergetic radiationless transition between two electronic states of different multiplicity, e.g. from T_1 to S_0. The spontaneous emission of a photon from the molecule in the excited state is termed *fluorescence*, if the spin multiplicity is retained. The corresponding process involving a change in spin multiplicity is termed *phosphorescence*, which typically involves a transition from the first excited triplet state T_1. As this transition is *spin-forbidden*, phosphorescence occurs on a much longer timescale than fluorescence. Fluorescence, as well as phosphorescence are following the *Kasha–Vavilov* rule, which states that quantum yield of the luminescence is independent of the excitation wavelength, i.e. the process occurs from the lowest vibrational level of the respective excited state.[51] As in the case of singlet excited states, ISC can also occur from a triplet state into a singlet state.

(a) Single photon excitations mainly occur into the S_1 state, although higher order excitations are possible if allowed *via* the selection rules.

Table 2.1 summarizes the above described photophysical processes together with their corresponding timescales.

Table 2.1. Summary of the photophysical processes described in the text and their corresponding time scales. Reproduced with permission from [46]. © 2009 John Wiley & Sons, Ltd.

Process	Abbreviation	Time scale / s
Absorption	–	10^{-15}
Internal conversion	IC	10^{-12}–10^{-6}
Intersystem crossing (S → T)	ISC	10^{-12}–10^{-6}
Intersystem crossing (T → S)	ISC	10^{-9}–10^{1}
Vibrational relaxation	VR	10^{-13}–10^{-12}
Fluorescence	–	10^{-9}–10^{-7}
Phosphorescence	–	10^{-6}–10^{-3}

2.2.2 Photochromic molecules

The first reports of the phenomenon later called “photochromism” date bake to the end of the 19th century, where Fritzsche described a molecular photochromism.[52] These observations have been termed *phototropy* and *phototropism*,[53] while the term *photochromism* was suggested by Hirshberg in 1950.[54]

Photochromic molecules respond to light as an external stimulus. Upon irradiation, the molecule undergoes a reversible transformation in geometry, polarity, as well as charge distribution.[55] Light as the stimulus has the advantage that it does not contaminate the system, is orthogonal to most other processes and non-toxic. In addition, light can be delivered with high spatial and temporal control, precise wavelength, as well as defined intensity.[56]

The photodynamic system of a photochromic molecule allows the population of a less stable or metastable state, as compared to the thermal ground state.[57] Figure 2.11 illustrates the differences between thermal and photodynamic equilibrium. In the thermal case (a), the two energy levels (**I**) and (**II**) are populated according to the Boltzmann distribution and is given by the equilibrium constant K_{eq}^{Δ}. Forward and backward reactions take place *via* the same transition state on the same potential energy surface (principle of microscopic reversibility).

In the dark case of the photodynamic system (b), the activation barrier is too high for thermal transformations. Upon irradiation with a suitable wavelength (c), the molecule can transit into an excited state, from which it can relax into state (**II**). The backward reaction can either take place spontaneously in the dark, or *via* irradiation with a different wavelength (d). As such, the equilibrium involves two different pathways and can involve

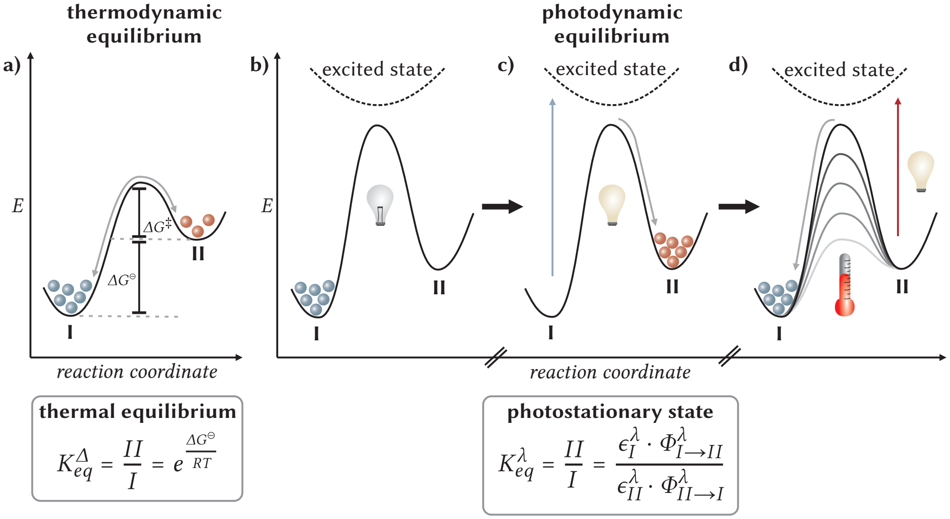
thermodynamic equilibrium
photodynamic equilibrium
a)
b)
c)
d)
E
E
excited state
excited state
excited state
$\Delta G^{\ddagger}$
$\Delta G^{\ominus}$
I
II
I
II
I
II
I
II
reaction coordinate
reaction coordinate
thermal equilibrium
$K_{eq}^{\Delta} = \frac{II}{I} = e^{\frac{\Delta G^{\ominus}}{RT}}$
photostationary state
$K_{eq}^{\lambda} = \frac{II}{I} = \frac{\epsilon_I^{\lambda} \cdot \Phi_{I\rightarrow II}^{\lambda}}{\epsilon_{II}^{\lambda} \cdot \Phi_{II\rightarrow I}^{\lambda}}$

Figure 2.11. Comparison between thermodynamic (a) and photodynamic (b–d) equilibria. The Boltzmann distribution dictates the population of the energy levels (I) and (II) in the thermal case (a) with the equilibrium constant K_{eq}^{Δ}. The difference between the energy levels is given by $\Delta G^{\ddagger}$ and $\Delta G^{\ominus}$. (b) Exclusive population of state (I) in the dark as a result of a high energy barrier. (c) Transition into an excited state upon irradiation and relaxation into state (II). (d) Depopulation of state (II) *via* thermal fading (T-type photochromism) or photo excitation (P-type photochromism). The photodynamic equilibrium constant K_{eq}^{λ} in this case is depicted below the graph and depends on the molar extinction coefficients and the quantum yields of the for- and backward reaction. [57] – Adapted with permission of The Royal Society of Chemistry.

the potential energy surface of an excited state, i.e. the principle of microscopic reversibility does not apply. The equilibrium constant for the resulting photostationary state (PSS) in the absence of thermal fading, i.e. the ratio between **(I)** and **(II)** under continuous irradiation with wavelength λ is given by K_{eq}^{λ}, which depends on the molar extinction coefficients ϵ_I^{λ} and ϵ_{II}^{λ}, as well as the quantum yields $\Phi_{I\rightarrow II}^{\lambda}$ and $\Phi_{II\rightarrow I}^{\lambda}$ of the two reactions. Depending on the energy barrier for the **(II)** to **(I)** backward reaction, photochromic molecules are classified as either *P-type* or *T-type*. For *P-type* molecules, the activation barrier is too high for a thermal reaction, resulting in a thermally bistable system. In contrast, *T-type* molecules are thermally labile, i.e. exhibit thermal depopulation of state **(II)**.

Figure 2.12 gives an overview over photochromic molecules. Two examples of *P-type* photochromic molecules are diarylethenes[58] and fulgides.[59] In these systems, the transformation in both directions is based on the electrocyclic [2_π+2_π+2_π] rearrangement, i.e. both isomerizations are photochemical reactions. Azobenzene[60] and flavylium systems[61] exhibit a (E)$\rightleftharpoons$(Z) double-bond isomerization and belong to the *T-type* photochromic molecules. Finally, SPs and spirooxazins[62] are also *T-type* photochromes, but undergo reversible photo activated cyclization/ring-opening reactions.

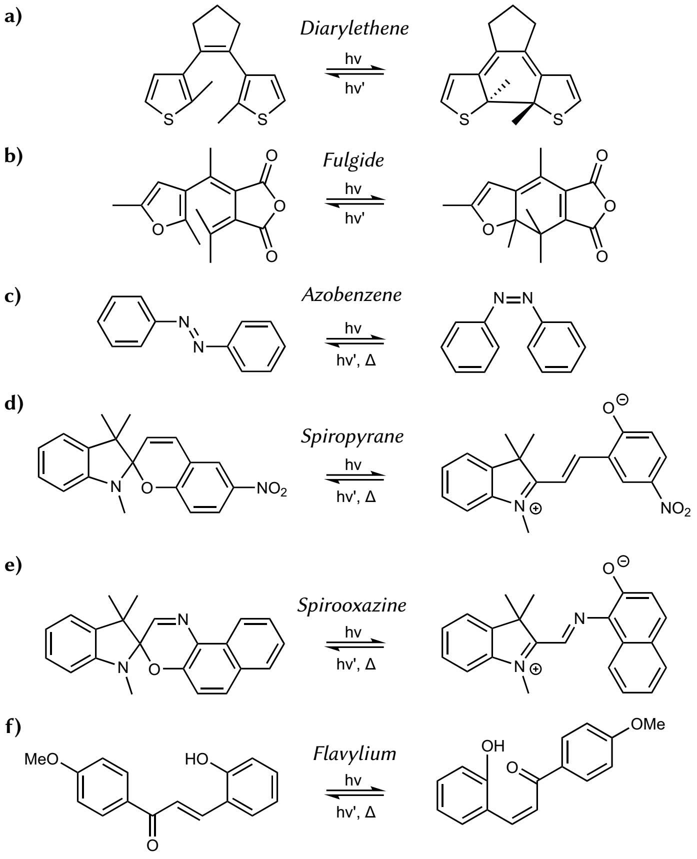
a)
Diarylethene
hv
hv'
S
S
S
S
b)
Fulgide
hv
hv'
O
O
O
O
O
O
O
O
c)
Azobenzene
hv
hv', Δ
N
N
N=N
d)
Spiropyrane
hv
hv', Δ
N
O
NO2
O⊖
N⊕
NO2
e)
Spirooxazine
hv
hv', Δ
N
N
O
O⊖
N
N⊕
f)
Flavylium
hv
hv', Δ
MeO
HO
O
OH
O
OMe

Figure 2.12. Most prominent families of molecular photochromic molecules. Diarylethenes (a) and fulgides (b) are examples of *P-type* photochromic molecules that isomerize *via* electrocyclic rearrangements. *T-type* photochromic molecules are for example azobenzenes (c) or flavylium molecules (f), which undergo (E)$\rightleftharpoons$(Z) double-bond isomerizations. Spiropyrans (d) and spirooxazins (e) are also *T-type* photochromes, but with reversible cyclization/ring-opening isomerizations.

Every class of photochromic molecules described above has its unique set of properties, which can be tuned to take into account the desired applications. Parameters include the quantum yields Φ, the molar extinction coefficients ϵ, the spectra shape of the absorption, the position of the PSS, the speed of switching and thermal stability of both isomers, and the resistance towards degradation (fatigue) of the photochrome.[56] The following section describes the photochemistry of SPs in more detail, which was exploited in Chapter 4 and 5 of the present thesis.

2.2.2.1 Spiropyrans

Fischer and Hirshberg were the first who described the photochemistry of SPs in the early 1960s.[63] The general structure of SPs and their photochromism is depicted in Scheme 2.3. The close-ring isomer is abbreviated as “SP”, while the open-ring isomer is abbreviated as “MC”, from the analogy to the structure of merocyanines. The MC form can either be drawn as a zwitterionic or a quinoidal structure, while the real structure is a hybrid of both.

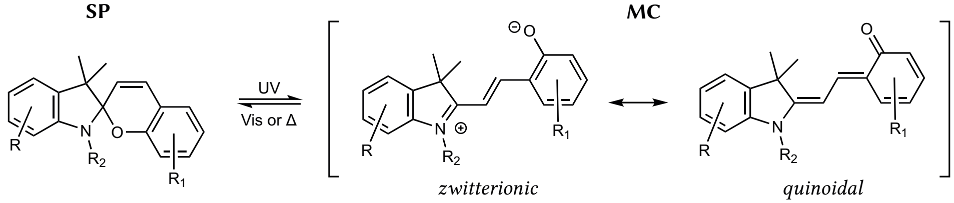

Scheme 2.3. General structure motif of the photochromic SP molecule and its open-ring MC isomer.

The unique properties of SPs compared to other photochromic molecules arise from the vastly different properties of the two isomers. First, the charge separation in the MC form results in a large electric dipole moment compared to the SP isomer.[64] Secondly, the structural differences between SP and MC geometries results in less occupied volume of the SP as compared to the MC form.[62c] Thirdly, the SP isomer is mostly transparent in the visible light region, whereas the MC form exhibits a strong absorption between 450–650 nm. In addition, the MC form shows strong fluorescence, while the SP form does not show significant emission.[65] Fourthly, the MC isomer is significantly more basic than the SP isomer and can be protonated at the oxygen atom.[66] Finally, the MC form also exhibits more affinity to other chemical species, such as metal ions or other zwitterionic species.[62c]

Synthesis The synthesis of SP molecules is straightforward and has been reviewed extensively.[53,62b,d,67] The most common methods are the condensation of a *N*-heterocyclic quaternary ammonium salt with a vicinal alkyl group with respect to the nitrogen (**a**) or the corresponding methylene base (**b**) with a 2-hydroxyarenealdehydes (**c**), i.e. salicylaldehydes, in refluxing ethanol solutions (see Scheme 2.4).[62c]

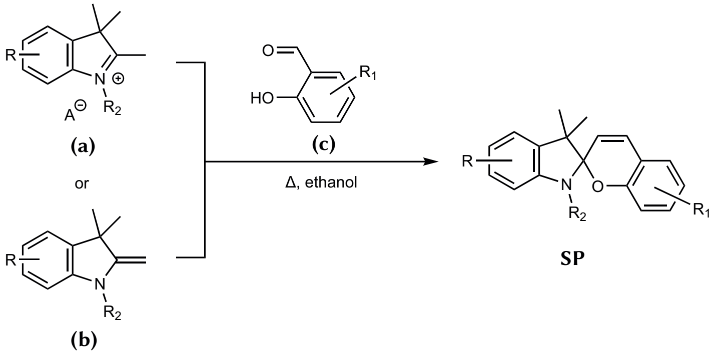

Scheme 2.4. The two most common synthesis strategies towards SP molecules. Condensation of a cyclic quaternary ammonium salt (a) or the corresponding methylene base (b) with a salicylaldehyde (c).

Isomerization mechanism The SP⇌MC isomerization can not only be triggered by light, but also by other stimuli, such as temperature[62d] (*thermochromism*), pH[68] (*acidochromism*), solvent polarity[69] (*solvatochromism*), metal ions,[70] redox potential[71] (*electrochromism*), or mechanical force[62d] (*mechanochromism*).

The *photochromism* and *acidochromism* of SPs is depicted in Scheme 2.5a).[62c] Transformation of SP (**1**) to MC (**2**) occurs *via* irradiation with UV light, while the reverse reaction is possible through irradiation with visible light or thermal fading. Upon protonation, the SP form (**1**) can be protonated towards SPH$^+$ (**3**). However, this species is not stable in solution and quickly ring-opens towards the protonated MCH$^+$ species (**4**), which is also indicated by the direct transformation of SP to MCH$^+$ in the middle. MCH$^+$ is also accessible *via* the MC form (**2**) at low pH values.

A comparison between the thermal and photochemical pathway of the SP to MC interconversion is illustrated in Scheme 2.5b). In the photochemical path on the top, irradiation with UV light around 365 nm gives rise to the MC isomer in a first-order process.[72] The heterolytic cleavage of the spiro C—O bond forms the *cis*-MC (**5**) isomer, which transforms into the *trans*-MC species (**6**) upon rotation about the central C—C bond. Interestingly, this ring-opening can also be achieved *via* two-photon excitation using near-infrared (NIR) irradiation,[70b,73] which will be exploited in Chapter 5 of the current thesis.

On the bottom half of Scheme 2.5b), the thermal SP to MC interconversion is depicted. In this case, the mechanism is a 6π electrocyclic ring-opening, which first results in the formation of the quinoidal form of the *cis*-MC isomer (**7**). Rotational isomerization towards *trans*-MC species (**8**) completes the transformation. The final MC structure is a hybrid of the two resonance structures (**6**) and (**8**).

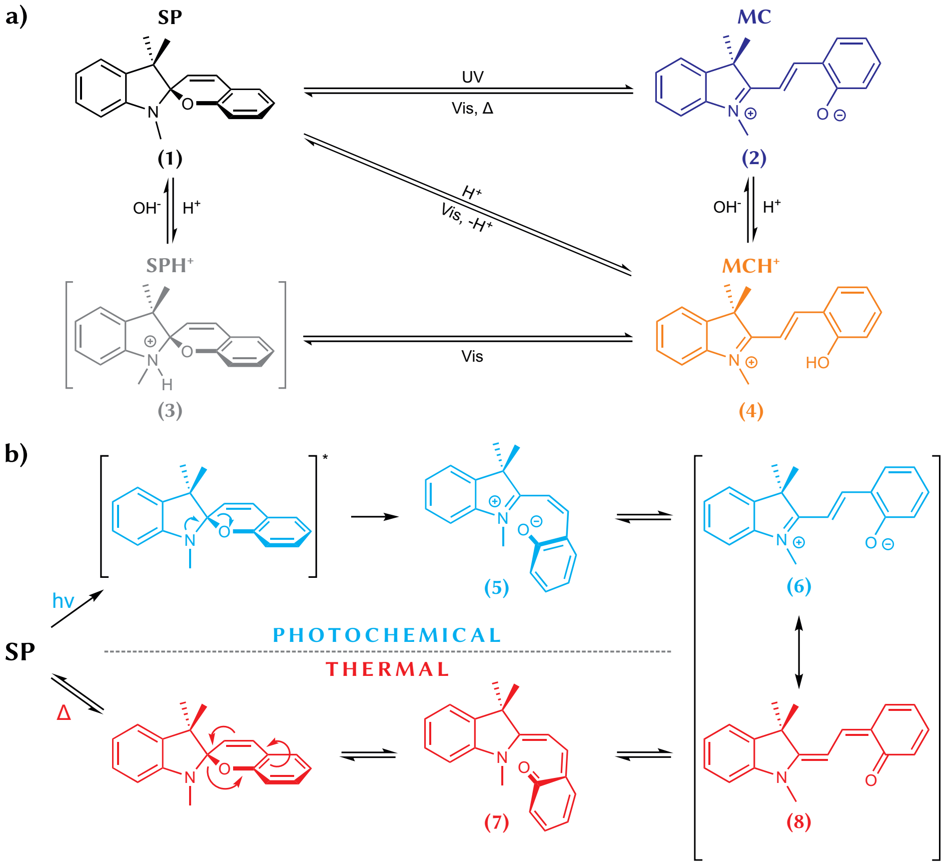

Scheme 2.5. a) *Photochromism* and *acidochromism* of SP molecules. Reversible transformations between the four states: SP (**1**), MC (**2**), protonated SP SPH⁺ (**3**), and protonated merocyanine MCH⁺ (**4**). b) Comparison between photochemical (top) and thermal ring-opening (bottom) mechanism. The resultant MC forms (**6**) and (**8**) are resonance structures of each other. [62c] – Adapted by permission of The Royal Society of Chemistry.

The mechanism and the involved excited species for the photochemical transformation has been investigated in great detail and can be divided in SP molecules without a nitro-group in the 6-position of the benzopyrane ring and those without substituents (see

Scheme 2.6a) and b), respectively).[68b,70a,74] For 6-nitro substituted SPs, excitation of SP into the singlet state is followed by ISC into ^{3}SP*. From here, ring-opening occurs towards the triplet state ^{3}MC*$_{perp}$, which transforms into ^{3}MC*$_{trans}$ through rotation. Additional ISC and IC results in the MC isomers CTC and TTC (for the description of the abbreviations, see Scheme 2.7 and discussion thereof). This mechanism is also called the *Görner–Chibisov* mechanism.[62a] In contrast, no triplet states are involved for SP

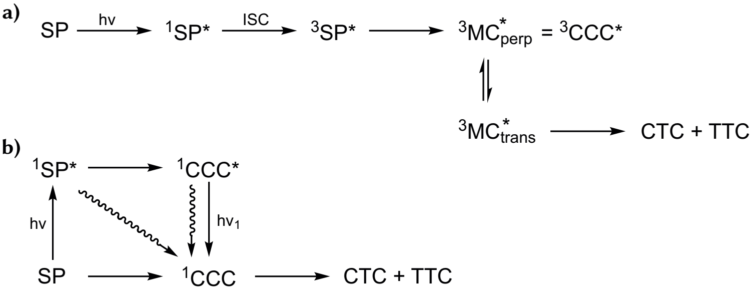

Scheme 2.6. a) *Görner–Chibisov* mechanism of the photo triggered ring-opening of SPs with a nitro-group in the 6-position of the benzopyran ring, involving triplet states. b) Ring-opening mechanism for SP molecules without an electron-withdrawing group in the 6-position only occurs *via* singlet excited states. Adapted with permission from [62d]. © 2004 American Chemical Society.

molecules without electron withdrawing groups in the 6-position of the benzopyrane ring (see Scheme 2.6b). Here, the SP can either directly ring-open towards the ^{1}CCC isomer (thermal way), or, upon irradiation, undergo the ring-opening from the ^{1}SP* state towards the ^{1}CCC* excited state, from which IC or irradiation with another wavelength results in the ^{1}CCC isomer. From here, rotational isomerization finally also results in the CTC and TTC MC isomers.[62a,d]

Scheme 2.7 illustrates the different possible isomers and their interconversion.[62a] Electrocyclic 6π ring-opening (thermally) or heterolytic C—O bond cleavage (photochemically) of *(R)*-SP in the top line yields a sterically strained intermediate, which rapidly converts to the nearly planar CTT MC isomer. The abbreviations highlighted in green are referring to the orientation relative to the two double bonds (*cis*, *trans*; C and T) and the central single bond (*s-cis*, *s-trans*; C, T). Only the *s-trans* isomers are depicted in Scheme 2.7, because the *s-cis* conformers are significantly higher in energy.[62b] Consecutive rotational isomerizations result in the formation of the CTC, TTC, and TTT isomers, from which the CTC and TTC are the thermodynamically most stable ones. Final ring-closure from the TTT form yields the *(S)*-SP stereoisomer. As depicted in the middle of Scheme 2.7, the MC forms can form supramolecular aggregates, which was exploited in Chapter 5 of the current thesis.

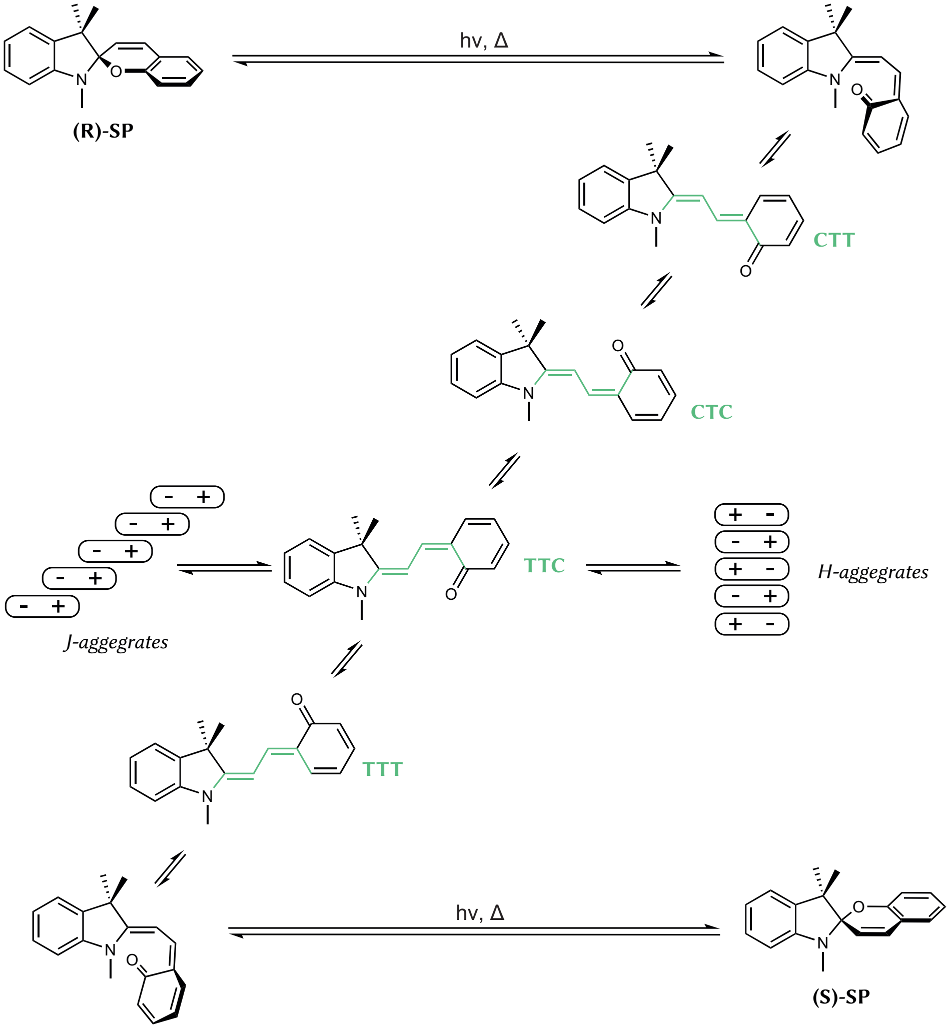

Scheme 2.7. Various MC isomer structures in solution and their interconversion through bond rotations. The MC isomers are capable to form supramolecular aggregates. Adapted with permission from [62d]. © 2004 American Chemical Society.

Aggregation of the MC isomer A result of the molecular structure of the MC isomer is its tendency to aggregate. The driving force for this aggregation behavior are mainly dipole–dipole interactions along with π–π stacking, which readily occurs in hydrophobic solvents.[75] The two different stacking possibilities are depicted in Scheme 2.7. Parallel "head-to-tail" arrangements of the MC dipoles are called *J-aggregates*, whereas antiparallel "side-by-side" stackings are referred to as *H-aggregates*.[62c] *J-aggregates*,[76] as well as *H-aggregates*[77] have been observed for SPs, and even exist in parallel.[78]

Krongauz *et al.* described the formation of SP-MC dimers, as well as charge-transfer (CT) complexes of small SP molecules resulting in the formation of supramolecular aggregates with a degree of association $>10^6$. The resulting macroscopic structures were in the micrometer range.[76a] In addition, aggregates of the type SP-MC, MC_n, and SP_nMC_m were described.[79] The aggregation stabilizes the MC isomers and strongly retards,[78a,80] or even suppresses[81] the ring-closing reaction.

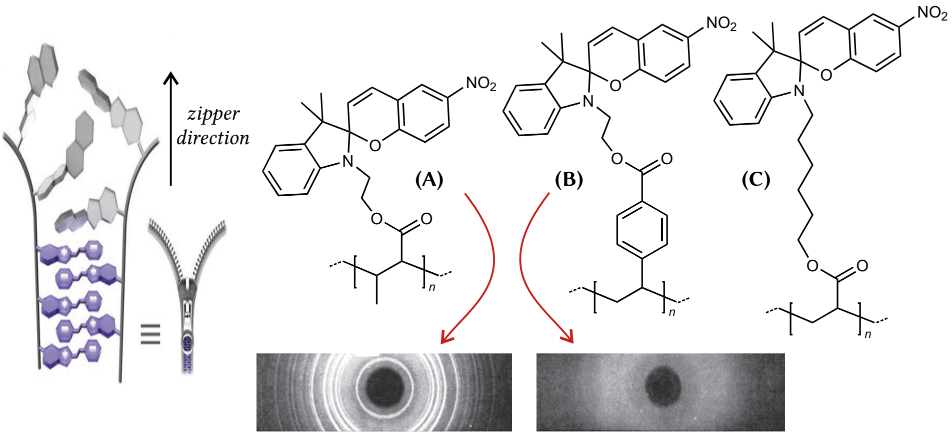

Figure 2.13. Illustration of the "zipper crystallization" found in SP-functionalized methacrylate polymers (**A**). Styrene- (**B**) or acrylate-based polymers (**C**) do not show such crystallization behavior. The X-ray powder diffraction of (**A**, left) and (**B**, right) are depicted below the structures. [62c] – Adapted by permission of The Royal Society of Chemistry.

For SP containing methacrylate copolymers, a mechanism termed "zipper crystallization" results in polymer crystals which are stable even at 150 °C.[77a,c,82] Interestingly, the authors demonstrated that styrene- or acrylate-type polymers did not show such behavior, which was attributed to the more rigid (styrene) or more flexible (acrylate) nature of the polymer backbone (see Figure 2.13).

Bell and co-workers exploited the strong tendency of SPs towards self-organization for UV-induced aggregation of colloidal silica particles functionalized with SP-bearing methacrylate polymers in toluene solution.[83] They showed that the UV-induced flocculation process was fully reversible upon visible light exposure and agitation.

George *et al.* combined the aggregation behavior of SP-functionalized colloids with direct laser writing (DLW, see Section 2.3).[73c] The local control of the aggregation behavior *via* a two-photon absorption (TPA) led to stable architectures in solution. The redispersal of the structures was achieved through ultrasonication in toluene or THF.

Metal complexation The photochemical or thermal SP→MC transformation results in the drastic alteration of the electron-donor ability of the ring oxygen of the molecule. The phenolate oxygen of the MC form can serve as a ligation center for various metal ions.[84] As such, the switching between the two isomers is of interest for applications, such as metal ion sensing under the influence of external stimuli, i.e. light, which was investigated in Chapter 4 of the current thesis. In the absence of additional ligation sites except the phenolate oxygen atom, the complex binding constants are rather weak and light induced ring-closure results in the expulsion of the metal ion.[62c,85]

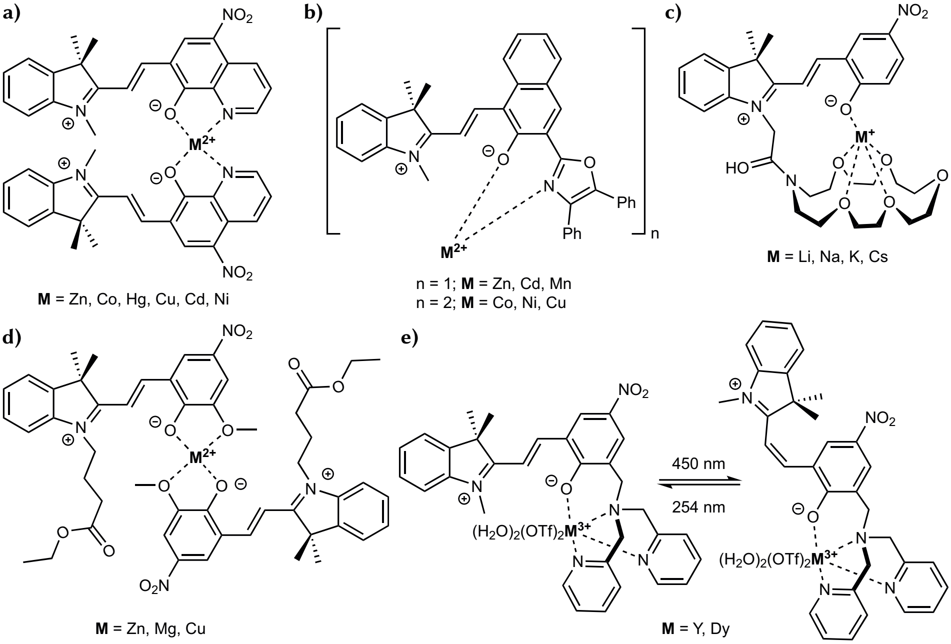

Figure 2.14. Various metal complexes of the open-ring MC isomer. An additional metal binding site is installed in all cases for the stabilization of the MC form.

First literature reports of SP molecules as photochromic metal sensors date back to the 1960s.[86] Later, Winkler and co-workers studied the metal-complexation of 6-nitro-spiro-[indolinepyridobenzopyran] (see Figure 2.14a).[87] Different stoichiometries depending on the metal and the SP substitution have been described, most of them belonging either to a MC:M^{n+} ratio of 2:1 or 1:1.

Another SP derivative and its metal complexation behavior are depicted in Figure 2.14b). Here, an additional binding site was provided by a 2-benzothiazolyl substituent in the *ortho*-position to the phenolate oxygen. Upon metal ion addition, 1:1 complexes were obtained for Zn$^{+\mathrm{II}}$, Cd$^{+\mathrm{II}}$, and Mn$^{+\mathrm{II}}$, while Co$^{+\mathrm{II}}$, Ni$^{+\mathrm{II}}$, and Cu$^{+\mathrm{II}}$ led to 2:1 stoichiometries.[88]

Very selective alkali metal chemosensors were achieved by the combination of SP molecules with crown ethers, which is depicted in Figure 2.14c).[89] While complexation with the oxygen containing SP occurs spontaneously in the dark, the corresponding spirobenzothiopyrane did not form the metal complex under dark conditions (not shown).[90]

Giordani and co-workers have synthesized metal complexes of Zn$^{+\mathrm{II}}$, Mg$^{+\mathrm{II}}$, and Cu$^{+\mathrm{II}}$ ions with SP molecules in a 2:1 ratio (see Figure 2.14d).[91] A methoxy group in ortho-position to the phenolate oxygen served as an additional binding site. The authors also proposed the participation of the ester moiety attached to the nitrogen atom of the indole ring in the metal complexation.

Selvanathan *et al.* reported the synthesis of Y$^{+\mathrm{III}}$ and Dy$^{+\mathrm{III}}$ complexes with a bis-(pyridinemethyl)amine substituted SP molecule.[92] They demonstrated, that the metal complexes undergo a photo triggered *trans*$\rightleftharpoons$*cis* isomerization of the MC ligand, while the coordination to metal is retained (see Figure 2.14d).

If attached to a polymeric backbone, selective detection of Cu$^{+\mathrm{II}}$ metal ions was demonstrated in the presence of Zn$^{+\mathrm{II}}$, Ni$^{+\mathrm{II}}$, and Co$^{+\mathrm{II}}$ ions.[93] Other reports have utilized SP end-functionalized poly(methyl methacrylate) (PMMA) for the selective and reversible dimerization of the polymer chains.[94] Locklin and co-workers demonstrated that the introduction of an ester moiety in close proximity to the phenolate oxygen can serve as an additional metal binding site for selective metal sensing in polymers.[95]

2.2.3 Photo triggered ligation techniques

Employing light as a trigger to control intra-, as well as intermolecular chemical reactions brings several advantages compared to the thermally overcoming of activation barriers. Not only can the chemist precisely define the light intensity, i.e. the number of photons reaching the desired target, but he can also tightly focus the light in arbitrary shapes in 2D, as well as in 3D space, and therefore obtain a spatial and temporal control over the chemical reaction process. The current thesis exploits various photo triggered ligation techniques for the end-functionalization of polymers and for surface lithography (see Chapter 3), as well as for 2D and 3D fabrication of microstructures *via* the use of DLW (refer to Chapter 5). The following section will review the literature about other photoligation techniques, before introducing the reactions employed in the present thesis in more detail.

To motivate why photo induced reactions can be superior to thermally-induced reactions, a quote from Balzani, Ceroni, and Juri who nicely visualize the remarkable difference, when going from thermal towards photochemical activation:[43]

> "For example, absorption of a 300 nm photon by naphthalene corresponds to an energy of 400 kJ mol^{-1}, comparable with the energy that would be taken up by naphthalene ... if it were immersed in a heat bath at 3000 K."

It becomes obvious, that the accessibility of reaction modes corresponding to high temperatures by photochemistry under mild conditions allow the synthesis of a plethora of molecules. In fact, the photo excited molecule should be regarded as a completely new species with different properties, as compared to the ground state molecule.[43]

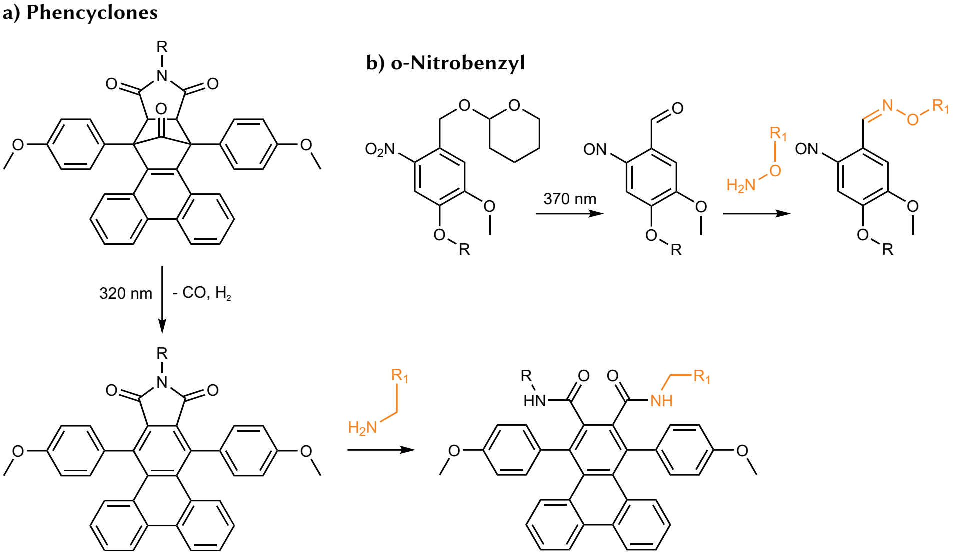

Figure 2.15. a) Photo activation of an *o*-nitrobenzyl (*o*-NB) derivative and reaction with an aminooxy derivative. b) *Diels–Alder* adducts of phencyclones release carbon monoxide and molecular hydrogen upon irradiation with 320 nm. Subsequent ring-opening with an amine gives the ligation product. R, R_1 = alkyl.

Photoligation chemistry has received significant attention in recent years and is nowadays routinely employed in organic synthesis,[43,46,96] polymer chemistry,[97] surface lithography,[98] polymer network formation,[99] as well as in 3D fabrication techniques, such as DLW.[100] All approaches exploit the inherent advantages of photochemistry, namely the spatial and temporal control over a reaction, as well as the low energy input into the reaction system, while simultaneously having the ability to access reaction manifolds not reachable *via* thermal activation.

Among the many reactions employed for photoligation chemistry, only the most prominent examples will be given here, ordered by the operating mechanism and the employed wavelength. This listing is of course far from being complete and the reader is referred to excellent reviews on the field.[46,101] Emerging research areas in photoligation chemistry include the search for reactions triggered *via* visible light[102] and some examples will be mentioned in the next part.

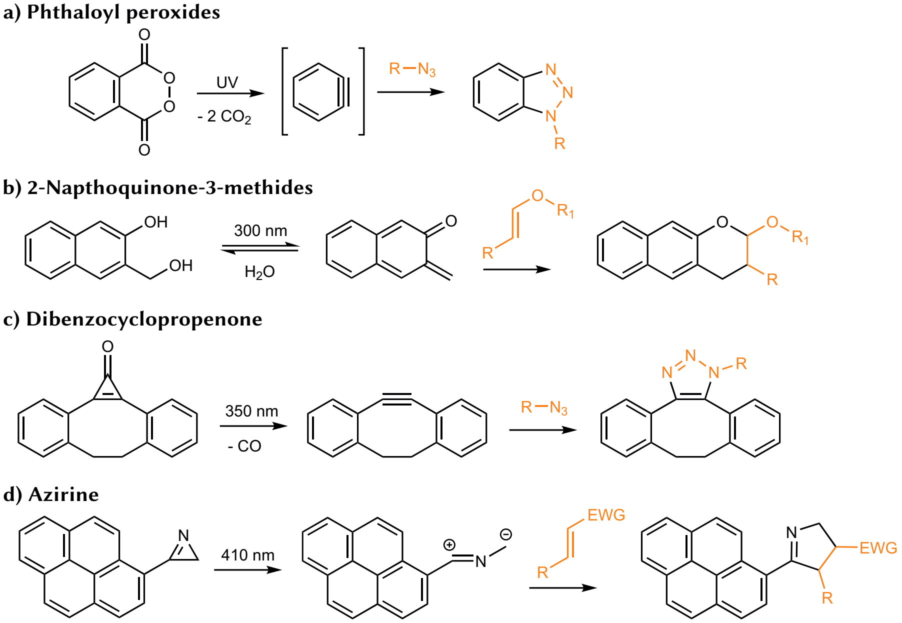

Figure 2.16. a) UV irradiation of phthaloyl peroxides releases CO_2 and forms highly reactive arynes, which are trapped by azides. b) 2-Napthoquinone-3-methides (*o*-NQMs) are generated *via* irradiation of 3-(hydroxymethyl)-2-naphthols and readily react in a hetero-*Diels–Alder* reaction with vinyl ethers. c) Dibenzocyclopropenones release CO upon irradiation, forming ring-strained dibenzocyclooctynes that react in a catalyst free cycloaddition with azides. d) Ring-opening of pyrene substituted azirines results in reactive nitrile ylides, which participate in 1,3-dipolar cycloadditions. EWG = electron withdrawing group; R, R_1 = alkyl.

Phencyclones can react in normal, as well as inverse electron demand *Diels–Alder* reactions[103] with dienophiles (refer to Figure 2.15, bottom), which subsequently releases carbon monoxide upon irradiation with a wavelength of 320 nm. The generated triphenylene imide derivatives can be ring-opened by amine nucleophiles in a following reaction step.[104] The well-known photochemistry of *o*-NB derivatives liberates a nitrosobenzaldehyde species,[105] which can be trapped in a bio-orthogonal fashion with aminooxy compounds, a reaction sequence referred to as photo triggered oxime ligation (see Figure 2.15, top).[106] Both reactions generate a reactive species under irradiation, which is subsequently reacting in a nucleophilic substitution.

Another group of photoligation reactions is generating highly reactive arynes under extrusion of small molecules or intramolecular rearrangements upon irradiation, which then react in cycloaddition reactions (see Figure 2.16). Phthaloyl peroxides have been shown to form highly reactive arynes upon UV irradiation and instantaneously react with azides in an 1,3-dipolar cycloaddition.[107] Popik and co-workers have utilized *o*-NQMs (a subclass of *o*-Quinone methides[108]) for hetero-*Diels–Alder* reactions with vinyl ethers.[109] They demonstrated the versatility of these reactive species in the spatial encoding of surfaces. *o*-NQMs can be generated *via* 350 nm irradiation from 3--(hydroxymethyl)-2-naphthols. They can either be trapped by nucleophiles or undergo an inverse-electron demand hetero-*Diels–Alder* reaction with electron-rich dienophiles.[110]

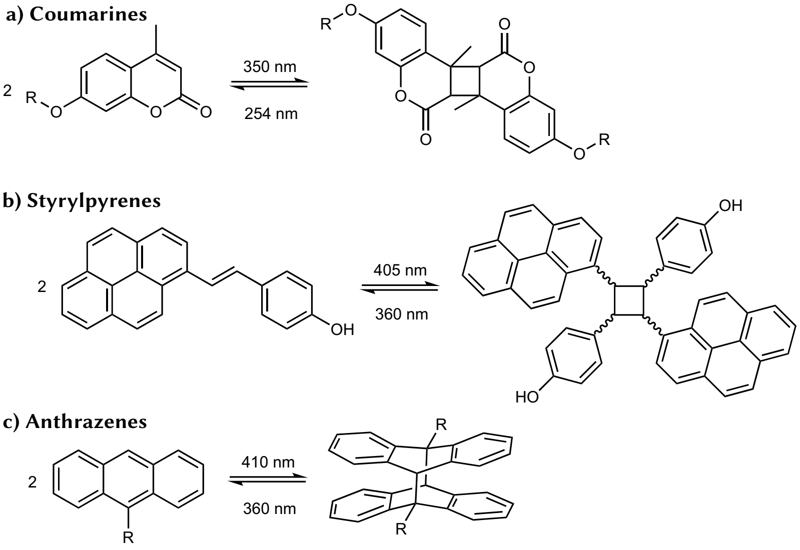

Figure 2.17. Three examples of reversible photoligation chemistry. The [2+2] cycloadditions of coumarines (a) and styrylpyrenes (b) triggered *via* irradiation with 350 nm and 405 nm, respectively. Only one isomer is depicted in each case. The dissociation is feasible with shorter wavelength in both cases. c) Photochemical [4+4] cycloaddition between two anthrazene molecules and the reverse reaction *via* 410 nm and 360 nm, respectively. R = alkyl.

Irradiation of dibenzocyclopropenones around 350 nm releases carbon monoxide and forms highly reactive dibenzocyclooctynes which can undergo catalyst-free 1,3-dipolar cycloadditions with azides.[111] Azirines form highly reactive nitrile ylides, i.e. 1,3-dipoles, upon irradiation, which undergo 1,3-dipolar cycloadditions with various substrates[112] and can even be triggered *via* visible light upon attachment of a pyrene substituent (see Figure 2.16, bottom).[113]

An emerging research area in photoligation chemistry is the search for photo reversible ligation techniques triggered with different wavelengths of light.[114] Figure 2.17 gives three examples, all belonging to the class of photochemically allowed [2+2] and [4+4] cycloadditions. Coumarines are known to form dimers upon irradiation with a wavelength of 350 nm. The reverse reaction is feasible with 254 nm and was employed for the cross-linking of polymers.[115] Recently, styrylpyrenes[116] have attracted new attention, and their reversible [2+2]-cycloaddition was exploited in polymer chemistry.[117] Again, attaching a pyrene substituent enabled the reaction to proceed in the visible light regime. The [4+4] dimerization of anthrazenes[118] has been employed in different fields, such as formation of single-chain nanoparticles (SCNPs),[119] polymer chemistry,[120] photo triggered assembly of nanomaterials,[121] and Claus *et al.* demonstrated their potential as a surface photoligation tool.[98a]

2.2.3.1 Thioaldehydes

Thioaldehydes are highly reactive compounds that are majorly formed *in situ* as they are converted very quickly. One possibility is the stabilization of the carbon-sulfur double bond with sterically bulky groups, being referred to as *thermodynamic stabilization*, but this approach will not be discussed in this introduction.[122] This section introduces the thioaldehyde chemistry and the possible reactions that can be used for photoligation chemistry, which was employed in Chapter 3 of the present thesis for surface functionalization *via* photo-lithography.

Thioaldehydes represent a highly unstable species compared to their oxygen analogues (aldehydes), as the energetic stabilization of the π-double bond decreases strongly when oxygen is substituted by sulfur ($\approx$30–40 kcal mol^{-1} difference between oxygen and sulfur, i.e. from a second- to a third-row element).[122] In literature, several methods for the generation of thioaldehydes have been described,[123] such as UV irradiation,[124] high temperatures,[125] flash photolysis,[126] or flash pyrolysis.[127]

One type of *in situ* generated thioaldehydes can be obtained by the decomposition of β-keto sulfides upon irradiation with UV light *via* a *Norrish Type II* reaction pathway.[128]

The *Norrish Type II* is a common photo induced reaction of alkyl ketones and related substrates. It refers to the elimination forming an enol and alkene after photo excitation and photo induced intramolecular γ-hydrogen atom abstraction. In contrast, the *Norrish Type I* reaction describes the homolytic cleavage of the α-bond of the excited carbonyl, which is often followed by decarbonylation of the acyl radical intermediate.[45b,129]

The group of Barner-Kowollik has employed phenacyl sulfide, which decomposes upon irradiation into a highly reactive thioaldehyde and acetophenone as a by-product. First literature reports utilizing this strategy date back into the late 1960s.[130] The photo excitation, as well as the subsequent reactions are depicted in Scheme 2.8. After the initial excitation of the phenacyl sulfide, γ-hydrogen abstraction (k_γ) and fragmentation occurs (*Norrish Type II* reaction), yielding the desired thioaldehyde species. As a by-product, the

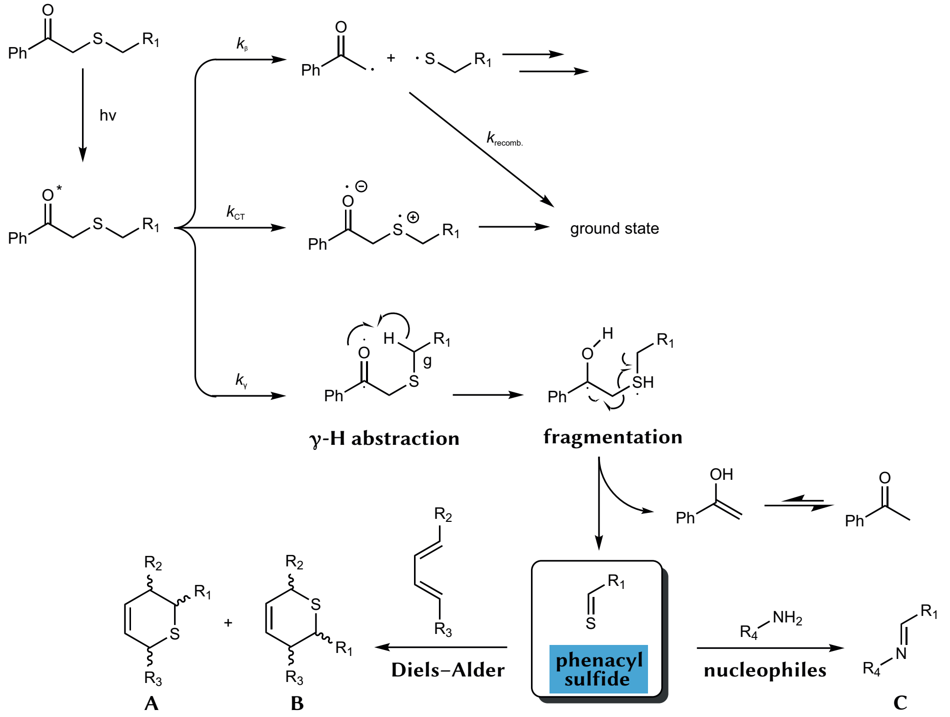

Scheme 2.8. Photo excitation of phenacyl sulfide and subsequent reactions: 1.) β-Cleavage resulting in two radicals, followed by recombination or side-reactions; 2.) CT and quenching towards the ground state; 3.) *Norrish type II* cleavage resulting in a thioaldehyde, which is trapped either by a diene in a hetero-*Diels–Alder* reaction to obtain products (**A**) and (**B**), or by a nucleophile, e.g. an alkoxy amine to obtain product (**C**). R_1, R_2, R_3, R_4 = alkyl.

enol tautomer of acetophenone is being formed, which undergoes rapid tautomerization towards acetophenone.

In a mechanistic study, Wagner and co-workers compared the depicted *Norrish Type II* reaction with two other possible reaction channels, namely the β-cleavage and CT.[131] The β-cleavage (k_{β}) results in two radicals, one of them being a sulfur centered radical. From this stage, either recombination ($k_{recomb.}$) towards the ground state molecule or further reactions involving the two radicals can occur (not shown). CT (k_{CT}) from the excited carbonyl towards a radical anion on the oxygen, as well as a radical cation on the sulfur represents the third reaction channel, which is subsequently quenched, reforming the initial phenacyl sulfide molecule. They demonstrated, that by introducing γ-hydrogen atoms, as well as performing the photoreaction in aprotic solvents considerably favors the desired *Norrish Type II* reaction channel.

In the presence of dienes, such as cyclopentadiene or alkoxydienes, the thioaldehyde can serve as a dienophile in a hetero-*Diels–Alder* reaction leading to the formation of cyclic thioethers (products **A** and **B** in Scheme 2.8). The regiochemistry of the adduct is determined by the electronic nature of the substituent R_1 on the thioaldehyde, as well as on the respective diene (R_2, and R_3). The regioselectivity can be explained by comparison of the molecular orbital coefficients of the lowest unoccupied molecular orbital (LUMO) of the dienophile (thioaldehyde) with the highest occupied molecular orbital (HOMO) of the respective diene.[122]

The highly reactive thioaldehyde can also react with suitable nucleophiles, for example thiols, alkoxy amines, or amines.[132] The reaction with an alkoxy amine is depicted in Scheme 2.8 on the lower right side (product **C**).

Despite their unstable nature, thioaldehydes are versatile intermediates in organic chemistry. They have been employed in natural product synthesis,[133] synthesis of thiazolines,[134] or complex ring closures.[135] They also have been shown to self-polymerize[136] and have been used in different cycloaddition reactions, such as [2+2], [3+2], and in the above mentioned [4+2] hetero-*Diels–Alder* reaction.[130b,133,137] Recently, Tuten *et al.* demonstrated that the substitution of the phenacyl moiety by a pyreneacyl group enables the red shifting of the photoreaction above 400 nm into the visible light regime.[138] Their approach utilizes the ability of the pyrene group to achieve visible light absorption of the corresponding pyreneacyl moiety.

In recent years, the photo triggered phenacyl sulfide ligation has been employed in the field of polymer chemistry, as well as for the functionalization of various surfaces. Examples are the ligation of end-functional polymers onto spherical and planar surfaces,[124,139] polymer end-group modifications,[132] sequence defined macromolecules,[140] cellulose functionalization,[141] and formation of SCNPs.[142] The photoligation chemistry was even extended into 3D in a DLW experiment to obtain dual functional free-standing 3D structures.[143]

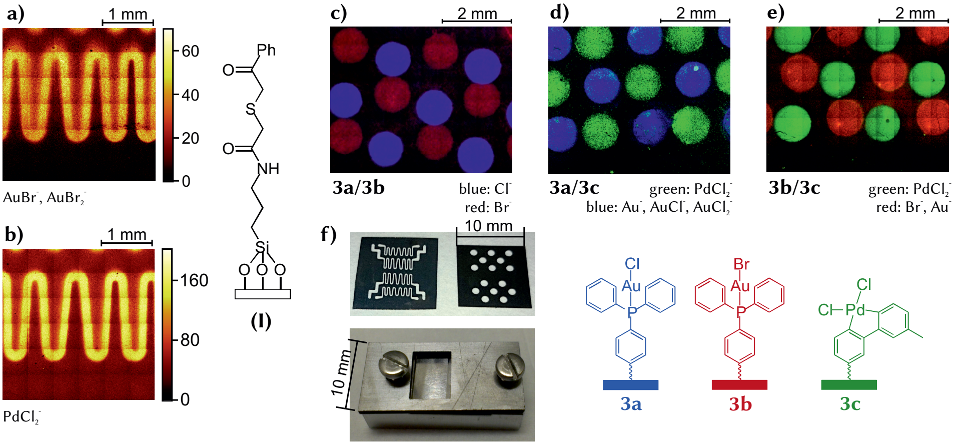

Figure 2.18. Spatially resolved immobilization of metal complexes (**3a**-**c**) onto silica surfaces employing a phenacyl sulfide functionalized silane (**I**). Single (**a,b**), as well as double functional (**c**-**e**) surfaces were characterized *via* time-of-flight secondary ion mass spectrometry (ToF-SIMS). The mass fragments used for creating the false-color images are given below each ToF-SIMS image. The shadow mask and surface holder are shown in **f**. Adapted with permission from [144]. © 2015 Wiley-VCH Verlag GmbH & Co. KGaA.

The photolithographic encoding of metal complexes onto silica surfaces was demonstrated employing gold, as well as palladium complexes, as depicted in Figure 2.18.[144] A phenacyl sulfide silane (**I**) was used as a surface anchor and metal complexes functionalized with sorbic alcohol as a diene (**3a**–**c**) were tethered onto the surface. Employing suitable shadow masks, single (Figure 2.18, **a** and **b**), as well as double functional metal complex surfaces (Figure 2.18, **c**–**e**) were obtained. The surfaces were characterized *via* ToF-SIMS, confirming the spatially resolved immobilization of the metal complexes.

2.2.3.2 Nitrile imine-mediated tetrazole-ene cycloaddition

Another versatile photo triggered ligation is the nitrile imine-mediated tetrazole-ene cycloaddition (NITEC). Here, a tetrazole releases nitrogen upon irradiation with UV light, forming a nitrile imine (see Scheme 2.9, 1st reaction). Initially described by Huisgen and coworkers in 1967 as a thermally triggered reaction,[145] this 1,3-dipolar cycloaddition has found widespread use in synthetic chemistry.[146] A general reaction scheme is depicted in Scheme 2.9. Starting from the tetrazol molecule, irradiation *via* UV light triggers the N_2 extrusion, forming the 1,3-dipole. From here, several reaction channels are possible, depending on the reaction partners. This section will introduce the chemistry behind the NITEC ligation and its variants with an emphasis on their application in surface patterning, which were employed for the spatially resolved surface patterning of metallopolymers in Chapter 3 of the current thesis.

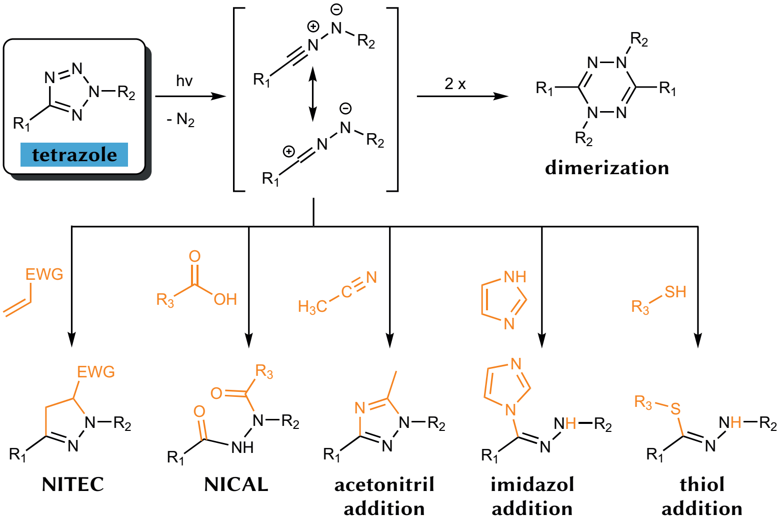

Scheme 2.9. Photo induced nitrile imine formation of a tetrazole and dimerization in the absence of reaction partners, yielding tetrazines (top row). In the presence of suitable reaction partners, from left to right: 1,3-dipolar cycloaddition with an electron deficient ene (NITEC), reaction with a carboxylic acid (NICAL), addition to the triple bond of acetonitrile, reaction with an amine, such as imidazole, and addition of a thiol. R_1, R_2 = aryl; R_3 = alkyl; EWG = electron withdrawing group.

In the absence of any reaction partner, nitrile imines stabilize *via* dimerization, forming tetrazines (see Scheme 2.9, top row). The nitrile imine can also react with electron deficient dipolarophiles such as maleimides or acrylates,[147] and even with non-activated double bonds due to its inherent high reactivity (see Scheme 2.9, bottom left).[148] While the predominant part of reports exploit the tetrazole chemistry for such NITEC reactions, the nitrile imine can react with various other functional groups. Heiler *et al.* exploited the self-dimerization of nitrile imines, which stabilize the reactive 1,3-dipoles in the absence of suitable reaction partners,[149] as well as the reaction with poly(acrylic acid) copolymers for the formation of SCNPs and established the term nitrile imine-carboxylic acid ligation (NICAL, see Scheme 2.9). Li *et al.* reported the reaction with carboxylic acids, as well as triple bonds (acetonitrile) and amines, such as imidazoles.[150] The authors made elegant use of cocktail experiments to compare the relative reactivities of the different functional groups. While already mentioned in the beginning of the tetrazole research area by Huisgen and co-workers in the 1960s,[151] Levkin and co-workers made use of the reactivity with thiols in solution and showed the capability for surface functionalization (see Scheme 2.9).[152] Lin and coworkers have published a variety of work based on NITEC and established the reaction as a bio-compatible ligation technique.[153–156] The Wagenknecht group published several papers utilizing the NITEC ligation as a tool for DNA labeling and fluorogenic sensing.[157]

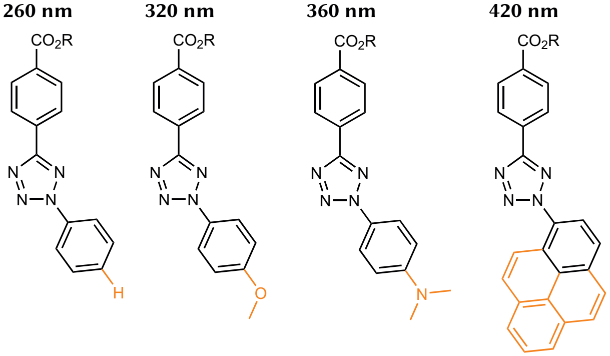

Figure 2.19. Different substitutions of the aryl group connected to the nitrogen atom of the tetrazole ring and the wavelengths reported to trigger the 1,3-dipole formation. From left to right: non-substituted tetrazole, push-pull substituted methoxy and *N*,*N*-dimethylamino tetrazoles, and pyrene functionalized tetrazole. R = alkyl.

In addition, tetrazoles were investigated regarding their activation wavelength by varying the two substituents of the tetrazole ring (R_1 and R_2 in Scheme 2.9). It was found that by careful substitution of the ring bound to the nitrogen atom of the tetrazole, a bathochromic shift of the activation wavelength could be achieved.[158] Structures of different tetrazoles together with their respective activation wavelengths are depicted in Figure 2.19. The core structure with a *para*-carboxylic acid ester on the carbon tetrazole ring atom and a phenyl ring on the nitrogen of the tetrazole ring can be activated *via* irradiation with 260 nm. Substitution of the *para*-position with electron donating substituents, such as methoxy or *N*,*N*-dimethylamino moieties results in push-pull tetrazoles, which can be triggered with 320 nm and 360 nm, respectively. Lederhose *et al.* substituted the aryl group connected to the nitrogen atom of the tetrazole ring by a pyrene moiety,[147] a concept also adopted for the thioaldehyde chemistry discussed in Section 2.2.3.1. They could push the trigger wavelength up to 420 nm and used the chemistry for small molecule ligation, as well as block copolymer formation. In another avenue, the same authors combined the pyrene tetrazole with upconverting nanoparticles

(UCNPs) and triggered the reaction with a 974 nm laser in the near-infrared region.[102a] They also demonstrated the ability of tissue penetration for possible medical applications. Lin and co-workers also achieved visible light triggered NITEC chemistry *via* oligothiophene-based extension of the tetrazole π-system.[159]

The NITEC ligation was also exploited for the spatially-resolved surface patterning of various substrates. Rodriguez-Emmenegger *et al.* investigated the NITEC ligation for poly(dopamine) (PDA) coated surfaces,[160] which is depicted in Figure 2.20. The spatially resolved immobilization of ATRP initiator molecules was achieved *via* NITEC. Subsequent surface-initiated ATRP (SI-ATRP) resulted in anti-fouling poly(oligoethylene glycol methyl ether methacrylate) brushes. In another approach, cellulose was used as a substrate and was functionalized with tetrazoles to enable photoligation capabilities.[161] Blasco *et al.* used silicon wafers as substrates and fabricated spatially resolved light-responsive azobenzene patterns *via* NITEC chemistry.[162] The NITEC reaction was also combined with the ligation of biomolecules onto a silicon surface in a reversible manner.[163] Lederhose *et al.* combined tetrazoles triggered by different wavelengths on a single substrate and were able to fabricate spatially resolved multifunctional surfaces.[98b]

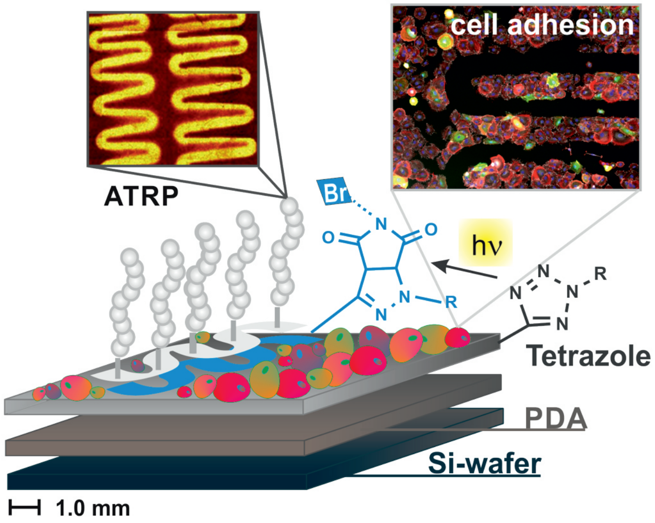

Figure 2.20. Example of a PDA coated silicon surface functionalized with tetrazole molecules. After NITEC ligation of an ATRP initiator, anti-fouling poly(oligoethylene glycol methyl ether methacrylate) brushes were grown from the surface and inhibited cell adhesion on the irradiated areas. Adapted with permission from [160]. © 2013 Wiley-VCH Verlag GmbH & Co. KGaA.

2.2.3.3 *ortho*-Quino dimethanes

The ability of *o*-alkyl aromatic ketones and aldehydes to form the corresponding hydroxy-*o*-quinodimethanes[164] was first described by Yang and Rivas in 1961.[165] They observed the photo induced *Diels–Alder* reaction between *o*-methylbenzophenone and dimethyl acetylenedicarboxylate upon ultraviolet irradiation. The photo induced tautomerization of *o*-alkyl aromatic ketones and aldehydes has later been termed *photoenolization* by Sammes and coworkers.[166] This section will introduce the chemistry of these molecules with a special emphasis on their photoligation properties, as these are employed for polymer functionalization in Chapter 3 of the current thesis. For a complete literature survey of *ortho*-quino dimethanes in synthetic chemistry, the reader referred to excellent reviews.[164,167]

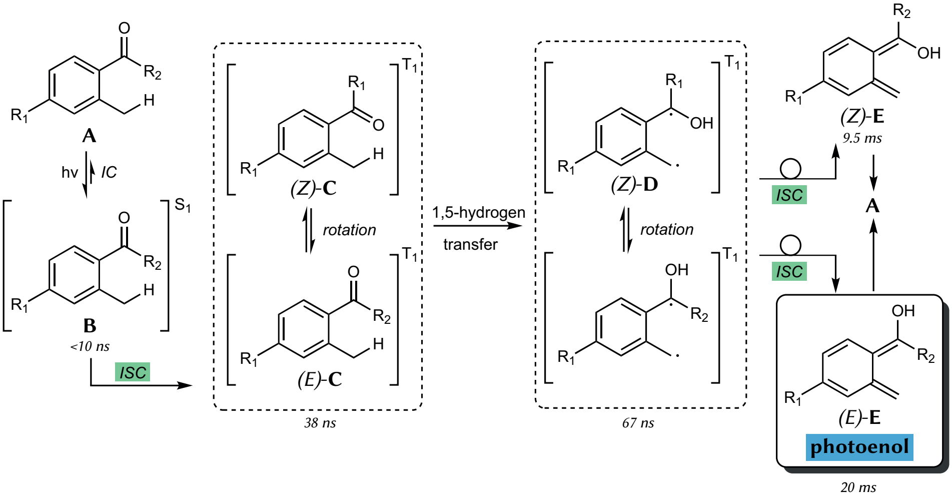

Scheme 2.10. Photoenolization mechanism of 2,4-dimethylbenzophenone with lifetimes of the different transient species as determined in oxygen free cyclohexane. A detailed description of the mechanism is given in the text. R_1 = methyl, R_2 = phenyl.

Porter and Tchir made an in-depth mechanistic study on several *o*-substituted benzophenones and established a detailed mechanistic description of the steps following the initial excitation.[168] The complete mechanism for the photo induced tautomerization of 2,4-dimethylbenzophenone is depicted in Scheme 2.10. The lifetimes of the different species are determined *via* laser flash photolysis in air-saturated cyclohexane. Starting with the excitation from the S_0 state **A** into the short lived S_1 state (n→π* transition of the carbonyl group), IC brings the S_1 state back to the ground state S_0. Alternatively, ISC can occur into the first triplet state (T_1). The initially formed *(E)*-**C** triplet can isomerize *via* rotation into the *(Z)*-**C** conformer, both having a lifetime of ≈38 ns. 1,5-Hydrogen shift leads in both cases to the 1,4-diradical conformers *(E)*-**D** and *(Z)*-**D**, which are also connected *via* a rotational isomerization and feature a lifetime of ≈67 ns. Subsequent rearrangement affords the two *o*-quinone species *(Z)*-**E** and *(E)*-**E**, with a lifetime of 9.5 ms and 20 ms, respectively. The lifetimes of the two *o*-quinone species (also referred to as *(E)*- and *(Z)*-enol) can be considerably increased when employing oxygen free solvent. In oxygen free cyclohexane, the lifetimes increase to 3.9 s for *(Z)*-**E** and 250 s for *(E)*-**E**, respectively. In principle, both *o*-quinone species can relax back to the ground state molecule **A**. *(Z)*-**E** quickly relaxes back to the ground state *via* a sigmatropic 1,5-hydrogen shift. For *(E)*-**E** however, the reketonization requires an intermolecular proton transfer and therefore increases the lifetime of this conformer.[167,169b] In addition, the lifetimes of the *o*-quinone species can vary considerably when changing substituents or solvent polarity.[164a,169b]

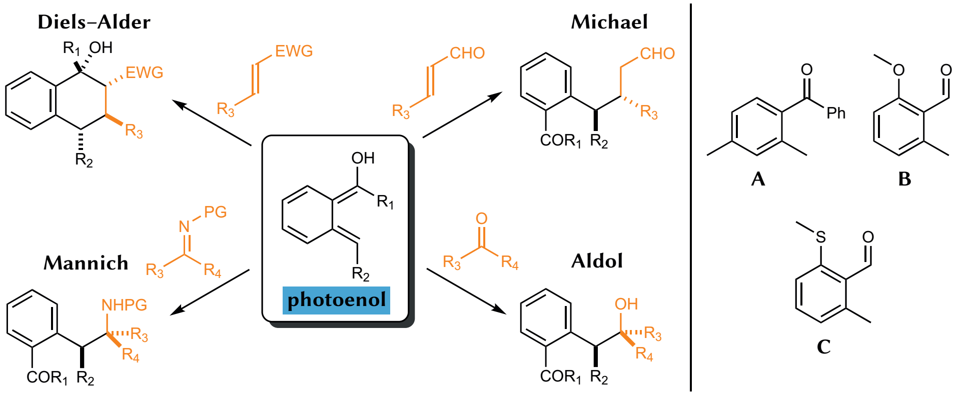

Figure 2.21. Left: Collection of photoenol reactivities with different substrates, namely *Diels–Alder*-, *Michael*-, *Aldol*-, and *Mannich*-type reactions. Reproduced with permission from [169b]. © 2018 Wiley-VCH Verlag GmbH & Co. KGaA. Right: Various photoenols described in literature. 2,4-Dimethylbenzophenone **A** as the first literature example, 2-methoxy-6-methylbenzaldehyde **B** as a widely employed photoenol precursor and 2-methyl-6-(methylthio)benzaldehyde **C** as a recently published photoenol triggered by visible light. R_1,R_2 = H, alkyl or phenyl; R_3,R_4 = alkyl; PG = protecting group; EWG = electron withdrawing group.

The *(E)*-enol (also referred to as photoenol or photo-caged diene in literature) can participate in different reactions depending on the reaction partner (see Figure 2.21, left side). The most prominent example is a *Diels–Alder* reaction with various dienophiles (see Figure 2.21). The photo induced tautomerization followed by a *Diels–Alder* reaction is termed photoenolization/*Diels–Alder* (PEDA) reaction sequence.[169b] The *(Z)*-enol does not show such reactivity, which can be explained by its short lifetime and steric hindrance.[164a] In a recent report, Melchiorre and co-workers reported an elegant approach towards an enantioselective organocatalytic variant of the PEDA reaction.[169] This will pave the way for employing the PEDA reaction sequence in enantioselective organocatalysis.[170] *Michael*-,[169a] *Aldol*-,[169a] and *Mannich*-type[169a] reactions complete the reaction toolbox offered by photoenols, as depicted in Figure 2.21.

Three examples of photoenol precursors are depicted in the right side of Figure 2.21. 2,4-Dimethylbenzophenone **A** constitutes the first example described in literature and detailed mechanistic investigations have been conducted, as described earlier. 2-Methoxy-6-methylbenzaldehyde **B** is a widely used motif in synthetic polymer chemistry and was also used in the current thesis (see Chapter 3). The free electron pair of the methoxy group in *ortho* position to the benzaldehyde plays an important role, as it significantly stabilizes the *(Z)*-enol *via* hydrogen bonding.[171] The last example, 2-methyl-6-(methylthio)benzaldehyde **C**, is the sulfur analogue of photoenol (**B**), which enabled a bathochromic shift of the activation wavelength into the visible light regime.[172]

In all of these reactions, a careful choice of the reaction conditions need to be made in order to minimize potential side-reactions, that can occur from the highly energetic *o*-quinone species. A collection of reported side-reactions is depicted in Figure 2.22. The formation of peroxides (**I**) in non-degassed solvents has been reported by Tchir and Findlay.[173] Murakami *et al.* reported the appearance of cyclobutane structures (**II**) upon radical combination from the triplet state of the photoenol.[174] Depending on the concentration of the photoenol precursor and the light intensity, different dimerization processes can occur. In diluted solution and with reduced light intensities, the photoenol can undergo a hetero-*Diels–Alder* reaction with the carbonyl group of a second photoenol precursor towards hemiacetal (**III**).[173] In the presence of high light intensities, such as in continuous-flow chemistry, the dimerization of two photoenol species can result in the formation of (**IV**) and (**V**). While (**IV**) is stable, (**V**) undergoes rearrangement towards the bisaldehyde structure of (**VI**).[175]

The PEDA reaction has been used for the total synthesis of natural products,[176] as well as a ligation tool in polymer chemistry. Specifically, the PEDA reaction enabled the formation of SCNPs,[177] realization of sequence-defined polymers[178,179] or the light-induced aggregation of nanostructures.[180] In addition, PEDA was also applied for surface functionalization[171,181] and was translated into the third dimension *via* 3D DLW,[182] sub-diffraction laser lithography,[183] and polymer network formation.[175]

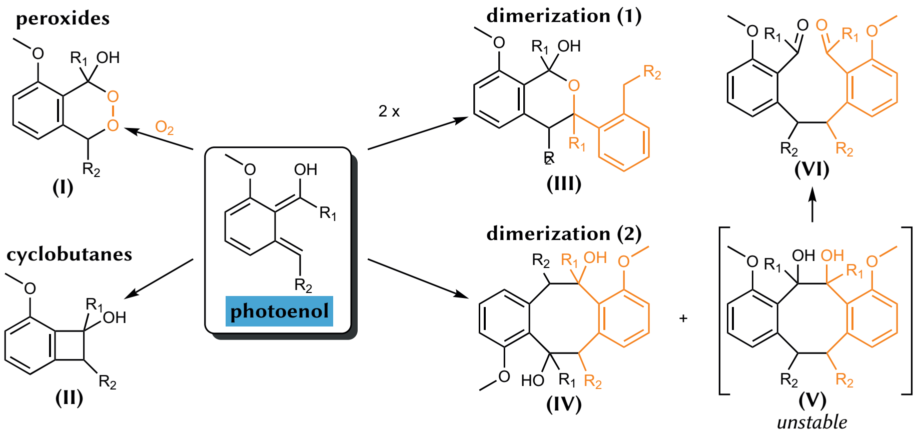

Figure 2.22. Reported side reactions of photoenols in the absence of suitable reaction partners. In oxygen containing solutions, the formation of peroxides (**I**) can occur. Cyclobutane formation towards (**II**) and hemiacetal formation with the carbonyl moiety of a second *o*-methyl benzaldehyde resulting in (**III**), has also been reported. Another dimerization is shown below, leading to dimers (**IV**) and (**V**). While (**IV**) is stable, (**V**) quickly rearranges towards bisaldehyde (**VI**). R_1 = H; R_2 = alkyl.

2.2.3.4 Spirothiopyrans

Spirothiopyrans (STPs) are a special subclass of the well-known SP photoswitch described in Section 2.2.2.1. This section will introduce this photoswitch and especially explain how it has been utilized as a photoligation tool. The light triggered chemistry of STPs is the subject of Chapter 5 of the current thesis.

In STPs, the oxygen atom bound to the spiro carbon atom is replaced by a sulfur atom. The first description of this molecule and its synthesis was published by Becker and Kolc in 1968.[184] Only recently, the versatile chemistry of this molecule was rediscovered.[185]

In analogy to the synthesis of SPs described in Section 2.2.2.1, the synthesis of STPs is feasible *via* condensation of the indoline base **III** with the benzopyrane ring system. Here, the salicyl aldehyde motif employed for SPs is exchanged by a thiosalicyl aldehyde **IV**, as depicted in Scheme 2.11, 2nd row. **IV** is readily obtained *via* a thermal *Newman–Kwart* rearrangement[186] of an *O*-aryl thiocarbamate **I** into a *S*-aryl thiocarbamate **II**,[187] see Scheme 2.11 upper row.

The substitution with sulfur has a pronounced effect on the photochemistry of the molecule. While the absorption of the STP shows only little change compared to its SP analogue, the ring-opened MC species causes a large bathochromic shift of the long-wavelength absorption band associated with the MC form up to 100 nm, almost tailing

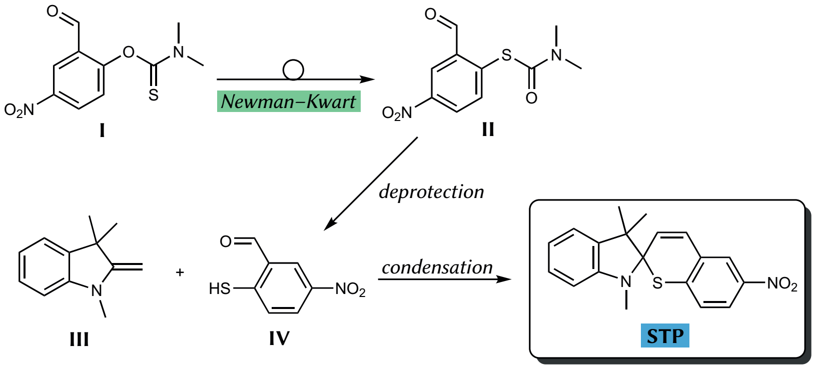

Scheme 2.11. General synthesis route for the preparation of STPs. *Newman–Kwart* rearrangement of *O*-aryl thiocarbamate **I** gives access to *S*-aryl thiocarbamate **II**. Condensation of an indoline base **III** with the *in situ* deprotected thiosalicyl aldehyde **IV** results in the formation of **STP**.

into the near-infrared region up to 900 nm.[187] This bathochromic shift can be explained by the lower electronegativity of sulfur compared to oxygen, which increases the effective charge that oscillates under irradiation with light.[188] It should be noted, that although the analogous selenopyrans have not been reported until now, selenochromenes, e.g. 2*H*-selenochromene, were synthesized with photochromic properties. They exhibit an absorption band of the MC species even beyond 900 nm and thus continue the trend as described when going from oxygen to sulfur.[189] The NIR absorption of these chromophores is beneficial for possible applications in data storage devices.[62d]

In contrast to the SP molecules, the photo coloration efficiency in STPs is considerably reduced (lower quantum yield) and the thermal fading of the MC form is faster than compared to SP.[190] This behavior has also been attributed to the reduced electronegativity of sulfur as compared to oxygen, which reduces the possibility to stabilize the negative charge at the hetero atom in the MC form. This difference is of great importance for applications, which exploit the rates of SP to MC interconversion. Miyashita and co-workers succeeded to crystallize the open MC form of a STP molecule under continuous irradiation. They characterized the MC form *via* several spectroscopic methods including NMR spectroscopy and emphasized the highly zwitterionic character of the MC form with a higher contribution of the thion form compared to the thiolate species in the solid state.[191]

In a recent study, Hirai and co-workers discovered that the free thiol of the MC form can effectively bind to gold nanoparticles (AuNPs). They observed a light-induced self-assembly of AuNPs in the presence of STP molecules.[185] Upon photo isomerization, the thiolate moiety of the MC form binds to the AuNPs, neutralizing the negative surface charge density on the AuNPs used for stabilization. In another study, they demonstrated that *via* structural change of the STP molecule, the aggregation can also occur spontaneously in the dark.[192]

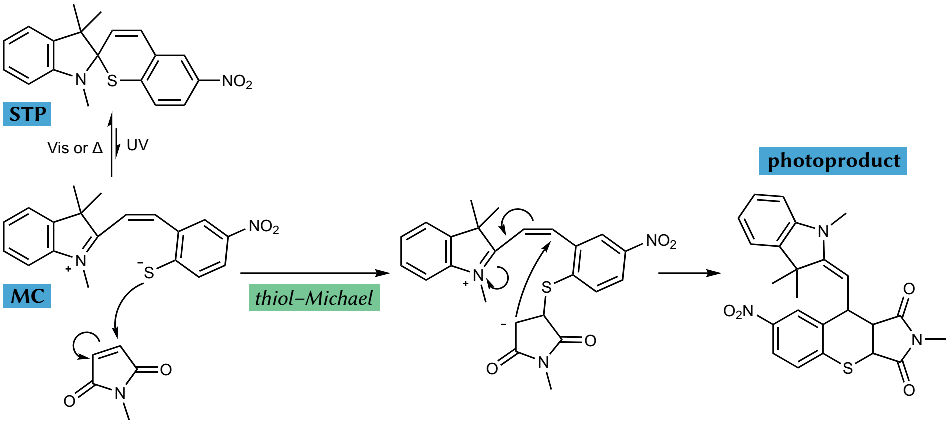

Scheme 2.12. Photo induced STP to MC isomerization and subsequent thiol-*Michael* reaction with a maleimide species as reported by Zhu and co-workers in [193].

After the rediscovery of the STP chemistry, Zhu and co-workers described the ability of the MC form to participate in a thiol-*Michael* reaction[194] in the presence of a *Michael*-acceptor, i.e. a maleimide.[193] They conducted small molecule studies, characterized the product *via* X-ray crystallography and made a mechanistic proposal for the new reaction, which is depicted in Scheme 2.12. The STP molecule in the dark does not react in the presence of the maleimide. Upon irradiation with UV light however, ring-opening towards the MC form occurs, which enables the nucleophilic attack of the thiophenolate anion on the *Michael*-acceptor, here a maleimide. Subsequent nucleophilic attack results in a six-membered heterocycle, which irreversibly leads to the photo adduct as depicted in Scheme 2.12. The entire reaction sequence can be described as a photo activated thiol-*Michael* reaction. In addition, they utilized the reaction between an acrylate based STP copolymer and a maleimide terminated polyethylene glycol (PEG) for the photo controlled formation of comb copolymers. Boulatov and co-workers demonstrated that the reaction can also be triggered *via* mechanical force, as the STP molecule features the same mechanochromism as known from SPs.[195] Inherent to a photo triggered process, the above described reaction opens up the possibility for temporal, as well as spatial control of the ligation, which was exploited in Chapter 5 of the current thesis.

2.3 3D laser lithography below the diffraction limit

The principle of stimulated emission depletion (STED) fluorescence microscopy was initially proposed by Stefan W. Hell in 1994[196] and led to a revolution in optical microscopy, which resulted in the Noble prize for Chemistry in 2014 together with Eric Betzig and William Moerner. Soon after these initial reports, a concept was proposed to adapt the resolution enhancement of STED for laser lithography.[197] This section will briefly introduce the STED principle for optical microscopy and its transfer to lithography, so-called STED-inspired lithography,[198] for which a new chemical system was developed in Chapter 5 of the current thesis in collaboration with Patrick Müller from the Wegener group at KIT.

2.3.1 The principle of STED

The concept of STED microscopy is based on the mechanism of conventional laser scanning confocal microscopy. The underlying principles are depicted in Figure 2.23. In laser scanning confocal microscopy, the excitation of a fluorophore from the ground state S_0 to a higher vibronic first excited singlet state S_1^* is followed by IC to the lowest vibronic state S_1 (refer to Figure 2.23a). From here, fluorescence brings the fluorophore back to a vibronic excited S_0^* state, from where IC leads again to the S_0 ground state. As the excitation area of the fluorophore and therefore also the area of fluorescence is a

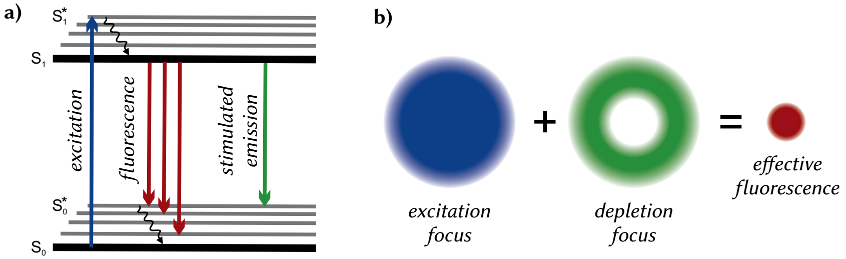

Figure 2.23. a) The principle of STED visualized by a *Jablonski* diagram. For a description, refer to the text. b) 2D intensity representation of the Gaussian shaped UV excitation laser (blue) and the visible light depletion laser with a point of zero intensity in the center (green). The effectively resulting fluorescent area is shown on the right (red).

result of the applied laser focus, the resulting microscopy image is diffraction limited. The relation between the excitation wavelength λ in a medium with refractive index n and the distance d between two objects that can still be resolved is given by the Abbe criterion[199] in Equation (2.21). NA stands for the numerical aperture of the objective lens collecting the incident light. The angle θ in Equation (2.21) is the half-opening angle of the lens of the microscope. As an example, the Abbe criterion allows a lateral resolution of $\approx$200 nm, when working with a green laser with 550 nm and a microscope with a numerical aperture of NA = 1.4.

$$d = \frac{\lambda}{2n\sin\theta} = \frac{\lambda}{2\mathrm{NA}} \tag{2.21}$$

In STED microscopy, a second laser, the so-called depletion laser, is applied in addition to the excitation laser. The energy of the depletion laser is adapted to the energy gap between the lowest S_1 and vibronic excited S_0^* states and its intensity distribution is depicted in Figure 2.23b in green color. Irradiation with such a wavelength can induce stimulated emission (SE) and is therefore able to bring the fluorophore back to the ground state by a radiationless process (green arrow in Figure 2.23a). After IC, the ground state S_0 is reached again. The light of the fluorophores that are brought back to the ground state *via* SE is spectrally filtered and therefore does not contribute to the fluorescence detected by the microscope.

The key point in achieving a resolution enhancement *via* SE is the shape of the applied depletion laser. A visualization for the 2D case is depicted in Figure 2.23b. The Gaussian shaped excitation laser (blue) with the highest intensity in the center is overlaid by the depletion laser with a point of zero intensity in the center (green), i.e. a donut shape. The area of the remaining effective fluorescence (red) is smaller than the value allowed from the Abbe limit. As such, sub-diffraction microscopy is feasible, being no longer dependent on the wavelength, but rather on the chromophore of the system as well as the laser performance. In addition, by increasing the depletion laser intensity, the remaining fluorescence area can in principle be reduced to an infinitesimal small area, ultimately ending up in the size of a single fluorescent molecule. A prerequisite of the system is the reversibility of the fluorophore switching, which needs to occur many times during the scanning of the picture. Lateral spatial resolutions ranging down to 10 nm were possible with STED microscopy, which is considerably below the diffraction limit.[200]

2.3.2 From direct laser writing towards STED-inspired lithography

After the great success in optical microscopy, the principle of STED was soon transferred to laser lithography, specifically DLW.[201] The working principle of DLW will be briefly introduced in this section, followed by the explanation how the STED principle can be transferred to achieve a resolution enhancement in the fabricated 2D and 3D structures made by DLW.

2.3.2.1 Direct laser writing

DLW is a laser lithography process for the fabrication of 2D and 3D materials in the nanometer range.[202] The writing laser is tightly focused into a spot inside the volume of a photoresist. The laser features high intensities, which results in two photon absorption (TPA) by the photoinitiator (PI) inside the photoresist.[202c] As such, the writing can be confined to a small volume element inside the photoresist, the so-called *voxel*, in analogy to the pixel element in 2D.[203] The TPA is crucial for the DLW process. Only by exploiting the non-linearity of the TPA, it is possible to achieve a voxel with a high axial resolution. In TPA, the absorption occurs *via* a virtual intermediate state. As a result, the photon energy of the incident light needs to be half the value of the one photon absorption (OPA) process. The absorption in TPA therefore scales with the square of the light intensity. Consequently, very short laser pulses of high energy are employed in DLW in order to favor the TPA over the OPA. The Abbe criterion needs to be modified for the TPA case and can be calculated *via* a modified equation, as shown in Equation (2.22).[203]

$$d = \frac{\lambda}{2\sqrt{2}\,\mathrm{NA}} \tag{2.22}$$

Applying Equation (2.22) for the above-mentioned example, the resolution achievable with a green laser with 550 nm and a numerical aperture of NA $= 1.4$ reduces to $\approx$140 nm. Therefore, the TPA is not only an essential feature of the DLW process, but also brings a benefit in terms of resolution.[203]

A DLW photoresist is typically composed of two active species: monomer and PI. The majority of DLW works *via* a multiphoton absorption polymerization (MAP) process.[202a,c,a,c] TPA of the PI into the first excited singlet state S_0 is followed by IC and ISC into the triplet state T_1 (see Figure 2.24a). From here, radical formation of the PI occurs and the radical species $R^\bullet$ starts the radical polymerization upon addition to monomer molecules M. For an efficient DLW process, ISC into the T_1 state needs to be

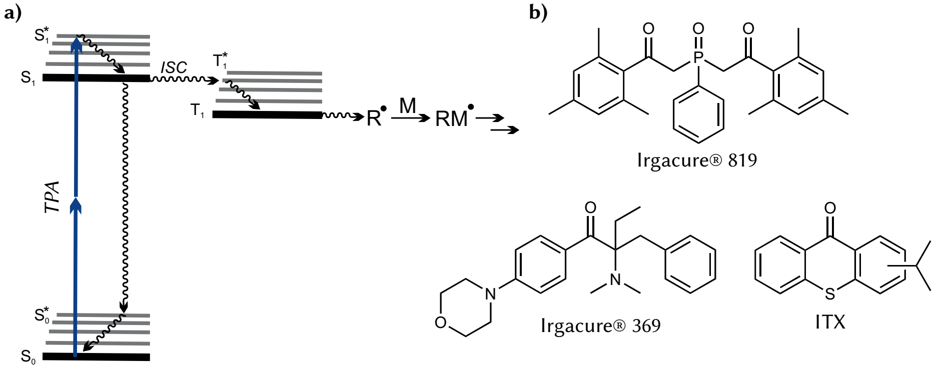

Figure 2.24. a) Principle of conventional DLW. TPA from S_0 into S_1 is followed by ISC and homolytic bond cleavage of the initiator, resulting in radicals $R^\bullet$ starting the polymerization of monomer M. b) Three structures of commercially available TPA PIs.

efficient. Otherwise, IC and radiationless deactivation can bring the initiator back to the S_0 ground state (see wavy arrows in Figure 2.24a). Three examples of PIs employed in DLW, namely Irgacure® 369, Irgacure® 819, and isopropylthioxanthone (ITX), are depicted in Figure 2.24b.[202b]

With these commercially available systems, microstructures with feature sizes down to 100 nm are possible.[204] Examples are the fabrication of photonic crystals,[205] cell scaffold structures,[206] lab-on-chip systems,[207] metamaterials,[208] or optical waveguides.[209]

2.3.2.2 STED-inspired lithography

With the above described DLW process, diffraction still limits the achievable linewidth and resolution of the fabricated microstructures. The idea behind so-called STED-inspired lithography is to adopt the principles of STED microscopy described in Section 2.3.1 for the lithographic process.[197] This concept was proposed soon after the invention of STED microscopy. The groups of Fourkas and McLeod were the first to demonstrate the feasibility of STED-inspired lithography in experiments.[210] As depicted in Figure 2.24a), the excitation of the laser in DLW leads to an irreversible reaction. Employing for example a common negative-tone photoresist, this results in the formation of an insoluble network upon radical polymerization in the exposed volume.

The idea of STED-inspired DLW is the incorporation of a second mechanism, accessing the system in some intermediate state and inhibiting the chemical reaction, leading to the network formation. The depletion channel is triggered by a second laser, operating at a different wavelength than the excitation laser. By adopting the spatial intensity distribution of the excitation and depletion laser in Figure 2.23b), the effectively exposed volume can be reduced by increasing the intensity of the depletion laser. Certain points need to be fulfilled for an effective depletion mechanism:

- The inhibition rate must be matched with the lifetime of the accessed intermediate state.
- The depletion needs to be reversible, i.e. reproduce the unexposed ground state, otherwise previously depleted regions would be insensitive for subsequent writing.
- The wavelengths of the two lasers must be well separated to avoid any “crosstalk” between activation and depletion.

While the depletion mechanism in STED microscopy is based on SE, several mechanisms can accomplish the depletion task in STED-inspired lithography.[203] In principle, any photo induced mechanism inhibiting the formation or propagation of the network forming radical polymerization can be employed as a depletion channel. Figure 2.25a)–c) summarizes several employed depletion mechanisms together with an exemplary system employed for STED lithography depicted in panel d).

The STED lithography mechanism depicted in Figure 2.25a) and directly adapts the principle of STED microscopy.[211] TPA of initiator molecules results in a S_0 to S_1 transition. From here, irradiation with the depletion laser brings the initiator back to the S_0 state *via* SE. This SE transition inhibits the ISC and subsequent radical formation, resulting in solid structures. An example following such a mechanism is 7-diethylamino-3-thenoyl coumarine (DETC). This dye can be excited *via* TPA at 800 nm and depleted by SE at 532 nm.[213]

Another dye first believed to follow the same mechanism[212] is depicted Figure 2.25d). ITX is excited *via* irradiation with femtosecond pulses centered at around 810 nm wavelength. The continuous-wave (CW) depletion laser operates at a wavelength of 532 nm into the fluorescence band of ITX. However, it has been shown that the depletion channel actually operates *via* an excited state absorption.[214] Linewidth reductions from 155 nm (no depletion) down towards 65 nm with the depletion laser switched on have been demonstrated with ITX.[212]

Figure 2.25b) shows a mechanism called resolution augmentation through photo induced deactivation (RAPID) lithography.[210a] Here, TPA is followed by the transition into a long-lived intermediate state. The exact nature of this intermediate state is still under investigation.[215] The molecule in the intermediate state can either relax back to

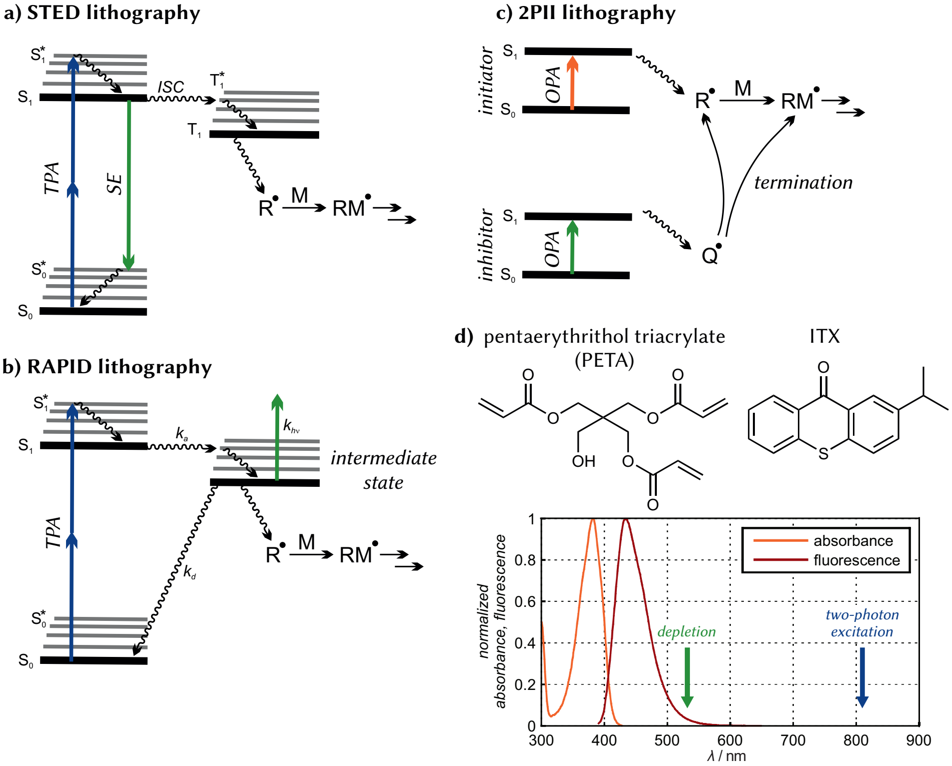
a) STED lithography
S1*
S1
ISC
T1*
T1
TPA
SE
R• M RM•
S0*
S0
b) RAPID lithography
S1*
S1
ka
khν
intermediate state
TPA
kd
R• M RM•
S0*
S0
c) 2PII lithography
initiator
S1
OPA
S0
R• M RM•
termination
inhibitor
S1
OPA
S0
Q•
d) pentaerythrithol triacrylate (PETA)
ITX
O
O
O
OH
O
O
O
S
normalized absorbance, fluorescence
1
0.8
0.6
0.4
0.2
0
300
400
500
600
700
800
900
λ / nm
absorbance
fluorescence
depletion
two-photon excitation

Figure 2.25. Different depletion mechanism employed for STED-inspired lithography. a) STED lithography: PI molecules are excited *via* TPA from S_0 to S_1. They relax back to the S_0 ground state *via* SE before ISC into the T_1 state and radical formation can occur. b) RAPID lithography: after TPA into S_1, transition into an intermediate state occurs (k_a), from which either radiationless decay with rate constant k_d or light excitation into a non-initiating product ($k_{h\nu}$) suppresses radical formation. c) 2PII lithography: initiator (orange), as well as inhibitor molecules (green) get excited *via* different wavelengths in an OPA process. d) Example of a photoresist system working through excited state absorption. PETA is employed as the cross-linking monomer and ITX as the initiator. The depletion (green), as well as the TPA wavelength (blue) for ITX are highlighted below in the absorption and fluorescence spectra measured in ethanol. Adapted with permission from [212]. © 2010 Wiley-VCH Verlag GmbH & Co. KGaA.

the ground state by a radiationless process with a rate k_d or *via* excitation of the depletion laser into a non-initiating product (green, $k_{h\nu}$). RAPID lithography was successfully applied to achieve sub-diffraction resolution malachite green carbinol base[210a] and ITX.[212]

Another mechanism called two-color photoinitiation/inhibition (2PII) lithography is drawn in Figure 2.25c).[210b,b,216] This mechanism operates *via* two OPA processes. One laser triggers the radical formation of an initiator molecule (orange), starting the radical polymerization of the monomer. The second laser (green) generates radicals from an inhibitor molecule, which terminates the propagating chain radicals of the polymerization. An inherent drawback of this mechanism is the irreversible consumption of inhibitor molecules inside the photoresist.

As all of the above-mentioned depletion mechanisms act *via* transformation of electronic states, they must be on the timescale of the fast and efficient dissociation of the initiator, which usually lies in the nanosecond regime.[217] Another approach to achieve sub-diffraction resolution is the photo control of the cross-linking chemistry itself, a mechanism also employed in Chapter 5 of the current thesis. The first example of such kind exploits the chemistry of photoenols discussed in Section 2.2.3.3 and was introduced by the groups of Barner-Kowollik and Wegener.[183]

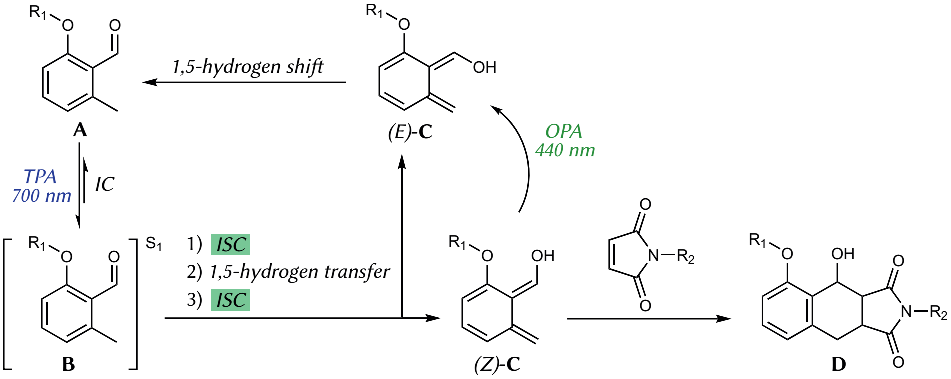

Scheme 2.13. Proposed mechanism for STED-inspired lithography based on the photo induced isomerization of photoenols. Starting from the ground state molecule (**A**), TPA brings the photoenol into the excited S_1 state (**B**). The three processes discussed in Scheme 2.10 generate the *(Z)*-**C** and *(E)*-**C** photoenols. The depletion laser, operating at 440 nm, triggers the *(Z)*- to *(E)*-isomerization of the photoenol and therefore suppresses the irreversible hetero-*Diels–Alder* reaction with a maleimide, resulting in the photoadduct (**D**).

The proposed mechanism is illustrated in Scheme 2.13. Photoenol (**A**) is excited *via* TPA of an 700 nm pulsed femtosecond laser to the S_1 state (**B**). Subsequent ISC, 1,5-

hydrogen transfer, and again ISC leads to the formation of the two photoenol species *(Z)*-**C** and *(E)*-**C**. A detailed mechanistic description of these processes was given in Scheme 2.10. While *(E)*-**C** quickly fades back towards the ground state molecule (**A**), *(Z)*-**C** can react in a hetero-*Diels–Alder* reaction with a dienophile, here a maleimide. The *Diels–Alder* adduct (**D**) is shown on the lower ride side. For the depletion channel, the photo induced isomerization of *(Z)*-**C** towards *(E)*-**C** is exploited.[218] The depletion laser diode is operated in CW mode at 440 nm and efficiently reduces the *(Z)*-**C** population. As such, the *Diels–Alder* reaction is also suppressed, which is necessary for the formation of a stable structure.

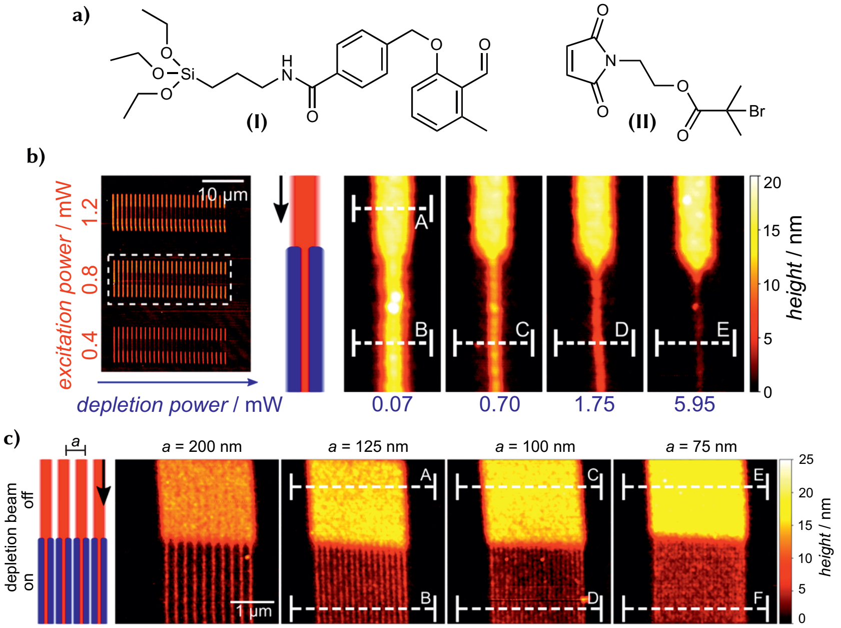
a)
O
Si
H
N
O
O
O
(I)
O
N
O
O
O
Br
(II)
b)
excitation power / mW
1.2
0.8
0.4
10 µm
depletion power / mW
A
B
C
D
E
0.07
0.70
1.75
5.95
20
15
10
5
0
height / nm
c)
a
depletion beam
off
on
a = 200 nm
a = 125 nm
a = 100 nm
a = 75 nm
1 µm
A
B
C
D
E
F
25
20
15
10
5
0
height / nm

Figure 2.26. a) Chemical structures of the photoenol-equipped silane (**I**) and the maleimide ATRP initiator (**II**). b) Linewidth reduction experiments visualized *via* AFM measurements of SI-ATRP grown polymer brushes. The excitation power is shown in red, while the depletion power is drawn in blue. c) Determination of the lateral resolution without (top) and with depletion (bottom) Lines are separated for depletion powers **B** and **C**, while **E** no longer lead to a clear periodic modulation. Adapted with permission from [183]. © 2017 American Chemical Society.

The authors were able to achieve sub-diffraction linewidth, as well as sub-diffraction resolution. A photoenol-bearing silane was attached to a glass substrate, and the employed maleimide was equipped with a bromine atom. Subsequent generation of polymer brushes consisting of poly(ethylene glycol) methyl ether methacrylate (PEGMEMA) prepared *via* SI-ATRP, and imaging *via* atomic-force microscopy (AFM) confirmed the successful writing. The employed photoenol silane (**I**)[171] and the maleimide ATRP initiator (**II**) are shown in Figure 2.26a).

In panel b), the AFM results of the linewidth reduction are presented. On the left side, the excitation power (red), as well as the depletion power (blue) are varied. For an excitation power of 0.8 mW, the zoom on the right side shows the decreasing linewidth when increasing the depletion power. Continuous lines are written for experiments (**B**-**E**). The smallest full width at half maximum (FWHM) is 54 nm for a depletion power of 1.75 mW (**E**).

Panel c) of Figure 2.26 shows the experiments to determine the lateral resolution, i.e. the smallest distance a between two sequentially written lines. Without the depletion laser switched on (top part), all lines are connected, regardless of the lattice constants. With the depletion laser turned on, a lateral resolution down to 100 nm (**D**) was achieved.

While this initial report demonstrated the possibility to exploit a chemical switch for STED-inspired lithography, the fabrication of free-standing microstructures was not possible with the employed surface functionalization approach.[183]

2.4 Spatially resolved surface functionalization

The following sections introduce methods for spatially resolved surface functionalization with a focus on photoligation approaches which has been previously introduced in Section 2.2.3. These approaches are employed in Chapter 3 of the current thesis for the spatially resolved immobilization of metallopolymers onto silicon substrates. The following sections are structured according to the consecutive steps typically undertaken in a surface functionalization experiment. These consist in the choice of a suitable substrate (see Section 2.4.1), with a focus on silicon substrates employed in the current thesis. The activation of the silicon surfaces and the formation of so-called self-assembled monolayers (SAMs) are discussed in Section 2.4.2.1 and Section 2.4.2.2, respectively. Different chemical strategies for the post-modification and/or photoligation of molecules onto the pre-coated surfaces are presented in Section 2.4.2.3. Finally, a literature overview of the different approaches for metallopolymer immobilization onto silicon substrates is given in Section 2.4.2.4. Figure 2.27 provides an illustration of the synthetic route in surface photoligation chemistry, as described in the following sections.

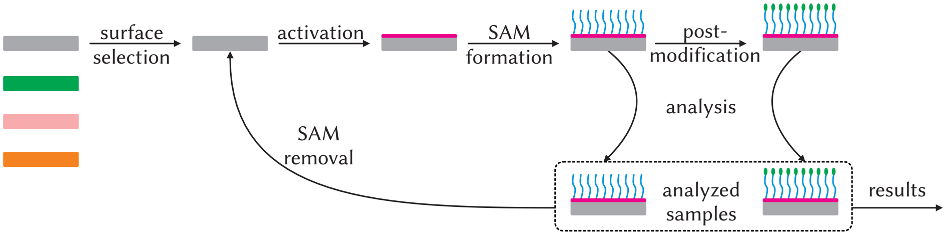

Figure 2.27. Illustration of a typical surface modification experiment. The individual steps are discussed in the following sections.

2.4.1 Substrates

First, the choice of substrate for the surface functionalization experiment must be considered. A plethora of materials has been reported to serve as suitable substrates for SAM formation and subsequent photoligation.[219] This section will shortly introduce different employed substrates, before focusing on silicon, which was employed in the present thesis. The choice of the substrate is dictated by the following chemistry and is dependent on the following chemical aspects:

- the chemical structure of attached SAMs,
- the specific binding interactions between substrate and coating agent,
- the final application of the surface-attached SAM, and
- the analytical tools available for characterization.

Substrates can be classified into different groups, according to their chemical composition and physical properties. Figure 2.28 illustrates selected surfaces, which are commonly employed in photoligation chemistry. The collection is limited to planar and solid substrates.

The most common substrate employed for surface functionalization is gold due to several reasons.[219a,b] It is by far the most studied surface material, with the ability to form very stable SAMs *via* thiol ligation. In addition, the handling of gold surfaces is facile, as gold is inert towards oxidation. Finally, many surface characterization techniques are compatible with gold. Other metals, which have been commonly employed as substrates in photoligation chemistry are silver,[220] copper,[220a] palladium,[221] platinum,[222] mercury,[223] or nickel.[224]

An advantage of metal oxides over bare metal substrates is the inherent oxide layer, which facilitates the SAM formation *via* chemical anchors attaching to the oxygen atoms. Many metal oxides have therefore served as SAM substrates, such as TiO_2,[225] ZrO_2,[225c,226] Al_2O_3,[227] Nb_2O_5,[227c] HfO_2,[226] or indium tin oxide (ITO).[228]

The surface functionalization of semiconductors offers the possibility for redox chemistry at the interface between the substrate and the SAM. With this respect, GaN,[229] GaAs,[229,230] or silicon[106,124,132,139a,162,231] have successfully been applied for photoligation chemistry. The surface chemistry of silicon will be discussed in more detail in the following sections (see also Chapter 3). Finally, other substrates are glass surfaces,[232] superconductors[233] or salts.[234] The advantage of glass substrates is the transparency over a wide range of wavelengths, opening many prospects for physical or chemical manipulation (see also Chapter 5).

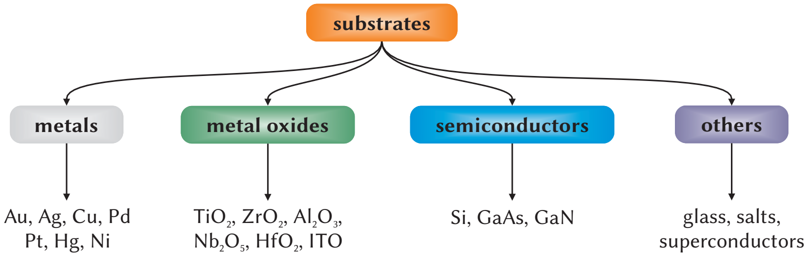

Figure 2.28. Overview of different substrates employed in photoligation chemistry. The materials are classified according to their physical properties into metals, metal oxides, semiconductors, and other substrates.

2.4.2 Silicon surfaces

This section presents the use of silicon materials, e.g. silicon wafers, as substrates, which are employed in Chapter 3 of the current thesis. The same principles discussed for Si wafers also hold true for glass substrates, which were employed for the STED-inspired lithography experiments in Chapter 5.

2.4.2.1 Activation strategies

The preparation of good quality SAMs requires a very clean surface and is a crucial step in the surface preparation. While rigorous cleaning is sufficient for most of the coinage metal substrates, silicon needs additional activation and cleaning.

The two most often used protocols to clean and activate silicon surfaces are plasma cleaning[235] or the immersion of the surface into a mixture of concentrated H_2SO_4 and H_2O_2 (2/1 vol%, known as piranha solution). Both methods result in the formation of a thin oxidized layer on the silicon surface with free hydroxyl moieties, acting as reactive groups for the SAM formation (see Figure 2.29, top left). The group of Finlayson-Pitts investigated and compared these two methods in detailed analytic studies.[236] In summary, they demonstrated that the cleaning with piranha solution results in a rougher and thicker oxide layer compared to plasma cleaning.

Another approach requires the treatment of the silicon surface with 1–2 vol% aqueous HF. Such a treatment results in the formation of hydrogen terminated silane at the silicon surface (see Figure 2.29, top right).[237]

In the current thesis, only piranha solution was used for surface activation (see Section 3.1).

2.4.2.2 Formation of self-assembled monolayers

After rigorous cleaning, the choice of suitable molecules for the formation of SAMs depends on the employed cleaning method. The whole process of activation and SAM formation is depicted in Figure 2.29.

When treated with 1–2 vol% aqueous HF, the free hydrogen-terminated silanes can react, for example, with organic peroxides,[231] terminal alkenes,[238] alkynes,[237] or diazonium salts.[239] In contrast to peroxides and diazonium salts, additional radical initiators are needed when working with alkenes or alkynes.[237] In all of these cases, the SAM formation follows a radical mechanism.[219b,237] The different chemical connectivities between substrate and SAM are depicted in the lower right side of Figure 2.29.

When piranha solution or plasma treatment is employed for surface activation, the free hydroxyl groups can react with either alcohols,[238] chlorosilanes,[219a] or silyl ethers,[124,162,219a,240] following a S_N2 reaction mechanism[219b] (see Figure 2.29, lower left side).

The driving force for the spontaneous formation of SAMs is the significant reduction in surface energy. In addition, the formation of the strong Si–O bonds further contributes to the process. Beside these thermodynamic reasons, entropic changes also need to be considered. As an example, employing alkylalkoxysilanes ($R{-}Si(OR')_3$), one molecule binding to the silicon surface releases three small molecules ($R'{-}OH$), which results in an increase in entropy. On the other hand, all molecules attached to the surface loses some degrees of freedom, which reduces the entropy. Adding up these two contributions, the net result is an overall increase in entropy. Wang *et al.* proposed a two-step process for the SAM formation of alkylchlorosilanes.[241] In the first step, condensation of the alkylchlorosilane with the surface-attached hydroxyl groups leads to the immobilization

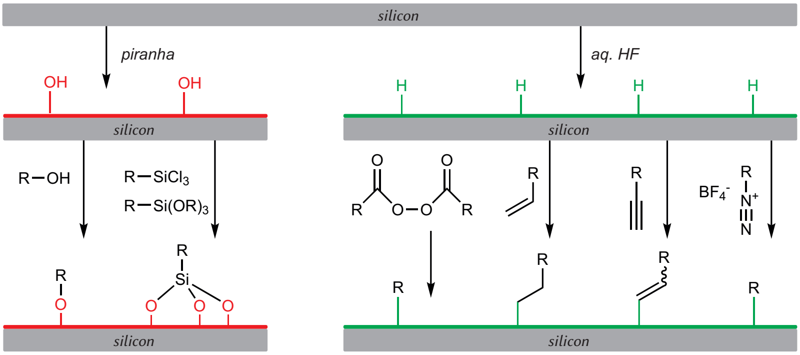

Figure 2.29. Activation *via* piranha (top left) or aqueous HF (top right) and subsequent SAM formation on silicon substrates based on various chemical connectivities.

of the silane. Subsequently, polycondensation of the attached silanes results in the final SAM.

For alkylalkoxysilanes, McGovern *et al.* proposed an alternative formation process.[242] They suggested that initial diffusion of surface moisture into the silane-containing solution, followed by partial condensation of the silanes and subsequent attachment to the silicon surface may be the mechanism of the SAM formation.

In both cases, the strict control of water content,[242] temperature,[243] choice of solvent system,[219b] and reaction time[243,244] is crucial for reproducible results.

2.4.2.3 Post-modification techniques

After successful formation of a SAM on the silicon substrate, several methods have been developed for further functionalization of the surface. Such post-modifications are necessary in cases were the desired functional group is not compatible with the SAM formation process. It is also advantageous to use silanes with low molecular weights for SAM formation in order to facilitate surface binding interactions of the coating agent. However, employing the concept of SAM formation on surfaces is not applicable to surface micro-patterning with spatial resolution. This section therefore summarizes different approaches for the post-modification of (mainly) silane based SAMs on silicon surfaces with a focus on spatially resolved techniques, as exploited in Chapter 3 of the current thesis.

A depiction of different surface modification strategies according to their chemical mechanism is presented in Figure 2.30.[219a] The post-modification strategies can be divided in two categories: non-covalent and covalent approaches.

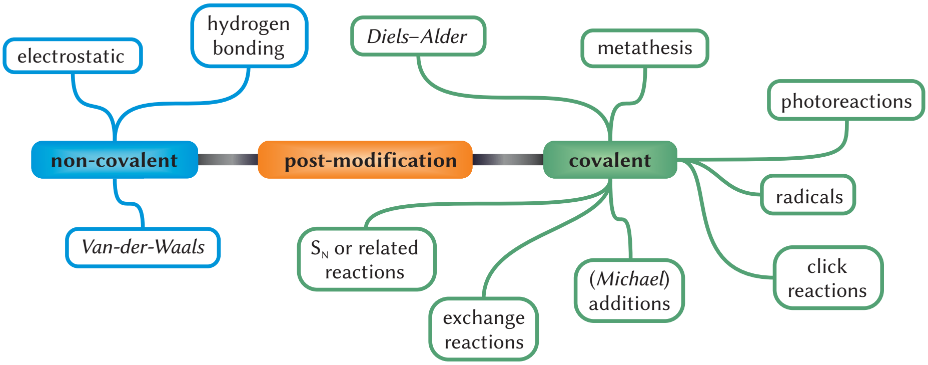
electrostatic
hydrogen bonding
Diels–Alder
metathesis
photoreactions
non-covalent
post-modification
covalent
radicals
Van-der-Waals
S_N or related reactions
(Michael) additions
click reactions
exchange reactions

Figure 2.30. Common examples of non-covalent (blue), as well as covalent (green) post-modification strategies.

Non-covalent interactions for post-modification strategies are shown on the left side of Figure 2.30. These include electrostatic interactions,[245] hydrogen bonding,[246] or *Van-der-Waals* interactions.[247]

On the right side of Figure 2.30, various post-modification routes involving covalent bond formations are summarized, including *Diels–Alder*-,[124,248] metathesis-,[249] photo-,[132,139a,250] radical-,[251] click-,[252] S_N -,[219a] as well as exchange reactions[219a] and (*Michael*) additions.[253]

While all of these approaches open up the opportunity for advanced surface modifications, only a few of them can be applied for the spatially resolved post-functionalization. Many examples can be found in the literature, including microcontact printing (µCP). Here, a microscopic stamp is loaded with the respective material and then directly pressed onto the surface. However, during µCP, no covalent bonds are formed between the modifying agent and the surface, which limits a widespread practical use.

Alternatively, many reactions displayed in Figure 2.30 can be triggered using light as an external stimulus. In combination with shadow masks, tailor-made surface patterns are accessible. Beside the STP chemistry described in Section 2.2.3.4, thioaldehyde, NITEC, as well as photoenol chemistry has been successfully applied for spatially resolved surface modifications, with common examples previously presented in Section 2.2.3.

2.4.2.4 Polymers on surfaces

The fabrication of polymer-functionalized surfaces is of emerging interest in applied chemistry and material sciences. Common examples include their use in surface wettability alteration,[254] opto-electronic devices,[255] heterogeneous catalysis,[256] lab on a chip system,[257] self-cleaning surfaces,[258] microfluidic devices,[259] smart membranes,[260] or thin film sensors.[261]

Hereby, the precise control over the polymer architecture, e.g. chain length, MWD, or metal content, is highly desirable and common strategies for the manufacturing of precision materials have been discussed in Section 2.1. Here, the focus is on the control of polymer surface immobilization, which is another key point in the formation of advanced functional material interfaces.

The surface decorating/functionalization with polymers can be achieved *via* three routes, namely the *grafting-to*, *grafting-from*, and *grafting-through* approaches (see Figure 2.31). Alternative strategies, such as the physisorption of polymers have been introduced as well. These mechanical patterning approaches include for example nanosphere lithography (NSL),[262] µCP,[263] or nanoimprint lithography (NIL).[264] While these techniques are attractive due to their high-throughput and low processing cost, they do not form covalent bonds between the surface and the polymers and therefore will not be discussed in this section.[265]

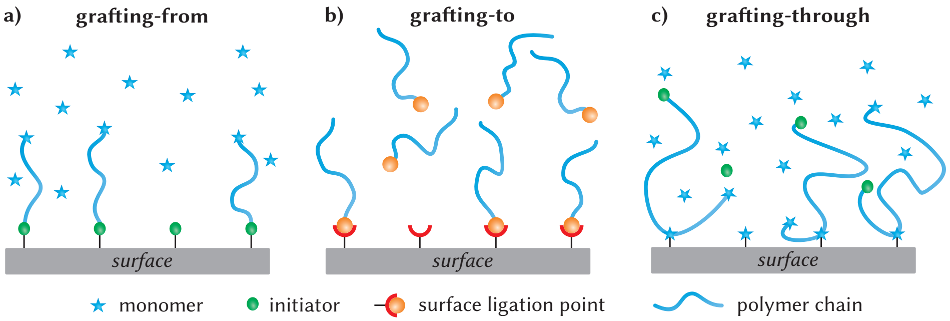

Figure 2.31. Different chemical strategies for the surface functionalization with polymers. a) *Grafting-from* polymerization through surface-attached initiator molecules. b) The *grafting-to* methodology utilizes pre-formed end-functionalized polymers in a ligation step. c) In the *grafting-through* approach, surface bound monomer units get incorporated into the growing polymer chain during a polymerization process.

When applying the *grafting-from* polymerization technique, polymer chain propagation proceeds directly at the substrate interface, which is equipped with surface-immobilized initiators (refer to Figure 2.31a).[266] Usually, an initiator for the polymerization is attached to the surface following one of the methods discussed in Section 2.4.2.3. Subsequent surface-initiated polymerization forms the desired materials. This approach has the advantage of the formation of densely packed polymer brushes attached to the surface.

However, it does lack the precise control over the polymer architecture, as the *grafting-from* polymerization is ill-defined compared to solution-based methods.

The *grafting-to* method utilizes end-functionalized polymers, which are tethered onto the substrate *via* various ligation protocols (see Figure 2.31b).[267] The surface is decorated with suitable moieties for the ligation, following the methods which have been previously discussed in Section 2.4.2.2 and Section 2.4.2.3. Instead of growing the polymer chains from the substrate, the pre-formed end-functionalized polymer is attached onto the surface. The advantage of this approach is the possibility to exploit the versatile toolbox of common RDRP techniques (e.g. RAFT, ATRP, ...) for the preparation of highly defined polymer architectures. The prepared polymers can be characterized with standard solution-based techniques, such as SEC or NMR spectroscopy, before attaching the polymer strands to the surface. However, it is reported that the surface coverage is typically lower compared to the *grafting-from* approach, due to the steric hindrance of already attached polymer chains.[268] In addition, the polymer composition determined in solution might differ from the actual distribution grafted onto the surface.[269]

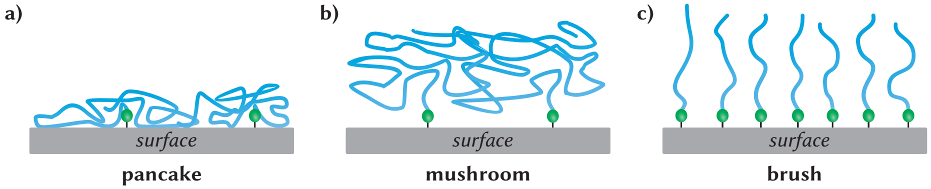

Figure 2.32. Classification of surface-immobilized polymers according to their grafting densities. a) The *pancake* regime in low grafting densities and bad solvents. b) The combination of good solvents and low grafting densities results in the *mushroom* regime. c) The *brush* regime is obtained with high grafting densities.

Finally, monomers, instead of initiators, are tethered onto the substrate following the *grafting-through* approach (refer to Figure 2.31c). Performing a bulk polymerization in presence of such surfaces, the growing polymer chains get chemically linked to the surface *via* incorporation of the surface-immobilized monomers.[270]

In all of the above-described approaches, the surface bound polymers are referred to as polymer brushes, i.e. as thin films, which are linked to the surface by one chain end of the respective polymer.[267a,271] Depending on the surface characteristics, such as covering density, MWD, etc., the surface-immobilized polymers can be classified according to their different conformations. These range from the so-called *pancake* (bad solvents) and *mushroom* regime (good solvents) at low grafting densities to the *brush* regime at high grafting densities (refer to Figure 2.32).[272] As previously discussed, the *brush* regime is usually obtained *via* the *grafting-from* approach, while the *grafting-to* and *grafting-through* approaches result in lower grafting densities.

2.4.2.5 Surface-immobilized metallopolymers

This section gives a brief summary on the preparation of metallopolymers on surfaces following the *grafting-to* method, as only *via* this route, precise control over the polymer architecture in solution, as well as the subsequent surface coverage is possible. Especially the possibility to characterize the polymers in solution is a big advantage on the way to tailor-made surfaces, as compared to the *grafting-from* approach. Surprisingly, reports on the surface functionalization with metallopolymers *via* the *grafting-to* approach are very rare compared to the *grafting-from* technique, which is intensively employed in surface-initiated metallopolymer formation.[273] In addition, the *grafting-to* method was applied in Chapter 3 of the present thesis, exploiting the above described advantages of the *grafting-to* approach.

While there are reports for the homogeneous coverage of silicon surfaces with end-functionalized metallopolymers, the spatially resolved immobilization of metallopolymers has not been reported yet. Therefore, two examples for the homogeneous surface fixation of metallopolymers *via* end-group ligation points is presented.

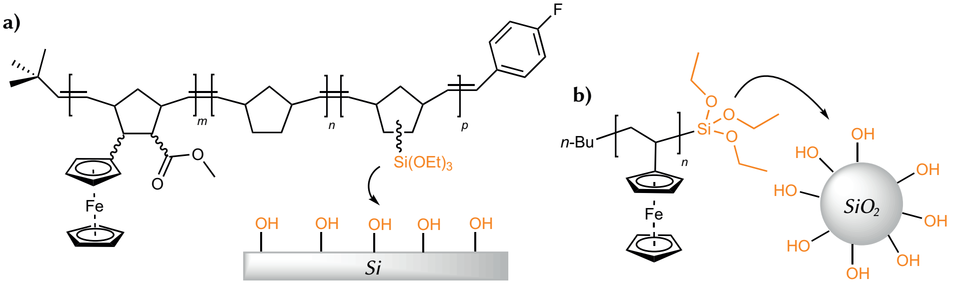

Figure 2.33. a) Homogeneous immobilization of a $Si(OEt)_3$-terminated ferrocene metallopolymer synthesized *via* ring-opening metathesis polymerization (ROMP) onto a silicon wafer.[274] b) Controlled anionic polymerization of vinylferrocene-terminated by a triethoxysilane moiety. Upon immobilization onto spherical silicon particles, redox-responsive surfaces are obtained.[275]

Schrock and coworkers were the first who reported the successful surface ligation of a ferrocene-containing metallopolymer in the early 1990s. The polymer was prepared by ROMP of a norbornene monomer. They introduced functional $Si(OEt)_3$ end groups, which enabled the surface ligation onto platinum, ITO, and *n*-doped silicon electrode surfaces through siloxane bond formation.[274] One of the employed metallopolymers is depicted in Figure 2.33a) together with the hydroxyl-terminated silicon surface.

Elbert *et al.* synthesized redox-responsive poly(vinylferrocene)-grafted silica nanoparticles *via* anionic polymerization and termination with a triethoxysilane moiety.[275] After immobilization of the metallopolymer in a *grafting-to* approach onto spherical silicon particles (see Figure 2.33b), the authors demonstrated the activity control of surface-attached Grubbs second generation type catalysts for ROMP polymerizations.

In conclusion, the spatially resolved immobilization of intact metallopolymers prepared through controlled polymerization techniques onto surfaces *via* the *grafting-to* method is attractive, as precise control of the polymer, as well as the surface structure is possible. Future applications are for example magnetic responsive materials, novel surface-coated electrodes, heterogeneous catalytic devices, stimuli-responsive surfaces, or bio-, as well as small molecule sensing devices.[27] In fact, the surface attachment of metallopolymers prepared *via* RDRP techniques has not been described so far. Despite these interesting application fields, the spatially resolved ligation of metallopolymers remains unexplored, which is the central point of Chapter 3 of the current thesis.

CHAPTER 3

Spatially resolved multiple metallopolymer surfaces by photolithography

Spatially resolved functional interfaces are of specific interest for various technological fields.[276] Examples include heterogeneous catalysis, were precise control over the spatial distribution of catalytically active metal centers is desired.[277] Here, the spatial control is achieved through the control over the crystal lattice of the underlying substrate, in which the metal centers are embedded. However, the spatially controlled attachment of homogenous catalysts onto a surface requires additional chemical strategies, such as photolithographic approaches. In addition, the performance of many organometallic catalysts attached onto solid substrates is inferior as compared to the homogeneous catalysis in solution.[278] The incorporation of such homogeneous catalysts into a surface anchored polymer chain can improve the performance, as more catalytic centers can be tethered onto a defined surface area, i.e. the metal loading per surface area is increased. In addition, the swelling behavior of the polymer chain is beneficial for the catalytic performance, as the catalytic centers are brought into a solution-like environment. As such, surface effects deteriorating the performance are reduced, while still taking advantage of the heterogeneous setup, such as the facile catalyst recovery. Ultimately, the utilization of RDRP protocols for the preparation of the metallopolymers enables additional control in the vertical dimension, e.g. *via* the $\bar{X}_n$ of the polymer or the local concentration of the catalyst through the functionalization degree. The use of a polymeric system additionally simplifies the synthetic strategy, as small organometallic complexes suffer from the necessity to synthesize each ligand-surface anchor system separately.

While there are several methods available for the spatially resolved anchoring of small molecules, as well as polymers on solid substrates (refer to Section 2.2.3 and 2.4.2.4), none of these techniques has been employed for the surface-ligation of metallopolymers, yet. The utilization of metallopolymers unifies the benefits of heterogeneous catalysis, surface photoligation and the simple preparation of polymers through RDRP techniques.

This chapter will introduce an approach for the spatially resolved immobilization of multiple metallopolymers onto silicon substrates *via* photolithographic techniques. For this purpose, surfaces are uniformly covered with a SAM of a photo active linker molecule (refer to Section 2.2.3), which is subsequently activated by light and reacts with the end-functionalized metallopolymers. Different lithographic masks enable the fabrication of arbitrary surface patterns with minimal equipment and on short timescales over large surface areas. (a)

3.1 Development of a surface ligation protocol

The first step of the method development was the choice of suitable photoligation protocols and their combination with a RDRP method. RAFT polymerization was chosen as the RDRP method, due to its versatility and the facile synthesis of functional RAFT agents for subsequent photoligation chemistry. A methacrylate-based polymer system was targeted, as functional methacrylate monomers feature a higher stability in comparison to their corresponding acrylates, while still featuring good solubility in polar organic solvents compared to styrene-based systems. ATRP was disregarded due to possible interference of the copper ions with ligand monomers, as well as metal ions of the metallopolymer backbone. NMP does not enable good control over methacrylates(b) and was therefore also not suitable for the chosen system. Two photoligation approaches were followed in the current thesis, namely phenacyl sulfide and tetrazole ligation chemistry. The surface anchor molecules are equipped with the photo active sites and the complementary groups are incorporated into the RAFT CTA R-group, which is depicted in Figure 3.1. The phenacyl sulfide photoligation on the left side (refer to Section 2.2.3.1) comprises a phenacyl sulfide silane **3** and either a dithiobenzoate **1** or trithiocarbonate **2** RAFT agent with a hexadiene-functionalized R-group. The utilization of the NITEC photoligation (refer to Section 2.2.3.2) is shown on the right hand consisting of a dithiobenzoate RAFT agent **4** with a furan-protected maleimide as the R-group and a tetrazole-functionalized silane **5** for the SAM formation onto the silicon surface.

(a) Parts of this chapter are reproduced or adapted from R. Müller, T. J. Feuerstein, V. Trouillet, S. Bestgen, P. W. Roesky, C. Barner-Kowollik, Spatially Resolved Multiple Metallopolymer Surfaces by Photolithography, *Chem. Eur. J.* **2018**, *24*, 18933–18943, with permission from Wiley-VCH Verlag GmbH & Co. KGaA © 2018. R. Müller designed and conducted all experiments unless otherwise stated. T. J. Feuerstein synthesized the phosphine ligand, parts of the bipyridine ligand, the metal complexes, and performed the metal-loading of the copolymers. V. Trouillet performed the ToF-SIMS and XPS measurements. S. Bestgen contributed to scientific discussions. P. W. Roesky, and C. Barner-Kowollik motivated and supervised the project and contributed to scientific discussions.

(b) The challenge for the NMP of methacrylates is the disproportionation reaction between the nitroxide and the growing radical, resulting in an alkene chain-end along with a hydroxylamine, which dominates over the reversible combination with the nitroxide, see also [279].

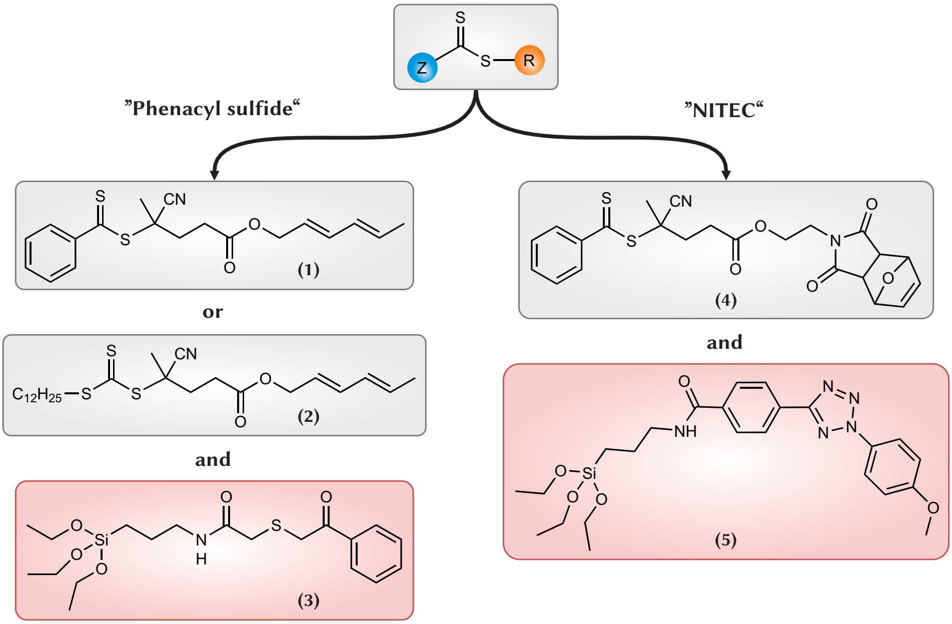

Figure 3.1. Two approaches for the photoligation of metallopolymers synthesized *via* RAFT polymerization onto silicon surfaces. Left side: phenacyl sulfide-functionalized silane **3** is coupled with RAFT agents **1** and **2**, bearing a hexadiene functionality in the R-group. Right side: a furan-protected maleimide on the R-group of CTA **4** enables the photoligation with the surface-attached tetrazole **5**.

3.1.1 Phenacylsulfide approach

The first route followed was the phenacyl sulfide approach on the left side of Figure 3.1. This chemistry was successfully applied in the authors group for the photolithographic encoding of metal complexes (refer to Figure 2.18)[144] and was therefore chosen as the initial methodology.

While the phenacyl sulfide silane **3** was synthesized according to literature,[124] the synthesis route for the RAFT agents **1** and **2** for subsequent photoligation is depicted in Figure 3.2a) and b), respectively.

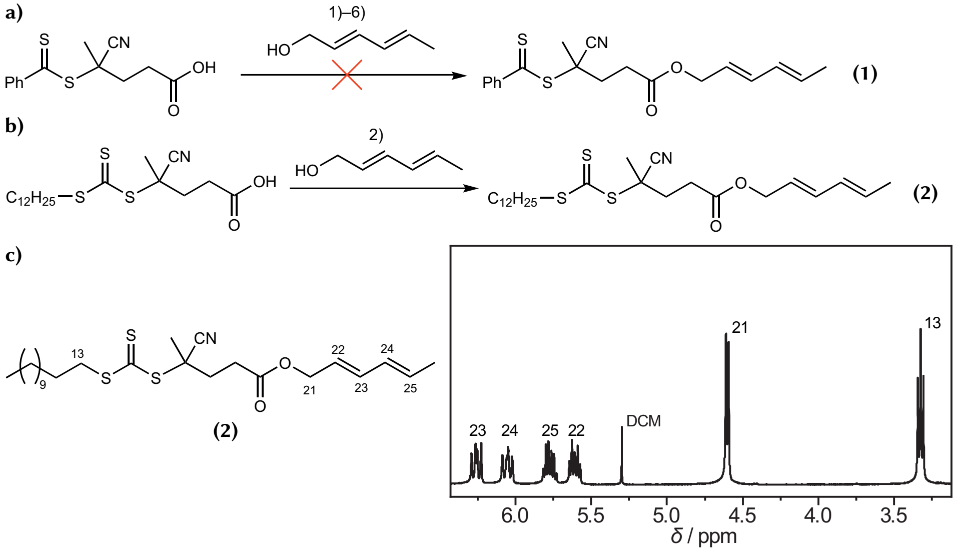

Figure 3.2. a) Unsuccessful attempted experiments to obtain CTA **1**: 1) EDC·HCl, DMAP, DCM; 2) DCC, DMAP, DCM; 3) DCC, PFP, DMAP, DCM; 4) EDC·HCl, OxymaPure®, $NaHCO_3$, $MeCN/H_2O$; 5) see 2) without (*2E*,*4E*)-hexadienol; 6) oxalyl chloride, DMF (cat.), DCM. b) Successful Steglich esterification of CDSTSP and (*2E*,*4E*)-hexadienol towards CTA **2**. c) ^1H NMR zoom in the spectrum of **2** with corresponding assignment, confirming the intact diene functionality (protons 21–25), as well as the Z-group *via* proton 13.

CTA synthesis CTA **1** was the first choice, as dithiobenzoate CTAs are very effective for the controlled polymerization of methacrylates. However, several attempts to esterify CPADB with (*2E*,*4E*)-hexadienol failed and resulted in the degradation of the dithiobenzoate moiety (see Figure 3.2a). Steglich esterification protocols with EDC or DCC resulted in degradation of the pink dithiobenzoate moiety and formation of a yellowish residual. Similar results were observed upon stabilizing the active ester *in situ* with pentafluorophenol (PFP) or OxymaPure®. Likewise, attempts to isolate the PFP active ester or activation of CPADB with oxalyl chloride were not successful.

The trithiocarbonate moiety features a higher stability compared to the dithiobenzoate group, while still being capable to control the polymerization of methacrylates. Starting from commercially available 4-cyano-4-((dodecylsulfanylthiocarbonyl)sulfanyl)pentanoic acid (CDSTSP), esterification with (*2E,4E*)-hexadienol employing DCC with catalytic amounts of DMAP led to successful formation of the target CTA **2** with a yield of 71 % (see Figure 3.2b). In the ^{1}H NMR spectrum of **2**, all proton resonances can be assigned, in particular the resonances associated with the Z-group (13), as well as the R-group (21–25) (see panel c).

Polymerization With the diene-functional CTA **2** at hand, the RAFT polymerization was first tested with methyl methacrylate in a homopolymerization (see Figure 3.3). A controlled polymerization was obtained in toluene solution with AIBN as the initiator at 60 °C. The SEC chromatograms of polymers **P1**–**P4** show a narrow and monomodal MWD with $\bar{M}_{\mathrm{n,SEC}}$ ranging from 3300–6500 g mol^{-1} and $Đ < 1.21$. For **P3**, the $\bar{M}_{\mathrm{n}}$ determined from ^{1}H NMR spectroscopy *via* integration of RAFT group protons 21 and the methoxy protons of the polymer backbone at 3.6 ppm affords a value of

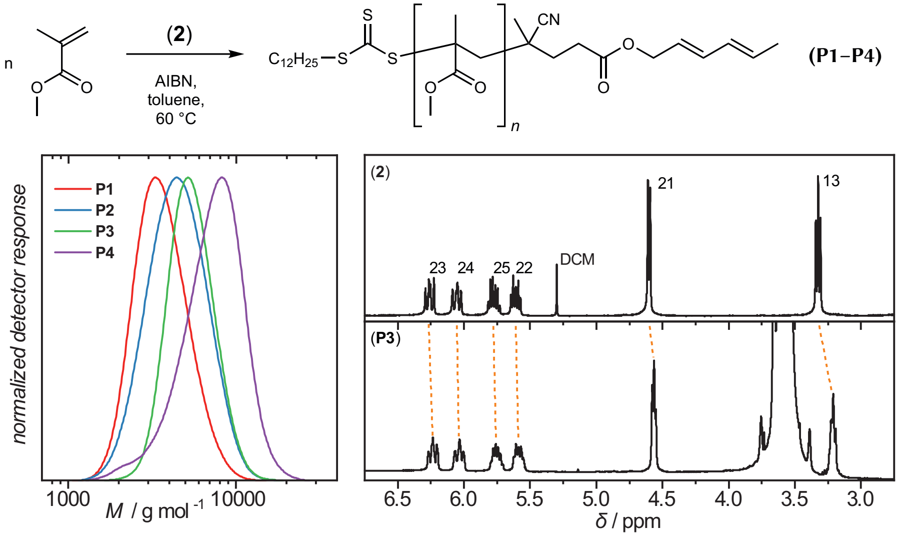

Figure 3.3. Results of the MMA homopolymerization with CTA **2**. The SEC traces of polymers **P1**–**P4** are shown on the left. The ^{1}H NMR spectra of **2** and **P3** on the right side confirm the intact diene functionality of the R-group, as well as the Z-group *via* protons 21–25 and 13, respectively.

$\bar{M}_{\mathrm{n,NMR}} = 4800$ g mol^{-1}, which is in good correlation to the SEC value of $\bar{M}_{\mathrm{n,SEC}} =$ 5100 g mol^{-1}. Importantly, the proton resonances 21–25 of the diene moiety stay unchanged during the radical polymerization, i.e. the conjugated double bonds are not reactive towards a radical attack, which is a prerequisite for the subsequent photoligation (see ^{1}H NMR spectra of **2** and **P3** in Figure 3.3).

Photoligation in solution With the end-functionalized homopolymers **P1**–**P4** at hand, the reactivity of the terminal diene moiety was first tested in solution, employing a phenacyl sulfide-terminated PEG **P5** ($\bar{M}_{\mathrm{n,SEC}} = 2900\,\mathrm{g\,mol^{-1}}$, $Đ = 1.04$). The SEC traces of the photoreaction between **P5** and **P1**, **P2**, and **P4** are depicted in Figure 3.4, together with the product traces **P6**–**P8**. The expected block copolymer formation between the end-functionalized polymers should result in a MW which is the sum of the two starting materials.(a) The calculated values for the photo induced hetero-*Diels–Alder* reaction are highlighted with *Photo-DA* in the graphs.

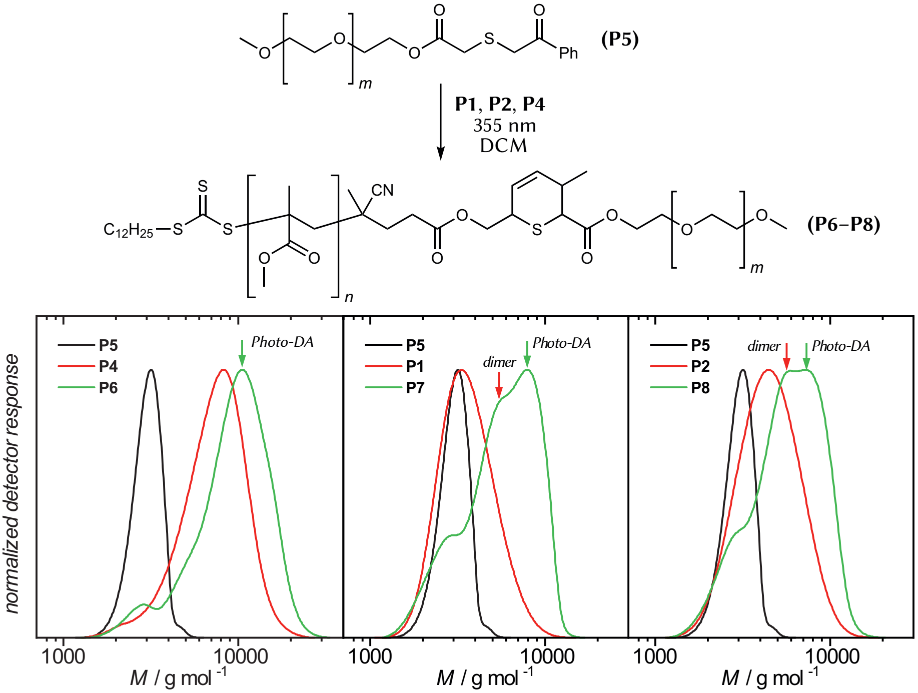

Figure 3.4. Photoligation reaction between phenacyl sulfide functionalized PEG **P5** and the diene equipped PMMA polymers **P1**, **P2**, and **P4**. The SEC traces for each reaction product **P6**–**P8**, as well as the starting materials, are depicted below the reaction scheme. Calculated MWs for the expected *Photo-DA* product and the *dimer* side-product are indicated with arrows.

(a) It should be noted that this calculation can only be regarded as a rough estimate, because the error from the SEC calibration must be considered as well.

A shift of the MW due to the formation of the block copolymers is observed in all cases. In the reaction between **P4** and **P5**, traces of residual PEG starting material are present due to stoichiometric imbalances. For the reactions of **P1** and **P2** with **P5**, a shoulder is observed in the product trace in addition to residual **P5**, with a MW that is twice the value of **P5** (indicated as *dimer*). This can be attributed to a possible side-reaction of the reactive thioaldehyde species that can dimerize (see also Scheme 2.8). As an example, the calculated MWs of the *dimer* and the *Photo-DA* products in the reaction between **P2** and **P5** are $M = 5800\,\mathrm{g\,mol^{-1}}$ and $M = 7700\,\mathrm{g\,mol^{-1}}$, respectively. The determined SEC peak values in the trace of **P8** are $M = 5900\,\mathrm{g\,mol^{-1}}$ and $M = 7300\,\mathrm{g\,mol^{-1}}$, which is in good correlation to the theoretical expectation.

Despite the observed side reaction, i.e. the formation of *dimer* PEG polymers, the reactivity of the diene functionalized PMMA polymers in the photochemical ligation was demonstrated in solution. It should be noted, that the side-reaction observed in solution should not interfere with the surface photoligation, since the phenacyl sulfide is covalently bound to the silicon surface and should therefore be hindered to form dimerization products. Accordingly, the photoligation was attempted on surfaces.

Photoligation on surfaces For the surface photoligation, silicon wafers were activated and covered with a SAM of the phenacyl sulfide silane **3** (refer to the experimental part on Page 184). In a typical surface experiment, a sample holder with or without shadow mask is assembled with the silicon wafer carrying the photo active SAM (see Figure 3.5a) and b). The assembled wafer is placed into a photo vial containing the polymer solution and irradiated from the side in a custom-build photo reactor (see Figure 3.5c) and d), for the spectral irradiances of the employed UV lamps refer to Figure A.24 and Figure A.25).

If no photo mask is used, the shape of the photo mask holder results in a rectangular irradiated area, whereas the residual surface area is not irradiated. Such a setup enables the characterization of the irradiated, as well as the dark areas of the surface in high-resolution X-ray photoelectron spectroscopy (XPS) measurements. In addition, the border of the irradiated area, i.e. the dark, as well as the irradiated part, can be characterized *via* ToF-SIMS. The setup without photo mask was employed for all screening experiments, before advancing to write particular patterns onto the surfaces with smaller feature sizes.

The photoreaction was conducted with polymer **P3** and no shadow mask (setup A, see Table A.2), as depicted in Figure 3.5e) (for experimental details, see Section 7.5). Surfaces **S1a**–**S1c** were analyzed *via* high-resolution XPS measurements. An additional reference surface **S1d** was prepared through immersion of surface **S1b** into polymer solution **P3** without irradiation. The results of the XPS measurements are summarized in Table 3.1. For **S1c**, **S1c-ir.** refers to the irradiated part, while **S1c-dark** describes the dark part of the surface (see grey and green parts in Figure 3.5e), respectively).

Starting with the activated surface **S1a**, only the underlying silicon substrate including the SiO_2 surface layer is detected.

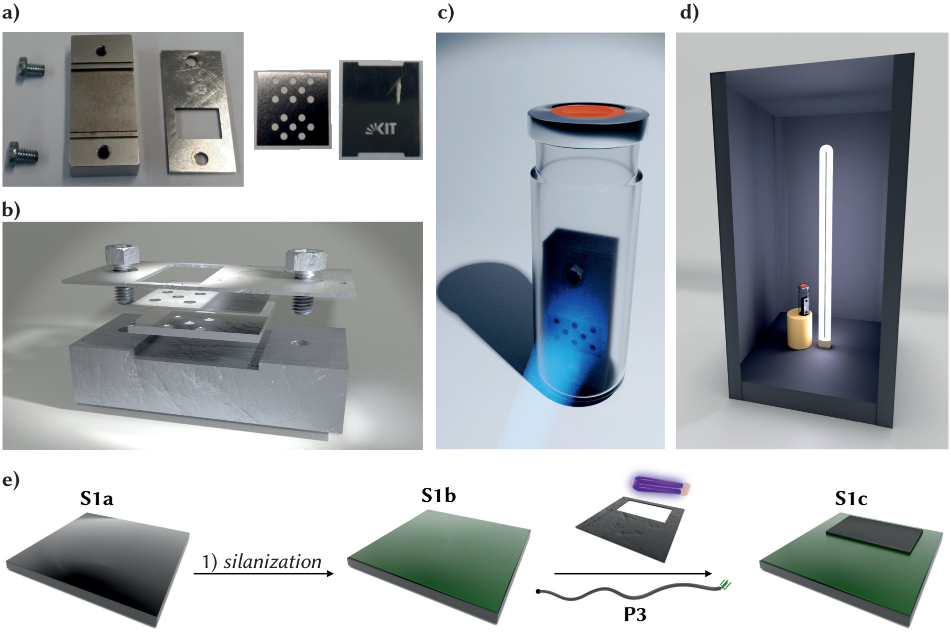

Figure 3.5. a) Picture of the photo mask holder next to the employed dotted and KIT-logo shadow masks. b) Illustration of the silicon wafer, photo mask holder, and a photo mask assembled for the reaction. If no photo mask is used, the shape of the c) Setup of the assembled photo mask holder in the photo vial containing the solution with the end-functionalized polymer. d) Scheme of the custom-build photo reactor equipped with an UV lamp. e) The activated silicon wafer **S1a** is uniformly covered with silane **3** (surface **S1b**) and irradiated with a rectangle shadow mask in the presence of polymer **P3** to obtain surface **S1c**. Adapted with permission from [280]. © 2018 Wiley-VCH Verlag GmbH & Co. KGaA.

The small C 1s value of 3.9 at% is the result of minor contamination. After the silanization, the N 1s and S $2p_{3/2}$ signals and the increase in the C 1s value in surface **S1b** correspond to the formed SAM of silane **3**. In addition, a decrease of the detected silicon substrate is an indirect measure of the successful SAM formation, since the penetration depth of the X-ray irradiation is constant, i.e. the formation of additional surface coverage attenuates the silicon substrate signal. The successful immobilization of polymer **P3** during irradiation should be detected through an increase in the C 1s value coming from the polymer backbone. Simultaneously, the silicon signal should be further reduced, as a consequence of the thicker surface layer. However, comparison of these values in the irradiated and dark parts of surface **S1c** does not show the expected trend. Instead, no significant change is observed and the N 1s and S $2p_{3/2}$ values of **S1c-ir.** do not vary either, when compared to **S1c-dark** or **S1b**. In combination with the values from the reference sample **S1d**, which are in a similar range than **S1c**, no evidence can be found for a successful immobilization of polymer **P3** on the surface.

Table 3.1. XPS analysis of the surface photoligation experiments employing polymer **P3** and silane **3**. All values are in atomic percent (at%).

surface	Si $2p_{3/2}$	C 1s	O 1s	N 1s	S $2p_{3/2}$
S1a	49.8	3.9	33.5	–	–
S1b	35.4	16.3	29.8	2.1	0.2
S1c-dark	34.4	14.6	30.3	2.2	0.2
S1c-ir.	34.0	17.4	29.6	2.2	0.2
S1d	35.5	13.2	31.0	2.0	0.2

Since the surface characterization cannot provide sufficient information about the chemical bonds in the surface layer, the reason for the failed photoligation remains unclear. Possible explanations might include the observed dimerization side-reaction observed in solution. If polymer **P3** is not in close proximity to the surface bound silane **3**, the photo generated thioaldehyde can undergo dimerization reactions with adjacent silane molecules and therefore reduce the surface activity towards ligation. Another point could arise from side-reactions of the trithiocarbonate moiety upon UV irradiation. Such groups are known to form reactive radicals under UV irradiation,[281] which can result in detrimental side-reactions.

In view of these results, the route towards surface immobilized metallopolymers employing the phenacyl sulfide photoligation chemistry was abandoned at this point and an alternative strategy *via* the use of NITEC photoligation chemistry was followed (see also right side of Figure 3.1).

3.1.2 NITEC approach

For the NITEC strategy outlined in Figure 3.1, a RAFT agent with an activated double bond needs to be synthesized. In order to circumvent the participation of the activated double bond in the radical polymerization, a furan-protected maleimide moiety was chosen. The structure of CTA **4** features a dithiobenzoate moiety with R-group that mimics the employed AIBN initiator.

CTA synthesis and polymerization In contrast to the difficulties in the esterification of CPADB with (*2E*,*4E*)-hexadienol in the synthesis towards CTA **1**, the esterification of CPADB with 2-(2-hydroxyethyl)-3a,4,7,7a-tetrahydro-1*H*-4,7-epoxyisoindole-1,3(2*H*)-dione (Mal-OH) using OxymaPure® as an active ester provided CTA **4** with an overall yield of 73 %.

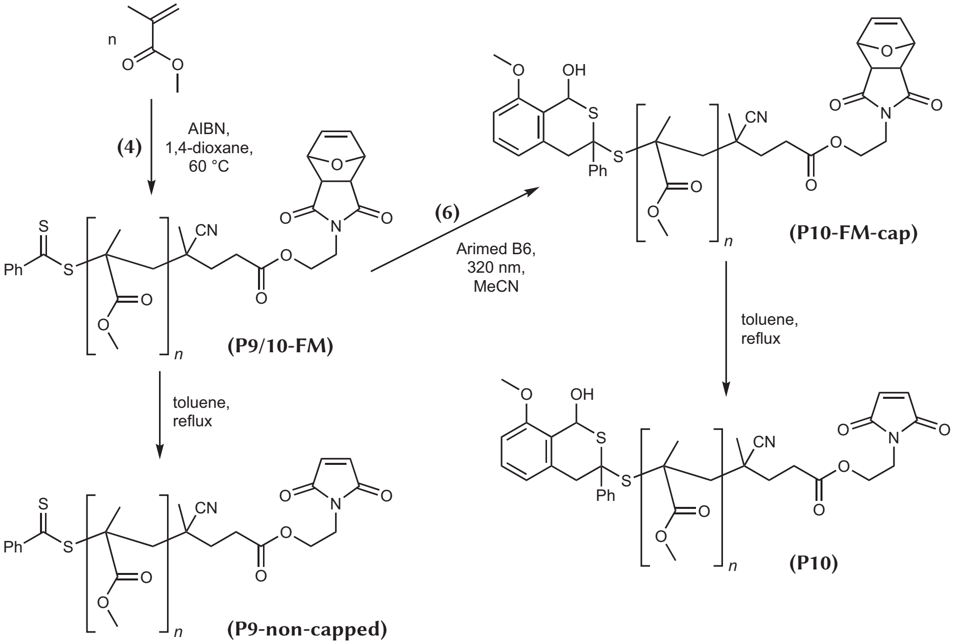

Scheme 3.14. RAFT polymerization of MMA with CTA **4** yields polymer **P9-FM** and **P10-FM**. Refluxing of **P9-FM** in toluene removes the furan protecting group towards polymer **P9-non-capped**. Capping of the dithiobenzoate moiety of **P10-FM** with photoenol precursor **6** delivers polymer **P10-FM-cap**, which is subsequently deprotected towards polymer **P10**.

The RAFT polymerization protocol of MMA with CTA **4** is depicted in Scheme 3.14. Homopolymers **P9-FM** and **P10-FM** were obtained as pink powders with narrow dispersity and a monomodal MWD ($\bar{M}_{\text{n,SEC}} = 2700\,\text{g mol}^{-1}$, $Đ = 1.18$, and $\bar{M}_{\text{n,SEC}} = 5500\,\text{g mol}^{-1}$, $Đ = 1.21$, respectively). First attempts to directly deprotect **P9-FM** in refluxing toluene and use the maleimide end-functionalized polymer **P9-non-capped** in the NITEC reaction were not successful. The expected immobilization of polymer **P9-non-capped** on surface **S2-non-capped** cannot be confirmed by the ToF-SIMS analysis, observing the specific PMMA fragments ($C_3H_3O^-$ and $C_4H_5O_2^-$, see Figure 3.7a). The dotted green line in the ToF-SIMS ion mappings divides the irradiated (top) from the dark part (bottom) of the surface. Similar to the results obtained by employing the phenacyl sulfide photoligation, the intact RAFT moiety does interfere with the NITEC reaction. This observation is attributed to radical formation and resulting undesired side-reactions of RAFT CTAs under UV light irradiation.[281]

Therefore, the dithiobenzoate group of **P10-FM** was reacted with 2-methoxy-6-methylbenzaldehyde (**6**) in a light-triggered hetero-*Diels–Alder* reaction towards polymer **P10-FM-cap**.(a) Subsequently, the capped polymer is deprotected, removing the furan, to yield the maleimide-functional polymer **P10** (refer to Scheme 3.14). This route was chosen over other possibilities to remove the RAFT group, as the reaction can be performed with an excess of **6** without the risk of side reactions, as for example polymer-polymer coupling in the case of radical CTA cleavage, see also Figure 2.4. The successful transformation

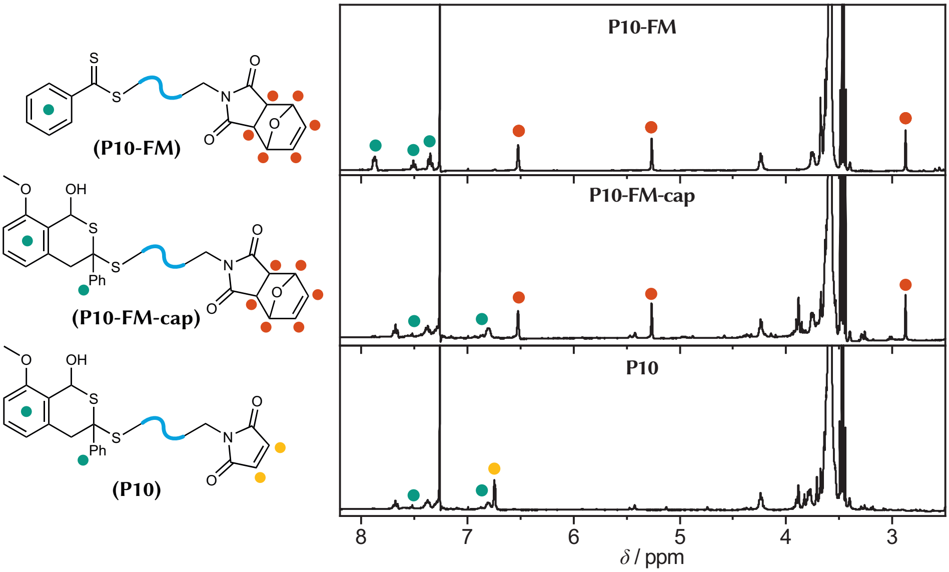

Figure 3.6. ^{1}H NMR spectra of the PMMA homopolymers **P10-FM** (top), **P10-FM-cap** (middle), and **P10** (bottom) recorded in $CDCl_3$. Representative protons described in the text are highlighted with colored circles in the structures (left side) and the spectra (right side). Adapted with permission from [280]. © 2018 Wiley-VCH Verlag GmbH & Co. KGaA.

(a) Unfortunately, the trithiocarbonate functionality in RAFT CTA **2** is not sufficiently activated to react in a similar hetero-*Diels–Alder* with **6**, while the corresponding dithiobenzoate CTA **1** was not accessible. Therefore, the capping protocol through photoreaction with **6** cannot be applied in the phenacyl sulfide approach.

of polymer **P10-FM** into **P10-FM-cap** and **P10** was followed by ^{1}H NMR spectroscopy and SEC (see Figure 3.6 and Figure A.33, respectively). In the ^{1}H NMR of **P10-FM**, the aromatic resonances from the dithiobenzoate group between 8–7.3 ppm (green) and the resonances of the furan-protected maleimide at 6.52, 5.26, and 2.87 ppm (red) prove the intact structure of the RAFT polymer ($\bar{M}_{\text{n,SEC}} = 5500\,\text{g}\,\text{mol}^{-1}$, $Đ = 1.21$).

In the first reaction step, the aromatic dithiobenzoate resonances in **P10-FM-cap** shift upon reaction with **6**, while the resonances associated with the furan protected maleimide remain unchanged. The SEC chromatogram of **P10-FM-cap** proves the structural integrity of the polymer during the reaction, as no significant change in the MW and dispersity is observed ($\bar{M}_{\text{n,SEC}} = 5700\,\text{g}\,\text{mol}^{-1}$, $Đ = 1.20$).

Finally, refluxing of **P10-FM-cap** in toluene removes the furan protecting group, yielding maleimide-functional polymer **P10** ($\bar{M}_{\text{n,SEC}} = 5700\,\text{g}\,\text{mol}^{-1}$, $Đ = 1.19$). In **P10**, the resonances arising from the furan protecting group vanish and a new resonance associated with the maleimide double bond appears at 6.75 ppm (yellow), while no change in the capped RAFT group is observed (green).

The employed synthetic strategy yields the maleimide end-functionalized polymer **P10** in a straightforward combination of the polymerization with two post-modification steps, in which the transformation of the dithiobenzoate moiety into a non-reactive species is the crucial step to obtain a successful surface photoligation.

Photoligation on surfaces Tetrazole-functionalized silane **5** was synthesized, for the photoligation of maleimide-terminated polymer **P10** onto silicon surfaces *via* NITEC chemistry.(a) Starting from (4-(2-(4-methoxyphenyl)-2*H*-tetrazol-5-yl)benzoic acid (Tet-acid), activation with 1,1′-carbonyldiimidazole (CDI) and addition of (3-aminopropyl)triethoxysilane (APTES) as the nucleophile without intermediate workup provides silane **5** in 73 % yield (for the structure of **5** see Figure 3.1). The SAM formation of **5** onto silicon wafers was conducted as described for the phenacyl sulfide silane **3**. Irradiation with the setup depicted in Figure 3.7b) (setup A) in the presence of polymer **P10** yields surface **S2**. In the ToF-SIMS mapping, the specific fragments $C_3H_3O^-$ and $C_4H_5O_2^-$ of the PMMA backbone are clearly visible in the irradiated area, while the dark part does not show any polymer attachment (for a summary of the specific fragments used for structure elucidation in the ToF-SIMS mappings see Table A.1). Beside the PMMA related fragments, ions arising from the photo capped RAFT end-group of polymer **S2** are detected in the irradiated areas (refer to Figure A.42). In combination with the molecular information about the polymer structure from the SEC and NMR measurements in solution, this constitutes additional evidence of the intact nature of the surface-ligated polymer. Furthermore, ion fragments from the tetrazole SAM are detected in the dark parts, which opens up the possibility for multi-step photoligation experiments, see discussion below. The C 1s XPS spectra of the dark part of **S2** does only show carbon

---

(a) The maleimide terminus on the R-group of polymer **P10** does also allow the photoligation *via* a surface bound photoenol (refer to Section 2.2.3.3). However, the synthesis of a silane-functional photoenol is a 5-step procedure,[171] while the tetrazole-bearing silane **5** can be prepared in 3 steps in high yield and was therefore preferred.

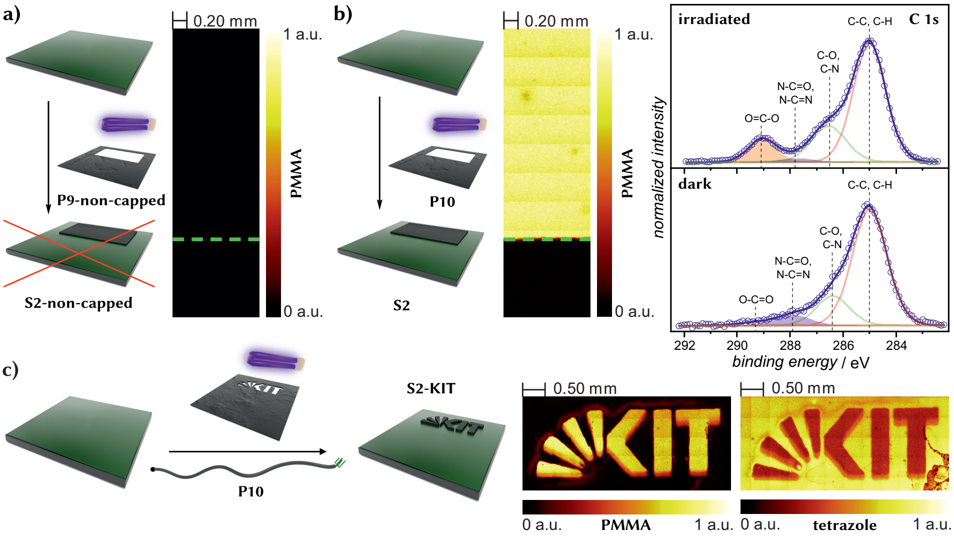

Figure 3.7. a) Reaction scheme and ToF-SIMS image of non-capped, furan deprotected **P9-non-capped** leading to surface **S2-non-capped**. The area above the dashed green line was irradiated. b) Successful surface attachment of capped, furan deprotected **P10** on surface **S2**. ToF-SIMS image (middle) and XPS analysis of C 1s (right) of the dark and irradiated areas. c) Photoligation of **P10** with a KIT logo mask yields surface **S2-KIT**. The ToF-SIMS analysis of the PMMA and tetrazole fragments is shown on the right. For ToF-SIMS fragments description refer to Table A.1. Adapted with permission from [280]. © 2018 Wiley-VCH Verlag GmbH & Co. KGaA.

species from the surface bound tetrazole silane **5**, i.e. C—C and C—H at 285.0 eV, C—O and C—N at 286.4 eV, N—C=O and N—C=N at 287.9 eV (filled in violet), and a small signal of the ester bond of silane **5** at 289.1 eV.[282] In contrast, the irradiated part of the surface shows a large increase of ester bonds on the surface at 289.1 eV (filled in orange) compared to the non-illuminated area. The absence of polymer related signals in the ToF-SIMS and XPS analysis of the dark parts confirm the exclusive covalent attachment of the polymer onto the surface without any physisorbed material. To further demonstrate the capabilities of the spatially resolved immobilization protocol, a KIT logo mask was employed for the preparation of surface **S2-KIT** with polymer **P10** (setup A-KIT, see

Figure 3.7c) and Table A.2). The ToF-SIMS mappings on the right side demonstrate the immobilization of **P10** according to the logo mask, while the dark area shows fragments arising from the SAM of tetrazole **5**.

The achievable lateral resolution in surface **S2-KIT** is limited through the lateral dimensions of the photo mask, since the size of the polymer molecules is far below the theoretical resolution, which is given by the Abbe criterion (see Equation (2.21). The smallest feature sizes of the KIT logo mask are width of the wedges with 160 µm.

The vertical resolution is physically governed by the size of the respective polymer. As the photoligation takes place at one polymer end-group, the size of the swollen polymer chain in solution and the orientation with respect to the surface interface dictates the vertical dimension. As the polymer is bound to the surface *via* a *grafting-to* approach, the conformation of the polymer chain results in a *pancake* or *mushroom* conformation (see Figure 2.32). Here, in contrast to the *brush* morphologies achievable *via* the *grafting-from* method, the polymer chain features a higher flexibility, which also impacts the vertical extent of the chain from the surface. In addition, the uniformity of the polymer surface layer is governed by the homogeneity of the underlying silicon substrate. As such, the preparation of the surface (here the treatment with piranha solution) has also an impact of the achievable surface homogeneity (see also discussion in Section 2.4.2.1).

In conclusion, the successful development of the polymer surface photoligation protocol *via* the NITEC chemistry was achieved with the PMMA homopolymer **P10**. In-depth ToF-SIMS and XPS characterization of the surface demonstrates the intact structure of the polymer on the surface *via* detection of all structural motifs also found in solution. The following sections will focus on the preparation of the metallopolymers, before utilizing the developed surface ligation protocol.

3.2 Metallopolymer synthesis

Ligand monomer synthesis For the ligand systems, triphenylphosphine and bipyridine functionalized MMA monomers were selected. Both ligands are widely used in coordination chemistry and ensure a broad range of applications for the prepared surfaces.[283]

The synthesis routes towards the triphenylphosphine **7** and bipyridine **9** functionalized MMA monomers are outlined in Scheme 3.15. [a] Ligand monomer 2-(methacryloyloxy)ethyl 4-(diphenylphosphaneyl) benzoate **7** was synthesized from 4-(diphenylphosphino)benzoic acid in a Steglich esterification employing *N,N′*,-diisopropylcarbodiimide (DIC) and catalytic 4-dimethylaminopyridine (DMAP) with 2-hydroxyethyl methacrylate (HEMA) as the nucleophile. **7** was obtained as a colorless oil in 94 % overall yield. The $^{31}P\{^1H\}$ NMR spectrum of **7** shows a single resonance at −5.1 ppm, indicating the high purity and absence of oxidized phosphorous species (see Figure 3.8, top left).

---

[a] The synthesis and characterization of **7**, **9** and steps 6)–7) of **9**, **9-Pt**, and **9-Pd** were performed by T. Feuerstein, see [280, 284].

Bipyridine-functionalized methacrylate **9** was synthesized from 4,4′-dimethyl-2,2′-bipyridine in four steps, whereby the first three steps were conducted without intermediate purification.[285] After initial *in situ* lithiation, substitution with 3-bromopropoxy-*tert*-butyl-dimethylsilane ($Br(CH_2)_3OTBDMS$) and deprotection of the TBDMS protecting group with tetrabutylammonium fluoride (TBAF) afforded 4-(4′-methyl-(2,2′-bipyridin)-4-yl)butan-1-ol **8** as a yellow oil. Subsequent esterification with methacryloyl chloride led to **9** (see Scheme 3.15b).

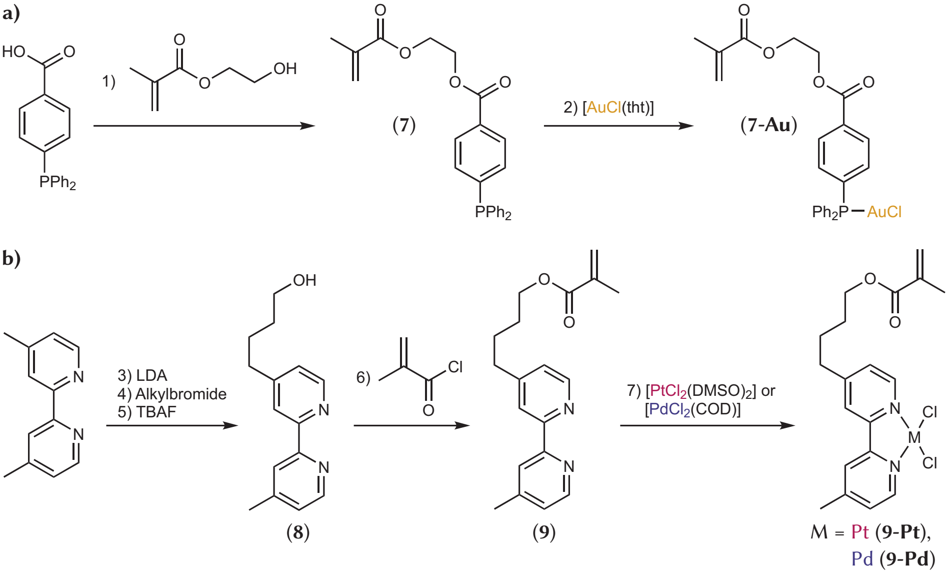

Scheme 3.15. a) Synthesis of triphenylphosphine monomer **7** and metal complexation towards **7-Au**. b) Bipyridine monomer synthesis **9** and metal complexation with platinum **9-Pt** or palladium **9-Pd**. Reagents and conditions: 1) HEMA, DIC, DMAP, DCM, r.t., 24 h; 2) [AuCl(tht)], DCM, r.t., 3 h; 3) LDA, THF, −78 °C, 1.5 h; 4) $Br(CH_2)_3OTBDMS$, r.t., 24 h; 5) TBAF, THF, r.t., 4 h; 6) methacryloyl chloride, NEt_3, DCM, 0 °C, 24 h; 7) $[PtCl_2(DMSO)_2]$, $CHCl_3$, reflux, 5 min or $[PdCl_2(COD)]$, DCM, r.t., 24 h. Adapted with permission from [280]. © 2018 Wiley-VCH Verlag GmbH & Co. KGaA.

Before conducting the polymerization with ligand monomers **7** and **9**, the metal complexation was tested with the monomers to establish a spectroscopic reference for the subsequent characterization of the metallopolymers. The reaction of **7** with a [AuCl(tht)] (tht = tetrahydrothiophene) solution in DCM yielded the metal complex **7-Au** as a pale-yellow powder. The phosphorous resonance in the $^{31}P\{^1H\}$ NMR spectrum of **7-Au** exhibits a shift from −5.1 ppm to 33.1 ppm compared to the free ligand **7** (see Figure 3.8a), which is in accordance to literature values.[286] The single resonance also confirms the high purity of the metal complex.

Bipyridine ligand monomer **9** was reacted with platinum and palladium precursor complexes to obtain the bis-chloro metal complexes. For platinum, reaction of **9** with $[PtCl_2(DMSO)_2]$ in refluxing $CHCl_3$ resulted in the formation of complex **9-Pt**. The corresponding palladium complex **9-Pd** was obtained *via* addition of **9** to a solution of $[PdCl_2(COD)]$ in DCM (COD = 1,5-cyclooctadiene). The ^1H NMR spectra of the free ligand **9** and the both metal complexes **9-Pt** and **9-Pd** is shown in Figure 3.8c). Both complexes exhibit characteristic chemical shifts for the aromatic proton resonances of the bipyridine ligand moiety, when being bound to the metal atoms. Despite the flexibility of

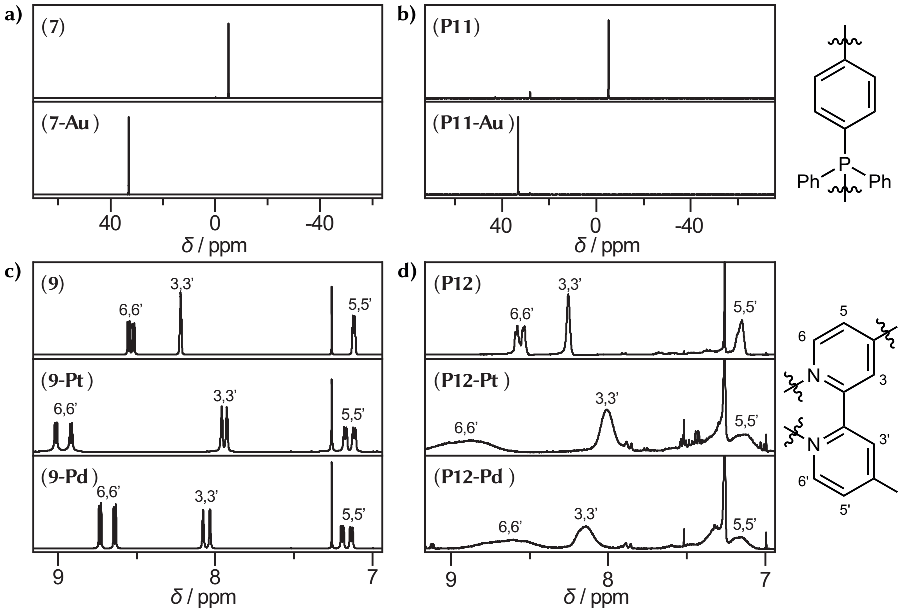

Figure 3.8. a) $^{31}P\{^1H\}$ NMR spectra of the ligand monomer **7** and the metal complex **7-Au**, next to the corresponding ligand copolymer **P11** and the metallopolymer **P11-Au** (b). c) ^1H NMR spectra of the ligand monomer **9** and the metal complexes **9-Pt** and **9-Pd**, next to the corresponding ligand copolymer **P12** and the metallopolymers **P12-Pt** and **P12-Pd** (d). For the resonance assignment refer to the schematic molecular structure. Adapted with permission from [280]. © 2018 Wiley-VCH Verlag GmbH & Co. KGaA.

the alkyl spacer between the bipyridine and the methacrylate unit, single crystals were obtained for **9-Pt** and **9-Pd** by recrystallization from methanol and characterized *via* X-ray diffraction (for the crystallographic description, see [284]). In summary, the results from X-ray crystallography confirm the structure determined by NMR spectroscopy.

Copolymerization and metal pre-loading In analogy to the preparation of homopolymer **P10**, the copolymerization of ligand monomers **7** and **9** was performed by RAFT polymerization with AIBN and CTA **4**. The polymerization and post-modification steps for both ligand copolymers is depicted in Scheme 3.16.

The comonomer feed ratio of the ligand monomers **7** and **9** was set to 15 mol% and 10 mol%, respectively. This resulted in an incorporation ratio of 13 mol% in the phosphine copolymer **P11-FM** and 10 mol% in the bipyridine copolymer **P12-FM**. These values are very similar to the feed ratios, which is a result of the similar molecular structure of the both ligand monomers compared to MMA.

P11-FM was obtained from the RAFT copolymerization of MMA and **7** ($\bar{M}_{\text{n,SEC}}$ = 10 200 g mol^{-1}, $Đ$ = 1.27). In the subsequent reaction step, the RAFT group of the purified polymer was reacted with **6** in a photo induced hetero-*Diels–Alder* reaction, yielding polymer **P11-FM-cap** ($\bar{M}_{\text{n,SEC}}$ = 10 400 g mol^{-1}, $Đ$ = 1.28, see Scheme 3.16). The excess of **6** was removed *via* precipitation of the polymer. Refluxing in toluene liberated furan and resulted in the maleimide end-functionalized ligand copolymer **P11** ($\bar{M}_{\text{n,SEC}}$ = 10 700 g mol^{-1}, $Đ$ = 1.35). Finally, polymer **P11** was purified through precipitation after the removal of the protecting group.

In the SEC traces of **P11-FM** and **P11-FM-cap**, a small high MW shoulder is detected, which might be attributed to a certain amount of transesterification in the diester of monomer **7** during the polymerization. The shoulder could also be the result of unwanted termination events during the polymerization at 60 °C. However, this interpretation is unlikely, as the detected shoulder keeps unchanged during the second photochemical reaction step but increases slightly during the heating step of the furan removal at 110 °C (see Figure A.34). This observation supports the transesterification as the reason for the high MW shoulder, as such an increase cannot be explained if the shoulder is a result of termination events during the polymerization. A possible solution to circumvent such transesterification events is to change the linker between the triphenylphosphine group and the methacrylate moiety of monomer **7**. However, the amount of transesterification is in an acceptable extent, as the synthetic effort to synthesize the corresponding *para*-alkyl substituted triphenylphosphine monomer is significantly higher, compared to the employed triphenylphosphine acid.

P12-FM, **P12-FM-cap**, and **P12** were obtained *via* a similar procedure as the phosphine copolymers through copolymerization of MMA with **9**. First, **P12-FM** ($\bar{M}_{\mathrm{n,SEC}}$ = 5900 g mol^{-1}, $Đ$ = 1.22) was end-group capped with **6** towards **P12-FM-cap** ($\bar{M}_{\mathrm{n,SEC}}$ = 6100 g mol^{-1}, $Đ$ = 1.22) and finally deprotected, yielding **P12** ($\bar{M}_{\mathrm{n,SEC}}$ = 6400 g mol^{-1}, $Đ$ = 1.25).

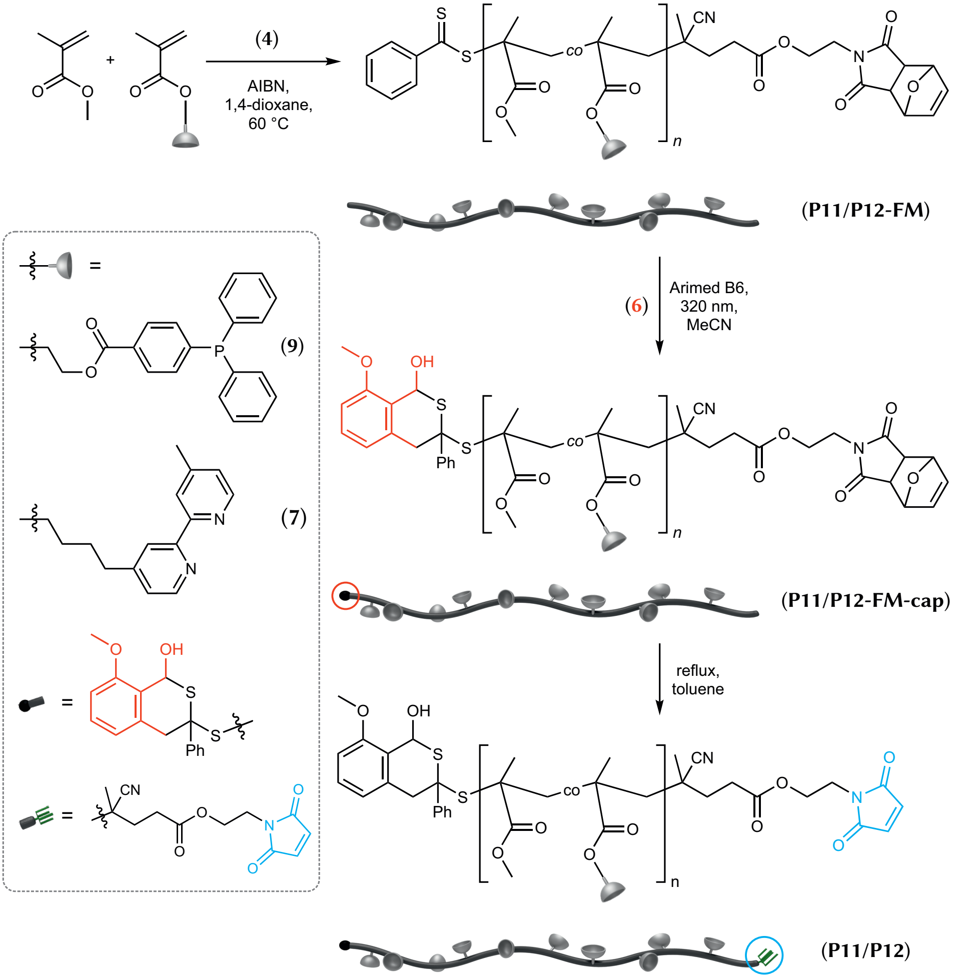
(4)
AIBN,
1,4-dioxane,
60 °C
(P11/P12-FM)
(6)
Arimed B6,
320 nm,
MeCN
(P11/P12-FM-cap)
reflux,
toluene
(P11/P12)
(9)
(7)
=
CN
co
n
Ph
OH

Scheme 3.16. Copolymerization of ligand monomers **7** and **9** with CTA **4**. The RAFT moiety of the obtained copolymers **P11-FM** and **P12-FM** is capped in a photo induced hetero-*Diels–Alder* reaction with **6**, yielding **P11-FM-cap** and **P12-FM-cap**, respectively. Refluxing in toluene affords the maleimide-functional ligand copolymers **P11** and **P12**. The graphical description of the polymers, as well as the end-groups, is employed for the rest of this thesis.

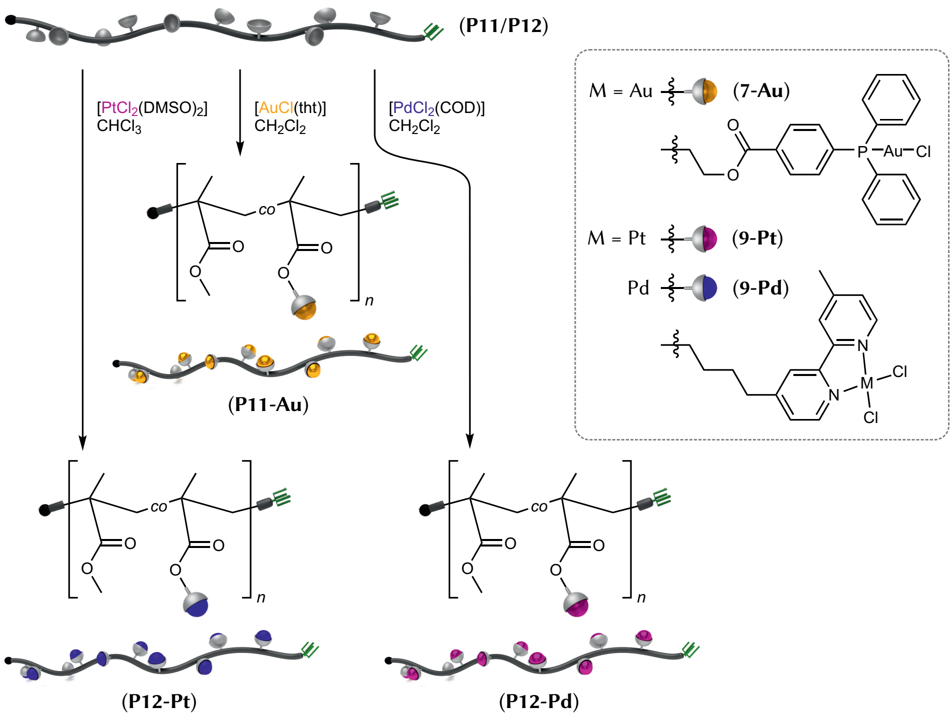

Scheme 3.17. Metal post-loading of **P11** towards **P11-Au** and **P12** towards **P12-Pt** and **P12-Pd**, respectively. The graphical description of the metallopolymers is employed for the rest of this thesis.

In contrast to **P11-FM**, **P11-FM-cap**, and **P11**, no transesterification events are observed in the SEC traces (see Figure A.35), as a result of the molecular structure of monomer **9**, which does not possess two ester moieties in close proximity. The small increase in the determined MW from **P12-FM** to **P12** is attributed to the removal of small oligomeric chains during each precipitation step during the post-modifications.

The metal complexation of ligand polymers **P11** and **P12** is depicted in Scheme 3.17. Table 3.2 summarizes the characterization of the ligand polymers **P11** and **P12** together with the respective metallopolymers **P11-Au**, **P12-Pt**, and **P12-Pd**.

P11 was treated with a solution of [AuCl(tht)] in DCM at room temperature to yield metallopolymer **P11-Au**. (a) The successful formation of the P−Au−Cl motif is evidenced through the shift of the phosphine resonance in the ^{31}P{^{1}H} NMR spectra of **P11** from −5.1 ppm to 33.1 ppm in **P11-Au** (see Figure 3.8b). Minor oxidized phosphine species in **P11** are completely removed after precipitation of **P11-Au**. The observed shifts are in excellent alignment with the values determined for the free ligand **7** and the corresponding metal complex **7-Au** (see Figure 3.8a). In addition, the single phosphine resonance observed for **P11-Au** is a strong indicator for the exclusive formation of mono-ligated phosphorous atoms, as depicted in Scheme 3.17. Another indicator for the successful metal complexation are the different absorption spectra of **P11** and **P11-Au** (see Figure A.18). The determined MW of **P11-Au** increases from 10 700 $\mathrm{g\,mol^{-1}}$ (**P11**) to 13 100 $\mathrm{g\,mol^{-1}}$, while the dispersity of $Đ = 1.28$ is slightly lower(a) as compared to the value of 1.35 for **P11** (for the SEC traces, see Figure A.36).

(a) Metal complexation of **P11** and purification of **P11-Au** *via* precipitation were performed by T. J. Feuerstein.

Table 3.2. Summary of ligand copolymers and metallopolymers for spatially resolved surface functionalization. Adapted with permission from [280]. © 2018 Wiley-VCH Verlag GmbH & Co. KGaA.

polymer	$\bar{M}_n$(a) / $\mathrm{g\,mol^{-1}}$	$Đ$ (a)	ratio of incorporated comonomer(b) / mol%
P11(c)	10 700	1.35	13
P11-Au	13 100	1.28	13
P12(d)	7400	1.19	10
P12-Pt	7000	1.17	10
P12-Pd	6100	1.19	10

(a) Estimated by SEC using THF as eluent and PMMA standards.
(b) Determined *via* ^{1}H NMR using characteristic resonances for MMA (δ = 3.59 ppm, 3H), **7** (δ = 4.65–4.06 ppm, 4H) and **9** (δ = 8.24 ppm, 2H), respectively.
(c) [MMA] : [**7**] : [**4**] : [AIBN] = 51 : 9 : 1 : 0.1. (d) [MMA] : [**9**] : [**4**] : [AIBN] = 54 : 6 : 1 : 0.1.

Two metallopolymers(b) were synthesized starting from bipyridine ligand copolymer **P12**. Stirring of **P12** in a solution of [$\mathrm{PtCl_2(DMSO)_2}$] in $\mathrm{CHCl_3}$ yielded metallopolymer **P12-Pt** ($\bar{M}_{\mathrm{n,SEC}} = 7000\,\mathrm{g\,mol^{-1}}$, $Đ = 1.17$). For the palladium complexation, reaction of **P12** with [$\mathrm{PdCl_2(COD)}$] in DCM resulted in metallopolymer **P12-Pd** ($\bar{M}_{\mathrm{n,SEC}} = 6100\,\mathrm{g\,mol^{-1}}$, $Đ = 1.19$; for SEC traces of **P12-Pt** and **P12-Pd**, see Figure A.37). The successful metal complexation is verified *via* ^{1}H NMR spectroscopy. The resonances of the bipyridine moiety in **P12-Pt** and **P12-Pd** shift in accordance with the model complexes **9-Pt** and **9-Pd** (see Figure 3.8c) and d). A line-broadening of the resonances in the polymer spectra is observed compared to the monomer complexes, which is a common observation in the ^{1}H NMR spectra of such metallopolymers.[287] The determined MWs of **P12-Pt** and **P12-Pd** differ slightly compared to **P12**, which is explained by a different hydrodynamic diameter of the metallopolymers in solution. The UV-Vis spectra of both metallopolymers differ significantly from the parent ligand copolymer **P12**, which supports the formation of the metal complexes (see Figure A.19). Importantly, similar to **P11-Au**, the MWD **P12-Pt** and **P12-Pd** remains monomodal, proving the absence of any cross-linking events during the complex formation.

(a) The lower value for the dispersity after several post-modification steps results most likely from the removal of low-MW material due to multiple precipitation steps.

(b) Metal complexation of **P12** and purification of **P12-Pt** and **P12-Pd** *via* precipitation were performed by T. J. Feuerstein.

Photostability When using the prepared metallopolymers in the photoligation experiments, the stability towards UV irradiation needs to be guaranteed. UV-Vis spectroscopy was therefore employed to probe the photostability of **P11-Au**, **P12-Pt**, and **P12-Pd** under UV exposure. Figure 3.9 shows the UV-Vis spectra before and after irradiation with the Arimed B6 lamp for 3 h, which is the time scale employed for the surface photoligation experiments. In all three cases, no significant spectral changes are observed after irradiation, evidencing the excellent UV stability of the metallopolymers. The slight increase of the absorption value in all cases after irradiation is attributed to a small amount of solvent evaporation during the photoreaction.

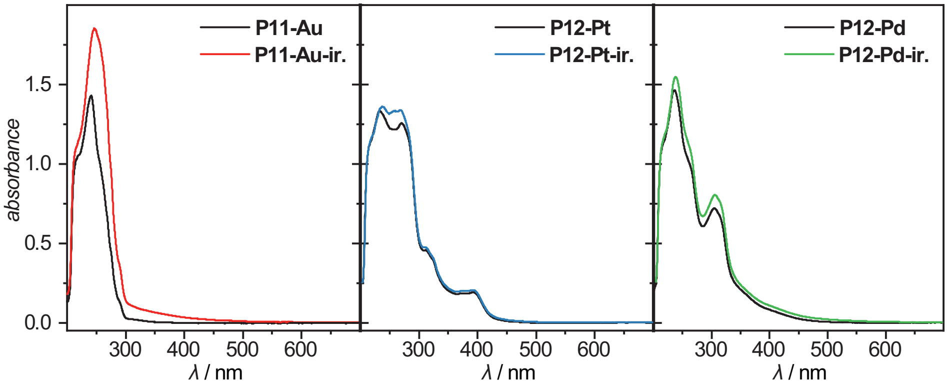

Figure 3.9. From left to right: UV-Vis spectra of the metallopolymers **P11-Au**, **P12-Pt**, and **P12-Pd** measured in 1,4-dioxane (1 mg mL^{-1}) before and after irradiation with the Arimed B6 lamp for 3 h.

The characterized ligand copolymers **P11** and **P12**, as well as the metallopolymers **P11-Au**, **P12-Pt**, and **P12-Pd** were subsequently employed in the surface photoligation protocol established in Section 3.1.2. Giving the stability of all metallopolymers towards UV irradiation, the spatially resolved surface-patterning can be achieved *via* two strategies: 1) photoligation of the ligand copolymers and subsequent metal loading of the attached polymer in analogy to the complexation in solution, or 2) direct photo patterning of the pre-loaded metallopolymers. Both strategies were investigated and compared in the present thesis. Starting with the immobilization of a single species onto the silicon wafer, setup A was employed for all experiments. The irradiated, as well as the dark parts of the rectangular shadow mask are sufficiently large to be characterized *via* high-resolution XPS measurements. In addition, the spatial resolution can be observed through ToF-SIMS mapping of the sharp line between the dark and the irradiated area.

3.3 Surface attachment

3.3.1 Post-loading approach

For the post-loading of ligand copolymers functionalized surfaces, the spatially resolved photoligation of polymers **P11** and **P12** was conducted employing setup A, as described for the preparation of the homopolymer surface **S2** (see Figure 3.10, top). The photoligation of **P11** delivered surface **S3**, while surface **S4** was prepared through immobilization of **P12**. The ToF-SIMS and XPS analysis of surfaces **S3** and **S4** is depicted in Figure 3.10. For the ToF-SIMS ion maps, the analyzed area is indicated by the rectangle in the schematic surface drawing with the dashed green line, separating the irradiated from the dark part of the surface.

For **S3**, the intact tetrazole silane **5** is visible in the dark area of the surface through the specific mass fragments $C_4H_2NO^+$, $C_6H_4NO^+$, $C_7H_7NO^+$, and $C_7H_8NO^+$, respectively. In addition, the underlying silicon substrate features an intense signal, as the penetration depth of the ion beam reaches through the SAM of the silane (see Figure A.45). In contrast, the irradiated area shows characteristic fragments arising from the PMMA backbone ($C_3H_3O^-$ and $C_4H_5O_2^-$), as well as from the phosphine comonomer **7** (C_6P^-, $C_6H_5P^-$, and $C_6H_4P^-$). The C 1s XPS spectra of **S3** additionally supports the successful spatial immobilization of **P11** through the increase of the ester bonds on the surface at 289.1 eV. The reduction of the N−C=O and N−C=N bounded carbon species at 288.2 eV,[288] stemming from the SAM of **5** in the irradiated area compared to the dark area also confirms the layer increase due to the polymer immobilization.

Surface **S4** gives nearly identical results, except that specific ions arising from the bipyridine ligand ($C_6H_6N^+$, $C_{11}N_2H_9^+$, and $C_{10}H_6N_2^+$) are detected in the ToF-SIMS instead of the phosphine species in **S3**. The N 1s XPS spectra of **S4** additionally confirms the immobilization of the bipyridine containing copolymer **P12** in the irradiated area (see Figure A.51). The dark area of **S4** is dominated by the signals at 402.7 eV and 400.2 eV arising from the surface bound tetrazole **5**.[162,289] In contrast, attachment of **P12** in the irradiated area results in a significant shift of the main nitrogen signal towards 398.9 eV. This value is assigned to the nitrogen in the bipyridine motif and matches the reported literature value of 399.0(1) eV for 2,2′-bipyridine.[290]

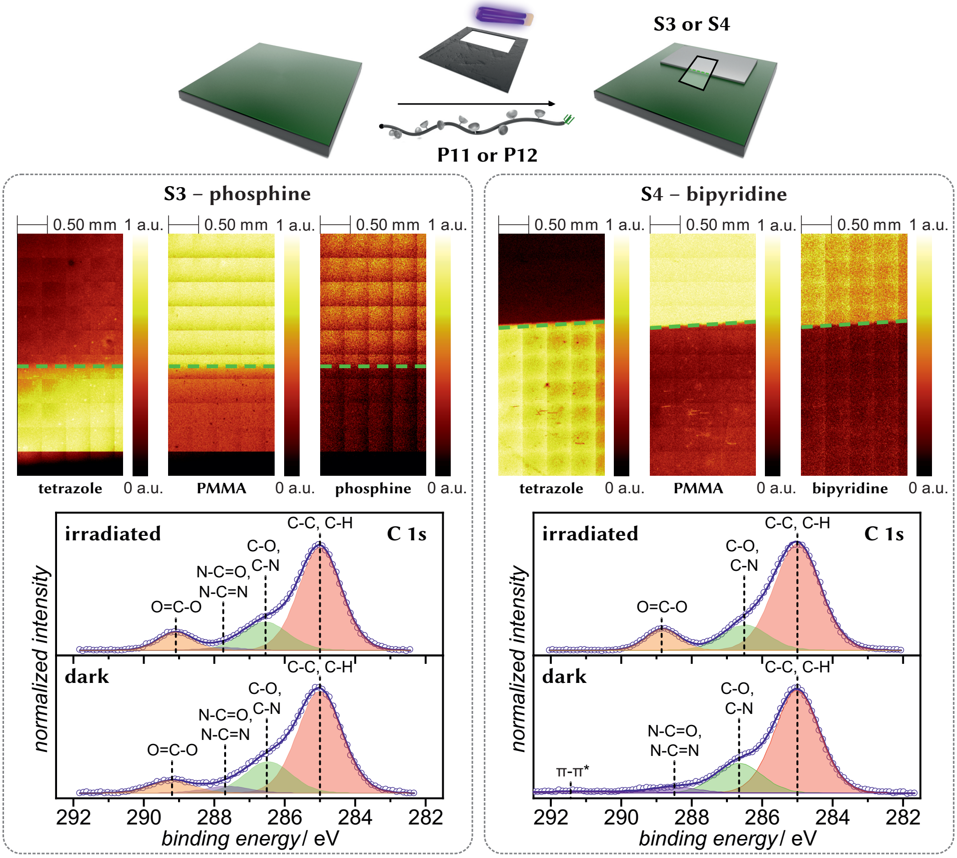

Figure 3.10. Surface photoligation of the free ligand copolymers **P11** and **P12**, yielding surfaces **S3** and **S4**, respectively. The rectangle in the schematic visualization represents the area analyzed *via* ToF-SIMS. The ToF-SIMS and XPS analysis of the phosphine copolymer surface **S3** (left) and **S4** (right) are depicted below. The dotted green line in the ToF-SIMS images indicates the line separating the dark from the irradiated area.

Upon confirmation of the successful spatial immobilization of the ligand copolymers **P11** and **P12**, the metal complexation of the ligand sites on the surface was attempted. The reaction setup is depicted in Figure 3.11 for the gold complexation of **S3** towards surface **S3-Au** (a) and the platinum complexation of **S4**, leading to surface **S4-Pt** (b).

For **S3-Au**, the post-loading was conducted in a similar manner as the complexation of **P11** in solution. The entire silicon wafer **S3** was immersed in solution of [AuCl(tht)] in DCM. In a first experiment, a qualitative investigation of the required incubation time for optimal complexation was performed. The surfaces were immersed in the gold solution for different time intervals, rinsed with DCM, and analyzed *via* ToF-SIMS (see Figure A.47). Already after 20 s, specific gold ions can be detected. After 30 min, a strong gold signal is observed in the previously irradiated area of **S3**. As can be seen in Figure 3.11a), the area covered with polymer **P11** in **S3** perfectly overlaps with the detected PMMA and gold fragments of **S3-Au**. This confirms that the complexation takes place exclusively in areas

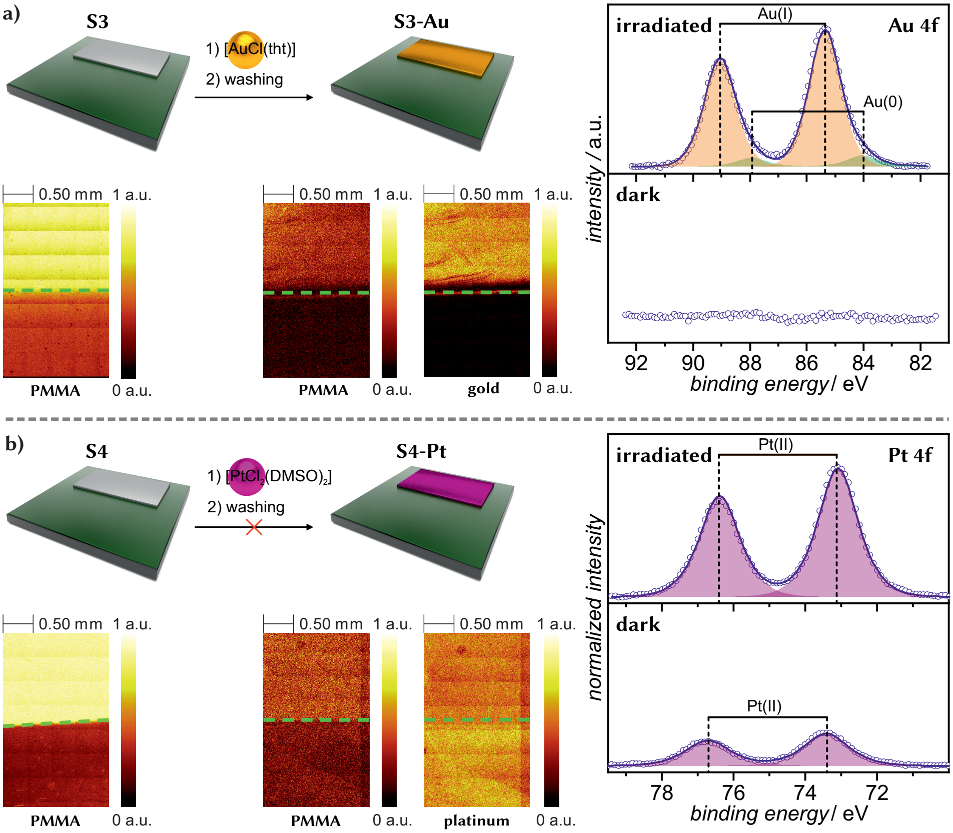

Figure 3.11. a) Post-loading with gold of surface **S3** towards surface **S3-Au**. b) Post-loading with platinum of surface **S4** towards surface **S4-Pt**. The ToF-SIMS analysis of the PMMA and metal characteristic ions is depicted below the surface drawings. The XPS spectra of Au 4f and Pt 4f in command of **S3-Au** and **S4-Pt** are shown on the right for the irradiated and dark areas of the surfaces. Adapted with permission from [280]. © 2018 Wiley-VCH Verlag GmbH & Co. KGaA.

that are covered with **P11**. Additional molecular information about the surface structure of **S3-Au** can be gained from the inspection of further ion fragments in the ToF-SIMS analysis (see Figure A.48). Specific signals associated with ligand **7** and also from the capped RAFT polymer end-group are detected in the initially irradiated area.

An intense $\mathrm{Au^{+I}}$ signal at 85.4 eV for Au $4f_{7/2}$[291] correlates with the ToF-SIMS findings, while it is completely absent in the dark area of the surface (see right side of Figure 3.11a). Small amounts of $\mathrm{Au^{0}}$ (84.0 eV for Au $4f_{7/2}$)[292] are attributed to a certain amount of metal precursor reduction during the experiment. The C 1s spectra are not altered as compared to **S3**, with a strong ester bond signal at 289.1 eV, stemming from the polymer backbone in the irradiated area and nitrogen bonded carbon arising from the surface bound tetrazole in the dark area (see Figure A.49). Unfortunately, a quantitative estimation of the complexation efficiency on the surface in analogy to the NMR characterization in solution cannot be made. For this, the P 2p doublet at ≈132 eV in the XPS spectra must be compared to the $\mathrm{Au^{+I}}$ signal at 85.4 eV. However, the phosphor signal overlaps with a plasmon loss peak of the underlying silicon substrate, which results in a very inaccurate determination of the phosphine content and thus the phosphine–gold ratio on the surface.

In contrast to the successful post-loading of **S3** towards **S3-Au**, the post-loading of **S4** employing the platinum precursor $[\mathrm{PtCl_2(DMSO)_2}]$ in $\mathrm{CHCl_3}$ was not successful. Figure 3.11b) shows the ToF-SIMS and XPS analysis of the surface **S4-Pt**. While surface **S4** shows the spatially resolved immobilization of **P12** *via* the PMMA fragments in the ToF-SIMS, the specific platinum fragments in **S4-Pt** are detected in the whole analyzed area. The Pt 4f and Cl 2p (see Figure A.53) XPS spectra are matching to the ToF-SIMS results, as $\mathrm{Pt^{+II}}$ and Pt—Cl bound $\mathrm{Cl^{-I}}$ are detected in the irradiated, as well as the dark areas of surface **S4-Pt**. Although the amount of $\mathrm{Pt^{+II}}$ and $\mathrm{Cl^{-I}}$ is lower in the dark area, these results clearly indicate a non-selective surface immobilization of platinum. The same results are obtained for the palladium complexation of **S3** in analogy to **P12-Pd** (not shown).

In conclusion, the complexation of pre-functionalized surfaces with metal complex precursors was successfully applied for gold on surface **S3-Au**, while the complexation of platinum or palladium on bipyridine-containing surface **P12** was non-selective.

3.3.2 Pre-loading approach

The photoligation of the metallopolymers **P11-Au**, **P12-Pt**, and **P12-Pd** should lead to a similar final surface structure as for the surfaces obtained *via* the post-loading approach.

The advantage in performing the complexation of the ligand copolymers in solution is the possibility of an in-depth molecular characterization of the metallopolymers without being restricted to ToF-SIMS and XPS surface analysis only.

Figure 3.12 shows the results for the direct photoligation of **P12-Pt** through setup A in analogy to the corresponding free ligand copolymer **P12** (see Figure 3.10). Notably, while the experimental setup was effective for **P12**, the immobilization of **P12-Pt** on surface **S5-long** was not successful. The ToF-SIMS analysis of **S5-long** does not show species related to metallopolymer **P12-Pt** (here PMMA, bipyridine, and platinum fragments). In addition, also the borderline between the irradiated and the dark area is not visible in the total ion count ToF-SIMS images, which is normally detectable even for unsuccessful ligations due to altered ionization probabilities of the irradiated area (see Figure A.54).

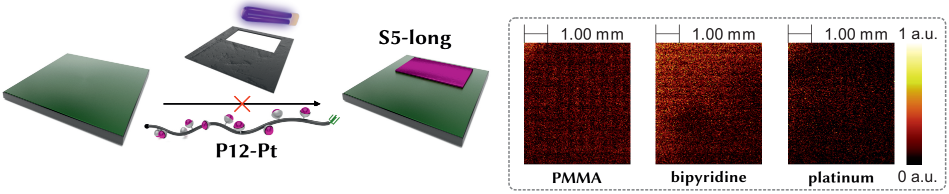

Figure 3.12. Unsuccessful photoligation of metallopolymer **P12-Pt** on surface **S5-long** with the ToF-SIMS analysis of **S5-long** showing no immobilized polymer with 6 cm distance between glass vial and irradiation source and 10 mm pathway through the **P12-Pt** metallopolymer solution.

These observations can be explained by revisiting the *Beer–Lambert* law regarding the employed photoligation setup. As the UV light of the irradiation source needs to penetrate the solution of the respective metallopolymer in order to trigger the NITEC reaction on the surface, the absorption inside the solution has a pronounced effect on the light intensity reaching the tetrazole SAM.

In comparison to the free ligand copolymer **P12**, an increased absorption for the metallopolymer **P12-Pt** is observed in the region between of 300–400 nm in which the NITEC reaction is triggered (see Figure A.19). Through combination of the measured spectral irradiance of the light source with the UV-Vis spectrum of metallopolymer **P12-Pt**, the effect of the absorption on the initially available irradiance is possible. A MATLAB script was utilized for calculating the spectral irradiance at any given penetration depth through an absorbing solution. (a) For the calculation of the individual molar extinction coefficients ϵ_λ of the **P12-Pt** solution, the molar concentration of **P12-Pt** was calculated

---

(a) The MATLAB script was developed with the help of Patrick Müller from the group of Prof. Wegener, KIT.

via the MW as determined by SEC (see Table 3.2). The capabilities of this approach are visualized in Figure 3.13.

In panel a), the absorption spectra of **P12-Pt** and the spectral irradiance measurement of the Arimed B6 lamp are depicted. By visual inspection, the **P12-Pt** solution has a notable absorption in the spectral range of 300–400 nm. Figure 3.13b) quantifies this observation on the irradiance for various penetration depths inside the **P12-Pt** solution. As an example, the initial irradiance at 320 nm is $E = 459\,\mathrm{mW\,m^{-2}\,nm^{-1}}$. Already after 1 mm inside the solution, this value is reduced by 62 %, whereas only 0.7 ‰ of the initial irradiance is available after 10 mm. A complete visualization of the 250–420 nm range is presented in Figure 3.13c) through a 3D surface plot. The complete spectral range 3D

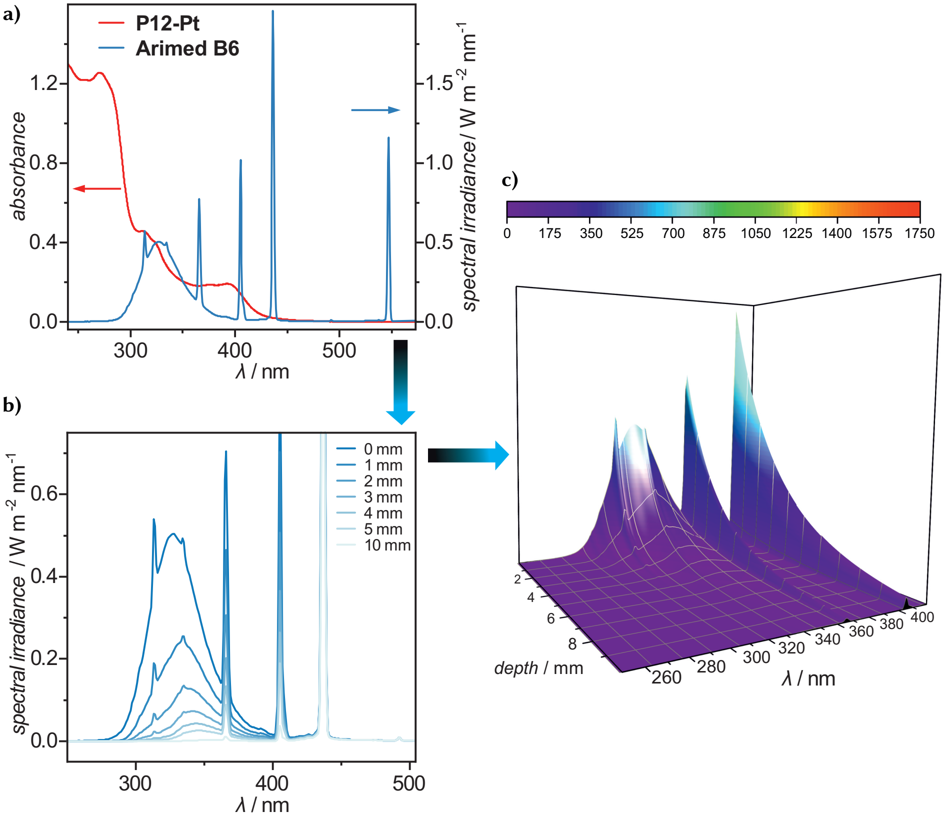

Figure 3.13. a) Overlay of the absorption spectrum of metallopolymer **P12-Pt** and the spectral irradiance of the Arimed B6 lamp. b) Effect of the **P12-Pt** solution absorption on the spectral irradiance after different penetration depths into the solution. c) 3D visualization of the decrease in available surface irradiance with a pronounced effect in the wavelength region around 320 nm.

surface plots of the spectral irradiances versus penetration depth for **P11-Au**, **P12-Pt**, and **P12-Pd** is given in Figure A.28, A.29, and A.30, respectively. Accordingly, the initially employed experimental setup was modified and the distance between the silicon surface and the wall of the glass vial was reduced from 10 to 2 mm (see Figure 3.14).

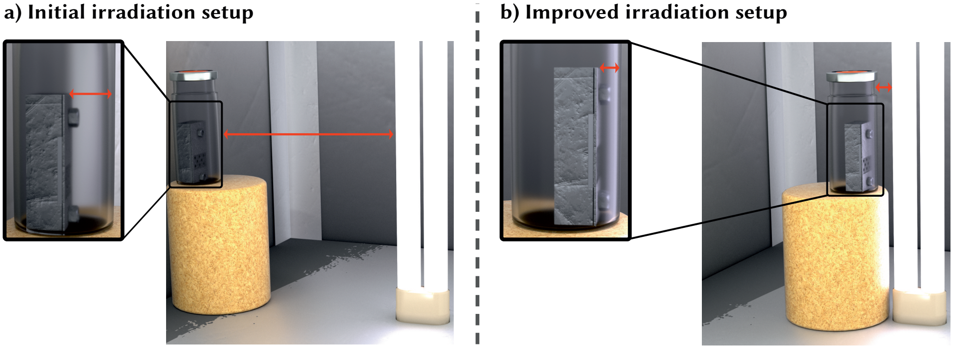

Figure 3.14. Visualization of the initial (a) and improved (b) experimental setup for surface photoligation. Compared to the initial setup, the distance between the irradiation source and the photo vial, as well as the distance between the silicon surface and the wall of the glass vial was shortened (red arrows). Adapted with permission from [280]. © 2018 Wiley-VCH Verlag GmbH & Co. KGaA.

In addition, the distance between the UV lamp and the photo vial was also reduced, which further increases the irradiance at the wafer surface. The dependency is illustrated in Figure 3.15. In panel a), the damping effect of the photo vial on the spectral irradiance is given. As the employed photo vial is made of standard laboratory glass ware, the cut-off is already starting to affect the range between 280–340 nm. Figure 3.15b) demonstrates the effect of the distance between the UV lamp and the photo vial, by reducing the distance from 6 to 2.5 cm. The red line only serves to guide the eye, as the inverse square law of the relationship between the irradiance from a point light source and the distance cannot be applied in this case because the Arimed B6 lamp is an elongated light source and the wall of the photo reactor also reflects incoming light.

Taking together these two changes of the experimental setup, a significant increase in the surface irradiance for all metallopolymers is achieved. Table 3.3 summarizes the effect for the initial and the improved irradiation setup. Polymer **P11-Au** only poorly absorbs light in the UV range and therefore exhibits only minor improvement upon adjustment. However, the absolute value of the irradiance is significantly higher as compared to the **P12-Pt** and **P12-Pd** metallopolymers. Here, the setup change results in an impressive increase in surface irradiance with a factor of 149 and 73 for **P12-Pt** and **P12-Pd**, respectively.

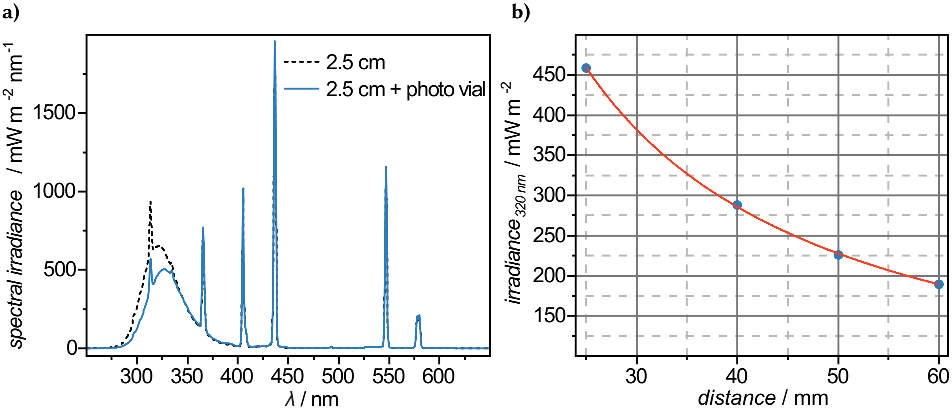

Figure 3.15. a) Spectral irradiance of the Arimed B6 UV lamp at 2.5 cm distance (dotted, black) and with a glass vial employed for the photoreactions placed between the lamp and the radiometric sensor (blue). b) Relationship between peak irradiance of the Arimed B6 lamp and the distance of the reaction vial towards the lamp. The red line only serves to guide the eye.

Table 3.3. Comparison of the initial and improved irradiation setup and the absolute gain in irradiance intensity at the wafer surface. Adapted with permission from [280]. © 2018 Wiley-VCH Verlag GmbH & Co. KGaA.

	initial setup$^{(a)}$	**improved setup**$^{(b)}$	
polymer	irradiance$_{280-400\,\mathrm{nm}}$ at wafer surface / mW m^{-2}	irradiance$_{280-400\,\mathrm{nm}}$ at wafer surface / mW m^{-2}	factor of improvement
P11-Au	8000	24 600	1.23
P12-Pt	45	6700	149
P12-Pd	85	6200	73

$^{(a)}$ 6 cm distance between glass vial and irradiation source and 10 mm pathway through the metallopolymer solution. $^{(b)}$ 2.5 cm distance between glass vial and irradiation source and 2 mm pathway through the metallopolymer solution.

Monofunctional patterning With the increased surface irradiance of the improved setup, the spatially resolved immobilization was successful for all metallopolymers, i.e. **P12-Pt**, **P12-Pd**, as well as **P11-Au** (see Figure 3.16). For the surface **S5**, the ToF-SIMS analysis clearly confirms the spatially resolved immobilization of the metallopolymer **P12-Pt** by the strong signal intensity of the PMMA, as well as the metal specific mass fragments in the irradiated area (see Figure 3.16a); for the PMMA and other fragments, refer to Figure A.55). Signals associated with the bipyridine ligand ($C_6H_6N^+$, $C_{11}N_2H_9^+$, $C_{10}H_6N_2^+$), as well as the capped RAFT group ($S_2O_2C_9H_9^+$, $S_2O_2C_{16}H_{17}^+$, and $S_2O_2C_{10}H_{12}^+$) are also detectable in the irradiated area, indicating the intact nature of the metallopolymer after the photoligation step. In contrast, the non-irradiated area of the surface remains

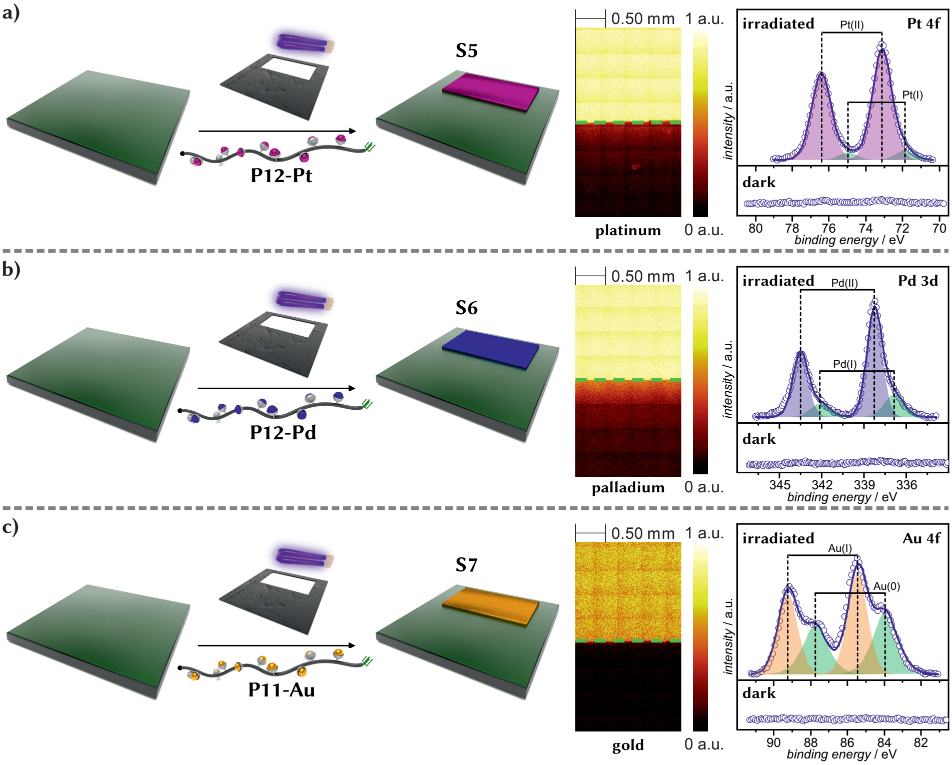

Figure 3.16. Spatially resolved surface immobilization of metallopolymers **P12-Pt** (a), **P12-Pd** (b), and **P11-Au** (c) *via* setup A. The ToF-SIMS and XPS analysis of the respective metal species are shown on the right. Adapted with permission from [280]. © 2018 Wiley-VCH Verlag GmbH & Co. KGaA.

unchanged. ToF-SIMS fragments of the remaining surface bound tetrazole, as well as a strong signal of the underlying silicon substrate are detectable in the dark area of **S5**. The XPS analysis of **S5** supports these findings by the increase of ester bonds in the irradiated area at 289.1 eV in the C 1s spectra compared to the dark area, where no ester bonds are detectable (see Figure A.56). In addition, the Pt 4f spectrum shows no metal complex in the non-irradiated area, whereas it is clearly visible through the Pt^{+II}

doublet at 73.1 eV (for Pt $4f_{7/2}$)[293] in the irradiated area (see Figure 3.16a). Traces of Pt^{+I} are detected as a small doublet at 71.9 eV (for Pt $4f_{7/2}$) and are probably due to a certain amount of photo reduction of the platinum complex during the irradiation step. Nevertheless, the predominant part of the surface bound platinum atoms are bound to the bipyridine ligand in the form of Pt^{+II}. The N 1s spectrum of the irradiated area does also differ significantly from the dark area. The signals in the non-irradiated area at 402.7 and 400.2 eV are assigned to the surface bound tetrazole species and are comparable to the free ligand surface **S4** (refer to Figure A.51). In contrast, the irradiated area is dominated by the nitrogen atoms of the platinum metal complex centered at 400.2 eV, which is attributed to the C=N−Pt binding motif. The N 1s spectrum shows an additional weak peak at 398.9 eV belonging to the nitrogen atoms in the aromatic rings of **P12-Pt**, whereas the tetrazole-assigned peak at 402.7 eV is absent. While non-irradiated area of the surface does not feature any chlorine species, the platinum-attached chlorine atoms are clearly visible at 198.1 eV (for Cl $2p_{3/2}$) in the Cl 2p spectra of the irradiated area.

The results of the ToF-SIMS and XPS analysis of the palladium containing surface **S6** are comparable to the results obtained from **S5**. Here, instead of the platinum signals, specific ions from the palladium-bipyridine complex are detected in the irradiated area in the ToF-SIMS analysis (see Figure 3.16b). All other ion species of **S6** detected in the ToF-SIMS exhibit a similar spatial distribution as observed for **S5** (see Figure A.57). The XPS spectra of **S6** shows Pd^{+II} species through the Pd 3d doublet at 338.3 eV (for Pd $3d_{5/2}$).[294] Similar to **S5**, a small amount of Pd^{+I} species is detected as a small doublet at 336.9 eV (for Pd $3d_{5/2}$). The C=N−Pd binding motif, as well as the palladium-bound chlorine atoms are detected exclusively in the irradiated area in the N 1s and Cl 2p spectra, respectively (see Figure A.58). In addition, the dark area of surface **S6** shows also an intact tetrazole species in the ToF-SIMS, as well as in the XPS spectrum (see Figure A.57 and A.58, respectively).

For surface **S7**, the ToF-SIMS and XPS measurements of the gold species are depicted in Figure 3.16c). In the ToF-SIMS, the surface-immobilized gold complex is detected through the Au^- ion. The additional detected $AuCl^-$ ion was not included in the evaluation, because its isotopic pattern overlaps with the $PtCl^-$ and $PtCl_2^-$ ions, which are employed for the detection of metallopolymer **P12-Pt**. Instead of the bipyridine ligand observed for **S5** and **S6**, the phosphine ligand is detected in the irradiated area *via* the C_6P^-, $C_6H_5P^-$, and $C_6H_4P^-$ ions, in combination with the fragment of the capped RAFT group (see Figure A.59). The non-irradiated area in the XPS spectrum is completely free of gold, whereas the irradiated area shows a strong signal for the Au^{+I} complex of the metallopolymer **P11-Au** at 85.4 eV (for Au $4f_{7/2}$), excellently matching the results obtained by the post-loading approach presented in Figure 3.11. However, the amount of detected

Au^0 species in the XPS spectrum is increased compared to the post-loading approach. Despite the UV-stability test of metallopolymer **P11-Au** (see Figure 3.9), this observation is indicating an increased photo reduction[295] in the photoligation step. An explanation for the exclusive occurrence of the Au^0 species in the irradiated area can be the formation of ligand-supported gold nanoclusters, for which the triphenylphosphine moieties of the polymer are literature known stabilizers.[292,296]

Bifunctional patterning As already discussed for the monofunctional metallopolymer surfaces, the tetrazole molecules in the non-irradiated surface areas are still intact for further functionalization, which opens up the unique possibility for multifunctional surface patterning. Having established the experimental setup for the monofunctional patterning, this section will describe the preparation of bifunctional surfaces employing two different metallopolymers.

The strategy for bifunctional surfaces is outlined in Scheme 3.18 for the preparation of surface **S8**, as an example of one combination. The procedure involves two consecutive photoligation experiments on the same silicon wafer. Here, the first photoligation of metallopolymer **P12-Pd** is conducted with point mask (I) (refer to Table A.2 for the description of the different shadow masks). Thereafter, the surface is thoroughly washed to remove all potentially physiosorbed metallopolymer on the surface. In the second irradiation step, metallopolymer **P12-Pt** was attached onto different areas of the surface by employing point mask (II). Again, the surface was carefully rinsed before analyzing it *via* ToF-SIMS and XPS. A condensed representation of the ToF-SIMS and XPS surface mappings is obtained by the overlay of the individual fragments/elements in a false color representation (see Figure 3.17a). The complete ToF-SIMS images and XPS elemental mappings can be found in Figure A.61 and A.62, respectively. A summary of all prepared

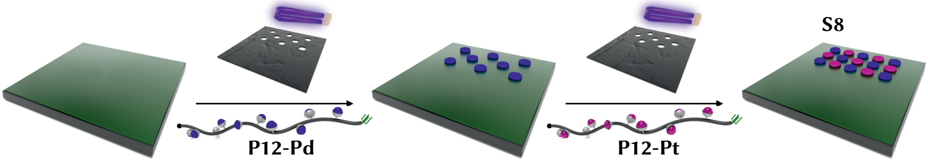

Scheme 3.18. Reaction sequence for the preparation of the bifunctional metallopolymer surface **S8**. The palladium metallopolymer **P12-Pd** is photochemically immobilized onto the surface with point mask (I) in the first reaction step, followed by platinum metallopolymer **P12-Pt** in the second surface reaction, employing point mask (II).

bifunctional surfaces is given Table 3.4 with the reaction sequence of the employed metallopolymers, as well as the references to the ToF-SIMS and XPS analysis.

Table 3.4. Summary of all bifunctional surfaces prepared *via* reaction setup B, i.e. point mask (I) in the first and point mask (II) in the second reaction step. The reaction sequence describes the order in which the two metallopolymers are tethered onto the silicon wafer. The detailed ToF-SIMS and XPS analytic can be found in the respective figures.

surface	reaction sequence	ToF-SIMS	XPS
S8	**P12-Pd**→**P12-Pt**	Figure A.61	Figure A.62
S8-rev	**P12-Pt**→**P12-Pd**	Figure A.63	Figure A.64
S9	**P12-Pd**→**P11-Au**	Figure A.65	Figure A.66
S9-rev	**P11-Au**→**P12-Pd**	Figure A.67	Figure A.68
S10	**P12-Pt**→**P11-Au**	Figure A.69	Figure A.70
S10-rev	**P11-Au**→**P12-Pt**	Figure A.71	Figure A.72

For surface **S8**, the analysis of the ToF-SIMS images clearly proves the bifunctional surface structure. The PMMA backbone signals ($C_3H_3O^-$, $C_4H_5O_2^-$), as well as the bipyridine and capped RAFT group fragments, are detected in all irradiated areas, as the metallopolymers **P12-Pd** and **P12-Pt** are both prepared from the same bipyridine functionalized ligand copolymer **P12**. In contrast, fragments associated with palladium are exclusively present in the area irradiated with point mask (I), while the platinum signals are only detected in the area of point mask (II).

Importantly, ions arising from the surface-bound tetrazole molecules are still observed in the non-irradiated areas on the final wafer **S8**, which implies the possibility for even further functionalization. It should be noted that the ion fragments from tetrazole **5** are solely not included in the false color overlays in Figure 3.17 because of software limitations, preventing the simultaneous overlay of the negative and positive ion modes. The sharp contrast between the dark and the irradiated areas further supports the spatially resolved nature of the photoligation process. (a)

The XPS chemical mapping of surface **S8** is depicted on the right side of Figure 3.17a). While the information on the oxidation state of the respective elements is accessible through the high-resolution XPS measurements discussed in the previous section, the snap map option of the spectrometer visualizes the spatial distribution of the various atoms present on the surface by rapid displacement of the sample stage, combined with a fast measurement (refer to the experimental section on Page 170). This technique

---

(a) For the achievable spatial resolution, the reader is referred to the discussion of the monofunctional surface of **S2-KIT** on Page 86.

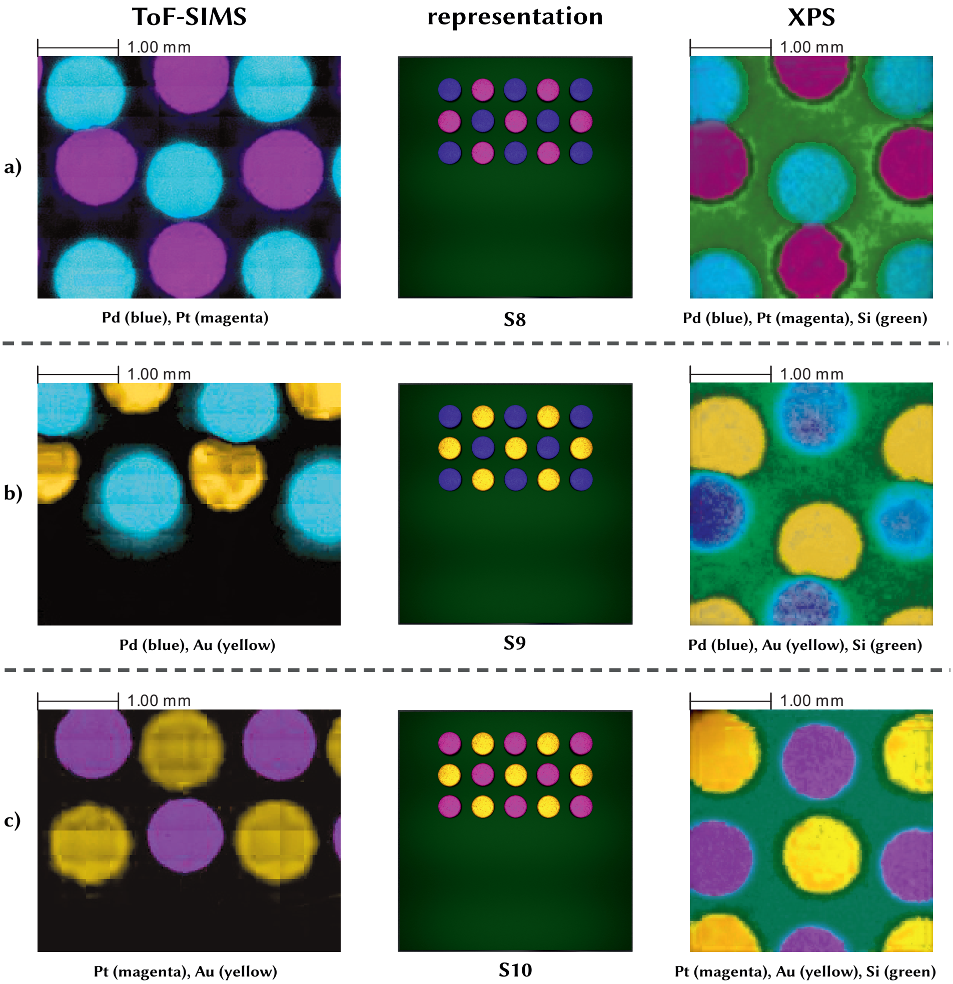

Figure 3.17. Three different combinations of the metallopolymers on a single surface for the fabrication of bifunctional metallopolymer surfaces **S8** (a), **S9** (b), and **S10** (c). A schematic overview of the surface patterning is given in the middle. The respective ToF-SIMS images are depicted on the left side, while the XPS chemical mappings are displayed in the right column. The color code is given below each picture.

enables the direct comparison of the surface structure with the results obtained from ToF-SIMS. In addition, it delivers information on the chemical oxidation state of every mapped element by a subsequent high-resolution XPS measurement at a defined location on the surface. Clearly, both analytical techniques condensed in the images given in Figure 3.17a) confirm the successful spatially resolved surface immobilization of **P12-Pd** and **P12-Pt** on different areas of surface **S8**.

In contrast to the ToF-SIMS imaging of the tetrazole ion fragments, the spatially resolved imaging of tetrazole **5** is not feasible with the XPS chemical mapping. The nitrogen atoms of **5** cannot be distinguished from the nitrogen atoms of the bipyridine ligand **9** in **P12-Pd** and **P12-Pt**, thus preventing the spatially resolved imaging. Instead, the underlying silicon substrate is visualized in the area in between the two metallopolymers as an indirect measurement of the tetrazole SAM due to the thinner surface coverage in the area only covered with **5**.

In order to investigate whether the order of the metallopolymer photoligation has an impact on the analytical outcome, the experiment was also conducted in reverse order, that is, employing first **P12-Pt**, and then **P12-Pd** in the second photoligation step, resulting in surface **S8-rev**. The results collated in Figure A.63 and Figure A.64 unambiguously confirm the versatility of the presented photoligation protocol. Both surfaces show identical analytical results, except for the location of the respective metallopolymers, proving that the reaction sequence has no impact on the final surface structure. A comparison between the ToF-SIMS images of **S8** and **S8-rev** is presented in Figure 3.18. As discussed for surface **S8** above, both surfaces show a similar spatial distribution of the tetrazole, PMMA, as well as the bipyridine ion fragments, while the palladium and platinum species are orthogonal to each other, as indicated by the arrows.

In addition to surfaces **S8** and **S8-rev**, all other possible combinations of the metallopolymers prepared in this thesis have been performed. Surface **S9** was prepared through the photoligation of **P12-Pd** followed by **P11-Au**, while the combination of **P12-Pt** and **P11-Au** was realized on surface **S10** (see Figure 3.17b) and c), respectively). Again, not only the different combinations, but also the order of the metallopolymer immobilization was varied, leading to surfaces **S9-rev** and **S10-rev**.

The gold metallopolymer **P11-Au** allows the detection of the phosphine and gold ion fragments in the respective areas in the ToF-SIMS mappings. Accordingly, the XPS mappings confirm the spatially resolved immobilization of **P11-Au** *via* the visualization of the Au 4f signals. It should be noted that the fast measurement in the snapmap mode does not allow a discrimination between $\mathrm{Au}^{+\mathrm{I}}$ and Au^{0} species, as observed for the monofunctional surface **S7** (see Figure 3.16c). As such, it can only be assumed that the

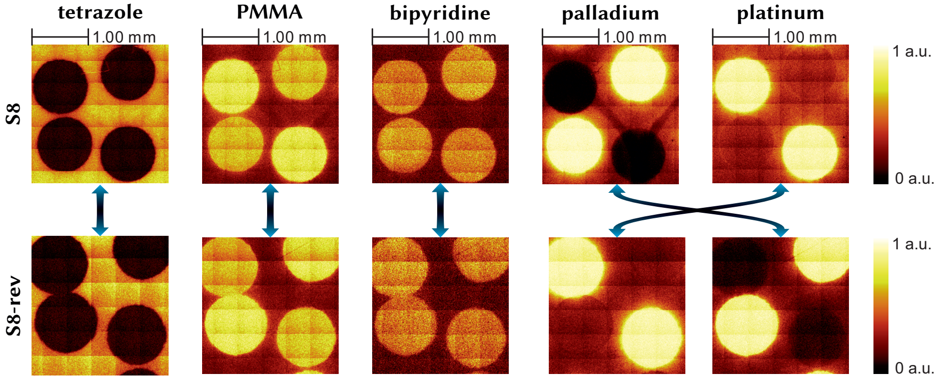

Figure 3.18. Comparison of the surfaces **S8** (1st row) and **S8-rev** (2nd row). The ToF-SIMS mappings of the tetrazole, PMMA, and bipyridine fragments are similar for both surfaces. In contrast, the palladium and platinum species swapped places.

observation made for **S7** can also be translated to the bifunctional surfaces **S9** and **S10**. Similar to the findings of **S8-rev**, the reverse order of metallopolymer immobilization in **S9-rev** and **S10-rev** does not influence the analytical findings, see Table 3.4 and analytical references therein.

Trifunctional patterning Two different strategies are followed for the fabrication of trifunctional surfaces, as outlined in Scheme 3.19. Surface setup C is depicted in panel a) and comprises three different shadow masks in consecutive reaction steps, namely point masks (III–V). Through this strategy, areas of the surface already covered with a metallopolymer attached in a previous reaction will not experience a second irradiation cycle. Consequently, the potential crosstalk between areas irradiated with multiple metallopolymers is prevented.

Surface **S11** is obtained after consecutive irradiation cycles of **P12-Pd** (point mask (III), 1st step), **P12-Pt** (point mask (IV), 2nd step), and **P11-Au** (point mask (V), 3rd step) on the same silicon wafer pre-functionalized with tetrazole **5**. The results of the ToF-SIMS, as well as the XPS measurements are shown in the Figure 3.19 (1st row). The two false color overlays of the individual ToF-SIMS (left) and XPS (right) images unambiguously confirm the successful spatially resolved immobilization of all three metallopolymers.

Signals from the PMMA backbone and the capped RAFT end group are detected in all areas covered with polymer, independent of the kind of metallopolymer (see Figure A.73). In contrast, the bipyridine ligand of **P12** is only detectable in the spots covered with either **P12-Pd** or **P12-Pd**, whereas the phosphine ligand of **P11** is solely found in the

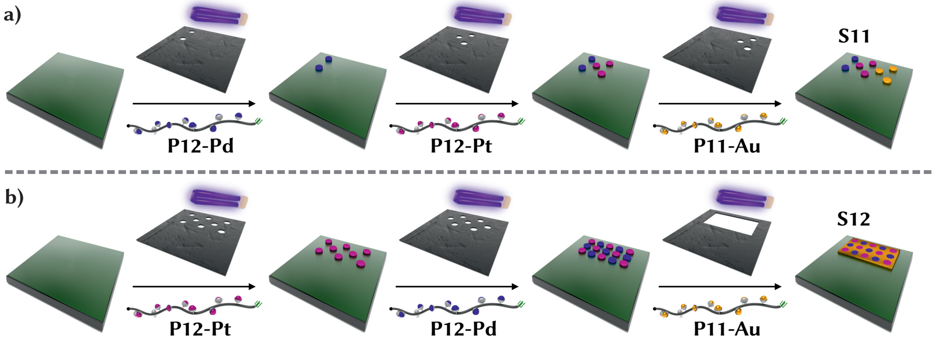

Scheme 3.19. The two different strategies for trifunctional surface patterning employed in this thesis. a) Immobilization of **P12-Pd** (point mask (III), 1st step), **P12-Pt** (point mask (IV), 2nd step), and **P11-Au** (point mask (V), 3rd step) towards surface **S11** *via* surface setup C. b) Immobilization of **P12-Pt** (point mask (I), 1st step), **P12-Pd** (point mask (II), 2nd step), and **P11-Au** (no mask, 3rd step) towards surface **S12** *via* surface setup D.

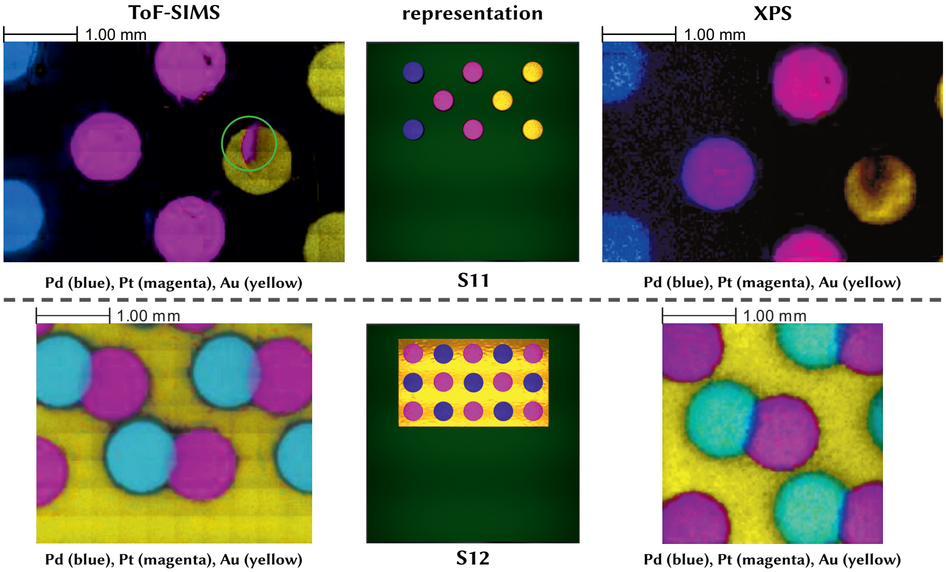

Figure 3.19. ToF-SIMS and XPS analytics of the trifunctional metallopolymer surfaces **S11** (1st row) and **S12** (2nd row). A schematic overview of the surface patterning is given in the middle. The respective ToF-SIMS images are depicted on the left side, while the XPS chemical mappings are displayed in the right column. The color code is given below each picture. The green circle in the ToF-SIMS image of **S11** indicates an area of the 3rd reaction step, which is partially functionalized with **P12-Pt** from the 2nd reaction.

area where **P11-Au** was immobilized. Importantly, the tetrazole moiety is still intact on the non-irradiated area, unaffected by even three irradiation cycles (including extensive washing steps and ultrasonication of the wafer). Hence, these results allow for even further functionalization of the silicon wafer with no general restriction on the number of different photoligation steps. Ultimately, the chemical XPS mappings fit well to the insights obtained from the ToF-SIMS analysis.

The green circle in the ToF-SIMS image of surface **S11** in Figure 3.19 indicates a small area in which **P12-Pt** was partially attached by accident in the second reaction step. Interestingly, no Au^- fragment stemming from the **P11-Au** metallopolymer is detected at this spot, which is already covered with **P12-Pt** from the previous step.

Interestingly, no Au^- fragment is observed at this spot in the detection of the **P11-Au** metallopolymer in this area already covered with **P12-Pt** from the previous step. This observation implicates that the surface coverage during the photoligation step is sufficiently dense to prevent further metallopolymer attachment in subsequent reaction steps.

Therefore, a second threefold experiment was performed in which the two point masks (I) and (II) were used in the first and second reaction step, while no shadow mask was used in the last reaction. In the last irradiation step, the entire surface is irradiated, which is already partially covered with two different metallopolymers (see Scheme 3.19b).

The results of the obtained surface **S12** are depicted in Figure 3.19 (2nd row). Again, all specific mass fragments in the ToF-SIMS analysis and the elemental XPS mappings support the immobilization of the metallopolymers in the targeted areas (see Figure A.77 and Figure A.78).

Importantly, no gold metallopolymer is detected in the area covered with **P12-Pt** and **P12-Pd** from the first and second reaction step, supporting the observation from surface **S11** that the surface coverage in each reaction step is sufficiently dense to prevent further attachment of another metallopolymer, here **P11-Au**, in the last step.

This robustness further simplifies the experimental setup for the fabrication of surfaces with multiple functionality. In addition, fully coated multifunctional metallopolymer surfaces can be readily obtained by employing one final irradiation step without any shadow mask, to fill up the interstitial space between the already functionalized areas.

In analogy to the bifunctional surface pattering, the order of the metallopolymer attachment was also varied for the trifunctional surfaces, see surfaces **S11-rev** and **S12-rev** in Table 3.5. A comparison between the ToF-SIMS analysis of the metal ion fragments of surface **S11** and **S11-rev** is depicted in Figure 3.20. While point mask (V) was used for the patterning of metallopolymer **P11-Au** in both cases, point mask (III) and (IV) were interchanged between **S11** and **S11-rev**. Clearly, the change in the reaction sequence of the palladium and platinum metallopolymer did not affect the successful pattering of all three metallopolymers, which is in good agreement with the observation made with the bifunctional surface patterns.

Table 3.5. Summary of all trifunctional metallopolymer surfaces fabricated in this thesis. For a description of the reaction setup, refer to Table A.2. The reaction sequence gives the order in which the three metallopolymers are tethered onto the silicon wafer. The detailed ToF-SIMS and XPS analytic can be found in the respective figures.

surface	setup	reaction sequence	ToF-SIMS	XPS
S11	C	**P12-Pd→P12-Pt→P11-Au**	Figure A.73	Figure A.74
S11-rev	C	**P12-Pt→P12-Pd→P11-Au**	Figure A.75	Figure A.76
S12	D	**P12-Pt→P12-Pd→P11-Au**	Figure A.77	Figure A.78
S12-rev	D	**P12-Pd→P12-Pt→P11-Au**	Figure A.79	Figure A.80

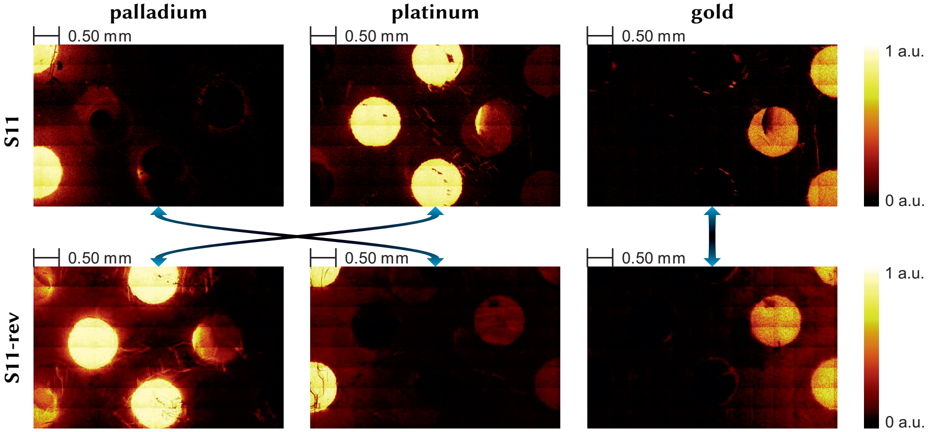

Figure 3.20. Comparison of the surfaces **S11** (1st row) and **S11-rev** (2nd row). The ToF-SIMS mappings of the palladium and platinum fragments swapped places, while the gold fragments are found on the same spots.

Layer thickness The information from the XPS and ToF-SIMS measurements were additionally used to assess an estimation of the thickness of the photoligated metallopolymers. In the employed ToF-SIMS analytical setup, and Regarding the operation mode of the bismuth ion source (Bi_3^+, 25 keV) in the employed ToF-SIMS instrument, the information withdrawn from the measurement equals a depth of 1 nm.[297]

As no silicon can be detected in areas covered with metallopolymers, the thickness must be above 1 nm in all studied cases (see for example Figure A.73). The information depth of the XPS analysis is related to the inelastic mean free path at a given X-ray photon energy. Consequently, the sampling depth has a value in the range of 8–10 nm.[298] The underlying silicon substrate is detected in all areas covered with metallopolymer, which therefore sets an upper limit for the layer thickness of the metallopolymer surface coverage (see entry for **S11-rev** and **S12** in Table 3.6). Hence, the thickness of the attached metallopolymers is in the range of 3–7 nm.

Interestingly, we observe differences between the three employed metallopolymers (see entry for **S11-rev** in Table 3.6). Here, the attenuation of the silicon signal in the XPS is between 50–60 % in the case of the palladium and platinum metallopolymers, whereas the gold metallopolymer only shows a decrease slightly below 40 % of the Si signal. These values suggest a higher layer thickness for the **P12-Pd** and **P12-Pt** metallopolymers as compared to the **P11-Au** metallopolymer. One possible explanation is the higher $\bar{X}_n$ of **P11-Au** compared to the two **P12** based metallopolymers (see Table 3.2). Therefore, the occupied volume of **P11-Au** also exceeds that of the two bipyridine metallopolymers, which results in a lower grafting density of the former through an increased interstitial space of the individual polymer chains on the surface (see also the discussion of the grafting regimes in Section 2.4.2.4).

Table 3.6. Concentration of silicon metal on different locations of the triple modified surfaces **S11-rev** and **S12**. For **S11-rev**, the decrease of the silicon signal with respect to the non-irradiated area is calculated. Adapted with permission from [280]. © 2018 Wiley-VCH Verlag GmbH & Co. KGaA.

surface	measured spot	Si^0 / at%	Si decrease / %
S11-rev	non-irradiated	43.1	–
	P12-Pt	16.5	62
	P12-Pd	21.5	50
	P11-Au	37.7	13
S12	**P12-Pt**	19.7	–
	P12-Pd	19.0	–
	P11-Au	32.5	–

3.4 Conclusion

In this chapter, the first method for the spatially resolved surface immobilization of different metallopolymers on a single surface, employing the versatile NITEC photochemistry for chemical bond formation was developed. The initially strategy *via* the use of photo generated thioaldehydes through phenacyl sulfides was also successfully applied in solution. However, the surface photoligation was not successful employing phenacyl sulfide functionalized silane **3** in combination with PMMA, which was end-functionalized with a diene moiety. The strategy, which was successful for the surface pattering of small organometallic complexes, was therefore abandoned for the photoligation of metallopolymers. Through the NITEC approach, mono-, bi- and even trifunctional metallopolymer surfaces with different metal combinations are fabricated. Preliminary studies on the PMMA homopolymer **P10** unraveled the need of capping the RAFT group by hetero-*Diels–Alder* chemistry, employing photochemically generated *o*-quinodimethanes from **6** as a key point to successfully perform the NITEC photoligation on the surface. The synthesis and characterization of various α-ω-functionalized metallopolymers capable of surface attachment, namely **P12-Pt**, **P12-Pd** and **P11-Au**, was established through RAFT polymerization in combination with the photochemical post-modification step.

The fabrication of gold metallopolymer surfaces is feasible through a post- or pre-loading approach, leading to the same surface structure. In contrast, the post-loading approach was not successful for the bipyridine based metallopolymers **P12-Pt** and **P12-Pd**. With in-depth surface characterization techniques, namely ToF-SIMS and spatially resolved XPS, unambiguous experimental support for the preserved chemical composition of the fabricated metallopolymer surfaces could be provided. In addition, the impact of the *Beer–Lambert* law on the photochemical surface ligation has been investigated. This effect is quantified through the correction of the spectral irradiance with the solution absorption. The developed MATLAB script in combination with the absorption spectrum of the solution containing the photo active molecules and the spectral irradiance of the employed irradiation source readily quantifies the key parameters for a successful surface photo-ligation. The herein introduced photoligation technique for spatially resolved multiple metallopolymer surface ligation can be transferred to other related surface ligation techniques, as the described interplay between solution absorption and successful immobilization can be universally applied for all photoligation systems. The spatial resolution employing this approach is in general only limited by the dimensions of the employed photo mask. The fabrication of bi- and even trifunctional metallopolymer surfaces is enabled by consecutive NITEC photoligation chemistry, ultimately leading to surfaces carrying three metallopolymers in close proximity. These multiple metallopolymer-decorated surfaces are potential candidates for the design of heterogeneous catalysis devices.

CHAPTER 4

Light-sensitive spiropyran-metal complexes

In the development of the spatially resolved surface photolithography protocol in Chapter 3, the photo triggered NITEC reaction was combined with the material class of metallopolymers. There, the photo triggered NITEC chemistry and the metal complexes in the metallopolymers do not interact with each other, despite being part of the same (macro)molecules. In contrast, this chapter will explore the photochemistry of organometallic complexes itself, for the potential creation of light-sensitive metallopolymers. Light-responsive metallopolymers are attractive for various technological fields, e.g. stimuli responsive materials, sensor applications, or the light-triggered control of catalysis activity. While the metallopolymers in Chapter 3 are prepared by the polymerization of widely used triphenylphosphine- and bipyridine-based ligand monomers, the creation of light-sensitive metallopolymers requires special ligands and monomers. The synthesized metal complexes in the current chapter are based on the chemistry of SPs, introduced in Section 2.2.2.1. In order to take advantage of the full toolbox of solution-based characterization methods, e.g. UV-Vis or NMR spectroscopy, the materials prepared in this chapter are not employed for surface ligation experiments, yet. This chapter will rather focus on the development and understanding of the photochemistry of SP-derived metal complexes for later usage as functional ligands in light-responsive metallopolymers. Nevertheless, the utilization of such light responsive materials with the surface photoligation chemistry of Chapter 3 will ultimately enable the preparation of light-responsive surfaces. While there are few reports on the combination of light-responsive SP-based molecules[62c,299] or organic polymers[69,75b,300] with surface chemistry, no reports on the fabrication of surfaces decorated with light-responsive SP metallopolymers can be found in literature.

The results in this chapter were obtained in close collaboration with M. Sc. T. J. Feuerstein from the group of Prof. P. W. Roesky (Institute for Inorganic Chemistry, Karlsruhe Institute of Technology). Parts of the synthesis and characterization performed by M. Sc. T. J. Feuerstein are included for consistency and are referenced at the respective places. First, the synthesis of new SP-based metal complexes will be discussed, followed by the investigation of their photochemical behavior. As a part of this investigation, the recently developed combination of light-emitting diode (LED) irradiation with NMR spectroscopy by Gschwind *et al.*[301] was significantly improved. The aim of this chapter is to synthesize suitable SP-based metal complexes and understand their photochemistry. After the insights gained from the small molecule studies, future work will aim to incorporate the SP-metal complexes into a polymer scaffold for potential applications in the realm of SCNP chemistry. In Figure 4.1, the motivation for the access to a light-responsive SP-metal complex SCNP system is shown. Through smart functionalization of the SP moiety, the polymer is non-reactive towards metal complexation in the dark. In contrast, the light-triggered SP⟶MC ring-opening in the presence of suitable metal precursors under dilute conditions results in an intramolecular chain collapse, i.e. the formation of a metal-containing SCNP. The metal extrusion and reformation of the polymer chain

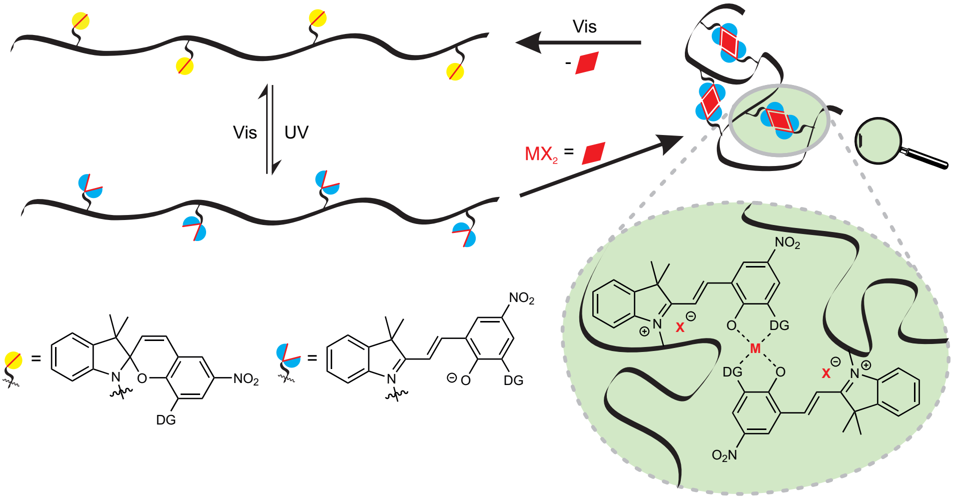

Figure 4.1. Proposal of a light-responsive SCNP based on the reversible intramolecular cross-linking of a SP-functionalized polymer with metal centers as cross-linking points.

is afterwards enabled by the light-triggered MC⟶SP isomerization through irradiation with visible light. The realization of the proposed properties of such a SP-based metallopolymer will be the driving force behind the investigations presented in the current chapter.

4.1 Synthesis of spiropyran-metal complexes

In all of the described metal complexes featuring SPs in their MC form as ligand sites, an additional binding site is necessary to sufficiently stabilize the metal complex and prevent a spontaneous thermal MC⟶SP ring-closure and therefore breakup of the metal complex (refer to the introduction on Page 36 and the complexes depicted in Figure 2.14). With this respect, a methoxy-group in *ortho*-position to the oxygen bound to the spiro-carbon atom serves as a readily available ligand site and was chosen for the synthesis of SP **10** according to Raston and co-workers[302] (see Scheme 4.20a). A related SP structure was also successfully employed by Giordani and co-workers[91] for the formation of SP-metal complexes (refer to Figure 2.14d).

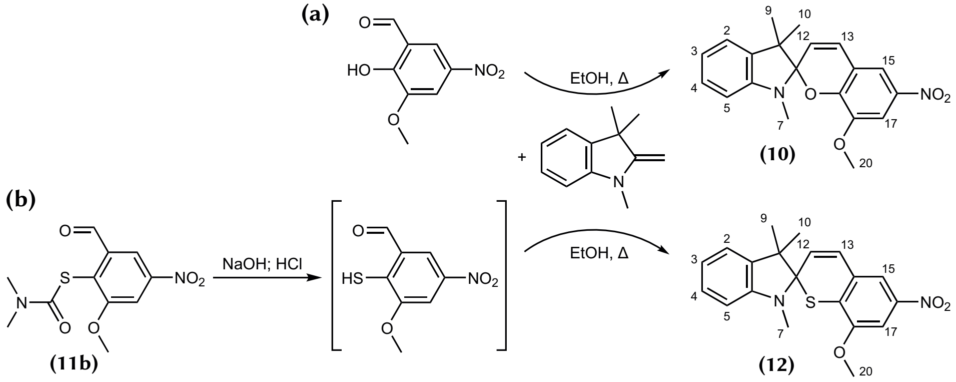

Scheme 4.20. a) Synthesis of 8-methoxy functionalized SP **10** as reported by Raston and co-workers.[302] b) Synthesis of the analogous STP **12** through *in situ* deprotection of **11b** towards the free thiophenol and subsequent condensation with 1,3,3-trimethyl-2-methyleneindoline.

SP **10** was obtained by refluxing an equimolar solution of 1,3,3-trimethyl-2-methyleneindoline and 3-methoxy-5-nitrosalicylaldehyde in ethanol. Concentration of the resulting solution and cooling yields **10** as green crystals in 83 % yield. In the top row of Figure 4.2, the ^{1}H NMR (left) and absorption spectra (right) of **10** are shown. The typical splitting of the two methyl group resonances 9 and 10 is visible, due to the fixed geometry of the spiro-center, resulting in their magnetic inequivalence, which is an

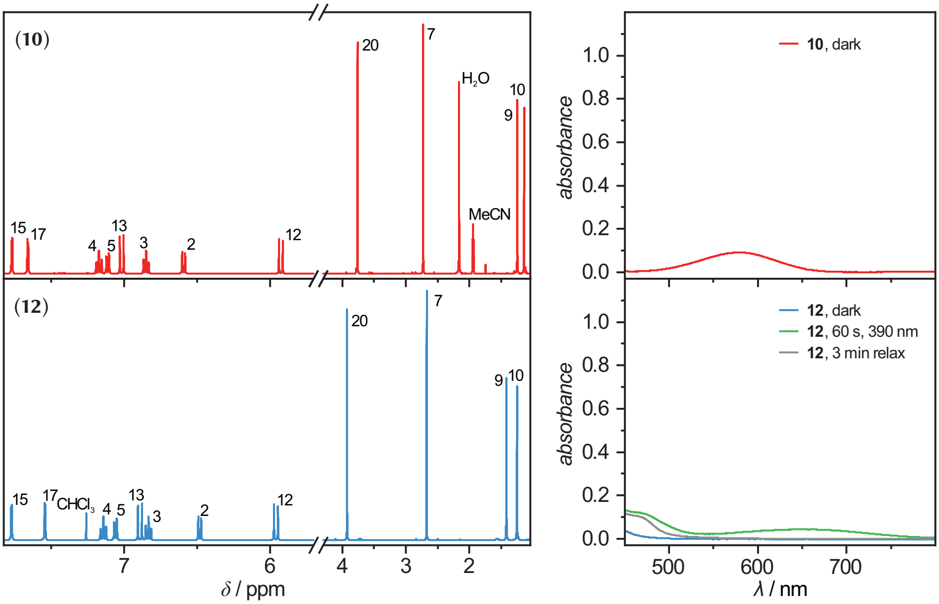

Figure 4.2. Left side: ^{1}H NMR spectra of **10** (top) and **12** (bottom) with the resonance assignments according to the labeling in Scheme 4.20. Right side: Corresponding absorption spectra of **10** (top) and **12** (bottom) in the dark. For **12**, the spectra of the PSS upon irradiation with a 390 nm LED and subsequent thermal relaxation in the dark are depicted as well. Measured in MeCN (30 µM, 1 cm cuvette).

indication for the closed SP structure. In addition, the vicinal coupling between the vinylic protons 12 and 13 with $^3J_\mathrm{c} = 10.4\,\mathrm{Hz}$ is typical for the *cis*-configuration in the closed SP structure. For the metal complexation to occur solely upon light-triggered SP⟶MC conversion (refer to Figure 4.1), the thermal equilibrium between the SP and the MC form must be located far on the SP side. However, an absorption band associated with the intensely colored MC form of **10** is visible in the absorption spectra centered at 580 nm. Given the large extinction coefficient of the MC form, which is significantly higher than the one from the SP form, the ratio of the SP:MC equilibrium cannot be determined *via* UV-Vis spectroscopy. However, upon closer inspection of the ^{1}H NMR spectra, the single resonance at 1.74 ppm can be assigned to the 6 magnetic equivalent geminal methyl proton resonances 9 and 10 of the MC form.[191,303] From the ^{1}H NMR integral ratios, the thermal equilibrium concentration of the MC form in CD_3CN is 1.9 mol%. The non-zero thermal equilibrium concentration of the MC form of **10** is likely to result in spontaneous metal complexation without the possibility to trigger the metal complexation *via* photochemistry. Various strategies for reducing the thermal MC equilibrium concentration have been proposed in literature, such as the substitution of the indol, as well as the chromene part of the molecule.[62d] Another possibility is to employ the analogous STP structure (see also Chapter 5), as these derivatives are known for their small thermal equilibrium concentration of the MC form.[184,187,188,190,191]

Therefore, STP **12** was synthesized through condensation of 1,3,3-trimethyl-2-methyleneindoline with the masked thiophenol **11b**, which was deprotected *in situ* under basic conditions (see Scheme 4.20b). **11b** was synthesized through reaction of 2-hydroxy-3-methoxy-5-nitrobenzaldehyde with *N*,*N*-dimethylthiocarbamoyl chloride and subsequent *Newman–Kwart* rearrangement (see also the synthesis of **14b** in Scheme 5.23b). Similar to the synthesis of **10**, **12** was obtained upon concentration and crystallization from ethanol in 72 % yield. In the bottom row of Figure 4.2, the ^{1}H NMR (left) and absorption spectra (right) of **12** are shown. Similar to the ^{1}H NMR spectrum of **10**, a splitting of the proton resonances 9 and 10 of the geminal methyl groups is observed, in addition to the vicinal coupling constant of $^3J_c = 10.9$ Hz between protons 12 and 13, fitting to the *cis*-configuration of the STP double bond. In contrast to **10**, no resonances associated with the MC isomer of **12** can be detected in the ^{1}H NMR spectrum. Accordingly, the absorption spectra of **12** does not show any absorption in the region of 500–800 nm, where an absorption band stemming from the MC form of STP molecules is expected (refer to the absorption spectrum in Figure 5.1). To examine, whether the photo triggered STP⟶MC isomerization is feasible with **12**, an irradiation experiment inside the UV-Vis cuvette was performed under simultaneous absorption measurement (for a description of the experimental setup, see Figure A.1). Upon irradiation with a 390 nm LED for 60 s, a broad absorption band rises at 650 nm, which is attributed to the PSS concentration of the MC isomer, together with a second absorption band at 470 nm. The small bump at 390 nm in the spectrum of the PSS is an artifact from the simultaneous irradiation with the 390 nm LED. Turning off the irradiation source results in the thermal fading of the MC absorption band after 3 min, while the absorption at 470 nm remains, indicating that this absorption band is most likely the result of an irreversible photo degradation product of **12**. Nevertheless, the absence of the MC form of **12** in the dark, together with its accessibility upon irradiation, renders STP **12** a good candidate for the application outlined in Figure 4.1.

Complexation studies with STP 12 The metal complexation studies of **12** were performed in the presence of metal salts, with the LED-UV-Vis setup employed for the PSS measurement of **12** (refer to Figure A.1). The strategy is outlined in Figure 4.3, in addition with the corresponding absorption measurements. Zinc and nickel perchlorate salts were

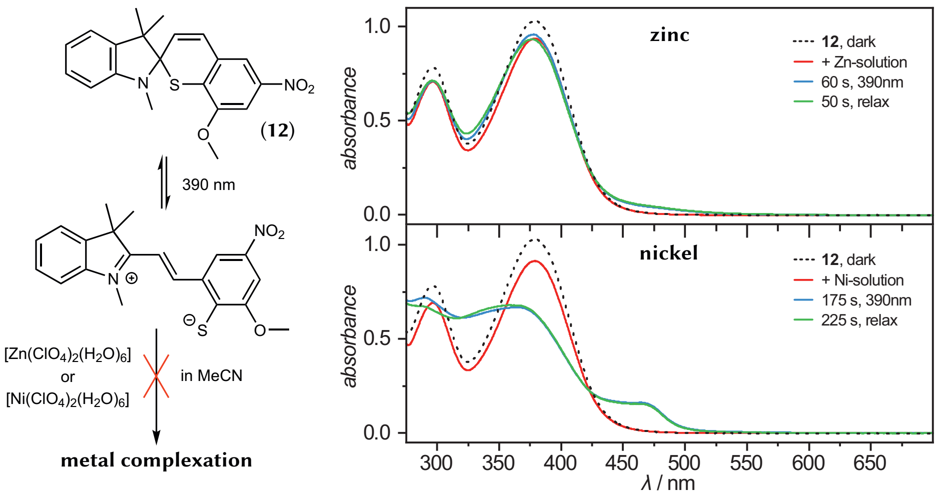

Figure 4.3. Non-successful experiments towards the formation of zinc and nickel complexes with **12** under irradiation with UV light. The absorption spectra of **12** and the mixture with 0.8 eq. of the zinc (top) and nickel (bottom) salts are shown, together with the PSS spectra upon irradiation with a 390 nm LED and the spectra after thermal relaxation in the dark.

employed for the test reactions, namely $[Zn(ClO_4)_2(H_2O)_6]$ and $[Ni(ClO_4)_2(H_2O)_6]$. A solution of **12** (2.1 mL, 30 µM in MeCN) was added into a quartz cuvette for the spectrum in the dark, serving as a reference. Thereafter, 0.8 eq. of the respective metal salt was added (0.1 mL, 540 µM in MeCN). The utilization of concentrated metal salt solution minimizes the influence of the dilution on the absorption spectra upon addition. Nevertheless, a small dilution effect is evident, when comparing the spectra of pure **12** with the two metal salt mixtures in Figure 4.3. More importantly, though, is the absence of metal complex associated absorption bands, confirms the inactivity of **12** to serve as a metal binding site in the dark. While the expected ration of MC/metal in the complexes equals 2 in both cases, a slight excess of 0.3 eq. is added to ensure a sufficiently large metal salt concentration for the anticipated complexation. However, upon irradiation of the mixed solutions with the 390 nm LED, no change in the absorption spectra is observed in both cases. In the experiment with zinc, the PSS spectrum, as well as the spectrum after 50 s relaxation in the dark, are similar to the spectrum of the mixture before irradiation. In the case of nickel, photo degradation of **12** is observed in analogy to the experiment for the irradiation of pure **12** in Figure 4.2. The expected metal complex formation should manifest itself in the rise of a broad absorption band in the region of 500–650 nm in analogy to comparable metal complexes.[91] In conclusion, while forming the MC isomer upon irradiation, STP **12** is not capable to form stable zinc or nickel complexes in solution. Therefore, further experiments will focus on the utilization of the oxygen SP analog **10** for the formation of metal complexes.

Complexation studies with SP 10 In contrast to the results obtained from the complexation experiments with STP **12**, SP **10** was successfully employed for the formation of zinc-, nickel-, calcium-, as well as lanthanum-SP metal complexes. However, the non-zero equilibrium concentration of the MC form of **10** in the dark leads to the spontaneous formation of the respective metal complexes, without the ability to trigger the complexation *via* light.[(a)] The formation and stoichiometry (from X-ray analysis) of the new SP-metal complexes is shown in Scheme 4.21.

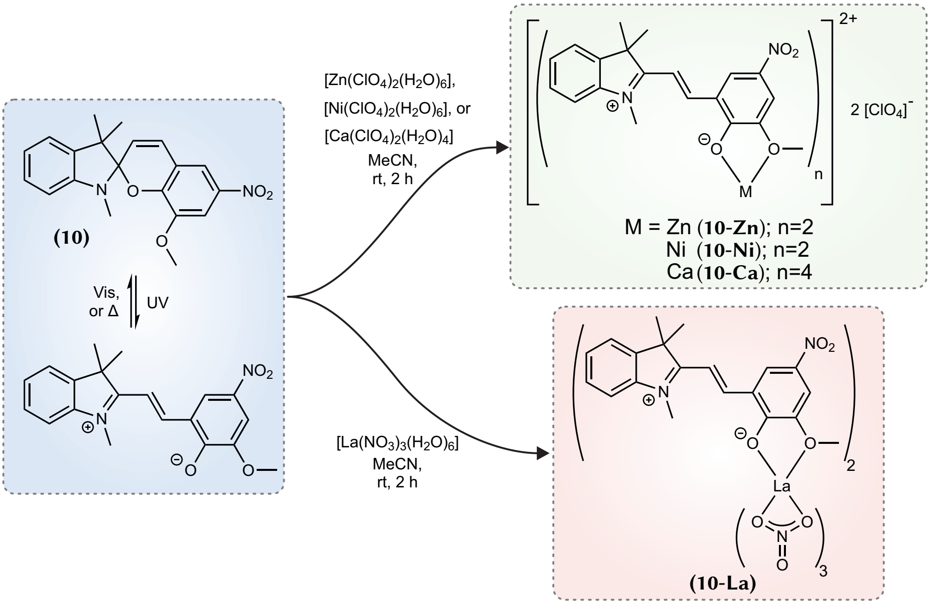

Scheme 4.21. Synthesis of SP-metal complexes with SP **10**. Reaction with $[Zn(ClO_4)_2(H_2O)_6]$ and $[Ni(ClO_4)_2(H_2O)_6]$ leads to the bischelated metal complexes **10-Zn** and **10-Ni**, respectively. The tetrachelated SP-calcium complex **10-Ca** is obtained through reaction with $[Ca(ClO_4)_2(H_2O)_4]$, while the reaction with $[La(NO_3)_3(H_2O)_6]$ leads to the bischelated lanthanum complex **10-La**, with 3 additional nitrate ions complementing the ligand sphere.

[(a)] The metal complexation, including the NMR spectroscopic characterization and the crystallization of single crystals suitable for X-ray analysis presented in this section were performed by M. Sc. T. J. Feuerstein. For the detailed experimental and spectroscopic description, see [284].

While the reaction with $[Zn(ClO_4)_2(H_2O)_6]$ and $[Ni(ClO_4)_2(H_2O)_6]$ results in bischelated metal complexes **10-Zn** and **10-Ni** with two MeCN molecules complementing the ligand sphere (not shown in Scheme 4.21), calcium is coordinated by 4 **10** molecules upon reaction with $[Ca(ClO_4)_2(H_2O)_4]$ in the complex **10-Ca**. In all of these cases, charged complexes are obtained with ClO_4^- as the counter ion. In contrast, the reaction with $[La(NO_3)_3(H_2O)_6]$ results in the non-charged complex **10-La**, in which the lanthanum is coordinated by two **10** molecules and three nitrate ions. The detailed NMR spectroscopic characterization of all complexes can be found in [284].

In Figure 4.4, the crystal structures of all prepared metal complexes of **10** are depicted. Hydrogen atoms are omitted for better visualization. In all cases, **10** is coordinated *via* the oxygen of the phenolate and the methoxy moiety of the MC form. Interestingly, while **10** in **10-Zn**, **10-Ni**, and **10-La** is coordinated as the TTC MC isomer, the coordination in **10-Ca** is realized *via* the TTT isomer (refer to Scheme 2.7).

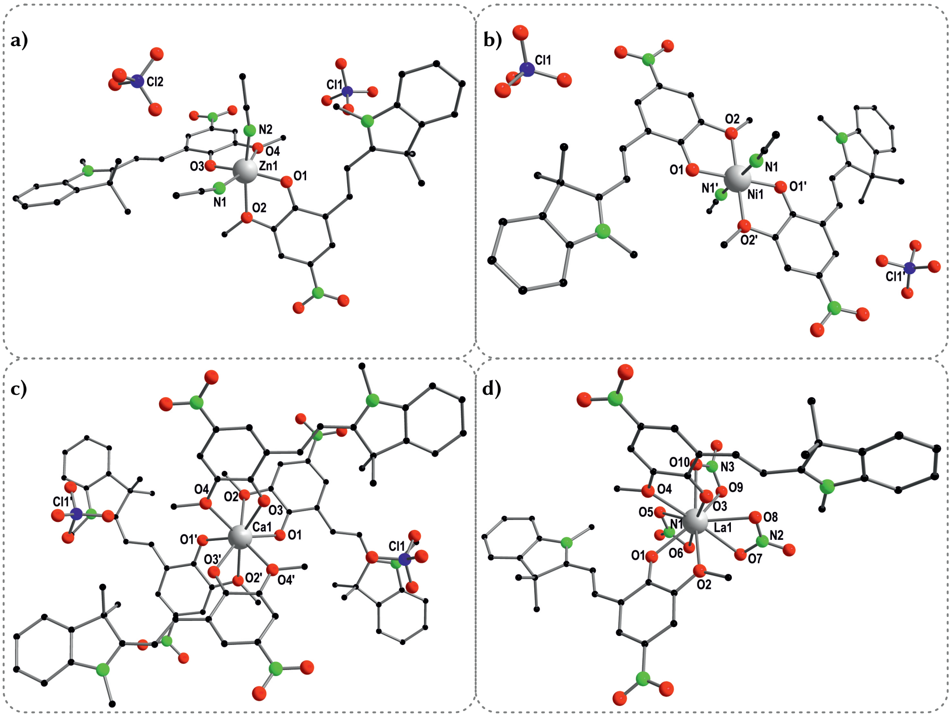

Figure 4.4. Crystal structures of **10-Zn** (a), **10-Ni** (b), **10-Ca** (c), and **10-La** (d). Hydrogen atoms are omitted for clarity. Adapted with permission from [284].

Recapitulating the anticipated application of the SP-metal complexes as cross-linking points for the formations of SCNPs (refer to Figure 4.1), the binding of at least two SP molecules to a single metal ion is crucial. While this condition is fulfilled in all synthesized metal complexes of **10** in Figure 4.4 in the solid state, the configuration of the complexes in solution might be different to the results obtained from X-ray crystallography. Therefore, the complex stoichiometries in solution were investigated *via* Job's method of continuous variations.[304]

The absorption spectra and the corresponding Job plot of **10-Zn** are depicted in Figure 4.5a) and b), respectively. In panel a), the spectrum of pure **10** ($X_{Zn} = 0.0$) does show the characteristic absorption band of the thermal equilibrium concentration of the MC form at 580 nm. In all other spectra, the formation of **10-Zn** is evident through the absorption band at 480 nm, which is used for the Job plot in panel b). The maximum of the absorption in the Job plot is directly correlated with the complex stoichiometry. Therefore, the maximum was determined *via* interpolation of the experimental points. Different methods have been proposed in literature for the interpolation equations in Job plot analysis, ranging from linear[305] to sophisticated models, involving several coupled equilibria.[306] Recent studies investigated the impact of coupled equilibria and association constants on the shape of the corresponding Job plot and pointed out the failure of simple linear models for weakly associated complexes.[307] The interpolation of the

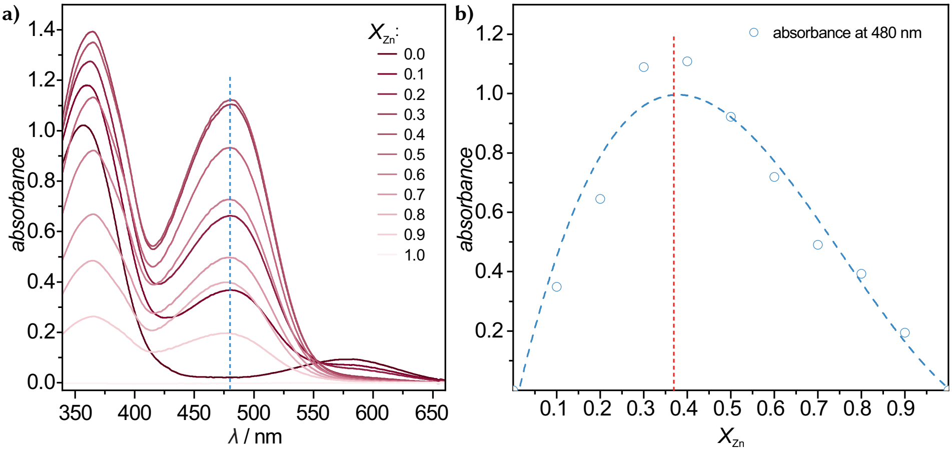

Figure 4.5. a) UV-Vis spectra of **10-Zn** for the determination of the complex stoichiometry using Job's method of continuous variations. The wavelength at 480 nm used for the Job's plot analysis is indicated with the dashed blue line. [**10**]+[**Zn**] = 95 µM in MeCN, measured in a 10 mm cuvette. b) Job's plot analysis of the spectra in a), with the maximum of the interpolated dashed blue line at $X_{Zn} = 0.37$.

Job's plot presented in the current thesis were performed using a polynomial equation of degree five, which is capable to represent all experimental values in sufficiently accurate manner. The determined maximum of $X_{Zn} = 0.37$ in Figure 4.5b) nicely correlates with the theoretical value of $X_{Zn} = 0.33$ for a $[(SP)_2M]$ complex with the 2:1 stoichiometry, thereby confirming the value for **10-Zn** in the crystalline state .

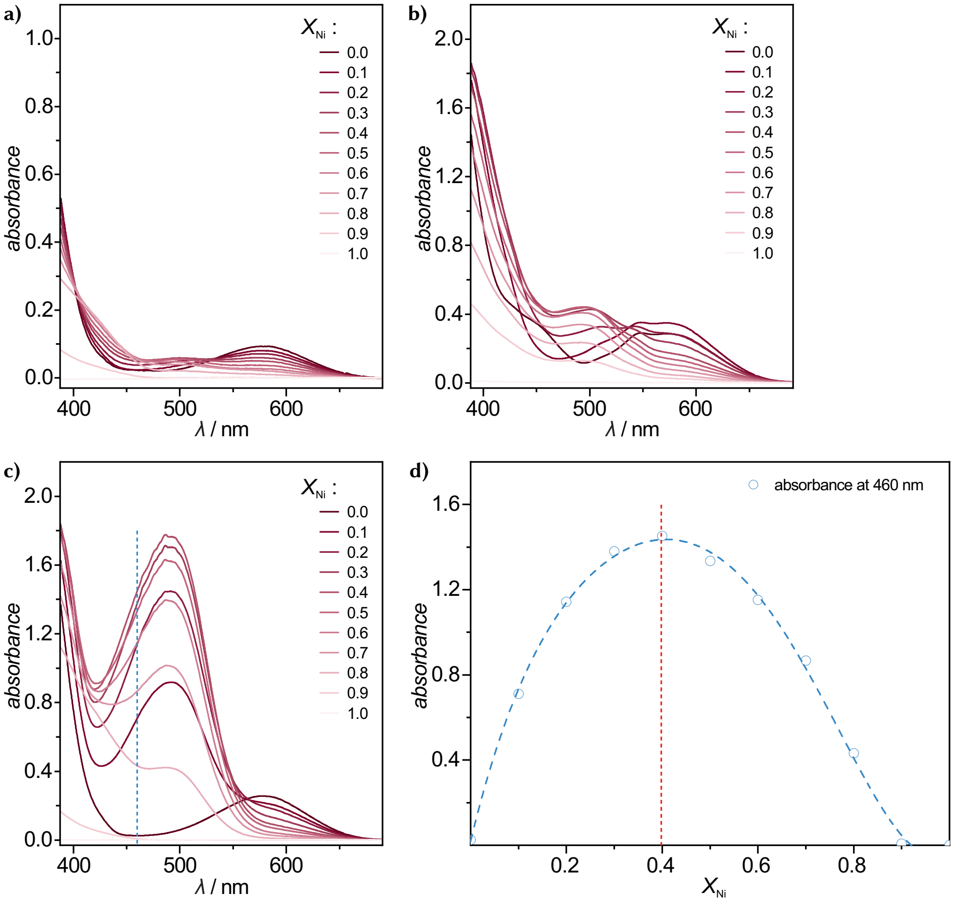

Figure 4.6. a)–c) UV-Vis spectra of **10-Ni** at different total concentrations of [**10**]+[**Ni**] = 95 µM (a), 0.55 mM (b), and 2.8 mM (c) in MeCN, measured in a 10, 5, and 1 mm cuvette, respectively. The absorption values at 460 nm in c) are used for the Job's plot analysis in d), which gives an interpolated maximum value at $X_{Ni} = 0.40$.

While the stoichiometry in solution equals the result from X-ray crystallography for **10-Zn**, a different result is obtained for **10-Ni** (see Figure 4.6). Using the same concentration also employed for the Job plot analysis of **10-Zn**, no clear determination of the complex stoichiometry *via* a Job plot is feasible (see Figure 4.6a). The spectra show multiple overlapping absorption bands stemming from the MC form of **10**, as well as **10**-derived nickel complexes of unknown stoichiometry. Increasing the concentration to 0.55 mM in panel b), the coexistence of the free MC form, as well as multiple absorption bands stemming from complexation products with nickel, is even more evident in the region of 450–650 nm. Finally, at a concentration of 2.8 mM, a single strong absorption band at 490 nm allows the determination of the corresponding complex stoichiometry. As the absorption values at 490 nm are already at the saturation threshold of the employed UV-Vis spectrometer, the absorption values in the shoulder at 460 nm are used for the determination of the stoichiometry. The Job plot is shown in panel d), with a determined maximum at $X_{\mathrm{Ni}} = 0.40$, which lies between the theoretical value of $X_{\mathrm{Ni}} = 0.33$ and $X_{\mathrm{Ni}} = 0.50$ of $[(\mathrm{SP})_2\mathrm{M}]$ and $[(\mathrm{SP})\mathrm{M}]$ stoichiometries, respectively. According to the available data and in contrast to complex **10-Zn**, **10-Ni** features a rather weak association constant, resulting in a complex mixture of multiple species at low concentrations. However, the $[(\mathrm{SP})_2\mathrm{M}]$ stoichiometry determined in the crystalline state seems to dominate at sufficiently high concentrations.

Similar observations have been made for the complexes **10-Ca** and **10-La** at low concentrations. However, as in the case of **10-Ni**, the predominant stoichiometry at higher concentrations equals the values determined from X-ray crystallography. The absorption spectra, including the Job plots for **10-Ca** and **10-La** can be found in Figure A.20–A.23.

In Table 4.1, the theoretical values from the stoichiometries determined *via* X-ray crystallography are listed next to the values determined through Job plot analysis in solution. Except for **10-Ni**, the determined values confirm the stoichiometry found in the crystalline state, rendering all prepared SP-metal complexes capable to serve as cross-linking points in the formation of SCNPs according to Figure 4.1.

Table 4.1. Comparison of the complex stoichiometries in the solid state (X-ray) with the values in solution determined *via* Job plot analysis.

complex	$\frac{[\mathrm{M}]}{[\mathrm{M}]+[\mathbf{10}]}$	
	X-ray	Job's plot
10-Zn	0.33	0.37
10-Ni	0.33	0.40
10-Ca	0.20	0.23
10-La	0.33	0.32

4.2 Photochemistry of spiropyran-metal complexes

After the elucidation of the complex stoichiometries, the photochemistry of the prepared metal complexes was investigated. For comparable SP-metal complexes, literature reports describe the photo induced dissociation of SP-metal complexes,[91] as well as photo triggered isomerizations in the MC ligand itself,[308] specifically a *cis*⇌*trans* isomerization of the central MC double bond. Therefore, the influence of light on the spectral behavior of the prepared metal complexes was first qualitatively investigated with the LED-UV-Vis setup described in Figure A.1.

4.2.1 LED-UV-Vis investigations

To assess the initial absorption spectra of the complex configuration in the crystalline state, the absorption spectra denoted as “after dissolving” in Figure 4.7 were measured directly after dissolving a small amount of crystalline material in the UV-Vis cuvette under vigorous stirring, which was filled with MeCN in advance. Due to the insolubility of crystalline **10-La** in MeCN, only the results for **10-Zn**, **10-Ni**, and **10-Ca** are shown in Figure 4.7a)–c), respectively.

For **10-Zn**, the initially strong absorption band at 480 nm shows a reduced intensity upon thermal equilibration after 6 h. This reduction is attributed to the non-zero concentration of uncomplexed **10** in solution, see also the discussion in Section 4.2.2. As such, the initial absorption spectrum measured directly after dissolution does correspond to the spectrum of **10-Zn**, while the spectrum after 6 h is in fact a mixture of **10-Zn** and **10**. Irradiating the obtained solution with a 390 nm LED for 30 s does result in a rapid fading of the absorption band at 480 nm, which is subsequently re-established in the dark after 1 h. This reversible photo induced transformation is repeated three times without any evidence of photo degradation and exhibits an isosbestic point at 304 nm. The presence of an isosbestic point is a strong indication of a reversible equilibrium between two species. However, UV-Vis spectroscopy is not capable to elucidate the structure of the second species, which is generated upon irradiation.

The investigation of **10-Ni** in Figure 4.7b) does not show a significant change of the initial absorption spectrum “after dissolution” and the thermally equilibrated spectrum after 1 min. This observation is not expected, as the results from the Job plot analysis in Figure 4.6 suggest a weaker association constant compared to **10-Zn**. As such, the initial absorption spectra of crystalline **10-Ni** should significantly differ from the thermally equilibrated spectrum. A possible explanation could be different kinetics of the complex dissociation. While the process is sufficiently slow for **10-Zn** to enable spectroscopic tracing *via* UV-Vis spectroscopy, the UV-Vis measurements might not be fast enough to capture the corresponding process in the case of **10-Ni**. Interestingly, a strong absorption band at 575 nm is rising upon subsequent irradiation with the 390 nm LED and reaches a PSS after 15 s. Similar to the observation of **10-Zn**, the thermally equilibrated spectrum of **10-Ni** is also re-established in the dark after 8 min. Recapitulating the specific wavelength for **10-Ni** at 490 nm and for the MC form of **10** at 580 nm (see Figure 4.6c) and Figure 4.2, respectively), the rising absorption band at 575 nm in Figure 4.7b) is attributed to the photo induced SP→MC transformation of uncomplexed **10** in solution.

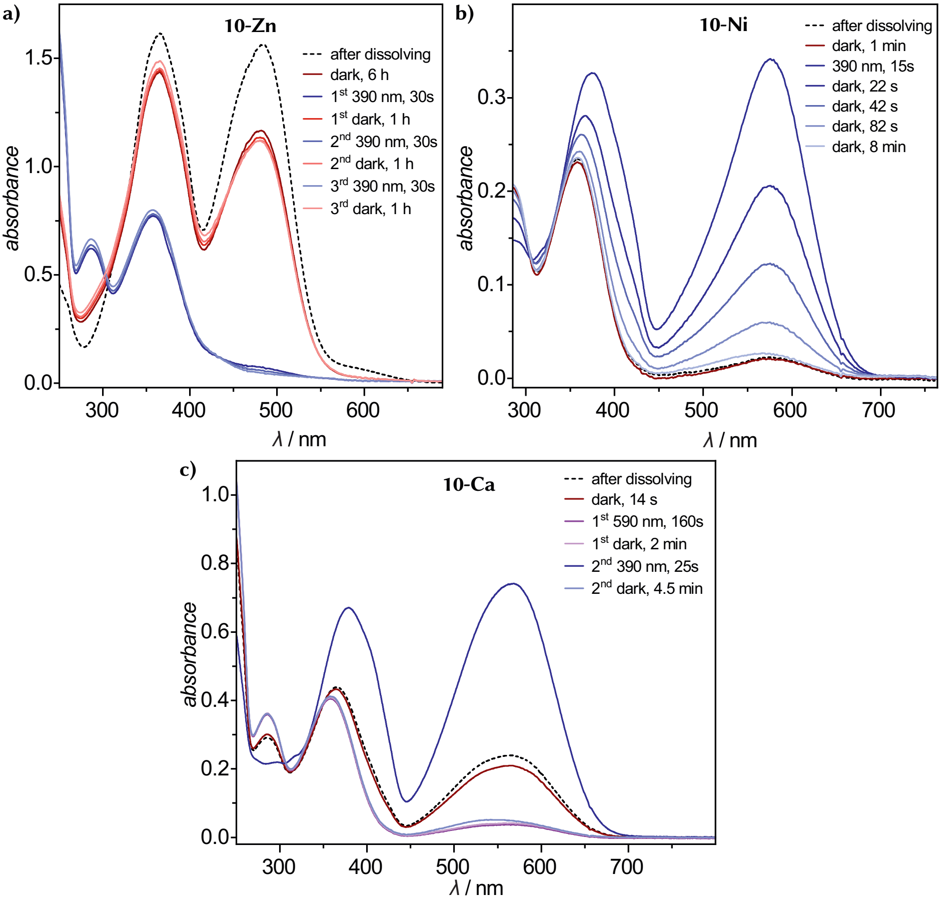

Figure 4.7. Absorption measurements of **10-Zn** (a), **10-Ni** (b), and **10-Ca** (c) under simultaneous irradiation with a 390 nm LED employing the setup described in Figure A.1. For **10-Ca**, a 590 nm LED was used in addition to the UV LED.

For **10-Ca**, an absorption band at 560 nm with a shoulder at ≈510 nm is visible in the spectrum after dissolution. Interestingly, irradiation of the broad absorption with a 590 nm LED results in a rapid decrease in the intensity of this band, which remains stable in the dark. Similar to **10-Ni**, a strong absorption at 560 nm is rising upon irradiation with the 390 nm LED. Again, thermal relaxation in the dark does re-establish the former spectrum, a process that was repeated two times. Regarding the absorption band at 510 nm of **10-Ca** in the concentrated solutions employed for the Job plot analysis (see Figure A.20), the shoulder at 510 nm in Figure 4.7c) is assigned to the tetracoordinated complex **10-Ca**, while the absorption band at 560 nm is related to the MC form of uncomplexed **10** in analogy to the results obtained for **10-Ni**. As such, the changes in the absorption spectra during irradiation with the 590 and 390 nm LED is dominated by the photo triggered SP⇌MC equilibrium of uncomplexed **10**. Therefore, the potential photochemistry of **10-Ca** cannot be investigated *via* this approach.

In summary, first indications of the photochemistry of the prepared SP-metal complexes could be assessed in the case of **10-Zn**, while the investigations of **10-Ni** and **10-Ca** are hampered by the significant impact of the SP⇌MC equilibrium of uncomplexed **10**. For this reason, and to gain a more precise molecular picture of the photochemistry of the prepared complexes, a recently introduced setup for the *in situ* irradiation of an NMR tube during the NMR measurement[301] was adapted for the investigation of the SP-metal complexes.

4.2.2 LED-NMR spectroscopy

The *in situ* irradiation of an NMR sample during the measurement inside the probe head of the NMR spectrometer was introduced by Gschwind and co-workers in 2013,[301] which is referred to as “LED-NMR spectroscopy” in the present thesis. Later, in 2018, Reibarkh and co-workers described methods for the measurement of quantum yields *via* LED-NMR spectroscopy though the use of various chemical actinometers to determine the light intensity inside the NMR tube.[309] LED-NMR spectroscopy has been employed for the elucidation of photochemical reaction mechanisms[310] and the investigation of photochromic azobenzene molecules.[311]

The LED-NMR setup of the present thesis is shown in Figure 4.8. The setup comprises an outer and inner NMR tube, which are fixed with spacers on the bottom and top of the outer tube. While the volume in between the outer and inner tube is filled with the analyte solution, the optical fiber is inserted into the inner tube. In the region that is filled with the analyte solution, the optical fiber is stripped and roughened to ensure a homogeneous emission of the light over the whole surface area. Instead of the roughening procedure through sand blasting published in the initial report by Gschwind and co-workers, it was found that the etching of the fiber tip with glass etching cream results in a very homogeneous surface wrinkling. In addition, the ability to monitor the etching process *in situ* further simplifies the roughening procedure (see Figure A.2 for detailed information). The employed 365 nm high-power LED is mounted on a custom-build metal adapter (see Figure 4.8b). A Peltier element below the adapter is actively cooling the LED and the heat dissipation is realized *via* attached cooling fins including a small fan. A commercially available cage plate is holding the LED fiber directly over the LED, thus ensuring an efficient coupling of the light inside the optical fiber.

The NMR measurements in this section were conducted together with M. Sc. T. J. Feuerstein from the group of Prof. P. W. Roesky (Institute for Inorganic Chemistry, Karlsruhe Institute of Technology), while the analysis of the obtained kinetic measurements and the interpretation of the results were performed by the author of the present thesis.

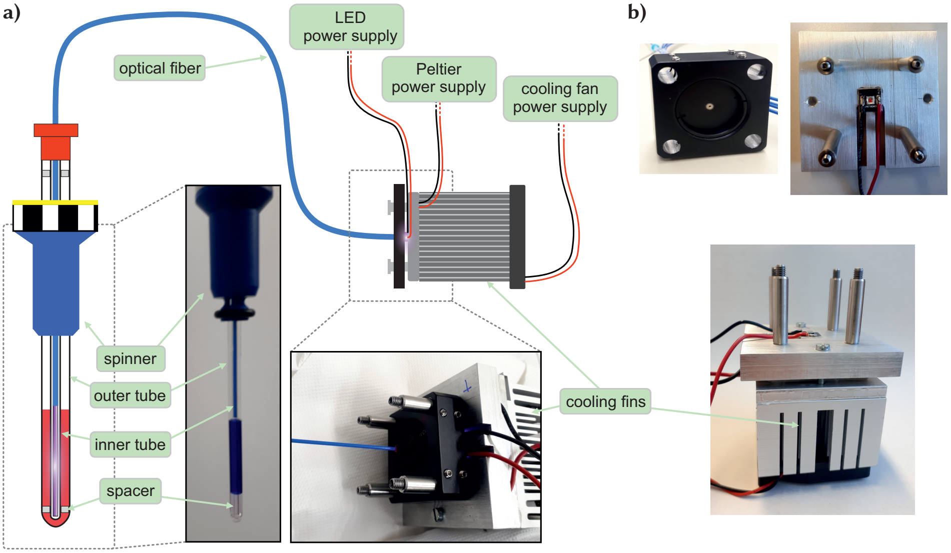

Figure 4.8. a) Schematic drawing of the setup for LED-NMR experiments including pictures of the real experimental setup. b) Picture of the cage plate with the inserted terminated fiber adapter, holding the optical fiber exactly centered over the LED (top left). Picture from the top (top right) and side (bottom) of the mounted LED inside the custom-build adapter with the cable channels and 4 rods to hold the cage plate on top of the LED.

Calibration of the LED-NMR setup through chemical actinometry Following the procedure described by Reibarkh and co-workers, the LED-NMR setup was calibrated directly inside the NMR probe head *via* the use of a chemical actinometer, namely *o*-nitrobenzaldehyde (*o*-NBA). Upon irradiation with 365 nm, *o*-NBA reacts towards *o*-nitrosobenzoic acid with a known quantum yield of $\Phi_{365} = 0.5$[312] (refer to Scheme 4.22). Solutions with different concentrations of *o*-NBA in CD_2Cl_2 were irradiated inside the NMR and the product formation of *o*-nitrosobenzoic acid was determined over time *via* integration of the proton resonance at 6.58 ppm. An adapted `zg2d`-Bruker pulse sequence with 33° flip angle was used for the kinetic measurements (the employed pulse sequence is given in Section A.1). The steady-state approach ensures the accuracy of the NMR quantitation (for a detailed description, see Page 168). In Figure 4.9a), the 99 mM sample of *o*-NBA is shown as an example for the determination of the initial product formation rate of *o*-nitrosobenzoic acid. The linear region in the beginning of the reaction is fitted, and the extracted reaction rates are plotted against the *o*-NBA concentration in Figure 4.9b).

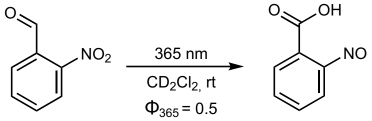

Scheme 4.22. Transformation of *o*-NBA towards *o*-nitrosobenzoic acid upon irradiation with 365 nm UV light.

The relation between the rate and the concentration of the unknown light intensity I_0 is given by Equation (4.1),

$$-\frac{\mathrm{d}[o\text{-NBA}]}{\mathrm{d}t} = I_0\Phi\left(1 - 10^{-\epsilon l[o\text{-NBA}]}\right) \tag{4.1}$$

$$f(x) = A\left(1 - e^{-\ln(10)zx}\right) \tag{4.2}$$

while Equation (4.2) was employed for the fitting with $A = I_0\Phi$ and $z = \epsilon l$. Φ is the known quantum yield of the reaction of $\Phi = 0.5$ and $\epsilon = 260\,\mathrm{M}^{-1}\,\mathrm{cm}^{-1}$ the molar attenuation coefficient of *o*-NBA.[309] With the specifications of the NMR tubes, the light path length l is calculated as $l = 0.84$ mm, resulting in a value of $z = 0.021\,84\,\mathrm{mM}^{-1}$.

From the fitting, A is determined as $A = 2.57(6)\,\mathrm{mM\,min}^{-1}$, from which the light intensity I_0 is calculated to $I_0 = 2 \cdot 2.57(6)\,\mathrm{meinstein\,L}^{-1}\,\mathrm{min}^{-1} = 5.14(6)\,\mathrm{meinstein\,L}^{-1}\,\mathrm{min}^{-1}$. Comparing this value with the one for the setup described by Reibarkh and co-workers of $I_0 = 1.41\,\mathrm{meinstein\,L}^{-1}\,\mathrm{min}^{-1}$,[309] the light intensity reaching the sample in the setup developed in the current thesis could be improved by 366 %. In addition, the coupling

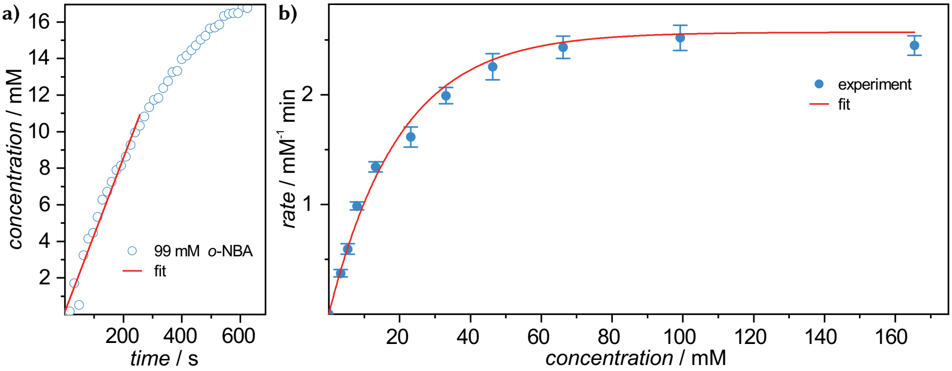

Figure 4.9. a) Concentration increase of *o*-nitrosobenzoic acid and linear fit for the determination of the initial product formation rate for the 99 mM sample of *o*-NBA. b) Experimental and fitted initial rates of product formation according to Scheme 4.22 for different concentrations of *o*-NBA using Equation (4.2).

efficiency of the employed setup was estimated by measuring the irradiance of the LED without the optical fiber at a distance of 1 cm with a spectroradiometer (see Figure A.26 and Figure A.27, respectively)(a) and comparison with the value determined from chemical actinometry. The irradiance F_0 measured with the spectroradiometer is given in units of watts per square meter ($\mathrm{W\,m^{-2}}$) with a value of $F_0 = 3167\,\mathrm{W\,m^{-2}}$ (see Figure A.27). Therefore, the light intensity $I_0 = 5.14\,\mathrm{meinstein\,L^{-1}\,min^{-1}}$ determined *via* chemical actinometry is converted according to:[312]

$$\begin{aligned}
F_0 &= I_0 \cdot l \cdot N_\mathrm{A} \cdot \frac{hc}{\lambda} \\
&= 5.14\,\mathrm{meinstein\,L^{-1}\,min^{-1}} \cdot 0.84\,\mathrm{mm} \cdot 6.022{\times}10^{23}\,\mathrm{mol^{-1}\,dm^{-3}} \\
&\quad \cdot \frac{6.63{\times}10^{-34}\,\mathrm{J\,s} \cdot 2.998{\times}10^{8}\,\mathrm{m\,s^{-1}}}{365\,\mathrm{nm}} \\
&= 6.44\,\mathrm{W\,m^{-2}}
\end{aligned} \tag{4.3}$$

In Equation (4.3), l is the light path in the NMR tube, N_A the Avogadro constant, and λ the irradiation wavelength,(b) resulting in a coupling efficiency of ≈0.7 %. This low value is not surprising, because the coupling into the fiber is done without any focusing lenses.

(a) The measurement of the irradiance directly at the position of the fiber tip was not possible, as the power of the LED was too high, resulting in the saturation of the employed spectroradiometer.

(b) For simplicity, only the photon energy of the peak wavelength at 365 nm is used as an average in the calculation, see also [312].

LED-NMR spectroscopy with SP 10 With the calibrated LED-NMR setup, the SP-metal complexes are investigated in the NMR with simultaneous irradiation of the 365 nm LED. However, SP **10** was first investigated without any metal salt present to get a spectral reference system and work out the capabilities of the developed setup.

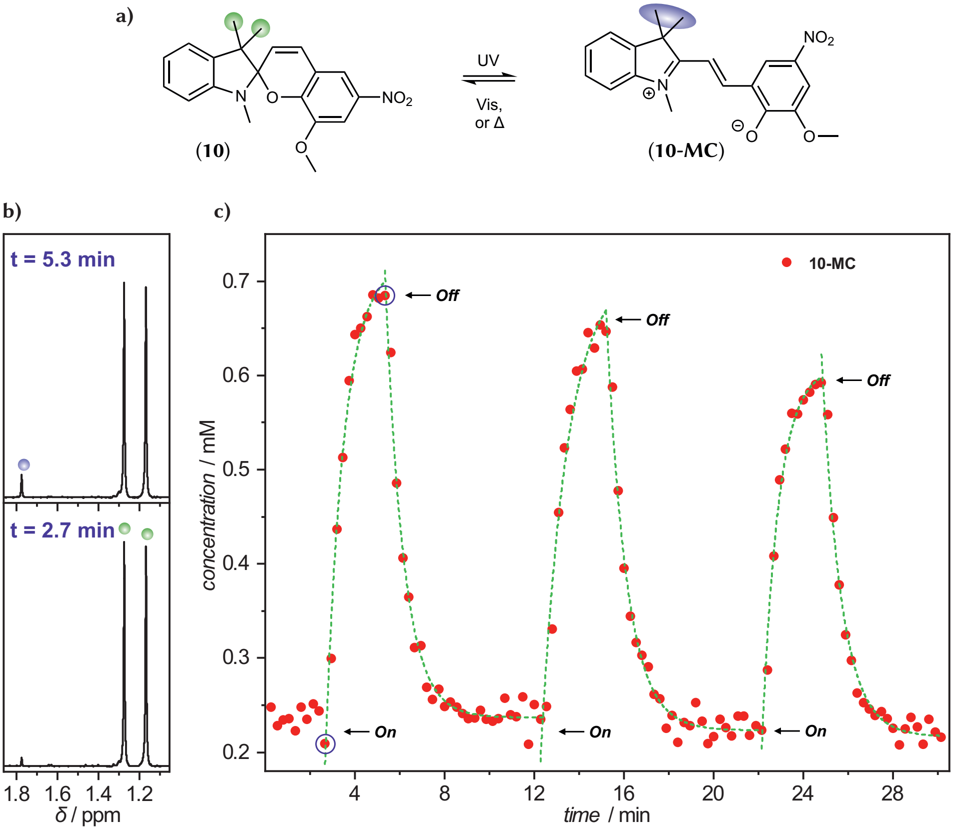

Figure 4.10. a) SP⇌MC equilibrium of **10** with highlighted proton resonances used for the integration of the LED-NMR kinetic experiment. b) Zoom into the ^{1}H NMR spectra before turning on the LED (bottom) and at the maximum **10-MC** concentration in the PSS under irradiation (top). c) Plot of the **10-MC** concentration vs. time with the on- and off-switching of the UV LED. The violet circles indicate the spectra, which are plotted in panel b).

In Figure 4.10a), the SP⇌MC equilibrium of **10** is shown with highlighted proton resonances used for the integration of the photo kinetic experiment, for which a zoom in is depicted in panel b). The spectrum at 2.7 min (bottom) is recorded in the dark, right before switching on the UV LED, while the spectrum after 5.3 min (top) is recorded in the PSS, i.e. at the maximum concentration of **10-MC** upon irradiation. Clearly, the resonance at 1.77 ppm stemming from the two CH_3-groups of **10-MC** is increasing after irradiation with UV light (violet, top), while the corresponding resonances of **10** decrease accordingly (green, bottom). In panel c), the integral of the labeled **10-MC** proton resonances is plotted against time and the on- and off-switching of the UV LED is indicated. Unfortunately, the determination of the quantum yield for the photo induced SP⟶MC transformation, as well as the rate coefficient for the thermal MC⟶SP reaction is not accessible with the available data, despite the known light intensity from the calibration *via* chemical actinometry. The reason is the presence of at least four coupled photo-, as well as thermal equilibria of the SP$\rightleftharpoons$MC system. Therefore, the dotted green mono exponential fits of the increase and decrease of the **10-MC** concentration vs. time are only included to guide the eye.

For the experiment shown in Figure 4.10, a 14.2 mM solution of **10** was prepared in CD_3CN and the equilibrium concentrations of **10** and **10-MC** were determined with quantitative NMR measurements prior to the start of the kinetic experiment (see the experimental section on Page 168 for a detailed description). The ratio between **10** and **10-MC** in the thermal equilibrium is 59/1. When switching on the LED, the concentration of **10-MC** increases rapidly from 0.23 mM to 0.69 mM, corresponding to a **10**/**10-MC** ratio of 20/1, i.e. an increase of the **10-MC** concentration of 300 %. After turning off the LED after 5.3 min, the thermal MC⟶SP reaction re-establishes the concentration value of **10-MC** found prior to irradiation. This sequence is repeated two more times, and a slight fatigue of **10** is visible, comparing the peak integral values of the three PSS spectra in Figure 4.10c). This first experiment with **10** serves as a valuable benchmark for the investigation of the **10**-derived metal complexes and demonstrates that the LED-NMR method can be used to monitor the SP$\rightleftharpoons$MC equilibrium of **10** *in situ* with the possibility to quantify the concentrations of **10**, as well as **10-MC**, which is not possible in the UV-Vis spectra in Figure 4.2, due to the unknown molar attenuation coefficient ϵ of **10-MC**.

LED-NMR spectroscopy with SP-metal complexes The results for the kinetic LED-NMR experiments with **10-Zn**, **10-Ca**, and **10-La** are shown in Figure 4.11, Figure 4.12, and Figure 4.13, respectively. The figures are structured in a similar manner than the results provided in Figure 4.10 for the investigation of pure **10**. For **10-Zn** and **10-Ca**, 0.62 and 0.61 mM solutions were prepared in CD_3CN by the dissolution of crystalline material. While the given concentrations refer to the theoretical values for 100 % SP-metal complex, the concentrations present at the start of the kinetic experiments correspond to the values of the thermal equilibrium, which were determined in quantitative NMR measurements before the kinetic run. Due to the insolubility of crystalline **10-La** (refer to the discussion of Figure 4.7), the solution for the experiment in Figure 4.13 was prepared by mixing of **10** and $[La(NO_3)_3(H_2O)_6]$ solutions in CD_3CN in a molar ratio of 2/1 with an effective concentration of 20.6 mM for **10-La**. The prepared **10-La** solution remained stable at room temperature for the time of the LED-NMR investigation, i.e. the formation of precipitate during the measurements was not observed.

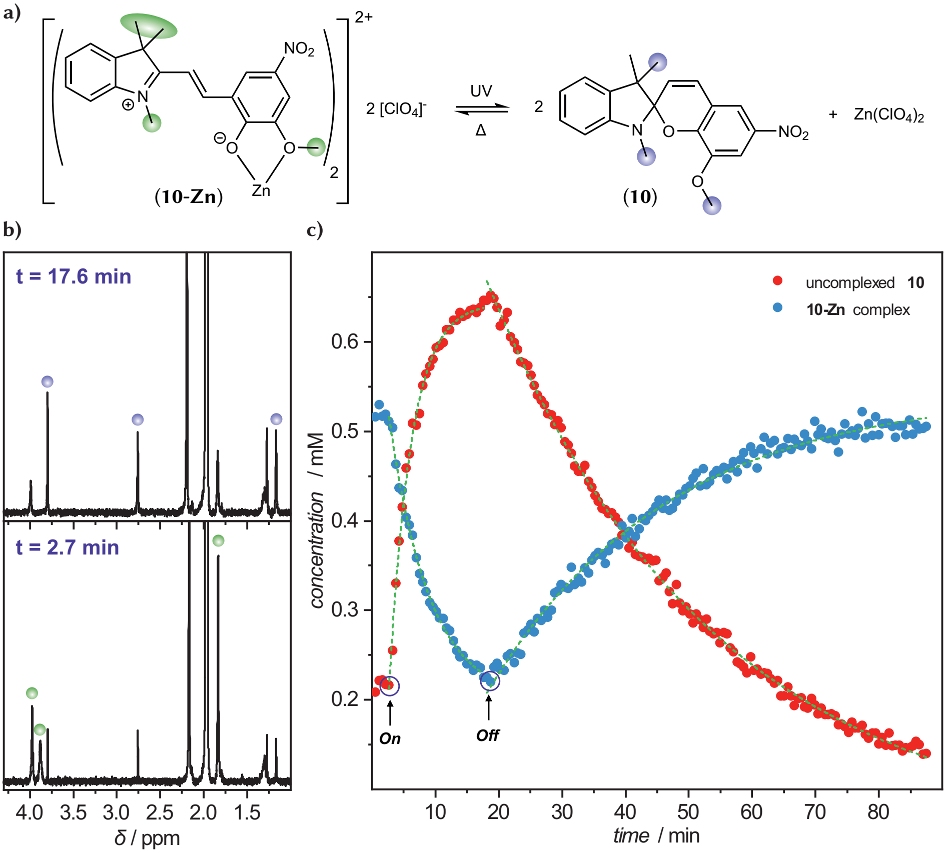

Figure 4.11. a) **10-Zn**$\rightleftharpoons$**10** equilibrium of **10-Zn** with highlighted proton resonances used for the integration of the LED-NMR kinetic experiment. b) Zoom into the ^{1}H NMR spectra before turning on the LED (bottom) and at the in the PSS under irradiation (top). c) Plot of the **10-Zn** and **10** concentration vs. time with the on- and off-switching of the UV LED. The experiment was performed with a 0.62 mM solution of **10-Zn** in CD_3CN. The violet circles indicate the spectra, which are plotted in panel b).

Attempts to investigate **10-Ni** were not successful, because the paramagnetic properties of the nickel center resulted in line broadening of the proton resonances, rendering the evaluation of the kinetic measurements impossible.

The concentrations for **10-Zn** and uncomplexed **10** in Figure 4.11 of 0.52 and 0.21 mM yield a **10-Zn** to **10** ratio of 2.4/1 for the thermal equilibrium. Upon irradiation with the 365 nm LED, the concentration of **10-Zn** decreases to 0.22 mM, while the concentration of uncomplexed **10** increases to 0.65 mM, until the PSS is reached after 17.6 min. This change corresponds to a **10-Zn** to **10** ratio of 1/3 in the PSS, i.e. the concentration of **10-Zn** is reduced by 58 % upon irradiation. It should be noted at this stage that the equilibrium shown in Figure 4.11a) does only include the bischelated **10-Zn** complex and the uncomplexed SP **10**. However, the presence of monochelated **10-Zn** species cannot be ruled out with the available data. The same statement does also hold true for the equilibria of **10-Ca** and **10-La** shown in Figure 4.12a) and Figure 4.13a), respectively. After turning off the UV LED, the system thermally relaxes back to a **10-Zn** to **10** ratio of 3.6/1, i.e. a concentration of 0.50 and 0.14 mM for **10-Zn** and **10**, respectively. The difference in the concentration of **10** compared to the start of the kinetic run is attributed to a superimposed photo degradation of **10** during the irradiation cycle. However, the ratio of **10-Zn** to **10** should not be influenced by a loss of **10** and might be due to an insufficient relaxation time of the system. Combining these results with the picture obtained from the LED-UV-Vis experiment in Figure 4.7a), are more detailed description of the photochemistry of **10-Zn** is possible. Upon dissolution of crystalline **10-Zn** in MeCN, the thermal equilibrium between **10-Zn** and uncomplexed **10** is established, which corresponds to the decrease in the UV-Vis absorption at 480 nm and the proton resonances for **10** in the ^{1}H NMR spectrum. During irradiation with UV light, the equilibrium concentration of **10-Zn** is reduced, which is related to the decrease in the 480 nm absorption band and the increase in the **10** integral in the ^{1}H NMR spectrum, a process that is reversible in the dark. Interestingly, the SP⟶MC transition of **10** is also triggered with the employed UV LED, although no MC-specific absorption band is visible in the absorption spectrum. Apparently, the PSS concentration of uncomplexed **10-MC** due to the rapid re-complexation with zinc is too low to be detected with UV-Vis spectroscopy.

A different picture is obtained for **10-Ca** in Figure 4.12 with a **10-Ca** to **10** ratio of 1/2.1 for the thermal equilibrium. Here, the irradiation with UV light leads to an increase in the concentration of the **10-Ca** complex from 0.40 to 0.48 mM of 20 % in the PSS. On the same time, the concentration of uncomplexed **10** is reduced from 0.84 to 0.58 mM, according to the stoichiometry in the equilibrium in Figure 4.12a). Similar to **10-Zn**, the photo induced shift of the equilibrium is reversible in the dark. Therefore, the increasing absorption band in the UV-Vis spectrum in Figure 4.7c) between 450–700 nm is not only caused by the SP→MC transition of uncomplexed **10**, but also a result of the higher **10-Ca** concentration in the PSS.

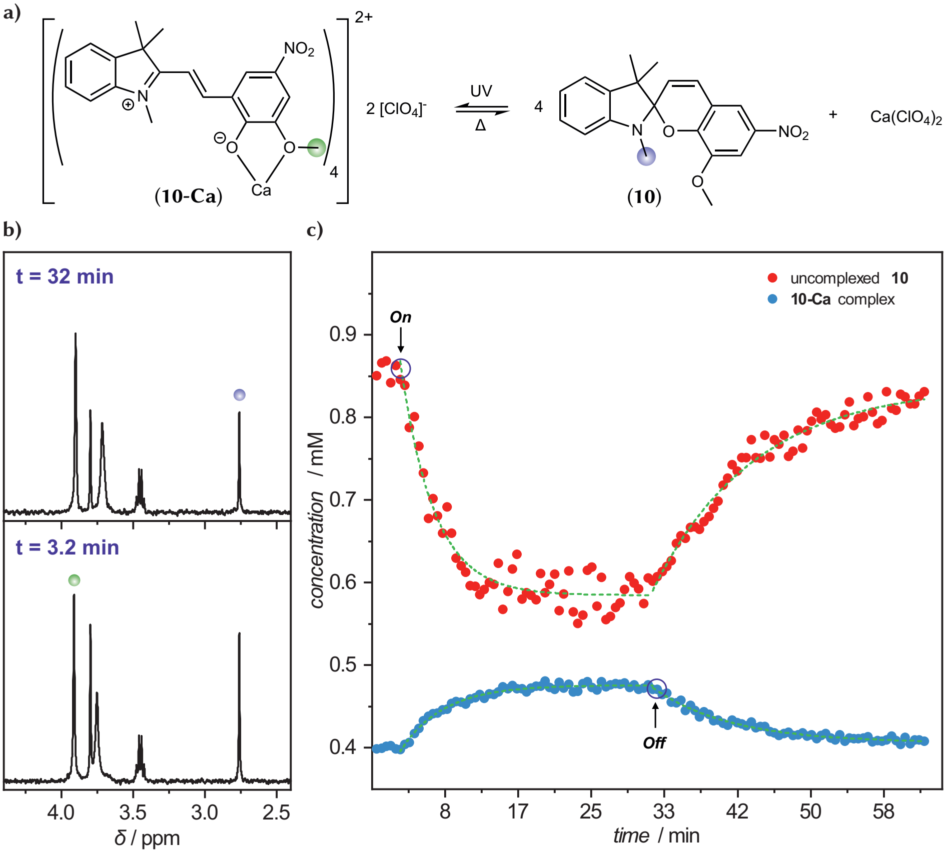

Figure 4.12. a) **10-Ca**$\rightleftharpoons$**10** equilibrium of **10-Ca** with highlighted proton resonances used for the integration of the LED-NMR kinetic experiment. b) Zoom into the ^{1}H NMR spectra before turning on the LED (bottom) and at the in the PSS under irradiation (top). c) Plot of the **10-Ca** and **10** concentration vs. time with the on- and off-switching of the UV LED. The experiment was performed with a 0.61 mM solution of **10-Ca** in CD_3CN. The violet circles indicate the spectra, which are plotted in panel b).

Finally, the photochemical properties of **10-La** are shown in Figure 4.13. The results are comparable to the observations made for **10-Zn**, that is, irradiation with the UV LED results in a shift of the **10-La**$\rightleftharpoons$**10** equilibrium towards the uncomplexed SP and the free metal salt, see panel a). Here, the **10-La** to **10** ratio is changed from 11.8/1 (thermal equilibrium) to 3/1 (PSS), i.e. the concentration of **10-La** is reduced by 10 % upon irradiation. Similar to the previous two SP-metal complexes, the photo induced changes of the **10-La**⇌**10** equilibrium are reversible in the dark.

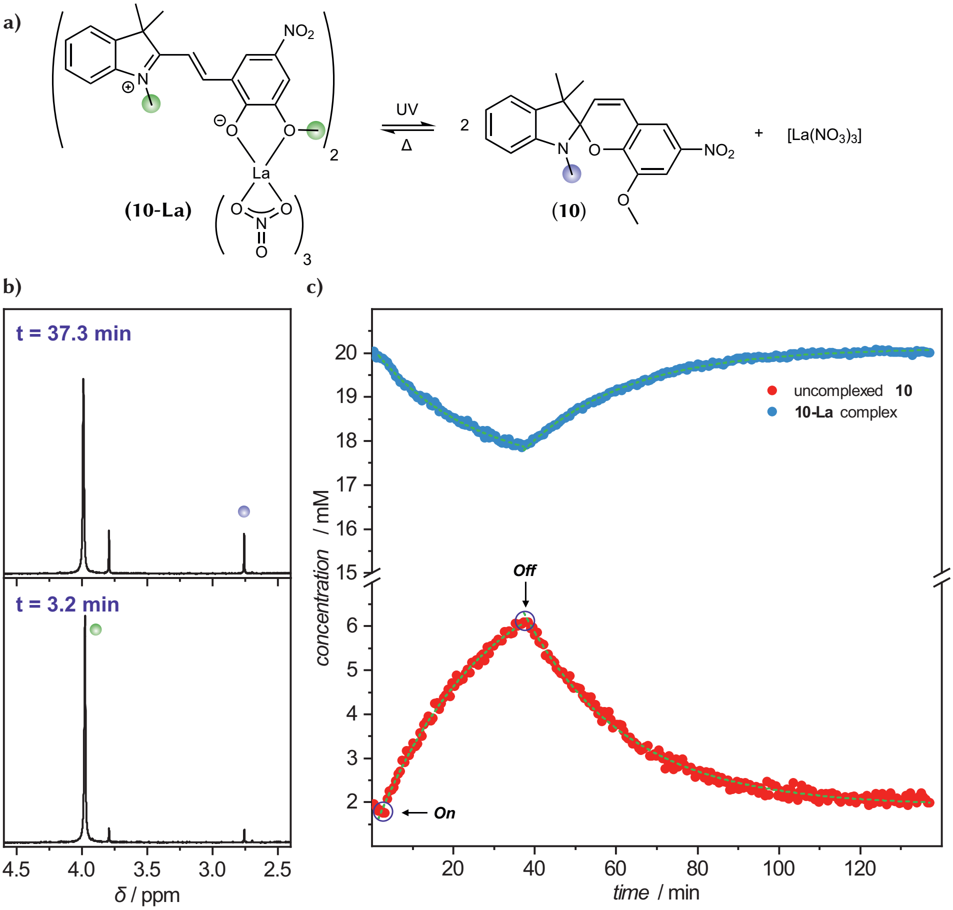

Figure 4.13. a) **10-La**⇌**10** equilibrium of **10-La** with highlighted proton resonances used for the integration of the LED-NMR kinetic experiment. b) Zoom into the ^{1}H NMR spectra before turning on the LED (bottom) and at the in the PSS under irradiation (top). c) Plot of the **10-La** and **10** concentration vs. time with the on- and off-switching of the UV LED. The experiment was performed with a 20.6 mM solution of **10-La** in CD$_3$CN. The violet circles indicate the spectra, which are plotted in panel b).

4.3 Conclusion

In this chapter, the synthesis of new SP-based metal complexes of zinc, nickel, calcium, as well as lanthanum was described. While complexation studies with the STP-based ligand **12** did not result in the formation of stable metal complexes, SP **10** served as a valuable ligand for all employed metal salts. The complex stoichiometries obtained *via* X-ray crystallography could be confirmed for the state in solution for all discussed complexes with the help of Job's method of continuous variations. It was found that values obtained from the Job plots differ for varying concentrations and approach the results from X-ray crystallography for concentrated solutions. Subsequently, the photochemistry of SP-metal complexes was investigated by means of LED-UV-Vis and LED-NMR spectroscopy. While only qualitative results can be obtained from the LED-UV-Vis measurements, the versatility of LED-NMR spectroscopy was exploited for the determination of the concentrations of the **12**-metal complexes, as well as uncomplexed **12** in the thermal equilibrium and the PSS. With this respect, the herein described LED-NMR setup was significantly improved compared to the setups described in literature regarding the light intensity reaching the analyte solution inside the NMR spectrometer. The gained understanding of the photochemistry of the described SP-metal complexes will pave the way for further experiments towards the application of such light-sensitive complexes in material science, as for example the formation of stimuli-responsive SCNPs shown in the motivation of this chapter (see Figure 4.1). With this application in mind, the controlled polymerization of **20** in analogy to copolymer **P15** developed in Chapter 5 of the current thesis can be a first starting point towards the realization of these materials.

CHAPTER 5

Photocaged ligation *via* spirothiopyrans

In the surface photoligation experiments in Chapter 3, challenges arise from the light absorption of the metallopolymer solution in the wavelength regime used to trigger the NITEC reaction on the surface. Such hurdles in tethering chromophores *via* light triggered ligation protocols are not limited to the photoligation of metallopolymers. It is therefore desirable to have the possibility to change the trigger wavelength of the photoligation chemistry into a wavelength regime were the substrates in solution are not absorbing the irradiation light to an extent, which compromises the successful photoligation on the surface.

This chapter will explore the chemistry of spirothiopyrans (STPs) for the photoligation on surfaces, including the possibility for STED-inspired lithography, as well as writing 3D structures *via* DLW. (a) While the photo triggered reaction between a ring-opened STP and a maleimide has first been described by Zhu and co-workers,[193] their report only exploits the photoligation chemistry in solution for the formation of comb copolymers (see Section 2.2.3.4 for the introduction of the reaction). Another report

---

(a) Parts of this chapter are reproduced or adapted from P. Müller, R. Müller, L. Hammer, C. Barner-Kowollik, M. Wegener, E. Blasco, STED-inspired Laser Lithography Based on Photoswitchable Spirothiopyran Moieties, *Chem. Mater.* **2019**, *31*, 1966–1972, with permission from [313] © 2019 American Chemical Society. P. Müller prepared the photoresist mixtures, conducted the lithography experiments, and the imaging of the surfaces. R. Müller synthesized all molecules and polymers and recorded the UV-Vis spectra unless stated otherwise. L. Hammer contributed to the synthesis and the solvent studies in the course of her master thesis under supervision of R. Müller, P. Müller, and E. Blasco.[314] C. Barner-Kowollik, M. Wegener, and E. Blasco participated in planning of experiments and discussion of experimental results.

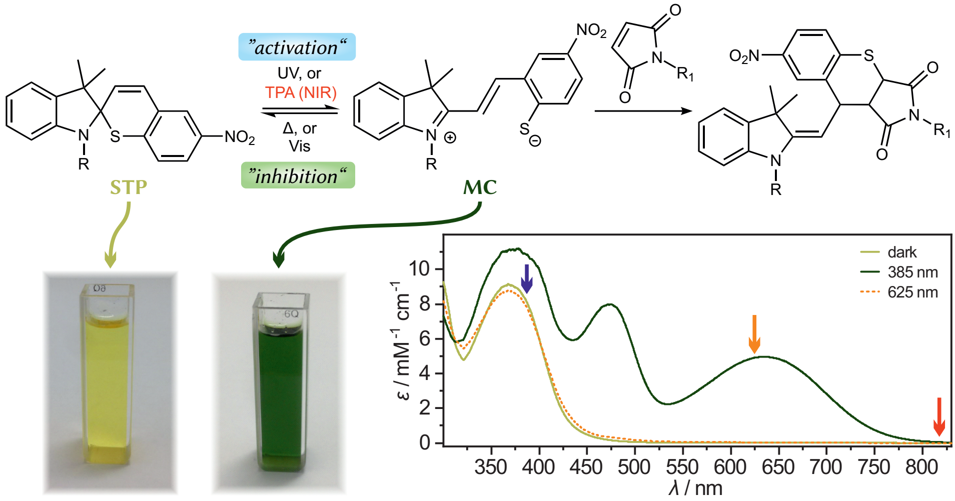

Figure 5.1. Top: photo triggered equilibrium between STP and MC. The MC form can react with a maleimide in a thiol-*Michael* reaction, resulting in an irreversible covalent connection. R = CH_2CH_2OH; R_1 = alkyl. DMSO solutions of STP and the PSS of MC are shown below the chemical structures. The UV-Vis spectrum shows a DMSO solution of STP in the dark (yellow), after irradiation with a 385 nm LED (green), and after subsequent irradiation with a 625 nm LED (dotted orange). The arrows indicate the wavelengths of the UV, as well as the visible light LED. The red arrow at 820 nm indicates the wavelength used to trigger the STP⟶MC transition *via* a TPA process.

by Zhang *et al.* demonstrated the possibility to trigger the thiol-*Michael* reaction *via* mechanochemistry.[195]

Another advantage of the STP molecules, so far unexplored, lies in the possibility to suppress the thiol-*Michael* reaction between the MC form and a maleimide through irradiation with visible light. As such, the photochemistry of STPs is well-suited for the STED-inspired lithography introduced in Section 2.3.2.2.

An adaption of the STED-inspired lithography concept to the photochemistry of STPs is depicted in Figure 5.1. DMSO solutions of the STP and the PST of the MC form are depicted below the chemical structures. The STP⟶MC transition can either be triggered by irradiation with UV light, or by a TPA process employing a strong NIR irradiation source. The possibility to trigger the isomerization through such a TPA process is one prerequisite for a successful application in STED-inspired lithography (refer to the discussion in Section 2.3.2.1). The wavelength of the NIR laser employed in this work is indicated with the red arrow at 820 nm in the UV-Vis spectrum in Figure 5.1. Another important feature of the system is the possibility to trigger the MC⟶STP ring-closure

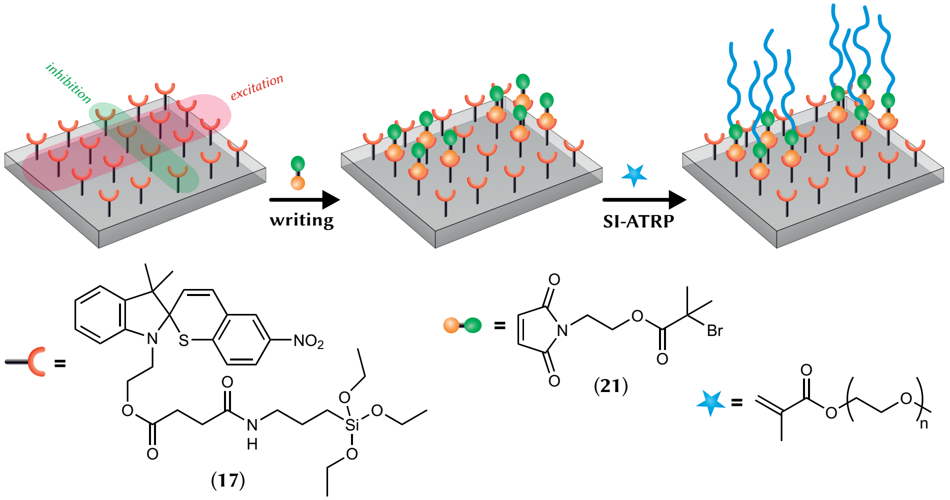

Figure 5.2. Surface functionalization approach utilizing the STP-maleimide reaction. A glass surface is covered with STP-functionalized silane **17**. The areas irradiated with the excitation, as well as the inhibition laser are highlighted in red and green, respectively. In the area where only the excitation laser is applied, the generated MC form reacts with the maleimide ATRP-initiator **21**. The reaction is suppressed in areas also irradiated with the inhibition laser. Subsequent SI-ATRP results in the formation of poly(ethylene glycol) methyl ether methacrylate brushes (blue lines), which are characterized *via* light microscopy or AFM.

with visible light. This opens up the possibility to photochemically prepare the system in analogy to the photoenol system described in Scheme 2.13 in Section 2.3.2.2.

During the work on this thesis, Vijayamohanan and co-workers proposed the idea to employ the STP system for super-resolution lithography.[315] They demonstrated the inhibition of the thiol-*Michael* reaction with green light in a macroscopic STP-functionalized PEG copolymer and a 4-arm PEG maleimide polymer and supported the proposed application in super-resolution lithography through photo kinetic modeling. However, they were not able to show an experimental microscopic proof of the proposed resolution increase.

5.1 Surface photoligation

The first approach employing the STP-maleimide reaction in surface photoligation experiments is outlined in Figure 5.2. Glass substrates are homogeneously covered with the STP-functionalized silane **17** in the first reaction step (not shown). Subsequently, the STP-covered glass surface is immersed in a solution containing the maleimide functionalized ATRP-initiator **21**. In the writing process, a pulsed femtosecond laser with a center wavelength of 750 nm[(a)] is used to trigger the STP→MC transition *via* a TPA only in the irradiated areas. A second CW laser diode at 640 nm is employed to trigger the MC→STP transition and therefore inhibit the thiol-*Michael* reaction. The inhibition laser is overlaid with the excitation laser, but only switched on in defined regions in order to suppress the covalent bond formation between the maleimide and the surface immobilized STP molecules. The established MC form on the surface reacts with the maleimide molecules present in the solution, resulting in the covalent linkage of the maleimide molecules onto the surface. In order to gain a visual feedback of the successful writing process, poly(ethylene glycol) methyl ether methacrylate brushes are grown from the surface through a SI-ATRP process and analyzed by AFM measurements. Such a protocol was also successfully applied for the writing on surfaces *via* the photoenol chemistry,[183] as depicted in Figure 2.26.

Synthesis While the synthesis of the maleimide-functionalized ATRP initiator **21** was performed following a literature procedure,[160] the synthetic strategy towards STP-functionalized silane **17** is outlined in Scheme 5.23.

The indol derivative **13** is readily obtained through an S_N2 reaction of 2,3,3-trimethylindoleine with 2-iodoethanole and subsequent grinding of the iodine salt with potassium hydroxide in 92 % overall yield (see panel a). For the chromene part of the STP molecule, a salicylaldehyde is transformed into the corresponding *O*-aryl thiocarbamate **14a** under basic conditions with *N*,*N*-dimethylthiocarbamoyl chloride. Upon refluxing of **14a** in toluene, the *Newman–Kwart* rearrangement results in the formation of the *S*-aryl thiocarbamate **14b** in 87 % overall yield. **14b** represents a bench stable protected thiophenol and the reaction can be easily scaled up for multigram synthesis. [(b)] For the synthesis of the hydroxy-functionalized STP **15**, **14b** is deprotected under basic conditions, acidified to obtain the free thiophenol, and reacted *in situ* with **13** in a condensation reaction, obtaining **15** in 76 % yield. Attempts to isolate and characterize the intermediate thiophenol were not successful. The transformation of **15** into the acid-functionalized STP **16** is accomplished *via* nucleophilic ring-opening of succinic anhydride under basic conditions in 60 % yield.

[(a)] A 750 nm pulsed femtosecond laser was used in the first experiments of the surface functionalization. Later, it was found that shifting the excitation laser to the 820 nm also indicated in Figure 5.1 results in a better spectral separation of the MC absorption band and the excitation laser.

[(b)] This reaction sequence is often employed to transform commercially available phenol derivatives into their corresponding thiophenol analogues, see [186c].

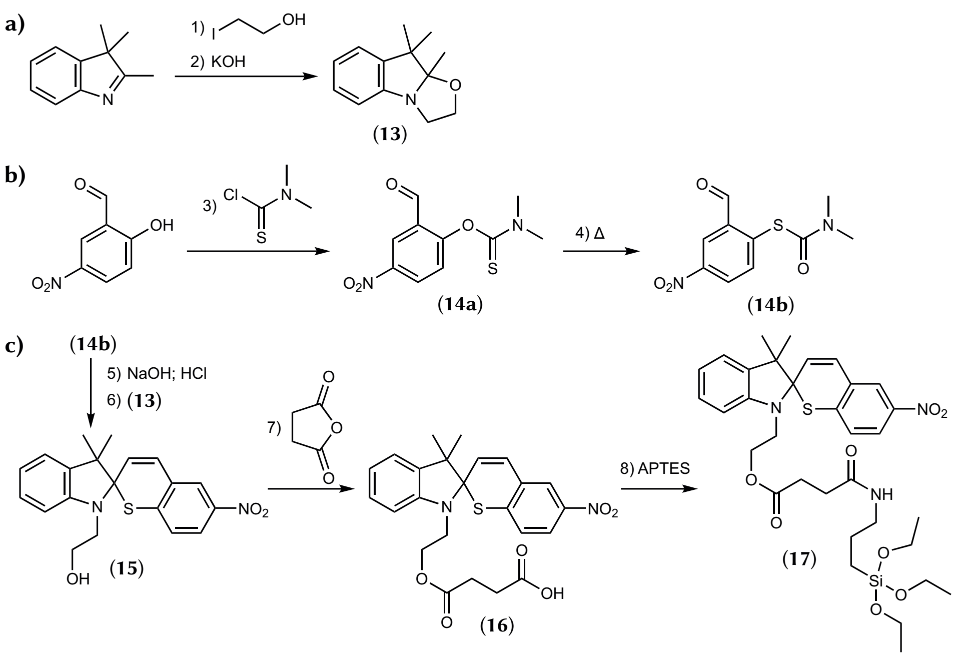

Scheme 5.23. Synthesis strategy towards STP-functionalized silane **17**. a) Synthesis of indol derivative **13**. b) Transformation of 5-nitrosalicylaldehyde into the masked salicylthioaldehyde **14b**. c) *In situ* deprotection of **14b** and condensation with **13** yields STP **15**, which is transformed into the free STP acid **16** *via* nucleophilic ring-opening of succinic anhydride, followed by amidation with APTES, yielding STP-silane **17**. 1) 2-Iodoethanole, MeCN, reflux; 2) KOH, grinding; 3) *N*,*N*-dimethylthiocarbamoyl chloride, DABCO, DMF; 4) toluene, reflux; 5) NaOH in MeOH, then HCl; 6) **13**, EtOH, reflux; 7) succinic anhydride, TEA, DMAP, 1,4-dioxane; 8) CDI, APTES, THF.

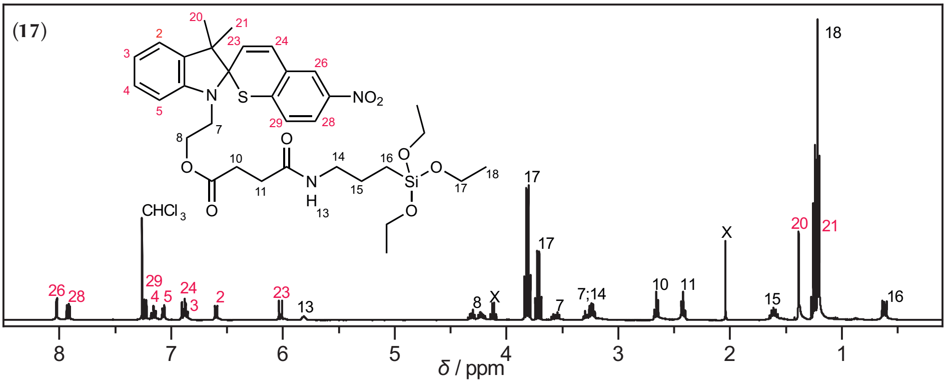

Figure 5.3. ^{1}H NMR spectrum of **17** recorded in $CDCl_3$. Proton resonances associated with the STP part of the molecule are highlighted in red. X = EtOAc.

The direct synthesis of the acid analogue of **15** has been described in literature,[193] but several attempts to reproduce the synthesis route resulted either in low yields or degradation of the starting materials (not shown). Therefore, the synthesis of **15** as an intermediate towards the free acid **16** was chosen, as both reactions can be easily scaled up and proceed in high yields. In the final step, the target silane functionalized STP **17** is obtained through activation of **16** with CDI and esterification with APTES in 64 % yield. This esterification protocol was already successfully employed for the synthesis of tetrazole-functionalized silane **5** in Section 3.1.2. Attempts to react **16** with APTES in standard Steglich esterification protocols employing DCC or EDC·HCl as activating agents were not successful and resulted in degradation of the STP moiety (not shown).

The ^{1}H NMR spectrum of **17** is depicted in Figure 5.3. The resonances of the STP part of the molecule are highlighted in red. The triethoxy silane moiety is represented through proton resonances 17 and 18, where the splitting of 17 into two parts is most probably caused by a partially hindered rotation of one of the ethoxy groups, which results in a slightly altered chemical shift. All other resonances are associated with the linker part between the STP and the silane group. The identity of **17** was additionally confirmed *via* ^{13}C NMR spectroscopy and HR-ESI-MS.

Photolithographic experiments on surface Initial studies of the photoswitching behavior of the STP chromophore, as well as the reaction of the MC form with a maleimide species were performed by L. Hammer in the course of her master thesis.[314] Employing STP derivative **15**, Hammer conducted UV-Vis studies under simultaneous irradiation with 385 nm and 590 nm LEDs for photochemical trigger of the STP$\rightleftharpoons$MC equilibrium. As the DLW process requires high boiling solvents to account for the thermal heating during the writing process, MeCN, DMSO, DMF, DMF/water, and anisole were chosen for the screening experiments with a concentration of 0.2 mM. While STP **15** was not stable under irradiation in anisole, MeCN, or DMF solutions, DMSO showed superior performance compared to the DMF/water mixture in the writing and development steps and was therefore chosen as the solvent of choice for the DLW experiments. (a)

With the STP-silane **17** and the maleimide-functionalized ATRP initiator **21** at hand, writing experiments as described in Figure 5.2 were conducted. Figure 5.4a) shows a light microscope image of a series of lines written with increasing excitation powers. In addition, the vertical position of the voxel is varied with respect to the surface interface.

(a) For detailed information about the photochemical switching behavior in various solvents, including the comparison between photo induced and thermal fading of the MC species, together with solution experiments demonstrating the ability to retard the reaction between the MC species of **15** and maleimide **21**, the reader is referred to [314].

The polymer brushes prepared through SI-ATRP after the DLW process are also analyzed *via* AFM, which is depicted in Figure 5.4b). The linewidth, as well as the height of the polymer brushes are increasing with the excitation power and show a saturation effect from ≈1 mW onwards (for an in-depth discussion of the saturation behavior, see [316]). While the depletion laser was not employed in this first writing experiment, the results confirm the applicability of the STP-maleimide chemistry for spatially resolved surface functionalization. Importantly, the employed DLW setup allows the fabrication of small feature sizes below 1 µm, even without the enhancements of STED-inspired DLW (see the line written with 0.26 mW in Figure 5.4b).

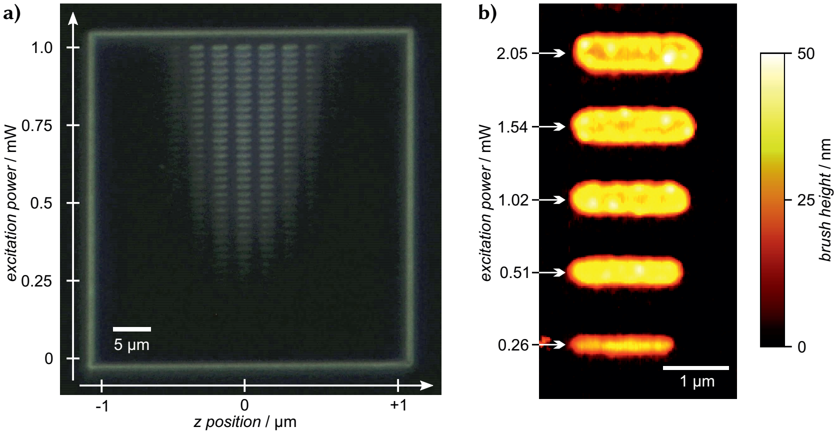

Figure 5.4. Lines of polymer brushes grown from the surface functionalized with silane **17** after photolithographic patterning of ATRP initiator **21** using only the excitation laser. a) Dark field light microscope image of the polymer brushes. The excitation energy is increased from bottom to top. b) False color AFM image of several lines written with varying excitation powers. The linewidth, as well as the height of the polymer brushes increases with the excitation energy. Adapted with permission from [316].

Having established the DLW process for the STP-maleimide system on the surface interface, an experiment shown in Figure 5.5 was conducted to investigate the expected depletion effect when employing a second laser beam at 640 nm. Panel a) shows the expected writing behavior for a STED-inspired lithographic experiment with the excitation and depletion powers increasing in the directions according to the inset. Starting with zero depletion laser power, the writing process begins at a certain threshold value of the excitation laser (point A). When increasing the depletion power, higher excitation powers to compensate the depletion effect are necessary to overcome the writing threshold (point B). The resulting envelope of such a writing experiment for a successful STED-inspired

DLW process is indicated with the black dotted line. The experimentally observed line pattern is depicted in the dark field light microscope image in Figure 5.5b). Clearly, the experiment does not follow the expected trend. Instead, the writing threshold decreases with increasing depletion powers for a fixed excitation power (dashed area C). This observation indicates an insufficient MC⟶STP conversion through the depletion laser. In addition, further increase of the depletion power results in the formation of structures even with no excitation laser switched on (dashed area D). This behavior is attributed to residual absorption of the STP molecule at the depletion laser wavelength, a phenomenon called *parasitic writing* in literature.[217] Different approaches were followed to reproduce the depletion effect present in solution[314] in surface writing experiments. However, none of the parameter changes, such as change of solvent, decreasing the depletion laser wavelength down to 532 nm, variation of the maleimide concentration, or lowering the grafting density of STP silane **17** through a co-grafting(a) with triethoxy(octyl)silane resulted in a successful depletion mechanism.

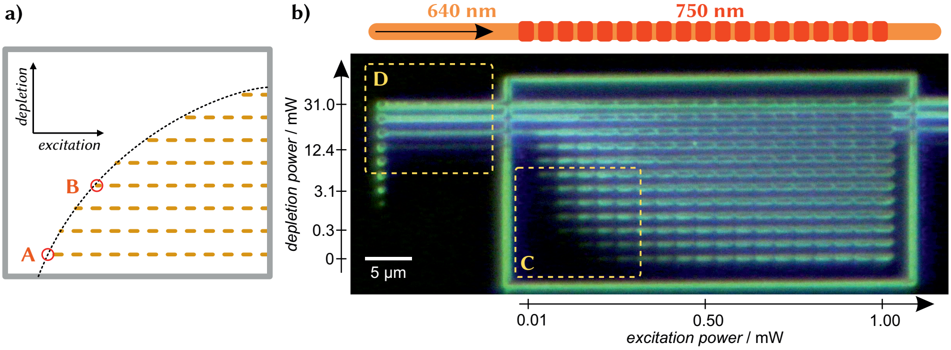

Figure 5.5. a) Expected depletion pattern when increasing the excitation and depletion laser powers according to the inset. b) Dark field light microscope image of a depletion test pattern. The depletion laser is fixed at a constant power in each line, while the excitation laser is switched on at the positions indicated on top and is varied in strength from left to right. Increasing the depletion power leads to a reduced excitation power needed to start the writing process (area C). If the depletion energy is too high, parasitic writing occurs even without switching on the excitation laser (area D). Adapted with permission from [316].

In conclusion, the surface photoligation approach was successfully applied for the immobilization of maleimide **21**. As such, these experiments are the first time the STP-maleimide reaction was employed for surface patterning and subsequent formation of polymer brushes *via* a SI-ATRP protocol. However, the expected reduction/inhibition of the reaction, when employing an additional depletion laser, could not be verified in this surface photoligation approach. Therefore, another strategy using STP-based negative-tone photoresists was followed.

(a) An effect on the switching behavior of sterically hindered SP molecules on surfaces compared to the properties in solution has been reported by Rosario *et al.* in [69].

5.2 Fabrication of 3D microstructures

Photoresist synthesis For the application of the STP-maleimide reaction in a photoresist, copolymers equipped with STP units, as well as maleimide functionalities were synthesized. The synthesis of a suitable STP monomer **18** is outlined in Scheme 5.24.

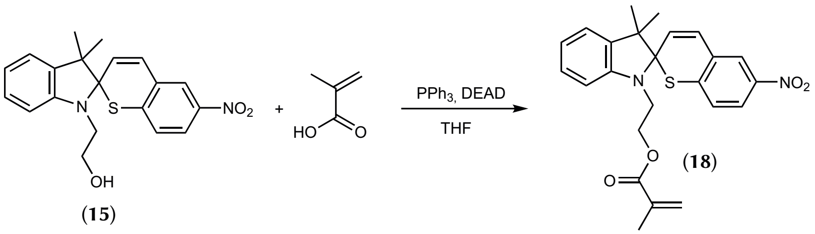

Scheme 5.24. *Mitsunobu* reaction between hydroxy-functionalized STP **15** and MAA, yielding STP monomer **18**.

For the synthesis of **18**, hydroxy-functionalized STP **15** was reacted with methacrylic acid (MAA) in a *Mitsunobu* reaction employing triphenylphosphine and diethyl azodicarboxylate (DEAD) in 50 % yield. Initial attempts to acetylate **15** with methacryloyl chloride were not successful and resulted in a complex product mixture. The diacetylated MC form **18a** of **15** was identified as the major side-product, which could not be separated from **18** *via* column chromatography (refer to Figure 5.6b). This observation is attributed to the thermal equilibrium concentration of the MC-form of **15** in solution and is in accordance to literature reports by Beshenko *et al.*,[317] who observed a similar behavior for the corresponding oxygen analogue of **15** (see structure **A-SP** in Figure 5.6a). Here, the desired acetylation product **A-SP1** is formed in addition to the side-product **A-MC2**, which is the acetylation product of the phenolate oxygen of the MC form of **A-SP**. Once the thermal equilibrium between **A-SP** and **A-MC** is established, further stabilization through back-biting of the hydroxyethyl moiety leads to the structure **A-MC1**, which is transformed into **A-MC2** upon acetylation (see Figure 5.6a).

For the reaction of **15** with methacryloyl chloride, the desired reaction product **18** is detected in the crude reaction mixture, but the diacetylated derivative **18a** is also present in the HR-ESI-MS spectrum with a significant amount (see Figure 5.6b).

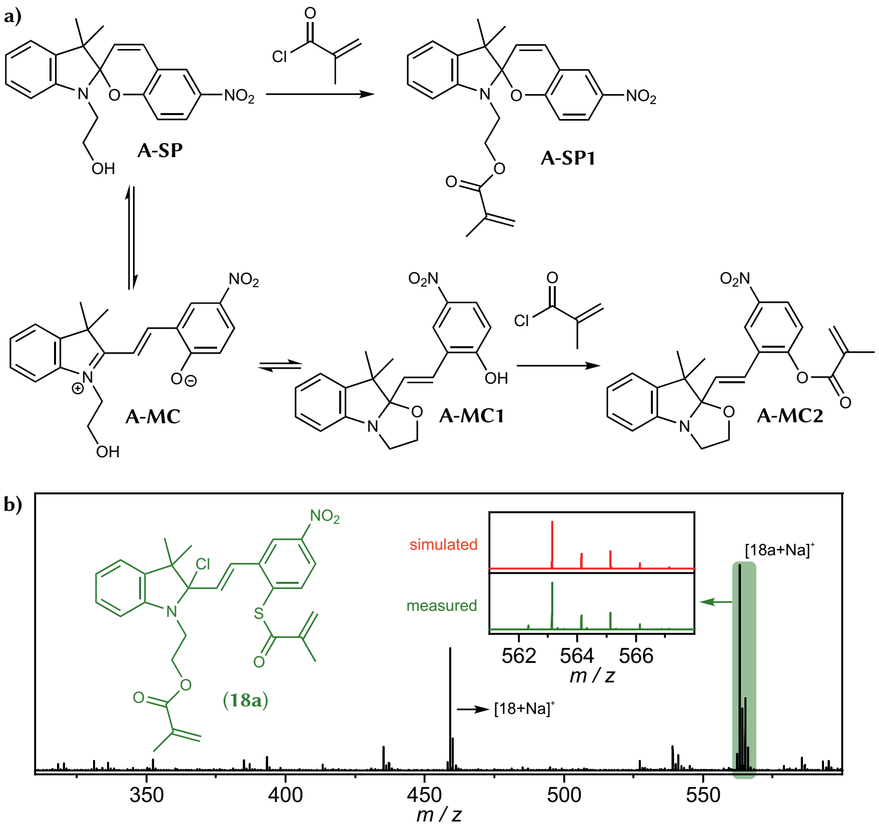

Figure 5.6. a) Formation of side-product **A-MC2** in the acetylation of **19** with methacryloyl chloride towards **A-SP1** *via* the **A-MC** and **A-MC1** merocyanine forms of **A-SP**, as described by Cherkashin and co-workers.[317] b) HR-ESI-MS spectrum of the crude reaction mixture of the reaction between **15** and methacryloyl chloride. Beside the desired STP monomer **18**, the main product of the reaction is the diacetylated derivative **18a**. The inset shows the experimental, as well as the simulated isotopic pattern of the $[\mathbf{18a}+\mathrm{Na}]^+$ ion.

Derivative **18a** is the product of the desired acetylation at the hydroxyethyl terminus of the indol fragment and an additional acetylation of the thiophenolate anion after SP→MC transformation of **15**. The charge compensation in the merocyanine structure is achieved through the addition of Cl^- at the former spiro-C atom, a reaction reported for halogen anions, as well as pseudohalogens.[318] Despite the small equilibrium concentration of the MC form of **15** in solution, which cannot be detected in UV-Vis or NMR spectroscopy, the fade of the MC form due to the acetylation reaction at the sulfur of the thiophenolate shifts the dynamic SP$\rightleftharpoons$MC equilibrium towards the product side, resulting in an non-selective reaction. In addition, the acidic environment in the reaction with methacryloyl chloride further contributes to the shift towards the protonated MC form of **15** in solution (refer to the *acidochromism* described in Scheme 2.5a). As such, the undesired outcome of this reaction procedure points out an important characteristic of spiro(thio)pyran functionalization chemistry. Although the concentration of the MC form is fairly small for many SP and STP molecules in solution, derivatization strategies always need to consider the chemical reactivity of the MC form as well, as the SP$\rightleftharpoons$MC equilibrium will re-establish the MC concentration during the reaction (*Le Châtelier's* principle).

With the STP monomer **18** at hand, a free radical copolymerization with MMA was conducted, yielding copolymers **P13a–d** (see Scheme 5.25a) and Figure A.38). For **P13a–c**, 1-dodecanethiol was used as a CT agent to adjust the MW of the final copolymer and the feed ratio of **18** was increased from **P13a** to **P13c** (see Table 5.1). **P13d** was synthesized without the CT agent, resulting in a higher MW of $\overline{M}_{\mathrm{n,SEC}} = 44\,000\ \mathrm{g\,mol^{-1}}$.

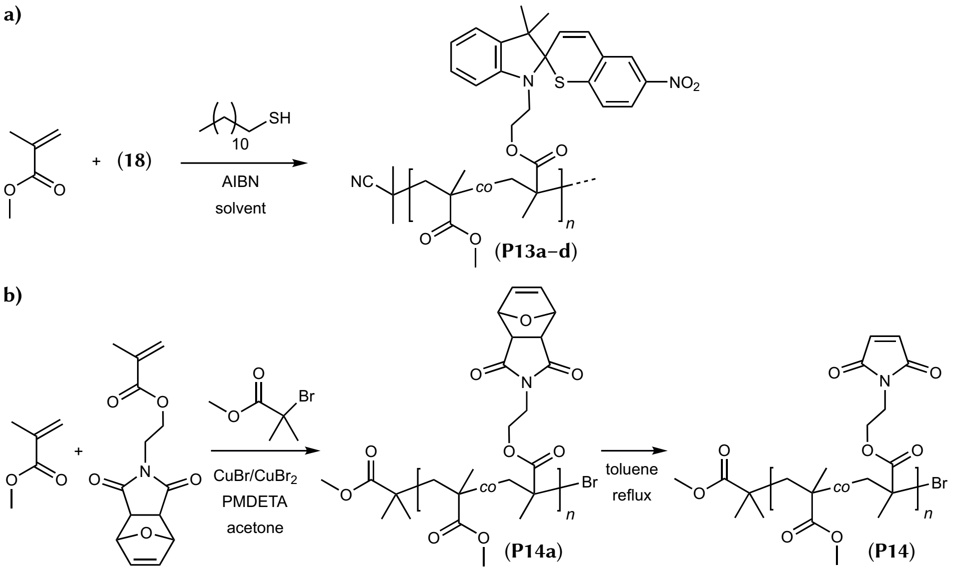

Scheme 5.25. a) FRP of MMA and **18** towards copolymers **P13a–d** with 1-dodecanethiol as CT agent. For **P13d**, no CT was added. b) ATRP of MMA and a furan-protected MMA monomer towards polymer **P14a**, which is deprotected towards maleimide-functionalized copolymer **P14**.

The synthesis of furan-protected methacrylate-based copolymer **P14a** ($\overline{M}_{\mathrm{n,SEC}} = 6400\ \mathrm{g\,mol^{-1}}$, Đ = 1.34, 17 mol% maleimide content) *via* ATRP using $\mathrm{CuBr/CuBr_2}$ with *N,N,N′,N″,N″*-pentamethyldiethylenetriamine (PMDETA) as the ligand and subsequent deprotection towards maleimide-functionalized copolymer **P14** were conducted by L.

Hammer in the course of her master thesis (see Scheme 5.25b) and Figure A.39).[314] A summary of the synthesized STP copolymers **P13a–d** and the maleimide-functionalized copolymer **P14** is given in Table 5.1.

Table 5.1. Summary of the STP- and maleimide-functionalized PMMA copolymers.

polymer	$\bar{M}_n$(a) / g mol^{-1}	$Đ$ (a)	ratio of incorporated comonomer(b) / mol%
P13a	6100	1.97	14
P13b	7600	1.55	27
P13c	8600	1.78	56
P13d	44 000	2.10	7
P14	6700	1.31	16

(a) Estimated by SEC using THF as eluent and PMMA standards.
(b) Determined *via* ^{1}H NMR using characteristic resonances for MMA (δ = 3.59 ppm, 3H), **18** (δ = 6.10–5.90 ppm, 1H), and the maleimide-MMA monomer (δ = 6.90–6.73 ppm, 2H), respectively.

Photoresist based on the STP-maleimide reaction With the STP- and maleimide-functionalized copolymers, photoresists for 3D writing experiments according to the procedure depicted in Figure 5.7a) were prepared.(a) For this particular DLW experiment, the photoresist consists of a mixture of **P13d** and **P14** (maleimide/STP units, 3/2) in an acetophenone-DMSO mixture with a total concentration of 25 wt%. The ability of the STP-functionalized polymers to transform into their corresponding MC structures was tested in acetophenone solution.

As an example, the UV-Vis spectrum of **P13a** (1 mg mL^{-1} in acetophenone) is shown in Figure 5.7b). No absorption in the wavelength region around 650 nm is detected (refer to the spectrum of the MC form of **15** in Figure 5.1). Upon continuous irradiation with a 365 nm LED, the PSS is established, and a broad absorption band centered at 700 nm is visible, which confirms the photoreactivity of the STP copolymer, here **P13a**.

The results of the 3D writing experiments are shown in the scanning electron microscopy (SEM) image in Figure 5.7c). The bridge structures feature free-standing elements, but show a pronounced shrinkage effect, when comparing the exposed volume element with the obtained 3D structure. The low structural quality of the STP-maleimide photoresist mixture is attributed to insufficient cross-linking. However, an increase in the concentration of STP, as well as maleimide functionalities per volume element was not possible, as the above described photoresist mixture was already at the upper solubility limit.

(a) For a detailed description of the writing procedure, as well as the experimental setup, including the preparation of the samples for AFM, SEM, and light microscopy, see [316].

In order assess the suppression of the cross-linking reaction *via* STED-inspired lithography, the excitation and depletion laser were overlaid according to the scheme in Figure 5.7d). While the 820 nm excitation laser was turned on the whole time, the depletion laser at 640 nm was only switched on in the right part of the line structure, which should result in a linewidth reduction. In the SEM image, a clear indication of an operating depletion mechanism is visible. However, the reduced linewidth in the right half of the written structure is accompanied with discontinuities and deteriorations, which renders the determination of the linewidth reduction impossible.

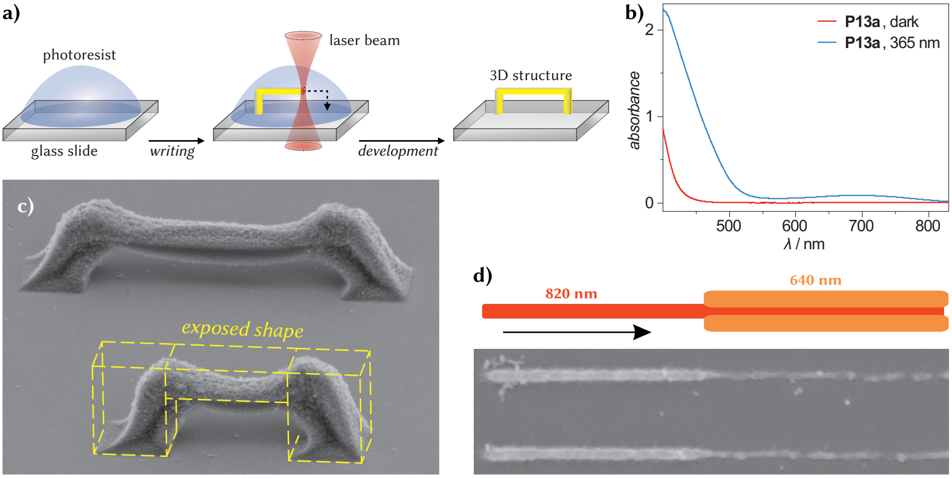

Figure 5.7. a) Schematic description of the processing steps towards 3D structures. A glass slide is covered with the photoresist mixture and the voxel of the DLW laser is scanned through the photoresist during the writing step. Free standing 3D structures are obtained after the removal of residual photoresist in the development step. b) Absorption spectra of **P13a** in the dark and under continuous irradiation with a 365 nm LED in the PSS. Spectra are recorded in 1 mg mL^{-1} acetophenone solution in a 1 mm cuvette. c) SEM image of two free-standing bridges suffering from pronounced shrinkage. d) SEM image of a depletion test experiment with the excitation and depletion laser foci according to the scheme above the image. c) and d) are adapted with permission from [316].

In summary, the photoresist mixture between STP and maleimide functional copolymers enabled the writing of free-standing 3D structures but suffered in terms of structure quality. In addition, a clear linewidth reduction through depletion of the MC form in defined areas is evidenced, but it was not possible to quantify the resolution enhancement due to the discontinuities in the written line structures.

Photoresist based on supramolecular aggregation Interestingly, an unexpected observation during the preparation of the above described experiments led to the development of a new photoresist, featuring a non-covalent interaction between STP-functionalized polymer chains. In Figure 5.8, a free-standing bridge (a) and pyramid structures (b) are fabricated with **P13a** in a 40 wt% acetophenone solution without any maleimide functionality being present in the photoresist mixture. Obviously, the formation of stable 3D structures cannot be explained by the above described photo triggered thiol-*Michael* reaction between a MC form and a maleimide species.

Instead, the formation of stable 3D structures is most likely the result of intra- and intramolecular aggregation of the formed MC species with other STPs, as well as MC moieties. Such a physical cross-linking has been extensively described for the oxygen SP analogue of the STP-MMA copolymers **P13a–d**. While Krongauz *et al.* were the first who reported such supramolecular aggregation for small SP molecules,[76a] different groups reported the aggregation of methacrylate-based polymers,[77a,c,82a,b] for which a mechanism called “zipper crystallization” describes the formation of aggregates between different polymer chains (see also discussion on Page 34 and references therein).

To further validate this interpretation of the structure-building mechanism in the STP-polymer structures in Figure 5.8, an analogous SP-functionalized copolymer was synthesized. Therefore, **13** was first reacted with 3-methoxy-5-nitrosalicylaldehyde in a condensation reaction towards the hydroxy-functionalized SP molecule **19** in 79 % yield. The *Mitsunobu* esterification of **19** with MAA yields the SP-monomer **20** in the second reaction step with a yield of 61 % (see Figure 5.9a). Subsequently, SP-containing

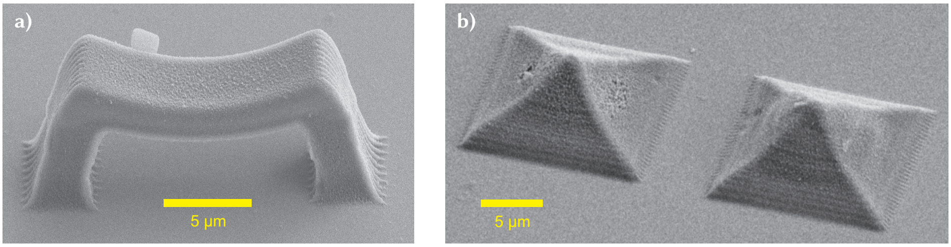

Figure 5.8. SEM images of a free-standing bridge structure (a) and two pyramidal structures (b), written with copolymer **P13a** in acetophenone (40 wt%). Adapted with permission from [313]. © 2019 American Chemical Society.

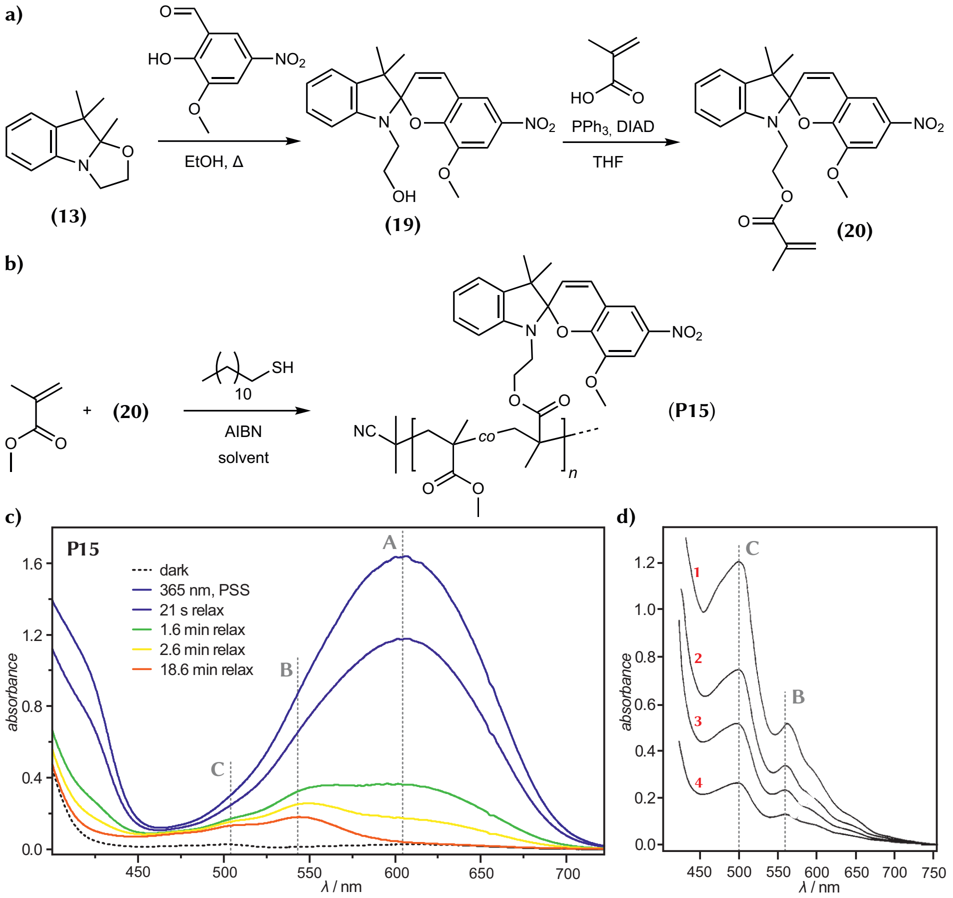

Figure 5.9. a) Synthesis of hydroxy-functionalized SP **19** through condensation of **13** with 3-methoxy-5-nitrosalicylaldehyde. Subsequent *Mitsunobu* reaction between **19** and MAA yields SP-monomer **20**. b) Synthesis of an SP-MMA copolymer **P15** in analogy to the STP-copolymers **P13a–c** with SP-monomer **20**. c) Absorption spectrum of **P15** in the dark and after irradiation with a 365 nm LED in the PSS. The MC form is detected through the absorption band centered at 605 nm (A). During thermal relaxation in the dark, two absorption bands with a hypsochromic shift build up at 544 nm (B) and 502 nm (C), which remain stable in solution. Spectra are recorded in 1 mg mL^{-1} acetophenone solution in a 1 mm cuvette. d) Absorption spectrum of thermally equilibrated solutions of a comparable SP-MMA copolymer in 2-methyltetrahydrofuran at different concentrations per monomer unit in a 2 mm cuvette: 0.2 M (1); 0.135 M (2); 0.1 M (3); 0.05 M (4). Adapted with permission from [319]. © 1981 American Chemical Society.

copolymer **P15** was synthesized in analogy to the STP-copolymers **P13a–c** *via* free radical copolymerization of **20** with MMA (see Figure 5.9b). Again, 1-dodecanethiol was employed as a CT agent, yielding copolymer **P15** ($\bar{M}_{\mathrm{n,SEC}} = 7300\,\mathrm{g\,mol^{-1}}$, $Đ = 1.58$, 16 mol% SP content). If the formation of stable structures upon DLW with **P13a** is due to supramolecular aggregation, a similar behavior is excepted, when employing SP-copolymer **P15**.

In Figure 5.9c), the absorption spectra of polymer **P15** in the dark does not show the absorption band associated with the MC form at around 600 nm. Upon irradiation with a 365 nm LED for 9 min, the PSS is reached, and a strong MC-absorption band centered at 605 nm (A) is visible. Upon thermal relaxation in the dark, the absorption band (A) associated with free MC-forms in solution vanishes completely after 19 min. Interestingly, two new absorption bands with a hypsochromic shift build up at 544 nm (B) and 502 nm (C) and remain stable in solution even after prolonged time. These are attributed to supramolecular *H-aggregates* of the type $\mathrm{MC_n}$ (B) and SP-MC aggregates (C) in **P15**.

As a comparison, the absorption spectra of an almost identical SP-MMA copolymer described by Goldburt *et al.* is depicted in Figure 5.9d).[319] Instead of monomer **20**, the authors used the corresponding monomer without the 8-methoxy moiety in the chromene part of the molecule. The thermally equilibrated solutions at different concentrations show the same distinct absorption bands with a hypsochromic shift with respect to the free MC-form at 500 and 560 nm, respectively. The authors attribute the absorption band at 500 nm to supramolecular complexes of the type SP-MC,[76a,79d] while the absorption band at 560 nm is assigned to *H-aggregates* of the type $\mathrm{MC_n}$.[77a–c]

Unfortunately, the small equilibrium constant of the STP$\rightleftharpoons$MC system in **P13a–d** and therefore the low concentration of the MC form in the PSS under continuous irradiation in analogy to the experiment shown in Figure 5.9c) did not allow a similar observation for the STP copolymers (see for example the PSS absorption spectrum of **P13a** in Figure 5.7b). Nevertheless, the analogy between the supramolecular aggregates reported in literature and the observations made with **P15**, together with the structural similarities between **P15** and **P13a–d**, strongly suggests a similar behavior for the STP-polymer system.

To gain additional evidence for this interpretation, polymer **P15** was employed in writing experiments similar to the ones for **P13a** in Figure 5.8. In fact, a stable 3D bridge structure is obtained with a comparable writing performance, structure quality, and shrinkage behavior as experienced for the STP polymer **P13a** (see Figure 5.10a). In Figure 5.10b), a depletion test pattern was written with varying excitation and depletion powers for each line in analogy to the pattern in Figure 5.5b). In principle, the application of polymer **P15** in STED-inspired lithography should also be possible, as the SP$\rightleftharpoons$MC

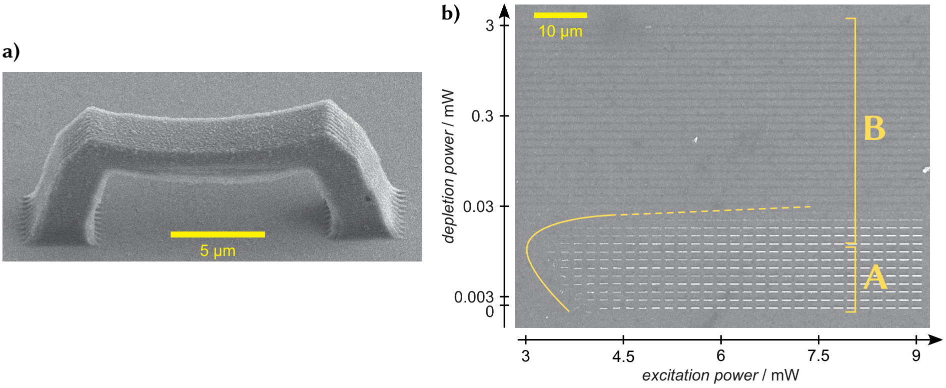

Figure 5.10. a) SEM image of a free-standing bridge structure written with a photoresist consisting of **P15** in acetophenone (40 wt%). Adapted with permission from [313]. © 2019 American Chemical Society. b) SEM image of a depletion test pattern employing the SP photoresist **P15**. Each line is written with a different excitation and depletion power. Parasitic writing in regime A is followed by the destructive regime B. Adapted with permission from [316].

equilibrium can be triggered with the same wavelengths as employed for the STP polymer. Unfortunately, the experiment in Figure 5.5b) does not follow the theoretical expectation. In regime A, the writing threshold decreases with increasing depletion powers, indicating *parasitic writing* right from the beginning, leaving no processing window for depletion. After further increase of the depletion power, a destruction of the written lines is observed (regime B).

It remains unclear, why the observed photo triggered MC⟶SP conversion cannot be translated to the STED-inspired lithography approach for the SP copolymer **P15** in contrast to the results of the STP copolymer **P13a** in combination with maleimide polymer **P14** in Figure 5.7d). Possible explanations can rely on the SP$\rightleftharpoons$MC equilibrium constant, which is far more shifted towards the MC form, with respect to the STP system. This becomes evident when comparing the PSS spectra between **P13a** and **P15** in Figure 5.7b) and Figure 5.9c), respectively. As such, the adjustment of the excitation, as well as the depletion laser powers might be outside the range for an effective structure formation. Therefore, despite the possibility to write stable 3D structures, polymer **P15** was not employed in further experiments towards STED-inspired lithography but represents a valuable system to validate the model of supramolecular aggregation as the course of stable structure formation in the STP polymer system.

5.3 Linewidth reduction through STED-inspired lithography

After the investigation of the cross-linking mechanism of the STP polymer structures in Figure 5.8, the possibility for STED-inspired lithography employing the STP copolymers **P13a–d** was tested. In Figure 5.11a), the SEM image of a depletion line pattern experiment in analogy to the one for the SP copolymer **P15** in Figure 5.10b) is depicted. Again, two different regimes can be identified. In contrast to the observation with **P15**, the threshold power first increases with higher depletion power (regime A), evidencing the successful depletion mechanism for the STP-based photoresist system. After raising the depletion power above 0.3 mW, the threshold power decreases again, which is an indication for the contribution of *parasitic writing* (regime B). However, a strong depletion effect is observed up to depletion powers of 0.3 mW in contrast to the SP photoresist, which can be exploited for STED-inspired lithography.

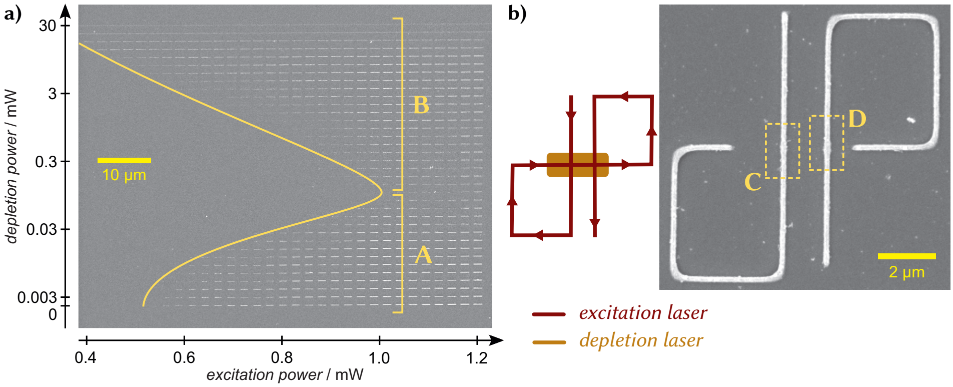

Figure 5.11. a) SEM image of a depletion test pattern employing the STP photoresist **P13a**. Each line is written with a different excitation and depletion power. Depletion regime A is followed by *parasitic writing* in regime B. b) Reversibility test of the depletion effect by writing a loop pattern. Previously written lines are not altered by the depletion laser (area C) and areas already irradiated with the depletion laser are still active in subsequent writing (area D). Adapted with permission from [313]. © 2019 American Chemical Society.

The reversibility of the depletion mechanism is investigated *via* the loop pattern depicted in Figure 5.11b). Following the writing direction, the depletion laser is only switched on in the central part that crosses the previously written vertical line (area C). This proves that the depletion laser does not damage previously written lines, i.e. the supramolecular aggregates are strong enough to withstand the depletion beam. In area D, the vertical line is written through a region already irradiated with the depletion laser, which is another key point, as the depletion laser does not lead to inactive polymer, i.e. the depletion laser does regenerate the STP form. In addition, the fact that stable structures are only possible in regions enriched which the MC form is further support for the cross-linking *via* supramolecular aggregates between the MC form and other MC, as well as STP molecules.

The bridge structure employing only polymer **P13a** shows a reduced shrinking behavior compared to the STP-maleimide photoresist mixture (compare Figure 5.7c) with Figure 5.8a), but the pillars of the bridge are still tilted inwards. Therefore, experiments employing all of the STP copolymers **P13a–d** listed in Table 5.1 were performed in saturated acetophenone solutions. The copolymers **P13a–c** are of comparable MW, while the STP monomer content increases from 14 (**P13a**) to 56 mol% (**P13c**). Polymer **P13d** features a higher MW at a reduced STP content of 7 mol%. In summary, the best writing results are obtained with polymer **P13a**, which is employed for all further writing experiments. Polymers **P13b** and **P13c** should in principle result in a more rigid structure due to the increased number of STP units, i.e. cross-linking points. However, the increased incorporation of STP monomer **18** into the copolymers reduces the solubility of the copolymers, which results in an overall lower STP density despite the higher STP-content per polymer chain. In contrast, increasing the MW of the copolymer in **P13d** should reduce the number of cross-linking points needed to overcome the gelation point, i.e. to form solid 3D structures. However, photoresist **P13d** shows an increased shrinkage behavior and lower structure quality compared to **P13a**, which can therefore be regarded as the sweet spot between MW of the copolymer and STP content. The photoresist mixture employed for all further experiments consists of **P13a** in a 40 wt% acetophenone solution.

As described in Figure 5.7d) for the STP-maleimide photoresist, a depletion line test was performed for polymer **P13a** to assess the achievable linewidth reduction through the depletion laser. In Figure 5.12a), a series of lines was written with fixed excitation powers and increasing depletion powers in the right part of the lines with the spatial intensity distribution of both lasers according to the scheme above the SEM image.

The linewidth with the depletion laser being on is reduced with increasing depletion power, until the line is not continuous anymore. Figure 5.12b) shows the determination of the FWHM for the highlighted area in panel a), with a FWHM linewidth of 31.2 nm. In addition, the FHWM of lines written at various depletion powers scales with the inverse square root of the depletion power, which is depicted in panel c). Such a scaling law is predicted for a STED-inspired lithographic process.[320] In the depletion experiment,

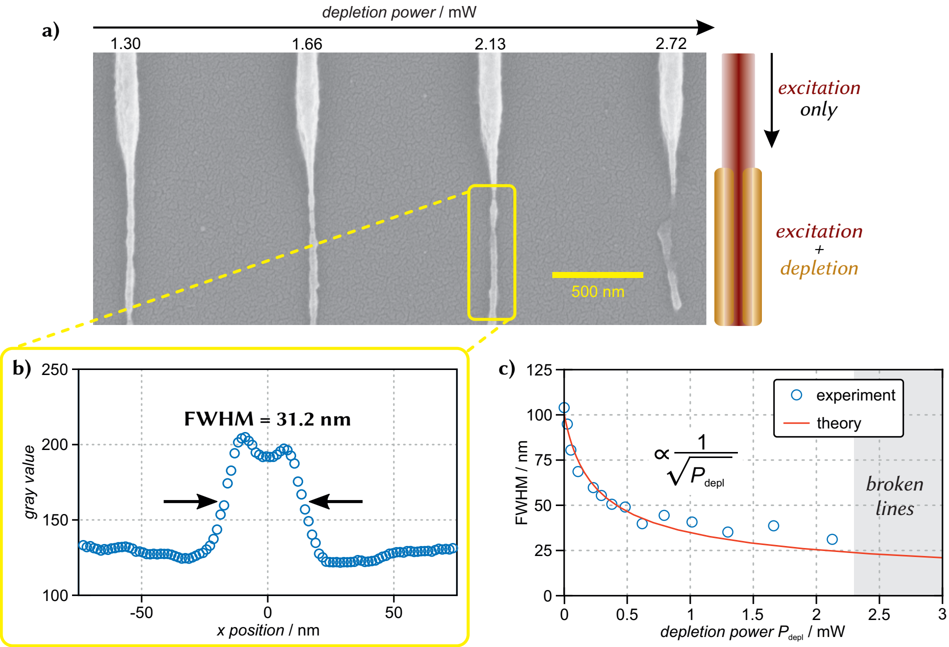

Figure 5.12. a) SEM image of linewidth reduction test *via* the depletion laser in the ride part of the lines for different depletion powers. The linewidth is decreasing with increasing depletion power until the lines become unstable and disconnected. b) Evaluation of the FWHM in the dashed area of a). c) The FWHM of lines written at different depletion powers is proportional to the inverse square root of the depletion power. Adapted with permission from [313]. © 2019 American Chemical Society.

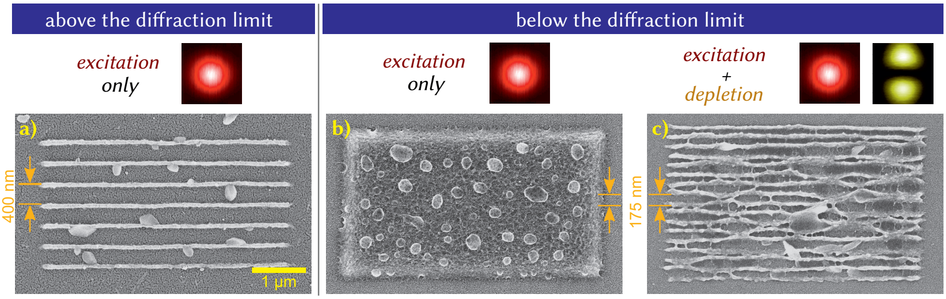
above the diffraction limit
below the diffraction limit
excitation only
excitation only
excitation + depletion
a)
b)
c)
400 nm
175 nm
1 µm

Figure 5.13. SEM image of gratings for the determination of the achievable resolution enhancement. a) Clearly separated lines are obtained for lattice constants greater than the diffraction limit of 207 nm (for the actual setup). For a lattice constant of 175 nm, using only the excitation laser leads to a single polymer block (b), while the lines are still separated employing the depletion laser in addition to the excitation laser (c). Adapted with permission from [313]. © 2019 American Chemical Society.

the thinnest achievable line without the depletion laser is 104 nm wide, employing an excitation power of 0.69 mW. In reducing the excitation power to 0.46 mW, the linewidth without depletion can also be reduced down to 55 nm, but the written lines are not continuous anymore. In summary, the linewidth employing the depletion laser is almost a factor 2 smaller than compared to the writing with only the excitation laser. It should be noted at this stage, that the observed linewidth reduction down to 31 nm constitutes the thinnest line written with STED-inspired lithography to date. As a comparison, Wollhofen *et al.* were able to achieve a FWHM linewidth of 34 nm employing an acrylate-based photoresist with DETC as the PI (for the mechanism in this case, see Figure 2.25a).[321]

Another important performance benchmark of a photoresist for STED-inspired lithography is the achievable resolution, i.e. the minimal distance between two elements. For the employed lithographic setup with a numerical aperture of NA $= 1.4$ and the excitation wavelength for the TPA of $\lambda = 820$ nm, the Abbe criterion predicts a minimal resolution of $d = 207$ nm (refer to Equation (2.22). In Figure 5.13a), a series of line gratings was written with a lattice constant of 400 nm. As the lattice constant is above the Abbe limit, the lines are well separated. In contrast, panel b) depicts a similar experiment with only the excitation laser being switched on. Here, the distance between adjacent lines is 175 nm, which is considerably smaller than the theoretical limit. Accordingly, the resulting structure consists of a single polymer block, i.e. the lines are not resolved anymore. When using the depletion laser to decrease the linewidth of the individual lines in panel c), the line pattern is again visible. However, the lines are not perfectly separated from each other. Such micro-bridge formation is observed for many negative-tone photoresist[322] and is attributed to swelling effects during the development of the written structures. Nevertheless, the STP photoresist shows a superior performance compared systems based on the FRP of acrylate monomers and allows for higher resolutions.[203]

5.4 Conclusion

This chapter has introduced the STP photoswitch for spatially resolved lithographic encoding of surfaces, as well as for the preparation of a photoresist based on the supramolecular aggregation of the MC form including the application in STED-inspired lithography.

The photo triggered reaction with the maleimide-functionalized ATRP initiator **21** and subsequent SI-ATRP enabled the lithographic encoding of glass substrates with polymer brushes (refer to Figure 5.2). The fabricated line structures feature brush heights between 25–50 nm with a width down to 0.4 µm. While the expected linewidth reduction through a depletion laser could not be translated from solution experiments onto surfaces with this approach, the possibility to fabricate spatially resolved structures employing the widely used maleimide anchoring moiety is a versatile new method for the fabrication of tailor-made surfaces. Importantly, the possibility to trigger the STP⟶MC conversion and therefore the reaction with the maleimide either at around 365–410 nm through OPA or *via* TPA at 820 nm is a great advance in the search for new trigger wavelengths in the toolbox of photolithographic protocols. As such, the adaption of the STP-maleimide reaction in the course of surface functionalization chemistry established in the current work is expected to enable new lithographic protocols in the near future.(a) Recapitulating the typical trigger wavelengths of molecules for other photolithographic processes, e.g. photoenols (≈320 nm), phenacyl sulfides (≈350 nm), or tetrazoles (320–410 nm), especially the possibility to trigger the STP at 820 nm should enable the adaption of *chromatic orthogonality*(b) for surface chemistry. To date, only few examples of such a selective bifunctional surface patterning *via chromatic orthogonality* have been reported.[98b,102a]

The synthesis of STP monomer **18** and copolymerization with MMA enabled the fabrication of a photoresist for DLW applications. In the first approach, the adaption of the STP-maleimide reaction for the cross-linking mechanism through blending of **P13d** with maleimide copolymer **P14** did not lead to a good quality of the written structures. However, it has been found that the STP copolymer itself is capable to form stable 3D structures in a DLW process through the formation of supramolecular aggregates of the MC form. This mechanism is supported by the similar behavior of the SP **P15** photoresist. The photo triggered STP⇌MC equilibrium enables the application of this one-component photoresist for STED-inspired lithography. In this regard, the TPA of an excitation laser at 820 nm for the STP⟶MC transformation and a depletion laser *via* an OPA process to trigger the MC⟶STP backward reaction at 640 nm was employed. The reversibility of the depletion reaction was demonstrated and a linewidth reduction of a factor 2 down to 31 nm has been achieved. This linewidth currently constitutes the thinnest lines written in STED-inspired lithography. In addition, the achievable resolution of the photoresist could also be pushed below the diffraction limit for this particular case, but the line gratings still exhibit swelling-induced deteriorations.

(a) In fact, during the writing up of the current thesis, Vijayamohanan and co-workers have published a report, in which they utilize the STP-maleimide in the same manner as described in the presented thesis for the immobilization of maleimide-functionalized fluorophores onto STP-silanized silicon surfaces, see [323].

(b) *Chromatic orthogonality* refers to the selective photoreaction of one chromophore among different chromophores. Other concepts in this context include *state selectivity* or *chromoselectivity*. For a detailed discussion of these different classes including a literature overview, the reader is referred to an excellent review from Fagnoni and co-workers.[324]

In conclusion, the STP chromophore has been introduced as a versatile photochromic molecule for the photoligation on surfaces, as well as the application in STED-inspired lithography, with superior performance compared to other reported photoresist formulations for sub-diffraction lithography.

CHAPTER 6

Concluding remarks

In the course of the present thesis, the first method for the spatially resolved surface immobilization of various metallopolymers on a single surface was developed, employing the versatile NITEC photochemistry . The in-depth analysis of the photoligation process identified crucial parameters for the successful immobilization of the metallopolymers, which are also valid for all other photo triggered surface ligation protocols. ToF-SIMS and spatially resolved XPS analysis of the prepared surfaces have demonstrated the preserved chemical composition of the fabricated metallopolymer surfaces. The introduced surface-ligation method is of high value for all related surface ligation techniques, as the described interplay between solution absorption and successful immobilization can be universally applied for all photoligation systems. The application of these functional metallopolymer surfaces in the realm of heterogeneous catalysis will be the next research step in this area. In the second part of the thesis, the photochemistry of spiro(thio)pyrans was investigated for the formation of light-sensitive SP-metal complexes, as well as the creation of a photoresist for the application in STED-inspired lithography. The irradiation of an NMR tube inside the NMR spectrometer in so-called LED-NMR experiments was introduced for the investigation of the prepared SP-metal complexes. It has been demonstrated that in combination with LED-UV-Vis experiments, a deeper understanding of the photo triggered processes is possible. Finally, the photo triggered reaction of the STP photoswitch with an electron deficient maleimide was used for the spatial encoding of surfaces for the first time. In addition, the preparation of a STP-based photoresist enabled the writing of structures below the diffraction limit, with the thinnest lines written with STED-inspired lithography to date.

CHAPTER 7

Experimental section

7.1 Materials

All starting materials and reagents were of analytic grade and used without further purification, if not declared otherwise. Acetic acid (100 %, p.a., VWR), acetonitrile (MeCN, p.a., VWR), (3-aminopropyl)triethoxysilane (APTES, 99 %, Acros Organics), ammonium chloride (99.5 %, Acros Organics), basic aluminum oxide (activity (I), Merck), benzene (99.8 %, anhydrous, Sigma Aldrich), 3-bromopropoxy-*tert*-butyldimethylsilane ($Br(CH_2)_3OTBDMS$, 97 %, abcr), *n*-butyllithium (1.6 M in *n*-hexane, Sigma Aldrich), 1,1′-carbonyldiimidazole (CDI, 97 %, Alfa Aesar), chloroform (VWR, p.a.), 4-cyano-4-((dodecylsulfanylthiocarbonyl)sulfanyl)pentanoic acid (CDSTSP, 97 %, Sigma Aldrich), cyclohexane (cC_6H_{12}, >97 %, VWR), dichloro(1,5-cyclooctadiene)palladium(II) (Pd 36.7 %, Alfa Aeser), dichloromethane (DCM, stabilized with ethanol, 99.8 %, VWR), *N,N′*-dicyclohexylcarbodiimid (DCC, 99 %, Sigma Aldrich), diethyl azodicarboxylate (DEAD, 97 %, Alfa Aesar), diethyl ether (>99 %, VWR), diisopropyl azodicarboxylate (DIAD, 98 %, Sigma Aldrich), *N,N′*-diisopropylcarbodiimide (DIC, 99 %, abcr), 4-dimethylaminopyridine (DMAP, 98 %, Acros Organics), 4,4′-dimethyl-2,2′-bipyridine (99 %, Acros Organics), *N,N*-dimethylformamide (DMF, p.a., Fisher Chemical), DMF (anhydrous, Acros Organics), *N,N*-dimethylthiocarbamoyl chloride (>97.0 %, TCI), 1,4-dioxane (>99 %, Acros), 4-(diphenylphosphino)benzoic acid (97 %, Acros Organics), ethanol (EtOH, 96 %, VWR), ethyl cyano(hydroxyimino)acetate (OxymaPure®, 99 %, Merck Millipore), 1-ethyl-3-(3-dimethylaminopropyl)carbodiimide hydrochloride (EDC·HCl, 99 %, Carl Roth), ethyl acetate (EtOAc, >99.5 %, VWR), (*2E,4E*)-hexadienol (97 %, Sigma Aldrich), hydrochloric acid (37 %, Carl Roth), hydrobromic acid (48 % aq., Sigma Aldrich), hydrogen peroxide (35 %, Carl Roth), hydroquinone (≥99 %, Sigma Aldrich), 2-hydroxy-3-methoxybenzaldehyde (>99.0 %, TCI), 2-hydroxy-3-methoxy-5-nitrobenzaldehyde (>99.0 %, TCI), 2-iodoethanole (99 %, stab. with copper, abcr), magnesium sulfate (dried, Carl Roth), methacrylic acid (MAA, 99.5 %, stabilized, Acros Organics), methacryloyl chloride (stabilized with 400 ppm 4-methoxyphenol, 97 %, Alfa Aesar), methanol (MeOH, p.a., VWR), 3-methyl-2-butanone (>99 %, TCI), methyl iodide (99 %, stab. with copper, Sigma-Aldrich), neutral aluminum oxide (activity (I), Merck), 4-nitrophenylhydrazine (96 %, 30 % in H_2O, Sigma-Aldrich), 5-nitrosalicylaldehyde (>97.0 %, TCI), oxalyl chloride (99 %, abcr), pentafluorophenol (PFP, 99 %, abcr), petroleum ether (40–60 °C, VWR), phosphorus pentoxide (≥99 %, powdered, Carl Roth), potassium hydroxide (≥85 %, in flakes, Carl Roth), *n*-propanol (≥99.5 %, VWR), tetrabutylammonium fluoride (TBAF, 1 M in THF, Sigma-Aldrich), tetrahydrofuran (THF, p.a., VWR), tetrahydrofuran (THF, anhydrous, Acros Organics), toluene (≥99.5 %, VWR), 2,3,3-trimethylindoleine (>97.0 %, TCI), 1,3,3-trimethyl-2-methyleneindoline (>96.0 %, TCI), triphenylphosphine (≥99.0 %, Merck Millipore), sodium hydrogen carbonate (99.5 %, Carl Roth), sodium hydroxide (99 %, Carl Roth), sodium sulfate (99 %, Carl Roth), sodium chloride (Carl Roth), sulfuric acid (96 %, Carl Roth), and 1,3,5-trioxane (Merck) were used as received. Methyl methacrylate (MMA, >99.5 %, Fisher Scientific), 2-hydroxyethyl methacrylate (HEMA, stabilized with <50 ppm monomethyl ether hydroquinone, >99 %, Sigma-Aldrich), and 1,4-dioxane (>99 %, Acros) were passed through a short column of basic alumina prior to use. Azobisisobutyronitrile (AIBN, Sigma-Aldrich) was recrystallized three times from methanol prior to use. Succinic anhydride was purified through sublimation and stored over P_2O_{10} in an exsiccator. For the surface reactions, acetone (electronics (MOS) grade, Fischer), Milli-Q® water Type 1, toluene (extra dry, Acros), 1,4-dioxane (99.5 %, extra dry, over molecular sieves, AcroSeal®, Acros Organics), MeCN (99.9 %, extra dry, over molecular sieves, AcroSeal®, Acros Organics), toluene (HPLC grade, Alfa Aesar), and DCM (synthesis grade, Fischer) were used. Triethylamine (TEA, 99.5 %, Sigma Aldrich) and diisopropylamine (Acros Organics) were distilled under reduced pressure. Deuterated solvents were obtained from Carl Roth GmbH (99.5 at% D). Silicon wafers were purchased from Si-Mat Silicon Materials (1 cm^2; type/dopant, P/boron; orientation <100>; resistivity, 1-30 Ω cm; thickness, 525(25) µm; TTV, <5 µm; front surface polished, back surface etched). Wafers were stored and transported in coin style single wafer shipper from SPS-EUROPE GmbH (25 mm, Art.-Nr. eCT1-25-ASSY-2-eM-01-BL, conductive polypropylene). The nitrogen stream was filtered by an activated charcoal filter (Supelco 24518). UV-Filter foil SFG10 (Art.-Nr. 100831) was purchased from METO*LIGHT*®. Arimed B6 UV lamp was purchased from Cosmedico® (36 W, Art.-Nr. 100-536-0060). Philips Cleo Compact PL-L 36W/09 2G11 UV lamp was purchased from

Philips® (36 W, EAN: 8711500642646). Light-emitting diodes (LEDs) were purchased from LUMITRONIX® and AVONEC®: 365 nm (Nichia® Art.-Nr. NVSU233B), 590 nm (Cree® Art.-Nr. XP-E2), 410–420 nm (AVONEC® Art.-Nr. 3W410420m), 380–390 nm (AVONEC® Art.-Nr. 10W380390m), 585–595 nm (AVONEC® Art.-Nr. 10W585595m), and 620–630 nm (AVONEC® Art.-Nr. 10W620630m). A power supply from EA Elektro-Automatik (EA-PS 2084-03B) was used for the LEDs and the Peltier cooling element. Fiber stripping tool (M44S63), multimode fiber (FP1000URT), and optical cage components (CP02T/M, ER1-P4, SM1LCM) were purchased from THORLABS®. Glass etching cream was purchased from Armour Etch® (Art.-Nr. 15-0150). NMR sample tubes for *in situ* irradiation were purchased from Rototec-Spintec GmbH (519-OUTER, 519-SPACER, 519-INNER). Glass photo vials (20 mL, clear glass, rounded bottom, long neck; VWR international, Art.-Nr. 548-0891) and aluminum caps with septa (central hole 10 mm; VWR international, Art. Nr. 548-0060) were purchased from VWR. Phenacyl sulfide-terminated PEG (**P5**) was kindly provided by Dr. Christiane Lang ($\bar{M}_{n,SEC} = 2900\,g\,mol^{-1}$, $Đ = 1.04$).[144] Maleimide-MMA copolymers **P14a** ($\bar{M}_{n,SEC} = 6400\,g\,mol^{-1}$, $Đ = 1.34$, 17 mol% maleimide content) and **P14** ($\bar{M}_{n,SEC} = 6700\,g\,mol^{-1}$, $Đ = 1.31$, 16 mol% maleimide content) were synthesized by L. Hammer in the course of her master thesis.[314] 2-Methoxy-6-methylbenzaldehyde (**6**),[325] 4-cyanopentanoic acid dithiobenzoate (CPADB),[326] 2-(2-hydroxyethyl)-3a,4,7,7a-tetrahydro-1*H*-4,7-epoxyisoindole-1,3(2*H*)-dione (Mal-OH),[327] 2-((2-oxo-2-phenylethyl)thio)-*N*-(3-(triethoxysilyl)propyl)acetamide (**3**),[124] 4-(2-(4-methoxyphenyl)-2*H*-tetrazol-5-yl)benzoic acid (Tet-acid),[160] and 2-(2,5-dioxo-2,5-dihydro-1*H*-pyrrol-1-yl)ethyl 2-bromo-2-methylpropanoate (**21**)[160] were synthesized according to the literature.

7.2 Analysis

Nuclear magnetic resonance spectroscopy

NMR spectra were recorded on a Bruker AM400 spectrometer at 298.0 K (400.3 MHz for ^{1}H and 100.7 MHz for ^{13}C, respectively). All NMR experiments were acquired employing standard pulse sequences from the Bruker library, if not stated otherwise. Chemical shifts are expressed in parts per million (ppm) and referenced on characteristic solvent resonances as internal standards for ^{1}H NMR and $^{13}C\{^{1}H\}$ NMR [$CDCl_3$: 7.26 ppm (^{1}H) and 77.16 ppm (^{13}C); CD_2Cl_2: 5.32 ppm (^{1}H) and 54.00 ppm (^{13}C); DMSO-d_6: 2.50 ppm (^{1}H) and 39.52 ppm (^{13}C); CD_3CN: 1.94 ppm (^{1}H) and 1.32 ppm (^{13}C); acetone-d_6: 2.05 ppm (^{1}H) and 29.84 ppm (^{13}C)]. 85 % Phosphoric acid was used as an external reference for $^{31}P\{^{1}H\}$ NMR. ^{1}H NMR are reported as follows: chemical shift (δ in ppm), multiplicity (s for singlet, bs for broad singlet, d for doublet, t for triplet, q for quartet, m for multiplet), coupling constant(s) (Hz), number of protons (concluded from the integrals), specific assignment. $^{13}C\{^1H\}$ NMR and $^{31}P\{^1H\}$ NMR spectra are reported in terms of chemical shift and specific assignment. NMR data processing was done using TopSpin (Bruker, version 3.2 pl7) and MestReNova (Mestrelab Research S.L., version 12.0) software. NMR assignments were made using a combination of 1D and 2D techniques, namely ^1H–^1H COSY (`cosygpppqf`), ^1H–^{13}C HMQC (`hmqcgpqf`), and ^1H–^{13}C HMBC (`hmbcgpndqf`).

***In situ* irradiation of NMR samples** NMR measurements with *in situ* irradiation with UV light was performed after a modified literature protocol.[309] The employed 365 nm LED was operated with a constant current of 1000 mA for all experiments.

For the chemical actinometry, solutions of *o*-NBA in CD_2Cl_2 (3.31, 5.29, 7.94, 13.2, 23.2, 33.1, 46.3, 66.2, 99.3, and 165 mM) were prepared with a total volume of 1 mL. 250 µL of the stock solutions were transferred into the assembled LED-NMR tube and directly placed inside the NMR spectrometer. For the metal complexes in Section 4.2.2, a similar volume of 250 µL was used with the concentrations given in the respective sections.

Samples were equilibrated for 5–10 min at 298.0 K and shimmed with the Bruker `topshim` au program. No spinning was used in all LED-NMR experiments. For quantitation of the NMR measurements, the steady-state approach was employed.[309] For all kinetic experiments, an adapted pseudo-2D experiment with the `zg2d`-pulse sequence from the standard Bruker library was used (the pulse sequence is given in Section A.1). As a compromise between sufficient signal-to-noise ratio and measurement speed, the flip angle was changed to 33°.

For the chemical actinometry, 32k complex data points were sampled within 2.93 s over a sweep width of 14 ppm. The transmitter frequency offset was set to 6 ppm. Other parameters were $DS = 0$ (dummy scans), $NS = 4$ (number of scans), $d1 = 1.06$ s (relaxation delay), and $d20 = 16$ s (delay between start of different 1D spectra). With these parameters, the delay between the individual 4 scans of every single 1D experiment equals the delay between different 1D experiments, i.e. the steady-state is maintained throughout the whole experiment. To ensure the steady-state condition in the beginning of the kinetic analysis, 10 dummy experiments were measured before the LED was switched on. Prior to Fourier transformation, the FIDs were zero filled to 128k data points and apodized with an exponential window function ($LB = 1.0$ Hz). Spectra were integrated in MestReNova with the “Concentration Graph” macro, in which the integral of *o*-nitrosobenzoic acid at 6.58 ppm was set to zero for the spectrum after the 10 dummy experiments. Plotting and fitting of the obtained concentrations was done with the OriginPro 2019 software package.

For the investigations of the SP-metal complexes, the number of scans added in every single 1D experiment was increased to NS = 8, the transmitter frequency offset to 5 ppm, and the delay between the individual 1D experiments to d20 = 32 s, keeping all other parameters unchanged. The initial 1D experiments for the determination of the thermal equilibrium concentrations of metal-complexes and free SP were conducted with a 33° pulse flip angle sampling 32k complex data points, DS = 4, NS = 32, 12 ppm sweep width, 3.41 s acquisition time, and d1 = 20 s to ensure sufficient relaxation for the quantitative analysis and the referencing of the kinetic measurements.

Size-exclusion chromatography

SEC measurements were performed on a Polymer Laboratories/Varian PL-SEC 50 Plus System and an Agilent 1200 system. The Polymer Laboratories/Varian PL-SEC 50 Plus System with an autosampler, a PLgel 5.0 µm bead-size guard column (50×7.5 mm) followed by one PLgel 5.0 µm Mixed E column (300×7.5 mm), one PLgel 5.0 µm Mixed C column (300×7.5 mm) and a differential refractive index (RI) detector using THF as the eluent at 35 °C with a flow rate of 1 mL min^{-1}. The Agilent 1200 system with an autosampler, a PLgel 5.0 µm bead size guard column (50×7.5 mm), one PLgel 5.0 µm Mixed E column (300×7.5 mm), three PLgel 5.0 µm Mixed C columns (300×7.5 mm) and a differential refractive index detector, as well as an UV detector using THF as eluent at 35 °C with a flow rate of 1 mL min^{-1}. The SEC systems were calibrated using linear polystyrene standards ranging from 380 g mol^{-1} to 2×10^6 g mol^{-1} (PSS ReadyCal) with the Mark-Houwink relationship for polystyrene (K = 14.1×10^3 mL g^{-1}, α = 0.7)[328] and linear poly(methyl methacrylate) standards ranging from 800 g mol^{-1} to 2×10^6 g mol^{-1} (PSS ReadyCal) with the Mark-Houwink relationship for poly(methyl methacrylate) (K = 12.8×10^3 mL g^{-1}, α = 0.69).[329] All samples were passed over 0.22 µm PTFE membrane filters prior to analysis.

Electrospray ionization mass spectrometry

ESI-MS spectra were recorded on a Q Exactive (Orbitrap) mass spectrometer (ThermoFisher Scientific, San Jose, CA, USA) equipped with a HESI II probe. The instrument was calibrated in the m/z range 74–1822 using a standard containing caffeine, Met-Arg-Phe-Ala acetate (MRFA) and a mixture of fluorinated phosphazenes (Ultramark 1621) (all from Sigma-Aldrich). A spray voltage of between 3.6 and 4.6 kV was used and nitrogen at a dimensionless sweep gas flow rate of 2 (approximately 3 L min^{-1}), as well as a dimensionless sheath gas flow rate of 5 to 10 were applied. The capillary temperature and the S-lens RF level were set to 320 °C and 62.0, respectively. The samples were dissolved with a concentration of 0.1 mg mL^{-1} in a mixture of THF and methanol (3/2 vol%) containing 100 µmol sodium trifluoroacetate or in pure DCM and infused with a flow of 5 µL min^{-1}. All samples were passed over 0.22 µm polytetrafluoroethylene (PTFE) membrane filters prior to analysis.

Ultraviolet-visible spectroscopy

All UV-Vis spectra were recorded on an USB4000 spectrometer together with a USB-ISS-UV-Vis device from Ocean Optics. The dissolved samples were measured using a 1 mm path length cell if not stated otherwise. Measurements were conducted in single strobe mode, the hold off time and pulse width were both set to 25 µs, the integration time was 26 µs, and electric dark correction was turned on. At least 20 scans were averaged and smoothed employing a boxcar smoothing value of 6. Both light sources were turned on with the UV lamp adjusted to 100 % and the visible lamp to 74 %, respectively. Spectra were collected from 200–800 nm and baseline corrected with respect to the pure solvent.

Spectral irradiance measurements

Spectral irradiance measurements were performed with a spectroradiometer SR600 equipped with a radiometric sensor with built-in diffuser for cosine correction from Opsytec Dr. Gröbel. The radiometric sensor was placed at the appropriate distance in an orthogonal manner towards the light source and the spectral irradiance was measured from 200–800 nm with active dark measurement and an offset factor of 1.15 in the range of 200–240 nm to account for scattering artifacts. The integration time was set between 2–2000 ms to ensure sufficient data quality above 80 %. Spectral corrections and raw data export were done using the USBSpec spectral software from Opsytec Dr. Gröbel.

X-ray photoelectron spectroscopy

XPS measurements were performed using a K-Alpha+ XPS spectrometer (ThermoFisher Scientific, East Grinstead, UK). All samples were analyzed using a micro-focused, monochromatic Al K_α X-ray source (400 µm spot size). The kinetic energy of the electrons was measured by a 180° hemispherical energy analyzer operated in the constant analyzer energy mode at 50 eV pass energy for elemental spectra. Data acquisition and processing using the Thermo Avantage software is described elsewhere.[330] The spectra were fitted with one or more Voigt profiles (binding energy uncertainty: ±0.2 eV). The analyzer transmission function, Scofield sensitivity factors,[331] and effective attenuation lengths (EALs) for photoelectrons were applied for quantification. EALs were calculated using the standard TPP-2M formalism.[332] All spectra were referenced to the C 1s peak of hydrocarbon at 285.0 eV binding energy controlled by means of the well-known photoelectron peaks of metallic Cu, Ag, and Au, respectively. The K-Alpha+ snapmap option was used to image the different structures with a spot of 100 µm. 7 Iterations were run to reach a better statistic. The obtained spectra were collapsed over the iterations and fitted either like described above or with the help of a principal component analysis routine to get better element mapping.

Time-of-flight secondary ion mass spectrometry

ToF-SIMS was performed on a TOF.SIMS5 instrument (ION-TOF GmbH, Münster, Germany). This spectrometer is equipped with a bismuth cluster primary ion source and a reflectron type time-of-flight analyzer. Ultra-high vacuum (UHV) base pressure was $<5\times10^{-9}$ mbar. For high mass resolution the Bi source was operated in the "high current bunched" mode providing short Bi_3^+ primary ion pulses at 25 keV energy and a lateral resolution of approx. 4 µm. The short pulse length of 1 ns allowed for high mass resolution. For imaging large fields of view the sample stage and the primary beam were scanned. Usually for 2–4 mm^2 fields of view 400×400 individual data points were recorded with 1 scan and 25 frames. 4 Adjacent points were binned to increase the dynamic range. Under these conditions, primary ion doses were kept below 10^{11} ions cm^{-2} (static SIMS limit) for all measurements. Spectra were calibrated on the omnipresent C^-, CH^-, C_2^-, C_3^-, C_4^- or on the C^+, CH^+, CH_2^+, CH_3^+, and Si^+ peaks. Based on these data sets, the chemical assignments for characteristic fragments were determined.

7.3 Synthesis of small molecules

All manipulations of air-sensitive materials were performed under rigorous exclusion of oxygen and moisture in Schlenk-type glassware on a dual manifold Schlenk line, interfaced to a high vacuum line (1×10^{-3} torr), or in an argon-filled glove box.

4-Cyano-4-(dodecylsulfanylthiocarbonyl) sulfanyl pentanoic acid 2,4-hexadienyl ester – (2)

CDSTSP (1.036 g, 2.57 mmol), (*2E,4E*)-hexadienol (0.761 g, 7.75 mmol), and DMAP (0.062 g, 0.507 mmol) were dissolved in 2.2 mL dry DCM and cooled to 0 °C. A solution of DCC (0.542 g, 2.63 mmol) in 2 mL dry DCM was added dropwise over 15 min. The reaction was stirred and brought to room temperature overnight (22 h). The white precipitate was filtered, 50 mL DCM was added, and the organic phase was washed with 0.5 M HCl (2×20 mL), saturated $NaHCO_3$ (40 mL), brine (20 mL), dried ($MgSO_4$), and purified *via* column chromatography [silica, cC_6H_{12}:EtOAc 15:1 (v:v)] yielding **2** as a yellow oil (0.88 g, 71 %). ^{1}H NMR (400.3 MHz, $CDCl_3$): δ(ppm) = 6.35–6.19 (m, 1H, H_{23}), 6.13–5.99 (m, 1H, H_{24}), 5.87–5.70 (m, 1H, H_{25}), 5.70–5.53 (m, 1H, H_{22}), 4.60 (d, $^3J=6.7$ Hz, 1H, H_{21}), 3.32 (t, $^3J=7.5$ Hz, 1H, H_{13}), 2.74–2.58 (m, 2H, H_{19}), 2.58–2.47 (m, 1H, H_{18}), 2.44–2.32 (m, 1H, H_{18}), 1.87 (s, 3H, H_{16}), 1.77 (d, $^3J = 6.8$ Hz, 3H, H_{26}), 1.73–1.64 (m, 2H, H_{11}), 1.41–1.20 (m, 18 H, H_{2-10}), 0.88 (t, $^3J=6.7$ Hz, 3H, H_1). $^{13}C\{^1H\}$ NMR (100.7 MHz, $CDCl_3$): δ(ppm) = 217.1 (C_{14}), 171.4 (C_{20}), 135.6 (C_{23}), 131.8 (C_{25}), 130.4 (C_{24}), 123.2 (C_{22}), 119.1 (C_{17}), 65.7 (C_{21}), 46.5 (C_{15}), 37.2 (C_{13}), 34.0 (C_{18}), 32.1, 30.0, 29.8, 29.7, 29.6, 29.5, 29.2, 29.1 (C_{2-10}, C_{19}), 27.8 (C_{11}), 25.0 (C_{16}), 18.3 (C_{26}), 14.3 (C_1). HR-ESI-MS (*m/z*): $[M+Na]^+$ calc. for $C_{25}H_{41}NO_2S_3$: 506.2192, found 506.2197.

2-(1,3-Dioxo-1,3,3a,4,7,7a-hexahydro-2*H*-4,7-epoxyisoindol-2-yl)ethyl 4-cyano-4-((phenylcarbonothioyl)thio)pentanoate – (4)

The synthesis of **4** was conducted using a modified literature procedure.[333] In a flame dried 50 mL Schlenk flask, CPADB (1.00 g, 3.58 mmol), Mal-OH (1.12 g, 5.37 mmol), DMAP (0.044 g, 0.36 mmol), and OxymaPure® (0.76 g, 5.37 mmol), were dissolved in acetonitrile (15 mL) and stirred for 5 min. The solution was cooled to 0 °C and EDC·HCl (1.03 g, 5.37 mmol) was added at once. The mixture was stirred at 0 °C for 1 h and at room temperature for 17 h. The solvent was removed under reduced pressure and the residue was redissolved in ethyl acetate (50 mL). The solution was washed (3×30 mL H_2O, 3×30 mL 1 M HCl, 30 mL brine), dried ($MgSO_4$), and the solvent was removed under reduced pressure. The raw product was purified *via* column chromatography [silica, cC_6H_{12}:EtOAc, 2:1

to 1:1 (v:v)] to obtain a pink oil (1.24 g, 2.63 mmol, 73 %). ^{1}H NMR (400.3 MHz, $CDCl_3$): δ(ppm) = 7.94–7.86 (m, 2H, H_3), 7.60–7.52 (m, 1H, H_1), 7.44–7.35 (m, 2H, H_2), 6.53–6.46 (m, 2H, H_{17}), 5.30–5.22 (m, 2H, H_{16}), 4.32–4.22 (m, 2H, H_{12}), 3.79–3.73 (m, 2H, H_{13}), 2.90–2.83 (m, 2H, H_{15}), 2.68–2.37 (m, 4H, $H_{9,10}$), 1.93 (s, 3H, H_7). ^{13}C{^{1}H} NMR (100.7 MHz, $CDCl_3$): δ(ppm) = 222.5 (C_5), 176.2 (C_{14}), 171.4 (C_{11}), 144.7 (C_4), 136.7 (C_{17}), 133.1 (C_1), 128.7 (C_2), 126.8 (C_3), 118.6 (C_8), 81.1 (C_{16}), 61.3 (C_{12}), 47.6 (C_{15}), 45.9 (C_6), 37.9 (C_{13}), 33.3 (C_{10}), 29.8 (C_9), 24.2 (C_7). HR-ESI-MS (*m/z*): $[M+Na]^+$ calc. for $C_{23}H_{22}N_2O_5S_2$: 493.0862, found 493.0866.

4-(2-(4-Methoxyphenyl)-2*H*-tetrazol-5-yl)-*N*-(3-(triethoxyilyl)propyl)benzamide – (5)

5 was synthesized using a modified literature procedure.[98b] Tet-acid (0.50 g, 1.7 mmol) and CDI (0.28 g, 1.7 mmol) were dispersed in 60 mL dry THF and stirred under argon at ambient temperature for 19 h. APTES (0.40 mL, 1.7 mmol) was added *via* syringe and the mixture was stirred under argon for 25 h. The solvent was removed at room temperature and the crude product was dissolved in DCM and purified *via* column chromatography [silica, cC_6H_{12}:EtOAc 1:2 (v:v)]. **5** was obtained as a white powder (0.62 g, 73 %). ^{1}H NMR (400.3 MHz, DMSO-d_6): δ(ppm) = 8.65 (t, $^3J = 5.6$ Hz, 1H, H_6), 8.27–8.19 (m, 2H, H_9), 8.12–8.01 (m, 4H, $H_{10,14}$), 7.28–7.18 (m, 2H, H_{15}), 3.87 (s, 3H, H_{17}), 3.75 (q, $^3J=7.0$ Hz, 6H, H_2), 3.27 (td, $^3J=7.0, 5.7$ Hz, 2H, H_5), 1.66–1.55 (m, 2H, H_4), 3.75 (t, $^3J=7.0$ Hz, 9H, H_1), 0.65–0.57 (m, 2H, H_3). ^{13}C{^{1}H} NMR (100.7 MHz, DMSO-d_6): δ(ppm) = 165.3 (C_7), 163.7 (C_{12}), 160.5 (C_{16}), 136.6 (C_{11}), 129.5 (C_8), 128.7 (C_{13}), 128.2 (C_{10}), 126.4 (C_9), 121.7 (C_{14}), 115.1 (C_{15}), 57.7 (C_2), 55.7 (C_{17}), 42.1 (C_5), 22.7 (C_4), 18.2 (C_1), 7.5 (C_3). HR-ESI-MS (*m/z*): $[M+MeOH+Na]^+$ calc. for $C_{24}H_{33}N_5O_5Si$: 522.2143, found 522.2120.

4-(4′-Methyl-[2,2′-bipyridin]-4-yl)butan-1-ol – (8)

A solution of freshly distilled diisopropylamine (1.67 mL, 11.9 mmol) in THF (10 mL) was cooled to −78 °C and slowly treated with *n*-butyllithium (1.6 M in *n*-hexane, 7.5 mL, 12 mmol). The resulting pale-yellow solution was stirred for 20 min and 4,4′-dimethyl-2,2′-bipyridine (2.0 g, 11 mmol) in THF (100 mL) was added dropwise. The mixture was stirred for 1.5 h at −78 °C, and $Br(CH_2)_3OTBDMS$ (2.77 mL, 11.9 mmol) in THF (20 mL) was added within 10 min. The reaction mixture was brought to room temperature overnight and was subsequently quenched by slow addition of water (10 mL). The solvent was removed under reduced pressure and the residue dissolved in DCM (50 mL), washed with water (3×20 mL), and dried ($MgSO_4$). The crude product was stirred for 4 h in a TBAF solution (1 M in THF, 16 mL) and diluted with Et_2O (50 mL). The resulting solution was washed with water (4×10 mL), concentrated $NaHCO_3$ solution (10 mL), brine (10 mL), and dried ($MgSO_4$). The crude product was purified by column chromatography [Alox N (III), cC_6H_{12}:EtOAc, 2:3 (v:v)]. **8** was obtained as a colorless oil (0.96 g, 37 %). ^{1}H NMR (400.3 MHz, $CDCl_3$): δ(ppm) = 8.53 (d, $^{3}J = 5.0$ Hz, 1H, $H_{6'}$), 8.50 (d, $^{3}J = 4.9$ Hz, 1H, H_6), 8.20 (d, $^{4}J = 1.7$ Hz, 2H, $H_{3,3'}$), 7.11 (dd, $^{3}J = 4.9$ Hz, $^{4}J = 1.7$ Hz, 2H, $H_{5,5'}$), 3.64 (t, $^{3}J = 6.4$ Hz, 2H, H_{10}), 2.70 (dd, $^{3}J = 4.9$ Hz, $^{4}J = 1.7$ Hz, 2H, H_7), 2.41 (s, 3H, $H_{7'}$), 2.10 (bs, 1H, H_{11}), 1.82–1.70 (m, 2H, H_8), 1.66–1.54 (m, 2H, H_9). $^{13}C\{^{1}H\}$ NMR (100.7 MHz, $CDCl_3$): δ(ppm) = 156.2 ($C_{2'}$), 156.1 (C_2), 152.5 (C_4), 149.1 ($C_{6'}$), 149.0 (C_6), 148.3 ($C_{4'}$), 124.8 ($C_{5'}$), 124.0 (C_5), 122.2 ($C_{3'}$), 121.4 (C_3), 62.5 (C_{10}), 35.3 (C_7), 32.3 (C_9), 26.7 (C_8), 21.3 ($C_{7'}$). HR-ESI-MS (*m/z*): $[M+Na]^+$ calc. for $C_{15}H_{18}N_2O$: 265.1311, found 265.1310.

8-Methoxy-1′,3′,3′-trimethyl-6-nitrospiro[chromene-2,2′-indoline] – (10)

10 was synthesized following a modified literature protocol.[302] 2-Hydroxy-3-methoxy-5-nitrobenzaldehyde (1.00 g, 5.08 mmol) and 1,3,3-trimethyl-2-methyleneindoline (0.88 g, 5.1 mmol) were dissolved in EtOH (120 mL) and heated to reflux for 5 h. The solvent was removed under reduced pressure and the raw product was recrystallized in EtOH (30 mL), filtered, washed (EtOH, water) and dried under high vacuum. **10** was obtained as yellow-green crystals (1.49 g, 83 %). ^{1}H NMR (400.3 MHz, CD_3CN): δ(ppm) = 7.77 (d, $^{4}J = 2.6$ Hz, 1H, H_{15}), 7.66 (d, $^{4}J = 2.6$ Hz, 1H, H_{17}), 7.17 (td, $^{3}J = 7.7$ Hz, $^{4}J = 1.3$ Hz, 1 H, H_4), 7.11 (ddd, $^{3}J = 7.3$ Hz, $^{4}J = 1.3$ Hz, $^{5}J = 0.6$ Hz, 1H, H_5), 7.02 (d, $^{3}J_c = 10.4$ Hz, 1H, H_{13}), 6.85 (td, $^{3}J = 7.4$ Hz, $^{4}J = 1.0$ Hz, 1H, H_4), 6.59 (dt, $^{3}J = 7.8$ Hz, $^{4}J = 0.7$ Hz, 1H, H_2), 5.93 (d, $^{3}J_c = 10.4$ Hz, 1H, H_{12}), 3.76 (s, 3H, H_{20}), 2.73 (s, 3H, H_7), 1.24 (s, 3H, H_9), 1.14 (s, 3H, H_{10}). $^{13}C\{^{1}H\}$ NMR (100.7 MHz, CD_3CN): δ(ppm) = 150.1 (C_{16}), 148.8 (C_6), 148.1 (C_{19}), 141.5 (C_{18}), 137.2 (C_1), 129.3 (C_{13}), 128.8 (C_4), 122.7 (C_5), 122.6 (C_{12}), 120.5 (C_3), 119.9 (C_{14}), 116.3 (C_{15}), 108.4 (C_{17}), 107.9 (C_2), 107.7 (C_{11}), 57.0 (C_{20}), 53.1 (C_8), 29.1 (C_7), 26.2 (C_{10}), 19.9 (C_9). HR-ESI-MS (*m/z*): $[M+H]^+$ calc. for $C_{20}H_{20}N_2O_4$: 353.1496, found 353.1490.

O-(2-Formyl-4-nitro-6-methoxyphenyl) dimethylcarbamothioate – (11b)

11b was synthesized following a modified literature protocol.[334] 2-Hydroxy-3-methoxy-5-nitrobenzaldehyde (3.00 g, 15.2 mmol), *N,N*-dimethylthiocarbamoyl chloride (2.83 g, 22.9 mmol), and triethylamine (4.22 mL, 30.4 mmol) were dissolved in dry DMF (90 mL) at room temperature and stirred overnight. The salt was removed by filtration the solvent was removed under reduced pressure. The residual was redissolved in EtOAc (50 mL), washed (water, 3×100 mL; brine, 50 mL), dried ($MgSO_4$), and the solvent was removed under reduced pressure to obtain *O*-(2-formyl-6-methoxy-4-nitrophenyl) dimethylcarbamothioate (**11a**), which was used without purification. **11a** was dissolved in toluene (200 mL) and refluxed for 20 h. The solvent was removed under reduced pressure and the raw product was purified by recrystallization (toluene/petroleum ether). **11b** was obtained as yellow crystals (2.26 g, 52 %). ^{1}H NMR (400.3 MHz, CDCl$_3$): δ(ppm) = 10.37 (s, 1H, H$_{10}$), 8.43 (d, ^4J = 2.4 Hz, 1H, H$_6$), 7.94 (d, ^4J = 2.3 Hz, 1H, H$_4$), 4.02 (s, 3H, H$_7$), 3.22 (s, 3H, H$_9$), 3.03 (s, 3H, H$_{9'}$). ^{13}C{^{1}H} NMR (100.7 MHz, CDCl$_3$): δ(ppm) = 189.2 (C$_{10}$), 163.2 (C$_8$), 161.0 (C$_3$), 149.8 (C$_5$), 140.0 (C$_1$), 128.7 (C$_2$), 115.1 (C$_6$), 109.4 (C$_4$), 57.3 (C$_7$), 37.5 (C$_{9,9'}$). HR-ESI-MS (*m/z*): **11b** was not ionizable.

8′-Methoxy-1,3,3-trimethyl-6′-nitrospiro[indoline-2,2′-thiochromene] – (12)

11b (0.42 g, 1.47 mmol) was dissolved in MeOH (52 mL). NaOH solution (1 M, 9.6 mL) was added at once to the stirred yellowish mixture, which instantly turned red. The solution was stirred at room temperature until the formation of precipitate (5 min) and HCl solution (15 mL, 1 M) was added at once. The solvent was removed under reduced pressure and the residual was extracted with EtOAc (50 mL), washed (3×50 mL brine/HCl), dried (MgSO$_4$), and the solvent was removed under reduced pressure. EtOH (100 mL) and 1,3,3-trimethyl-2-methyleneindoline (0.26 g, 1.5 mmol) were added and the mixture was refluxed for 6 h. The resultant was recovered by filtration and recrystallized from EtOH, yielding **12** as yellow needles (0.39 g, 72 %). ^{1}H NMR (400.3 MHz, CDCl$_3$): δ(ppm) = 7.77 (d, ^4J = 2.2 Hz, 1H, H$_{15}$), 7.54 (d, ^4J = 2.2 Hz, 1H, H$_{17}$), 7.14 (td, ^3J = 7.7 Hz, ^4J = 1.3 Hz, 1H, H$_4$), 7.06 (ddd, ^3J = 7.3 Hz, ^4J = 1.3 Hz, ^5J = 0.5 Hz, 1H, H$_5$), 6.89 (d, ^3J_c = 11.0 Hz, 1H, H$_{13}$), 6.83 (td, ^3J = 7.4 Hz, ^4J = 1.0 Hz, 1H, H$_3$), 6.48 (dt, ^3J = 7.7 Hz, ^4J = 0.7 Hz, 1H, H$_2$), 5.96 (d, ^3J_c = 10.9 Hz, 1H, H$_{12}$), 3.93 (s, 3H, H$_{20}$), 2.67 (s, 3H, H$_7$), 1.42 (s, 3H, H$_9$), 1.25 (s, 3H, H$_{10}$). ^{13}C{^{1}H} NMR (100.7 MHz, CDCl$_3$): δ(ppm) = 155.0 (C$_{18}$), 147.7 (C$_6$), 144.6 (C$_{19}$), 136.4 (C$_1$), 132.5 (C$_{16}$), 130.8 (C$_{13}$), 129.4 (C$_{14}$), 128.0 (C$_4$), 123.8 (C$_{12}$), 122.1 (C$_{15}$), 119.9 (C$_3$), 116.7 (C$_{15}$), 107.6 (C$_2$), 103.8 (C$_{17}$), 88.4 (C$_{11}$), 56.5 (C$_{20}$), 52.5 (C$_8$), 30.7 (C$_7$), 24.6 (C$_{10}$), 22.4 (C$_9$). HR-ESI-MS (*m/z*): [M+Na]$^+$ calc. for C$_{20}$H$_{20}$N$_2$O$_3$S: 391.1087, found 391.1089.

9,9,9a-Trimethyl-2,3,9,9a-tetrahydrooxazolo[3,2-a]indole – (13)

13 was synthesized following a modified literature protocol.[335] A mixture of 2,3,3-trimethylindoleine (3.6 mL, 22 mmol) and 2-iodoethanole (2.3 mL, 29 mmol) in MeCN (35 mL) were refluxed under N$_2$ atmosphere for 4 h. The solvent was removed under reduced pressure and the violet solid was grinded with KOH (2.1 g, 37 mmol) until the color changed from violet to orange. Benzene (40 mL) and water (10 mL) were added and the aqueous phase was discarded. The organic phase was washed (3×10 mL water, 20 mL brine), dried (MgSO$_4$), and the solvent was removed under reduced pressure. **13** was obtained as a red oil (4.19 g, 92 %). ^{1}H NMR (400.3 MHz, CDCl$_3$): δ(ppm) = 7.14

(td, $^3J = 7.6$ Hz, $^4J = 1.3$ Hz, 1H, H_3), 7.08 (ddd, $^3J = 7.4$ Hz, $^4J = 1.4$ Hz, $^5J = 0.5$ Hz, 1H, H_2), 6.93 (td, $^3J = 7.4$ Hz, $^4J = 1.0$ Hz, 1H, H_4), 6.76 (dt, $^3J = 7.8$ Hz, $^4J = 0.7$ Hz, 1H, H_5), 3.84 (ddd, $^3J = 7.8, 6.6$ Hz, $^2J = 3.0$ Hz, 1H, H_8), 3.73 (ddd, $^3J = 9.8, 6.8$ Hz, $^2J = 3.0$ Hz, 1H, H_7), 3.63–3.47 (m, 2H, $H_{7,8}$), 1.43 (s, 3H, H_{10}), 1.39 (s, 3H, H_{13}), 1.19 (s, 3H, H_{11}). $^{13}C\{^1H\}$ NMR (100.7 MHz, $CDCl_3$): δ(ppm) = 150.7 (C_6), 140.1 (C_1), 127.6 (C_3), 122.5 (C_2), 121.8 (C_4), 112.1 (C_5), 109.1 (C_{12}), 63.1 (C_8), 50.2 (C_7), 47.1 (C_9), 28.2 (C_{11}), 20.9 (C_{10}), 17.7 (C_{13}). HR-ESI-MS (*m/z*): $[M+H]^+$ calc. for $C_{13}H_{17}NO$: 204.1383, found 204.1384.

(*S*)-(2-Acetyl-4-nitrophenyl) dimethylcarbamothioate – (14b)

14b was synthesized following a modified literature protocol.[185,334] 5-Nitrosalicylaldehyde (5.00 g, 29.9 mmol), *N*,*N*-dimethylthiocarbamoyl chloride (5.69 g, 46.9 mmol), and DABCO (6.71 g, 59.8 mmol) were dissolved in dry DMF (160 mL) at 0 °C under inert atmosphere. The solution was stirred at 0 °C for 15 min. and at ambient temperature for 22 h. The salt was removed by filtration the solvent was removed under reduced pressure. Brine (100 mL) was added and the solution was extracted with EtOAc (2×100 mL), washed (3×100 mL water/brine), dried ($MgSO_4$), and the solvent was removed under reduced pressure to obtain *O*-(2-formyl-4-nitrophenyl) dimethylcarbamothioate (**14a**), which was used without purification. **14a** was dissolved in toluene (500 mL) and refluxed for 22 h. The solvent was removed under reduced pressure and the raw product was purified by recrystallization (toluene/petroleum ether). **14b** was obtained as beige crystals (6.64 g, 87 %). ^1H NMR (400.3 MHz, $CDCl_3$): δ(ppm) = 10.27 (s, 1H, H_7), 8.81 (d, $^4J = 2.6$ Hz, 1H, H_2), 8.37 (dd, $^3J = 8.5$ Hz, $^4J = 2.6$ Hz, 1H, H_4), 7.78 (d, $^3J = 8.5$ Hz, 1H, H_5), 3.19 (s, 3H, H_9), 3.05 (s, 3H, H_9). $^{13}C\{^1H\}$ NMR (100.7 MHz, $CDCl_3$): δ(ppm) = 188.7 (C_6), 163.4 (C_1), 148.9 (C_3), 139.7 (C_2), 138.3 (C_4), 127.2 (C_5), 123.6 (C_{12}), 37.6 (C_8), 37.3 (C_7). HR-ESI-MS (*m/z*): $[M+Na]^+$ calc. for $C_{10}H_{10}N_2O_4S$: 277.0254, found 277.0253.

1-(2-Hydroxyethyl),3,3-trimethyl-6′-nitrospiro[indoline-2,2′-thiochromene] – (15)

14b (1.00 g, 3.93 mmol) was dissolved in methanol (140 mL). NaOH solution (1 M, 26 mL) was added at once under vigorous stirring. The pale-yellow solution turned instantly red and was stirred until the formation of precipitate (4 min). HCl solution (1 M, 40 mL) was added at once and the solvent was removed under reduced pressure. Diethyl ether (50 mL) and water (30 mL) were added to the residue and the aqueous phase was discarded. The organic phase was washed (3×50 mL brine/HCl), dried ($MgSO_4$) and the solvent was removed. **13** (0.86 g, 3.9 mmol) and EtOH (92 mL) were added and the mixture was refluxed for 4 h, cooled to ambient temperature and stored in the freezer. The precipitate was collected *via* filtration, washed with cold EtOH and dried under high vacuum. **15** was obtained as yellow crystals (1.11 g, 76 %). ^{1}H NMR (400.3 MHz, DMSO-d_6): δ(ppm) = 8.24 (d, ^4J = 2.5 Hz, 1H, H_{17}), 7.94 (dd, ^3J = 8.7 Hz, ^4J = 2.6 Hz, 1H, H_{19}), 7.42 (d, ^3J = 8.7 Hz, 1H, H_{15}), 7.13–7.06 (m, 2H, $H_{4,5}$), 6.78 (td, ^3J = 7.4 Hz, ^4J = 0.9 Hz, 1H, H_3), 6.61 (dd, ^3J = 8.1 Hz, ^4J = 0.9 Hz, 1H, H_2), 6.16 (d, ^3J_c = 11.0 Hz, 1H, H_{14}), 4.79 (t, ^3J = 5.6 Hz, 1H, H_9), 3.64–3.49 (m, 2H, H_8), 3.34–3.24 (m, 1H, H_7), 3.10–3.00 (m, 1H, H_7), 1.31 (s, 3H, H_{11}), 1.14 (s, 3H, H_{12}). ^{13}C{^{1}H} NMR (100.7 MHz, DMSO-d_6): δ(ppm) = 147.0 (C_6), 144.3 (C_{16}), 143.1 (C_{18}), 135.6 (C_1), 130.3 (C_{15}), 129.4 (C_{21}), 127.6 (C_4), 126.6 (C_{20}), 125.0 (C_{14}), 123.2 (C_{17}), 122.6 (C_{19}), 122.1 (C_5), 119.2 (C_3), 106.9 (C_2), 89.9 (C_{13}), 59.2 (C_8), 52.9 (C_{10}), 47.7 (C_7), 24.2 (C_{12}), 21.5 (C_{11}). HR-ESI-MS (*m/z*): [M+Na]$^+$ calc. for $C_{20}H_{20}N_2O_3S$: 391.1087, found 391.1088.

4-(2-(3,3-Dimethyl-6′-nitrospiro[indoline-2,2′-thiochromen]-1-yl)ethoxy)-4-oxobutanoic acid – (16)

In a flame dried Schlenk flask, **15** (0.20 g, 0.54 mmol), DMAP (9.2 mg, 75 µmol), and succinic anhydride (66.2 mg, 0.66 mmol) were dissolved in anhydrous 1,4-dioxane (4.6 mL). TEA (0.09 mL, 0.7 mmol) was added and the solution was stirred at 50 °C for 14 h. Additional succinic anhydride (64 mg, 0.64 mmol) was added and the solution was heated at 60 °C for 29 h. The mixture was diluted with EtOAc (5 mL), washed (4×2 mL H_2O/HCl, 2 mL brine), dried ($MgSO_4$), and the solvent was removed under reduced pressure. The raw product was recrystallized from EtOH, yielding **16** as a yellow powder (154 mg, 60 %). In the ^{1}H NMR spectrum, protons 11 and 12 are overlapping with the residual solvent peak in DMSO-d_6 but can be resolved in acetone-d_6. However, the carbon resonances of 11 and 12 overlap with the residual solvent signal in the ^{13}C{^{1}H} NMR spectrum in acetone-d_6. Only the spectral assignments in DMSO-d_6 are presented here, while both deuterated solvents were employed for the resonance assignment. ^{1}H NMR (400.3 MHz, DMSO-d_6): δ(ppm) = 12.22 (s, 1H, H_{12}), 8.24 (d, ^4J = 2.5 Hz, 1H, H_{20}), 7.95 (dd, ^3J = 8.7 Hz, ^4J = 2.5 Hz, 1H, H_{22}), 7.42 (d, ^3J = 8.7 Hz, 1H, H_{23}), 7.19 (d, ^3J_c = 11.0 Hz, 1H, H_{18}), 7.13–7.06 (m, 2H, $H_{3,5}$), 6.82 (td, ^3J = 7.4 Hz, ^4J = 0.9 Hz, 1H, H_4), 6.69 (dd, ^3J = 8.1 Hz, ^4J = 0.9 Hz, 1H, H_2), 6.12 (d, ^3J_c = 11.0 Hz, 1H, H_{17}), 4.30–4.14 (m, 2H, H_8), 3.45 (ddd, ^2J = 14.9 Hz, ^3J = 7.7, 5.5 Hz, 1H, H_7), 3.23 (dt, ^2J = 14.8 Hz, ^3J = 5.0 Hz, 1H, H_7), 2.56–2.43 (m, 4H, $H_{10,11}$), 1.31 (s, 3H, H_{14}), 1.13 (s, 3H, H_{15}). ^{13}C{^{1}H} NMR (100.7 MHz, DMSO-d_6): δ(ppm) = 173.3 (C_{12}), 172.1 (C_9), 146.5 (C_{21}), 144.4 (C_6), 142.6 (C_{24}), 135.7 (C_{19}), 130.8 (C_{18}), 129.1 (C_1), 127.7 (C_5), 126.7 (C_{23}), 124.2 (C_{17}), 123.3 (C_{20}), 122.7 (C_{22}), 122.2 (C_3), 119.7 (C_4), 107.0 (C_2), 89.7 (C_{16}), 61.9 (C_8), 52.8 (C_{13}), 44.0 (C_7), 28.7 (C_{11}), 28.6 (C_{10}), 24.1 (C_{15}), 21.5 (C_{14}). HR-ESI-MS (*m/z*): [M+Na]$^+$ calc. for $C_{24}H_{24}N_2O_6S$: 491.1247, found 491.1251.

2-(3,3-Dimethyl-6′-nitrospiro[indoline-2,2′-thiochromen]-1-yl)ethyl 4-oxo-4-((3-(triethoxysilyl)propyl)amino)butanoate – (17)

In a flame dried Schlenk flask, **16** (0.33 g, 0.71 mmol) and CDI (0.12 mg, 0.71 mmol) were dissolved in anhydrous THF (5 mL) and the mixture was stirred at room temperature for 21 h. APTES (0.17 mL, 0.73 mmol) was added dropwise and the reaction mixture was stirred at ambient temperature for 23 h. The solvent was removed under reduced pressure and the crude product was purified *via* column chromatography [silica, $c\text{C}_6\text{H}_{12}$:EtOAc, 2:1⟶1:1 (v:v)]. **17** was obtained as a yellow oil (0.30 g, 64 %). ^{1}H NMR (400.3 MHz, CDCl$_3$): δ(ppm) = 8.02 (d, ^4J = 2.4 Hz, 1H, H$_{26}$), 7.92 (dd, ^3J = 8.6 Hz, ^4J = 2.5 Hz, 1H, H$_{28}$), 7.23 (d, ^3J = 8.6 Hz, 1H, H$_{29}$), 7.16 (td, ^3J = 7.7 Hz, ^4J = 1.3 Hz, 1H, H$_4$), 7.07 (dd, ^3J = 7.2 Hz, ^4J = 1.3 Hz, 1H, H$_5$), 6.89 (d, ^3J_c = 11.0 Hz, 1H, H$_{24}$), 6.87 (td, ^3J = 7.7 Hz, ^4J = 1.3 Hz, 1H, H$_3$), 6.60 (d, ^3J = 7.8 Hz, 1H, H$_2$), 6.02 (d, ^3J_c = 11.0 Hz, 1H, H$_{23}$), 5.81 (bs, 1H, H$_{13}$), 4.36–4.17 (m, 2H, H$_8$), 3.81 (q, ^3J = 7.0 Hz, 4H, H$_{17}$), 3.72 (q, ^3J = 7.1 Hz, 2H, H$_{17}$), 3.56 (ddd, ^2J = 14.9 Hz, ^3J = 7.0, 6.2 Hz, 1H, H$_7$), 3.34–3.17 (m, 3H, H$_{7,14}$), 2.71–2.59 (m, 2H, H$_{10}$), 2.47–2.35 (m, 2H, H$_{11}$), 1.68–1.53 (m, 2H, H$_{15}$), 1.39 (s, 3H, H$_{20}$), 1.24 (t, ^3J = 7.1 Hz, 3H, H$_{18}$), 1.22 (t, ^3J = 7.1 Hz, 6H, H$_{18}$), 1.21 (s, 3H, H$_{21}$), 0.69–0.55 (m, 2H, H$_{16}$). ^{13}C{^{1}H} NMR (100.7 MHz, CDCl$_3$): δ(ppm) = 173.0 (C$_9$), 171.1 (C$_{12}$), 146.9 (C$_6$), 144.9 (C$_{30}$), 143.4 (C$_{27}$), 136.0 (C$_1$), 130.9 (C$_{24}$), 129.1 (C$_{25}$), 128.1 (C$_4$), 126.5 (C$_{29}$), 124.6 (C$_{23}$), 123.5 (C$_{26}$), 122.9 (C$_{28}$), 122.4 (C$_5$), 120.3 (C$_3$), 107.2 (C$_2$), 89.8 (C$_{22}$), 62.8 (C$_8$), 58.6 (C$_{17}$), 58.6 (C$_{17}$), 53.2 (C$_{19}$), 44.5 (C$_7$), 42.1 (C$_{14}$), 31.0 (C$_{11}$), 29.6 (C$_{10}$), 24.4 (C$_{20}$), 23.0 (C$_{15}$), 22.2 (C$_{21}$), 18.6 (C$_{18}$), 18.4 (C$_{18}$), 7.9 (C$_{16}$). HR-ESI-MS (*m/z*): [M+Na]$^+$ calc. for $\text{C}_{33}\text{H}_{45}\text{N}_3\text{O}_8\text{SSi}$: 694.2589, found 694.2599.

2-(3,3-Dimethyl-6′-nitrospiro[indoline-2,2′-thiochromen]-1-yl)ethyl methacrylate – (18)

15 (500 mg, 1.36 mmol) and triphenylphosphine (641 mg, 2.44 mmol) were dissolved in dry THF (6 mL). The solution was cooled to 0 °C and MAA (0.21 mL, 2.4 mmol) was added dropwise. The mixture was stirred at 0 °C for 5 min and a solution of DEAD (0.39 mL, 2.4 mmol) in dry THF (4.5 mL) was added dropwise. The solution was stirred at 0 °C for 30 min and at ambient temperature for 22 h. The solvent was evaporated at ambient temperature and the crude product was purified *via* column chromatography [silica, $c\text{C}_6\text{H}_{12}$:EtOAc, 10:1 (v:v)]. **18** was obtained as a yellow powder (298 mg, 50 %). ^{1}H NMR (400.3 MHz, CDCl$_3$): δ(ppm) = 8.02 (d, ^4J = 2.4 Hz, 1H, H$_{20}$), 7.93 (dd, ^3J = 8.6 Hz, ^4J = 2.5 Hz, 1H, H$_{22}$), 7.24 (d, ^3J = 8.7 Hz, 1H, H$_{23}$), 7.17 (td, ^3J = 7.7 Hz, ^4J = 1.3 Hz, 1H, H$_4$), 7.08 (dd, ^3J = 7.3 Hz, ^4J = 1.2 Hz, 1H, H$_5$), 6.88 (td, ^3J = 7.5 Hz, ^4J = 1.0 Hz, 1H, H$_3$), 6.87 (d, ^3J_c = 10.9 Hz, 1H, H$_{17}$), 5.59 (t, ^4J = 1.6 Hz, 1H, H$_{11}$), 4.42–4.26 (m, 2H, H$_8$), 3.62 (ddd, ^2J = 15.0 Hz, ^3J = 7.1, 6.1 Hz, 1H, H$_7$), 3.33 (dt, ^2J = 14.9 Hz, ^3J = 5.6 Hz, 1H, H$_7$), 1.94 (dd,

^4J = 1.6, 1.0 Hz, 3H, H_{12}), 1.40 (s, 3H, H_{14}), 1.22 (s, 3H, H_{15}). $^{13}C\{^1H\}$ NMR (100.7 MHz, $CDCl_3$): δ(ppm) = 167.3 (C_9), 146.9 (C_6), 144.9 (C_{19}), 143.5 (C_{21}), 136.2 (C_{10}), 136.0 (C_1), 130.8 (C_{18}), 129.1 (C_{24}), 128.1 (C_4), 126.6 (C_{23}), 126.1 (C_{11}), 124.6 (C_{17}), 123.5 (C_{20}), 122.9 (C_{22}), 122.4 (C_5), 120.3 (C_3), 107.3 (C_2), 90.0 (C_{16}), 62.8 (C_8), 53.2 (C_{13}), 44.6 (C_7), 24.3 (C_{15}), 22.2 (C_{14}), 18.5 (C_{12}). HR-ESI-MS (*m/z*): $[M+Na]^+$ calc. for $C_{24}H_{24}N_2O_4S$: 459.1349, found 459.1348.

2-(8-Methoxy-3′,3′-dimethyl-6-nitrospiro[chromene-2,2′-indolin]-1′-yl)ethan-1-ol – (19)

19 was synthesized following a modified literature protocol.[336] **13** (7.26 g, 35.7 mmol) and 3-methoxy-5-nitrosalicylaldehyde (7.04 g, 35.7 mmol) were dissolved in EtOH (280 mL) and heated to reflux for 8 h. The solvent was removed under reduced pressure and the raw product was recrystallized from EtOH, filtered, washed (EtOH, petroleum ether) and dried under high vacuum. **19** was obtained as green-golden crystals (10.8 g, 79 %). ^1H NMR (400.3 MHz, CD_3CN): δ(ppm) = 7.77 (d, ^4J = 2.6 Hz, 1H, H_{17}), 7.66 (d, ^4J = 2.6 Hz, 1H, H_{19}), 7.15 (td, ^3J = 7.7 Hz, ^4J = 1.3 Hz, 1H, H_4), 7.11 (dd, ^3J = 7.4 Hz, ^4J = 1.0 Hz, 1H, H_5), 6.98 (d, ^3J_c = 10.4 Hz, 1H, H_{15}), 6.84 (td, ^3J = 7.4 Hz, ^4J = 1.0 Hz, 1H, H_3), 6.66 (d, ^3J = 7.8 Hz, 1H, H_2), 5.97 (d, ^3J_c = 10.4 Hz, 1H, H_{14}), 3.77 (s, 3H, H_{22}), 3.66 (dq, ^2J = 12.4 Hz, ^3J = 6.3 Hz, 1H, H_8), 3.56 (dq, ^2J = 11.5 Hz, ^3J = 5.9 Hz, 1H, H_8), 3.37 (dt, ^2J = 14.8 Hz, ^3J = 6.8 Hz, 1H, H_7), 3.23 (dt, ^2J = 14.8 Hz, ^3J = 5.6 Hz, 1H, H_7), 2.79 (t, ^3J=6.0 Hz, 1H, H_9), 1.23 (s, 3H, H_{11}), 1.14 (s, 3H, H_{12}). $^{13}C\{^1H\}$ NMR (100.7 MHz, CD_3CN): δ(ppm) = 150.0 (C_{18}), 148.3 (C_6), 148.1 (C_{20}), 141.6 (C_{21}), 136.9 (C_1), 128.9 (C_{15}), 128.7 (C_4), 123.3 (C_{14}), 122.8 (C_5), 120.3 (C_3), 119.8 (C_{16}), 116.3 (C_{17}), 108.4 (C_{19}), 108.1 (C_{13}), 107.7 (C_2), 60.8 (C_8), 57.0 (C_{22}), 53.6 (C_{10}), 46.8 (C_7), 26.2 (C_{12}), 19.8 (C_{11}). HR-ESI-MS (*m/z*): $[M+Na]^+$ calc. for $C_{21}H_{22}N_2O_5$: 405.1421, found 405.1420.

2-(8-Methoxy-3′,3′-dimethyl-6-nitrospiro[chromene-2,2′-indolin]-1′-yl)ethyl methacrylate – (20)

Triphenylphosphine (688 mg, 2.62 mmol) and **19** (1.00 g, 2.62 mmol) were dissolved in dry THF (17 mL). The solution was cooled to 0 °C and MAA (0.23 mL, 2.6 mmol) was added dropwise. The mixture was stirred at 0 °C for 5 min and a solution of DIAD (0.55 mL, 2.8 mmol) in dry THF (3 mL) was added dropwise over 15 min. The solution was stirred at 0 °C for 30 min and at ambient temperature for 22 h. The solvent was evaporated at ambient temperature and the crude product was purified *via* column chromatography [Alox N (I), cC_6H_{12}:EtOAc gradient]. **20** was obtained as a blue solid (722 mg, 61 %). ^1H NMR (400.3 MHz, $CDCl_3$): δ(ppm) = 7.69 (d, ^4J= 2.6 Hz, 1H, H_{20}), 7.62 (d, ^4J= 2.5 Hz,

1H, H_{22}), 7.19 (td, $^{3}J = 7.7$ Hz, $^{4}J = 1.2$ Hz, 1H, H_4), 7.08 (dd, $^{3}J = 7.3$ Hz, $^{4}J = 1.2$ Hz, 1H, H_5), 6.88 (td, $^{3}J = 7.4$ Hz, $^{4}J = 0.9$ Hz, 1H, H_3), 6.84 (td, $^{3}J = 7.4$ Hz, $^{4}J = 1.0$ Hz, 1H, H_3), 6.86 (d, $^{3}J_{\mathrm{c}} = 10.3$ Hz, 1H, H_{18}), 6.70 (d, $^{3}J = 7.8$ Hz, 1H, H_2), 6.06 (t, $^{4}J = 1.3$ Hz, 1H, H_{11}), 5.85 (d, $^{3}J_{\mathrm{c}} = 10.3$ Hz, 1H, H_{17}), 5.55 (t, $^{4}J = 1.7$ Hz, 1H, H_{11}), 4.29 (t, $^{3}J = 6.3$ Hz, 2H, H_8), 3.75 (s, 3H, H_{25}), 3.60 (dt, $^{2}J = 15.2$ Hz, $^{3}J = 6.7$ Hz, 1H, H_7), 3.47 (dt, $^{2}J = 15.2$ Hz, $^{3}J = 6.0$ Hz, 1 H, H_7), 1.91 (d, $^{4}J = 1.2$ Hz, 3H, H_{12}), 1.27 (s, 3H, H_{14}), 1.16 (s, 3H, H_{15}). $^{13}C\{^{1}H\}$ NMR (100.7 MHz, $CDCl_3$): δ(ppm) = 167.4 (C_9), 149.3 (C_{24}), 147.5 (C_{23}), 146.8 (C_6), 140.7 (C_{21}), 136.2 (C_{10}), 135.9 (C_1), 128.4 (C_{18}), 127.8 (C_4), 126.0 (C_{11}), 122.0 (C_{17}), 121.9 (C_5), 119.8 (C_3), 118.4 (C_{19}), 115.5 (C_{20}), 108.0 (C_{22}), 106.8 (C_2), 106.6 (C_{16}), 62.8 (C_8), 56.4 (C_{25}), 52.9 (C_{13}), 42.4 (C_7), 26.1 (C_{15}), 19.1 (C_{14}), 18.5 (C_{12}). HR-ESI-MS (*m/z*): $[M+Na]^+$ calc. for $C_{25}H_{26}N_2O_6$: 473.1683, found 473.1685.

7.4 Polymerizations

Diene-functional PMMA polymers (P1–P4)

MMA (0.941 mg, 9.40 mmol), **2** (45.3 µg, 94 µmol) and AIBN (1.7 µg, 10 µmol) were dissolved in toluene (1.50 mL). The solution was divided in half and transferred into two 10 mL Schlenk flasks. The mixtures were deoxygenated by four consecutive freeze-pump-thaw cycles and the flasks were subsequently placed in a pre-heated oil bath at 60 °C for 3 h (**P1**) and 5 h (**P2**). The polymerizations were stopped through freezing in liquid nitrogen and exposure to air. Residual monomer and solvent were removed under reduced pressure and the polymers were purified by precipitating three times from DCM in an excess of cold cC_6H_{12}:Et_2O [8:2 (v:v)] and dried under high vacuum. **P1** and **P2** were obtained as yellow powders. **P1**: $\bar{M}_{\mathrm{n,SEC}} = 3300\,\mathrm{g\,mol^{-1}}$, $Đ = 1.14$; **P2**: $\bar{M}_{\mathrm{n,SEC}} = 4000\,\mathrm{g\,mol^{-1}}$, $Đ = 1.18$.

In a 25 mL Schlenk flask, MMA (1.859 mg, 18.57 mmol), **2** (91.6 µg, 189 µmol) and AIBN (3.4 µg, 21 µmol) were dissolved in toluene (3.0 mL). The mixture was deoxygenated by three consecutive freeze-pump-thaw cycles and the flask was subsequently placed in a pre-heated oil bath at 60 °C for 5.5 h. The polymerization was stopped through freezing in liquid nitrogen and exposure to air. Residual monomer and solvent were removed under reduced pressure and the polymer was purified by precipitating three times from DCM in an excess of cold cC_6H_{12}:Et_2O [1:1 (v:v)] and dried under high vacuum. **P3** was obtained as a yellow powder: $\bar{M}_{\mathrm{n,SEC}} = 5100\,\mathrm{g\,mol^{-1}}$, $Đ = 1.18$.

In a 10 mL Schlenk flask, MMA (0.937 mg, 9.35 mmol), **2** (48.2 µg, 100 µmol) and AIBN (1.6 µg, 10 µmol) were dissolved in toluene (4.0 mL). The mixture was deoxygenated by three consecutive freeze-pump-thaw cycles and the flask was subsequently placed in a pre-heated oil bath at 60 °C for 22.5 h. The polymerization was stopped through freezing in liquid nitrogen and exposure to air. Residual monomer and solvent were removed under reduced pressure and the polymer was purified by precipitating three times from DCM in an excess of cold MeOH and dried under high vacuum. **P4** was obtained as a yellow powder: $\bar{M}_{\mathrm{n,SEC}} = 6500\,\mathrm{g\,mol^{-1}}$, $Đ = 1.21$.

Maleimide functional PMMA polymers (P9-FM, P9-non-capped, P10-FM, P10-FM-cap, and P10)

In a 50 mL round bottom flask, MMA (2.13 ml, 20.0 mmol), **4** (157 mg, 0.333 mmol) and AIBN (5.6 mg, 0.033 mmol) were dissolved in 1,4-dioxane (7.87 mL). The mixture was deoxygenated by three consecutive freeze-pump-thaw cycles and the flask was subsequently placed in a pre-heated oil bath at 60 °C for 24 h. The polymerization was stopped through freezing in liquid nitrogen and exposure to air. Residual monomer and solvent were removed under reduced pressure and the polymer was purified by precipitating three times from DCM in an excess of cold $c\mathrm{C_6H_{12}}$:$\mathrm{Et_2O}$ [8:2 (v:v)] and dried under high vacuum. **P10-FM** was obtained as a pink powder: $\bar{M}_{\mathrm{n,SEC}} = 5500\,\mathrm{g\,mol^{-1}}$, $Đ = 1.21$. For **P9-FM**, the same procedure as for **P10-FM** was applied, but the polymerization was stopped after 3.5 h. **P9-FM**: $\bar{M}_{\mathrm{n,SEC}} = 2900\,\mathrm{g\,mol^{-1}}$, $Đ = 1.17$.

For **P9-non-capped**, **P9-FM** (831 mg) was dissolved in dry toluene (80 mL) and percolated with nitrogen for 1 h. The solution was refluxed for 3 h and the solvent was removed under reduced pressure. The polymer was purified by precipitating two times from DCM in an excess of cold $c\mathrm{C_6H_{12}}$ and dried under high vacuum. **P9-non-capped** was obtained as an off-white powder: $\bar{M}_{\mathrm{n,SEC}} = 2700\,\mathrm{g\,mol^{-1}}$, $Đ = 1.18$.

For **P10-FM-cap**, **P10-FM** was dissolved in MeCN ($15\,\mathrm{mg\,mL^{-1}}$) and **6** (5 eq.) was added. The solution was percolated with nitrogen for 30 min and the flask was irradiated in a custom-made photoreactor at room temperature under constant stirring with an Arimed B6 lamp from 2.5 cm distance. After 2 h, the solvent was removed under reduced pressure and the polymer was purified by precipitating three times from DCM in an excess of cold $c\mathrm{C_6H_{12}}$:$\mathrm{Et_2O}$ [8:2 (v:v)] and dried under high vacuum. **P10-FM-cap** was obtained as a white powder: $\bar{M}_{\mathrm{n,SEC}} = 5700\,\mathrm{g\,mol^{-1}}$, $Đ = 1.20$.

P10-FM-cap was dissolved in toluene ($10\,\mathrm{mg\,mL^{-1}}$) and heated under reflux for 4 h. The solvent was removed under reduced pressure and the polymer was purified by precipitating three times from DCM in an excess of cold $c\mathrm{C_6H_{12}}$:$\mathrm{Et_2O}$ [8:2 (v:v)] and dried under high vacuum. **P10** was obtained as a white powder: $\bar{M}_{\mathrm{n,SEC}} = 5700\,\mathrm{g\,mol^{-1}}$, $Đ = 1.19$.

Phosphine ligand copolymers

In a 50 mL round bottom flask, **4** (89.2 mg, 190 µmol), AIBN (3.0 mg, 18 µmol), MMA (1.00 ml, 9.39 mmol) and **7** (703 mg, 1.68 mmol) were dissolved in 1,4-dioxane (4.6 mL). The mixture was deoxygenated by three consecutive freeze-pump-thaw cycles and the flask was subsequently placed in a pre-heated oil bath at 60 °C for 24 h. The polymerization was stopped through freezing in liquid nitrogen and exposure to air. Residual monomer and solvent were removed under reduced pressure and the polymer was purified by precipitating three times from DCM in an excess of $c\text{C}_6\text{H}_{12}$:Et_2O [8:2 (v:v)] and dried under high vacuum. **P11-FM** was obtained as a pink powder: $\bar{M}_{\text{n,SEC}} = 10\,200\ \text{g mol}^{-1}$, $Đ = 1.27$.

A solution of **P11-FM** was prepared in MeCN ($16\ \text{mg mL}^{-1}$). To this, **6** (5 eq.) was added and the solution was percolated with nitrogen for 30 min. The flask was placed in a custom-made photoreactor and irradiated at room temperature with an Arimed B6 lamp from 2.5 cm distance while being stirred. After 2.5 h, the solvent was removed under vacuum and the residue was redissolved in a minimum amount of DCM, precipitated two times in an excess of $c\text{C}_6\text{H}_{12}$:Et_2O [8:2 (v:v)] and dried under high vacuum. **P11-FM-cap** was obtained as a white powder: $\bar{M}_{\text{n,SEC}} = 10\,400\ \text{g mol}^{-1}$, $Đ = 1.28$.

A solution of **P11-FM-cap** in toluene ($21\ \text{mg mL}^{-1}$) was heated under reflux for 4 h. The solvent was removed under vacuum and the residue was re-dissolved in a minimum amount of DCM, precipitated two times in an excess of *n*-hexane/Et_2O [8:2 (v:v)] and dried under high vacuum. **P11** was obtained as a white powder: $\bar{M}_{\text{n,SEC}} = 10\,700\ \text{g mol}^{-1}$, $Đ = 1.35$.

Bipyridine ligand copolymers

In a 50 mL round bottom flask, **4** (178 mg, 378 µmol), AIBN (6.7 mg, 41 µmol), MMA (2.19 ml, 20.6 mmol), and **9** (708 mg, 2.28 mmol) were dissolved in 1,4-dioxane (9.2 mL). The mixture was deoxygenated by three consecutive freeze-pump-thaw cycles and the flask was subsequently placed in a pre-heated oil bath at 60 °C for 24 h. The polymerization was stopped through freezing in liquid nitrogen and exposure to air. The solvent was removed under vacuum and the residue was re-dissolved in a minimum amount of DCM, precipitated three times in an excess of *n*-hexane/Et_2O [8:2 (v:v)] and dried under high vacuum. **P12-FM** was obtained as a pink powder: $\bar{M}_{\text{n,SEC}} = 5900\ \text{g mol}^{-1}$, $Đ = 1.22$.

A solution of **P12-FM** was prepared in MeCN ($34\ \text{mg mL}^{-1}$). To this, **6** (5 eq.) was added and the solution was percolated with nitrogen for 30 min. The flask was then placed in a custom-made photoreactor and irradiated at room temperature while being stirred with an Arimed B6 lamp from 2.5 cm distance. After 2.5 h, the solvent was removed under vacuum and the residue was redissolved in a minimum amount of DCM and precipitated two times in an excess of *n*-hexane/Et_2O [8:2 (v:v)] and dried under high vacuum. **P12-FM-cap** was obtained as a white powder: $\bar{M}_{n,SEC} = 6100\,g\,mol^{-1}$, $Đ = 1.22$.

A solution of **P12-FM-cap** in toluene ($20\,mg\,mL^{-1}$) was heated under reflux for 4 h. The solvent was removed under vacuum and the residue was re-dissolved in a minimum amount of DCM, precipitated two times in an excess of *n*-hexane/Et_2O [8:2 (v:v)] and dried under high vacuum. **P12** was obtained as a white powder: $\bar{M}_{n,SEC} = 6400\,g\,mol^{-1}$, $Đ = 1.25$.

Spirothiopyran-MMA copolymers (P13a–d)

In a 10 mL Schlenk flask, MMA (147 mg, 1.46 mmol), **18** (161 mg, 0.369 mmol), 1-dodecanethiol (8.9 mg, 44 µmol), and AIBN (6.7 mg, 41 µmol) were dissolved in toluene (2.84 mL). The mixture was deoxygenated by three consecutive freeze-pump-thaw cycles and the flask was subsequently placed in a pre-heated oil bath at 65 °C for 17.5 h. The polymerization was stopped through freezing in liquid nitrogen and exposure to air. Residual monomer and solvent were removed under reduced pressure and the polymer was purified by precipitating three times from DCM in an excess of cold methanol and dried under high vacuum. **P13a** was obtained as a yellow powder: $\bar{M}_{n,SEC} = 6100\,g\,mol^{-1}$, $Đ = 1.97$, 14 mol% SPT content (NMR).

In a 10 mL Schlenk flask, MMA (42.6 mg, 0.425 mmol), **18** (80.3 mg, 0.184 mmol), 1-dodecanethiol (2.5 mg, 12 µmol), and AIBN (2.1 mg, 13 µmol) were dissolved in toluene (0.96 mL). The mixture was deoxygenated by three consecutive freeze-pump-thaw cycles and the flask was subsequently placed in a pre-heated oil bath at 65 °C for 17 h. The polymerization was stopped through freezing in liquid nitrogen and exposure to air. Residual monomer and solvent were removed under reduced pressure and the polymer was purified by precipitating three times from DCM in an excess of cold methanol and dried under high vacuum. **P13b** was obtained as a yellow powder: $\bar{M}_{n,SEC} = 7600\,g\,mol^{-1}$, $Đ = 1.55$, 27 mol% SPT content (NMR).

In a 10 mL Schlenk flask, MMA (9.6 mg, 96 µmol), **18** (92.8 mg, 0.213 mmol), 1-dodecanethiol (1.4 mg, 6.9 µmol), and AIBN (1.0 mg, 6.1 µmol) were dissolved in toluene (0.99 mL). The mixture was deoxygenated by three consecutive freeze-pump-thaw cycles and the flask was subsequently placed in a pre-heated oil bath at 65 °C for 17 h. The polymerization was stopped through freezing in liquid nitrogen and exposure to air. Residual monomer and solvent were removed under reduced pressure and the polymer was purified by precipitating three times from DCM in an excess of cold methanol and dried under high vacuum. **P13c** was obtained as a yellow powder: $\bar{M}_{\text{n,SEC}} = 8600\,\text{g}\,\text{mol}^{-1}$, $Đ = 1.78$, 56 mol% STP content (NMR).

In a 10 mL Schlenk flask, MMA (0.75 mL, 7.0 mmol), **18** (300 mg, 0.687 mmol), and AIBN (2.4 mg, 15 µmol) were dissolved in 1,4-dioxane (5 mL). The mixture was deoxygenated by three consecutive freeze-pump-thaw cycles and the flask was subsequently placed in a pre-heated oil bath at 65 °C for 23 h. The polymerization was stopped through freezing in liquid nitrogen and exposure to air. Residual monomer and solvent were removed under reduced pressure and the polymer was purified by precipitating two times from DCM in an excess of cold methanol and dried under high vacuum. **P13d** was obtained as a yellow powder: $\bar{M}_{\text{n,SEC}} = 44\,000\,\text{g}\,\text{mol}^{-1}$, $Đ = 2.10$, 7 mol% STP content (NMR).

SP-MMA copolymer (P15)

In a 10 mL Schlenk flask, MMA (98.0 mg, 0.976 mmol), **20** (109 mg, 0.242 mmol), 1-dodecanethiol (6.1 mg, 37 µmol), and AIBN (4.1 mg, 25 µmol) were dissolved in toluene (1.89 mL). The mixture was deoxygenated by three consecutive freeze-pump-thaw cycles and the flask was subsequently placed in a pre-heated oil bath at 70 °C for 13.5 h. The polymerization was stopped through freezing in liquid nitrogen and exposure to air. Residual monomer and solvent were removed under reduced pressure and the polymer was purified by precipitating three times from DCM in an excess of cold methanol and dried under high vacuum. **P15** was obtained as a blue powder: $\bar{M}_{\text{n,SEC}} = 7300\,\text{g}\,\text{mol}^{-1}$, $Đ = 1.58$, 16 mol% SP content (NMR).

7.5 Surface reactions

All silicon wafer manipulations were carried out with gloves and surgical masks employing ceramic tweezers. A continuous solvent film on the polished side of the wafers was maintained during all experimental steps until the final drying step in a stream of nitrogen.

Activation of silicon wafers Silicon wafers were separately placed in 10 ml glass vials with the polished surface pointing upwards, 4 ml freshly prepared piranha solution [H_2O_2:H_2SO_4, 1:2 (v:v)] was added, the glass vials were sealed with a plastic lid and placed on a pre-heated metal plate at 80 °C for 1 h. The wafers were rinsed with water, dried in a stream of nitrogen, and placed with the polished surface pointing upwards into head space vials (Pyrex, 20 mm diameter), which were crimped airtight using styrene/butadiene rubber seals with PTFE inner liner and degassed for 10 min with nitrogen. The activated, dried, and sealed wafers were immediately used for subsequent silanization.

Silanization of silicon wafers The respective silane was dissolved in dry toluene (4 mM) and percolated with nitrogen for 10 min. To each activated silicon wafer, 1 ml of silane solution was added and the sealed glass vials were placed on a pre-heated metal plate at 50 °C for 4 h and stored at ambient temperature until usage (8–24 h) under exclusion from light. The wafers were rinsed with an excess of toluene and DCM, dried under a stream of nitrogen and either used directly for the surface encoding steps or stored in single wafer shippers until usage at ambient temperature (maximum 1 week).

Photoreactions employing shadow masks The wafers were assembled in the photo mask holder with or without shadow mask (see Figure 3.5a–c) and placed upright in a head space vial (Pyrex, 20 mm diameter). The vials were crimped airtight using styrene/butadiene rubber seals with PTFE inner liner and percolated with nitrogen for 10 min. A solution of the respective reaction partner was prepared in a separate vial (1 mg $\mathrm{mL^{-1}}$ in anhydrous 1,4-dioxane, 5 mL total volume), percolated with nitrogen for 10 min, passed through a 0.22 µm PTFE membrane filter and transferred into the vial containing the assembled wafer. The vial was irradiated with UV light (Philips Cleo Compact PL-L for phenacyl sulfide and Arimed B6 for NITEC reactions) in a custom-build photoreactor from 2.5 cm distance (see Figure 3.5d). The distance between the inner glass wall of the vial and the wafer surface was 2 mm unless stated otherwise. The solution was diluted with DCM and the photo mask holder was disassembled while being immersed in a head space vial with DCM. All metal parts were sonicated in DCM for 15 min, washed with DCM, dried under a stream of nitrogen, and stored in a dry and dust free environment for further experiments. The functionalized silicon wafers were washed with DCM, sonicated for 2 min in acetone, washed with DCM, sonicated for 2 min in toluene, washed with DCM and finally dried in a stream of nitrogen and stored in single wafer shippers.

For the metal post-loading of phosphine and bipyridine functionalized surfaces, the silicon wafers containing the ligand polymer **P11** or **P12** on the irradiated areas were placed in head space vials (Pyrex, 20 mm diameter), crimped airtight using styrene/butadiene rubber seals with PTFE inner liner and percolated with nitrogen for 10 min.

For **P11**, a stock solution of chloro(tetrahydrothiophene)gold(I) was prepared (4 mM in DCM). DCM was transferred into the wafer-containing vial *via* syringe (1 mL) and left at ambient temperature for 5 min after which 1 mL of the gold stock solution was added *via* syringe and left at ambient temperature for another 30 min (if not stated otherwise) under exclusion from light and gentle shaking.

For **P12**, a stock solution of *cis*-dichlorobis(dimethyl sulfoxide)platinum(II) was prepared (4 mM in chloroform). Chloroform was transferred into the wafer-containing vial *via* syringe (1 mL) and left at 65 °C for 5 min after which 1 mL of the platinum stock solution was added *via* syringe and left at 65 °C for another 30 min under exclusion from light and gentle shaking.

The functionalized silicon wafers were washed with DCM, sonicated for 2 min in acetone, washed with DCM, sonicated for 2 min in toluene, washed with DCM, dried in a stream of nitrogen and stored in single wafer shippers.

Bibliography

[1] R. F. T. Stepto, *Pure Appl. Chem.* **2009**, *81*, 351–353.

[2] R. J. Young, P. A. Lovell, *Introduction to polymers*, 3rd ed., CRC Press Taylor & Francis Group, Boca Raton, USA, **2011**, p. 668.

[3] J. Chiefari, Y. K. Chong, F. Ercole, J. Krstina, J. Jeffery, T. P. T. Le, R. T. A. Mayadunne, G. F. Meijs, C. L. Moad, G. Moad, E. Rizzardo, S. H. Thang, *Macromolecules* **1998**, *31*, 5559–5562.

[4] D. Charmot, P. Corpart, H. Adam, S. Zard, T. Biadatti, G. Bouhadir, *Macromol. Symp.* **2000**, *150*, 23–32.

[5] *Handbook of RAFT Polymerization*, 1st ed., (Ed.: C. Barner-Kowollik), Wiley-VCH Verlag GmbH & Co. KGaA, Weinheim, Germany, **2008**, p. 543.

[6] S. Perrier, *Macromolecules* **2017**, *50*, 7433–7447.

[7] D. J. Keddie, G. Moad, E. Rizzardo, S. H. Thang, *Macromolecules* **2012**, *45*, 5321–5342.

[8] G. Moad, E. Rizzardo, S. H. Thang, *Polym. Int.* **2011**, *60*, 9–25.

[9] (a) G. Moad, Y. Chong, A. Postma, E. Rizzardo, S. H. Thang, *Polymer* **2005**, *46*, 8458–8468; (b) A. P. Vogt, B. S. Sumerlin, *Soft Matter* **2009**, *5*, 2347–2351; (c) X.-P. Qiu, F. M. Winnik, *Macromol. Rapid Commun.* **2006**, *27*, 1648–1653; (d) S.-S. Zhang, S.-K. Cao, S. Wang, Q.-L. Zhao, J.-Z. Chen, K. Cui, Z. Ma, *RSC Adv.* **2015**, *5*, 91140–91146.

[10] (a) Y. Wu, Y. Zhou, J. Zhu, W. Zhang, X. Pan, Z. Zhang, X. Zhu, *Polym. Chem.* **2014**, *5*, 5546–5550; (b) R. W. Lewis, R. A. Evans, N. Malic, K. Saito, N. R. Cameron, *Polym. Chem.* **2017**, *8*, 3702–3711.

[11] (a) C. L. McCormick, A. B. Lowe, *Acc. Chem. Res.* **2004**, *37*, 312–325; (b) R. Plummer, D. J. T. Hill, A. K. Whittaker, *Macromolecules* **2006**, *39*, 8379–8388.

[12] L. Petton, A. E. Ciolino, M. M. Stamenović, P. Espeel, F. E. Du Prez, *Macromol. Rapid Commun.* **2012**, *33*, 1310–1315.

[13] R. Barbey, S. Perrier, *ACS Macro Lett.* **2013**, *2*, 366–370.

[14] P. J. Roth, F. D. Jochum, R. Zentel, P. Theato, *Biomacromolecules* **2010**, *11*, 238–244.

[15] M. R. Whittaker, Y.-K. Goh, H. Gemici, T. M. Legge, S. Perrier, M. J. Monteiro, *Macromolecules* **2006**, *39*, 9028–9034.

[16] (a) Y. K. Chong, G. Moad, E. Rizzardo, S. H. Thang, *Macromolecules* **2007**, *40*, 4446–4455; (b) M. Chen, K. P. Ghiggino, E. Rizzardo, S. H. Thang, G. J. Wilson, *Chem. Commun.* **2008**, *0*, 1112–1114; (c) M. Destarac, C. Kalai, A. Wilczewska, L. Petit, E. Van Gramberen, S. Z. Zard in *Controlled/Living Radical Polymerization*, Washington, DC, USA, **2006**, Chapter 38, pp. 564–577.

[17] E. H. Discekici, S. L. Shankel, A. Anastasaki, B. Oschmann, I.-H. Lee, J. Niu, A. J. McGrath, P. G. Clark, D. S. Laitar, J. R. de Alaniz, C. J. Hawker, D. J. Lunn, *Chem. Commun.* **2017**, *53*, 1888–1891.

[18] C. P. Jesson, C. M. Pearce, H. Simon, A. Werner, V. J. Cunningham, J. R. Lovett, M. J. Smallridge, N. J. Warren, S. P. Armes, *Macromolecules* **2017**, *50*, 182–191.

[19] (a) A. Postma, T. P. Davis, G. Moad, M. S. O'Shea, *Macromolecules* **2005**, *38*, 5371–5374; (b) A. Postma, T. P. Davis, R. A. Evans, G. Li, G. Moad, M. S. O'Shea, *Macromolecules* **2006**, *39*, 5293–5306; (c) J. Xu, J. He, D. Fan, W. Tang, Y. Yang, *Macromolecules* **2006**, *39*, 3753–3759.

[20] (a) Y. Ao, J. He, X. Han, Y. Liu, X. Wang, D. Fan, J. Xu, Y. Yang, *J. Polym. Sci. Part A: Polym. Chem.* **2007**, *45*, 374–387; (b) A. Favier, B. Luneau, J. Vinas, N. Laïssaoui, D. Gigmes, D. Bertin, *Macromolecules* **2009**, *42*, 5953–5964.

[21] I.-H. Lee, E. H. Discekici, S. L. Shankel, A. Anastasaki, J. Read de Alaniz, C. J. Hawker, D. J. Lunn, *Polym. Chem.* **2017**, *8*, 7188–7194.

[22] A. J. Inglis, S. Sinnwell, T. P. Davis, C. Barner-Kowollik, M. H. Stenzel, *Macromolecules* **2008**, *41*, 4120–4126.

[23] (a) A. J. Inglis, M. H. Stenzel, C. Barner-Kowollik, *Macromol. Rapid Commun.* **2009**, *30*, 1792–1798; (b) N. K. Guimard, J. Ho, J. Brandt, C. Y. Lin, M. Namazian, J. O. Mueller, K. K. Oehlenschlaeger, S. Hilf, A. Lederer, F. G. Schmidt, M. L. Coote, C. Barner-Kowollik, *Chem. Sci.* **2013**, *4*, 2752–2759; (c) M. Langer, J. Brandt, A. Lederer, A. S. Goldmann, F. H. Schacher, C. Barner-Kowollik, *Polym. Chem.* **2014**, *5*, 5330–5338; (d) K. Pahnke, J. Brandt, G. Gryn'ova, P. Lindner, R. Schweins, F. G. Schmidt, A. Lederer, M. L. Coote, C. Barner-Kowollik, *Chem. Sci.* **2015**, *6*, 1061–1074.

[24] D. Varadharajan, G. Delaittre, *Polym. Chem.* **2016**, *7*, 7488–7499.

[25] T. Gruendling, K. K. Oehlenschlaeger, E. Frick, M. Glassner, C. Schmid, C. Barner-Kowollik, *Macromol. Rapid Commun.* **2011**, *32*, 807–812.

[26] (a) G. R. Whittell, I. Manners, *Adv. Mater.* **2007**, *19*, 3439–3468; (b) *Frontiers in Transition Metal-Containing Polymers*, 1st ed., (Eds.: A. S. Abd-El-Aziz, I. Manners), John Wiley & Sons, Inc., Hoboken, NJ, USA, **2007**, p. 533; (c) *Macromolecule-Metal Complexes*, 1st ed., (Eds.: F. Ciardelli, E. Tsuchida, D. Wöhrle), Springer-Verlag Berlin, Berlin, Germany, **1996**, p. 318.

[27] C. G. Hardy, J. Zhang, Y. Yan, L. Ren, C. Tang, *Prog. Polym. Sci.* **2014**, *39*, 1742–1796.

[28] (a) C. U. Pittman, A. Hirao, *J. Polym. Sci. Polym. Chem. Ed.* **1977**, *15*, 1677–1686; (b) C. U. Pittman, A. Hirao, *J. Polym. Sci. Polym. Chem. Ed.* **1978**, *16*, 1197–1209; (c) C. U. Pittman, C. C. Lin, *J. Polym. Sci. Polym. Chem. Ed.* **1979**, *17*, 271–275.

[29] (a) D. A. Foucher, B. Z. Tang, I. Manners, *J. Am. Chem. Soc.* **1992**, *114*, 6246–6248; (b) F. Jökle, R. Rulkens, G. Zech, J. A. Massey, I. Manners, *J. Am. Chem. Soc.* **2000**, *122*, 4231–4232; (c) R. Rulkens, D. P. Gates, D. Balaishis, J. K. Pudelski, D. F. McIntosh, A. J. Lough, I. Manners, *J. Am. Chem. Soc.* **1997**, *119*, 10976–10986.

[30] (a) M. Weck, *Polym. Int.* **2007**, *56*, 453–460; (b) R. Shunmugam, G. N. Tew, *Macromol. Rapid Commun.* **2008**, *29*, 1355–1362.

[31] M. Rehahn, *Acta Polym.* **1998**, *49*, 201–224.

[32] (a) M. O. Wolf, *Adv. Mater.* **2001**, *13*, 545–553; (b) M. O. Wolf, *J. Inorg. Organomet. Polym. Mater.* **2006**, *16*, 189–199.

[33] T. R. Cook, Y.-R. Zheng, P. J. Stang, *Chem. Rev.* **2013**, *113*, 734–777.

[34] (a) C. Ulbricht, C. R. Becer, A. Winter, D. Veldman, U. S. Schubert, *Macromol. Rapid Commun.* **2008**, *29*, 1919–1925; (b) C. Feng, Z. Shen, D. Yang, Y. Li, J. Hu, G. Lu, X. Huang, *J. Polym. Sci. Part A: Polym. Chem.* **2009**, *47*, 4346–4357; (c) S. Zhai, J. Shang, D. Yang, S. Wang, J. Hu, G. Lu, X. Huang, *J. Polym. Sci. Part A: Polym. Chem.* **2012**, *50*, 811–820; (d) C. G. Hardy, L. Ren, T. C.

Tamboue, C. Tang, *J. Polym. Sci. Part A: Polym. Chem.* **2011**, *49*, 1409–1420; (e) C. G. Hardy, L. Ren, S. Ma, C. Tang, *Chem. Commun.* **2013**, *49*, 4373–4375; (f) Y. Yan, J. Zhang, Y. Qiao, M. Ganewatta, C. Tang, *Macromolecules* **2013**, *46*, 8816–8823.

[35] (a) A. Wild, K. Babiuch, M. König, A. Winter, M. D. Hager, M. Gottschaldt, A. Prokop, U. S. Schubert, *Chem. Commun.* **2012**, *48*, 6357–6359; (b) M. Baumert, J. Fröhlich, M. Stieger, H. Frey, R. Mülhaupt, H. Plenio, *Macromol. Rapid Commun.* **1999**, *20*, 203–209; (c) L. A. Mîinea, L. B. Sessions, K. D. Ericson, D. S. Glueck, R. B. Grubbs, *Macromolecules* **2004**, *37*, 8967–8972; (d) L. B. Sessions, L. A. Mîinea, K. D. Ericson, D. S. Glueck, R. B. Grubbs, *Macromolecules* **2005**, *38*, 2116–2121; (e) C. Ott, C. Ulbricht, R. Hoogenboom, U. S. Schubert, *Macromol. Rapid Commun.* **2012**, *33*, 556–561; (f) D. A. Poulsen, B. J. Kim, B. Ma, C. S. Zonte, J. M. J. Fréchet, *Adv. Mater.* **2010**, *22*, 77–82; (g) P. T. Furuta, L. Deng, S. Garon, M. E. Thompson, J. M. J. Fréchet, *J. Am. Chem. Soc.* **2004**, *126*, 15388–15389.

[36] A. M. Breul, J. Schöfer, E. Altuntas, M. D. Hager, A. Winter, B. Dietzek, J. Popp, U. S. Schubert, *J. Inorg. Organomet. Polym. Mater.* **2013**, *23*, 74–80.

[37] (a) A. M. Breul, I. Rabelo de Moraes, R. Menzel, M. Pfeffer, A. Winter, M. D. Hager, S. Rau, B. Dietzek, R. Beckert, U. S. Schubert, *Polym. Chem.* **2014**, *5*, 2715–2724; (b) B. Happ, J. Kübel, M. G. Pfeffer, A. Winter, M. D. Hager, B. Dietzek, S. Rau, U. S. Schubert, *Macromol. Rapid Commun.* **2015**, *36*, 671–677; (c) B. Happ, C. Friebe, A. Winter, M. D. Hager, U. S. Schubert, *Eur. Polym. J.* **2009**, *45*, 3433–3441.

[38] C. Ulbricht, C. R. Becer, A. Winter, U. S. Schubert, *Macromol. Rapid Commun.* **2010**, *31*, 827–833.

[39] S. Bode, R. K. Bose, S. Matthes, M. Ehrhardt, A. Seifert, F. H. Schacher, R. M. Paulus, S. Stumpf, B. Sandmann, J. Vitz, A. Winter, S. Hoeppener, S. J. Garcia, S. Spange, S. van der Zwaag, M. D. Hager, U. S. Schubert, *Polym. Chem.* **2013**, *4*, 4966–4973.

[40] (a) M. Shi, A.-L. Li, H. Liang, J. Lu, *Macromolecules* **2007**, *40*, 1891–1896; (b) Z.-P. Xiao, Z.-H. Cai, H. Liang, J. Lu, *J. Mater. Chem.* **2010**, *20*, 8375–8381.

[41] J. Zhang, L. Ren, C. G. Hardy, C. Tang, *Macromolecules* **2012**, *45*, 6857–6863.

[42] B. Happ, J. Schäfer, R. Menzel, M. D. Hager, A. Winter, J. Popp, R. Beckert, B. Dietzek, U. S. Schubert, *Macromolecules* **2011**, *44*, 6277–6287.

[43] V. Balzani, P. Ceroni, A. Juris, *Photochemistry and photophysics: concepts, research, applications*, 1st ed., Wiley-VCH Verlag GmbH & Co. KGaA, Weinheim, Germany, **2014**, p. 502.

[44] (a) G. Ciamician, *Science* **1912**, *36*, 385–394; (b) A. Albini, M. Fagnoni, *ChemSusChem* **2008**, *1*, 63–66.

[45] (a) C. H. Bamford, R. G. W. Norrish, *J. Chem. Soc.* **1938**, *0*, 1544–1554; (b) R. G. W. Norrish, M. E. S. Appleyard, *J. Chem. Soc.* **1934**, *0*, 874–880.

[46] P. Klán, J. Wirz, *Photochemistry of Organic Compounds: From Concepts to Practice*, 1st ed., John Wiley & Sons, Ltd, Chichester, UK, **2009**, p. 582.

[47] M. Born, R. Oppenheimer, *Ann. Phys.* **1927**, *389*, 457–484.

[48] (a) J. Franck, E. G. Dymond, *Trans. Faraday Soc.* **1926**, *21*, 536–542; (b) E. Condon, *Phys. Rev.* **1926**, *28*, 1182–1201; (c) E. U. Condon, *Phys. Rev.* **1928**, *32*, 858–872.

[49] J. M. Hollas, *Modern spectroscopy*, 4th ed., John Wiley & Sons, Inc., Chichester, England, **2004**, p. 452.

[50] A. Jablonski, *Nature* **1933**, *131*, 839–840.

[51] M. Kasha, *Discuss. Faraday Soc.* **1950**, *9*, 14–19.

[52] J. Fritzsche, *Compt. Rend. Acad. Sci.* **1867**, *69*, 1035–1037.

[53] *Organic Photochromic and Thermochromic Compounds, Volume 1: Main Photochromic Families*, 1st ed., (Eds.: J. C. Crano, R. J. Guglielmetti), Kluwer Academic Publishers, New York, USA, **2002**, p. 378.

[54] Y. Hirshberg, *Compt. Rend. Acad. Sci.* **1950**, *231*, 903.

[55] H. Bouas-Laurent, H. Dürr, *Pure Appl. Chem.* **2001**, *73*, 639–665.

[56] M. M. Lerch, W. Szymański, B. L. Feringa, *Chem. Soc. Rev.* **2018**, *47*, 1910–1937.

[57] M. Kathan, S. Hecht, *Chem. Soc. Rev.* **2017**, *46*, 5536–5550.

[58] M. Irie, *Chem. Rev.* **2000**, *100*, 1685–1716.

[59] Y. Yokoyama, T. Gushiken, T. Ubukata in *Molecular Switches*, (Eds.: B. L. Feringa, W. R. Browne), Wiley-VCH Verlag GmbH & Co. KGaA, Weinheim, Germany, **2011**, pp. 81–95.

[60] H. M. D. Bandara, S. C. Burdette, *Chem. Soc. Rev.* **2012**, *41*, 1809–1825.

[61] F. Pina, J. Parola, R. Gomes, M. Maestri, V. Balzani in *Molecular Switches*, (Eds.: B. L. Feringa, W. R. Browne), Wiley-VCH Verlag GmbH & Co. KGaA, Weinheim, Germany, **2011**, pp. 181–226.

[62] (a) V. I. Minkin in *Molecular Switches*, (Eds.: B. L. Feringa, W. R. Browne), Wiley-VCH Verlag GmbH & Co. KGaA, Weinheim, Germany, **2011**, pp. 37–80; (b) V. I. Minkin, *Russ. Chem. Rev.* **2013**, *82*, 1–26; (c) R. Klajn, *Chem. Soc. Rev.* **2014**, *43*, 148–184; (d) V. I. Minkin, *Chem. Rev.* **2004**, *104*, 2751–2776.

[63] (a) Y. Hirshberg, E. Fischer, *J. Chem. Soc.* **1953**, *0*, 629–636; (b) Y. Hirshberg, E. Fischer, *J. Chem. Phys.* **1953**, *21*, 1619–1620; (c) Y. Hirshberg, E. Fischer, *J. Chem. Phys.* **1955**, *23*, 1723–1723.

[64] (a) Q. Shen, Y. Cao, S. Liu, M. L. Steigerwald, X. Guo, *J. Phys. Chem. C* **2009**, *113*, 10807–10812; (b) M. Levitus, G. Glasser, D. Neher, P. F. Aramendía, *Chem. Phys. Lett.* **1997**, *277*, 118–124; (c) M. Bletz, U. Pfeifer-Fukumura, U. Kolb, W. Baumann, *J. Phys. Chem. A* **2002**, *106*, 2232–2236.

[65] J. Chen, F. Zeng, S. Wu, *ChemPhysChem* **2010**, *11*, 1036–1043.

[66] A. A. García, S. Cherian, J. Park, D. Gust, F. Jahnke, R. Rosario, *J. Phys. Chem. A* **2000**, *104*, 6103–6107.

[67] *Photochromism*, 2nd ed., (Eds.: H. Dürr, H. Bouas-Laurent), Elsevier BV., Amsterdam, The Netherlands, **2003**, p. 1218.

[68] (a) F. M. Raymo, S. Giordani, *J. Am. Chem. Soc.* **2001**, *123*, 4651–4652; (b) J. T. C. Wojtyk, A. Wasey, N.-N. Xiao, P. M. Kazmaier, S. Hoz, C. Yu, R. P. Lemieux, E. Buncel, *J. Phys. Chem. A* **2007**, *111*, 2511–2516; (c) S.-R. Keum, K.-B. Lee, P. M. Kazmaier, E. Buncel, *Tetrahedron Lett.* **1994**, *35*, 1015–1018.

[69] R. Rosario, D. Gust, M. Hayes, F. Jahnke, J. Springer, A. A. Garcia, *Langmuir* **2002**, *18*, 8062–8069.

[70] (a) C. Lenoble, R. S. Becker, *J. Phys. Chem.* **1986**, *90*, 62–65; (b) D. A. Parthenopoulos, P. M. Rentzepis, *Science* **1989**, *245*, 843–845.

[71] K. Wagner, R. Byrne, M. Zanoni, S. Gambhir, L. Dennany, R. Breukers, M. Higgins, P. Wagner, D. Diamond, G. G. Wallace, D. L. Officer, *J. Am. Chem. Soc.* **2011**, *133*, 5453–5462.

[72] H. Görner, *Phys. Chem. Chem. Phys.* **2001**, *3*, 416–423.

[73] (a) S. Konorov, A. Zheltikov, *Opt. Express* **2003**, *11*, 2440–2445; (b) O. Ivashenko, J. T. van Herpt, B. L. Feringa, P. Rudolf, W. R. Browne, *Langmuir* **2013**, *29*,

4290–4297; (c) M. C. George, A. Mohraz, M. Piech, N. S. Bell, J. A. Lewis, P. V. Braun, *Adv. Mater.* **2009**, *21*, 66–70; (d) A. S. Dvornikov, J. Malkin, P. M. Rentzepis, *J. Phys. Chem.* **1994**, *98*, 6746–6752.

[74] (a) Z. Tian, W. Wu, W. Wan, A. D. Q. Li, *J. Am. Chem. Soc.* **2011**, *133*, 16092–16100; (b) S. Krysanov, M. Alfimov, *Chem. Phys. Lett.* **1982**, *91*, 77–80; (c) M. Irie, A. Menju, K. Hayashi, *Macromolecules* **1979**, *12*, 1176–1180; (d) J. Whelan, D. Abdallah, J. Wojtyk, E. Buncel, *J. Mater. Chem.* **2010**, *20*, 5727–5735.

[75] (a) C. P. McCoy, L. Donnelly, D. S. Jones, S. P. Gorman, *Tetrahedron Lett.* **2007**, *48*, 657–661; (b) S. Samanta, J. Locklin, *Langmuir* **2008**, *24*, 9558–9565.

[76] (a) V. A. Krongauz, E. S. Goldburt, *Nature* **1978**, *271*, 43–45; (b) M. Matsumoto, T. Nakazawa, R. Azumi, H. Tachibana, Y. Yamanaka, H. Sakai, M. Abe, *J. Phys. Chem. B* **2002**, *106*, 11487–11491; (c) T. Seki, K. Ichimura, E. Ando, *Langmuir* **1988**, *4*, 1068–1069; (d) P. Uznanski, *Langmuir* **2003**, *19*, 1919–1922; (e) Y. Unuma, A. Miyata, *Thin Solid Films* **1989**, *179*, 497–502.

[77] (a) I. Cabrera, V. Krongauz, *Macromolecules* **1987**, *20*, 2713–2717; (b) E. Goldburt, V. Krongauz, *Macromolecules* **1986**, *19*, 246–247; (c) E. Goldburt, F. Shvartsman, S. Fishman, V. Krongauz, *Macromolecules* **1984**, *17*, 1225–1230.

[78] (a) H. Tomioka, T. Itoh, *J. Chem. Soc. Chem. Commun.* **1991**, *0*, 532–533; (b) Y. Wu, C. Zhang, X. Qu, Z. Liu, Z. Yang, *Langmuir* **2010**, *26*, 9442–9448.

[79] (a) V. A. Krongauz, *Isr. J. Chem.* **1979**, *18*, 304–311; (b) V. D. Arsenov, V. S. Marevtsev, M. I. Cherkashin, *Bull. Acad. Sci. USSR Div. Chem. Sci.* **1984**, *33*, 1806–1809; (c) V. D. Arsenov, A. A. Parshutkin, V. S. Marevtsev, M. I. Cherkashin, *Bull. Acad. Sci. USSR Div. Chem. Sci.* **1984**, *33*, 1799–1806; (d) V. Krongauz, J. Kiwi, M. Grötzel, *J. Photochem.* **1980**, *13*, 89–97.

[80] T. Seki, K. Ichimura, *J. Phys. Chem.* **1990**, *94*, 3769–3775.

[81] H. Eckhardt, A. Bose, V. Krongauz, *Polymer* **1987**, *28*, 1959–1964.

[82] (a) E. Goldburt, F. Shvartsman, V. Krongauz, *Macromolecules* **1984**, *17*, 1876–1878; (b) Y. Kalisky, D. J. Williams, *Macromolecules* **1984**, *17*, 292–296.

[83] N. S. Bell, M. Piech, *Langmuir* **2006**, *22*, 1420–1427.

[84] (a) J. D. Winkler, K. Deshayes, B. Shao, *J. Am. Chem. Soc.* **1989**, *111*, 769–770; (b) J.-W. Zhou, Y.-T. Li, X.-Q. Song, *J. Photochem. Photobiol. A* **1995**, *87*, 37–42.

[85] T. Suzuki, T. Kato, H. Shinozaki, *Chem. Commun.* **2004**, *0*, 2036–2037.

[86] L. Taylor, J. Nicholson, R. Davis, *Tetrahedron Lett.* **1967**, *8*, 1585–1588.

[87] (a) J. D. Winkler, C. M. Bowen, V. Michelet, *J. Am. Chem. Soc* **1998**, *120*, 3237–3242; (b) L. Evans, G. E. Collins, R. E. Shaffer, V. Michelet, J. D. Winkler, *Anal. Chem.* **1999**, *71*, 5322–5327; (c) G. E. Collins, L.-S. Choi, K. J. Ewing, V. Michelet, C. M. Bowen, J. D. Winkler, *Chem. Commun.* **1999**, *0*, 321–322.

[88] (a) N. A. Voloshin, A. V. Chernyshev, S. O. Bezuglyi, A. V. Metelitsa, E. N. Voloshina, V. I. Minkin, *Russ. Chem. Bull.* **2008**, *57*, 151–158; (b) A. V. Chernyshev, N. A. Voloshin, I. M. Raskita, A. V. Metelitsa, V. I. Minkin, *J. Photochem. Photobiol. A* **2006**, *184*, 289–297; (c) M. I. Zakharova, C. Coudret, V. Pimienta, J. C. Micheau, S. Delbaere, G. Vermeersch, A. V. Metelitsa, N. Voloshin, V. I. Minkin, *Photochem. Photobiol. Sci.* **2010**, *9*, 199–207.

[89] (a) K. Kimura, M. Kaneshige, T. Yamashita, M. Yokoyama, *J. Org. Chem.* **1994**, *59*, 1251–1256; (b) K. Kimura, H. Tokuhisa, M. Kaneshige, T. Yamashita, M. Yokoyama,

Mol. Cryst. Liq. Cryst. Sci. Technol. Sect. A. Mol. Cryst. Liq. Cryst. **1994**, *246*, 173–176.

[90] K. Kimura, H. Sakamoto, M. Nakamura, *Bull. Chem. Soc. Jpn.* **2003**, *76*, 225–245.

[91] M. Baldrighi, G. Locatelli, J. Desper, C. B. Aakeröy, S. Giordani, *Chem. Eur. J.* **2016**, *22*, 13976–13984.

[92] P. Selvanathan, V. Dorcet, T. Roisnel, K. Bernot, G. Huang, B. Le Guennic, L. Norel, S. Rigaut, *Dalton Trans.* **2018**, *47*, 4139–4148.

[93] T. Suzuki, Y. Hirahara, K. Bunya, H. Shinozaki, *J. Mater. Chem.* **2010**, *20*, 2773–2779.

[94] (a) R. Byrne, C. Ventura, F. Benito Lopez, A. Walther, A. Heise, D. Diamond, *Biosens. Bioelectron.* **2010**, *26*, 1392–1398; (b) C. Ventura, R. Byrne, F. Audouin, A. Heise, *J. Polym. Sci. Part A: Polym. Chem.* **2011**, *49*, 3455–3463.

[95] (a) K. H. Fries, J. D. Driskell, S. Samanta, J. Locklin, *Anal. Chem.* **2010**, *82*, 3306–3314; (b) K. H. Fries, J. D. Driskell, G. R. Sheppard, J. Locklin, *Langmuir* **2011**, *27*, 12253–12260.

[96] (a) *Photochemical Key Steps in Organic Synthesis*, (Eds.: J. Mattay, A. G. Griesbeck), Wiley-VCH Verlag GmbH, Weinheim, Germany, **1994**, p. 350; (b) N. Hoffmann, *Chem. Rev.* **2008**, *108*, 1052–1103; (c) *CRC handbook of organic photochemistry and photobiology*, 3rd ed., (Eds.: A. G. Griesbeck, M. Oelgemöller, F. Ghetti), CRC Press Taylor & Francis Group, Boca Raton, USA, **2012**, p. 1607.

[97] (a) K. Ichimura in *Organic Photochromic Thermochromic Compounds*, (Eds.: J. C. Crano, R. Guglielmetti), Kluwer Academic/Plenum Publishers, New York, USA, **1999**, Chapter 1, pp. 9–63; (b) *Dyes and Chromophores in Polymer Science*, 1st ed., (Eds.: J. Lalevée, J.-P. Fouassier), John Wiley & Sons, Inc., Hoboken, USA, **2015**, p. 451.

[98] (a) T. K. Claus, S. Telitel, A. Welle, M. Bastmeyer, A. P. Vogt, G. Delaittre, C. Barner-Kowollik, *Chem. Commun.* **2017**, *53*, 1599–1602; (b) P. Lederhose, D. Abt, A. Welle, R. Müller, C. Barner-Kowollik, J. P. Blinco, *Chem. Eur. J.* **2018**, *24*, 576–580.

[99] E. Blasco, M. Wegener, C. Barner-Kowollik, *Adv. Mater.* **2017**, *29*, 1604005.

[100] C. Barner-Kowollik, M. Bastmeyer, E. Blasco, G. Delaittre, P. Müller, B. Richter, M. Wegener, *Angew. Chem. Int. Ed.* **2017**, *56*, 15828–15845.

[101] (a) S. Arumugam, S. V. Orski, N. E. Mbua, C. McNitt, G.-J. Boons, J. Locklin, V. V. Popik, *Pure Appl. Chem.* **2013**, *85*, 1499–1513; (b) M. A. Tasdelen, Y. Yagci, *Angew. Chem. Int. Ed.* **2013**, *52*, 5930–5938.

[102] (a) P. Lederhose, Z. Chen, R. Müller, J. P. Blinco, S. Wu, C. Barner-Kowollik, *Angew. Chem. Int. Ed.* **2016**, *55*, 12195–12199; (b) J. T. Offenloch, M. Gernhardt, J. P. Blinco, H. Frisch, H. Mutlu, C. Barner-Kowollik, *Chem. Eur. J.* **2019**, *25*, 3700–3709.

[103] T. Sasaki, K. Kanematsu, K. Iizuka, *J. Org. Chem.* **1976**, *41*, 1105–1112.

[104] T. Pauloehrl, A. Welle, M. Bruns, K. Linkert, H. G. Börner, M. Bastmeyer, G. Delaittre, C. Barner-Kowollik, *Angew. Chem. Int. Ed.* **2013**, *52*, 9714–9718.

[105] P. Klán, T. Šolomek, C. G. Bochet, A. Blanc, R. Givens, M. Rubina, V. Popik, A. Kostikov, J. Wirz, *Chem. Rev.* **2013**, *113*, 119–191.

[106] T. Pauloehrl, G. Delaittre, M. Bruns, M. Meißler, H. G. Börner, M. Bastmeyer, C. Barner-Kowollik, *Angew. Chem. Int. Ed.* **2012**, *51*, 9181–9184.

[107] (a) A. W. Gann, J. W. Amoroso, V. J. Einck, W. P. Rice, J. J. Chambers, N. A. Schnarr, *Org. Lett.* **2014**, *16*, 2003–2005; (b) D. Chang, D. Zhu, L. Shi, *J. Org. Chem.*

2015, *80*, 5928–5933; (c) J. Torres-Alacan, *J. Org. Chem.* **2016**, *81*, 1151–1156.

[108] (a) R. W. Van De Water, T. R. Pettus, *Tetrahedron* **2002**, *58*, 5367–5405; (b) *Quinone Methides*, 1st ed., (Ed.: S. E. Rokita), John Wiley & Sons, Inc., Hoboken, USA, **2009**, p. 431.

[109] S. Arumugam, V. V. Popik, *J. Am. Chem. Soc.* **2011**, *133*, 15730–15736.

[110] H. Wang, Y. Wang, K.-L. Han, X.-J. Peng, *J. Org. Chem.* **2005**, *70*, 4910–4917.

[111] A. A. Poloukhtine, N. E. Mbua, M. A. Wolfert, G.-J. Boons, V. V. Popik, *J. Am. Chem. Soc.* **2009**, *131*, 15769–15776.

[112] R. K. V. Lim, Q. Lin, *Chem. Commun.* **2010**, *46*, 7993.

[113] J. O. Mueller, F. G. Schmidt, J. P. Blinco, C. Barner-Kowollik, *Angew. Chem. Int. Ed.* **2015**, *54*, 10284–10288.

[114] H. Frisch, D. E. Marschner, A. S. Goldmann, C. Barner-Kowollik, *Angew. Chem. Int. Ed.* **2018**, *57*, 2036–2045.

[115] Y. Chen, J.-D. Wu, *J. Polym. Sci. Part A: Polym. Chem.* **1994**, *32*, 1867–1875.

[116] (a) N. Kovalenko, A. Abdukadyrov, V. Gerko, M. Alfimov, *J. Photochem.* **1980**, *12*, 59–65; (b) N. P. Kovalenko, A. Abdukadirov, V. I. Gerko, M. V. Alfimov, *J. Appl. Spectrosc.* **1980**, *32*, 607–612.

[117] (a) V. X. Truong, F. Li, F. Ercole, J. S. Forsythe, *ACS Macro Lett.* **2018**, *7*, 464–469; (b) D. E. Marschner, H. Frisch, J. T. Offenloch, B. T. Tuten, C. R. Becer, A. Walther, A. S. Goldmann, P. Tzvetkova, C. Barner-Kowollik, *Macromolecules* **2018**, *51*, 3802–3807.

[118] F. Fages, J.-P. Desvergne, I. Frisch, H. Bouas-Laurent, *J. Chem. Soc. Chem. Commun.* **1988**, *0*, 1413–1415.

[119] P. G. Frank, B. T. Tuten, A. Prasher, D. Chao, E. B. Berda, *Macromol. Rapid Commun.* **2014**, *35*, 249–253.

[120] (a) K. Rameshbabu, Y. Kim, T. Kwon, J. Yoo, E. Kim, *Tetrahedron Lett.* **2007**, *48*, 4755–4760; (b) P. Payamyar, M. Servalli, T. Hungerland, A. P. Schütz, Z. Zheng, A. Borgschulte, A. D. Schlüter, *Macromol. Rapid Commun.* **2015**, *36*, 151–158.

[121] A. R. Smith, D. F. Watson, *Chem. Mater.* **2010**, *22*, 294–304.

[122] R. Okazaki in *Organosulfur Chemistry, Vol. 1*, (Ed.: P. Page), Academic Press, **1995**, Chapter 5, pp. 225–258.

[123] W. M. McGregor, D. C. Sherrington, *Chem. Soc. Rev.* **1993**, *22*, 199–204.

[124] M. Glassner, K. K. Oehlenschlaeger, A. Welle, M. Bruns, C. Barner-Kowollik, *Chem. Commun.* **2013**, *49*, 633–635.

[125] J. E. Baldwin, R. C. G. Lopez, *J. Chem. Soc. Chem. Commun.* **1982**, 1029–1030.

[126] E. Vedejs, D. A. Perry, *J. Am. Chem. Soc.* **1983**, *105*, 1683–1684.

[127] H. G. Giles, R. A. Marty, P. D. Mayo, *Can. J. Chem.* **1976**, *54*, 537–542.

[128] (a) M. C. Caserio, W. Lauer, T. Novinson, *J. Am. Chem. Soc.* **1970**, *92*, 6082–6084; (b) A. E.-A. M. Gaber, *Phosphorus. Sulfur. Silicon Relat. Elem.* **1997**, *129*, 135–145.

[129] C. Chatgilialoglu, D. Crich, M. Komatsu, I. Ryu, *Chem. Rev.* **1999**, *99*, 1991–2070.

[130] (a) B. M. Trost, *J. Am. Chem. Soc.* **1967**, *89*, 138–142; (b) E. Vedejs, T. H. Eberlein, D. J. Mazur, C. K. McClure, D. A. Perry, R. Ruggeri, E. Schwartz, J. S. Stults, D. L. Varie, *J. Org. Chem.* **1986**, *51*, 1556–1562; (c) E. Vedejs, T. H. Eberlein, D. L. Varie, *J. Am. Chem. Soc.* **1982**, *104*, 1445–1447.

[131] P. J. Wagner, M. J. Lindstrom, *J. Am. Chem. Soc.* **1987**, *109*, 3062–3067.

[132] T. Pauloehrl, A. Welle, K. K. Oehlenschlaeger, C. Barner-Kowollik, *Chem. Sci.* **2013**, *4*, 3503–3507.

[133] G. W. Kirby, *Phosphorus. Sulfur. Silicon Relat. Elem.* **1993**, *74*, 17–29.

[134] E. Vedejs, S. Fields, *J. Org. Chem.* **1988**, *53*, 4663–4667.

[135] S. S.-M. Choi, G. W. Kirby, *J. Chem. Soc. Perkin Trans. 1* **1991**, *0*, 3225–3233.

[136] G. Opitz, *Angew. Chem. Int. Ed.* **1967**, *6*, 107–123.

[137] G. Hofstra, J. Kamphuis, H. Bos, *Tetrahedron Lett.* **1984**, *25*, 873–876.

[138] B. T. Tuten, J. P. Menzel, K. Pahnke, J. P. Blinco, C. Barner-Kowollik, *Chem. Commun.* **2017**, *53*, 4501–4504.

[139] (a) M. Kaupp, A. S. Quick, C. Rodriguez-Emmenegger, A. Welle, V. Trouillet, O. Pop-Georgievski, M. Wegener, C. Barner-Kowollik, *Adv. Funct. Mater.* **2014**, *24*, 5649–5661; (b) O. Altintas, M. Glassner, C. Rodriguez-Emmenegger, A. Welle, V. Trouillet, C. Barner-Kowollik, *Angew. Chem. Int. Ed.* **2015**, *54*, 5777–5783.

[140] N. Zydziak, F. Feist, B. Huber, J. O. Mueller, C. Barner-Kowollik, *Chem. Commun.* **2015**, *51*, 1799–1802.

[141] T. Tischer, T. K. Claus, K. K. Oehlenschlaeger, V. Trouillet, M. Bruns, A. Welle, K. Linkert, A. S. Goldmann, H. G. Börner, C. Barner-Kowollik, *Macromol. Rapid Commun.* **2014**, *35*, 1121–1127.

[142] T. K. Claus, J. Zhang, L. Martin, M. Hartlieb, H. Mutlu, S. Perrier, G. Delaittre, C. Barner-Kowollik, *Macromol. Rapid Commun.* **2017**, *38*, 1700264.

[143] T. K. Claus, B. Richter, V. Hahn, A. Welle, S. Kayser, M. Wegener, M. Bastmeyer, G. Delaittre, C. Barner-Kowollik, *Angew. Chem. Int. Ed.* **2016**, *55*, 3817–3822.

[144] C. Lang, S. Bestgen, A. Welle, R. Müller, P. W. Roesky, C. Barner-Kowollik, *Chem. Eur. J.* **2015**, *21*, 14728–14731.

[145] J. S. Clovis, A. Eckell, R. Huisgen, R. Sustmann, *Chem. Ber.* **1967**, *100*, 60–70.

[146] A. Padwa, M. Dharan, J. Smolanoff, S. I. Wetmore, *J. Am. Chem. Soc.* **1973**, *95*, 1945–1954.

[147] P. Lederhose, K. N. R. Wüst, C. Barner-Kowollik, J. P. Blinco, *Chem. Commun.* **2016**, *52*, 5928–5931.

[148] J. Willenbacher, K. N. R. Wuest, J. O. Mueller, M. Kaupp, H.-A. Wagenknecht, C. Barner-Kowollik, *ACS Macro Lett.* **2014**, *3*, 574–579.

[149] R. Darkow, U. Hartmann, G. Tomaschewski, *React. Funct. Polym.* **1997**, *32*, 195–207.

[150] Z. Li, L. Qian, L. Li, J. C. Bernhammer, H. V. Huynh, J.-S. Lee, S. Q. Yao, *Angew. Chem. Int. Ed.* **2016**, *55*, 2002–2006.

[151] (a) R. Huisgen, J. Sauer, M. Seidel, *Chem. Ber.* **1961**, *94*, 2503–2509; (b) R. Huisgen, R. Grashey, M. Seidel, H. Knupfer, R. Schmidt, *Justus Liebigs Ann. Chem.* **1962**, *658*, 169–180.

[152] W. Feng, L. Li, C. Yang, A. Welle, O. Trapp, P. A. Levkin, *Angew. Chem. Int. Ed.* **2015**, *54*, 8732–8735.

[153] Y. Wang, C. I. Rivera Vera, Q. Lin, *Org. Lett.* **2007**, *9*, 4155–4158.

[154] W. Song, Y. Wang, J. Qu, Q. Lin, *J. Am. Chem. Soc.* **2008**, *130*, 9654–9655.

[155] W. Song, Y. Wang, J. Qu, M. M. Madden, Q. Lin, *Angew. Chem. Int. Ed.* **2008**, *47*, 2832–2835.

[156] W. Song, Y. Wang, Z. Yu, C. I. R. Vera, J. Qu, Q. Lin, *ACS Chem. Biol.* **2010**, *5*, 875–885.

[157] (a) M. Merkel, K. Peewasan, S. Arndt, D. Ploschik, H.-A. Wagenknecht, *ChemBioChem* **2015**, *16*, 1541–1553; (b) M. Merkel, S. Arndt, D. Ploschik, G. B. Cserép, U. Wenge, P. Kele, H.-A. Wagenknecht, *J. Org. Chem.* **2016**, *81*, 7527–7538; (c) B. Lehmann, H.-A. Wagenknecht, *Org. Biomol. Chem.* **2018**, *16*, 7579–7582.

[158] E. Blasco, Y. Sugawara, P. Lederhose, J. P. Blinco, A.-M. Kelterer, C. Barner-

Kowollik, *ChemPhotoChem* **2017**, *1*, 159–163.

[159] P. An, Z. Yu, Q. Lin, *Chem. Commun.* **2013**, *49*, 9920–9922.

[160] C. Rodriguez-Emmenegger, C. M. Preuss, B. Yameen, O. Pop-Georgievski, M. Bachmann, J. O. Mueller, M. Bruns, A. S. Goldmann, M. Bastmeyer, C. Barner-Kowollik, *Adv. Mater.* **2013**, *25*, 6123–6127.

[161] (a) M. Dietrich, G. Delaittre, J. P. Blinco, A. J. Inglis, M. Bruns, C. Barner-Kowollik, *Adv. Funct. Mater.* **2012**, *22*, 304–312; (b) T. Tischer, C. Rodriguez-Emmenegger, V. Trouillet, A. Welle, V. Schueler, J. O. Mueller, A. S. Goldmann, E. Brynda, C. Barner-Kowollik, *Adv. Mater.* **2014**, *26*, 4087–4092; (c) A. Hufendiek, A. Carlmark, M. A. R. Meier, C. Barner-Kowollik, *ACS Macro Lett.* **2016**, *5*, 139–143; (d) D. Hoenders, J. Guo, A. S. Goldmann, C. Barner-Kowollik, A. Walther, *Mater. Horizons* **2018**, *5*, 560–568.

[162] E. Blasco, M. Piñol, L. Oriol, B. V. K. J. Schmidt, A. Welle, V. Trouillet, M. Bruns, C. Barner-Kowollik, *Adv. Funct. Mater.* **2013**, *23*, 4011–4019.

[163] T. Gegenhuber, D. Abt, A. Welle, S. özbek, A. S. Goldmann, C. Barner-Kowollik, *J. Mater. Chem. B* **2017**, *5*, 4993–5000.

[164] (a) J. L. Charlton, M. Alauddin, *Tetrahedron* **1987**, *43*, 2873–2889; (b) J. L. Segura, N. Martín, *Chem. Rev.* **1999**, *99*, 3199–246.

[165] N. C. Yang, C. Rivas, *J. Am. Chem. Soc.* **1961**, *83*, 2213–2213.

[166] P. G. Sammes, *Tetrahedron* **1976**, *32*, 405–422.

[167] P. Klán, J. Wirz, A. D. Gudmundsdottir, *Photoenolization and Its Applications*, 3. ed., (Eds.: A. G. Griesbeck, G. Francesco, M. Oelgemöller), CRC Press/-Taylor & Francis, Boca Raton, USA, **2012**, Chapter 26, p. 1694.

[168] (a) G. Porter, M. F. Tchir, *J. Chem. Soc. D* **1970**, *0*, 1372; (b) G. Porter, M. F. Tchir, *J. Chem. Soc. A* **1971**, *0*, 3772–3777.

[169] (a) L. Dell'Amico, A. Vega-Peñaloza, S. Cuadros, P. Melchiorre, *Angew. Chem. Int. Ed.* **2016**, *55*, 3313–3317; (b) S. Cuadros, P. Melchiorre, *Eur. J. Org. Chem.* **2018**, *2018*, 2884–2891.

[170] D. W. C. MacMillan, *Nature* **2008**, *455*, 304–308.

[171] T. Pauloehrl, G. Delaittre, V. Winkler, A. Welle, M. Bruns, H. G. Börner, A. M. Greiner, M. Bastmeyer, C. Barner-Kowollik, *Angew. Chem. Int. Ed.* **2012**, *51*, 1071–1074.

[172] F. Feist, J. P. Menzel, T. Weil, J. P. Blinco, C. Barner-Kowollik, *J. Am. Chem. Soc.* **2018**, *140*, 11848–11854.

[173] D. M. Findlay, M. F. Tchir, *J. Chem. Soc. Chem. Commun.* **1974**, *0*, 514–515.

[174] N. Ishida, T. Yano, T. Yuhki, M. Murakami, *Chem. - An Asian J.* **2017**, *12*, 1905–1908.

[175] T. Krappitz, F. Feist, I. Lamparth, N. Moszner, H. John, J. P. Blinco, T. R. Dargaville, C. Barner-Kowollik, *Mater. Horizons* **2019**, *6*, 81–89.

[176] (a) G. A. Kraus, Y. Wu, *J. Org. Chem.* **1992**, *57*, 2922–2925; (b) K. C. Nicolaou, D. Gray, J. Tae, *Angew. Chem. Int. Ed.* **2001**, *40*, 3679; (c) K. C. Nicolaou, D. L. F. Gray, J. Tae, *J. Am. Chem. Soc.* **2004**, *126*, 613–627.

[177] (a) O. Altintas, J. Willenbacher, K. N. R. Wuest, K. K. Oehlenschlaeger, P. Krolla-Sidenstein, H. Gliemann, C. Barner-Kowollik, *Macromolecules* **2013**, *46*, 8092–8101; (b) E. Blasco, B. T. Tuten, H. Frisch, A. Lederer, C. Barner-Kowollik, *Polym. Chem.* **2017**, *8*, 5845–5851.

[178] N. Zydziak, W. Konrad, F. Feist, S. Afonin, S. Weidner, C. Barner-Kowollik, *Nat. Commun.* **2016**, *7*, 13672.

[179] W. Konrad, F. R. Bloesser, K. S. Wetzel, A. C. Boukis, M. A. R. Meier, C. Barner-Kowollik, *Chem. Eur. J.* **2018**, *24*, 3413–3419.

[180] L. Chen, M. Xu, J. Hu, Q. Yan, *Macromolecules* **2017**, *50*, 4276–4280.

[181] A. Kerbs, P. Mueller, M. Kaupp, I. Ahmed, A. S. Quick, D. Abt, M. Wegener, C. M. Niemeyer, C. Barner-Kowollik, L. Fruk, *Chem. Eur. J.* **2017**, *23*, 4990–4994.

[182] A. S. Quick, H. Rothfuss, A. Welle, B. Richter, J. Fischer, M. Wegener, C. Barner-Kowollik, *Adv. Funct. Mater.* **2014**, *24*, 3571–3580.

[183] P. Mueller, M. M. Zieger, B. Richter, A. S. Quick, J. Fischer, J. B. Mueller, L. Zhou, G. U. Nienhaus, M. Bastmeyer, C. Barner-Kowollik, M. Wegener, *ACS Nano* **2017**, *11*, 6396–6403.

[184] R. S. Becker, J. Kolc, *J. Phys. Chem.* **1968**, *72*, 997–1001.

[185] Y. Shiraishi, K. Tanaka, E. Shirakawa, Y. Sugano, S. Ichikawa, S. Tanaka, T. Hirai, *Angew. Chem. Int. Ed.* **2013**, *52*, 8304–8308.

[186] (a) H. Kwart, E. R. Evans, *J. Org. Chem.* **1966**, *31*, 410–413; (b) M. S. Newman, H. A. Karnes, *J. Org. Chem.* **1966**, *31*, 3980–3984; (c) G. C. Lloyd-Jones, J. D. Moseley, J. S. Renny, *Synthesis* **2008**, *3*, 661–689.

[187] S. Arakawa, H. Kondo, J. Seto, *Chem. Lett.* **1985**, *14*, 1805–1808.

[188] Y. D. Khamchukov, V. G. Luchina, V. S. Marevtsev, *Russ. Chem. Bull.* **1997**, *46*, 1094–1098.

[189] B. Lukjanow, M. Knjazschanski, J. Rewinski, L. Niworozschkin, W. Minkin, *Tetrahedron Lett.* **1973**, *14*, 2007–2010.

[190] S.-i. Tamura, N. Asai, J. Seto, *Bull. Chem. Soc. Jpn.* **1989**, *62*, 358–361.

[191] M. Hirano, K. Osakada, H. Nohira, A. Miyashita, *J. Org. Chem.* **2002**, *67*, 533–540.

[192] Y. Shiraishi, H. Tanaka, H. Sakamoto, S. Ichikawa, T. Hirai, *RSC Adv.* **2015**, *5*, 77572–77580.

[193] Z. Liu, T. Liu, Q. Lin, C. Bao, L. Zhu, *Angew. Chem. Int. Ed.* **2015**, *54*, 174–178.

[194] D. P. Nair, M. Podgórski, S. Chatani, T. Gong, W. Xi, C. R. Fenoli, C. N. Bowman, *Chem. Mater.* **2014**, *26*, 724–744.

[195] H. Zhang, F. Gao, X. Cao, Y. Li, Y. Xu, W. Weng, R. Boulatov, *Angew. Chem. Int. Ed.* **2016**, *55*, 3040–3044.

[196] S. W. Hell, J. Wichmann, *Opt. Lett.* **1994**, *19*, 780–782.

[197] S. Hell, S. Jakobs, L. Kastrup, *Appl. Phys. A Mater. Sci. Process.* **2003**, *77*, 859–860.

[198] (a) L. Li, R. R. Gattass, E. Gershgoren, H. Hwang, J. T. Fourkas, *Science* **2009**, *324*, 910–913; (b) T. F. Scott, B. A. Kowalski, A. C. Sullivan, C. N. Bowman, R. R. McLeod, *Science* **2009**, *324*, 913–917.

[199] E. Abbe, *Arch. für Mikroskopische Anat.* **1873**, *9*, 413–418.

[200] E. Rittweger, K. Y. Han, S. E. Irvine, C. Eggeling, S. W. Hell, *Nat. Photonics* **2009**, *3*, 144–147.

[201] (a) H.-B. Sun, S. Kawata in *NMR • 3D Anal. • Photopolymerization. Adv. Polym. Sci.* Springer-Verlag, Berlin, Germany, **2006**, Chapter 3, pp. 169–273; (b) *Multiphoton lithography: techniques, materials and applications*, 1st ed., (Eds.: J. Stampfl, R. Liska, A. Ovsianikov), Wiley-VCH Verlag GmbH & Co. KGaA, Weinheim, Germany, **2017**, p. 386.

[202] (a) H.-B. Sun, S. Kawata in *NMR • 3D Anal. • Photopolymerization. Adv. Polym. Sci.* Springer-Verlag, Berlin, Germany, **2006**, Chapter 3, pp. 169–273; (b) C. N. LaFratta, J. T. Fourkas, T. Baldacchini, R. A. Farrer, *Angew. Chem. Int. Ed.* **2007**, *46*, 6238–6258; (c) *Multiphoton lithography: techniques, materials and applications*, 1st ed., (Eds.: J. Stampfl, R. Liska,

A. Ovsianikov), Wiley-VCH Verlag GmbH & Co. KGaA, Weinheim, Germany, **2017**, p. 386.

[203] J. Fischer, M. Wegener, *Laser Photonics Rev.* **2013**, *7*, 22–44.

[204] (a) M. Farsari, B. N. Chichkov, *Nat. Photonics* **2009**, *3*, 450–452; (b) M. Malinauskas, M. Farsari, A. Piskarskas, S. Juodkazis, *Phys. Rep.* **2013**, *533*, 1–31.

[205] M. Deubel, G. von Freymann, M. Wegener, S. Pereira, K. Busch, C. M. Soukoulis, *Nat. Mater.* **2004**, *3*, 444–447.

[206] (a) A. M. Greiner, B. Richter, M. Bastmeyer, *Macromol. Biosci.* **2012**, *12*, 1301–1314; (b) F. Klein, B. Richter, T. Striebel, C. M. Franz, G. von Freymann, M. Wegener, M. Bastmeyer, *Adv. Mater.* **2011**, *23*, 1341–1345.

[207] B.-B. Xu, Y.-L. Zhang, H. Xia, W.-F. Dong, H. Ding, H.-B. Sun, *Lab Chip* **2013**, *13*, 1677–1690.

[208] T. Frenzel, M. Kadic, M. Wegener, *Science* **2017**, *358*, 1072–1074.

[209] M. Rezem, A. Günther, M. Rahlves, B. Roth, E. Reithmeier, *Procedia Technol.* **2016**, *26*, 517–523.

[210] (a) L. Li, R. R. Gattass, E. Gershgoren, H. Hwang, J. T. Fourkas, *Science* **2009**, *324*, 910–913; (b) T. F. Scott, B. A. Kowalski, A. C. Sullivan, C. N. Bowman, R. R. McLeod, *Science* **2009**, *324*, 913–917.

[211] T. A. Klar, S. Jakobs, M. Dyba, A. Egner, S. W. Hell, *Proc. Natl. Acad. Sci.* **2000**, *97*, 8206–8210.

[212] J. Fischer, G. von Freymann, M. Wegener, *Adv. Mater.* **2010**, *22*, 3578–3582.

[213] J. Fischer, M. Wegener, *Adv. Mater.* **2012**, *24*, OP65–OP69.

[214] T. J. A. Wolf, J. Fischer, M. Wegener, A.-N. Unterreiner, *Opt. Lett.* **2011**, *36*, 3188–3190.

[215] M. P. Stocker, L. Li, R. R. Gattass, J. T. Fourkas, *Nat. Chem.* **2011**, *3*, 223–227.

[216] K. C. Johnson, *Appl. Opt.* **2014**, *53*, J7–J18.

[217] J. Fischer, J. B. Mueller, A. S. Quick, J. Kaschke, C. Barner-Kowollik, M. Wegener, *Adv. Opt. Mater.* **2015**, *3*, 221–232.

[218] (a) J. C. Netto-Ferreira, J. C. Scaiano, *J. Am. Chem. Soc.* **1991**, *113*, 5800–5803; (b) A. P. Pelliccioli, P. Klán, M. Zabadal, J. Wirz, *J. Am. Chem. Soc.* **2001**, *123*, 7931–7932.

[219] (a) J. C. Love, L. a. Estroff, J. K. Kriebel, R. G. Nuzzo, G. M. Whitesides, *Chem. Rev.* **2005**, *105*, 1103–69; (b) A. Ulman, *Chem. Rev.* **1996**, *96*, 1533–1554.

[220] (a) P. E. Laibinis, G. M. Whitesides, D. L. Allara, Y. T. Tao, A. N. Parikh, R. G. Nuzzo, *J. Am. Chem. Soc.* **1991**, *113*, 7152–7167; (b) M. M. Walczak, C. Chung, S. M. Stole, C. A. Widrig, M. D. Porter, *J. Am. Chem. Soc.* **1991**, *113*, 2370–2378.

[221] (a) J. C. Love, D. B. Wolfe, R. Haasch, M. L. Chabinyc, K. E. Paul, G. M. Whitesides, R. G. Nuzzo, *J. Am. Chem. Soc.* **2003**, *125*, 2597–2609; (b) A. Carvalho, M. Geissler, H. Schmid, B. Michel, E. Delamarche, *Langmuir* **2002**, *18*, 2406–2412.

[222] Z. Li, S.-C. Chang, R. S. Williams, *Langmuir* **2003**, *19*, 6744–6749.

[223] N. Muskal, I. Turyan, D. Mandler, *J. Electroanal. Chem.* **1996**, *409*, 131–136.

[224] Z. Mekhalif, F. Laffineur, N. Couturier, J. Delhalle, *Langmuir* **2003**, *19*, 637–645.

[225] (a) H.-G. Chen, X.-D. Wu, Q.-Q. Yu, S.-R. Yang, D.-P. Wang, W.-Z. Seen, *Chinese J. Chem.* **2010**, *20*, 1467–1471; (b) R. Helmy, A. Y. Fadeev, *Langmuir* **2002**, *18*, 8924–8928; (c) S. Pawsey, K. Yach, L. Reven, *Langmuir* **2002**, *18*, 5205–5212.

[226] A. Y. Fadeev, R. Helmy, S. Marcinko, *Langmuir* **2002**, *18*, 7521–7529.

[227] (a) C. E. Taylor, D. K. Schwartz, *Langmuir* **2003**, *19*, 2665–2672; (b) D. L. Allara, R. G. Nuzzo, *Langmuir* **1985**, *1*, 52–

66; (c) G. Höhner, R. Hofer, I. Klingenfuss, *Langmuir* **2001**, *17*, 7047–7052.

[228] (a) T. L. Breen, P. M. Fryer, R. W. Nunes, M. E. Rothwell, *Langmuir* **2002**, *18*, 194–197; (b) Y. Koide, M. W. Such, R. Basu, G. Evmenenko, J. Cui, P. Dutta, M. C. Hersam, T. J. Marks, *Langmuir* **2003**, *19*, 86–93.

[229] W. C. Hughes, S. E. Koh, B. H. Augustine, J. M. Polefrone in Proc. Electrochem. Soc. *Vol. 2001 – 1*, **2001**, p. 213.

[230] S. Ye, G. Li, H. Noda, K. Uosaki, M. Osawa, *Surf. Sci.* **2003**, *529*, 163–170.

[231] M. R. Linford, C. E. D. Chidsey, *J. Am. Chem. Soc.* **1993**, *115*, 12631–12632.

[232] J. Gun, J. Sagiv, *J. Colloid Interface Sci.* **1986**, *112*, 457–472.

[233] (a) K. Chen, F. Xu, C. A. Mirkin, R.-K. Lo, K. S. Nanjundaswamy, J.-P. Zhou, J. T. McDevitt, *Langmuir* **1996**, *12*, 2622–2624; (b) K. Chen, C. A. Mirkin, R.-K. Lo, J. Zhao, J. T. McDevitt, *J. Am. Chem. Soc.* **1995**, *117*, 6374–6375.

[234] S. C. D'Andrea, K. Swaminathan Iyer, I. Luzinov, A. Y. Fadeev, *Colloids Surf. B* **2003**, *32*, 235–243.

[235] T. Desmet, R. Morent, N. De Geyter, C. Leys, E. Schacht, P. Dubruel, *Biomacromolecules* **2009**, *10*, 2351–2378.

[236] T. M. McIntire, S. R. Smalley, J. T. Newberg, A. S. Lea, J. C. Hemminger, B. J. Finlayson-Pitts, *Langmuir* **2006**, *22*, 5617–5624.

[237] J. M. Buriak, *Chem. Rev.* **2002**, *102*, 1271–1308.

[238] T. L. Niederhauser, Y.-Y. Lua, G. Jiang, S. D. Davis, R. Matheson, D. A. Hess, I. A. Mowat, M. R. Linford, *Angew. Chem. Int. Ed.* **2002**, *41*, 2353–2356.

[239] M. P. Stewart, F. Maya, D. V. Kosynkin, S. M. Dirk, J. J. Stapleton, C. L. McGuiness, D. L. Allara, J. M. Tour, *J. Am. Chem. Soc.* **2004**, *126*, 370–378.

[240] L. Nebhani, P. Gerstel, P. Atanasova, M. Bruns, C. Barner-Kowollik, *J. Polym. Sci. Part A: Polym. Chem.* **2009**, *47*, 7090–7095.

[241] M. Wang, K. M. Liechti, Q. Wang, J. M. White, *Langmuir* **2005**, *21*, 1848–1857.

[242] M. E. McGovern, K. M. R. Kallury, M. Thompson, *Langmuir* **1994**, *10*, 3607–3614.

[243] P. Silberzan, L. Leger, D. Ausserre, J. J. Benattar, *Langmuir* **1991**, *7*, 1647–1651.

[244] (a) S. R. Wasserman, Y. T. Tao, G. M. Whitesides, *Langmuir* **1989**, *5*, 1074–1087; (b) R. Banga, J. Yarwood, A. M. Morgan, B. Evans, J. Kells, *Langmuir* **1995**, *11*, 4393–4399.

[245] (a) K. Boschkova, J. J. R. Stålgren, *Langmuir* **2002**, *18*, 6802–6806; (b) M. Mrksich, C. S. Chen, Y. Xia, L. E. Dike, D. E. Ingber, G. M. Whitesides, *Proc. Natl. Acad. Sci.* **1996**, *93*, 10775–10778.

[246] (a) A. S. Goldstein, P. A. DiMilla, *J. Biomed. Mater. Res.* **2002**, *59*, 665–675; (b) J. T. Elliott, A. Tona, J. T. Woodward, P. L. Jones, A. L. Plant, *Langmuir* **2003**, *19*, 1506–1514; (c) X.-L. Sun, C. L. Stabler, C. S. Cazalis, E. L. Chaikof, *Bioconjug. Chem.* **2006**, *17*, 52–57.

[247] P. Brandani, P. Stroeve, *Macromolecules* **2003**, *36*, 9492–9501.

[248] M. N. Yousaf, M. Mrksich, *J. Am. Chem. Soc.* **1999**, *121*, 4286–4287.

[249] (a) I. M. Rutenberg, O. A. Scherman, R. H. Grubbs, W. Jiang, E. Garfunkel, Z. Bao, *J. Am. Chem. Soc.* **2004**, *126*, 4062–4063; (b) M. Weck, J. J. Jackiw, R. R. Rossi, P. S. Weiss, R. H. Grubbs, *J. Am. Chem. Soc.* **1999**, *121*, 4088–4089; (c) J. K. Lee, K.-B. Lee, D. J. Kim, I. S. Choi, *Langmuir* **2003**, *19*, 8141–8143.

[250] (a) W. S. Dillmore, M. N. Yousaf, M. Mrksich, *Langmuir* **2004**, *20*, 7223–7231;

(b) K. Lee, F. Pan, G. T. Carroll, N. J. Turro, J. T. Koberstein, *Langmuir* **2004**, *20*, 1812–1818.

[251] (a) R. Paul, R. Schmidt, J. Feng, D. J. Dyer, *J. Polym. Sci. Part A: Polym. Chem.* **2002**, *40*, 3284–3291; (b) R. Schmidt, T. Zhao, J.-B. Green, D. J. Dyer, *Langmuir* **2002**, *18*, 1281–1287.

[252] (a) J. P. Collman, N. K. Devaraj, C. E. D. Chidsey, *Langmuir* **2004**, *20*, 1051–1053; (b) P. Tingaut, R. Hauert, T. Zimmermann, *J. Mater. Chem.* **2011**, *21*, 16066–16076.

[253] B. T. Houseman, E. S. Gawalt, M. Mrksich, *Langmuir* **2003**, *19*, 1522–1531.

[254] B. Xin, J. Hao, *Chem. Soc. Rev.* **2010**, *39*, 769–782.

[255] O. Ostroverkhova, *Handbook of organic materials for optical and (Opto)electronic devices: properties and applications*, 1st ed., Woodhead Publishing Ltd, Cambridge, UK, **2013**, p. 832.

[256] (a) J. Xiang, C.-L. Ho, W.-Y. Wong, *Polym. Chem.* **2015**, *6*, 6905–6930; (b) S. Bellemin-Laponnaz, T. Achard, D. Bissessar, Y. Geiger, A. Maisse-François, *Coord. Chem. Rev.* **2017**, *332*, 38–47; (c) K. Y. Zhang, S. Liu, Q. Zhao, W. Huang, *Coord. Chem. Rev.* **2016**, *319*, 180–195.

[257] V. C. Romao, S. A. M. Martins, J. Germano, F. A. Cardoso, S. Cardoso, P. P. Freitas, *ACS Nano* **2017**, *11*, 10659–10664.

[258] V. V. Tarabara in *Nanotechnol. Appl. Clean Water*, (Eds.: N. Savage, J. Duncan, R. Sustich, M. Diallo, A. Street), William Andrew Inc. Published by Elsevier Inc., **2009**, Chapter 5, pp. 59–75.

[259] K. Kadimisetty, S. Malla, J. F. Rusling, *ACS Sensors* **2017**, *2*, 670–678.

[260] C. Laberty-Robert, K. Vallé, F. Pereira, C. Sanchez, *Chem. Soc. Rev.* **2011**, *40*, 961–1005.

[261] (a) P. Bertoncello, R. J. Forster, *Biosens. Bioelectron.* **2009**, *24*, 3191–3200; (b) B. Naidji, J. Husson, A. Et Taouil, E. Brunol, J.-B. Sanchez, F. Berger, J.-Y. Rauch, L. Guyard, *Synth. Met.* **2016**, *221*, 214–219.

[262] (a) C. Acikgoz, X. Y. Ling, I. Y. Phang, M. A. Hempenius, D. N. Reinhoudt, J. Huskens, G. J. Vancso, *Adv. Mater.* **2009**, *21*, 2064–2067; (b) X. Y. Ling, C. Acikgoz, I. Y. Phang, M. A. Hempenius, D. N. Reinhoudt, G. J. Vancso, J. Huskens, *Nanoscale* **2010**, *2*, 1455–1460; (c) L. Fritea, F. Haddache, B. Reuillard, A. Le Goff, K. Gorgy, C. Gondran, M. Holzinger, R. Săndulescu, S. Cosnier, *Electrochem. Commun.* **2014**, *46*, 75–78.

[263] M. Ginzburg, M. J. MacLachlan, S. M. Yang, N. Coombs, T. W. Coyle, N. P. Raju, J. E. Greedan, R. H. Herber, G. A. Ozin, I. Manners, *J. Am. Chem. Soc.* **2002**, *124*, 2625–2639.

[264] C. Acikgoz, B. Vratzov, M. A. Hempenius, G. J. Vancso, J. Huskens, *ACS Appl. Mater. Interfaces* **2009**, *1*, 2645–2650.

[265] *Functional polymer films*, 1st ed., (Eds.: W. Knoll, R. C. Advincula), Wiley-VCH Verlag & Co. KGaA, Weinheim, Germany, **2011**, p. 1080.

[266] (a) S. Edmondson, V. L. Osborne, W. T. S. Huck, *Chem. Soc. Rev.* **2004**, *33*, 14–22; (b) R. Barbey, L. Lavanant, D. Paripovic, N. Schüwer, C. Sugnaux, S. Tugulu, H.-A. Klok, *Chem. Rev.* **2009**, *109*, 5437–5527; (c) H.-A. Klok, J. Genzer, *ACS Macro Lett.* **2015**, *4*, 636–639.

[267] (a) *Polymer brushes: synthesis, characterization, applications*, 1st ed., (Eds.: R. C. Advincula, W. J. Brittain, K. C. Caster, J. Rühe), Wiley-VCH Verlag GmbH & Co. KGaA, Weinheim, Germany, **2004**, p. 483; (b) *Surface-Initiated Polymerization I*, 1st ed., (Ed.: R. Jordan), Springer-Verlag, Berlin, Germany, **2006**, p. 202.

[268] L. Michalek, L. Barner, C. Barner-Kowollik, *Adv. Mater.* **2018**, *30*, 1706321.

[269] L. Michalek, K. Mundsinger, C. Barner-Kowollik, L. Barner, *Polym. Chem.* **2019**, *10*, 54–59.

[270] (a) M. Bialk, O. Prucker, J. Rühe, *Colloids Surfaces A Physicochem. Eng. Asp.* **2002**, *198-200*, 543–549; (b) M. Henze, D. Mädge, O. Prucker, J. Rühe, *Macromolecules* **2014**, *47*, 2929–2937; (c) P. Datta, J. Genzer, *J. Polym. Sci. Part A: Polym. Chem.* **2016**, *54*, 263–274.

[271] *Polymers at interfaces*, 1st ed., (Eds.: G. J. Fleer, M. A. C. Stuart, J. M. H. M. Scheutjens, T. Cosgrove, B. Vincent), Chapman & Hall, London, UK, **1998**, p. 502.

[272] (a) D. Dimitrov, A. Milchev, K. Binder, *Macromol. Symp.* **2007**, *252*, 47–57; (b) J. O. Zoppe, N. C. Ataman, P. Mocny, J. Wang, J. Moraes, H.-A. Klok, *Chem. Rev.* **2017**, *117*, 1105–1318; (c) Y. Wang, X. Shu, J. Liu, Q. Ran, *Soft Matter* **2018**, *14*, 2077–2083; (d) *Polymer Surfaces and Interfaces*, 1st ed., (Ed.: M. Stamm), Springer-Verlag, Berlin, Germany, **2008**, p. 324.

[273] (a) B. Y. Kim, E. L. Ratcliff, N. R. Armstrong, T. Kowalewski, J. Pyun, *Langmuir* **2010**, *26*, 2083–2092; (b) J. Elbert, H. Didzoleit, C. Fasel, E. Ionescu, R. Riedel, B. Stühn, M. Gallei, *Macromol. Rapid Commun.* **2015**, *36*, 597–603; (c) M. Mazurowski, M. Gallei, J. Li, H. Didzoleit, B. Stühn, M. Rehahn, *Macromolecules* **2012**, *45*, 8970–8981; (d) J. Elbert, F. Krohm, C. Rüttiger, S. Kienle, H. Didzoleit, B. N. Balzer, T. Hugel, B. Stühn, M. Gallei, A. Brunsen, *Adv. Funct. Mater.* **2014**, *24*, 1591–1601; (e) J. Elbert, M. Gallei, C. Rüttiger, A. Brunsen, H. Didzoleit, B. Stühn, M. Rehahn, *Organometallics* **2013**, *32*, 5873–5878.

[274] D. Albagli, G. C. Bazan, R. R. Schrock, M. S. Wrighton, *J. Am. Chem. Soc.* **1993**, *115*, 7328–7334.

[275] J. Elbert, J. Mersini, N. Vilbrandt, C. Lederle, M. Kraska, M. Gallei, B. Stühn, H. Plenio, M. Rehahn, *Macromolecules* **2013**, *46*, 4255–4267.

[276] (a) P. Anikeeva, C. M. Lieber, J. Cheon, *Acc. Chem. Res.* **2018**, *51*, 987–987; (b) P. Yang, W. Yang, *Chem. Rev.* **2013**, *113*, 5547–5594; (c) E. J. Park, G. T. Carroll, N. J. Turro, J. T. Koberstein, *Soft Matter* **2009**, *5*, 36–50.

[277] J. M. Thomas, W. J. Thomas, *Principles and practice of heterogeneous catalysis*, 2nd ed., Wiley-VCH, Weinheim, Germany, **2015**, p. 767.

[278] (a) S. Hübner, J. G. de Vries, V. Farina, *Adv. Synth. Catal.* **2016**, *358*, 3–25; (b) J.-M. Basset, F. Lefebvre, C. Santini, *Coord. Chem. Rev.* **1998**, *178-180*, 1703–1723.

[279] E. Guégain, Y. Guillaneuf, J. Nicolas, *Macromol. Rapid Commun.* **2015**, *36*, 1227–1247.

[280] R. Müller, T. J. Feuerstein, V. Trouillet, S. Bestgen, P. W. Roesky, C. Barner-Kowollik, *Chem. Eur. J.* **2018**, *24*, 18933–18943.

[281] M. L. Allegrezza, Z. M. DeMartini, A. J. Kloster, Z. A. Digby, D. Konkolewicz, *Polym. Chem.* **2016**, *7*, 6626–6636.

[282] J. Laun, W. Marchal, V. Trouillet, A. Welle, A. Hardy, M. K. Van Bael, C. Barner-Kowollik, T. Junkers, *Langmuir* **2018**, *34*, 3244–3255.

[283] (a) K. K. Chow, W. Levason, C. A. McAuliffe in *Transit. Met. Complexes Phosphorus, Arsen. Antimony Ligands*, Macmillan Education UK, London, UK, **1973**, pp. 33–204; (b) C. Kaes, A. Katz, M. W. Hosseini, *Chem. Rev.* **2000**, *100*, 3553–3590; (c) H. Lang, *Polyhedron* **2018**, *139*, 50–62.

[284] T. J. Feuerstein, Dissertation, Karlsruher Institut für Technologie (KIT), Karlsruhe, Germany, **2019**.

[285] V. Marin, E. Holder, U. S. Schubert, *J. Polym. Sci. Part A: Polym. Chem.* **2004**, *42*, 374–385.

[286] S. Attar, W. H. Bearden, N. W. Alcock, E. C. Alyea, J. H. Nelson, *Inorg. Chem.* **1990**, *29*, 425–433.

[287] A. C. W. Leung, J. K.-H. Hui, J. H. Chong, M. J. MacLachlan, *Dalton Trans.* **2009**, 5199–5210.

[288] (a) T. Tischer, R. Gralla-Koser, V. Trouillet, L. Barner, C. Barner-Kowollik, C. Lee-Thedieck, *ACS Macro Lett.* **2016**, *5*, 498–503; (b) G. Zorn, L.-H. Liu, L. Árnadóttir, H. Wang, L. J. Gamble, D. G. Castner, M. Yan, *J. Phys. Chem. C* **2014**, *118*, 376–383.

[289] C. Buten, S. Lamping, M. Körsgen, H. F. Arlinghaus, C. Jamieson, B. J. Ravoo, *Langmuir* **2018**, *34*, 2132–2138.

[290] V. I. Nefjedov, J. V. Salin, D. Walther, E. Uhlig, E. Dinjus, *Zeitschrift für Chemie* **2010**, *17*, 190–191.

[291] M. P. Casaletto, A. Longo, A. Martorana, A. Prestianni, A. M. Venezia, *Surf. Interface Anal.* **2006**, *38*, 215–218.

[292] A. Taketoshi, M. Haruta, *Chem. Lett.* **2014**, *43*, 380–387.

[293] D. Skomski, C. D. Tempas, K. A. Smith, S. L. Tait, *J. Am. Chem. Soc.* **2014**, *136*, 9862–9865.

[294] L. B. Belykh, N. I. Skripov, V. V. Akimov, V. L. Tauson, T. P. Stepanova, F. K. Schmidt, *Russ. J. Gen. Chem.* **2013**, *83*, 2260–2268.

[295] (a) M. Harada, S. Kizaki, *Cryst. Growth Des.* **2016**, *16*, 1200–1212; (b) M. Quinn, G. Mills, *J. Phys. Chem.* **1994**, *98*, 9840–9844; (c) E. Gachard, H. Remita, J. Khatouri, B. Keita, L. Nadjo, Belloni, Jacqueline, *New J. Chem.* **1998**, *22*, 1257–1265.

[296] (a) D. Astruc, M.-C. Daniel, *Chem. Rev.* **2004**, *104*, 293–346; (b) G. Schmid, B. Corain, *Eur. J. Inorg. Chem.* **2003**, *2003*, 3081–3098; (c) A. Caragheorgheopol, V. Chechik, *Phys. Chem. Chem. Phys.* **2008**, *10*, 5029–5041.

[297] S. Muramoto, J. Brison, D. G. Castner, *Anal. Chem.* **2012**, *84*, 365–372.

[298] *Surface analysis by Auger and X-ray photoelectron spectroscopy*, (Eds.: D. Briggs, J. T. Grant), IM Publications LLP, Chichester, UK, **2003**, pp. XI, 899.

[299] B. C. Bunker, B. I. Kim, J. E. Houston, R. Rosario, A. A. Garcia, M. Hayes, D. Gust, S. T. Picraux, *Nano Lett.* **2003**, *3*, 1723–1727.

[300] Y. S. Park, Y. Ito, Y. Imanishi, *Macromolecules* **1998**, *31*, 2606–2610.

[301] C. Feldmeier, H. Bartling, E. Riedle, R. Gschwind, *J. Magn. Reson.* **2013**, *232*, 39–44.

[302] S. Ciampi, P. K. Eggers, N. L. Haworth, N. Darwish, P. Wagner, M. L. Coote, G. G. Wallace, C. L. Raston, *Chem. Commun.* **2015**, *51*, 4815–4818.

[303] A. Seegerer, P. Nitschke, R. M. Gschwind, *Angew. Chem. Int. Ed.* **2018**, *57*, 7493–7497.

[304] (a) I. Ostromisslensky, *Berichte der Dtsch. Chem. Gesellschaft* **1911**, *44*, 268–273; (b) P. Job, *Ann. Chim.* **1928**, *9*, 113–203; (c) P. Job, *Ann. Chim.* **1936**, *6*, 97–144.

[305] (a) K. Klausen, F. Langmyhr, *Anal. Chim. Acta* **1963**, *28*, 335–340; (b) E. Bruneau, D. Lavabre, G. Levy, J. C. Micheau, *J. Chem. Educ.* **1992**, *69*, 833.

[306] (a) E. Asmus, *Z. Anal. Chem.* **1961**, *183*, 401–412; (b) E. Asmus, *Z. Anal. Chem.* **1961**, *183*, 321–333; (c) E. J. Olson, P. Bühlmann, *J. Org. Chem.* **2011**, *76*, 8406–8412.

[307] (a) E. J. Olson, P. Bühlmann, *J. Org. Chem.* **2011**, *76*, 8406–8412; (b) F. Ulatowski, K. Dąbrowa, T. Bałakier, J. Jurczak, *J. Org. Chem.* **2016**, *81*, 1746–1756.

[308] (a) H. Görner, A. K. Chibisov, *J. Chem. Soc. Faraday Trans.* **1998**, *94*, 2557–2564; (b) A. K. Chibisov, H. Görner, *Chem. Phys.* **1998**, *237*, 425–442.

[309] Y. Ji, D. A. DiRocco, C. M. Hong, M. K. Wismer, M. Reibarkh, *Org. Lett.* **2018**, *20*, 2156–2159.

[310] (a) D. M. Schultz, F. Lévesque, D. A. DiRocco, M. Reibarkh, Y. Ji, L. A. Joyce, J. F. Dropinski, H. Sheng, B. D. Sherry, I. W. Davies, *Angew. Chem. Int. Ed.* **2017**, *56*, 15274–15278; (b) D. Lehnherr, Y. Ji, A. J. Neel, R. D. Cohen, A. P. J. Brunskill, J. Yang, M. Reibarkh, *J. Am. Chem. Soc.* **2018**, *140*, 13843–13853.

[311] (a) J. Kind, L. Kaltschnee, M. Leyendecker, C. M. Thiele, *Chem. Commun.* **2016**, *52*, 12506–12509; (b) L. Čechová, J. Kind, M. Dračínský, J. Filo, Z. Janeba, C. M. Thiele, M. Cigáň, E. Procházková, *J. Org. Chem.* **2018**, *83*, 5986–5998.

[312] K. L. Willett, R. A. Hites, *J. Chem. Educ.* **2000**, *77*, 900.

[313] P. Müller, R. Müller, L. Hammer, C. Barner-Kowollik, M. Wegener, E. Blasco, *Chem. Mater.* **2019**, *31*, 1966–1972.

[314] L. Hammer, Master thesis, Karlsruhe Institute of Technology (KIT), Karlsruhe, Germany, **2017**.

[315] H. Vijayamohanan, E. F. Palermo, C. K. Ullal, *Chem. Mater.* **2017**, *29*, 4754–4760.

[316] P. Müller, PhD thesis, Karlsruhe Institute of Technology (KIT), Karlsruhe, Germany, **2019**, pp. VII, 184.

[317] S. I. Beshenko, N. A. Zaichenko, V. V. Buzaev, V. D. Ermakova, M. I. Cherkashin, *Bull. Acad. Sci. USSR Div. Chem. Sci.* **1978**, *27*, 556–558.

[318] (a) Y. Shiraishi, K. Adachi, M. Itoh, T. Hirai, *Org. Lett.* **2009**, *11*, 3482–3485; (b) M. Dagilienė, V. Martynaitis, V. Kriščiūnienė, S. Krikštolaitytė, A. Šačkus, *ChemistryOpen* **2015**, *4*, 363–369.

[319] V. A. Krongauz, E. S. Goldburt, *Macromolecules* **1981**, *14*, 1382–1386.

[320] B. Harke, J. Keller, C. K. Ullal, V. Westphal, A. Schönle, S. W. Hell, *Opt. Express* **2008**, *16*, 4154–4162.

[321] R. Wollhofen, J. Katzmann, C. Hrelescu, J. Jacak, T. A. Klar, *Opt. Express* **2013**, *21*, 10831–10840.

[322] (a) W. Limm, D. Stanton, G. P. Dimnik, M. A. Winnik, B. A. Smith, *J. Appl. Polym. Sci.* **1988**, *35*, 2099–2116; (b) T. Tanaka, M. Morigami, N. Atoda, *Jpn. J. Appl. Phys.* **1993**, *32*, 6059–6064; (c) K. Nakazawa, E. Shiobara, M. Asano, Y. Sato, S. Tanaka, Y. Oonishi, *Jpn. J. Appl. Phys.* **1999**, *38*, 1569–1574.

[323] H. Vijayamohanan, P. Bhide, D. Boyd, Z. Zhou, E. F. Palermo, C. K. Ullal, *Langmuir* **2019**, *35*, 3871–3879.

[324] S. Protti, D. Ravelli, M. Fagnoni, *Photochem. Photobiol. Sci.* **2019**, *18*, 2094–2101.

[325] K. K. Oehlenschlaeger, J. O. Mueller, N. B. Heine, M. Glassner, N. K. Guimard, G. Delaittre, F. G. Schmidt, C. Barner-Kowollik, *Angew. Chem. Int. Ed.* **2013**, *52*, 762–766.

[326] S. H. Thang, Y. K. Chong, R. T. A. Mayadunne, G. Moad, E. Rizzardo, *Tetrahedron Lett.* **1999**, *40*, 2435–2438.

[327] W. H. Heath, F. Palmieri, J. R. Adams, B. K. Long, J. Chute, T. W. Holcombe, S. Zieren, M. J. Truitt, J. L. White, C. G. Willson, *Macromolecules* **2008**, *41*, 719–726.

[328] H. L. Wagner, *J. Phys. Chem. Ref. Data* **1985**, *14*, 1101–1106.

[329] A. Rudin, H. L. W. Hoegy, *J. Polym. Sci. Part A: Polym. Chem.* **1972**, *10*, 217–235.

[330] K. L. Parry, A. G. Shard, R. D. Short, R. G. White, J. D. Whittle, A. Wright, *Surf. Interface Anal.* **2006**, *38*, 1497–1504.

[331] J. Scofield, *J. Electron. Spectrosc. Relat. Phenom.* **1976**, *8*, 129–137.

[332] S. Tanuma, C. J. Powell, D. R. Penn, *Surf. Interface Anal.* **1994**, *21*, 165–176.

[333] Y. Wang, B. a. Aleiwi, Q. Wang, M. Kurosu, *Org. Lett.* **2012**, *14*, 4910–4913.

[334] R. Romagnoli, P. G. Baraldi, C. Lopez-Cara, D. Preti, M. Aghazadeh Tabrizi, J. Balzarini, M. Bassetto, A. Brancale, X.-h. Fu, Y. Gao, J. Li, S.-z. Zhang, E. Hamel, R. Bortolozzi, G. Basso, G. Viola, *J. Med. Chem.* **2013**, *56*, 9296–9309.

[335] (a) D. Liu, W. Chen, K. Sun, K. Deng, W. Zhang, Z. Wang, X. Jiang, *Angew. Chem. Int. Ed.* **2011**, *50*, 4103–4107; (b) G. O'Bryan, B. M. Wong, J. R. McElhanon, *ACS Appl. Mater. Interfaces* **2010**, *2*, 1594–1600.

[336] E. L. Zaitseva, A. L. Prokhoda, L. N. Kurkovskaya, R. R. Shifrina, N. S. Kardash, D. A. Drapkina, V. A. Krongauz, *Chem. Heterocycl. Compd.* **1975**, *9*, 1233–1239.

List of Figures

2.1 Different kinds of polymer topologies. (a) linear, (b) brush, (c) ring, (d) star, (e) cross-linked, and (f) branched star. 5

2.2 Examples of various polymer compositions as described in the text. 7

2.3 a) Guidelines for the selection of suitable R- and Z-groups depending on the monomer structure. For the Z-groups, values of k_{α} decrease and k_{β} increase from left to right. For the R-groups, k_{β} decrease from left to right. Abbreviations: MMA = methyl methacrylate, Sty = styrene, MA = methyl acrylate, AM = acrylamide, AN = acrylonitrile, VAc = vinyl acetate, and NVP = *N*-vinylpyrrolidone. Adapted with permission from [7]. © 2012 American Chemical Society. b) Examples of RAFT agents for the monomer classes described below. 15

2.4 Examples for the post-modification of the RAFT group into various other functional groups as described in the text. 17

2.5 Classifications of metallopolymers according to Rehan (a) and Wolf (b). . . . 18

2.6 Selection of metal complex bearing monomers, which were directly polymerized in a RAFT process. 19

2.7 a) Phosphorescent $\mathrm{Ir}^{+\mathrm{III}}$ emitter containing metallopolymer *via* a post-loading approach. The inset shows the polymer structure, as well as the UV-Vis and emission spectra. Adapted with permission from [38]. © 2010 Wiley-VCH Verlag GmbH & Co. KGaA. b) Polymer structure of a terpyridine containing copolymer and subsequent metal complexation with cadmium resulting in network formation with self-healing capabilities. Pictures after scratching (**I**) and after annealing at 100 °C for 16 h (**II**). [39] – Adapted by permission of The Royal Society of Chemistry. 20

2.8 The electromagnetic spectrum with the energy in electron volt (eV), the equivalent wavelength (nm) and the corresponding frequency (Hz). The spectrum is separated into different regimes as described in the gray horizontal bar. A zoom-in into of the visible light region is depicted below with the different perception of colors. 23

2.9 Primary steps after the interaction between light with the energy *hv* and a molecule A. A chemical reaction with the rate constant k_{p} leads to the formation of product P (top). Luminescence associated with the rate k_{r} to the ground state A and release of a photon with energy *hv* (middle). Non-radiative deactivation can occur *via* heat dissipation with a rate k_{nr} (bottom). 24

2.10 a) Schematic explanation of vertical electronic transitions from a ground state Ψ_i to an excited state Ψ_f. E is the energy scale and Q the nuclear coordinates of the respective molecule. E_ab represents the energy of a vibronic transition from $\Psi_{\mathrm{v=a}} \leftarrow \Psi_{\mathrm{v=b}}$. b) *Jablonski* diagram, depicting the energy levels of a molecule with the possible intramolecular photo processes as described in the text. Adapted with permission from [43]. © 2014 Wiley-VCH Verlag GmbH & Co. KGaA. 26

2.11 Comparison between thermodynamic (a) and photodynamic (b–d) equilibria. The Boltzmann distribution dictates the population of the energy levels (I) and (II) in the thermal case (a) with the equilibrium constant K_{eq}^{Δ}. The difference between the energy levels is given by $\Delta G^{\ddagger}$ and $\Delta G^{\ominus}$. (b) Exclusive population of state (I) in the dark as a result of a high energy barrier. (c) Transition into an excited state upon irradiation and relaxation into state (II). (d) Depopulation of state (II) *via* thermal fading (T-type photochromism) or photo excitation (P-type photochromism). The photodynamic equilibrium constant K_{eq}^{λ} in this case is depicted below the graph and depends on the molar extinction coefficients and the quantum yields of the for- and backward reaction. [57] – Adapted with permission of The Royal Society of Chemistry. 28

2.12 Most prominent families of molecular photochromic molecules. Diarylethenes (a) and fulgides (b) are examples of *P-type* photochromic molecules that isomerize *via* electrocyclic rearrangements. *T-type* photochromic molecules are for example azobenzenes (c) or flavylium molecules (f), which undergo $(E)\rightleftharpoons(Z)$ double-bond isomerizations. Spiropyrans (d) and spirooxazins (e) are also *T-type* photochromes, but with reversible cyclization/ring-opening isomerizations. 29

2.13 Illustration of the "zipper crystallization" found in SP-functionalized methacrylate polymers (**A**). Styrene- (**B**) or acrylate-based polymers (**C**) do not show such crystallization behavior. The X-ray powder diffraction of (**A**, left) and (**B**, right) are depicted below the structures. [62c] – Adapted by permission of The Royal Society of Chemistry. 35

2.14 Various metal complexes of the open-ring MC isomer. An additional metal binding site is installed in all cases for the stabilization of the MC form. . . . 36

2.15 a) Photo activation of an *o*-nitrobenzyl (*o*-NB) derivative and reaction with an aminooxy derivative. b) *Diels–Alder* adducts of phencyclones release carbon monoxide and molecular hydrogen upon irradiation with 320 nm. Subsequent ring-opening with an amine gives the ligation product. R, R_1 = alkyl. 38

2.16 a) UV irradiation of phthaloyl peroxides releases CO_2 and forms highly reactive arynes, which are trapped by azides. b) 2-Napthoquinone-3-methides (*o*-NQMs) are generated *via* irradiation of 3-(hydroxymethyl)-2-naphthols and readily react in a hetero-*Diels–Alder* reaction with vinyl ethers. c) Dibenzocyclopropenones release CO upon irradiation, forming ring-strained dibenzocyclooctynes that react in a catalyst free cycloaddition with azides. d) Ring-opening of pyrene substituted azirines results in reactive nitrile ylides, which participate in 1,3-dipolar cycloadditions. EWG = electron withdrawing group; R, R_1 = alkyl. 39

2.17 Three examples of reversible photoligation chemistry. The [2+2] cycloadditions of coumarines (a) and styrylpyrenes (b) triggered *via* irradiation with 350 nm and 405 nm, respectively. Only one isomer is depicted in each case. The dissociation is feasible with shorter wavelength in both cases. c) Photochemical [4+4] cycloaddition between two anthrazene molecules and the reverse reaction *via* 410 nm and 360 nm, respectively. R = alkyl. 40

2.18 Spatially resolved immobilization of metal complexes (**3a-c**) onto silica surfaces employing a phenacyl sulfide functionalized silane (**I**). Single (**a,b**), as well as double functional (**c-e**) surfaces were characterized *via* time-of-flight secondary ion mass spectrometry (ToF-SIMS). The mass fragments used for creating the false-color images are given below each ToF-SIMS image. The shadow mask and surface holder are shown in **f**. Adapted with permission from [144]. © 2015 Wiley-VCH Verlag GmbH & Co. KGaA. 44

2.19 Different substitutions of the aryl group connected to the nitrogen atom of the tetrazole ring and the wavelengths reported to trigger the 1,3-dipole formation. From left to right: non-substituted tetrazole, push-pull substituted methoxy and *N,N*-dimethylamino tetrazoles, and pyrene functionalized tetrazole. R = alkyl. 46

2.20 Example of a PDA coated silicon surface functionalized with tetrazole molecules. After NITEC ligation of an ATRP initiator, anti-fouling poly(oligoethylene glycol methyl ether methacrylate) brushes were grown from the surface and inhibited cell adhesion on the irradiated areas. Adapted with permission from [160]. © 2013 Wiley-VCH Verlag GmbH & Co. KGaA. . . . 47

2.21 Left: Collection of photoenol reactivities with different substrates, namely *Diels–Alder*-, *Michael*-, *Aldol*-, and *Mannich*-type reactions. Reproduced with permission from [169b]. © 2018 Wiley-VCH Verlag GmbH & Co. KGaA. Right: Various photoenols described in literature. 2,4-Dimethylbenzophenone **A** as the first literature example, 2-methoxy-6-methylbenzaldehyde **B** as a widely employed photoenol precursor and 2-methyl-6-(methylthio)benzaldehyde **C** as a recently published photoenol triggered by visible light. R_1,R_2 = H, alkyl or phenyl; R_3,R_4 = alkyl; PG = protecting group; EWG = electron withdrawing group. 49

2.22 Reported side reactions of photoenols in the absence of suitable reaction partners. In oxygen containing solutions, the formation of peroxides (**I**) can occur. Cyclobutane formation towards (**II**) and hemiacetal formation with the carbonyl moiety of a second *o*-methyl benzaldehyde resulting in (**III**), has also been reported. Another dimerization is shown below, leading to dimers (**IV**) and (**V**). While (**IV**) is stable, (**V**) quickly rearranges towards bisaldehyde (**VI**). R_1 = H; R_2 = alkyl. 51

2.23 a) The principle of STED visualized by a *Jablonski* diagram. For a description, refer to the text. b) 2D intensity representation of the Gaussian shaped UV excitation laser (blue) and the visible light depletion laser with a point of zero intensity in the center (green). The effectively resulting fluorescent area is shown on the right (red). 54

2.24 a) Principle of conventional DLW. TPA from S_0 into S_1 is followed by ISC and homolytic bond cleavage of the initiator, resulting in radicals $R^\bullet$ starting the polymerization of monomer M. b) Three structures of commercially available TPA PIs. 57

2.25 Different depletion mechanism employed for STED-inspired lithography. a) STED lithography: PI molecules are excited *via* TPA from S_0 to S_1. They relax back to the S_0 ground state *via* SE before ISC into the T_1 state and radical formation can occur. b) RAPID lithography: after TPA into S_1, transition into an intermediate state occurs (k_a), from which either radiationless decay with rate constant k_d or light excitation into a non-initiating product (k_{hv}) suppresses radical formation. c) 2PII lithography: initiator (orange), as well as inhibitor molecules (green) get excited *via* different wavelengths in an OPA process. d) Example of a photoresist system working through excited state absorption. PETA is employed as the cross-linking monomer and ITX as the initiator. The depletion (green), as well as the TPA wavelength (blue) for ITX are highlighted below in the absorption and fluorescence spectra measured in ethanol. Adapted with permission from [212]. © 2010 Wiley-VCH Verlag GmbH & Co. KGaA. 59

2.26 a) Chemical structures of the photoenol-equipped silane (**I**) and the maleimide ATRP initiator (**II**). b) Linewidth reduction experiments visualized *via* AFM measurements of SI-ATRP grown polymer brushes. The excitation power is shown in red, while the depletion power is drawn in blue. c) Determination of the lateral resolution without (top) and with depletion (bottom) Lines are separated for depletion powers **B** and **C**, while **E** no longer lead to a clear periodic modulation. Adapted with permission from [183]. © 2017 American Chemical Society. 61

2.27 Illustration of a typical surface modification experiment. The individual steps are discussed in the following sections. 63

2.28 Overview of different substrates employed in photoligation chemistry. The materials are classified according to their physical properties into metals, metal oxides, semiconductors, and other substrates. 64

2.29 Activation *via* piranha (top left) or aqueous HF (top right) and subsequent SAM formation on silicon substrates based on various chemical connectivities. 66

2.30 Common examples of non-covalent (blue), as well as covalent (green) post-modification strategies. 67

2.31 Different chemical strategies for the surface functionalization with polymers. a) *Grafting-from* polymerization through surface-attached initiator molecules. b) The *grafting-to* methodology utilizes pre-formed end-functionalized polymers in a ligation step. c) In the *grafting-through* approach, surface bound monomer units get incorporated into the growing polymer chain during a polymerization process. 68

2.32 Classification of surface-immobilized polymers according to their grafting densities. a) The *pancake* regime in low grafting densities and bad solvents. b) The combination of good solvents and low grafting densities results in the *mushroom* regime. c) The *brush* regime is obtained with high grafting densities. 69

2.33 a) Homogeneous immobilization of a Si(OEt)$_3$-terminated ferrocene metallopolymer synthesized *via* ring-opening metathesis polymerization (ROMP) onto a silicon wafer.[274] b) Controlled anionic polymerization of vinylferrocene-terminated by a triethoxysilane moiety. Upon immobilization onto spherical silicon particles, redox-responsive surfaces are obtained.[275] 70

3.1 Two approaches for the photoligation of metallopolymers synthesized *via* RAFT polymerization onto silicon surfaces. Left side: phenacyl sulfide-functionalized silane **3** is coupled with RAFT agents **1** and **2**, bearing a hexadiene functionality in the R-group. Right side: a furan-protected maleimide on the R-group of CTA **4** enables the photoligation with the surface-attached tetrazole **5**. 75

3.2 a) Unsuccessful attempted experiments to obtain CTA **1**: 1) EDC·HCl, DMAP, DCM; 2) DCC, DMAP, DCM; 3) DCC, PFP, DMAP, DCM; 4) EDC·HCl, OxymaPure®, NaHCO$_3$, MeCN/H$_2$O; 5) see 2) without (*2E*,*4E*)-hexadienol; 6) oxalyl chloride, DMF (cat.), DCM. b) Successful Steglich esterification of CDSTSP and (*2E*,*4E*)-hexadienol towards CTA **2**. c) ^{1}H NMR zoom in the spectrum of **2** with corresponding assignment, confirming the intact diene functionality (protons 21–25), as well as the Z-group *via* proton 13. 76

3.3 Results of the MMA homopolymerization with CTA **2**. The SEC traces of polymers **P1**–**P4** are shown on the left. The ^{1}H NMR spectra of **2** and **P3** on the right side confirm the intact diene functionality of the R-group, as well as the Z-group *via* protons 21–25 and 13, respectively. 77

3.4 Photoligation reaction between phenacyl sulfide functionalized PEG **P5** and the diene equipped PMMA polymers **P1**, **P2**, and **P4**. The SEC traces for each reaction product **P6**–**P8**, as well as the starting materials, are depicted below the reaction scheme. Calculated MWs for the expected *Photo-DA* product and the *dimer* side-product are indicated with arrows. 78

3.5 a) Picture of the photo mask holder next to the employed dotted and KIT-logo shadow masks. b) Illustration of the silicon wafer, photo mask holder, and a photo mask assembled for the reaction. If no photo mask is used, the shape of the c) Setup of the assembled photo mask holder in the photo vial containing the solution with the end-functionalized polymer. d) Scheme of the custom-build photo reactor equipped with an UV lamp. e) The activated silicon wafer **S1a** is uniformly covered with silane **3** (surface **S1b**) and irradiated with a rectangle shadow mask in the presence of polymer **P3** to obtain surface **S1c**. Adapted with permission from [280]. © 2018 Wiley-VCH Verlag GmbH & Co. KGaA. 80

3.6 ^{1}H NMR spectra of the PMMA homopolymers **P10-FM** (top), **P10-FM-cap** (middle), and **P10** (bottom) recorded in $CDCl_3$. Representative protons described in the text are highlighted with colored circles in the structures (left side) and the spectra (right side). Adapted with permission from [280]. © 2018 Wiley-VCH Verlag GmbH & Co. KGaA. 83

3.7 a) Reaction scheme and ToF-SIMS image of non-capped, furan deprotected **P9-non-capped** leading to surface **S2-non-capped**. The area above the dashed green line was irradiated. b) Successful surface attachment of capped, furan deprotected **P10** on surface **S2**. ToF-SIMS image (middle) and XPS analysis of C 1s (right) of the dark and irradiated areas. c) Photoligation of **P10** with a KIT logo mask yields surface **S2-KIT**. The ToF-SIMS analysis of the PMMA and tetrazole fragments is shown on the right. For ToF-SIMS fragments description refer to Table A.1. Adapted with permission from [280]. © 2018 Wiley-VCH Verlag GmbH & Co. KGaA. 85

3.8 a) $^{31}P\{^1H\}$ NMR spectra of the ligand monomer **7** and the metal complex **7-Au**, next to the corresponding ligand copolymer **P11** and the metallopolymer **P11-Au** (b). c) ^{1}H NMR spectra of the ligand monomer **9** and the metal complexes **9-Pt** and **9-Pd**, next to the corresponding ligand copolymer **P12** and the metallopolymers **P12-Pt** and **P12-Pd** (d). For the resonance assignment refer to the schematic molecular structure. Adapted with permission from [280]. © 2018 Wiley-VCH Verlag GmbH & Co. KGaA. 88

3.9 From left to right: UV-Vis spectra of the metallopolymers **P11-Au**, **P12-Pt**, and **P12-Pd** measured in 1,4-dioxane ($1\,mg\,mL^{-1}$) before and after irradiation with the Arimed B6 lamp for 3 h. 93

3.10 Surface photoligation of the free ligand copolymers **P11** and **P12**, yielding surfaces **S3** and **S4**, respectively. The rectangle in the schematic visualization represents the area analyzed *via* ToF-SIMS. The ToF-SIMS and XPS analysis of the phosphine copolymer surface **S3** (left) and **S4** (right) are depicted below. The dotted green line in the ToF-SIMS images indicates the line separating the dark from the irradiated area. 95

3.11 a) Post-loading with gold of surface **S3** towards surface **S3-Au**. b) Post-loading with platinum of surface **S4** towards surface **S4-Pt**. The ToF-SIMS analysis of the PMMA and metal characteristic ions is depicted below the surface drawings. The XPS spectra of Au 4f and Pt 4f in command of **S3-Au** and **S4-Pt** are shown on the right for the irradiated and dark areas of the surfaces. Adapted with permission from [280]. © 2018 Wiley-VCH Verlag GmbH & Co. KGaA. 96

3.12 Unsuccessful photoligation of metallopolymer **P12-Pt** on surface **S5-long** with the ToF-SIMS analysis of **S5-long** showing no immobilized polymer with 6 cm distance between glass vial and irradiation source and 10 mm pathway through the **P12-Pt** metallopolymer solution. 98

3.13 a) Overlay of the absorption spectrum of metallopolymer **P12-Pt** and the spectral irradiance of the Arimed B6 lamp. b) Effect of the **P12-Pt** solution absorption on the spectral irradiance after different penetration depths into the solution. c) 3D visualization of the decrease in available surface irradiance with a pronounced effect in the wavelength region around 320 nm. 99

3.14 Visualization of the initial (a) and improved (b) experimental setup for surface photoligation. Compared to the initial setup, the distance between the irradiation source and the photo vial, as well as the distance between the silicon surface and the wall of the glass vial was shortened (red arrows). Adapted with permission from [280]. © 2018 Wiley-VCH Verlag GmbH & Co. KGaA. 100

3.15 a) Spectral irradiance of the Arimed B6 UV lamp at 2.5 cm distance (dotted, black) and with a glass vial employed for the photoreactions placed between the lamp and the radiometric sensor (blue). b) Relationship between peak irradiance of the Arimed B6 lamp and the distance of the reaction vial towards the lamp. The red line only serves to guide the eye. 101

3.16 Spatially resolved surface immobilization of metallopolymers **P12-Pt** (a), **P12-Pd** (b), and **P11-Au** (c) *via* setup A. The ToF-SIMS and XPS analysis of the respective metal species are shown on the right. Adapted with permission from [280]. © 2018 Wiley-VCH Verlag GmbH & Co. KGaA. 102

3.17 Three different combinations of the metallopolymers on a single surface for the fabrication of bifunctional metallopolymer surfaces **S8** (a), **S9** (b), and **S10** (c). A schematic overview of the surface patterning is given in the middle. The respective ToF-SIMS images are depicted on the left side, while the XPS chemical mappings are displayed in the right column. The color code is given below each picture. 106

3.18 Comparison of the surfaces **S8** (1st row) and **S8-rev** (2nd row). The ToF-SIMS mappings of the tetrazole, PMMA, and bipyridine fragments are similar for both surfaces. In contrast, the palladium and platinum species swapped places. 108

3.19 ToF-SIMS and XPS analytics of the trifunctional metallopolymer surfaces **S11** (1^{st} row) and **S12** (2^{nd} row). A schematic overview of the surface patterning is given in the middle. The respective ToF-SIMS images are depicted on the left side, while the XPS chemical mappings are displayed in the right column. The color code is given below each picture. The green circle in the ToF-SIMS image of **S11** indicates an area of the 3^{rd} reaction step, which is partially functionalized with **P12-Pt** from the 2^{nd} reaction. 109

3.20 Comparison of the surfaces **S11** (1^{st} row) and **S11-rev** (2^{nd} row). The ToF-SIMS mappings of the palladium and platinum fragments swapped places, while the gold fragments are found on the same spots. 111

4.1 Proposal of a light-responsive SCNP based on the reversible intramolecular cross-linking of a SP-functionalized polymer with metal centers as cross-linking points. 116

4.2 Left side: ^{1}H NMR spectra of **10** (top) and **12** (bottom) with the resonance assignments according to the labeling in Scheme 4.20. Right side: Corresponding absorption spectra of **10** (top) and **12** (bottom) in the dark. For **12**, the spectra of the PSS upon irradiation with a 390 nm LED and subsequent thermal relaxation in the dark are depicted as well. Measured in MeCN (30 µM, 1 cm cuvette). 118

4.3 Non-successful experiments towards the formation of zinc and nickel complexes with **12** under irradiation with UV light. The absorption spectra of **12** and the mixture with 0.8 eq. of the zinc (top) and nickel (bottom) salts are shown, together with the PSS spectra upon irradiation with a 390 nm LED and the spectra after thermal relaxation in the dark. 120

4.4 Crystal structures of **10-Zn** (a), **10-Ni** (b), **10-Ca** (c), and **10-La** (d). Hydrogen atoms are omitted for clarity. Adapted with permission from [284]. 122

4.5 a) UV-Vis spectra of **10-Zn** for the determination of the complex stoichiometry using Job's method of continuous variations. The wavelength at 480 nm used for the Job's plot analysis is indicated with the dashed blue line. [**10**]+[**Zn**] = 95 µM in MeCN, measured in a 10 mm cuvette. b) Job's plot analysis of the spectra in a), with the maximum of the interpolated dashed blue line at $X_{Zn} = 0.37$. 123

4.6 a)–c) UV-Vis spectra of **10-Ni** at different total concentrations of [**10**]+[**Ni**] = 95 µM (a), 0.55 mM (b), and 2.8 mM (c) in MeCN, measured in a 10, 5, and 1 mm cuvette, respectively. The absorption values at 460 nm in c) are used for the Job's plot analysis in d), which gives an interpolated maximum value at $X_{Ni} = 0.40$. 124

4.7 Absorption measurements of **10-Zn** (a), **10-Ni** (b), and **10-Ca** (c) under simultaneous irradiation with a 390 nm LED employing the setup described in Figure A.1. For **10-Ca**, a 590 nm LED was used in addition to the UV LED. . 127

4.8 a) Schematic drawing of the setup for LED-NMR experiments including pictures of the real experimental setup. b) Picture of the cage plate with the inserted terminated fiber adapter, holding the optical fiber exactly centered over the LED (top left). Picture from the top (top right) and side (bottom) of the mounted LED inside the custom-build adapter with the cable channels and 4 rods to hold the cage plate on top of the LED. 129

4.9 a) Concentration increase of *o*-nitrosobenzoic acid and linear fit for the determination of the initial product formation rate for the 99 mM sample of *o*-NBA. b) Experimental and fitted initial rates of product formation according to Scheme 4.22 for different concentrations of *o*-NBA using Equation (4.2). . 131

4.10 a) SP$\rightleftharpoons$MC equilibrium of **10** with highlighted proton resonances used for the integration of the LED-NMR kinetic experiment. b) Zoom into the ^{1}H NMR spectra before turning on the LED (bottom) and at the maximum **10-MC** concentration in the PSS under irradiation (top). c) Plot of the **10-MC** concentration vs. time with the on- and off-switching of the UV LED. The violet circles indicate the spectra, which are plotted in panel b). 132

4.11 a) **10-Zn**$\rightleftharpoons$**10** equilibrium of **10-Zn** with highlighted proton resonances used for the integration of the LED-NMR kinetic experiment. b) Zoom into the ^{1}H NMR spectra before turning on the LED (bottom) and at the in the PSS under irradiation (top). c) Plot of the **10-Zn** and **10** concentration vs. time with the on- and off-switching of the UV LED. The experiment was performed with a 0.62 mM solution of **10-Zn** in CD_3CN. The violet circles indicate the spectra, which are plotted in panel b). 134

4.12 a) **10-Ca**$\rightleftharpoons$**10** equilibrium of **10-Ca** with highlighted proton resonances used for the integration of the LED-NMR kinetic experiment. b) Zoom into the ^{1}H NMR spectra before turning on the LED (bottom) and at the in the PSS under irradiation (top). c) Plot of the **10-Ca** and **10** concentration vs. time with the on- and off-switching of the UV LED. The experiment was performed with a 0.61 mM solution of **10-Ca** in CD_3CN. The violet circles indicate the spectra, which are plotted in panel b). 136

4.13 a) **10-La**$\rightleftharpoons$**10** equilibrium of **10-La** with highlighted proton resonances used for the integration of the LED-NMR kinetic experiment. b) Zoom into the ^{1}H NMR spectra before turning on the LED (bottom) and at the in the PSS under irradiation (top). c) Plot of the **10-La** and **10** concentration vs. time with the on- and off-switching of the UV LED. The experiment was performed with a 20.6 mM solution of **10-La** in CD_3CN. The violet circles indicate the spectra, which are plotted in panel b). 137

5.1 Top: photo triggered equilibrium between STP and MC. The MC form can react with a maleimide in a thiol-*Michael* reaction, resulting in an irreversible covalent connection. R = CH_2CH_2OH; R_1 = alkyl. DMSO solutions of STP and the PSS of MC are shown below the chemical structures. The UV-Vis spectrum shows a DMSO solution of STP in the dark (yellow), after irradiation with a 385 nm LED (green), and after subsequent irradiation with a 625 nm LED (dotted orange). The arrows indicate the wavelengths of the UV, as well as the visible light LED. The red arrow at 820 nm indicates the wavelength used to trigger the STP→MC transition *via* a TPA process. 140

5.2 Surface functionalization approach utilizing the STP-maleimide reaction. A glass surface is covered with STP-functionalized silane **17**. The areas irradiated with the excitation, as well as the inhibition laser are highlighted in red and green, respectively. In the area where only the excitation laser is applied, the generated MC form reacts with the maleimide ATRP-initiator **21**. The reaction is suppressed in areas also irradiated with the inhibition laser. Subsequent SI-ATRP results in the formation of poly(ethylene glycol) methyl ether methacrylate brushes (blue lines), which are characterized *via* light microscopy or AFM. 141

5.3 ^1H NMR spectrum of **17** recorded in $CDCl_3$. Proton resonances associated with the STP part of the molecule are highlighted in red. X = EtOAc. 143

5.4 Lines of polymer brushes grown from the surface functionalized with silane **17** after photolithographic patterning of ATRP initiator **21** using only the excitation laser. a) Dark field light microscope image of the polymer brushes. The excitation energy is increased from bottom to top. b) False color AFM image of several lines written with varying excitation powers. The linewidth, as well as the height of the polymer brushes increases with the excitation energy. Adapted with permission from [316]. 145

5.5 a) Expected depletion pattern when increasing the excitation and depletion laser powers according to the inset. b) Dark field light microscope image of a depletion test pattern. The depletion laser is fixed at a constant power in each line, while the excitation laser is switched on at the positions indicated on top and is varied in strength from left to right. Increasing the depletion power leads to a reduced excitation power needed to start the writing process (area C). If the depletion energy is too high, parasitic writing occurs even without switching on the excitation laser (area D). Adapted with permission from [316]. 146

5.6 a) Formation of side-product **A-MC2** in the acetylation of **19** with methacryloyl chloride towards **A-SP1** *via* the **A-MC** and **A-MC1** merocyanine forms of **A-SP**, as described by Cherkashin and co-workers.[317] b) HR-ESI-MS spectrum of the crude reaction mixture of the reaction between **15** and methacryloyl chloride. Beside the desired STP monomer **18**, the main product of the reaction is the diacetylated derivative **18a**. The inset shows the experimental, as well as the simulated isotopic pattern of the [**18a**+Na]$^+$ ion. 148

5.7 a) Schematic description of the processing steps towards 3D structures. A glass slide is covered with the photoresist mixture and the voxel of the DLW laser is scanned through the photoresist during the writing step. Free standing 3D structures are obtained after the removal of residual photoresist in the development step. b) Absorption spectra of **P13a** in the dark and under continuous irradiation with a 365 nm LED in the PSS. Spectra are recorded in 1 mg $\mathrm{mL^{-1}}$ acetophenone solution in a 1 mm cuvette. c) SEM image of two free-standing bridges suffering from pronounced shrinkage. d) SEM image of a depletion test experiment with the excitation and depletion laser foci according to the scheme above the image. c) and d) are adapted with permission from [316]. 151

5.8 SEM images of a free-standing bridge structure (a) and two pyramidal structures (b), written with copolymer **P13a** in acetophenone (40 wt%). Adapted with permission from [313]. © 2019 American Chemical Society. 152

5.9 a) Synthesis of hydroxy-functionalized SP **19** through condensation of **13** with 3-methoxy-5-nitrosalicylaldehyde. Subsequent *Mitsunobu* reaction between **19** and MAA yields SP-monomer **20**. b) Synthesis of an SP-MMA copolymer **P15** in analogy to the STP-copolymers **P13a–c** with SP-monomer **20**. c) Absorption spectrum of **P15** in the dark and after irradiation with a 365 nm LED in the PSS. The MC form is detected through the absorption band centered at 605 nm (A). During thermal relaxation in the dark, two absorption bands with a hypsochromic shift build up at 544 nm (B) and 502 nm (C), which remain stable in solution. Spectra are recorded in 1 mg $\mathrm{mL^{-1}}$ acetophenone solution in a 1 mm cuvette. d) Absorption spectrum of thermally equilibrated solutions of a comparable SP-MMA copolymer in 2-methyltetrahydrofuran at different concentrations per monomer unit in a 2 mm cuvette: 0.2 M (1); 0.135 M (2); 0.1 M (3); 0.05 M (4). Adapted with permission from [319]. © 1981 American Chemical Society. 153

5.10 a) SEM image of a free-standing bridge structure written with a photoresist consisting of **P15** in acetophenone (40 wt%). Adapted with permission from [313]. © 2019 American Chemical Society. b) SEM image of a depletion test pattern employing the SP photoresist **P15**. Each line is written with a different excitation and depletion power. Parasitic writing in regime A is followed by the destructive regime B. Adapted with permission from [316]. . 155

5.11 a) SEM image of a depletion test pattern employing the STP photoresist **P13a**. Each line is written with a different excitation and depletion power. Depletion regime A is followed by *parasitic writing* in regime B. b) Reversibility test of the depletion effect by writing a loop pattern. Previously written lines are not altered by the depletion laser (area C) and areas already irradiated with the depletion laser are still active in subsequent writing (area D). Adapted with permission from [313]. © 2019 American Chemical Society. 156

5.12 a) SEM image of linewidth reduction test *via* the depletion laser in the ride part of the lines for different depletion powers. The linewidth is decreasing with increasing depletion power until the lines become unstable and disconnected. b) Evaluation of the FWHM in the dashed area of a). c) The FWHM of lines written at different depletion powers is proportional to the inverse square root of the depletion power. Adapted with permission from [313]. © 2019 American Chemical Society. 158

5.13 SEM image of gratings for the determination of the achievable resolution enhancement. a) Clearly separated lines are obtained for lattice constants greater than the diffraction limit of 207 nm (for the actual setup). For a lattice constant of 175 nm, using only the excitation laser leads to a single polymer block (b), while the lines are still separated employing the depletion laser in addition to the excitation laser (c). Adapted with permission from [313]. © 2019 American Chemical Society. 158

A.1 Setup for the irradiation of a solution in a quartz cuvette with simultaneous absorption measurement. The cuvette is equipped with a magnetic stirring bar and inserted into the UV-Vis spectrometer, which is placed above a magnetic stirrer. The LED is attached onto a passive cooling element and placed upside down on top of the cuvette. The potential interference of the LED irradiation and the UV-Vis measurement is minimized through the 90° angle between the LED light beam and the light path of the spectrometer. . . 228

A.2 Images of the etching procedure of the stripped optical fiber with glass etching cream. a) After the 1^{st} etching, most of the light is still leaking from the tip of the fiber. b) Illumination of the fiber during the etching procedure enables real-time monitoring of the surface wrinkling. c) After several etching iterations, the optical fiber is homogeneously emitting the light over the whole surface area. 229

A.3 ^{1}H NMR (top) and ^{13}C NMR (bottom) spectrum of **2** recorded in $CDCl_3$. For resonance assignment refer to the schematic molecular structure. 236

A.4 ^{1}H NMR (top) and ^{13}C NMR (bottom) spectrum of **4** recorded in $CDCl_3$. For resonance assignment refer to the schematic molecular structure. X = EtOAc and cC$_6$H$_{12}$. 237

A.5 ^{1}H NMR (top) and ^{13}C NMR (bottom) spectrum of **5** recorded in DMSO-d_6. For resonance assignment refer to the schematic molecular structure. X = H_2O. 238

A.6 ^{1}H NMR (top) and ^{13}C NMR (bottom) spectrum of **8** recorded in $CDCl_3$. For resonance assignment refer to the schematic molecular structure. 239

A.7 ^{1}H NMR (top) and ^{13}C NMR (bottom) spectrum of **10** recorded in CD_3CN. For resonance assignment refer to the schematic molecular structure. X = H_2O. 240

A.8 ^{1}H NMR (top) and ^{13}C NMR (bottom) spectrum of **11b** recorded in $CDCl_3$. For resonance assignment refer to the schematic molecular structure. X = H_2O. 241

A.9 ^{1}H NMR (top) and ^{13}C NMR (bottom) spectrum of **12** recorded in $CDCl_3$. For resonance assignment refer to the schematic molecular structure. 242

A.10 ^1H NMR (top) and ^{13}C NMR (bottom) spectrum of **13** recorded in $CDCl_3$. For resonance assignment refer to the schematic molecular structure. 243
A.11 ^1H NMR (top) and ^{13}C NMR (bottom) spectrum of **14b** recorded in $CDCl_3$. For resonance assignment refer to the schematic molecular structure. X = toluene. 244
A.12 ^1H NMR (top) and ^{13}C NMR (bottom) spectrum of **15** recorded in DMSO-d_6. For resonance assignment refer to the schematic molecular structure. X = EtOH, H_2O. 245
A.13 ^1H NMR (top) and ^{13}C NMR (bottom) spectrum of **16** recorded in DMSO-d_6. For resonance assignment refer to the schematic molecular structure. 246
A.14 ^1H NMR (top) and ^{13}C NMR (bottom) spectrum of **17** recorded in $CDCl_3$. For resonance assignment refer to the schematic molecular structure. X = EtOAc. 247
A.15 ^1H NMR (top) and ^{13}C NMR (bottom) spectrum of **18** recorded in $CDCl_3$. For resonance assignment refer to the schematic molecular structure. X = cC_6H_{12}. 248
A.16 ^1H NMR (top) and ^{13}C NMR (bottom) spectrum of **19** recorded in CD_3CN. For resonance assignment refer to the schematic molecular structure. X = H_2O. 249
A.17 ^1H NMR (top) and ^{13}C NMR (bottom) spectrum of **20** recorded in $CDCl_3$. For resonance assignment refer to the schematic molecular structure. X = cC_6H_{12}, H_2O, grease. 250
A.18 UV-Vis spectra of copolymer **P11** and the metallopolymer **P11-Au** measured in 1,4-dioxane (1 mg mL^{-1}). 251
A.19 UV-Vis spectra of copolymer **P12** and the metallopolymers **P12-Pt** and **P12-Pd** measured in 1,4-dioxane (1 mg mL^{-1}). 251
A.20 UV-Vis spectra of **10-Ca** for the determination of the complex stoichiometry using Job's method of continuous variations. The wavelength at 580 nm used for the Job's plot analysis is indicated with the dashed blue line. [**10**]+[**Ca**] = 2.8 mM in MeCN, measured in a 1 mm cuvette. 252
A.21 Job's plot analysis of the spectra in Figure A.20. The maximum of the interpolated dashed blue line lies at $X_{\mathrm{Ca}} = 0.23$. 252
A.22 UV-Vis spectra of **10-La** for the determination of the complex stoichiometry using Job's method of continuous variations. The wavelength at 530 nm used for the Job's plot analysis is indicated with the dashed blue line. [**10**]+[**La**] = 2.8 mM in MeCN, measured in a 1 mm cuvette. 253
A.23 Job's plot analysis of the spectra in Figure A.20. The maximum of the interpolated dashed blue line lies at $X_{\mathrm{La}} = 0.32$. 253
A.24 Spectral irradiance of the Philips Cleo Compact PL-L UV lamp employed for the phenacyl sulfide photoreactions. Measured at a distance of 6 cm in the custom-build photoreactor. 254
A.25 Spectral irradiance of the Arimed B6 UV lamp employed for the NITEC and photoenol photoreactions. Measured at a distance of 2.5 cm in the custom-build photoreactor. 254
A.26 Spectral irradiance of the 365 nm LED employed for the LED-NMR experiments. Measured at a distance of 1 cm for various LED currents. 255

A.27 Irradiance of the 365 nm LED employed for the LED-NMR experiments integrated from 330–420 nm, plotted against the applied LED current, and fitted to a cubic polynomial function. The operation mode for the LED-NMR experiments is indicated. 255
A.28 3D Surface plot of the relationship between the spectral irradiance of the light source after passing through the reaction solution of **P11-Au** (1 mg mL^{-1} in 1,4-dioxane) at arbitrary distances. 256
A.29 3D Surface plot of the relationship between the spectral irradiance of the light source after passing through the reaction solution of **P12-Pt** (1 mg mL^{-1} in 1,4-dioxane) at arbitrary distances. 256
A.30 3D Surface plot of the relationship between the spectral irradiance of the light source after passing through the reaction solution of **P12-Pd** (1 mg mL^{-1} in 1,4-dioxane) at arbitrary distances. 257
A.31 SEC traces of the PMMA homopolymers **P1**, **P2**, **P3**, and **P4**. 258
A.32 SEC traces of the PMMA homopolymers **P9-FM** and **P9-non-capped**. . . . 258
A.33 SEC traces of the PMMA homopolymers **P10-FM**, and **P10-FM-cap**, and **P10**. 259
A.34 SEC traces of the three prepared phosphine ligand copolymers **P11-FM**, **P11-FM-cap**, and **P11**. 259
A.35 SEC traces of the three prepared bipyridine ligand copolymers **P12-FM**, **P12-FM-cap**, and **P12**. 260
A.36 SEC traces of the free phosphine ligand copolymer **P11** and the gold functionalized metallopolymer **P11-Au**. 260
A.37 SEC traces of the free bipyridine ligand copolymer **P12** and the platinum and palladium metallopolymers **P12-Pt** and **P12-Pd**, respectively. 261
A.38 SEC traces of the STP-containing copolymers **P13a–d**. 261
A.39 SEC traces of the maleimide-containing copolymers **P14a** (furan protected) and **P14**. 262
A.40 SEC trace of the SP-containing copolymer **P15**. 262
A.41 ToF-SIMS spectra of **S2-non-capped**. Positive polarity (top), negative polarity (bottom). 265
A.42 ToF-SIMS spectra of **S2**. Positive polarity (top), negative polarity (bottom). . 266
A.43 C 1s XPS spectra of **S2**. 267
A.44 ToF-SIMS spectra of **S2-KIT**. Positive polarity (top), negative polarity (bottom). 268
A.45 ToF-SIMS spectra of **S3**. Positive polarity (top), negative polarity (bottom). . 269
A.46 C 1s and Cl 2p XPS spectra of **S3**. 270
A.47 ToF-SIMS spectra of **S3-Au** for various immersion times *t* of the surface into the metal salt solution. 271
A.48 ToF-SIMS spectra of **S3-Au**. Positive polarity (top), negative polarity (bottom). 271
A.49 C 1s and Au 4f XPS spectra of **S3-Au**. 272
A.50 ToF-SIMS spectra of **S4**. Positive polarity (top), negative polarity (bottom). . 273
A.51 C 1s and N 1s XPS spectra of **S4**. 274
A.52 ToF-SIMS spectra of **S4-Pt**. Positive polarity (top), negative polarity (bottom). 275
A.53 C 1s, N 1s, Cl 2p, and Pt 4f XPS spectra of **S4-Pt**. 276
A.54 ToF-SIMS spectra of **S5-long**. Positive polarity (top), negative polarity (bottom). 277

A.55 ToF-SIMS spectra of **S5**. Positive polarity (top), negative polarity (bottom). . 278
A.56 C 1s, N 1s, Cl 2p, and Pt 4f XPS spectra of **S5**. 279
A.57 ToF-SIMS spectra of **S6**. Positive polarity (top), negative polarity (bottom). . 280
A.58 C 1s, N 1s, Cl 2p and Pd 3d XPS spectra of **S6**. 281
A.59 ToF-SIMS spectra of **S7**. Positive polarity (top), negative polarity (bottom). . 282
A.60 C 1s and Au 4f XPS spectra of **S7**. 283
A.61 ToF-SIMS spectra of **S8**. Positive polarity (top), negative polarity (bottom). . 284
A.62 XPS mappings of **S8**. 285
A.63 ToF-SIMS spectra of **S8-rev**. Positive polarity (top), negative polarity (bottom). 286
A.64 XPS mappings of **S8-rev**. 287
A.65 ToF-SIMS spectra of **S9**. Positive polarity (top), negative polarity (bottom). . 288
A.66 XPS mappings of **S9**. 289
A.67 ToF-SIMS spectra of **S9-rev**. Positive polarity (top), negative polarity (bottom). 290
A.68 XPS mappings of **S9-rev**. 291
A.69 ToF-SIMS spectra of **S10**. Positive polarity (top), negative polarity (bottom). 292
A.70 XPS mappings of **S10**. 293
A.71 ToF-SIMS spectra of **S10-rev**. Positive polarity (top), negative polarity (bottom). 294
A.72 XPS mappings of **S10-rev**. 295
A.73 ToF-SIMS spectra of **S11**. Positive polarity (top), negative polarity (bottom). 296
A.74 XPS mappings of **S11**. 297
A.75 ToF-SIMS spectra of **S11-rev**. Positive polarity (top), negative polarity (bottom). 298
A.76 XPS mappings of **S11-rev**. 299
A.77 ToF-SIMS spectra of **S12**. Positive polarity (top), negative polarity (bottom). 300
A.78 XPS mappings of **S12**. 301
A.79 ToF-SIMS spectra of **S12-rev**. Positive polarity (top), negative polarity (bottom). 302
A.80 XPS mappings of **S12-rev**. 303

List of Tables

2.1 Summary of the photophysical processes described in the text and their corresponding time scales. Reproduced with permission from [46]. © 2009 John Wiley & Sons, Ltd. 27

3.1 XPS analysis of the surface photoligation experiments employing polymer **P3** and silane **3**. All values are in atomic percent (at%). 81

3.2 Summary of ligand copolymers and metallopolymers for spatially resolved surface functionalization. Adapted with permission from [280]. © 2018 Wiley-VCH Verlag GmbH & Co. KGaA. 92

3.3 Comparison of the initial and improved irradiation setup and the absolute gain in irradiance intensity at the wafer surface. Adapted with permission from [280]. © 2018 Wiley-VCH Verlag GmbH & Co. KGaA. 101

3.4 Summary of all bifunctional surfaces prepared *via* reaction setup B, i.e. point mask (I) in the first and point mask (II) in the second reaction step. The reaction sequence describes the order in which the two metallopolymers are tethered onto the silicon wafer. The detailed ToF-SIMS and XPS analytic can be found in the respective figures. 105

3.5 Summary of all trifunctional metallopolymer surfaces fabricated in this thesis. For a description of the reaction setup, refer to Table A.2. The reaction sequence gives the order in which the three metallopolymers are tethered onto the silicon wafer. The detailed ToF-SIMS and XPS analytic can be found in the respective figures. 111

3.6 Concentration of silicon metal on different locations of the triple modified surfaces **S11-rev** and **S12**. For **S11-rev**, the decrease of the silicon signal with respect to the non-irradiated area is calculated. Adapted with permission from [280]. © 2018 Wiley-VCH Verlag GmbH & Co. KGaA. 112

4.1 Comparison of the complex stoichiometries in the solid state (X-ray) with the values in solution determined *via* Job plot analysis. 125

5.1 Summary of the STP- and maleimide-functionalized PMMA copolymers. . . 150

A.1 Description of ToF-SIMS fragments and their aliases used for structure elucidation in the ToF-SIMS mappings. 263

A.2 Description of the surface reaction setups with the employed shadow masks. The different shadow masks are depicted below the table. 264

List of Schemes

2.1 The four steps in a FRP mechanism. *Initiation* can be divided in two steps, namely the formation of radicals by an initiator molecule I_2 (1a) and the addition to a double bond of a monomer M (1b). 2) *Propagation* of the polymerization, adding more monomers to the propagating chain. 3) *Chain transfer* reactions can occur with transfer agents T. *Termination via combination* of two radical species (4a) and through a *disproportionation* process (4b). 8

2.2 Mechanism of a RAFT polymerization, starting with the *initiation* (1). Growing polymer chains are transformed into macroRAFT agents in the *pre-equilibrium* (**2a**) and the released $R^\bullet$ radicals re-initiate upon addition to monomer (**2b**). *Propagation* (**3**) and *termination* (**5**) events are overlaid by the *core-equilibrium* (**4**), in which constant addition/fragmentation between active polymer chains $P_n^\bullet$ and $P_m^\bullet$ and dormant CTA bearing polymer chains occurs. 13

2.3 General structure motif of the photochromic SP molecule and its open-ring MC isomer. 30

2.4 The two most common synthesis strategies towards SP molecules. Condensation of a cyclic quaternary ammonium salt (a) or the corresponding methylene base (b) with a salicylaldehyde (c). 31

2.5 a) *Photochromism* and *acidochromism* of SP molecules. Reversible transformations between the four states: SP (**1**), MC (**2**), protonated SP SPH^+ (**3**), and protonated merocyanine MCH^+ (**4**). b) Comparison between photochemical (top) and thermal ring-opening (bottom) mechanism. The resultant MC forms (**6**) and (**8**) are resonance structures of each other. [62c] – Adapted by permission of The Royal Society of Chemistry. 32

2.6 a) *Görner–Chibisov* mechanism of the photo triggered ring-opening of SPs with a nitro-group in the 6-position of the benzopyran ring, involving triplet states. b) Ring-opening mechanism for SP molecules without an electron-withdrawing group in the 6-position only occurs *via* singlet excited states. Adapted with permission from [62d]. © 2004 American Chemical Society. . . 33

2.7 Various MC isomer structures in solution and their interconversion through bond rotations. The MC isomers are capable to form supramolecular aggregates. Adapted with permission from [62d]. © 2004 American Chemical Society. 34

2.8 Photo excitation of phenacyl sulfide and subsequent reactions: 1.) β-Cleavage resulting in two radicals, followed by recombination or side-reactions; 2.) CT and quenching towards the ground state; 3.) *Norrish type II* cleavage resulting in a thioaldehyde, which is trapped either by a diene in a hetero-*Diels–Alder* reaction to obtain products (**A**) and (**B**), or by a nucleophile, e.g. an alkoxy amine to obtain product (**C**). R_1, R_2, R_3, R_4 = alkyl. 42

2.9 Photo induced nitrile imine formation of a tetrazole and dimerization in the absence of reaction partners, yielding tetrazines (top row). In the presence of suitable reaction partners, from left to right: 1,3-dipolar cycloaddition with an electron deficient ene (NITEC), reaction with a carboxylic acid (NICAL), addition to the triple bond of acetonitrile, reaction with an amine, such as imidazole, and addition of a thiol. R_1, R_2 = aryl; R_3 = alkyl; EWG = electron withdrawing group. 45

2.10 Photoenolization mechanism of 2,4-dimethylbenzophenone with lifetimes of the different transient species as determined in oxygen free cyclohexane. A detailed description of the mechanism is given in the text. R_1 = methyl, R_2 = phenyl. 48

2.11 General synthesis route for the preparation of STPs. *Newman–Kwart* rearrangement of *O*-aryl thiocarbamate **I** gives access to *S*-aryl thiocarbamate **II**. Condensation of an indoline base **III** with the *in situ* deprotected thiosalicyl aldehyde **IV** results in the formation of **STP**. 52

2.12 Photo induced STP to MC isomerization and subsequent thiol-*Michael* reaction with a maleimide species as reported by Zhu and co-workers in [193]. . 53

2.13 Proposed mechanism for STED-inspired lithography based on the photo induced isomerization of photoenols. Starting from the ground state molecule (**A**), TPA brings the photoenol into the excited S_1 state (**B**). The three processes discussed in Scheme 2.10 generate the *(Z)*-**C** and *(E)*-**C** photoenols. The depletion laser, operating at 440 nm, triggers the *(Z)*- to *(E)*-isomerization of the photoenol and therefore suppresses the irreversible hetero-*Diels–Alder* reaction with a maleimide, resulting in the photoadduct (**D**). 60

3.14 RAFT polymerization of MMA with CTA **4** yields polymer **P9-FM** and **P10-FM**. Refluxing of **P9-FM** in toluene removes the furan protecting group towards polymer **P9-non-capped**. Capping of the dithiobenzoate moiety of **P10-FM** with photoenol precursor **6** delivers polymer **P10-FM-cap**, which is subsequently deprotected towards polymer **P10**. 82

3.15 a) Synthesis of triphenylphosphine monomer **7** and metal complexation towards **7-Au**. b) Bipyridine monomer synthesis **9** and metal complexation with platinum **9-Pt** or palladium **9-Pd**. Reagents and conditions: 1) HEMA, DIC, DMAP, DCM, r.t., 24 h; 2) [AuCl(tht)], DCM, r.t., 3 h; 3) LDA, THF, −78 °C, 1.5 h; 4) $Br(CH_2)_3OTBDMS$, r.t., 24 h; 5) TBAF, THF, r.t., 4 h; 6) methacryloyl chloride, NEt_3, DCM, 0 °C, 24 h; 7) $[PtCl_2(DMSO)_2]$, $CHCl_3$, reflux, 5 min or $[PdCl_2(COD)]$, DCM, r.t., 24 h. Adapted with permission from [280]. © 2018 Wiley-VCH Verlag GmbH & Co. KGaA. 87

3.16 Copolymerization of ligand monomers **7** and **9** with CTA **4**. The RAFT moiety of the obtained copolymers **P11-FM** and **P12-FM** is capped in a photo induced hetero-*Diels–Alder* reaction with **6**, yielding **P11-FM-cap** and **P12-FM-cap**, respectively. Refluxing in toluene affords the maleimide-functional ligand copolymers **P11** and **P12**. The graphical description of the polymers, as well as the end-groups, is employed for the rest of this thesis. . 90

3.17 Metal post-loading of **P11** towards **P11-Au** and **P12** towards **P12-Pt** and **P12-Pd**, respectively. The graphical description of the metallopolymers is employed for the rest of this thesis. 91

3.18 Reaction sequence for the preparation of the bifunctional metallopolymer surface **S8**. The palladium metallopolymer **P12-Pd** is photochemically immobilized onto the surface with point mask (I) in the first reaction step, followed by platinum metallopolymer **P12-Pt** in the second surface reaction, employing point mask (II). 104

3.19 The two different strategies for trifunctional surface patterning employed in this thesis. a) Immobilization of **P12-Pd** (point mask (III), 1st step), **P12-Pt** (point mask (IV), 2nd step), and **P11-Au** (point mask (V), 3rd step) towards surface **S11** *via* surface setup C. b) Immobilization of **P12-Pt** (point mask (I), 1st step), **P12-Pd** (point mask (II), 2nd step), and **P11-Au** (no mask, 3rd step) towards surface **S12** *via* surface setup D. 109

4.20 a) Synthesis of 8-methoxy functionalized SP **10** as reported by Raston and co-workers.[302] b) Synthesis of the analogous STP **12** through *in situ* deprotection of **11b** towards the free thiophenol and subsequent condensation with 1,3,3-trimethyl-2-methyleneindoline. 117

4.21 Synthesis of SP-metal complexes with SP **10**. Reaction with [$Zn(ClO_4)_2(H_2O)_6$] and [$Ni(ClO_4)_2(H_2O)_6$] leads to the bischelated metal complexes **10-Zn** and **10-Ni**, respectively. The tetrachelated SP-calcium complex **10-Ca** is obtained through reaction with [$Ca(ClO_4)_2(H_2O)_4$], while the reaction with [$La(NO_3)_3(H_2O)_6$] leads to the bischelated lanthanum complex **10-La**, with 3 additional nitrate ions complementing the ligand sphere. 121

4.22 Transformation of *o*-NBA towards *o*-nitrosobenzoic acid upon irradiation with 365 nm UV light. 130

5.23 Synthesis strategy towards STP-functionalized silane **17**. a) Synthesis of indol derivative **13**. b) Transformation of 5-nitrosalicylaldehyde into the masked salicylthioaldehyde **14b**. c) *In situ* deprotection of **14b** and condensation with **13** yields STP **15**, which is transformed into the free STP acid **16** *via* nucleophilic ring-opening of succinic anhydride, followed by amidation with APTES, yielding STP-silane **17**. 1) 2-Iodoethanole, MeCN, reflux; 2) KOH, grinding; 3) *N*,*N*-dimethylthiocarbamoyl chloride, DABCO, DMF; 4) toluene, reflux; 5) NaOH in MeOH, then HCl; 6) **13**, EtOH, reflux; 7) succinic anhydride, TEA, DMAP, 1,4-dioxane; 8) CDI, APTES, THF. 143

5.24 *Mitsunobu* reaction between hydroxy-functionalized STP **15** and MAA, yielding STP monomer **18**. 147

5.25 a) FRP of MMA and **18** towards copolymers **P13a–d** with 1-dodecanethiol as CT agent. For **P13d**, no CT was added. b) ATRP of MMA and a furan-protected MMA monomer towards polymer **P14a**, which is deprotected towards maleimide-functionalized copolymer **P14**. 149

A.26 Attachment of **P9-non-capped** on surface **S2-non-capped** (setup A). 265
A.27 Attachment of **P10** on surface **S2** (setup A). 266
A.28 Attachment of **P10** on surface **S2-KIT** (setup A). 268
A.29 Attachment of **P11** on surface **S3** (setup A). 269
A.30 Attachment of **P11** and subsequent post-loading with a [AuCl(tht)] solution towards surface **S3-Au** (setup A). 271
A.31 Attachment of **P12** on surface **S4** (setup A). 273
A.32 Attachment of **P12** and subsequent post-loading with a [$PtCl_2(DMSO)_2$] solution towards surface **S4-Pt** (setup A). 275
A.33 Attachment of **P12-Pt** on surface **S5-long** with a long irradiation pathway through the metallopolymer solution (setup A). 277
A.34 Attachment of **P12-Pt** on surface **S5** (setup A). 278
A.35 Attachment of **P12-Pd** on surface **S6** (setup A). 280
A.36 Attachment of **P11-Au** on surface **S7** (setup A). 282
A.37 Attachment of **P12-Pd** and **P12-Pt** on surface **S8** (setup B). 283
A.38 Attachment of **P12-Pt** and **P12-Pd** on surface **S8-rev** (setup B). 286
A.39 Attachment of **P12-Pd** and **P11-Au** on surface **S9** (setup B). 288
A.40 Attachment of **P11-Au** and **P12-Pd** on surface **S9-rev** (setup B). 290
A.41 Attachment of **P12-Pt** and **P11-Au** on surface **S10** (setup B). 292
A.42 Attachment of **P11-Au** and **P12-Pt** on surface **S10-rev** (setup B). 294
A.43 Attachment of **P12-Pd**, **P12-Pt**, and **P11-Au** on surface **S11** (setup C). . . . 296
A.44 Attachment of **P12-Pt**, **P12-Pd**, and **P11-Au** on surface **S11-rev** (setup C). . 298
A.45 Attachment of **P12-Pt**, **P12-Pd**, and **P11-Au** on surface **S12** (setup D). . . . 300
A.46 Attachment of **P12-Pd**, **P12-Pt**, and **P11-Au** on surface **S12-rev** (setup D). . 302

APPENDIX A

Appendix

A.1 Pulse sequence for LED-NMR kinetic experiments

```
;zg2d_30
;avance-version (12/01/11)
;pseudo 2D sequence
;
;$$CLASS=HighRes
;$$DIM=2D
;$$TYPE=
;$$SUBTYPE=
;$$COMMENT=Modified by Rouven Müller to use 30 degree flip angle instead of 90

#include <Avance.incl>
#include <Delay.incl>

”DELTA=d20-((d1+aq)*(ns+ds))-30m”

”acqt0=-p1*0.66/3.1416”

1 ze
  30m
2 DELTA
3 d1
  p1*0.33 ph1
  go=3 ph31
  30m wr #0 if #0 ze
  lo to 2 times td1
exit

ph1=0 2 2 0 1 3 3 1
```

```
ph31=0 2 2 0 1 3 3 1

;pl1 : f1 channel - power level for pulse (default)
;p1 : f1 channel - 90 degree high power pulse
;d1 : relaxation delay; 1-5 * T1
;d20: delay between start of different 1D spectra
;ns: 1 * n
;td1: number of experiments

;$Id: zg2d,v 1.6.8.1 2012/01/31 17:56:41 ber Exp $
```

A.2 Setup for LED-UV-Vis measurements

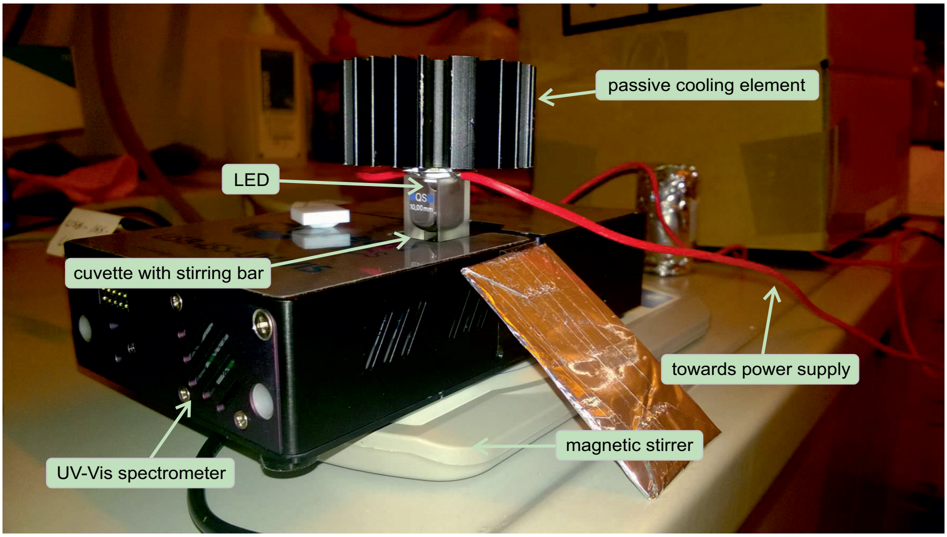
passive cooling element
LED
cuvette with stirring bar
towards power supply
magnetic stirrer
UV-Vis spectrometer

Figure A.1. Setup for the irradiation of a solution in a quartz cuvette with simultaneous absorption measurement. The cuvette is equipped with a magnetic stirring bar and inserted into the UV-Vis spectrometer, which is placed above a magnetic stirrer. The LED is attached onto a passive cooling element and placed upside down on top of the cuvette. The potential interference of the LED irradiation and the UV-Vis measurement is minimized through the 90° angle between the LED light beam and the light path of the spectrometer.

A.3 Setup for LED-NMR measurements

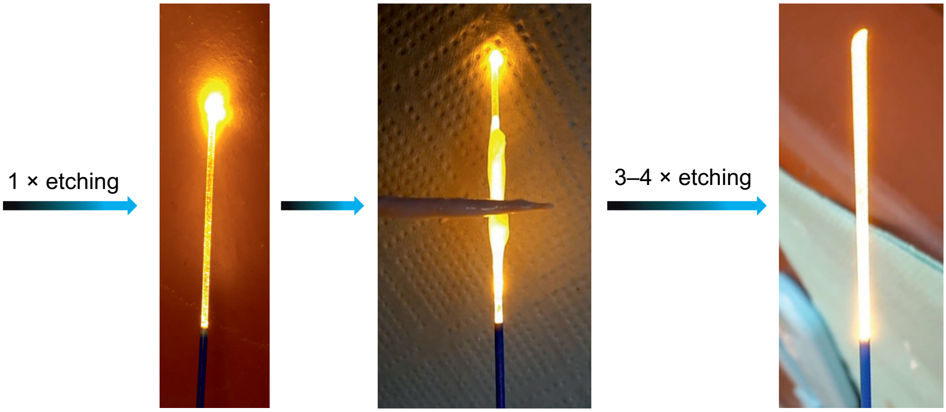

Figure A.2. Images of the etching procedure of the stripped optical fiber with glass etching cream. a) After the 1st etching, most of the light is still leaking from the tip of the fiber. b) Illumination of the fiber during the etching procedure enables real-time monitoring of the surface wrinkling. c) After several etching iterations, the optical fiber is homogeneously emitting the light over the whole surface area.

A.4 MATLAB Script for absorption corrected spectral intensity

The MATLAB script for absorption corrected spectral intensity calculations needs two input files. First, the UV-Vis spectra as a .txt-file in the format as exported from the OceanOptics software, for which an example including the header is given below:

```
Data from UVVis-filename.txt Node

Date: Thu Nov 23 09:51:24 CET 2018
User: username
Spectrometer: USB4J01072
Trigger mode: 0
Integration Time (sec): 3,020000E-2
Scans to average: 100
Electric dark correction enabled: true
Nonlinearity correction enabled: false
Boxcar width: 6
```

```
XAxis mode: Wavelengths
Number of Pixels in Spectrum: 3648
>>>>>Begin Spectral Data<<<<<
176,59012 0,15318592
176,8105137 0,16792531
177,03089514 0,17661932
 ⋮
```

The 2nd input file is the spectral intensity measurement of the light source in the .dat-format as exported from the USBSpec spectral software, for which also an example including the header is given below:

```
[Common]
DecimalSep=,
DateSep=.
DateFormat=dd/MM/yyyy
TimeSep=:
TimeFormat=hh:mm:ss

[Measurement Info]
Integration time [ms]=1301,24795436859
Spectra start [nm]=200
Spectra end [nm]=800
Spectra Resolution [nm]=0,6
Dark measurement=YES
Averaging=200
Measurement date=21.11.2017
Measurement time=12:51:17
File name=Photometer-filename.dat
Spectral correction=absolut
Calibration file=69DIF20160222.SpecCal

[Manipulation]
Mathematical manipulation[1]=

[Memo]
Memo[1]=

[Measurement Setup]
Auto integration time=NO
continuous measurement=NO
Transmission measurement=NO
Dynamic measurement=NO
Flash active=NO
Output active=NO
Trigger input active=NO
```

```

[Offset Info]
Offset active=YES

[Hardware Info]
Serial number=#840 320 0069
Start Pixel=13
Dispersion=0,6047
Device DLL=$0499
CPU Version=$0082

[Calculations]
UV-C [mW/m²]=-18,8722101724828
UV-B [mW/m²]=2038,26866111501
UV-A [mW/m²]=8169,02761508168
Lux [Lux]=1114,70201075884
Erythema [mW/m²]=501,827074298747
Pigment [mW/m²]=8389,27927931011

[Spectra]
Name=Opsytec Dr. Groebel Spectra
Unit=mW/m²/nm
Dose Unit=mW/m²
LUX kor=0,001
CAL kor=1
UU=4
Amax=82,9272755016403
Lines=1001
Data: Photometer-filename
200,00 -5,1202858E-01
200,60 2,3112685E+00
201,20 -1,5222480E+00
 ⋮
```

With these two input files, the MATLAB script given below calculates the spectral intensity of the light source at arbitrary penetration depths through the absorbing solution:

```matlab
function PlotIntensityDepth()

% Absorption calculator
% first adapt these values, then execute script

filename_UVVis = 'UVVis-filename.txt';
filename_Photometer = 'Photometer-filename.dat';

% UV-Vis measurement
```

```
c_UVVis = 0.25; % mmol/l - concentration of solution in UV Vis
d_UVVis = 1; % mm - width of UV-Vis solution/vial
UVVis_spectrum_normalized = 0; % 0 or 1 - normalize spectrum to 1 (instead of physical units)

% Photometer
lamp_spectrum_normalized = 0; % 0 or 1 - normalize spectrum to 1 (instead of physical units)

% target solution
c_solution = 0.25; % mmol/l - concentration of target solution

% plot parameters
lambda_min = 200; % nm - lower end of spectrum
lambda_max = 800; % nm - upper end of spectrum
lambda_step = 1; % nm - step size of spectrum
depth = 10; % mm - maximum depth for simulation
depth_step = 0.01; % mm - depth step size

% read in data files
fid1 = fopen(filename_UVVis);
data_UVVis = textscan(fid1,'%s\t%s','HeaderLines',14);
fclose(fid1);
data_UVVis = str2double(strrep([data_UVVis{1} data_UVVis{2}],',','.'));

fid2 = fopen(filename_Photometer);
data_Photometer = textscan(fid2,'%s\t%s','HeaderLines',63);
fclose(fid2);
data_Photometer = str2double(strrep([data_Photometer{1} data_Photometer{2}],',','.'));

%grid
z = 0:depth_step:depth;
nm = lambda_min:lambda_step:lambda_max;

%interpolate data
data_interp_UVVis = interp1(data_UVVis(:,1),data_UVVis(:,2),nm);
data_interp_Photometer = interp1(data_Photometer(:,1),data_Photometer(:,2),nm);

%data cosmetics
data_interp_UVVis(data_interp_UVVis<0) = 0;
data_interp_Photometer(data_interp_Photometer<0) = 0;

% calculate epsilon and intensity
epsilon = data_interp_UVVis / c_UVVis / d_UVVis; % unit: l/mmol / mm
intensity = data_interp_Photometer; % unit: mW/m²

%normalize
if UVVis_spectrum_normalized
```

```
   epsilon = epsilon./max(epsilon);
end
if lamp_spectrum_normalized
   intensity = intensity./max(intensity);
end

%create calculation matrices
[~,Z] = meshgrid(nm,z);
Eps = repmat(epsilon,size(Z,1),1);
Int = repmat(intensity,size(Z,1),1);

% the actual calculation
result = Int .* 10.^(-Z .* Eps * c_solution);

% plotting everything
f = figure('Units', 'normal', 'Position', [0.05 0.05 .8 .8 ]);

% spectra plot
subgroup1 = uipanel('Parent',f ,'Units','normal','Position',[0 .5 .5 .5],'BorderType','none');
subgroup1_axes = axes('Parent',subgroup1,'Units','normal','Position',[0.1 0.2 .8 .7]);
yyaxis left
plot(nm,epsilon,'Parent',subgroup1_axes)
if UVVis_spectrum_normalized
   ylabel('epsilon (norm.)')
else
   ylabel('epsilon (l/mmol/mm)')
end
yyaxis right
plot(nm,intensity)
xlabel('wavelength (nm)')
if lamp_spectrum_normalized
   ylabel('intensity (norm.)')
else
   ylabel('intensity (mW/m²)')
end

% false color plot
subgroup2 = uipanel('Parent',f ,'Units','normal','Position',[.5 0 .5 1],'BorderType','none');
subgroup2_axes = axes('Parent',subgroup2,'Units','normal','Position',[0.1 0.1 .8 .8]);
imagesc(nm,z,result,'Parent',subgroup2_axes)
c = colorbar;
if lamp_spectrum_normalized
   c.Label.String = 'intensity (norm.)';
else
   c.Label.String = 'intensity (mW/m²)';
end
```

```
xlabel('wavelength (nm)')
ylabel('depth (mm)')

current_line = 1;

% slice plot
subgroup3 = uipanel('Parent',f ,'Units','normal','Position',[0 0 .5
     .5],'BorderType','none');
subgroup3_axes = axes('Parent',subgroup3,'Units','normal','Position',[0.1 0.25 .8 .7]);
subgroup3_controls = uipanel('Parent',subgroup3,'Units', 'normal', 'Position', [0 0 1
     .1],'BorderType','none');
h = plot(nm,result(current_line,:),'Parent',subgroup3_axes);
xlabel('wavelength (nm)')
title('intensity spectrum at selected depth')
if lamp_spectrum_normalized
   ylabel('intensity (norm.)')
   ylim([0 1]);
else
   ylabel('intensity (mW/m²)')
   tmp = ylim;
   ylim(tmp);
end

% save data into file
save('filename.mat','result')

% interactive controls
uicontrol('Style', 'text','Parent',subgroup3_controls,'Position', [20 10 100
     20],'String','depth (mm)');
sld = uicontrol('Style',
     'slider','Min',z(1),'Max',z(end),'Value',z(current_line),'Parent',
      subgroup3_controls,'Position', [120 10 320 20],'Callback', @sliderchange);
edt = uicontrol('Style',
     'edit','String',num2str(z(current_line)),'Parent',subgroup3_controls,'Position',
     [460 10 100 20],'Callback', @editchange);
button = uicontrol('Style', 'pushbutton','String','Save
     spectrum','Parent',subgroup3_controls,'Position', [580 10 100 20],'Callback',
     @savedata);

function sliderchange(source,event)
      current_line = find(source.Value<=z,1);
      h.YData = result(current_line,:);
      edt.String = num2str(z(current_line));
end

function editchange(source,event)
      value = str2double(source.String);
      if value >= 0 && value <= z(end)
```

```
            current_line = find(value<=z,1);
        end
        h.YData = result(current_line,:);
        sld.Value = z(current_line);
end

function savedata(source,event)
        savefile = uiputfile('*.*');
        if savefile ~= 0
            dlmwrite(savefile,[h.XData' h.YData']);
        end
end

end
```

A.5 NMR spectra

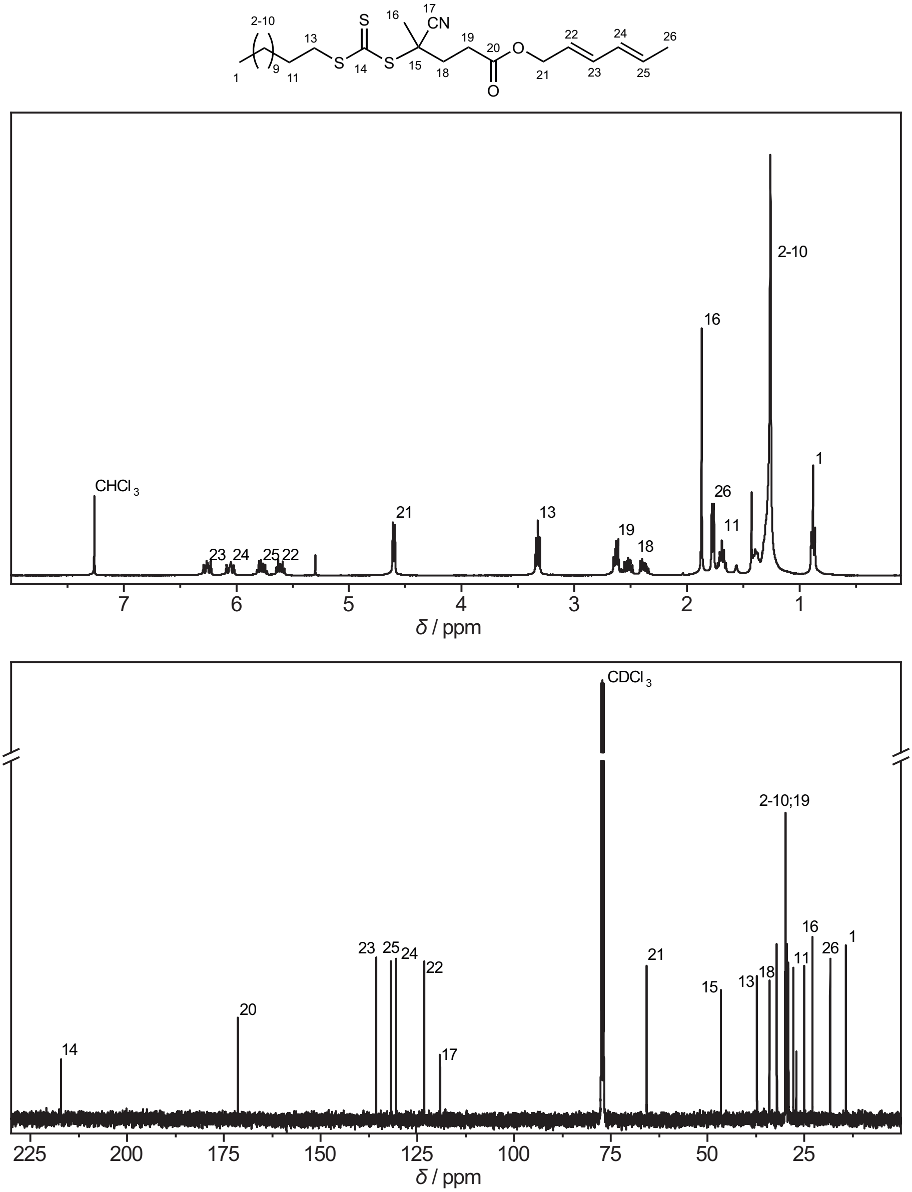

Figure A.3. ^{1}H NMR (top) and ^{13}C NMR (bottom) spectrum of **2** recorded in CDCl$_3$. For resonance assignment refer to the schematic molecular structure.

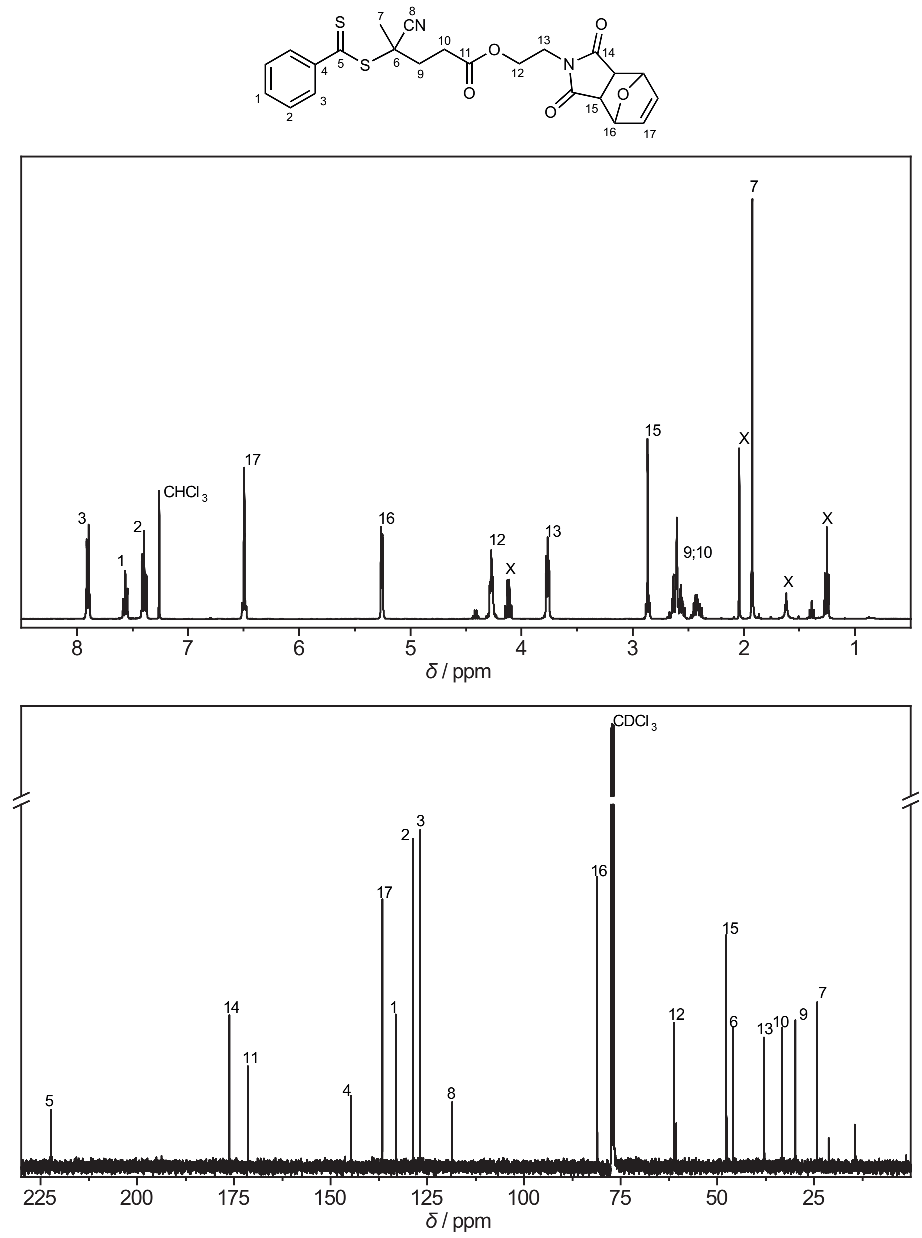

Figure A.4. ^{1}H NMR (top) and ^{13}C NMR (bottom) spectrum of **4** recorded in $CDCl_3$. For resonance assignment refer to the schematic molecular structure. X = EtOAc and cC_6H_{12}.

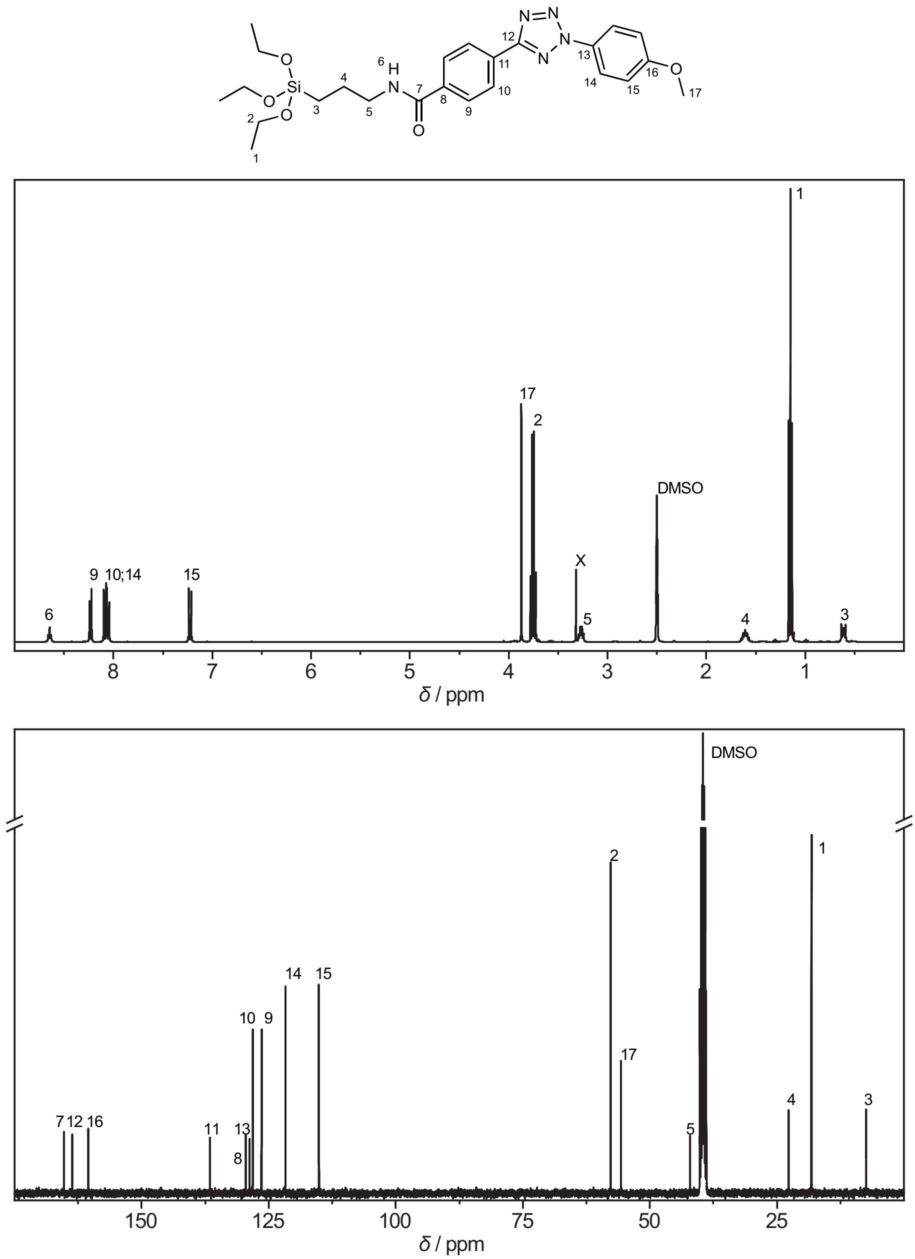

Figure A.5. ^{1}H NMR (top) and ^{13}C NMR (bottom) spectrum of **5** recorded in DMSO-d_6. For resonance assignment refer to the schematic molecular structure. X = H_2O.

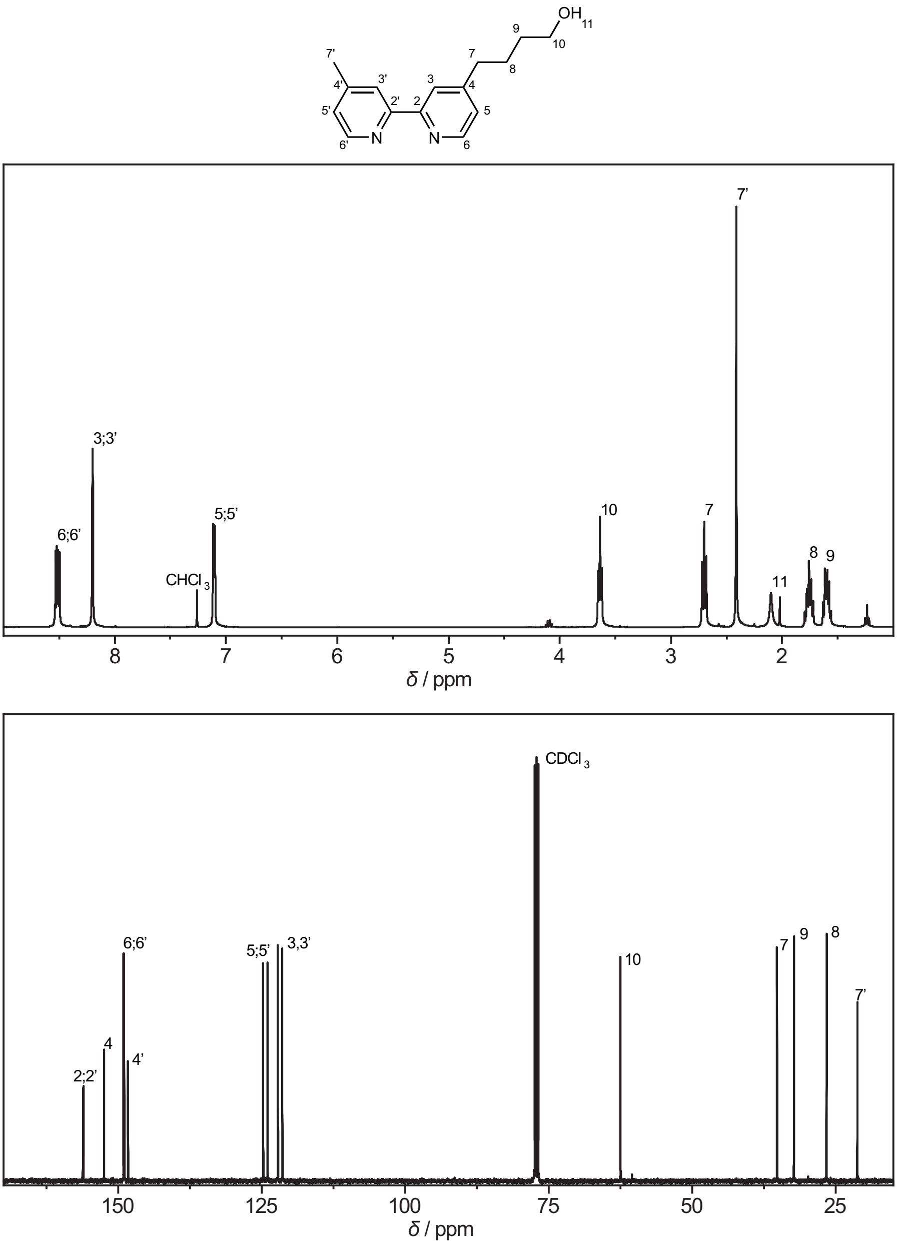

Figure A.6. ^{1}H NMR (top) and ^{13}C NMR (bottom) spectrum of **8** recorded in CDCl$_3$. For resonance assignment refer to the schematic molecular structure.

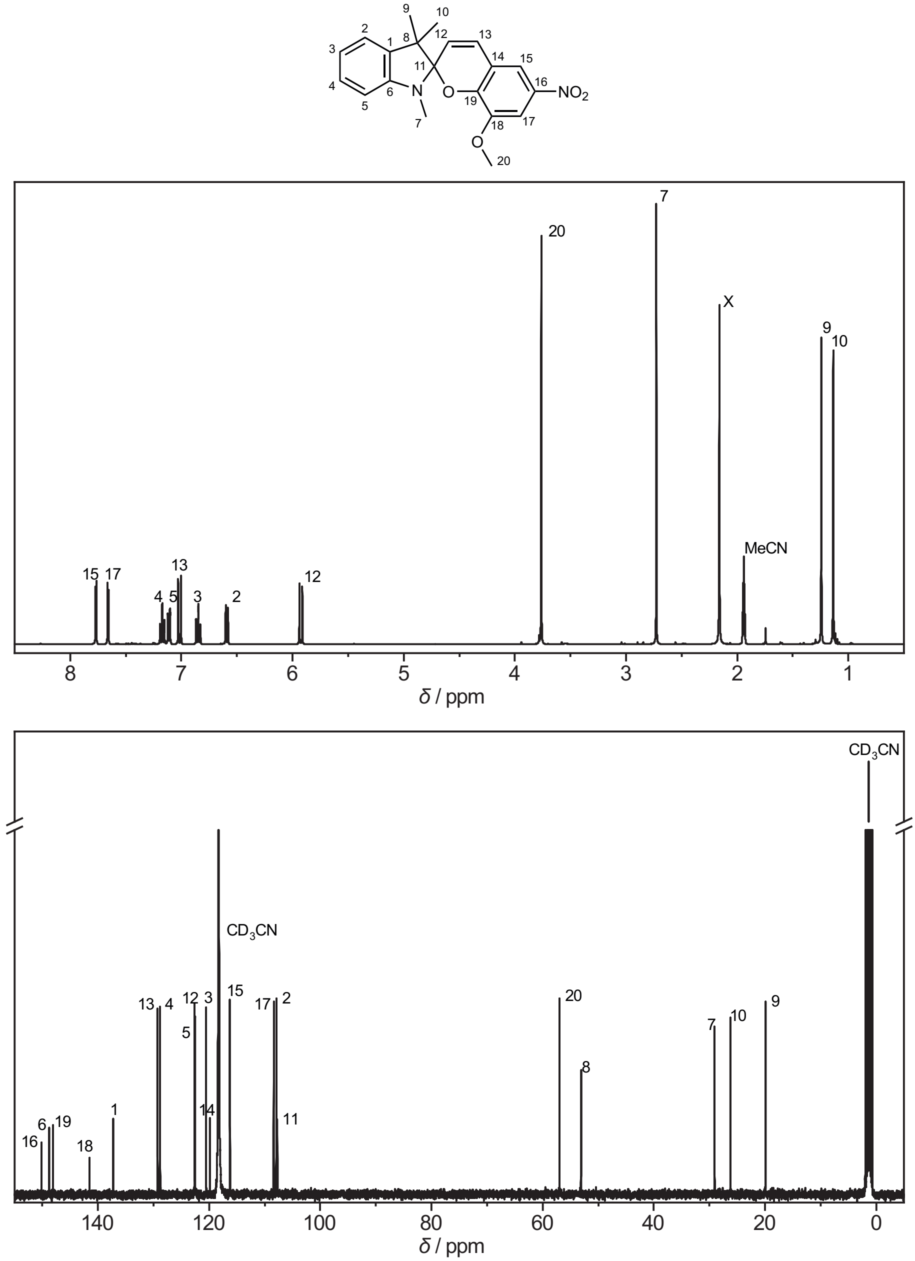

Figure A.7. ^{1}H NMR (top) and ^{13}C NMR (bottom) spectrum of **10** recorded in CD_3CN. For resonance assignment refer to the schematic molecular structure. X = H_2O.

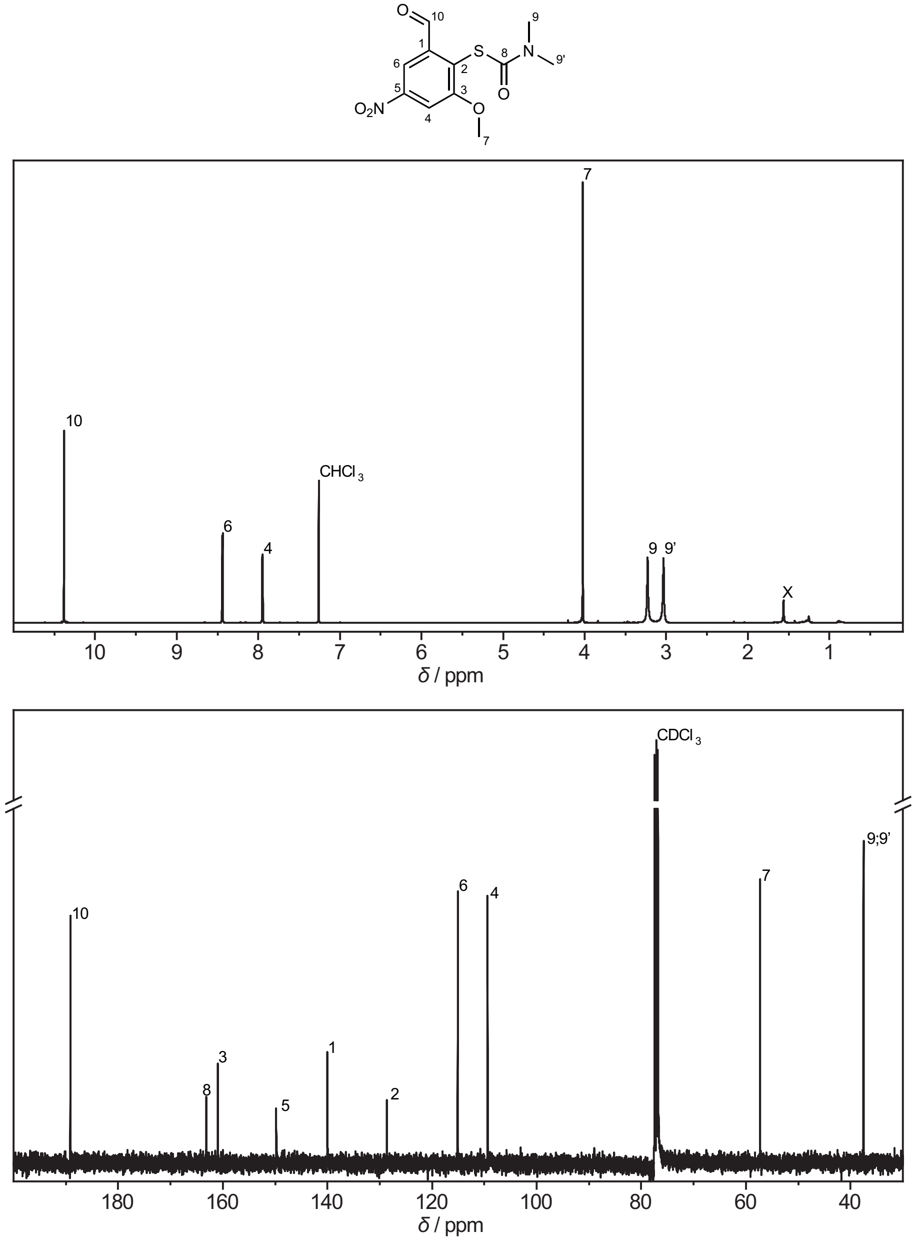

Figure A.8. ^{1}H NMR (top) and ^{13}C NMR (bottom) spectrum of **11b** recorded in $CDCl_3$. For resonance assignment refer to the schematic molecular structure. X = H_2O.

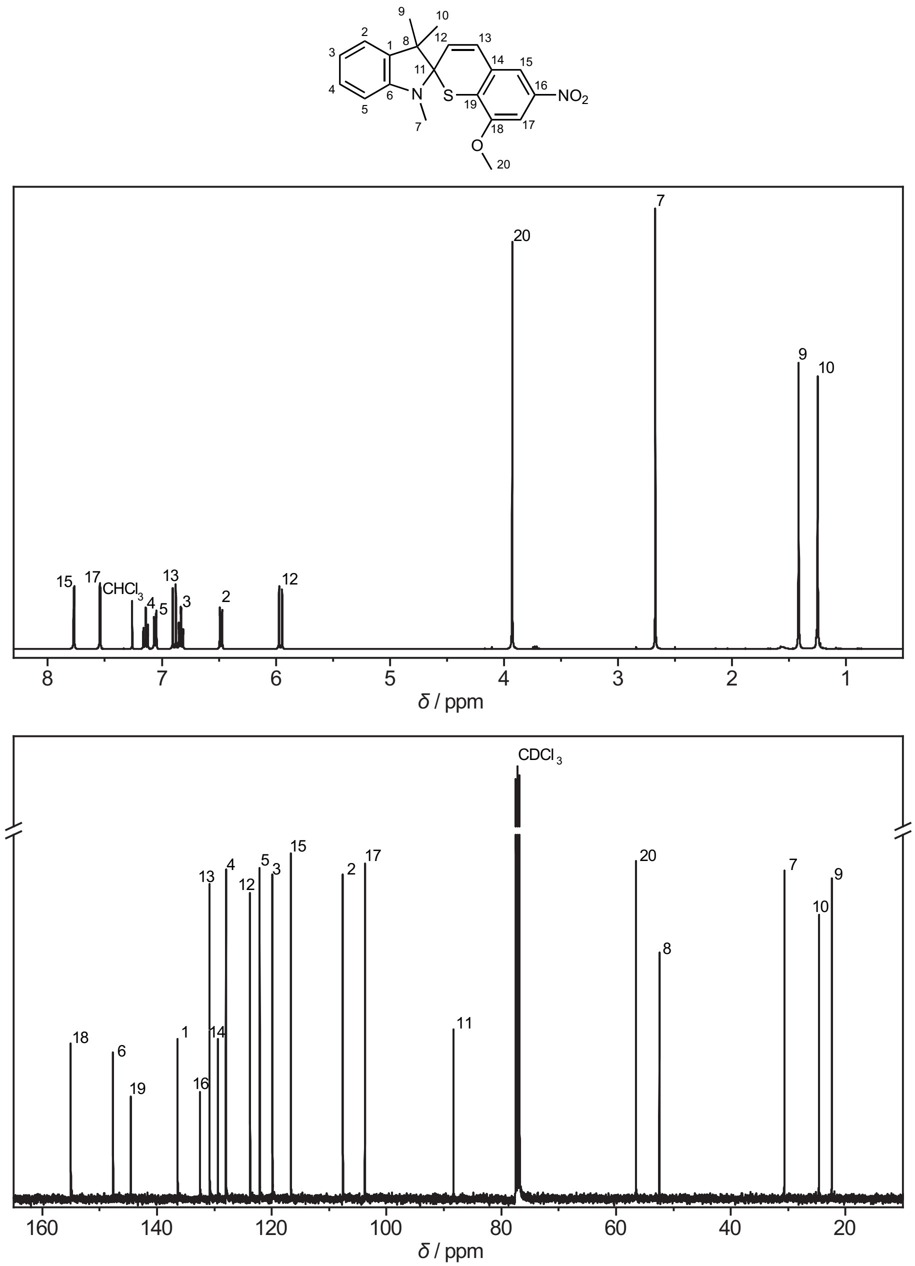

Figure A.9. ^{1}H NMR (top) and ^{13}C NMR (bottom) spectrum of **12** recorded in $CDCl_3$. For resonance assignment refer to the schematic molecular structure.

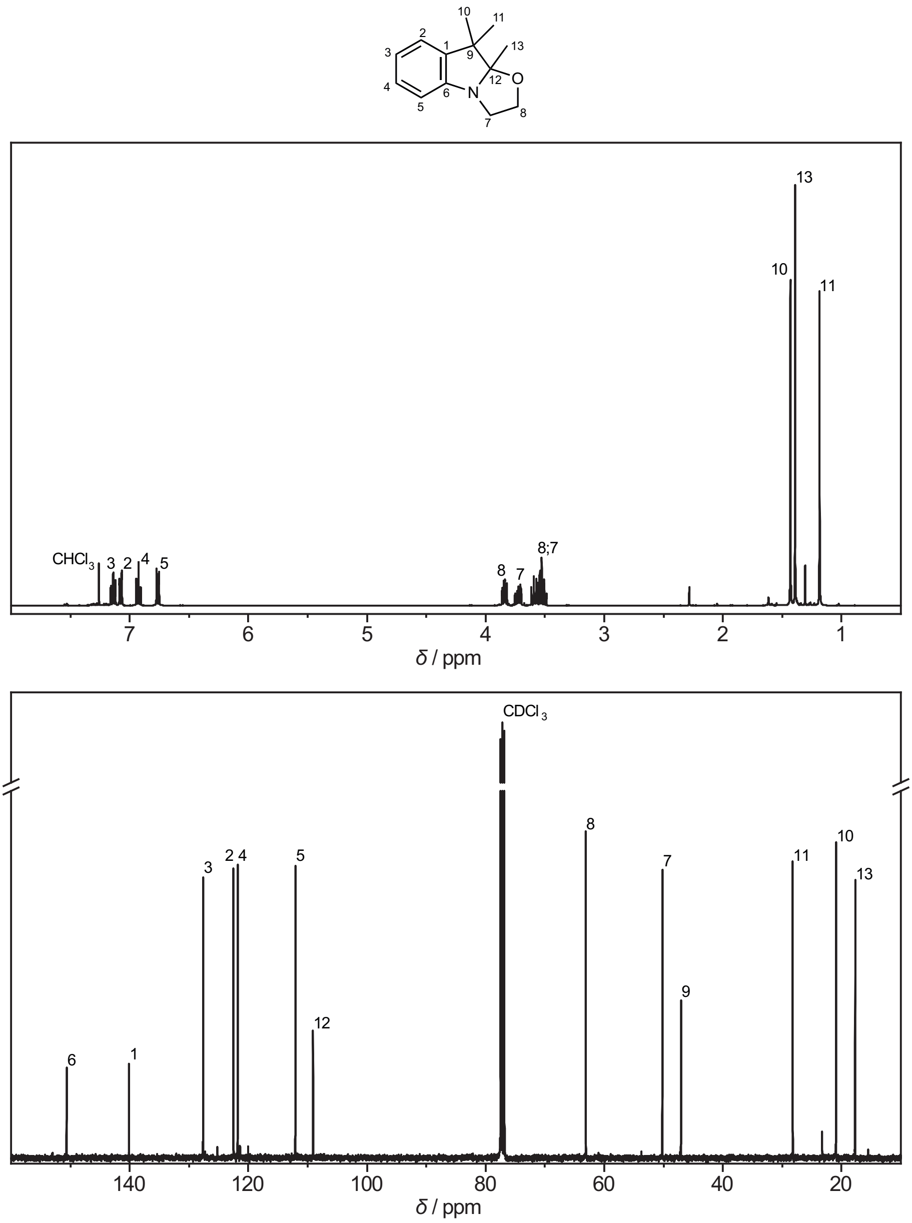

Figure A.10. ^{1}H NMR (top) and ^{13}C NMR (bottom) spectrum of **13** recorded in CDCl$_3$. For resonance assignment refer to the schematic molecular structure.

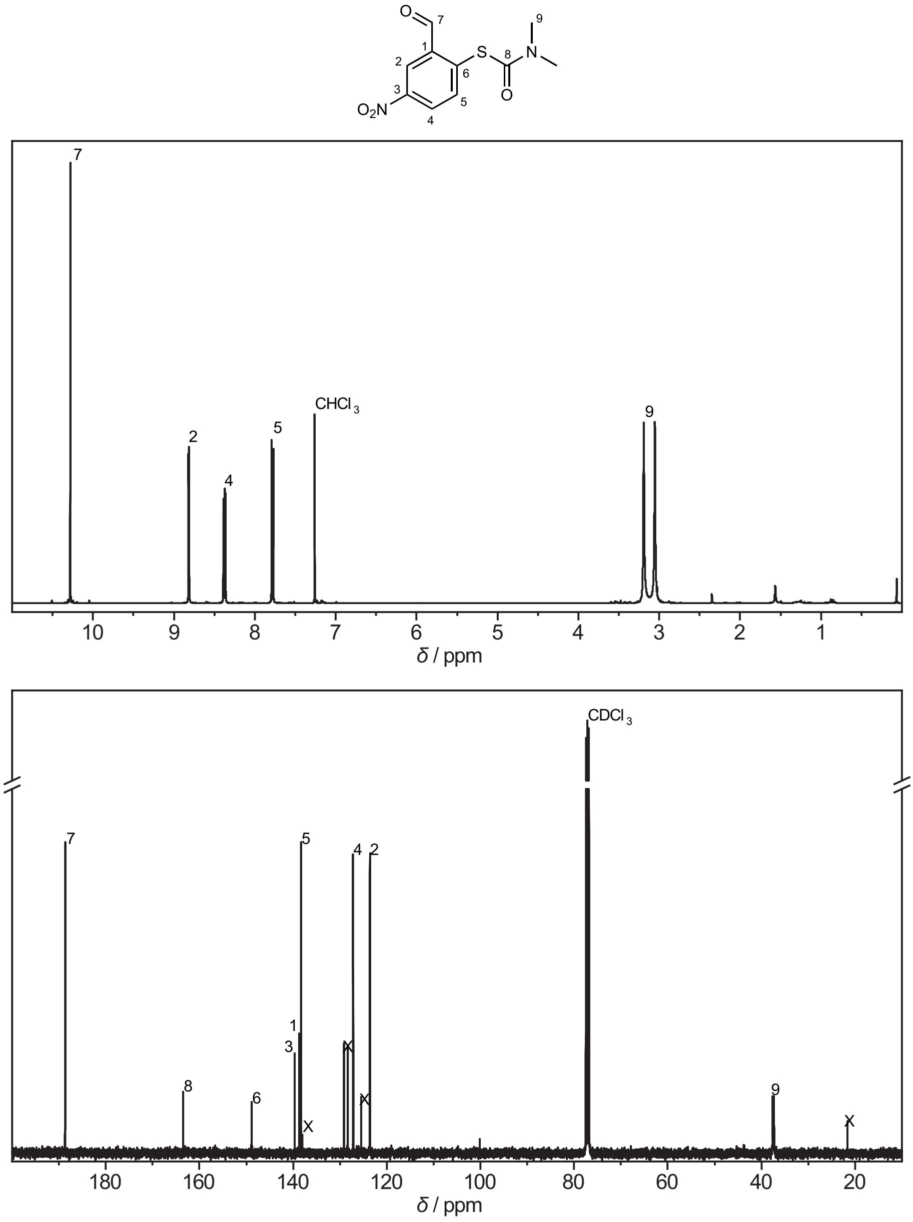

Figure A.11. ^{1}H NMR (top) and ^{13}C NMR (bottom) spectrum of **14b** recorded in CDCl$_3$. For resonance assignment refer to the schematic molecular structure. X = toluene.

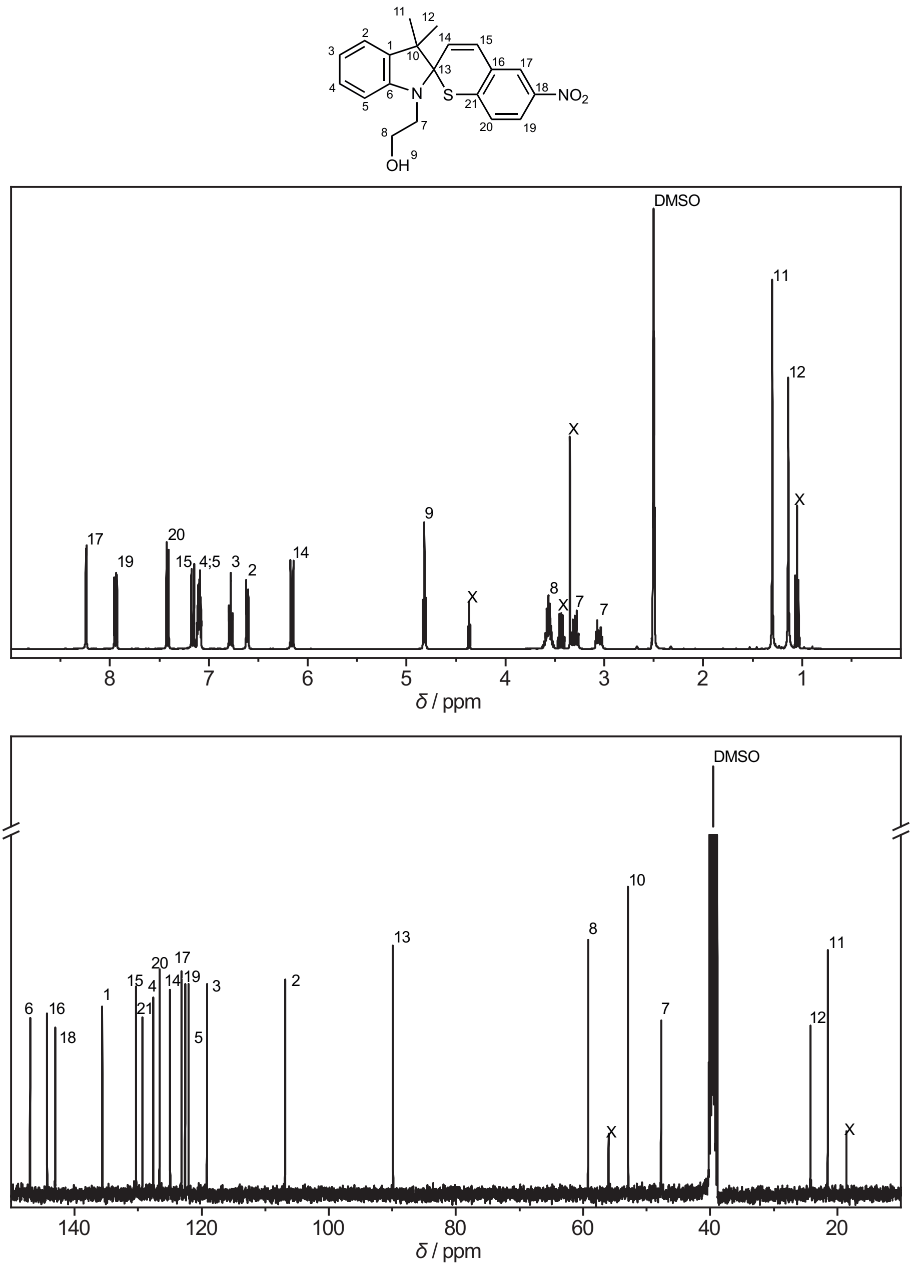

Figure A.12. ^{1}H NMR (top) and ^{13}C NMR (bottom) spectrum of **15** recorded in DMSO-d_6. For resonance assignment refer to the schematic molecular structure. X = EtOH, H_2O.

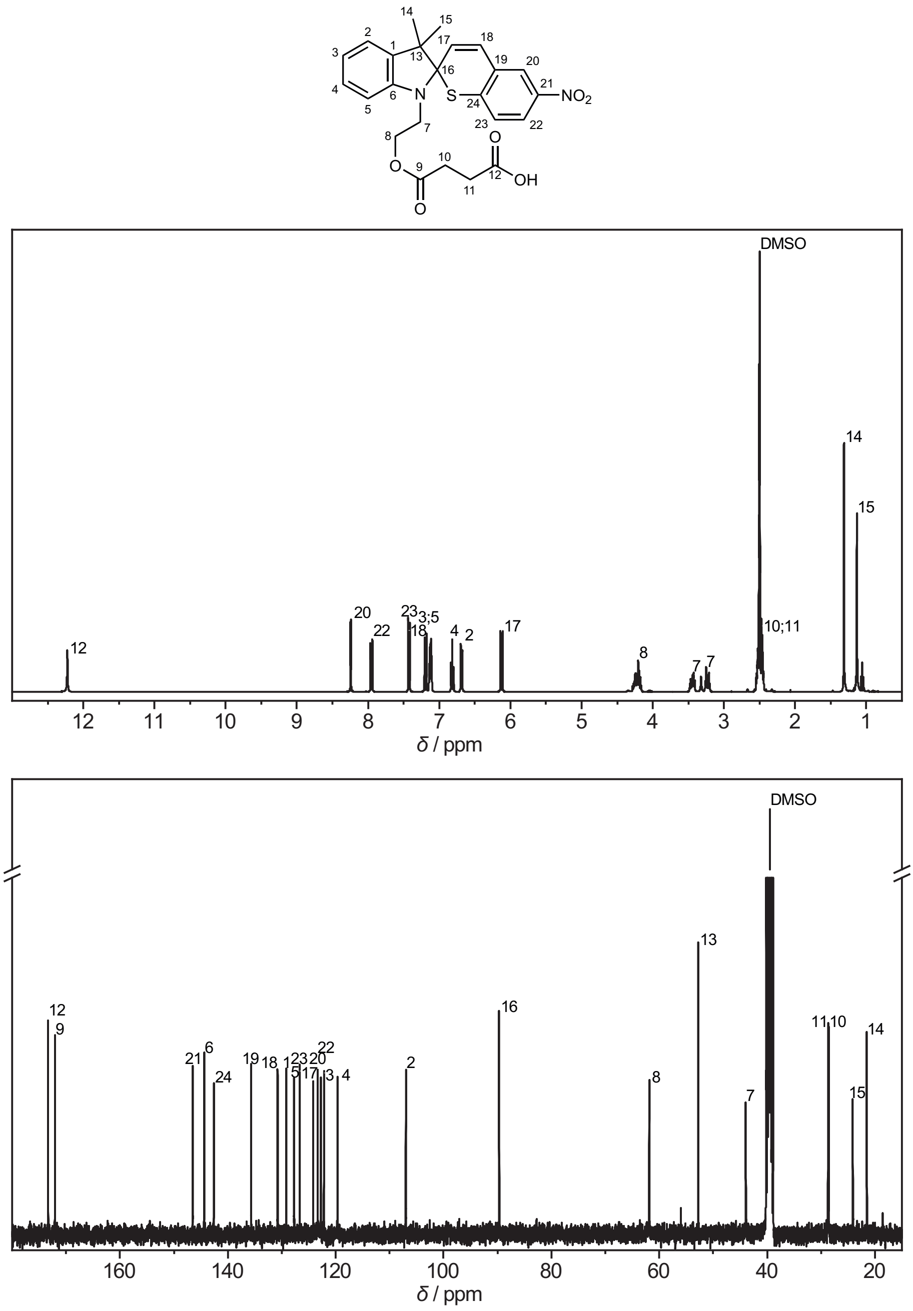

Figure A.13. ^{1}H NMR (top) and ^{13}C NMR (bottom) spectrum of **16** recorded in DMSO-d_6. For resonance assignment refer to the schematic molecular structure.

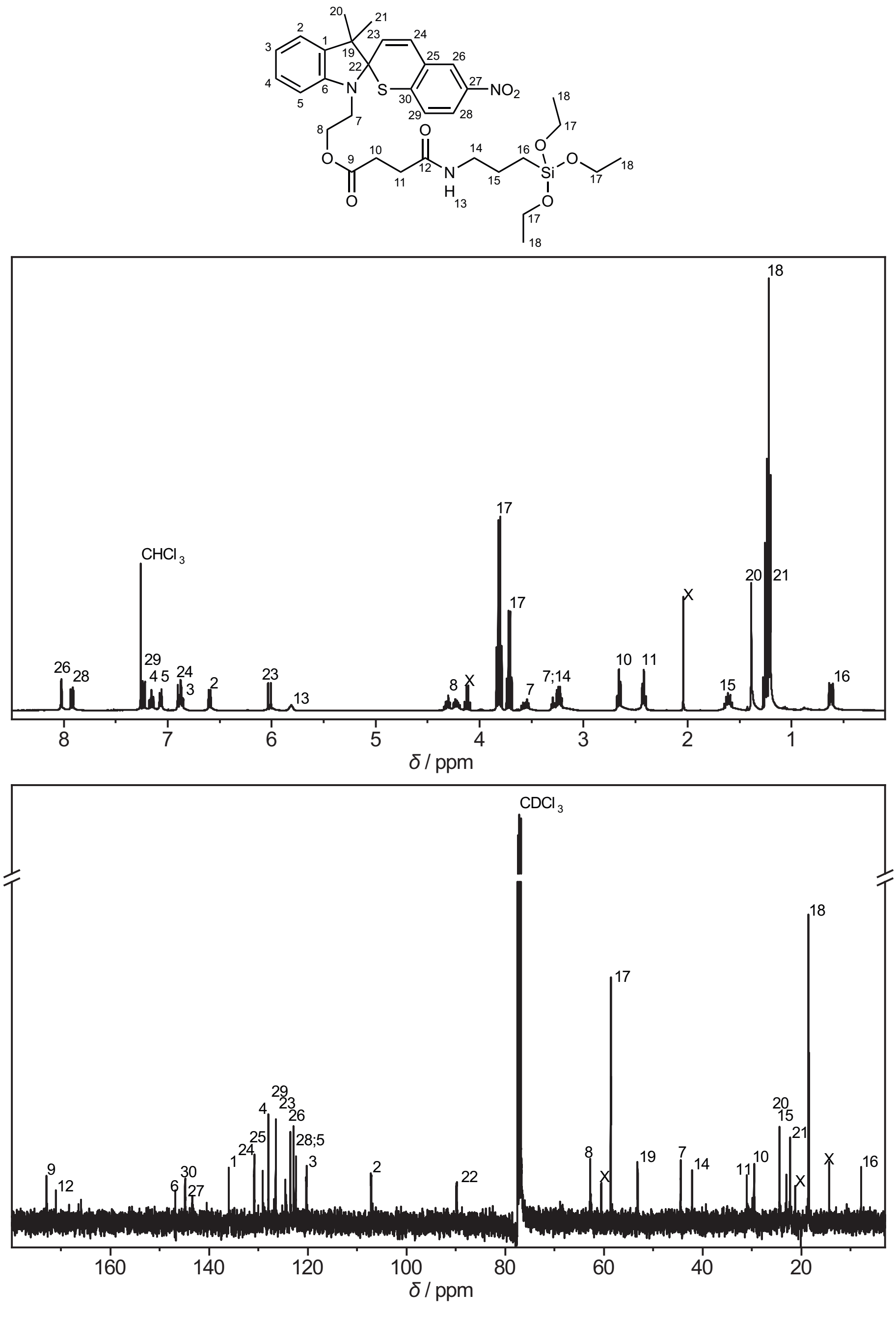

Figure A.14. ^{1}H NMR (top) and ^{13}C NMR (bottom) spectrum of **17** recorded in $CDCl_3$. For resonance assignment refer to the schematic molecular structure. X = EtOAc.

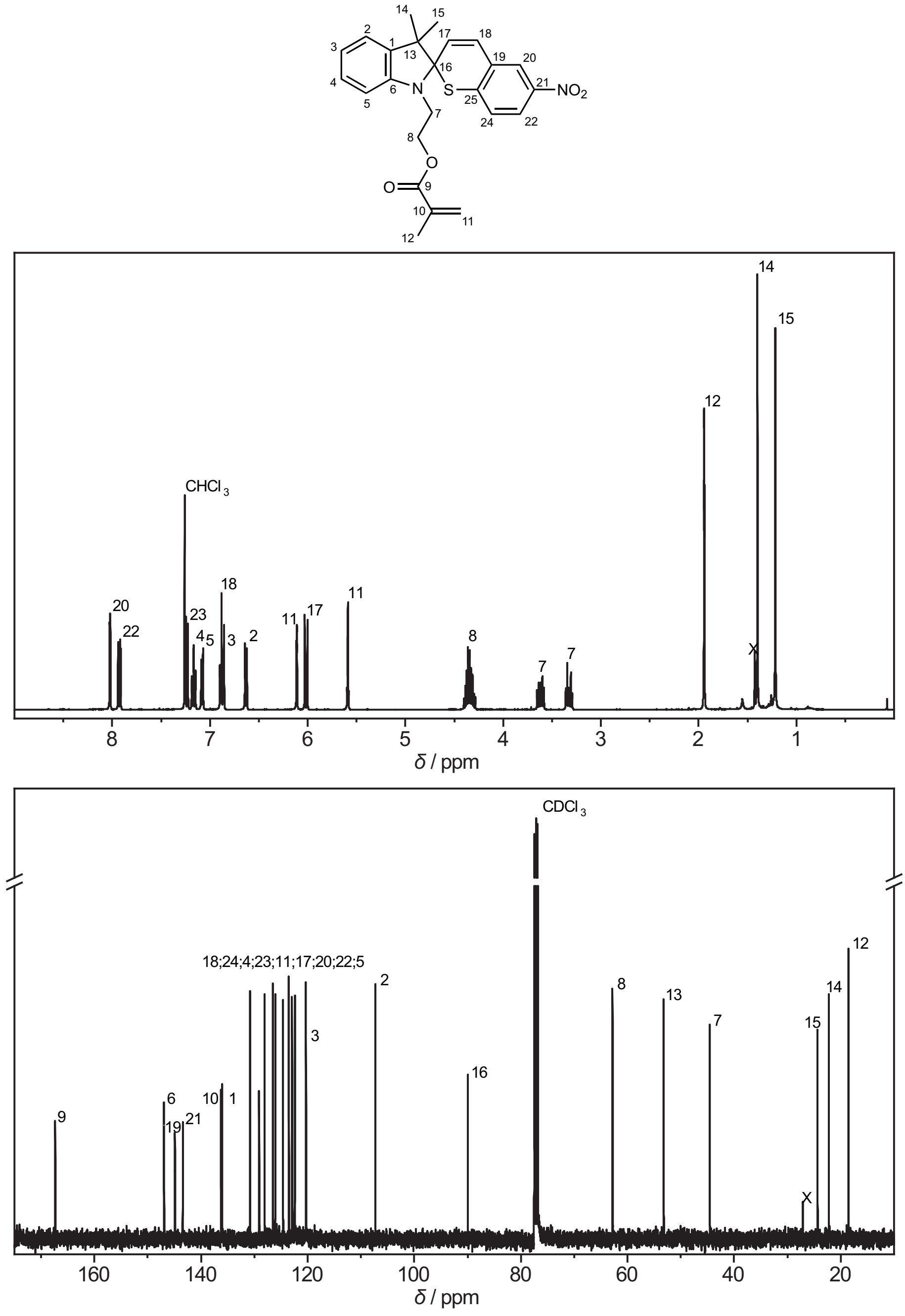

Figure A.15. ^{1}H NMR (top) and ^{13}C NMR (bottom) spectrum of **18** recorded in $CDCl_3$. For resonance assignment refer to the schematic molecular structure. X = $c$$C_6H_{12}$.

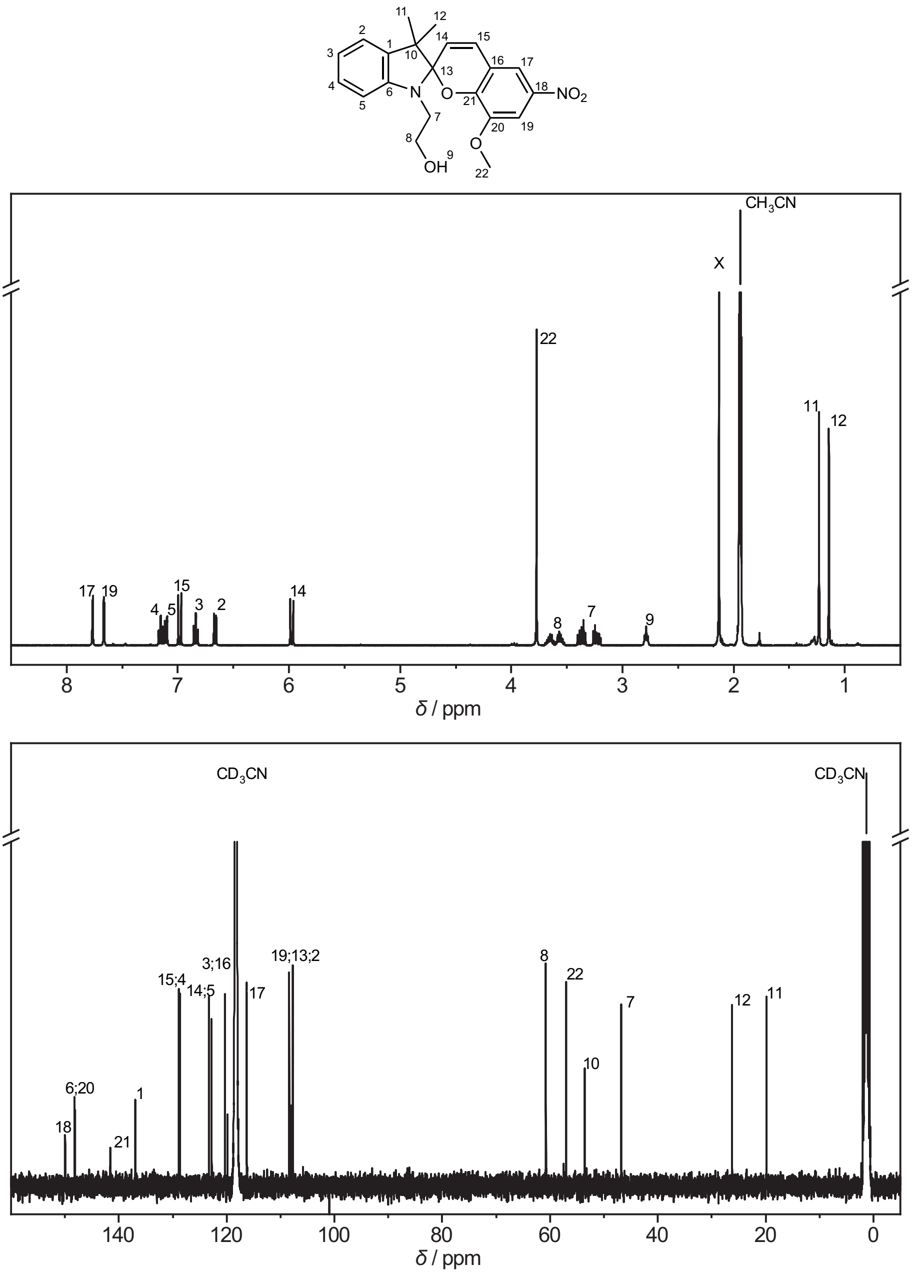

Figure A.16. ^{1}H NMR (top) and ^{13}C NMR (bottom) spectrum of **19** recorded in CD_3CN. For resonance assignment refer to the schematic molecular structure. X = H_2O.

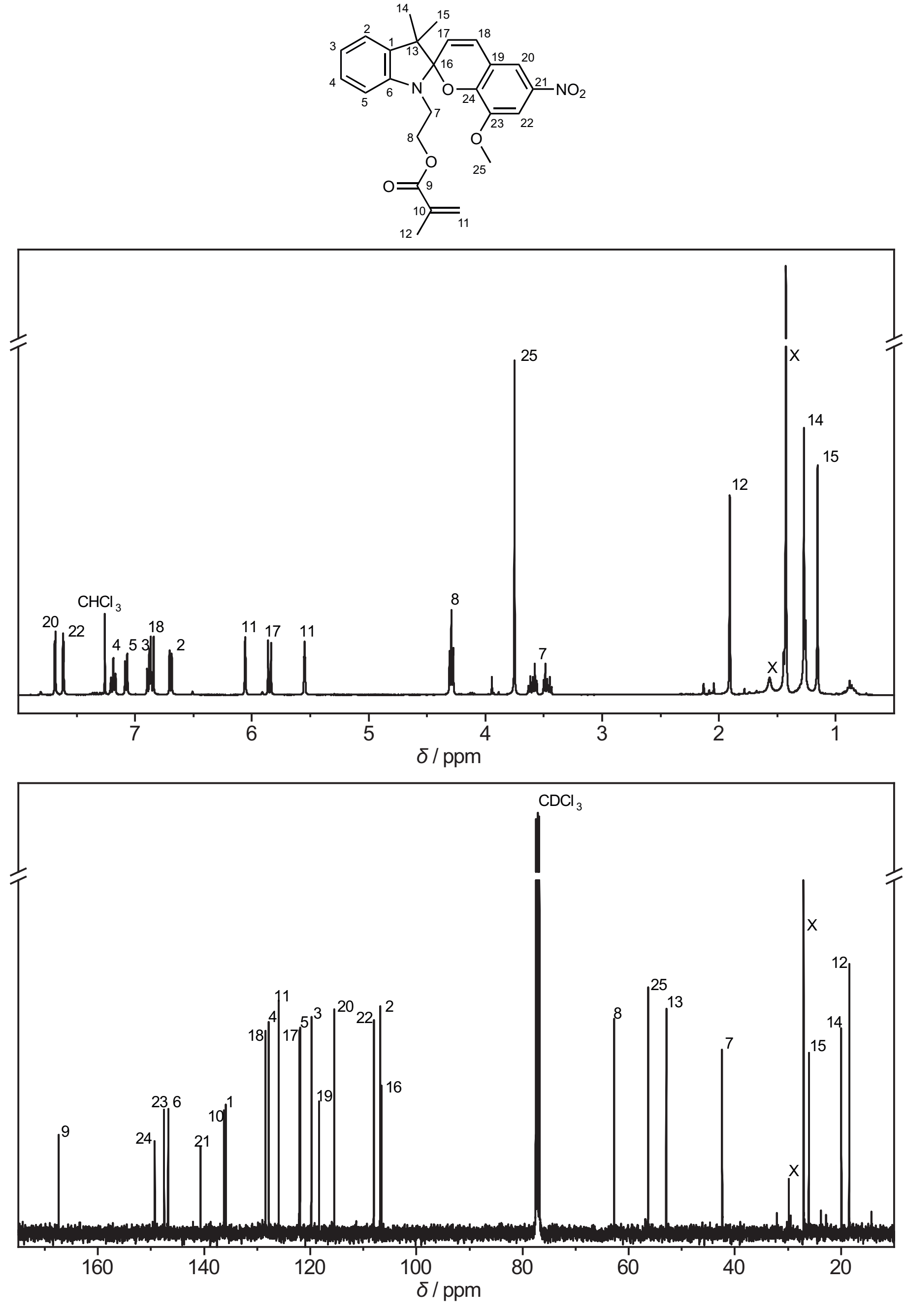

Figure A.17. ^{1}H NMR (top) and ^{13}C NMR (bottom) spectrum of **20** recorded in $CDCl_3$. For resonance assignment refer to the schematic molecular structure. X = cC_6H_{12}, H_2O, grease.

A.6 UV-Vis spectra

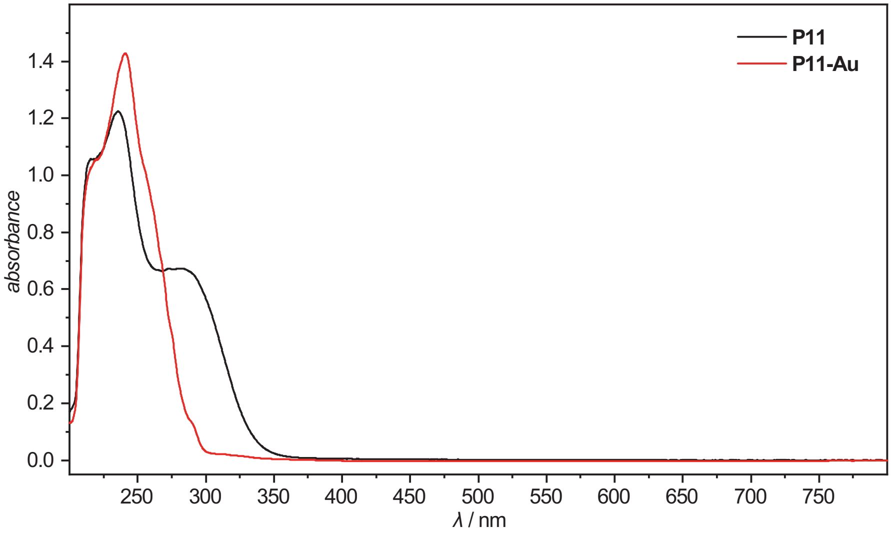

Figure A.18. UV-Vis spectra of copolymer **P11** and the metallopolymer **P11-Au** measured in 1,4-dioxane (1 mg mL^{-1}).

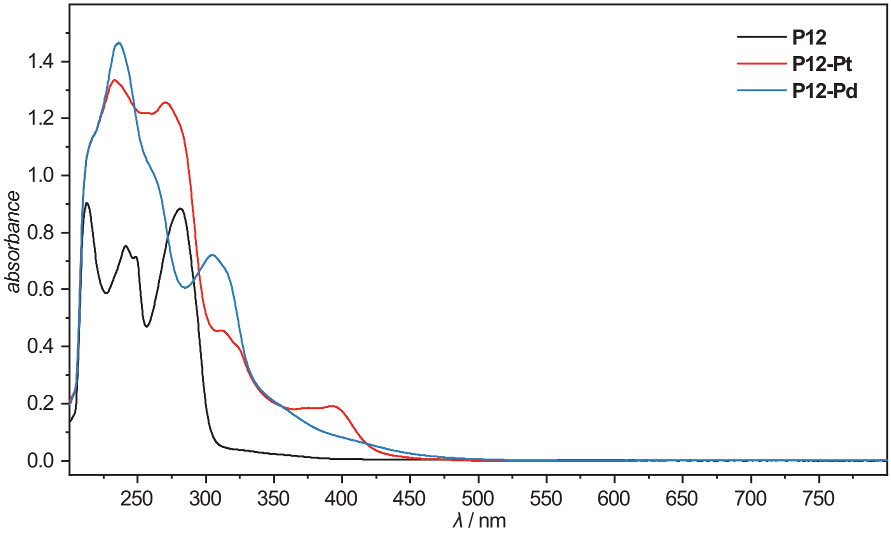

Figure A.19. UV-Vis spectra of copolymer **P12** and the metallopolymers **P12-Pt** and **P12-Pd** measured in 1,4-dioxane (1 mg mL^{-1}).

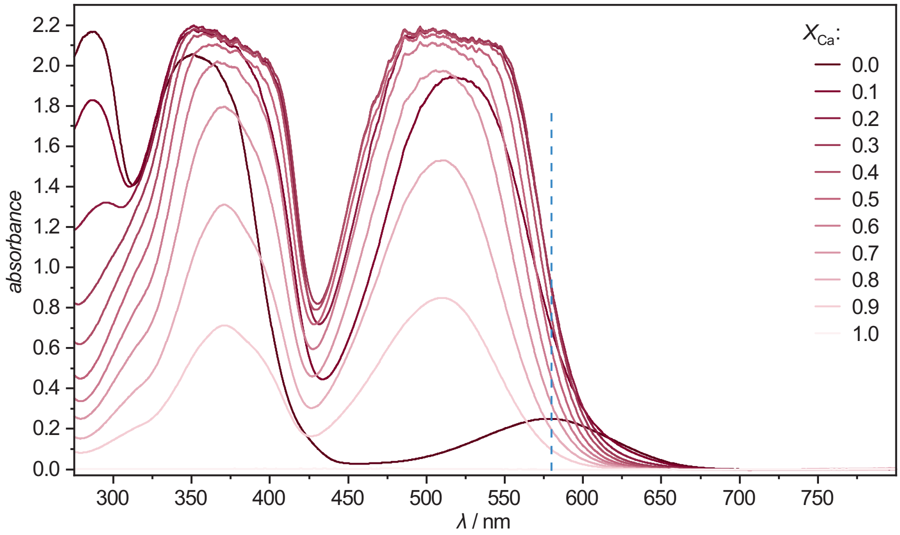

Figure A.20. UV-Vis spectra of **10-Ca** for the determination of the complex stoichiometry using Job's method of continuous variations. The wavelength at 580 nm used for the Job's plot analysis is indicated with the dashed blue line. [**10**]+[**Ca**] = 2.8 mM in MeCN, measured in a 1 mm cuvette.

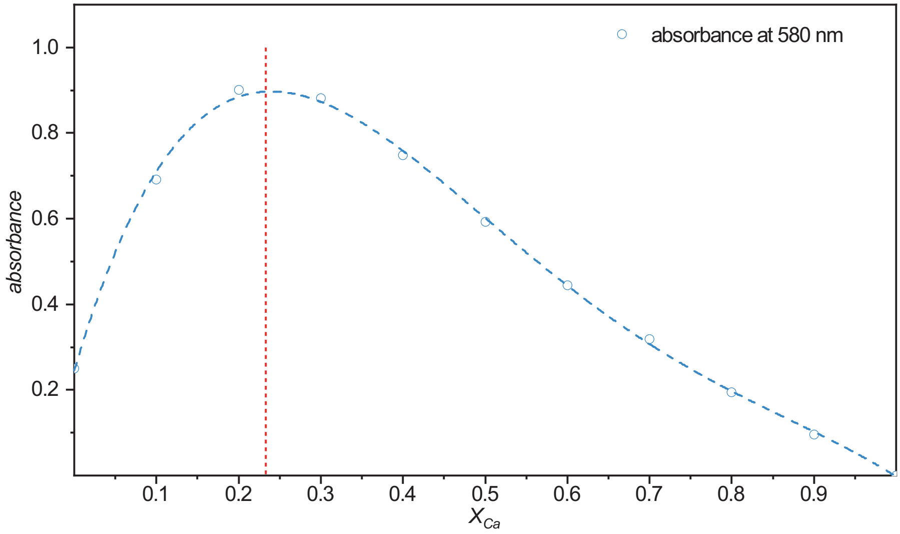

Figure A.21. Job's plot analysis of the spectra in Figure A.20. The maximum of the interpolated dashed blue line lies at $X_{\mathrm{Ca}} = 0.23$.

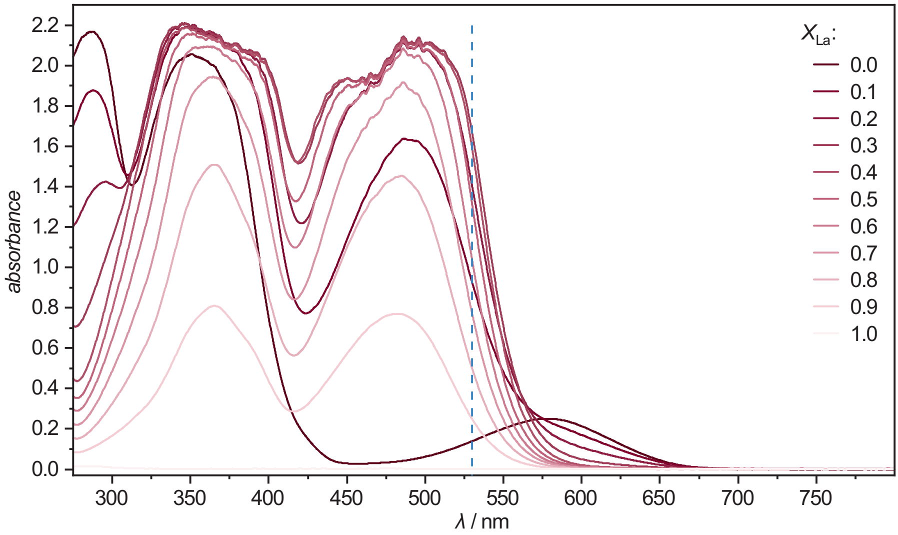

Figure A.22. UV-Vis spectra of **10-La** for the determination of the complex stoichiometry using Job's method of continuous variations. The wavelength at 530 nm used for the Job's plot analysis is indicated with the dashed blue line. [**10**]+[**La**] = 2.8 mM in MeCN, measured in a 1 mm cuvette.

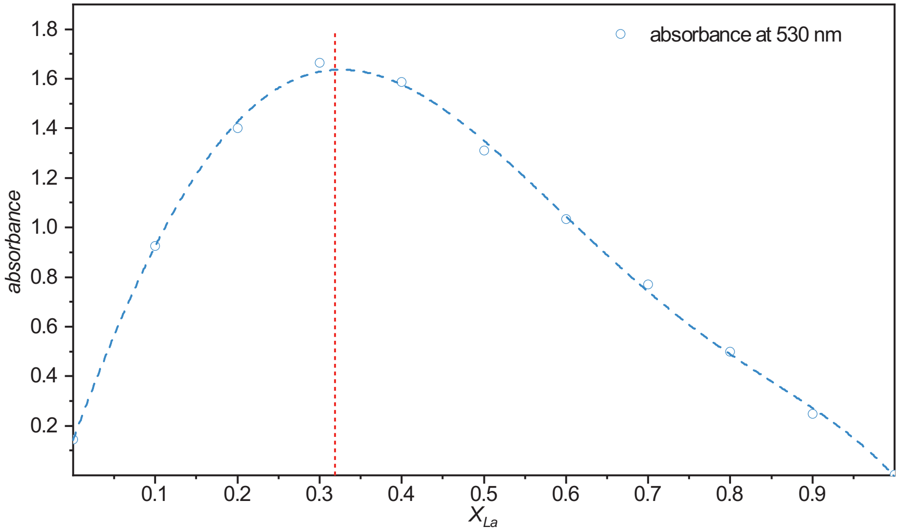

Figure A.23. Job's plot analysis of the spectra in Figure A.20. The maximum of the interpolated dashed blue line lies at $X_{\mathrm{La}} = 0.32$.

A.7 Emission spectra

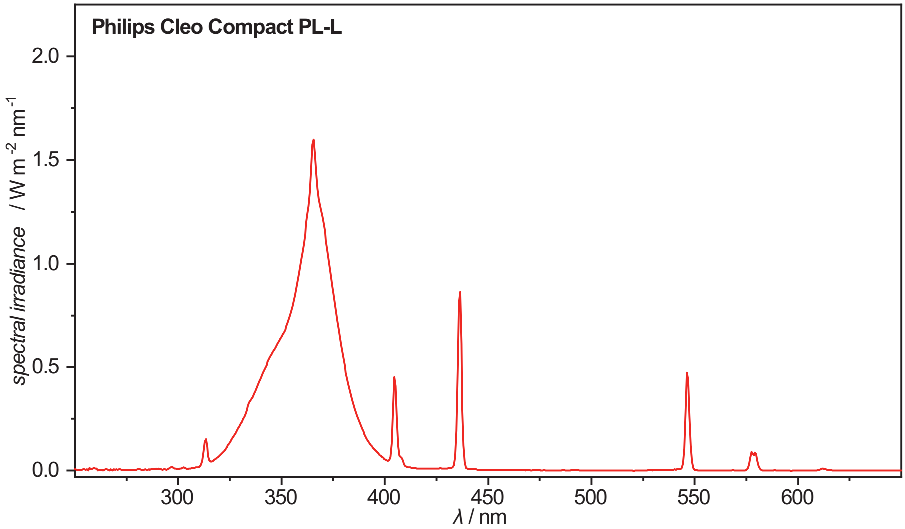

Figure A.24. Spectral irradiance of the Philips Cleo Compact PL-L UV lamp employed for the phenacyl sulfide photoreactions. Measured at a distance of 6 cm in the custom-build photoreactor.

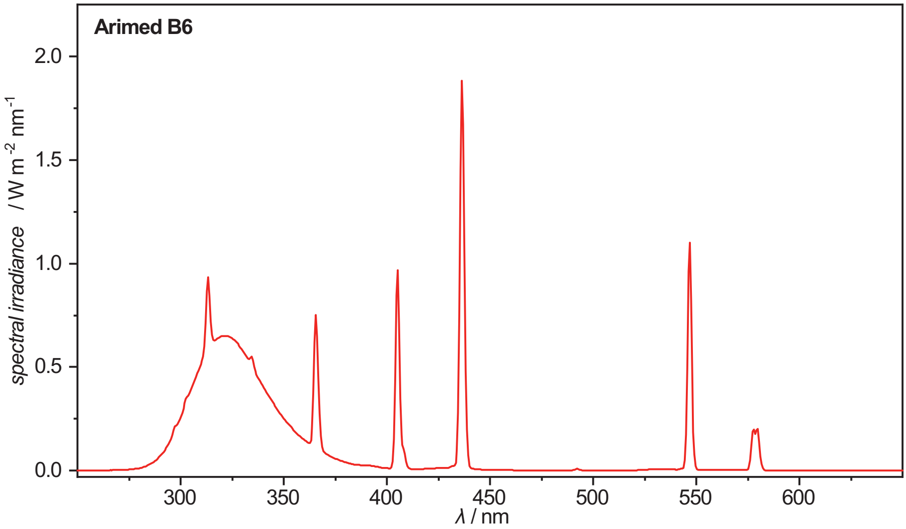

Figure A.25. Spectral irradiance of the Arimed B6 UV lamp employed for the NITEC and photoenol photoreactions. Measured at a distance of 2.5 cm in the custom-build photoreactor.

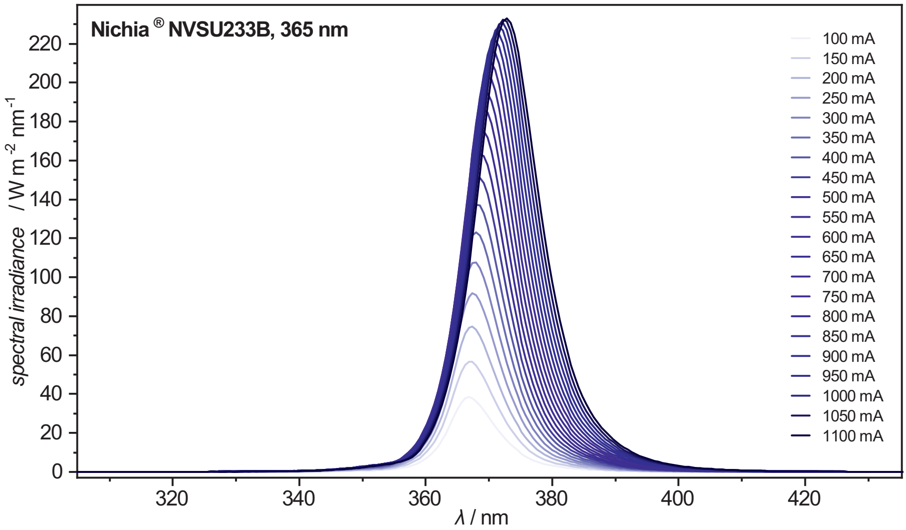

Figure A.26. Spectral irradiance of the 365 nm LED employed for the LED-NMR experiments. Measured at a distance of 1 cm for various LED currents.

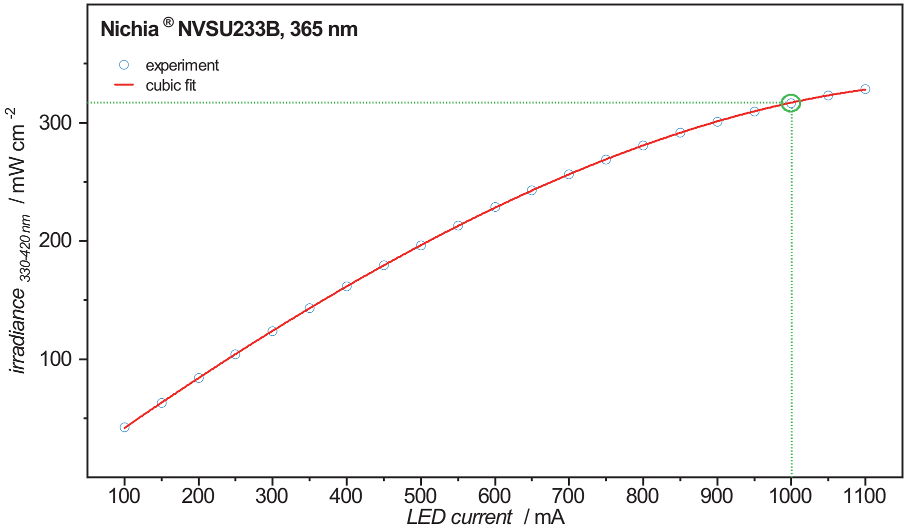

Figure A.27. Irradiance of the 365 nm LED employed for the LED-NMR experiments integrated from 330–420 nm, plotted against the applied LED current, and fitted to a cubic polynomial function. The operation mode for the LED-NMR experiments is indicated.

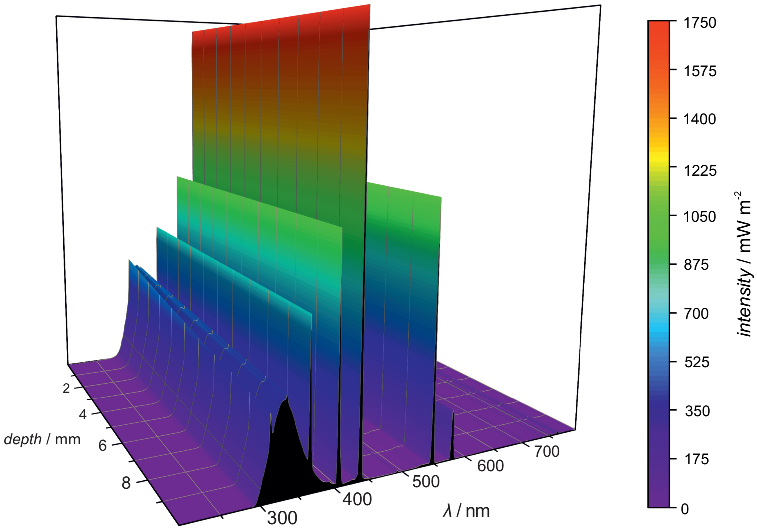

Figure A.28. 3D Surface plot of the relationship between the spectral irradiance of the light source after passing through the reaction solution of **P11-Au** (1 mg mL^{-1} in 1,4-dioxane) at arbitrary distances.

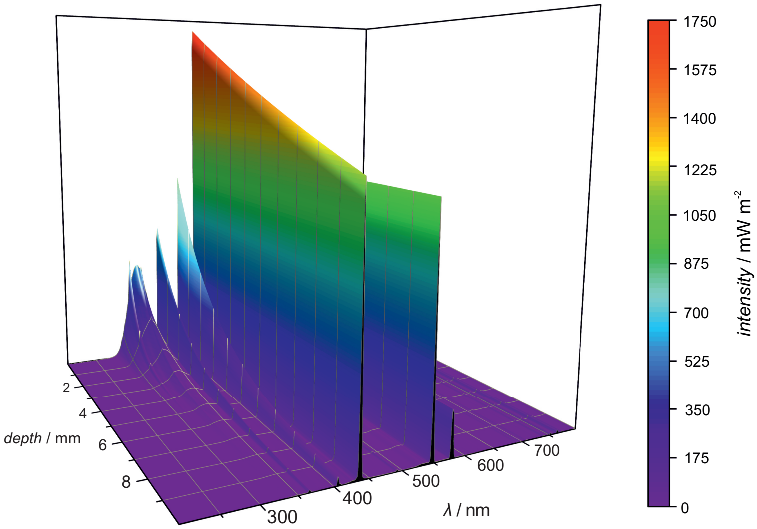

Figure A.29. 3D Surface plot of the relationship between the spectral irradiance of the light source after passing through the reaction solution of **P12-Pt** (1 mg mL^{-1} in 1,4-dioxane) at arbitrary distances.

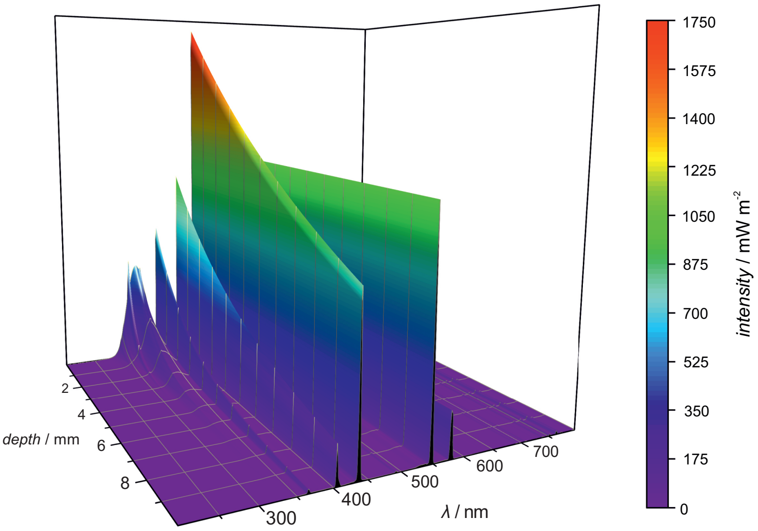

Figure A.30. 3D Surface plot of the relationship between the spectral irradiance of the light source after passing through the reaction solution of **P12-Pd** (1 mg mL^{-1} in 1,4-dioxane) at arbitrary distances.

A.8 SEC chromatograms

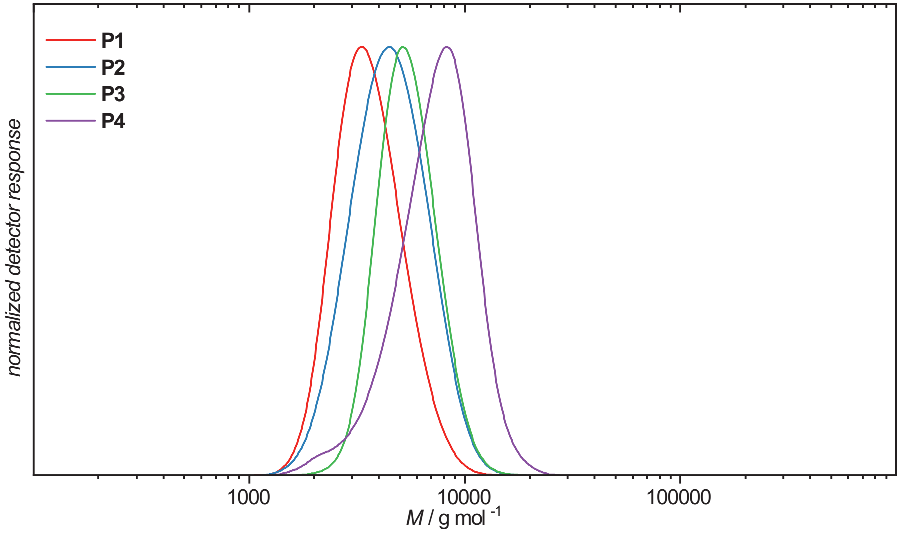

Figure A.31. SEC traces of the PMMA homopolymers **P1**, **P2**, **P3**, and **P4**.

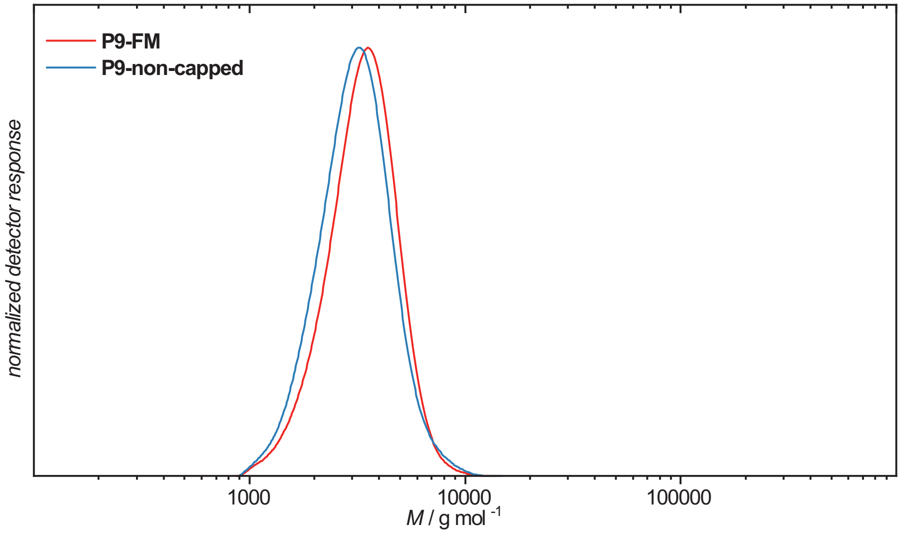

Figure A.32. SEC traces of the PMMA homopolymers **P9-FM** and **P9-non-capped**.

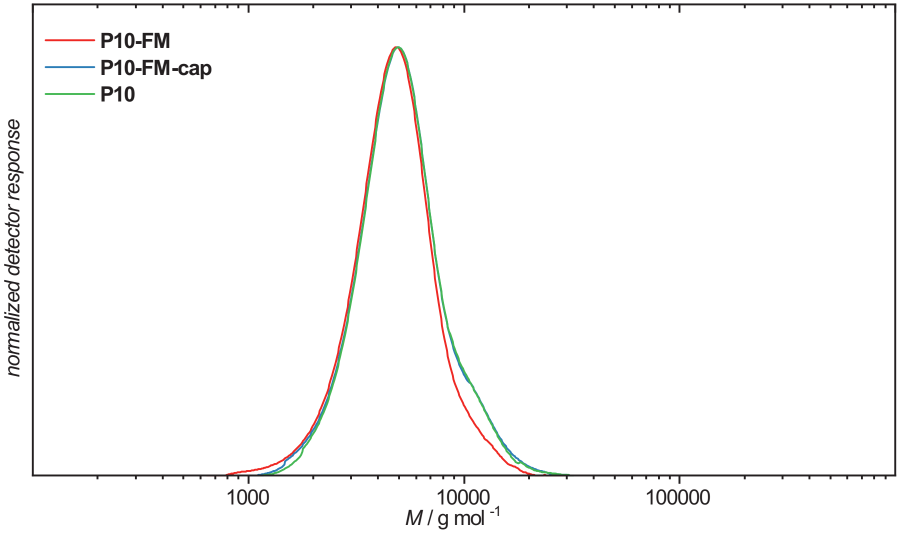

Figure A.33. SEC traces of the PMMA homopolymers **P10-FM**, and **P10-FM-cap**, and **P10**.

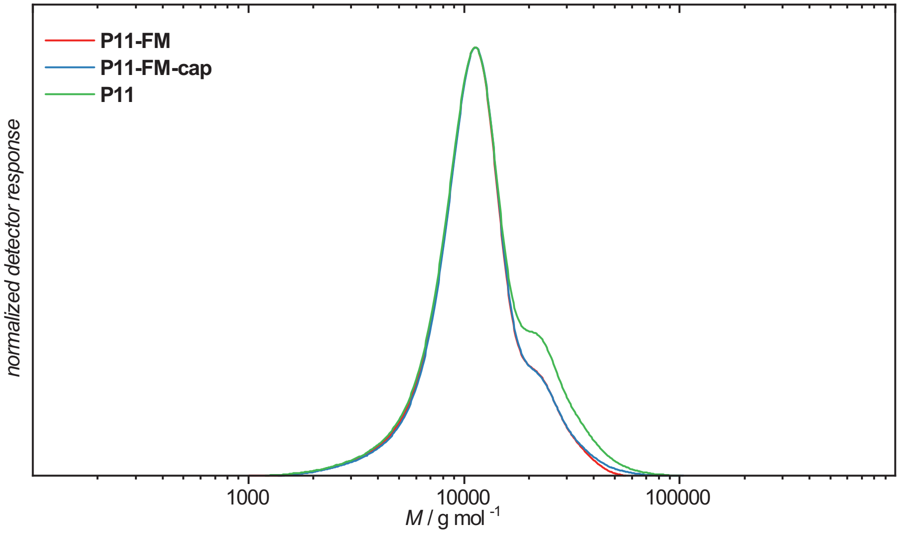

Figure A.34. SEC traces of the three prepared phosphine ligand copolymers **P11-FM**, **P11-FM-cap**, and **P11**.

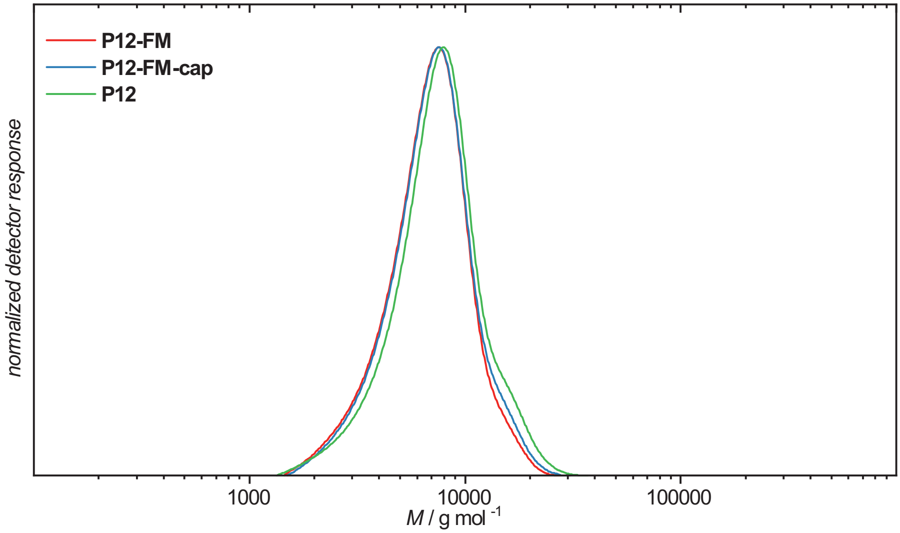

Figure A.35. SEC traces of the three prepared bipyridine ligand copolymers **P12-FM**, **P12-FM-cap**, and **P12**.

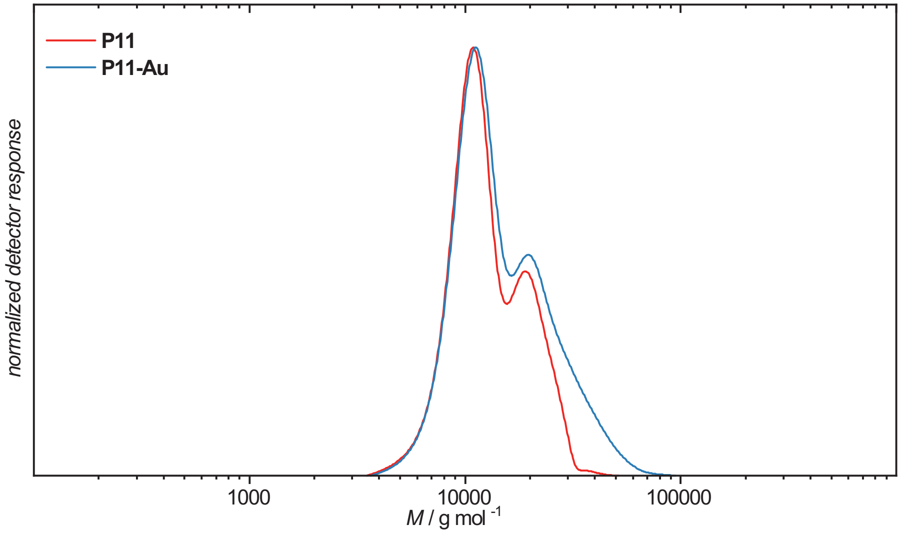

Figure A.36. SEC traces of the free phosphine ligand copolymer **P11** and the gold functionalized metallopolymer **P11-Au**.

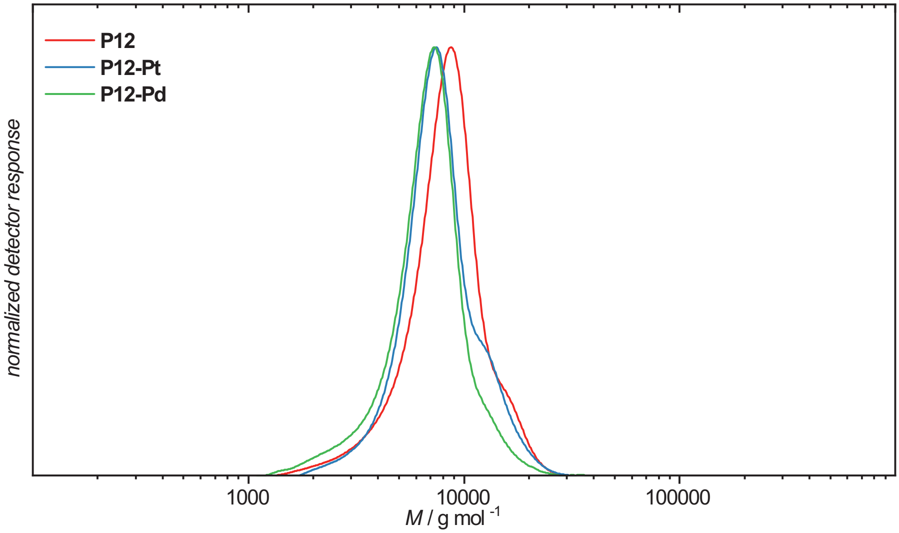

Figure A.37. SEC traces of the free bipyridine ligand copolymer **P12** and the platinum and palladium metallopolymers **P12-Pt** and **P12-Pd**, respectively.

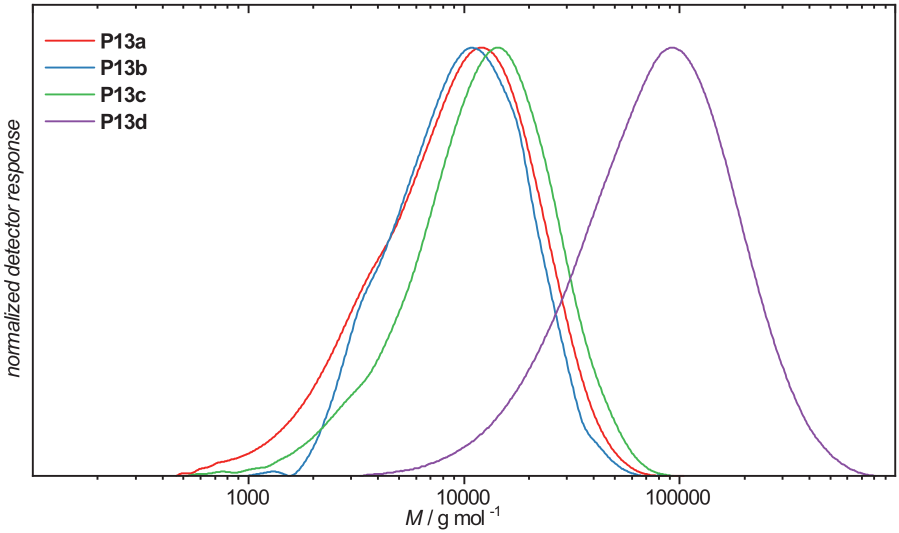

Figure A.38. SEC traces of the STP-containing copolymers **P13a–d**.

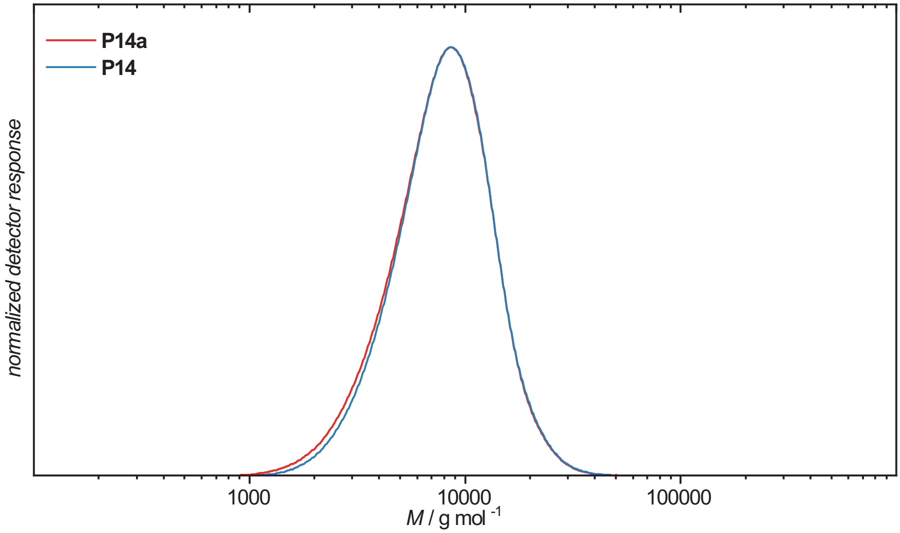

Figure A.39. SEC traces of the maleimide-containing copolymers **P14a** (furan protected) and **P14**.

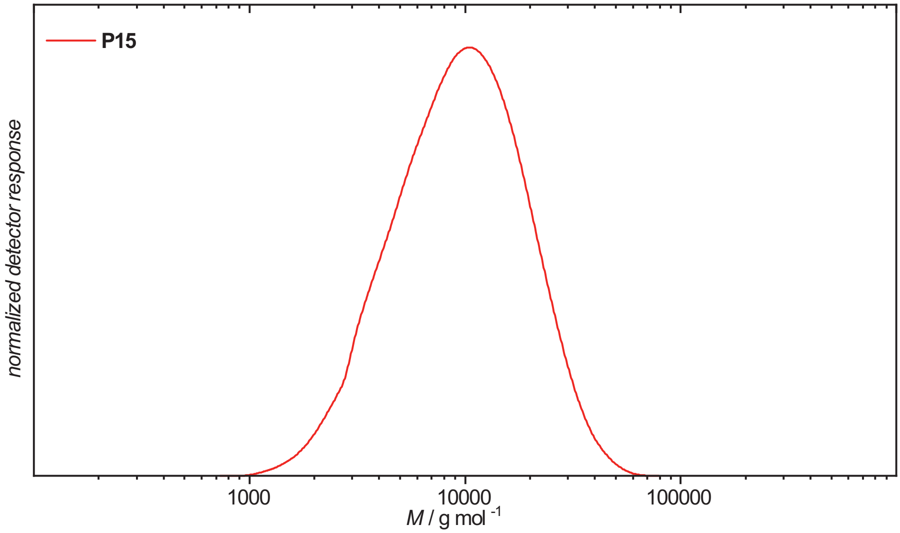

Figure A.40. SEC trace of the SP-containing copolymer **P15**.

A.9 ToF-SIMS and XPS analysis

Table A.1. Description of ToF-SIMS fragments and their aliases used for structure elucidation in the ToF-SIMS mappings.

alias	description	characteristic fragments used for mappings	
		negative polarity	positive polarity
total	total ion count	All ions	All ions
silicon	residual substrate signal	–	Si^+
tetrazole	surface anchored tetrazole	–	$C_4H_2NO^+$, $C_6H_4NO^+$, $C_7H_7NO^+$, $C_7H_8NO^+$
RAFT group	capped dithiobenzoate RAFT moiety	–	$S_2O_2C_9H_9^+$, $S_2O_2C_{16}H_{17}^+$, $S_2O_2C_{10}H_{12}^+$
bipyridine	ligand **9**	–	$C_6H_6N^+$, $C_{11}N_2H_9^+$, $C_{10}H_6N_2^+$
PMMA	PMMA polymer backbone	$C_3H_3O^-$, $C_4H_5O_2^-$	–
phosphine	ligand **7**	C_6P^-, $C_6H_5P^-$, $C_6H_4P^-$	–
gold	**7-AuCl** complex in the copolymer	$Au^{-(a)}$	–
platinum	**9-PtCl$_2$** complex in the copolymer	Pt^-, $PtCl_2^-$	–
palladium	**9-PdCl$_2$** complex in the copolymer	Pd^-, $PdCl_2^-$	–

(a) Only Au^- was used, as the isotopic pattern of the $AuCl^-$ ion is overlapping with isotopic patterns of the $PtCl^-$ and $PtCl_2^-$ ions, respectively.

Table A.2. Description of the surface reaction setups with the employed shadow masks. The different shadow masks are depicted below the table.

surface reaction setup	employed shadow masks step 1)	step 2)	step 3)
A	no mask	–	–
A-KIT	KIT mask	–	–
B	point mask (I)	point mask (II)	–
C	point mask (III)	point mask (IV)	point mask (V)
D	point mask (I)	point mask (II)	no mask

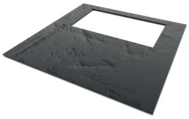

no mask

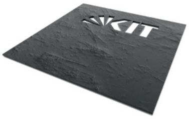

KIT mask

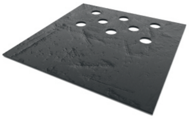

point mask (I)

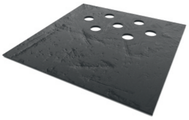

point mask (II)

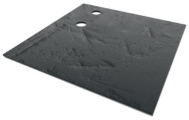

point mask (III)

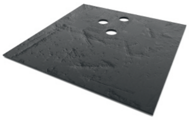

point mask (IV)

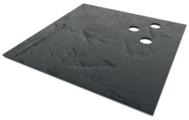

point mask (V)

A.9.1 Monofunctional patterning

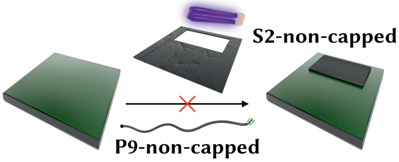
S2-non-capped
P9-non-capped

Scheme A.26. Attachment of **P9-non-capped** on surface **S2-non-capped** (setup A).

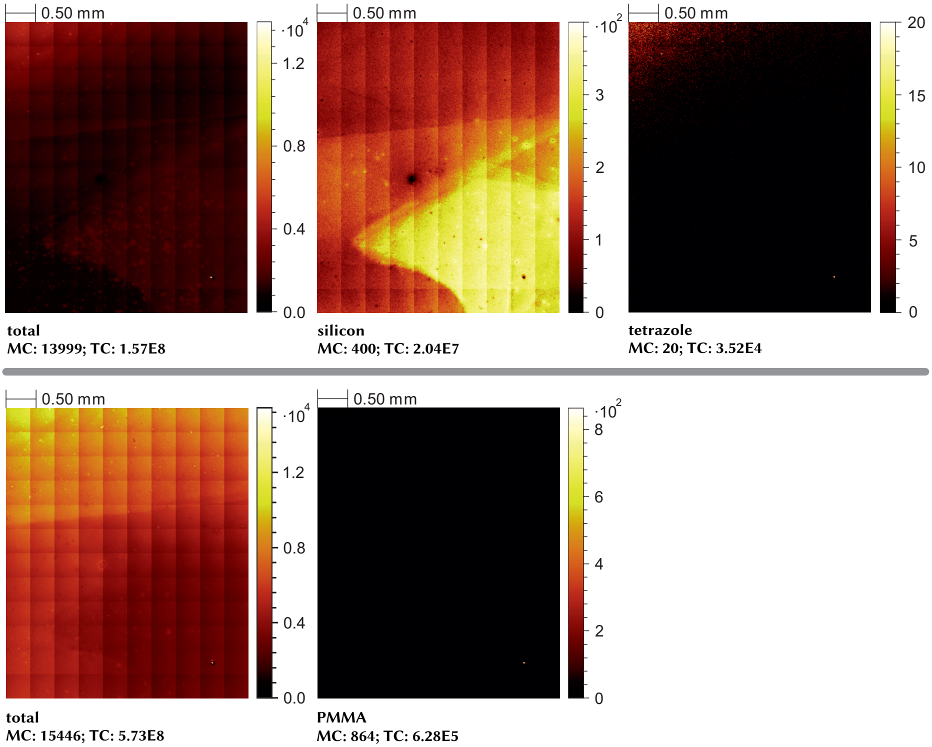

Figure A.41. ToF-SIMS spectra of **S2-non-capped**. Positive polarity (top), negative polarity (bottom).

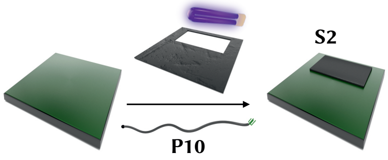

Scheme A.27. Attachment of **P10** on surface **S2** (setup A).

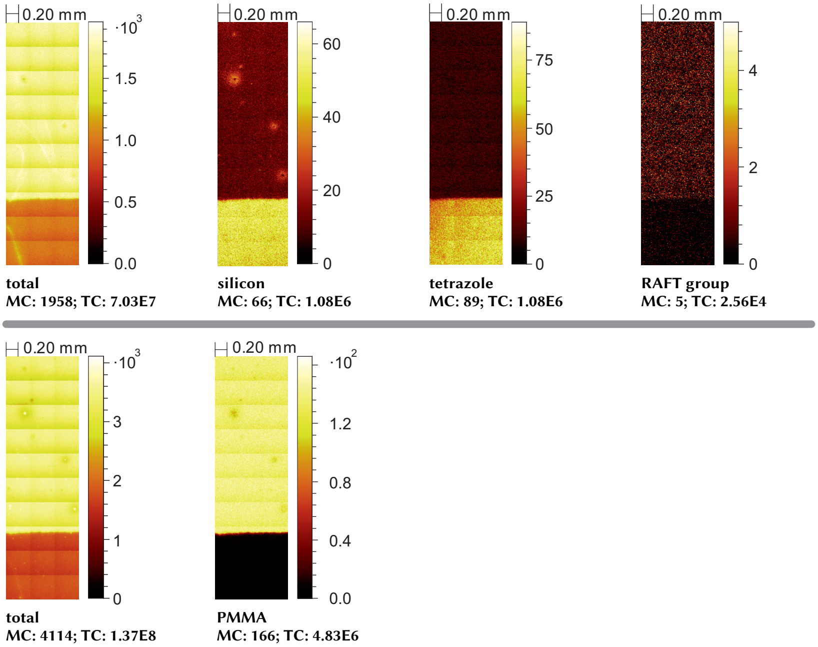

total
MC: 1958; TC: 7.03E7

silicon
MC: 66; TC: 1.08E6

tetrazole
MC: 89; TC: 1.08E6

RAFT group
MC: 5; TC: 2.56E4

total
MC: 4114; TC: 1.37E8

PMMA
MC: 166; TC: 4.83E6

Figure A.42. ToF-SIMS spectra of **S2**. Positive polarity (top), negative polarity (bottom).

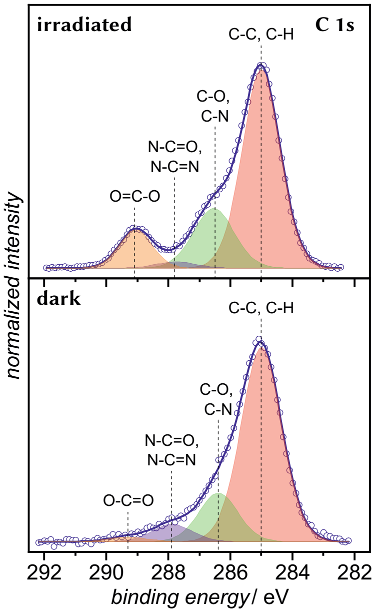

Figure A.43. C 1s XPS spectra of **S2**.

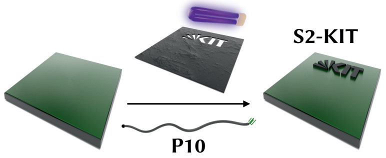

Scheme A.28. Attachment of **P10** on surface **S2-KIT** (setup A).

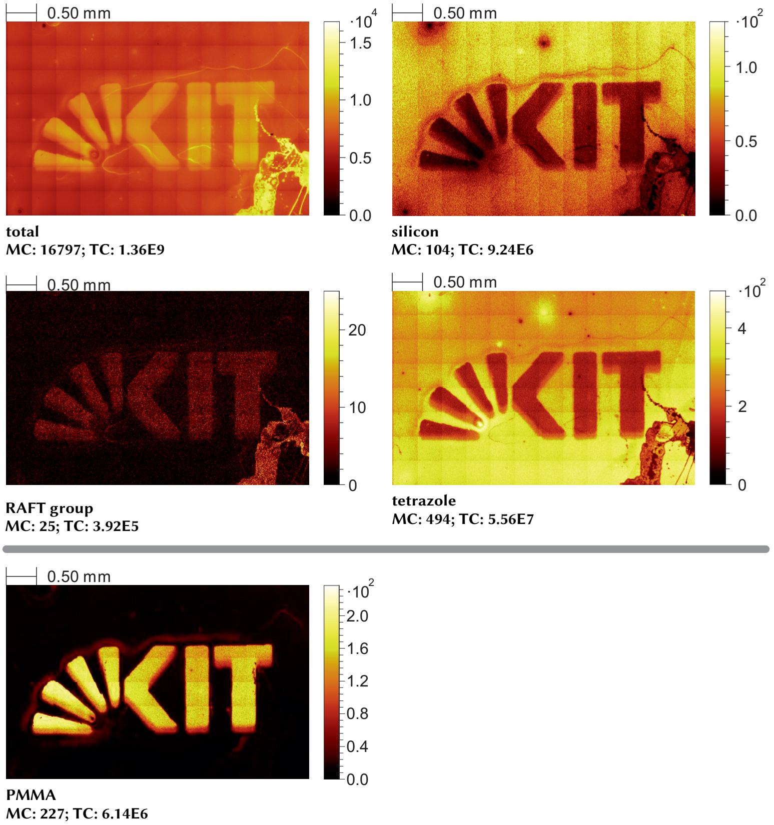

total
MC: 16797; TC: 1.36E9

silicon
MC: 104; TC: 9.24E6

RAFT group
MC: 25; TC: 3.92E5

tetrazole
MC: 494; TC: 5.56E7

PMMA
MC: 227; TC: 6.14E6

Figure A.44. ToF-SIMS spectra of **S2-KIT**. Positive polarity (top), negative polarity (bottom).

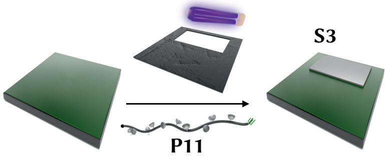

Scheme A.29. Attachment of **P11** on surface **S3** (setup A).

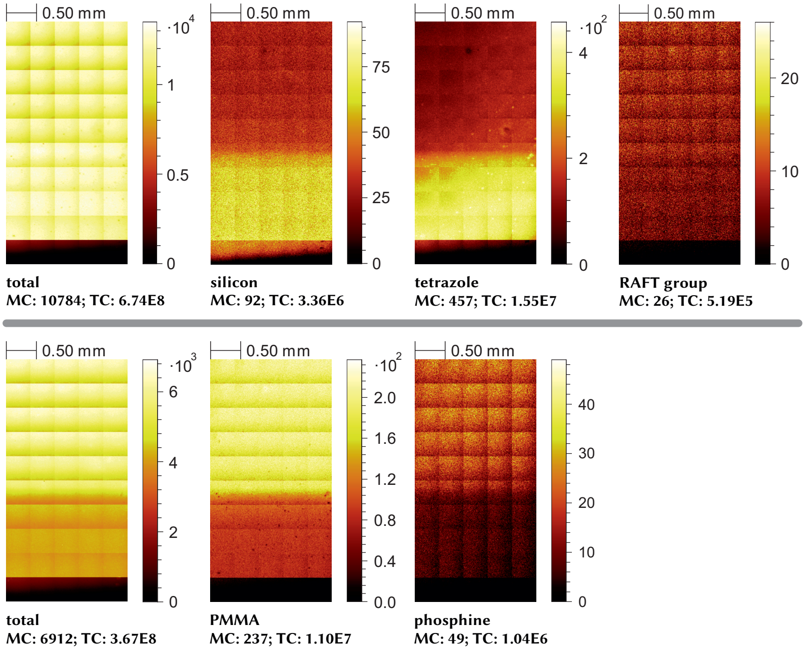

Figure A.45. ToF-SIMS spectra of **S3**. Positive polarity (top), negative polarity (bottom).

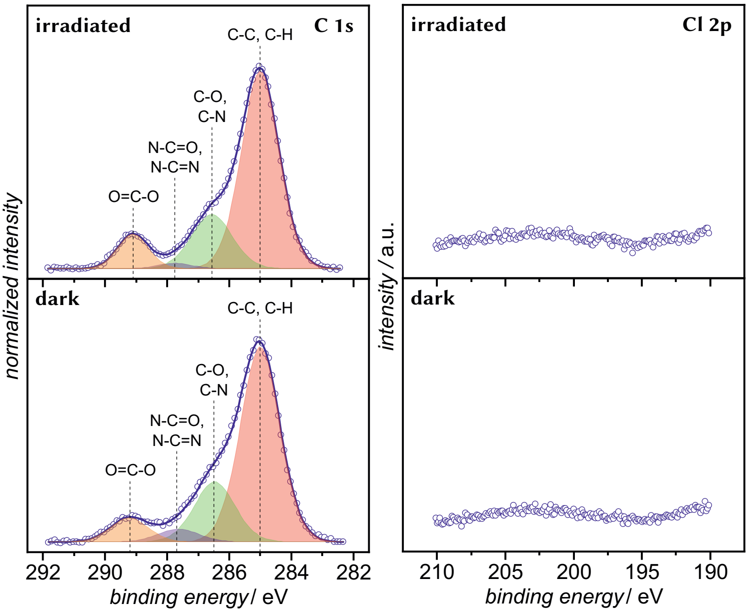

Figure A.46. C 1s and Cl 2p XPS spectra of **S3**.

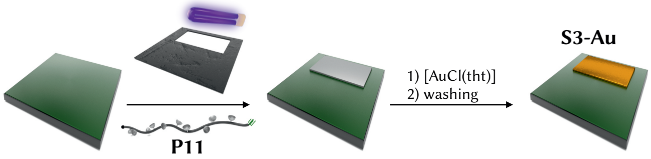

Scheme A.30. Attachment of **P11** and subsequent post-loading with a [AuCl(tht)] solution towards surface **S3-Au** (setup A).

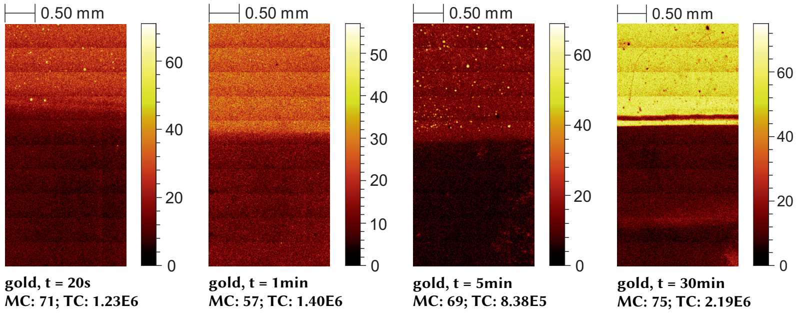

gold, t = 20s
MC: 71; TC: 1.23E6

gold, t = 1min
MC: 57; TC: 1.40E6

gold, t = 5min
MC: 69; TC: 8.38E5

gold, t = 30min
MC: 75; TC: 2.19E6

Figure A.47. ToF-SIMS spectra of **S3-Au** for various immersion times t of the surface into the metal salt solution.

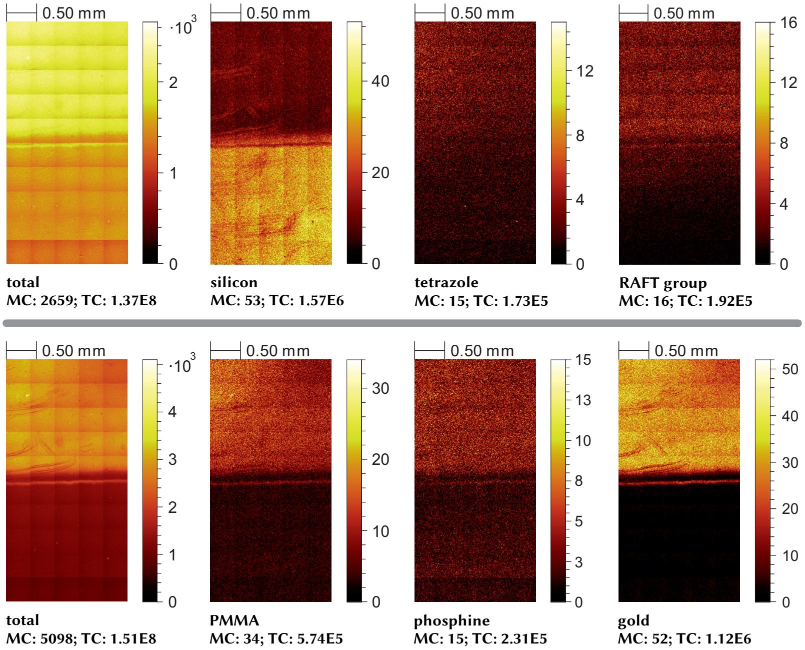

total
MC: 2659; TC: 1.37E8

silicon
MC: 53; TC: 1.57E6

tetrazole
MC: 15; TC: 1.73E5

RAFT group
MC: 16; TC: 1.92E5

total
MC: 5098; TC: 1.51E8

PMMA
MC: 34; TC: 5.74E5

phosphine
MC: 15; TC: 2.31E5

gold
MC: 52; TC: 1.12E6

Figure A.48. ToF-SIMS spectra of **S3-Au**. Positive polarity (top), negative polarity (bottom).

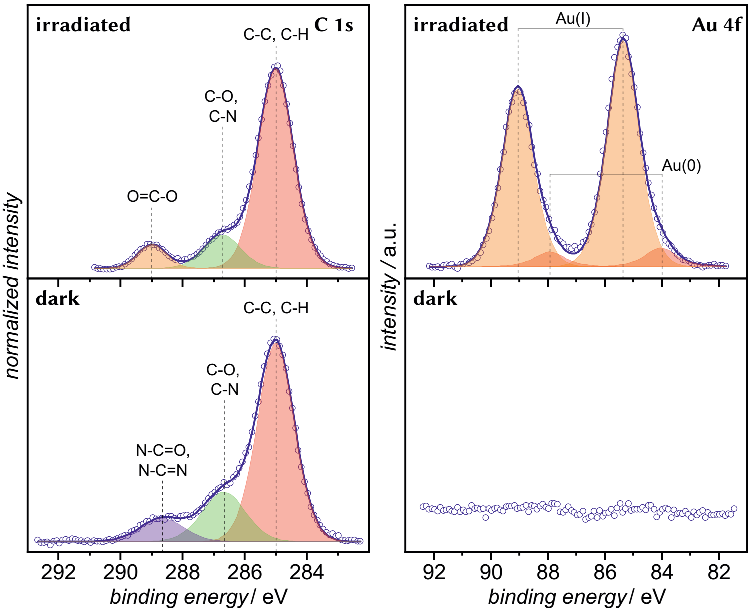

Figure A.49. C 1s and Au 4f XPS spectra of **S3-Au**.

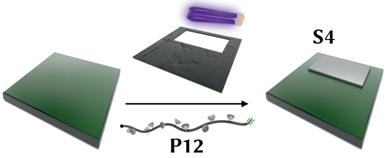

Scheme A.31. Attachment of **P12** on surface **S4** (setup A).

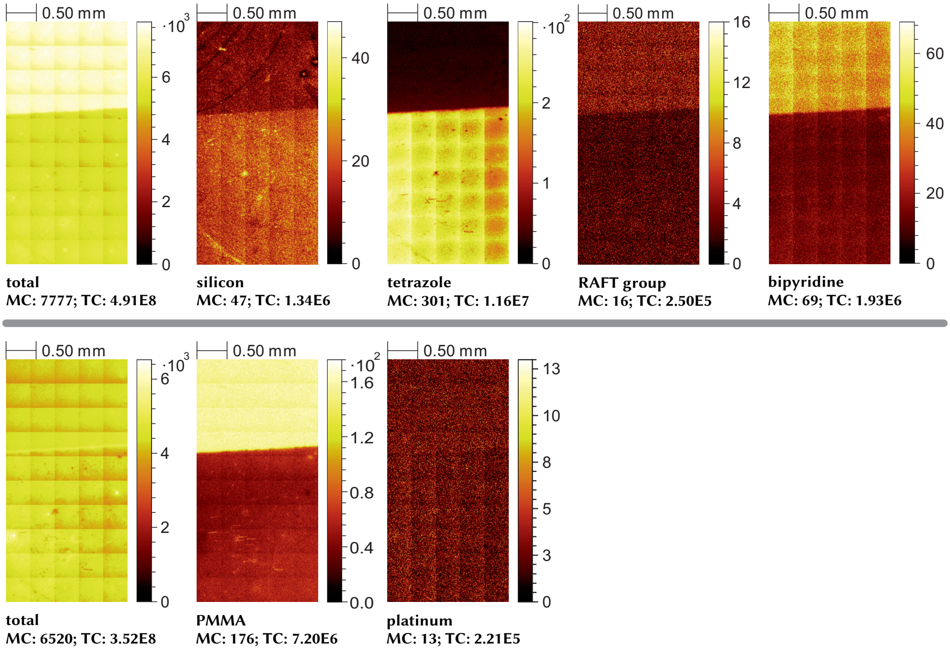

total
MC: 7777; TC: 4.91E8

silicon
MC: 47; TC: 1.34E6

tetrazole
MC: 301; TC: 1.16E7

RAFT group
MC: 16; TC: 2.50E5

bipyridine
MC: 69; TC: 1.93E6

total
MC: 6520; TC: 3.52E8

PMMA
MC: 176; TC: 7.20E6

platinum
MC: 13; TC: 2.21E5

Figure A.50. ToF-SIMS spectra of **S4**. Positive polarity (top), negative polarity (bottom).

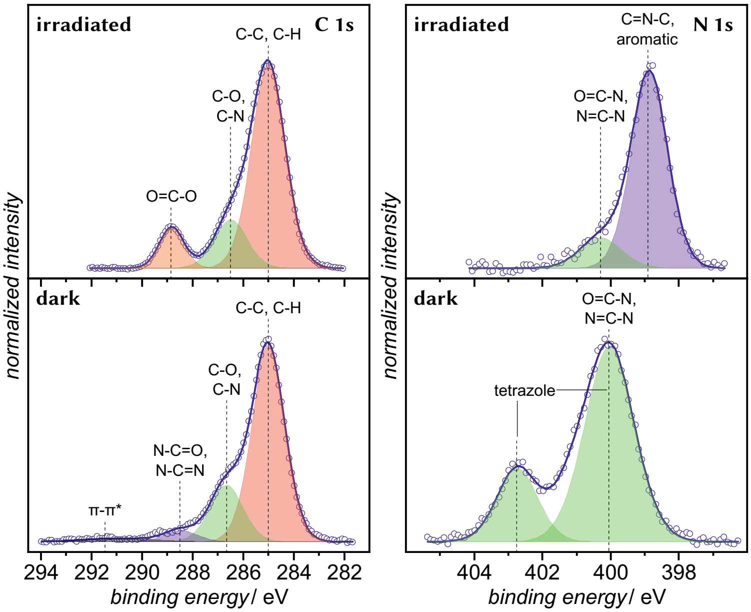

Figure A.51. C 1s and N 1s XPS spectra of **S4**.

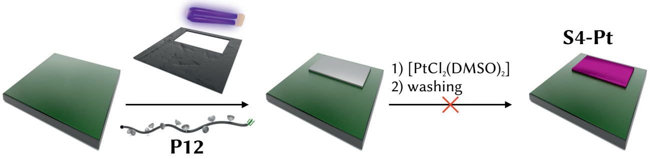
S4-Pt
1) [PtCl$_2$(DMSO)$_2$]
2) washing
P12

Scheme A.32. Attachment of **P12** and subsequent post-loading with a [PtCl$_2$(DMSO)$_2$] solution towards surface **S4-Pt** (setup A).

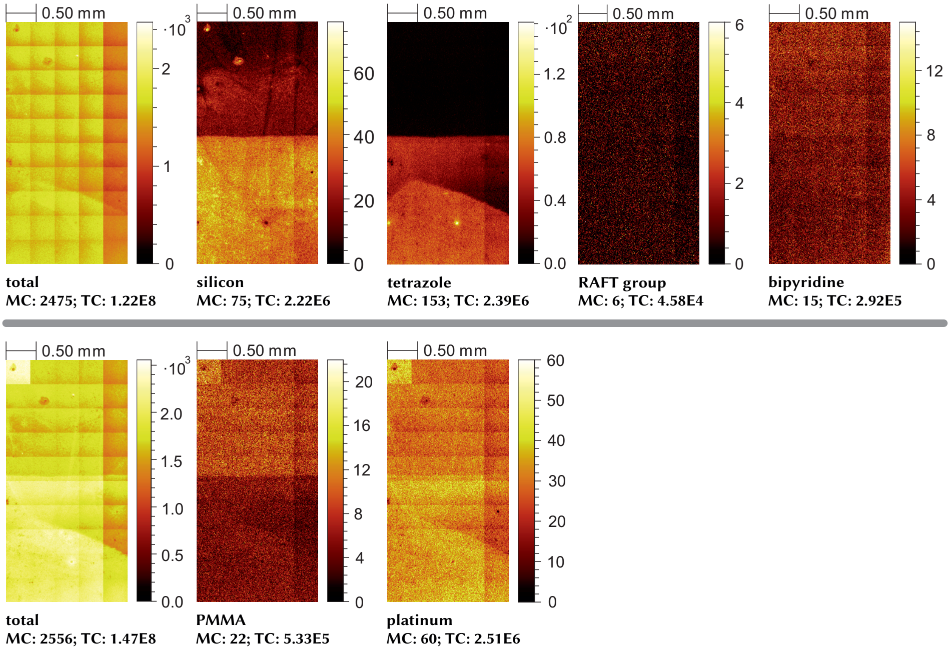

Figure A.52. ToF-SIMS spectra of **S4-Pt**. Positive polarity (top), negative polarity (bottom).

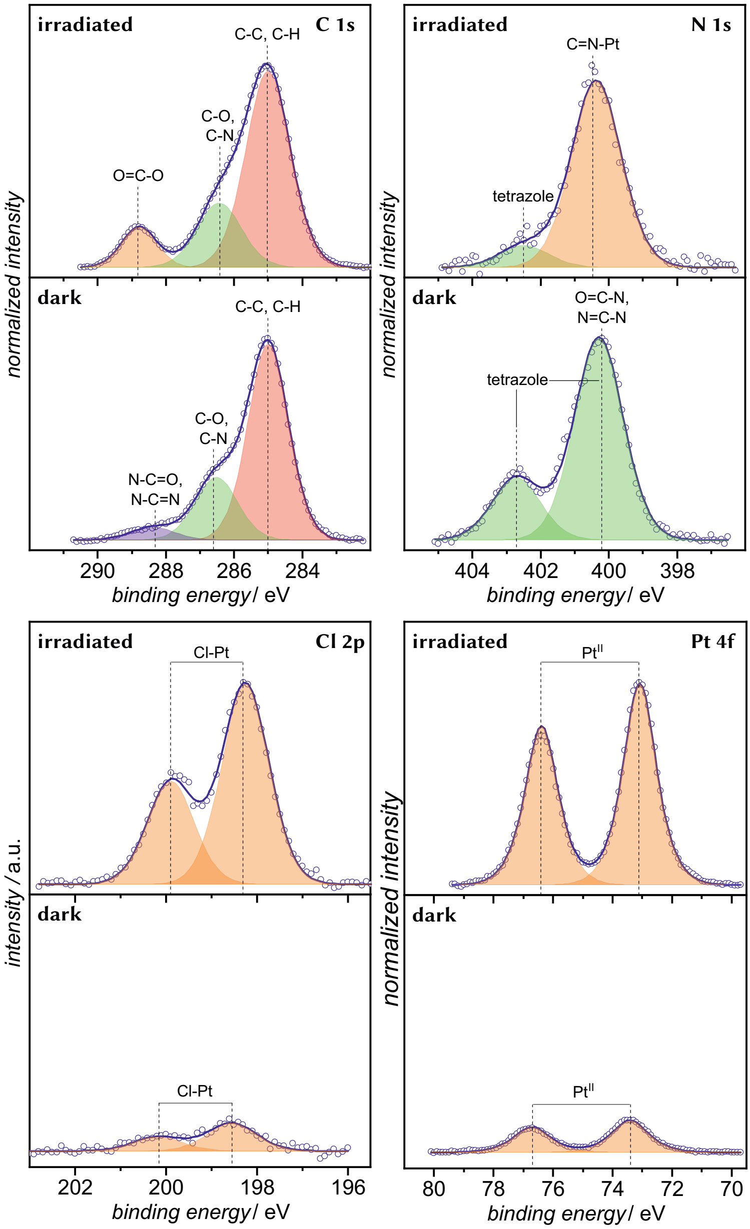

Figure A.53. C 1s, N 1s, Cl 2p, and Pt 4f XPS spectra of **S4-Pt**.

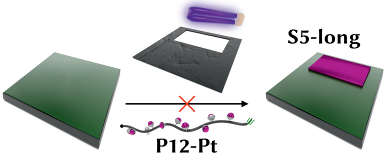

Scheme A.33. Attachment of **P12-Pt** on surface **S5-long** with a long irradiation pathway through the metallopolymer solution (setup A).

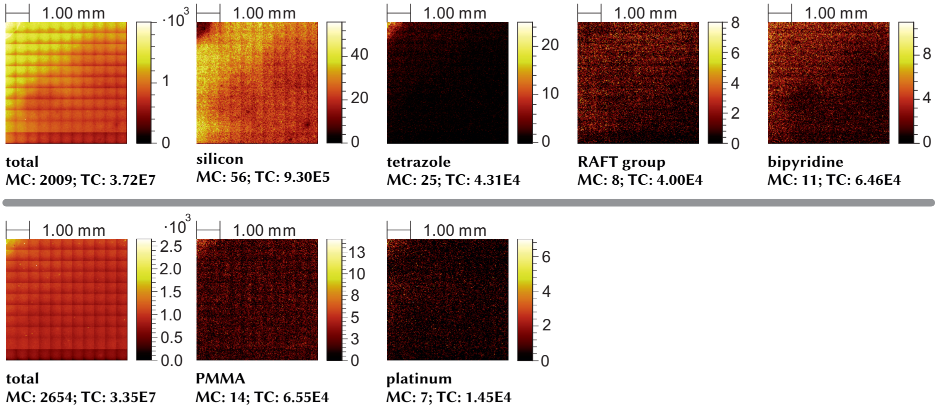

Figure A.54. ToF-SIMS spectra of **S5-long**. Positive polarity (top), negative polarity (bottom).

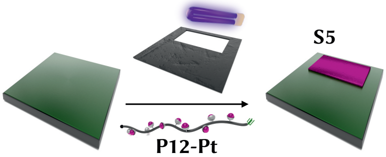

Scheme A.34. Attachment of **P12-Pt** on surface **S5** (setup A).

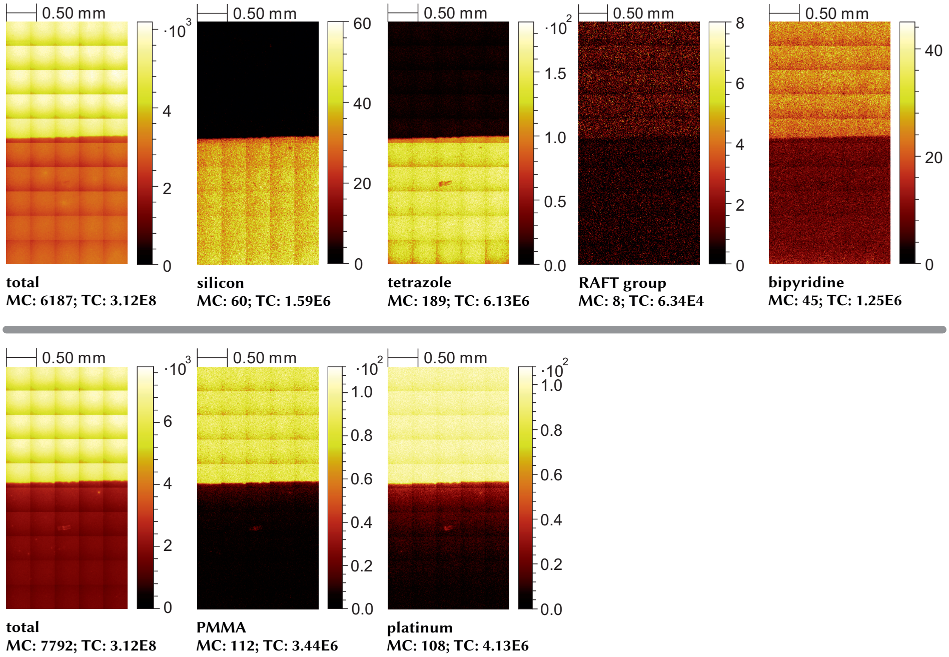

Figure A.55. ToF-SIMS spectra of **S5**. Positive polarity (top), negative polarity (bottom).

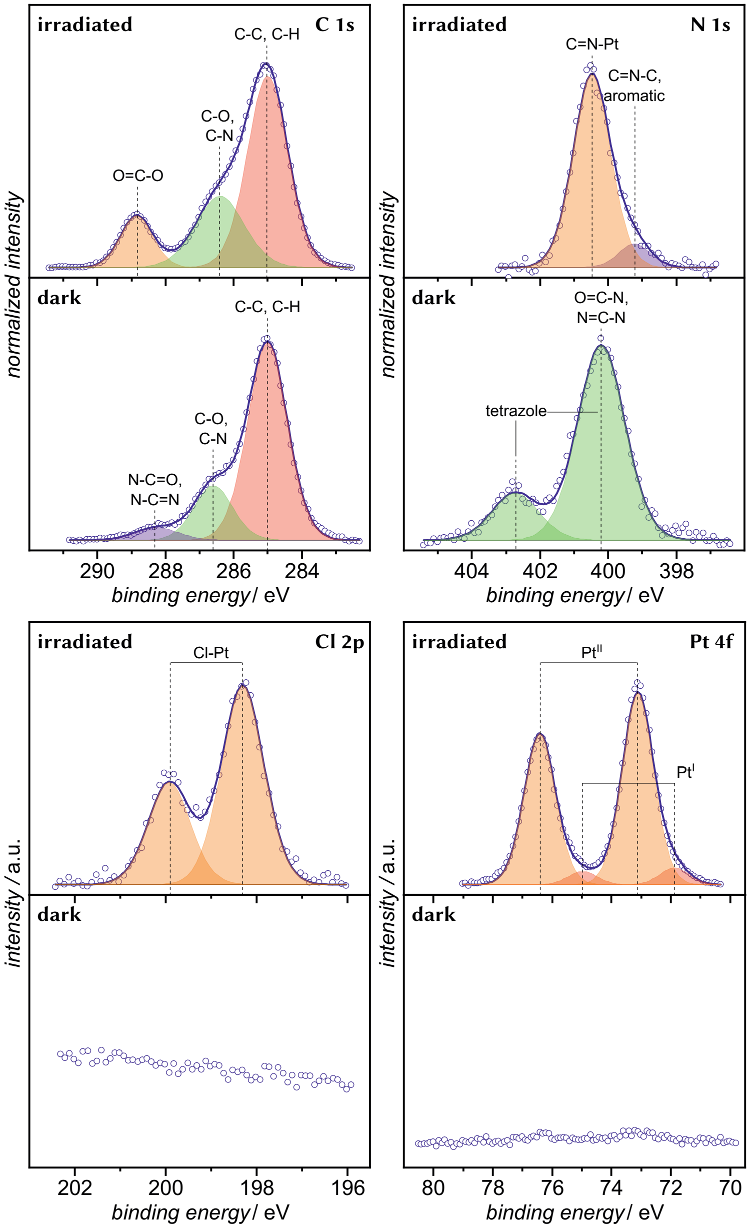

Figure A.56. C 1s, N 1s, Cl 2p, and Pt 4f XPS spectra of **S5**.

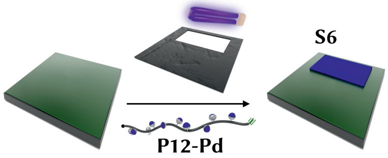

Scheme A.35. Attachment of **P12-Pd** on surface **S6** (setup A).

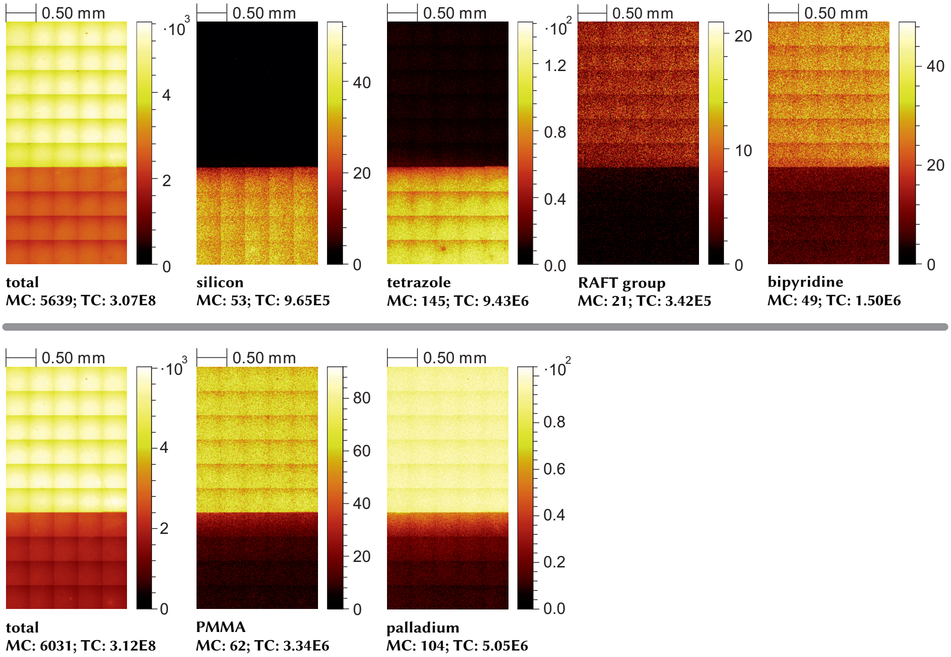

total
MC: 5639; TC: 3.07E8

silicon
MC: 53; TC: 9.65E5

tetrazole
MC: 145; TC: 9.43E6

RAFT group
MC: 21; TC: 3.42E5

bipyridine
MC: 49; TC: 1.50E6

total
MC: 6031; TC: 3.12E8

PMMA
MC: 62; TC: 3.34E6

palladium
MC: 104; TC: 5.05E6

Figure A.57. ToF-SIMS spectra of **S6**. Positive polarity (top), negative polarity (bottom).

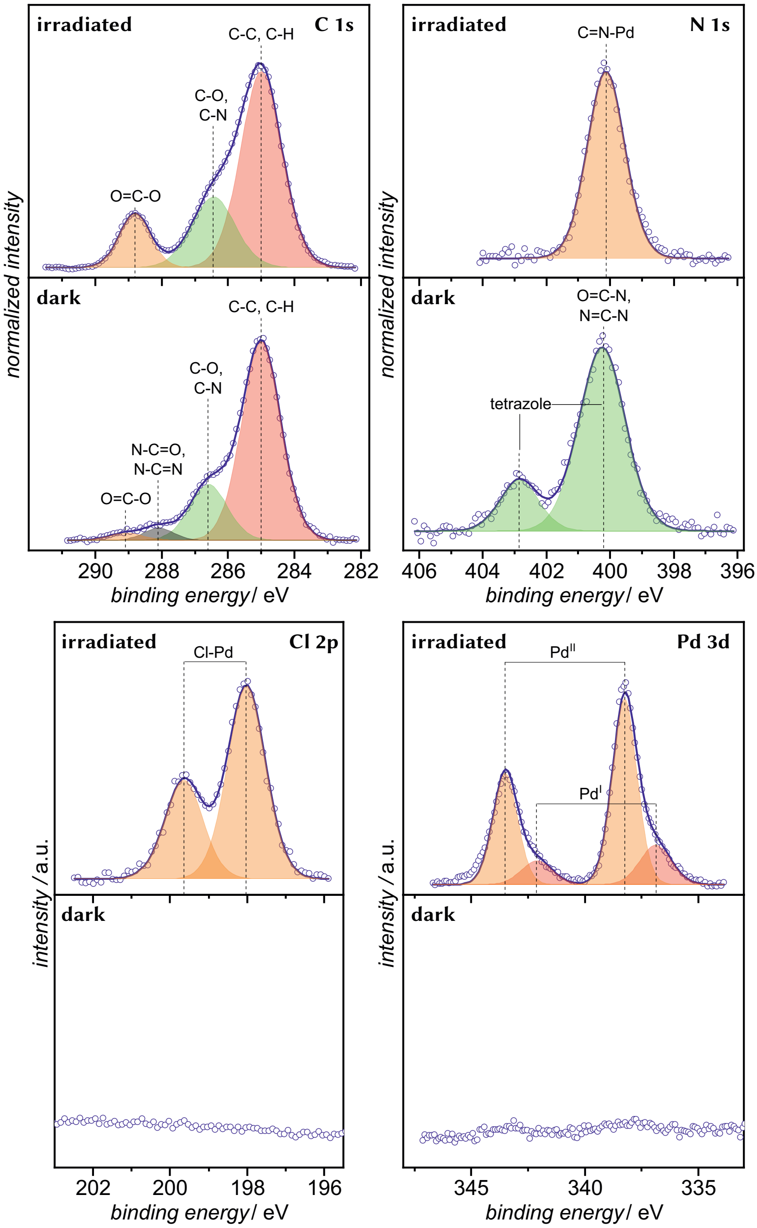

Figure A.58. C 1s, N 1s, Cl 2p and Pd 3d XPS spectra of **S6**.

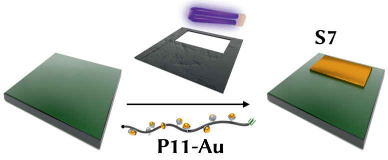

Scheme A.36. Attachment of **P11-Au** on surface **S7** (setup A).

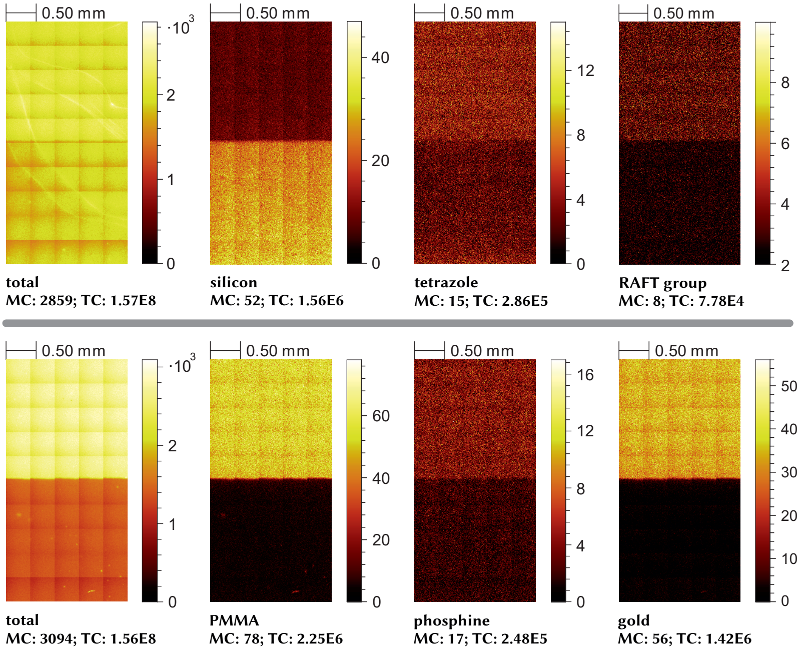

Figure A.59. ToF-SIMS spectra of **S7**. Positive polarity (top), negative polarity (bottom).

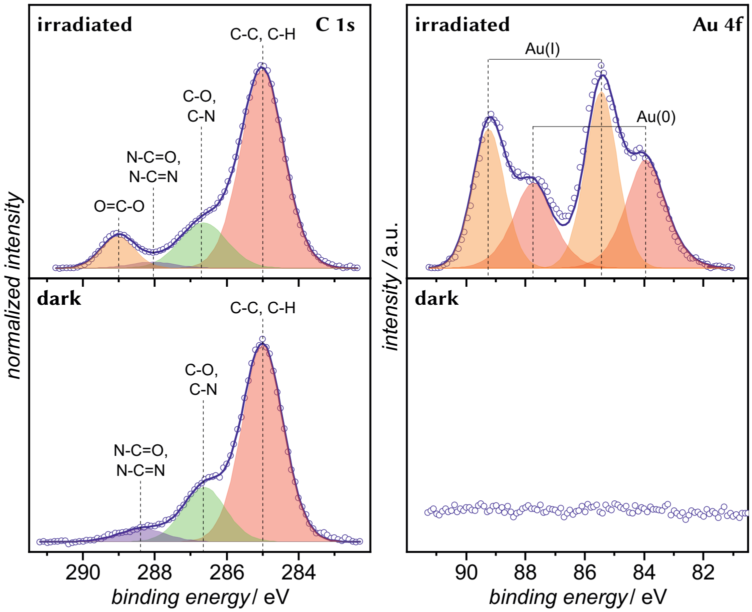

Figure A.60. C 1s and Au 4f XPS spectra of **S7**.

A.9.2 Bifunctional patterning

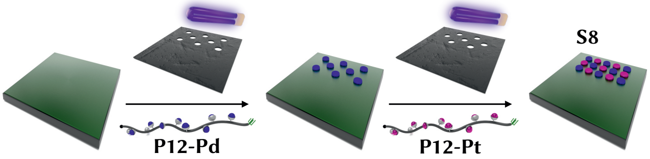

Scheme A.37. Attachment of **P12-Pd** and **P12-Pt** on surface **S8** (setup B).

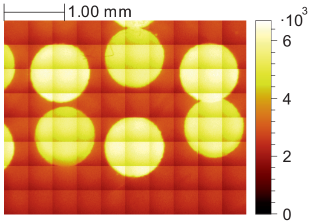

total
MC: 6694; TC: 4.68E8

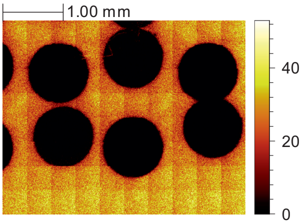

silicon
MC: 53; TC: 2.19E6

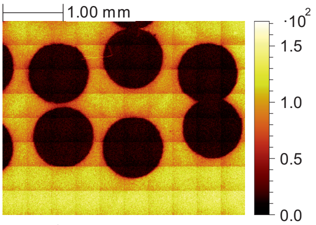

tetrazole
MC: 172; TC: 8.90E6

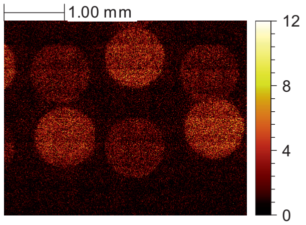

RAFT group
MC: 12; TC: 1.71E5

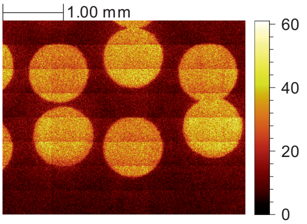

bipyridine
MC: 61; TC: 2.42E6

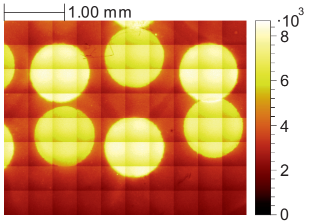

total
MC: 8679; TC: 5.87E8

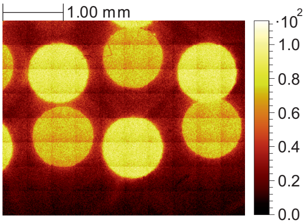

PMMA
MC: 114; TC: 5.90E6

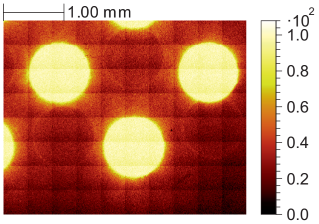

platinum
MC: 108; TC: 5.90E5

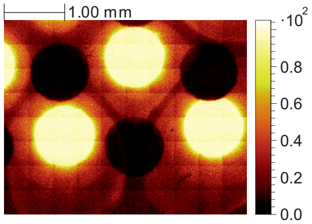

palladium
MC: 105; TC: 5.08E6

Figure A.61. ToF-SIMS spectra of **S8**. Positive polarity (top), negative polarity (bottom).

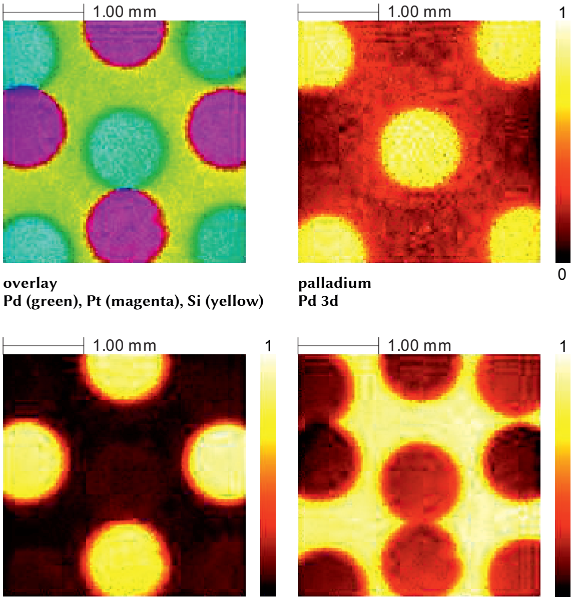

overlay
Pd (green), Pt (magenta), Si (yellow)

palladium
Pd 3d

platinum
Pt 4f

silicon
Si 2p

Figure A.62. XPS mappings of **S8**.

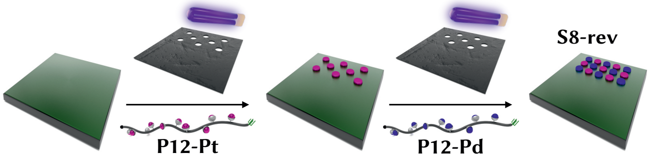

Scheme A.38. Attachment of **P12-Pt** and **P12-Pd** on surface **S8-rev** (setup B).

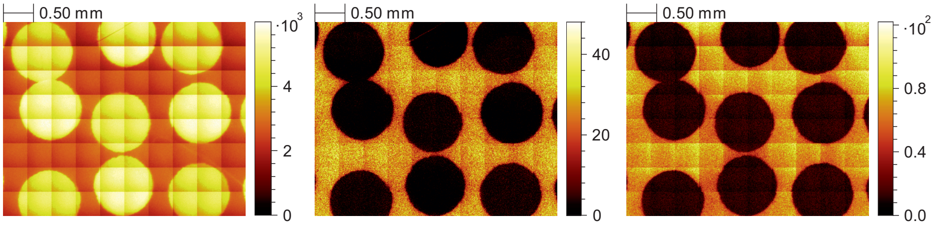

total
MC: 5998; TC: 4.60E8

silicon
MC: 48; TC: 1.71E6

tetrazole
MC: 122; TC: 4.82E6

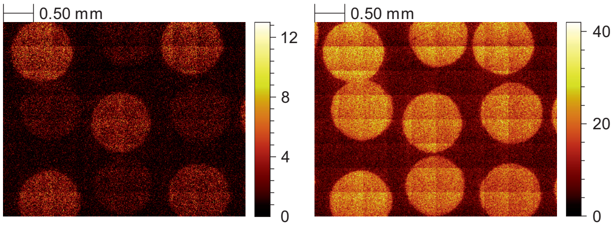

RAFT group
MC: 13; TC: 2.00E5

bipyridine
MC: 42; TC: 1.76E6

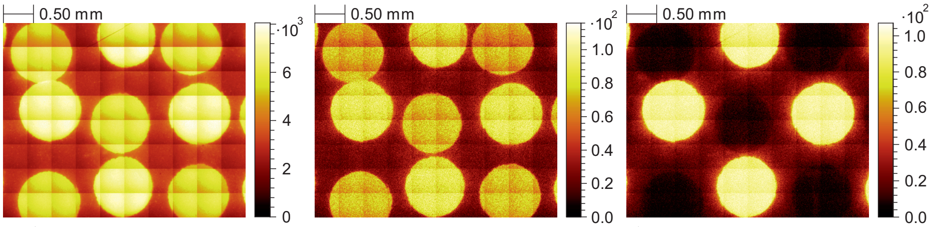

total
MC: 8057; TC: 3.89E8

PMMA
MC: 116; TC: 6.99E6

platinum
MC: 107; TC: 4.74E6

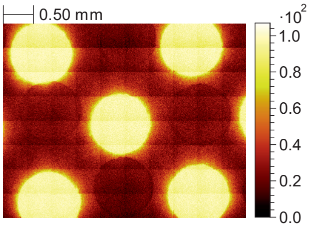

palladium
MC: 107; TC: 6.50E6

Figure A.63. ToF-SIMS spectra of **S8-rev**. Positive polarity (top), negative polarity (bottom).

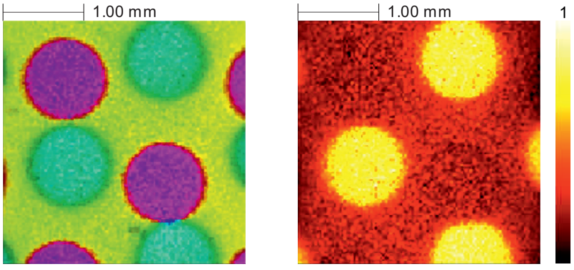

overlay
Pd (green), Pt (magenta), Si (yellow)

palladium
Pd 3d

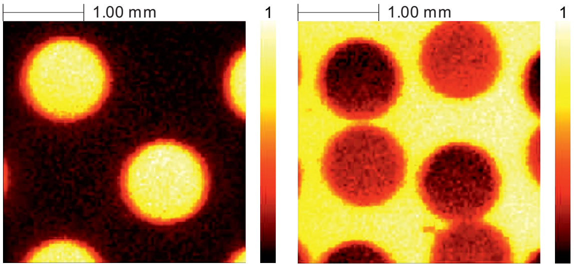

platinum
Pt 4f

silicon
Si 2p

Figure A.64. XPS mappings of **S8-rev**.

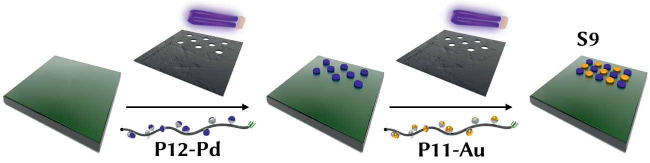

Scheme A.39. Attachment of **P12-Pd** and **P11-Au** on surface **S9** (setup B).

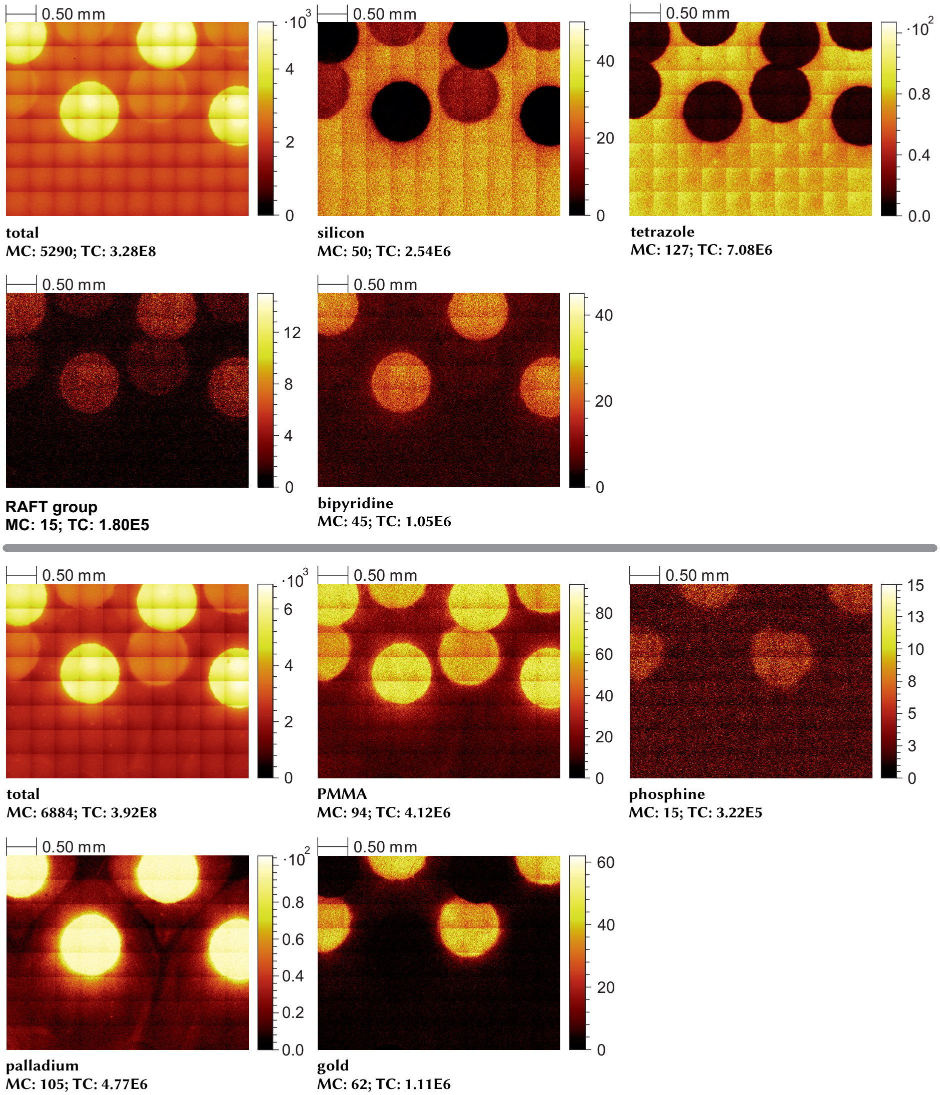

total
MC: 5290; TC: 3.28E8

silicon
MC: 50; TC: 2.54E6

tetrazole
MC: 127; TC: 7.08E6

RAFT group
MC: 15; TC: 1.80E5

bipyridine
MC: 45; TC: 1.05E6

total
MC: 6884; TC: 3.92E8

PMMA
MC: 94; TC: 4.12E6

phosphine
MC: 15; TC: 3.22E5

palladium
MC: 105; TC: 4.77E6

gold
MC: 62; TC: 1.11E6

Figure A.65. ToF-SIMS spectra of **S9**. Positive polarity (top), negative polarity (bottom).

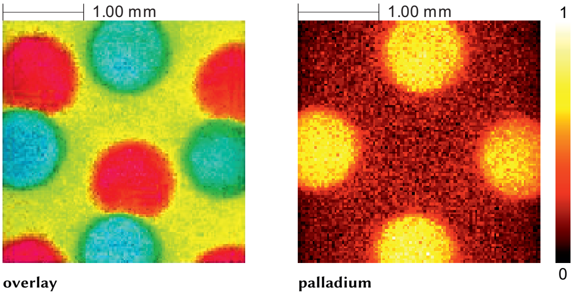

overlay
Pd (blue), Au (red), Si (yellow)

palladium
Pd 3d

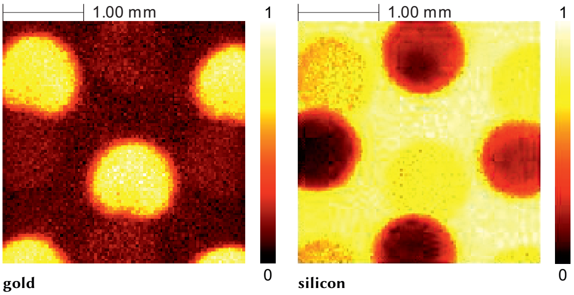

gold
Au 4f

silicon
Si 2p

Figure A.66. XPS mappings of **S9**.

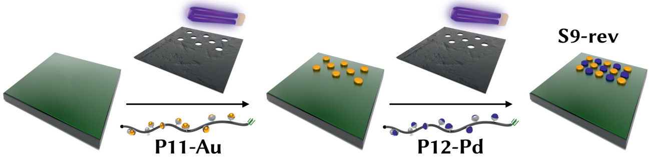

Scheme A.40. Attachment of **P11-Au** and **P12-Pd** on surface **S9-rev** (setup B).

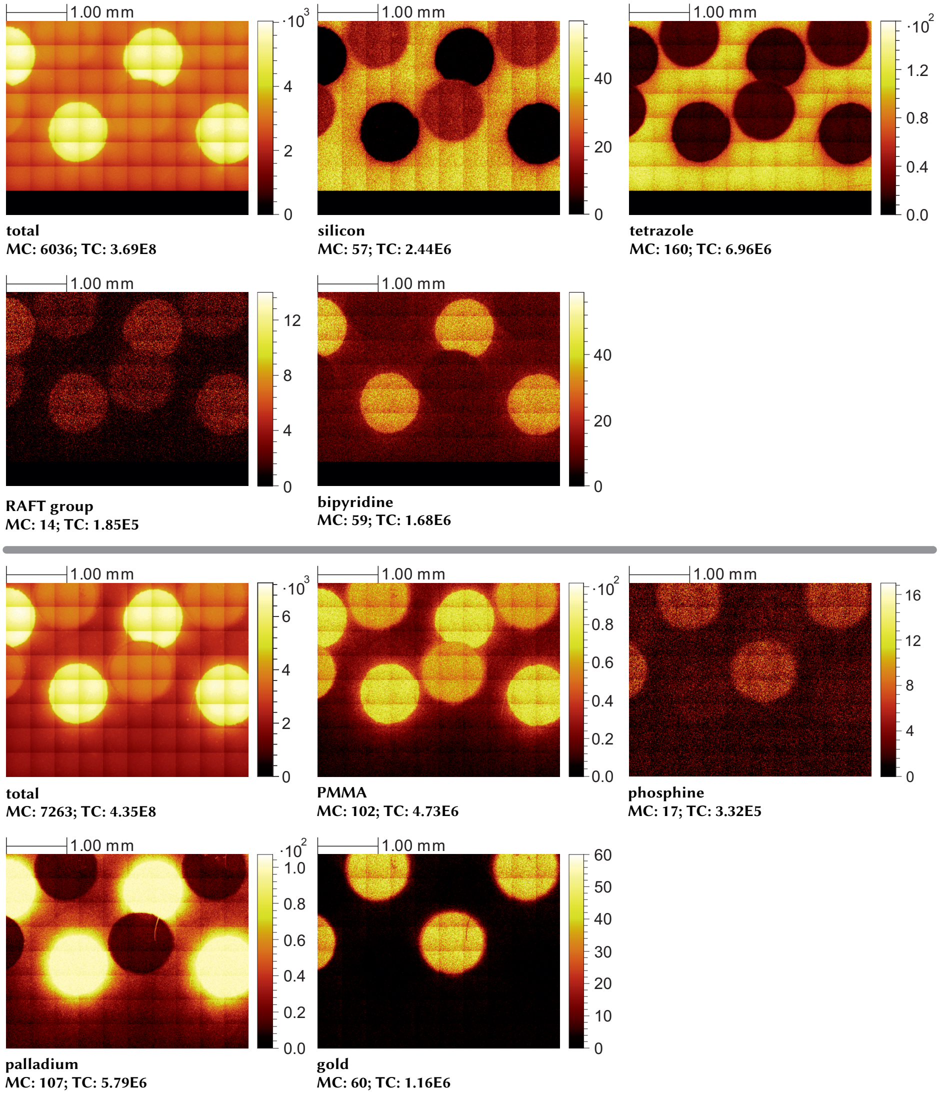

total
MC: 6036; TC: 3.69E8

silicon
MC: 57; TC: 2.44E6

tetrazole
MC: 160; TC: 6.96E6

RAFT group
MC: 14; TC: 1.85E5

bipyridine
MC: 59; TC: 1.68E6

total
MC: 7263; TC: 4.35E8

PMMA
MC: 102; TC: 4.73E6

phosphine
MC: 17; TC: 3.32E5

palladium
MC: 107; TC: 5.79E6

gold
MC: 60; TC: 1.16E6

Figure A.67. ToF-SIMS spectra of **S9-rev**. Positive polarity (top), negative polarity (bottom).

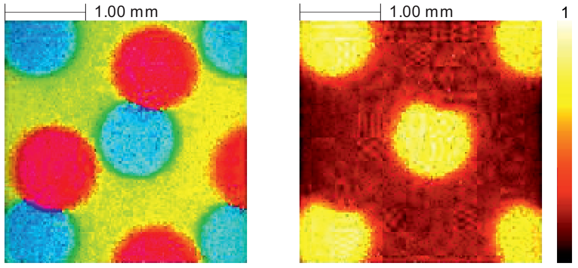

overlay
Pd (blue), Au (red), Si (yellow)

palladium
Pd 3d

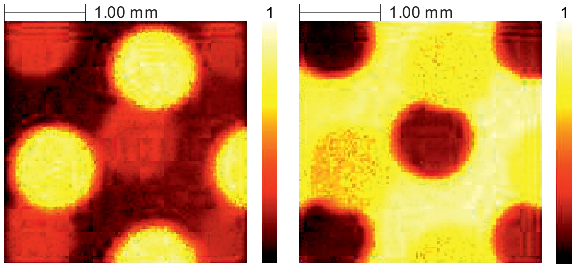

gold
Au 4f

silicon
Si 2p

Figure A.68. XPS mappings of **S9-rev**.

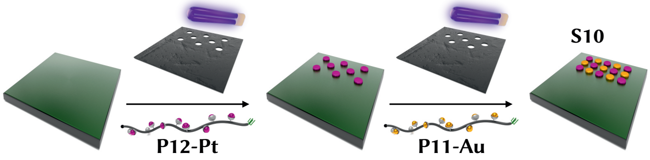

Scheme A.41. Attachment of **P12-Pt** and **P11-Au** on surface **S10** (setup B).

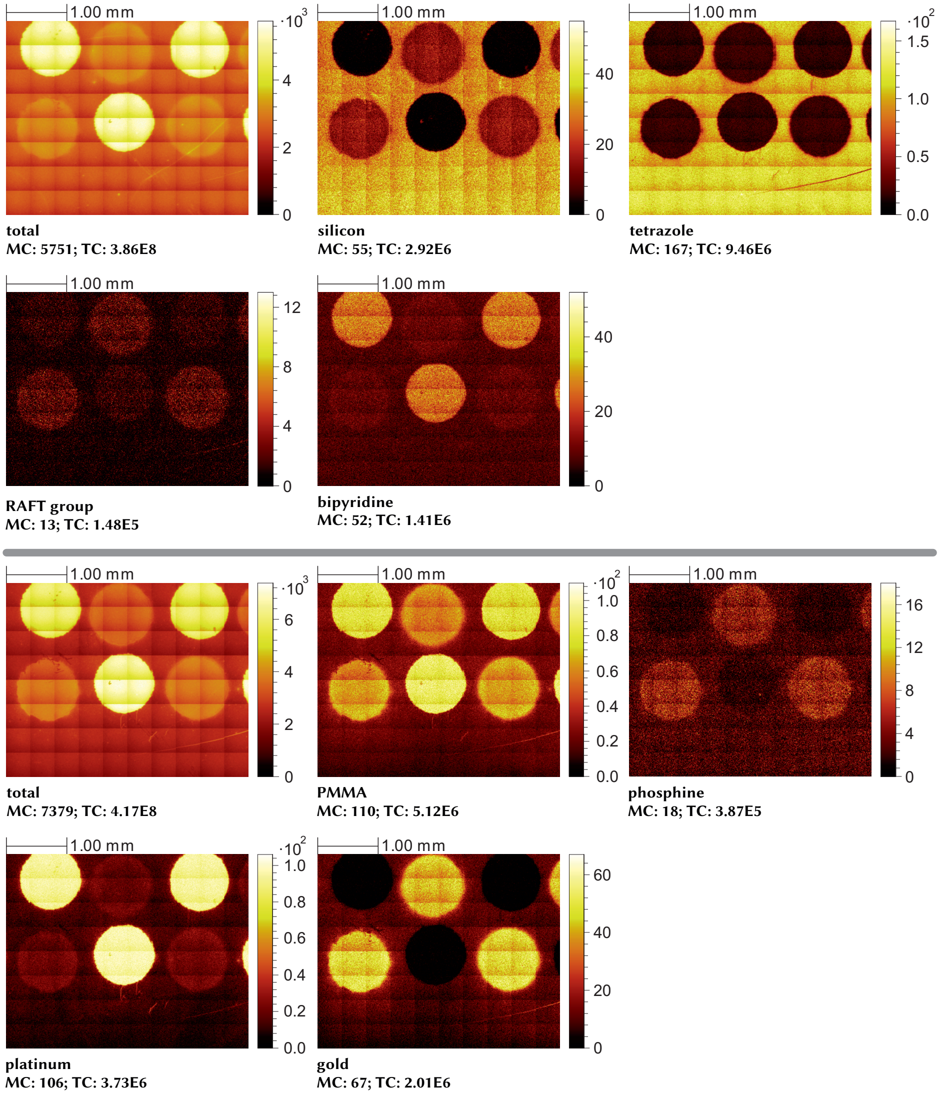

total
MC: 5751; TC: 3.86E8

silicon
MC: 55; TC: 2.92E6

tetrazole
MC: 167; TC: 9.46E6

RAFT group
MC: 13; TC: 1.48E5

bipyridine
MC: 52; TC: 1.41E6

total
MC: 7379; TC: 4.17E8

PMMA
MC: 110; TC: 5.12E6

phosphine
MC: 18; TC: 3.87E5

platinum
MC: 106; TC: 3.73E6

gold
MC: 67; TC: 2.01E6

Figure A.69. ToF-SIMS spectra of **S10**. Positive polarity (top), negative polarity (bottom).

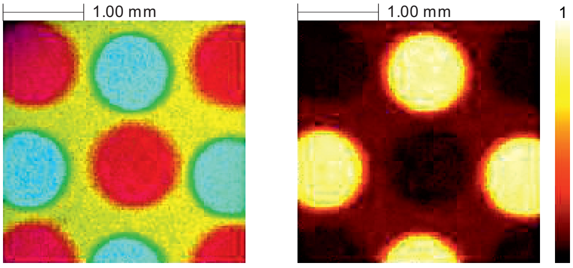

overlay
Pt (blue), Au (red), Si (yellow)

platinum
Pt 4f

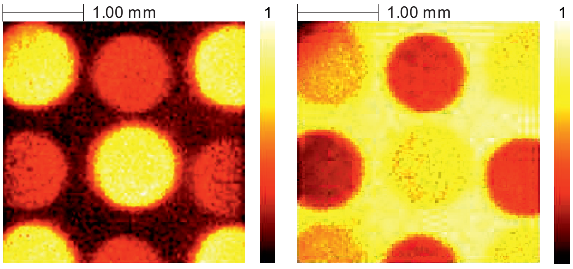

gold
Au 4f

silicon
Si 2p

Figure A.70. XPS mappings of **S10**.

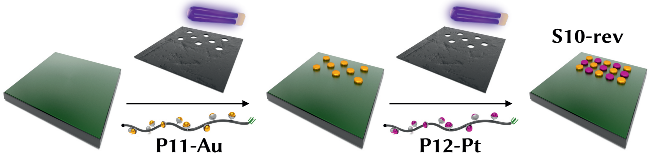

Scheme A.42. Attachment of **P11-Au** and **P12-Pt** on surface **S10-rev** (setup B).

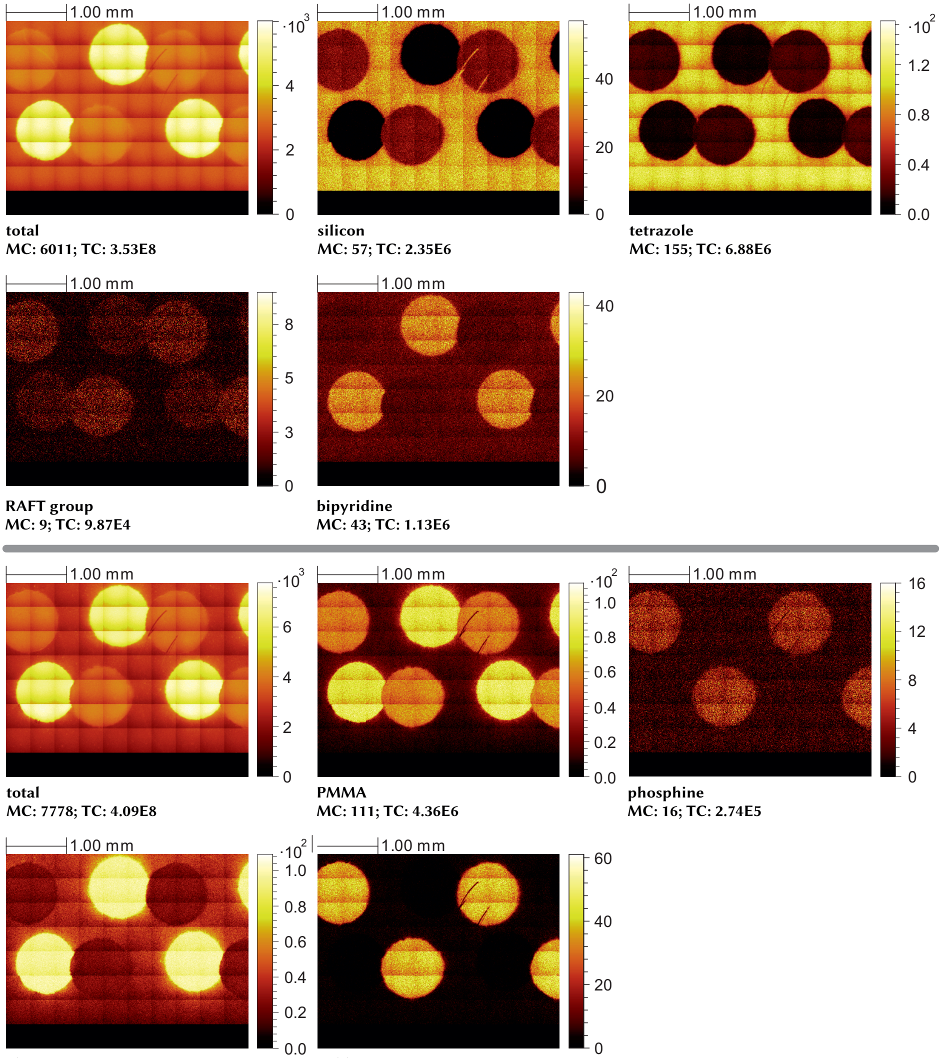

total
MC: 6011; TC: 3.53E8

silicon
MC: 57; TC: 2.35E6

tetrazole
MC: 155; TC: 6.88E6

RAFT group
MC: 9; TC: 9.87E4

bipyridine
MC: 43; TC: 1.13E6

total
MC: 7778; TC: 4.09E8

PMMA
MC: 111; TC: 4.36E6

phosphine
MC: 16; TC: 2.74E5

platinum
MC: 109; TC: 5.09E6

gold
MC: 61; TC: 1.21E6

Figure A.71. ToF-SIMS spectra of **S10-rev**. Positive polarity (top), negative polarity (bottom).

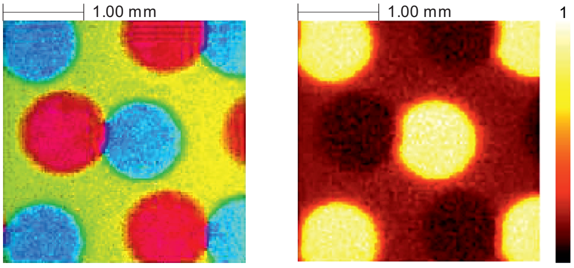

overlay
Pt (blue), Au (red), Si (yellow)

platinum
Pt 4f

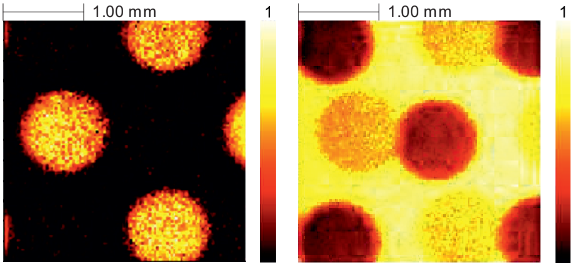

gold
Au 4f

silicon
Si 2p

Figure A.72. XPS mappings of **S10-rev**.

A.9.3 Trifunctional patterning

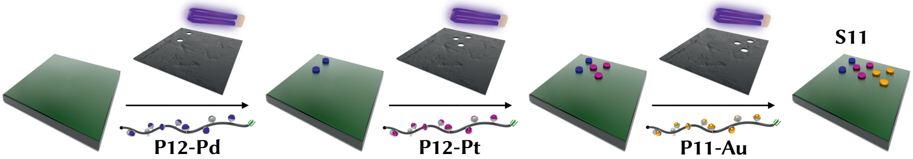

Scheme A.43. Attachment of **P12-Pd**, **P12-Pt**, and **P11-Au** on surface **S11** (setup C).

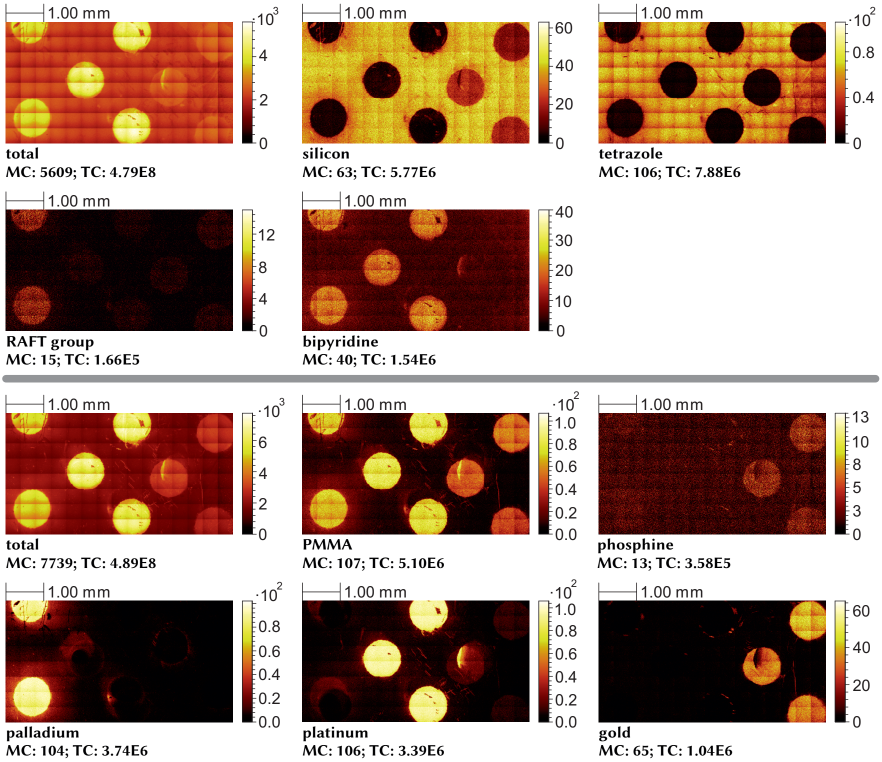

Figure A.73. ToF-SIMS spectra of **S11**. Positive polarity (top), negative polarity (bottom).

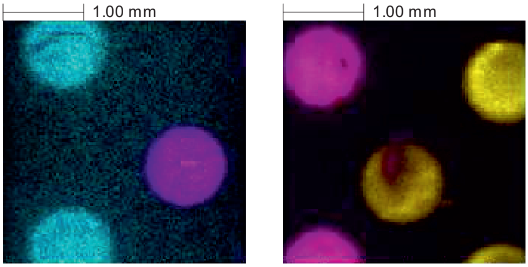

overlay left wafer side
Pd (cyan), Pt (magenta)

overlay right wafer side
Pt (magenta), Au (yellow)

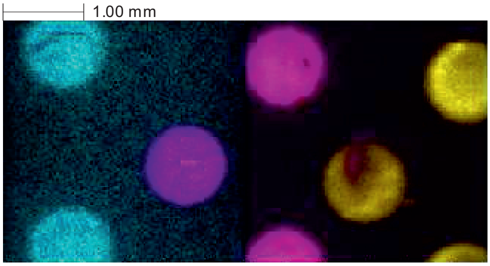

overall picture
Pd (cyan), Pt (magenta), Au (yellow)

Figure A.74. XPS mappings of **S11**.

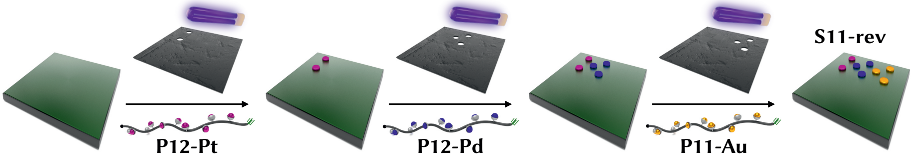
S11-rev
P12-Pt
P12-Pd
P11-Au

Scheme A.44. Attachment of **P12-Pt**, **P12-Pd**, and **P11-Au** on surface **S11-rev** (setup C).

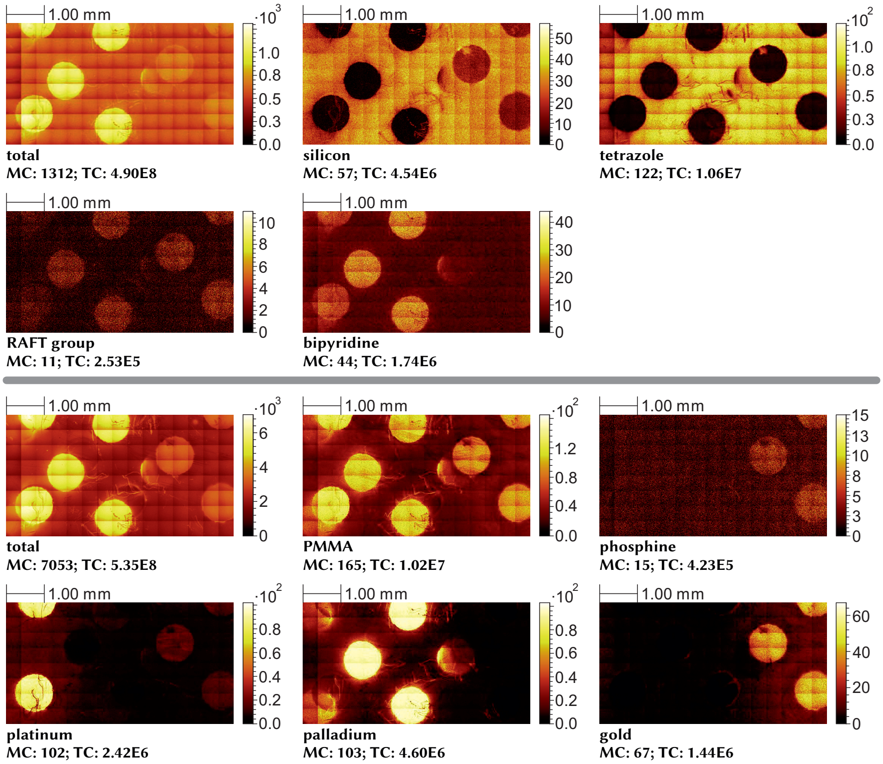

Figure A.75. ToF-SIMS spectra of **S11-rev**. Positive polarity (top), negative polarity (bottom).

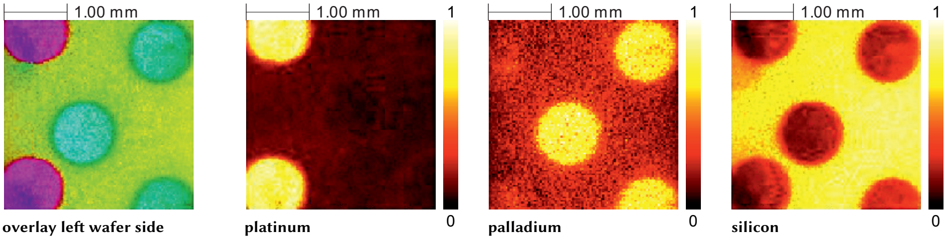

overlay left wafer side
Pt (magenta), Pd (cyan),
Si (yellow)

platinum
Pt 4f

palladium
Pd 3d

silicon
Si 2p

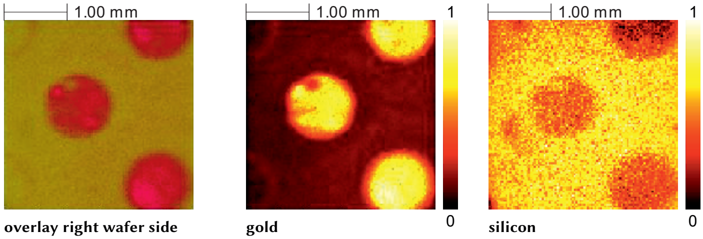

overlay right wafer side
Au (red), Si (yellow)

gold
Au 4f

silicon
Si 2p

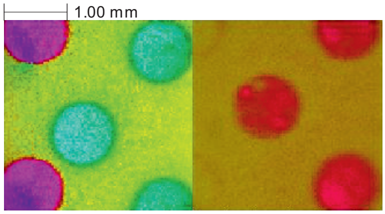

overall picture
Pt (magenta), Pd (cyan), Au (red), Si (yellow)

Figure A.76. XPS mappings of **S11-rev**.

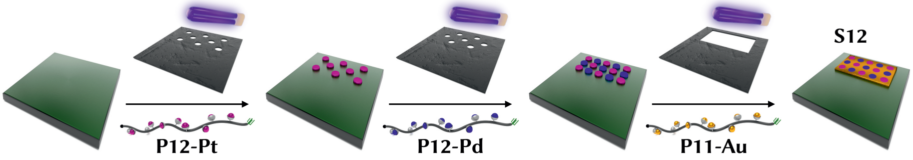

Scheme A.45. Attachment of **P12-Pt**, **P12-Pd**, and **P11-Au** on surface **S12** (setup D).

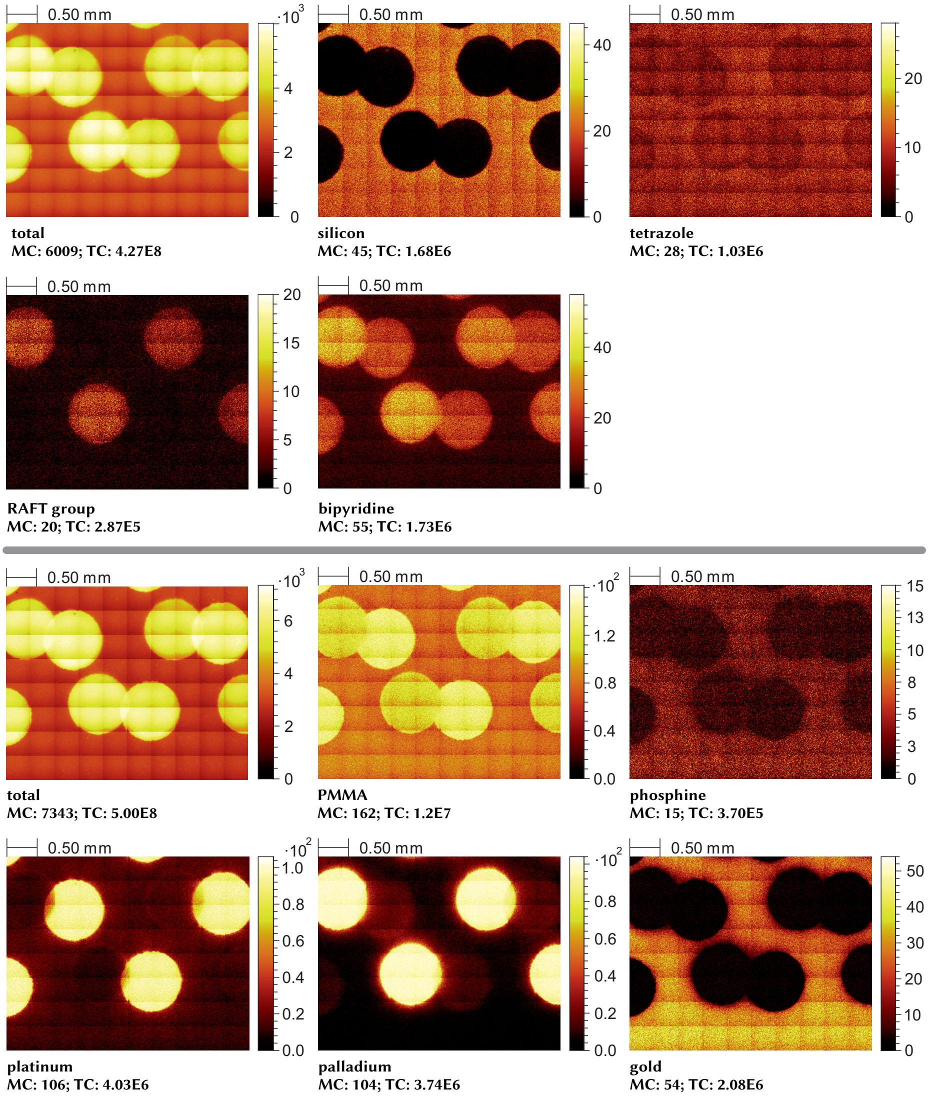

total
MC: 6009; TC: 4.27E8

silicon
MC: 45; TC: 1.68E6

tetrazole
MC: 28; TC: 1.03E6

RAFT group
MC: 20; TC: 2.87E5

bipyridine
MC: 55; TC: 1.73E6

total
MC: 7343; TC: 5.00E8

PMMA
MC: 162; TC: 1.2E7

phosphine
MC: 15; TC: 3.70E5

platinum
MC: 106; TC: 4.03E6

palladium
MC: 104; TC: 3.74E6

gold
MC: 54; TC: 2.08E6

Figure A.77. ToF-SIMS spectra of **S12**. Positive polarity (top), negative polarity (bottom).

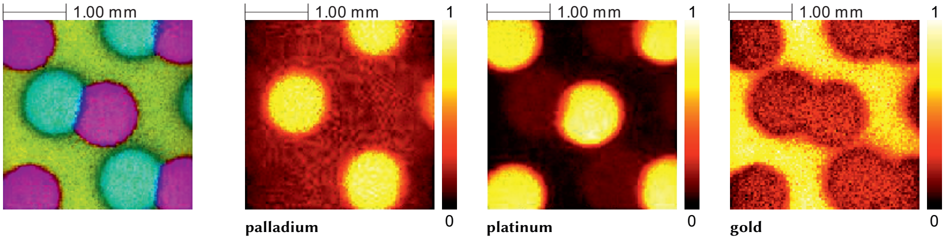
1.00 mm
1.00 mm
1
0
1.00 mm
1
0
1.00 mm
1
0

palladium
Pd 3d

platinum
Pt 4f

gold
Au 4f

Figure A.78. XPS mappings of **S12**.

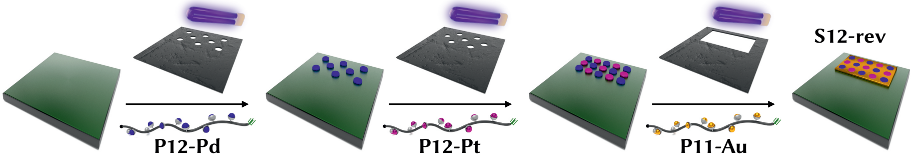

Scheme A.46. Attachment of **P12-Pd**, **P12-Pt**, and **P11-Au** on surface **S12-rev** (setup D).

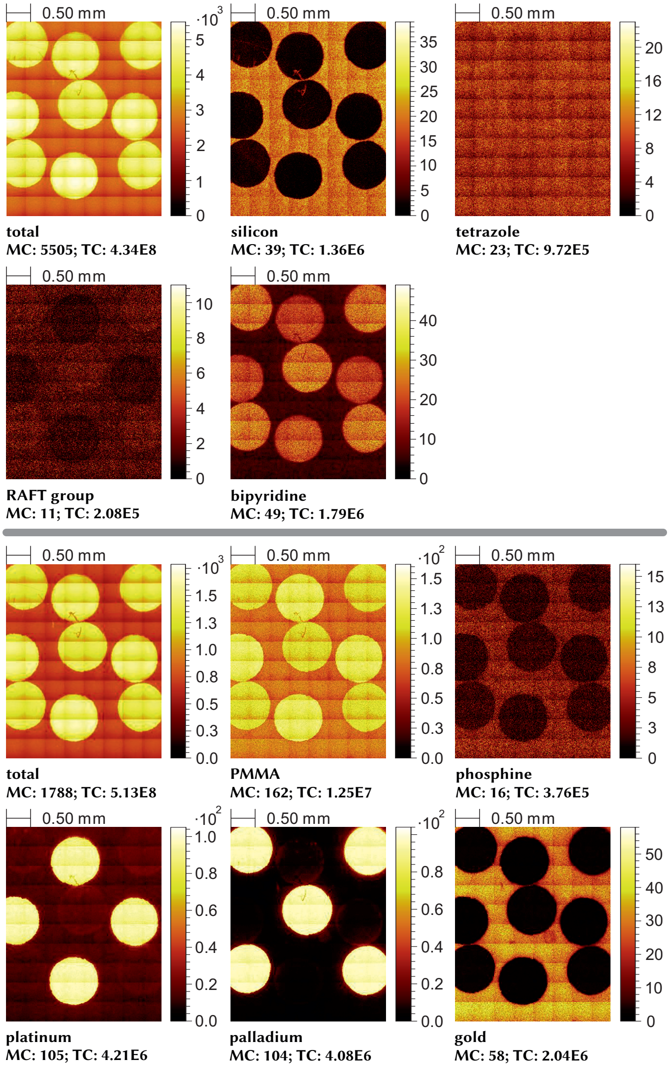

total
MC: 5505; TC: 4.34E8

silicon
MC: 39; TC: 1.36E6

tetrazole
MC: 23; TC: 9.72E5

RAFT group
MC: 11; TC: 2.08E5

bipyridine
MC: 49; TC: 1.79E6

total
MC: 1788; TC: 5.13E8

PMMA
MC: 162; TC: 1.25E7

phosphine
MC: 16; TC: 3.76E5

platinum
MC: 105; TC: 4.21E6

palladium
MC: 104; TC: 4.08E6

gold
MC: 58; TC: 2.04E6

Figure A.79. ToF-SIMS spectra of **S12-rev**. Positive polarity (top), negative polarity (bottom).

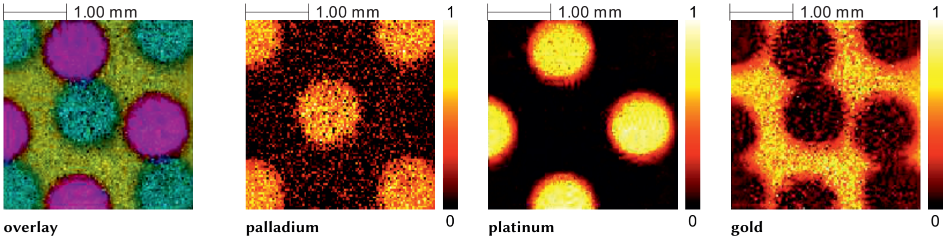
1.00 mm
1.00 mm
1
0
1.00 mm
1
0
1.00 mm
1
0

overlay
Pd (cyan), Pt (magenta),
Au (yellow)

palladium
Pd 3d

platinum
Pt 4f

gold
Au 4f

Figure A.80. XPS mappings of **S12-rev**.

Publications and conference contributions

Refereed journal publications

[6] **STED-inspired Laser Lithography Based on Photoswitchable Spirothiopyran Moieties**[†]
P. Müller,[*] **R. Müller**,[*] L. Hammer, C. Barner-Kowollik, M. Wegener, E. Blasco, *Chem. Mater.* **2019**, *31*, 1966–1972.

[5] **Spatially Resolved Multiple Metallopolymer Surfaces by Photolithography**[†]
R. Müller,[*] T. J. Feuerstein,[*] V. Trouillet, S. Bestgen, P. W. Roesky, C. Barner-Kowollik, *Chem. Eur. J.* **2018**, *24*, 18933–18943.

[4] **Exploiting λ-Orthogonal Photoligation for Layered Surface Patterning**
P. Lederhose, D. Abt, A. Welle, **R. Müller**, C. Barner-Kowollik, J. P. Blinco, *Chem. Eur. J.* **2018**, *24*, 576–580.

[3] **The Para-Fluoro-Thiol Ligation in Water**
H. Turgut, C. A. Schmidt, P. Wadhwani, A. Welle, **R. Müller**, G. Delaittre, *Polym. Chem.* **2017**, *8*, 1288–1293.

[2] **Near Infrared Photoinduced Coupling Reactions Assisted by Upconversion Nanoparticles**
P. Lederhose, Z. Chen, **R. Müller**, J. P. Blinco, S. Wu, C. Barner-Kowollik, *Angew. Chem. Int. Ed.* **2016**, *55*, 12195–12199.

[†] Publications arising from the current thesis.

[*] These authors contributed equally.

[1] **Photolithographic Encoding of Metal Complexes**
C. Lang, S. Bestgen, A. Welle, **R. Müller**, P. W. Roesky, C. Barner-Kowollik, *Chem. Eur. J.* **2015**, *21*, 14728–14731.

Conference contributions

[3] **Spatially Resolved Multiple Surface Patterning of Metallopolymers**‡
R. Müller, T. Feuerstein, V. Trouillet, P. W. Roesky, C. Barner-Kowollik, *Biennial Meeting of the GDCh-Division of Macromolecular Chemistry*, **September 2018**, Karlsruhe, Germany. (oral presentation)

[2] **Photo Induced Ligation towards Spatially Resolved Multiple Metallopolymer Surfaces**‡
R. Müller, T. Feuerstein, V. Trouillet, S. Bestgen, P. W. Roesky, C. Barner-Kowollik, *4th Functional Polymeric Materials Conference*, **June 2018**, Nassau, Bahamas. (poster presentation)

[1] **Spatially Resolved Surface Patterning of Metallopolymers**‡
R. Müller, T. Feuerstein, S. O. Steinmüller, V. Trouillet, P. W. Roesky, C. Barner-Kowollik, *Advanced Polymers via Macromolecular Engineering*, **May 2017**, Ghent, Belgium. (poster presentation)

---

‡ Conference contributions arising from the current thesis.

Acknowledgements

At this point, I want to thank a number of people that have contributed in various ways to the completion of the present thesis.

First, I want to express my gratitude to Prof. Dr. Christopher Barner-Kowollik for giving me the opportunity to work on this project, the support, and the suggestions during my doctorate and also for his ever open ear to new ideas.

I would also thank Prof. Dr. Peter W. Roesky for the fruitful collaboration and especially for his time to serve as the second examiner and reviewer for the present thesis.

A big thank goes to the collaboration partners involved in different projects of this thesis, namely M. Sc. Thomas Feuerstein from the group of Prof. Dr. Peter W. Roesky, Dr. Patrick Müller from the group of Prof. Dr. Martin Wegener, and Dr. Eva Blasco from the group of Prof. Dr. Christopher Barner-Kowollik. It was a great pleasure to work with you during the time of my thesis. Your work significantly contributed to the results presented in this thesis.

I also want to thank Dr. Alexander Welle and Dipl.-Ing. Vanessa Trouillet for the ToF-SIMS and XPS analysis presented in Chapter 3 of this thesis.

During the work on this thesis, I had the pleasure to supervise several excellent students. I thank M. Sc. Larissa Hammer for her excellent work on spirothiopyrans during her master thesis. Your investigations paved the way for the results presented in Chapter 5. I also thank M. Sc. Mario Eck for his preliminary studies on spirothiopyrans in the course of his Vertiefer lab course. In addition, I would like to thank M. Sc. Christian Schmitt, M. Sc. Fabian Hundemer, M. Sc. Lukas Bangert, and M. Sc. Tobias Glöckler for their synthesis work during their HiWi time in our group.

I also want to mention the great effort and dedication of Prof. Dr. Christopher Barner-Kowollik, Prof. Dr. Peter W. Roesky, Prof. Dr. Manfred Wilhelm, Prof. Dr. Michael A. R. Meier, Dr. Dominik Voll, and Cornelia Weber they put into the SFB1176, which also funded my doctorate.

A big thank goes also to the present and former administrative site of the Barner-Kowollik group, namely to Dr. Eva Blasco, Katharina Elies, Dr. Anja Goldmann, Dr. Maria

Schneider, Vincent Schüler, and Evelyn Stühring. The effort you put into the "group behind the group" is outstanding!

The work on this thesis would not have been possible without the many good colleagues I worked with in the group of Prof. Dr. Christopher Barner-Kowollik. I would like to thank the whole past and present Macroarc group, especially Dr. Tanja Claus, Dr. Thomas Gegenhuber, M. Sc. Jeroen De Neve, Dr. Michael Kaupp, M. Sc. Waldemar Konrad, Dr. Christiane Lang, Dr. Marcel Langer, Dr. Paul Lederhose, Dr. Kai Pahnke, M. Sc. Tanja Rieder, and Dr. Andrew Vogt.

I also thank Dr. Eva Blasco, Dr. Thomas Gegenhuber, Dr. Patrick Müller, and Dr. Hendrik Woehlk for their time to proof read parts of my thesis and for their inspiring comments, hints, and for finding many typos and errors in my thesis. Your work made the present thesis a more enjoyable read!

I am very grateful to have many good friends beside work. I especially want to thank Dr. Sebastian Link and Dr. David Rombach for their friendship and support in all the last years. I am really grateful to call you my friends!

I want to thank my parents, my sister, my grandparents and all members of my family. It is due to your constant support and belief that I am at this point where I stand right now.

Finally, I want to thank my girlfriend Sarah, for her affection, her support, and for always putting a smile on my face. You made me the greatest gift of all and I'm really looking forward to the time to come!

He who knows the goal, can decide.
He who decides, finds peace.
He who finds peace, feels safe.
He who feels safe, can reflect.
He who reflects, can improve things.

Confucius (551 - 479 B.C.)